

Mine engineering geological disaster forecasting, monitoring, and prevention

Edited by

Jie Chen, Wei Liu, Qingsheng Bai and Xuanmei Fan

Published in

Frontiers in Earth Science

Frontiers in Environmental Science



FRONTIERS EBOOK COPYRIGHT STATEMENT

The copyright in the text of individual articles in this ebook is the property of their respective authors or their respective institutions or funders. The copyright in graphics and images within each article may be subject to copyright of other parties. In both cases this is subject to a license granted to Frontiers.

The compilation of articles constituting this ebook is the property of Frontiers.

Each article within this ebook, and the ebook itself, are published under the most recent version of the Creative Commons CC-BY licence. The version current at the date of publication of this ebook is CC-BY 4.0. If the CC-BY licence is updated, the licence granted by Frontiers is automatically updated to the new version.

When exercising any right under the CC-BY licence, Frontiers must be attributed as the original publisher of the article or ebook, as applicable.

Authors have the responsibility of ensuring that any graphics or other materials which are the property of others may be included in the CC-BY licence, but this should be checked before relying on the CC-BY licence to reproduce those materials. Any copyright notices relating to those materials must be complied with.

Copyright and source acknowledgement notices may not be removed and must be displayed in any copy, derivative work or partial copy which includes the elements in question.

All copyright, and all rights therein, are protected by national and international copyright laws. The above represents a summary only. For further information please read Frontiers' Conditions for Website Use and Copyright Statement, and the applicable CC-BY licence.

ISSN 1664-8714
ISBN 978-2-83251-056-8
DOI 10.3389/978-2-83251-056-8

About Frontiers

Frontiers is more than just an open access publisher of scholarly articles: it is a pioneering approach to the world of academia, radically improving the way scholarly research is managed. The grand vision of Frontiers is a world where all people have an equal opportunity to seek, share and generate knowledge. Frontiers provides immediate and permanent online open access to all its publications, but this alone is not enough to realize our grand goals.

Frontiers journal series

The Frontiers journal series is a multi-tier and interdisciplinary set of open-access, online journals, promising a paradigm shift from the current review, selection and dissemination processes in academic publishing. All Frontiers journals are driven by researchers for researchers; therefore, they constitute a service to the scholarly community. At the same time, the *Frontiers journal series* operates on a revolutionary invention, the tiered publishing system, initially addressing specific communities of scholars, and gradually climbing up to broader public understanding, thus serving the interests of the lay society, too.

Dedication to quality

Each Frontiers article is a landmark of the highest quality, thanks to genuinely collaborative interactions between authors and review editors, who include some of the world's best academicians. Research must be certified by peers before entering a stream of knowledge that may eventually reach the public - and shape society; therefore, Frontiers only applies the most rigorous and unbiased reviews. Frontiers revolutionizes research publishing by freely delivering the most outstanding research, evaluated with no bias from both the academic and social point of view. By applying the most advanced information technologies, Frontiers is catapulting scholarly publishing into a new generation.

What are Frontiers Research Topics?

Frontiers Research Topics are very popular trademarks of the *Frontiers journals series*: they are collections of at least ten articles, all centered on a particular subject. With their unique mix of varied contributions from Original Research to Review Articles, Frontiers Research Topics unify the most influential researchers, the latest key findings and historical advances in a hot research area.

Find out more on how to host your own Frontiers Research Topic or contribute to one as an author by contacting the Frontiers editorial office: frontiersin.org/about/contact

Mine engineering geological disaster forecasting, monitoring, and prevention

Topic editors

Jie Chen — Chongqing University, China

Wei Liu — Chongqing University, China

Qingsheng Bai — Freiberg University of Mining and Technology, Germany

Xuanmei Fan — Chengdu University of Technology, China

Citation

Chen, J., Liu, W., Bai, Q., Fan, X., eds. (2022). *Mine engineering geological disaster forecasting, monitoring, and prevention*. Lausanne: Frontiers Media SA.
doi: 10.3389/978-2-83251-056-8

The author declares that the research was conducted in the absence of any commercial or financial relationships that could be construed as a potential conflict of interest.

Table of contents

06	Editorial: Mine engineering geological disaster forecasting, monitoring, and prevention Jie Chen
09	Experimental Study on the Effect of Key Factors on the Soil–Water Characteristic Curves of Fine-Grained Tailings Baofeng Cao, Yakun Tian, Rong Gui and Yong Liu
17	On-Site Measurement on Compaction Characteristics of Coal Gangue and Surface Subsidence Disaster in Deep Backfilling Mining Jiaqi Wang, Qiang Zhang, Wei Yin, Shengming Qi, Difa Gao and Dan Ma
27	An Object-Oriented Approach for the Recursive Numeration and Visualization of the Key Strata of Coal Mines Chun Xu, Keping Zhou, Xin Xiong and Yan Lu
38	Experimental Study on Gangue Backfilling Materials Improved by Soda Residue and Field Measurement of Surface Subsidence Wei Yin, Kun Zhang, Shenyang Ouyang, Xiaomin Bai, Wenjie Sun and Jingru Zhao
52	Mechanism of Rock Bursts Induced by the Synthetic Action of “Roof Bending and Rock Pillar Prying” in Subvertical Extra-Thick Coal Seams Zhenhua Wu, Peng-Zhi Pan, Jianqiang Chen, Xudong Liu, Shuting Miao and Peiyang Yu
68	Deterioration and Cavity of Surrounding Rocks at the Bottom of Tunnel Under the Combined Action of Heavy-Haul Load and Groundwater: An Experimental Study Zheng Li, Kunping Chen, Ziqiang Li, Weiwei Huang and Xinsheng Wang
77	Tailings Dam Break: The Influence of Slurry with Different Concentrations Downstream Xuanyi Chen, Xiaofei Jing, Yulong Chen, Changshu Pan and Wensong Wang
88	Rainfall Infiltration Process of a Rock Slope with Considering the Heterogeneity of Saturated Hydraulic Conductivity Qingqing Zhang, Laigui Wang and Huabin Zhang
104	Study on Mechanical Problems of Complex Rock Mass by Composite Material Micromechanics Methods: A Literature Review Junzhao He, Yunan Li, Yuling Jin, Anming Wang, Yumin Zhang, Jinchao Jia, Hei Song and Dong Liang
114	Regional Characteristics of Porosity and Permeability of Dahebian Syncline Coal and Its Application Fuping Zhao and Yuanlong Wei

- 128 **Experimental Study on Strength and Permeability Characteristics of Cemented Rock-Tailings Backfill**
Huafu Qiu, Fushun Zhang, Weibo Sun, Lang Liu, Yujiao Zhao and Chao Huan
- 137 **Study on Mechanical Properties of Shale Under Different Loading Rates**
Yuanlong Wei, Lingyun Zhao, Tao Yuan and Wei Liu
- 150 **Influence of Crack Spacing/Layer Thickness Value on Reflection Crack Propagation Mechanism Under Low Temperatures**
Chunyan Bao, Qi Liu, Yingjie Xia, Yi Cui, Zongyong Cao, Yidong Qian, Minghao Liu, Chaoqian Mu and Hongliang Wang
- 164 **Research on Deformation and Fracture Characteristics of the Fractured Rock Mass Under Coupling of Heavy Rainfall Infiltration and Mining Unloading**
Menglai Wang, Xiaoshuang Li, Shun Yang, Lin Teng, Qiusong Chen and Song Jiang
- 179 **Characteristics of Stress Field and Damage Law of Coal Rock in Residual Pillar of Top Slice and Its Application**
Fengfeng Wu, Xin Yu, Gaoliang Zhao, Beiju Du, Bo Lv and Jian Zhang
- 190 **A New Repeated Mining Method With Preexisting Damage Zones Filled for Ultra-Thick Coal Seam Extraction – Case Study**
Liang Chen, Dongsheng Zhang, Gangwei Fan, Shizhong Zhang, Xufeng Wang and Wei Zhang
- 204 **Early Warning Method for Coal and Gas Outburst Prediction Based on Indexes of Deep Learning Model and Statistical Model**
Chong Wang, Like Wei, Haiyong Hu, Jiren Wang and Mengfeng Jiang
- 221 **Study on the Overburden Failure Law of High-Intensity Mining in Gully Areas With Exposed Bedrock**
Tan Yi, Xu Han, Yan Weitao, Guo Wenbing, Bai Erhu, Qi Tingye, Yin Dawei, Hao Bingyuan, Cheng Hao and Shao Minghao
- 231 **3D Visualization Monitoring and Early Warning System of a Tailings Dam—Gold Copper Mine Tailings Dam in Zijinshan, Fujian, China**
Wen Nie, Minghua Luo, Yunmin Wang and Ruixiang Li
- 245 **Research on Roof Cutting Pressure Relief of the Gob-Side Entry Retaining With Roadside Backfilling**
Kun Zhang, Changyou Liu, Hanrui Zhang, Xin Yue and Huaidong Liu
- 260 **Experimental Study on Coal and Gas Outburst Risk in Strong Outburst Coal Under Different Moisture Content**
Zhuang Lu, Liang Wang, Mingzhe Lv, Yang Lei, Hao Wang and Qingquan Liu

- 273 **Analysis of Failure Mechanics and Energy Evolution of Sandstone Under Uniaxial Loading Based on DIC Technology**
Like Wei, Qiang Yuan, Yiwei Ren, Deyi Jiang, Dingding Zhang, Yongliang Liu, Yunlong Zou and Shicong Ren
- 284 **Coordinated slag Disposal From Horizontal Boreholes During Hydraulic Cutting Based on Two-Phase Flow Theory**
Yongjiang Zhang, Fei Ji and Quanle Zou
- 298 **Surrounding Rock Damage Characteristics and Support Optimization of Roadway in Soft Gas-Rich Coal Seam Under the Condition of Penetrating Hydraulic Reaming**
Xu Han, Kai Zhang, Xinran Xue and Bailong Ma
- 310 **Severe Damage Law on the Ground Surface Induced by High-Strength Mining: A Case Study From the Shendong Coal Field in China**
Weitao Yan, Junting Guo, Junjie Chen, Yi Tan, Shaoge Yan and Yueguan Yan
- 320 **Research on 3D Development Characteristics of Water-Conducting Fractured Zone Based on Field Measurement**
Dong Feng, Enke Hou, Shuangming Wang, Xiaoshen Xie, Feng Yuan, Liangliang Guo, Gang Wang, Yongli Xie and Zhen Chen



OPEN ACCESS

EDITED AND REVIEWED BY

Federico Di Traglia,
Istituto Nazionale di Oceanografia e di
Geofisica Sperimentale, Italy

*CORRESPONDENCE

Jie Chen,
jichen023@cqu.edu.cn

SPECIALTY SECTION

This article was submitted to
Geohazards and Georisks,
a section of the journal
Frontiers in Earth Science

RECEIVED 20 September 2022

ACCEPTED 20 October 2022

PUBLISHED 01 December 2022

CITATION

Chen J (2022), Editorial: Mine
engineering geological disaster
forecasting, monitoring,
and prevention.
Front. Earth Sci. 10:1049480.
doi: 10.3389/feart.2022.1049480

COPYRIGHT

© 2022 Chen. This is an open-access
article distributed under the terms of the
[Creative Commons Attribution License](#)
(CC BY). The use, distribution or
reproduction in other forums is
permitted, provided the original
author(s) and the copyright owner(s) are
credited and that the original
publication in this journal is cited, in
accordance with accepted academic
practice. No use, distribution or
reproduction is permitted which does
not comply with these terms.

Editorial: Mine engineering geological disaster forecasting, monitoring, and prevention

Jie Chen*

School of Resources and Safety Engineering, Chongqing University, Chongqing, China

KEYWORDS

mine engineering, geological disaster, disaster prevention, disaster monitoring, disaster forecasting, early warning

Editorial on the Research Topic

[Mine engineering geological disaster forecasting, monitoring, and prevention](#)

Due to the gradual depletion of shallow resources and the deepening of resource extraction depth, the engineering geological conditions are more complex. High ground stress, high temperature, high osmotic pressure, strong mining disturbance, and complex geological structure have led to a more frequent occurrence of geological disasters in mines. The common geological disasters mainly include mine water inrush, rock and coal burst (as shown in [Figure 1](#)), roof accident, coal and gas protrusion, surface subsidence, fault activation, high steep slope instability, water pollution, and so on. Given the increasing prominence of mine engineering geological hazards and the serious threat to mine safety production, the research on the prediction, monitoring, and prevention of mine geological hazards has become urgent. To this end, Research Topic researched on regional geological characteristics, state of ground stress, nature of surrounding rocks, and support strategies. Furthermore, the disaster-causing mechanism of mine geological hazards, monitoring approaches, and prevention and control techniques were studied and provide an important guarantee for the safe development of mine resources and economic development.

The study of the disaster-causing mechanism of mine geological hazards will help to understand the causes and processes of disaster occurrence in essence and to provide theoretical support for disaster prevention and control. The mechanical property and deformation law of surrounding rock are always the important research content in disaster-causing mechanism of mine geological hazards, and also the focuses of Research Topic. To reveal the causes of dynamic hazards in rock engineering, [Wei et al.](#) analyzed the uniaxial damage mechanics and energy evolution law of sandstone using the DIC technique, explored the uncoordinated evolution of the deformation displacement field of rock mass, and revealed the fracture development and failure mode of sandstone specimens under uniaxial compression conditions. [Wei et al.](#) investigated the effect of loading rate on the mechanical and fracture properties of shale and found that the peak

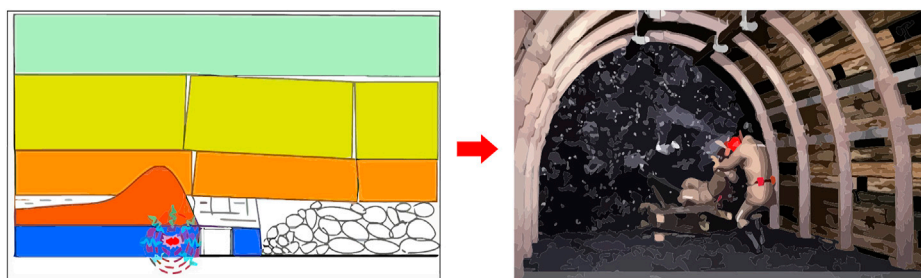


FIGURE 1
Schematic diagram of rock and coal burst disaster.

strength and elastic modulus of shale increased with increasing the loading rate, but there was no significant pattern in Poisson's ratio. [Wu et al.](#) researched the mechanism of impact ground pressure in a sub-vertical extra-thick coal seam under the control of a "roof-rock pillar" by numerical simulation and microseismic analysis, which revealed that the superposition of dynamic disturbance caused by roof and pillar failure and high static stress in a coal seam is the cause of rock burst in the B3 + 6 coal seam. In addition, [He et al.](#) reviewed the application of micromechanical methods in mechanics of complex rock masses and provided a new approach to analyze the mechanic law of the disaster-causing mechanism. [Yi et al.](#) analyzed the characteristics of overburden movement and the law of surface movement in areas with exposed bedrock, which explained the causes of sudden water explosion disasters.

The research on the action mechanism of water on coal/rock/soil is also an important topic of mine geological disaster theory. The influence of water not only leads to the redistribution of chemical elements between coal/rock/soil and water, but also leads to the changes in the microstructure and mechanical properties of coal/rock/soil, then inducing engineering geological disasters. [Lu et al.](#) studied the risk of coal and gas outburst under different water content, which provided new insights for the theoretical study of coal and gas outburst and the hydraulic prevention and control measures of coal and gas outburst. [Wang et al.](#) used PFC numerical calculation software to study the mechanical properties and fracture propagation characteristics of fractured rock mass under the coupling effect of heavy rainfall infiltration and mining unloading. It was found that the compressive strength and peak strain of the rock decreased as the pore water pressure of the rock increased, and the pore water pressure accelerated the destruction process of the rock. [Zhang et al.](#) proposed a saturated-unsaturated seepage random field model to analyze the effects of rainfall intensity, rainfall duration, and spatial variability of the saturated hydraulic coefficient on the infiltration process and stability of unsaturated rocky slopes, which provides reference significance for the risk assessment of

rainfall infiltration-induced slope geological hazards. [Zhao and Wei](#) conducted a systematic study on the porosity and permeability of coal from two areas of the Dahebian landslide in the Liupanshui coalfield and found that the internal mechanism of permeability loss is related to fracture closure and plastic deformation caused by confining pressure. [Cao et al.](#) investigated the effects of key factors (gradient, temperature, and initial dry density) on the soil-water characteristic curves of fine-grained tailings dams, which provided the support for stability assessment and prediction of unsaturated tailings dams. To understand the risk of tailings pond failure, [Chen et al.](#) studied the flow characteristics of slurries with different concentrations in tailings dams and conducted a series of flume experiments to obtain the flow characteristics such as inundated height, impact force, and velocity at 30%, 40%, 50%, and 60% concentrations.

The development of disaster monitoring technology has a crucial impact on the prediction and prevention of mine geological disasters. Its main task is to monitor the spatial evolution information and inducing factors of geological disasters, and to obtain continuous spatial deformation data to the maximum extent. The research of disaster monitoring technology can effectively predict and prevent the occurrence of disasters. For example, in the safety monitoring of tailings dams, [Nie et al.](#) developed a 3D visual early warning system for tailings dams by combining the GIS (geographic information system), ARIMA (autoregressive comprehensive moving average model) and 3S (RS, GIS, GPS) technologies to predict phreatic line changes and tailings dam deformation. The system solves the problems of low visualization of monitoring data, poor management of various data, and prediction and early warning of the point-surface combination. For the monitoring and warning of surrounding rock stability, [Xu et al.](#) proposed an object-oriented method combined with an improved recursive algorithm to realize the visual computation of key strata. Then, the object-oriented application was developed and applied in the Xia Dian coal mine in Shanxi, verifying the practicality and efficiency of the method. For the coal gas outburst disaster, [Wang](#)

et al. proposed an early warning method for predicting coal and gas emergencies based on the deep learning model and statistical model indicators, which has advantages in predicting emergencies. For the monitoring of sudden water accidents in coal mines, it is crucial to accurately grasp the development height of the water-conducting fractured zone. To this end, Feng et al. used a combination of drilling and 3D seismic exploration to study the 3D development characteristics of the water-conducting fractured zone in the middle and deep coal seam mining. The height and morphology of the water-conducting fractured zone were measured using the first mining face of Xiaobodang No.1 mine as an example.

Disaster prevention and control are the most critical tasks of Research Topic after understanding potential engineering disasters. For example, for the potential roof collapse disaster caused by the empty area or irregular damage zone left by coal mining, Chen et al. proposed a damage zone filling repeated mining method based on the analysis of the disaster state when the working face passes through the existing damage zone, which provides an effective practical reference for preventing roof collapse hazards. In the goaf backfilling, gangue is often used as the main solid backfilling material. Therefore, Wang et al. established the laboratory coal gangue compaction test system and carried out research on the compaction characteristics (such as stress-strain, stress volume density, and stress-deformation modulus) of coal gangue in deep backfilling mining. Through monitoring the surface subsidence, it is found that the backfilling technology with an initial compression force of 2.5 MPa can effectively control the surface subsidence. Yin et al. used alkali slag-modified gangue backfill material to further improve the surface settlement control. Qiu et al. conducted uniaxial compression strength tests and permeability tests to investigate the strength and permeability characteristics of cemented tailings backfill with different cement-sand ratios and different waste rock contents. To control the deformation of mine surrounding rock and ensure its stability, Wu et al. studied the load concentration of the coal pillar and the goaf floor, as well as the stress distribution characteristics of the coal pillar area before and after the top slice, and determined the suitable location of the lower slice roadway in the residual pillar area after top slicing of thick coal seam, which achieved a better effect of surrounding rock management. To better prevent the

collapse deformation of the roadway, Han et al. proposed an optimized support scheme by analyzing the deformation damage characteristics of the roadway surrounding rock caused by penetrating hydraulic reaming using ground-penetrating radar technology. To ensure the stability of the gob-side entry when experiencing quick subsidence of the hard roof, Zhang et al. researched roof-cutting pressure relief of the gob-side entry retaining with roadside backfilling, by establishing a roof-cutting mechanical model and using a numerical simulation. In addition, coal and gas protrusion, as an extremely serious dynamic hazard, seriously threatens the safe production of coal mines. Zhang et al. conducted a study on coordinated slag disposal from horizontal boreholes during hydraulic cutting based on two-phase flow theory, which could result in 4.5 times higher average net gas extraction in coal mines compared with conventional boreholes, 25 times higher gas permeability coefficient, and more than double the effective extraction radius.

Author contributions

The author confirms being the sole contributor of this work and has approved it for publication.

Conflict of interest

The author declares that the research was conducted in the absence of any commercial or financial relationships that could be construed as a potential conflict of interest.

Publisher's note

All claims expressed in this article are solely those of the authors and do not necessarily represent those of their affiliated organizations, or those of the publisher, the editors and the reviewers. Any product that may be evaluated in this article, or claim that may be made by its manufacturer, is not guaranteed or endorsed by the publisher.



Experimental Study on the Effect of Key Factors on the Soil–Water Characteristic Curves of Fine-Grained Tailings

Baofeng Cao[†], Yakun Tian[†], Rong Gui^{*} and Yong Liu^{*}

School of Resource and Environment and Safety Engineering, University of South China, Hengyang, China

OPEN ACCESS

Edited by:

Qingsheng Bai,
Freiburg University of Mining and
Technology, Germany

Reviewed by:

Dan Ma,
China University of Mining and
Technology, China
Hao Wu,
China University of Mining and
Technology, China

*Correspondence:

Rong Gui
2009000507@usc.edu.cn
Yong Liu
liuyong81668@163.com

[†]These authors have contributed
equally to this work

Specialty section:

This article was submitted to
Soil Processes,
a section of the journal
Frontiers in Environmental Science

Received: 19 May 2021

Accepted: 08 July 2021

Published: 30 August 2021

Citation:

Cao B, Tian Y, Gui R and Liu Y (2021)
Experimental Study on the Effect of
Key Factors on the Soil–Water
Characteristic Curves of Fine-
Grained Tailings.
Front. Environ. Sci. 9:710986.
doi: 10.3389/fenvs.2021.710986

The soil–water characteristic curve (SWCC) is an essential parameter for studying the mechanical properties of unsaturated tailings, and it plays an important role in stability assessment and prediction of unsaturated tailings dams. In this paper, the matrix suction was measured indirectly by a filter paper-based method to investigate the effects of key factors (gradation, temperature, and initial dry density) on the soil–water characteristic curves of fine-grained tailings, and the Van Genuchten model was adopted to obtain the empirical equation of SWCC and to verify the accuracy of experimental results. The results showed the following: 1) the Van Genuchten model fits well the relationship between matric suction and volumetric moisture content of fine-grained tailings, indicating that experimental data determined by filter paper-based method is accurate and appropriate; 2) at the same volumetric moisture content, the matrix suction increased with decreasing average particle size, and the decrease in temperature will increase the matrix suction and water-holding capacity of fine-grained tailings, and the matrix suction of the tailings in summer is 38.3% lower than that in winter under the natural volumetric moisture content (14.0%); 3) when the saturation degree of fine-grained tailings is less than 60%, the greater the initial dry density, the better the water-holding capacity and matrix suction.

Keywords: fine-grained tailings, filter paper-based method, unsaturated tailings, Van Genuchten model, soil water characteristic curve (SWCC)

INTRODUCTION

As the hydraulic structure for tailings storage, tailings reservoir is one of the major hazardous sources for the mining enterprises. The operational status of a tailings reservoir is directly related to the operation of mining enterprises and the safety of the lives and properties of people living downstream. In recent years, fine-grained tailings have become the primary dam-building materials of tailings reservoirs due to the pervasiveness of fine-grained mineral processing technology in China. The physical and mechanical properties of these fine-grained tailings with small average particle sizes and poor permeability are more vulnerable to environmental factors than coarse-grained tailings. The changes in rainfall intensity, temperature, and the dry–wet cycle will affect the matric suction and cohesion of unsaturated fine-grained tailings, resulting in instability of the tailings dam (Lersow, 2010; Ma et al., 2021).

The soil–water characteristic curve (SWCC), as an important parameter of unsaturated soil, shows the relationship curve between moisture content and suction. The changing trend of the curve reflects the water holding capacity and porosity characteristics of the soil, and many engineering properties such as hydraulic conductivity, shear strength, coefficient of diffusion, etc. can be estimated from it (Fredlund and Rahardjo, 1993). The previous research results show that gradation, temperature, and initial dry density are the key factors affecting the SWCC of tailings, so it is necessary to quantitatively evaluate the effect of key factors on the SWCC to analyze the stability of the unsaturated part of the tailings dam. There are many instruments available for measuring the matric suction, such as the Tensiometer Method (Marinho et al., 2008), Pressure apparatus (Bechtold et al., 2018; Jiang et al., 2020), Electrical resistance blocks (Zeitoun et al., 2021), etc., and indirect methods, such as the Filter paper-based method (Mahler and Mendes, 2005; Fattah et al., 2021), Empirical method (Kern, 1995), etc. During the past few decades, many empirical models have been developed to predict SWCC, such as the Van-Genuchten (1980), Brooks-Corey (1964), Fredlund and Xing (1994), Gardner (1958), etc., and researchers also compared and evaluated the applicability and consistency of various empirical models (Matlan et al., 2015; Fattah et al., 2021). Based on this, the scholars investigated the SWCC of clay (Tripathy et al., 2014; Li et al., 2017), sand (Yan and Zhang, 2015), and expansive soil (Tamer et al., 2017; Ahmed et al., 2018), and they analyzed the effect of dry density (Birle et al., 2008; Gallage and Uchimura, 2010), void ratio (Heshmati and Motahari, 2015), grain size distribution (Chen et al., 2018; Zhai et al., 2020), and temperature (ElKeshky, 2011; Qiao et al., 2019) on the SWCC.

Although many studies have been conducted to analyze the SWCC of various soils, none of these investigations have highlighted a comprehensive evaluation of the effect of key factors on SWCC of fine-grained tailings from the microscopic mechanism. And fine-grained tailings are significantly different in physical properties and mechanical behavior from the general soil due to the complex mineral composition, high content of fine particles. The results of previous studies show that gradation, temperature, and initial dry density have the most significant influence on the physical and mechanical properties of unsaturated tailings. Therefore, in this paper, the matrix suction was determined by filter paper-based method to investigate the effect of gradation, temperature, and initial dry density on the SWCC of fine-grained tailings. In addition, the Van Genuchten model, as the most widely used mathematical model for fitting SWCC, was adopted to verify the accuracy of the experimental results in this paper. The fitting parameters and empirical equations for the SWCC were also obtained to provide a basis for mechanical properties, seepage calculations, and stability evaluation of fine-grained tailings dam.

MATERIALS AND EXPERIMENTS

Experimental Principle

The filter paper-based method is a widely used method to indirectly measure the matric suction of soil, which has the advantages of low price, ease of operation, and large

measurement range, but it must, however, be measured under an environment of a certain humidity and temperature. When a dry filter paper is placed on or in a soil sample for a few days, the filter paper will absorb the moisture from soil by evaporation and capillary action, and the moisture can be balanced between the soil and the filter paper at last. After moisture equilibration, the matrix suction of the soil was determined by a recommended rate formula according to the volumetric moisture content of the filter paper.

“Whatman No.203” quantitative filter paper of 70 mm diameters and hardened low ash was used to determine the matrix suction of tailings. The matrix suction was rated based on the rate formula recommended by ASTM D5298-10 (2010) with the following Eq. 1 (Fredlund and Rahardjo, 1993):

$$\begin{aligned} \lg S &= 5.493 - 0.0767w_f & w_f \leq 47\% \\ \lg S &= 2.470 - 0.0120w_f & w_f > 47\% \end{aligned} \quad (1)$$

where S is the suction, kPa; and

w_f is the volumetric moisture content of filter paper.

The Van Genuchten model was used to obtain the empirical equation of the SWCC. The mathematical expression of Van Genuchten models is shown in Eq. 2 (Van-Genuchten, 1980):

$$\theta = \theta_r + \frac{\theta_s - \theta_r}{[1 + (\alpha\psi)^n]^m} \quad (2)$$

where θ is the volumetric moisture content (%), θ_r, θ_s are the residual and saturated volumetric moisture content, which can be determined by a test, and ψ is the suction (kPa). α, n, m are the fitting parameter, where α is associated with air-entry value (kPa): the smaller the α value, the greater the air-entry value and water-holding capacity of the soil. m, n are associated with the residual volumetric moisture content and the slope of the SWCC, respectively, $m = 1 - 1/n$. The value of n, m related to the particle size distribution and pore size of soil: the more uniform the particle size distribution and the smaller the porosity, the smaller the n, m value.

Experimental Materials and Specimen Preparation

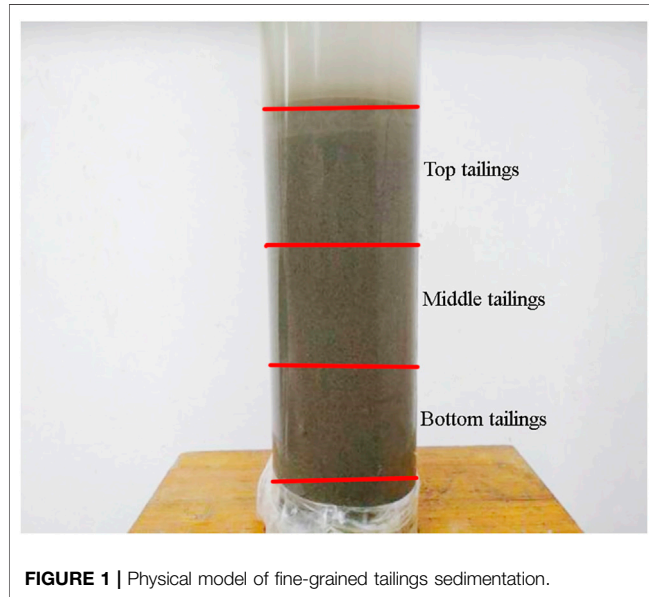
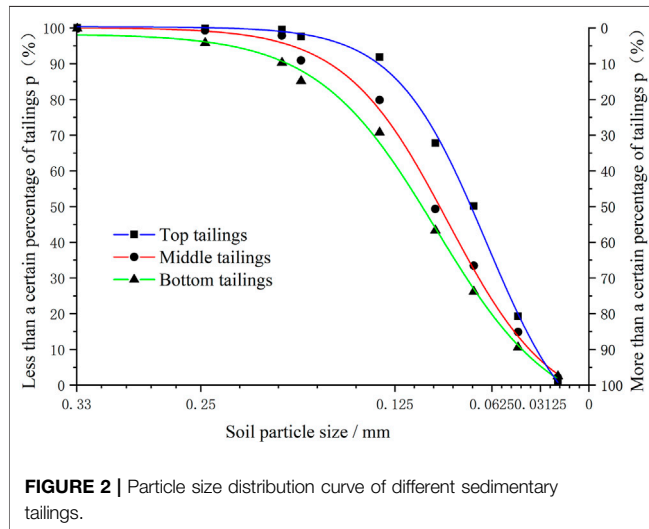
The raw tailings were chosen came from the discharge outlet of the Gao Wanqiu tailings reservoir in Hunan province, China. The physical properties of the raw tailings were determined according to ASTM recommended test methods (ASTM D2216-19, 2019; ASTM D854-14, 2014; ASTM D7263-21, 2021), as shown in Table 1.

The particle size distribution of tailings samples was determined by a Screening Test (ASTM D6913-04, 2017), and the particle sizes smaller than 0.074 mm were determined by the Winner 2,000 Laser Particle Size Analyzer (Zhang et al., 2015). The experimental results showed that the mass of tailings with particle diameters lower than 200 mesh (0.074 mm) accounts for more than 30% of the total mass.

A physical model of fine-grained tailings sedimentation was established by an acrylic tube with an inner diameter of 20 cm and a height of 100 cm to obtain the tailings with

TABLE 1 | Physical properties of the fine-grained tailings.

Raw material	Natural density $\rho(\text{g}/\text{cm}^3)$	Volumetric moisture content%	Pore ratio e	Relative density G_s	Dry density $\rho_d(\text{g}/\text{cm}^3)$
Tailings sample	1.42	14.0	1.11	2.68	1.27

**FIGURE 1** | Physical model of fine-grained tailings sedimentation.**FIGURE 2** | Particle size distribution curve of different sedimentary tailings.

different gradations. The raw tailings and water were put into the physical model in a mass ratio of 1:2 and stirred evenly with a wooden stick for 10 min. After the fine-grained tailings were deposited, the water was discharged out of the tube. Along the direction of gravity sedimentation, the tailings were divided equally into three layers (top tailings, middle tailings, and bottom tailings) from top to bottom of the model, as shown in **Figure 1**. The volumetric water content of the saturated tailings at the top, middle, and

bottom of the physical model were *in-situ* measured by RS-485 Soil Moisture Sensor before the water was drained out, which was 44, 41, and 38%, respectively.

The sedimentary tailings were sampled in the middle of each layer, and the particle characteristics of each tailings sample were analyzed by screening test and laser particle size analysis. Additionally, the particle size distribution curve of different sedimentary tailings was plotted according to experimental results, as shown in **Figure 2**.

The particle characteristics of different sedimentary tailings were calculated according to **Figure 2**, and the results are shown in **Table 2**.

Raw tailings with different burial depths have different porosity and dry density under the confining pressure. To determine the effect of different initial dry densities on the matrix suction of fine-grained tailings, the raw tailings with a volumetric moisture content of 14% were compacted under the vertical pressure of 0, 150, and 300 kPa, which are roughly consistent with gravity stress of tailings at burial depths of 0, 10, and 20 m, respectively. In addition, the initial dry densities of tailings under the vertical pressure of 0, 150, and 300 kPa were calculated as 1.27, 1.41, and 1.55 g/cm^3 , respectively.

Experimental Procedures

First, dry the tailings samples with a thermostatic drying chamber (105~110°C) for no less than 10 h.

Second, wet the dry tailings samples to different volumetric moisture content (3, 6, 9, 12, 15, 18, 21, 24, 27, 30, 33, and 36% up to saturation moisture content), respectively. Tailings samples with different moisture content are made into cylindrical specimens, and the specimens are placed into sealed jars for 2 days to allow for the tailings and water homogenization.

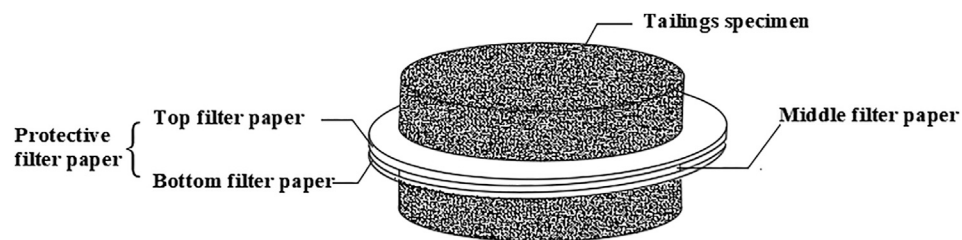
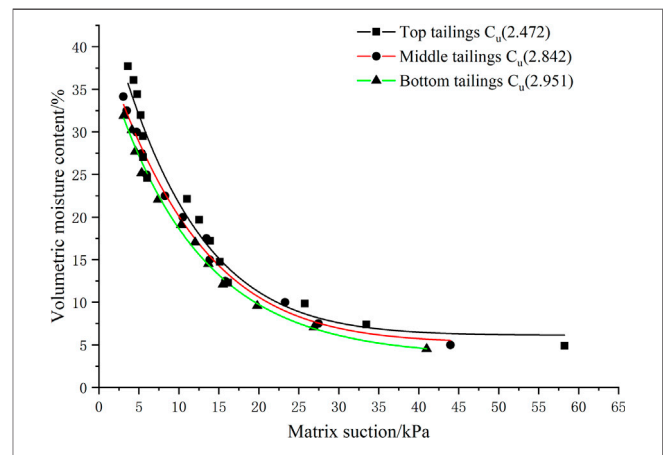
Third, put three sheets of filter paper baked over 2 h into the tailings specimens, the top and bottom filter paper are designed to protect the middle filter paper from damage, as shown in **Figure 3**. Weigh the mass of middle filter paper with a High-precision Electronic Scale before placing it into the tailings specimens.

Fourth, place the tailings specimen with the filter paper into the sealed jar, and place the sealed jar into a constant temperature and humidity box for 7 days to balance the moisture content between the filter paper and fine-grained tailings. Then keep the box with constant humidity, and change the temperature of the box to investigate the effect of temperature on the soil–water characteristic curve. Tailings specimens in the sealed jar are shown in **Figure 4**.

Fifth, take the middle filter paper out of the tailings specimen, and measure its mass within 30 s, as the filter paper is sensitive to moisture, and calculate the volumetric moisture content of filter paper.

TABLE 2 | The particle characteristics of different sedimentary tailings.

Specimens	Effective particle size d_{10}/mm	Median particle size d_{50}/mm	Restricted particle size d_{60}/mm	Nonuniformity coefficient C_u
Top tailings	0.036	0.056	0.089	2.472
Middle tailings	0.038	0.071	0.108	2.842
Bottom tailings	0.041	0.078	0.121	2.951

**FIGURE 3 |** Position relationship between tailings specimens and filter paper.**FIGURE 4 |** Tailings specimens in the sealed jar.**FIGURE 5 |** The experimental data and best-fit SWCC of tailings at different gradations.**TABLE 3 |** Fitting parameters of the Van Genuchten model for the SWCC of tailings at different gradations.

Samples	n	m	α/kPa	$R^2(\text{COD})$
Top tailings	2.49	0.598	0.125	0.952
Middle tailings	2.57	0.611	0.134	0.981
Bottom tailings	2.68	0.627	0.137	0.972

Sixth, calculate the matrix suction S of the fine-grained tailings by Eq. 1 according to the volumetric moisture content of filter paper.

Last, use the Van Genuchten model to obtain the empirical equation of SWCC and to verify the accuracy of experimental results.

RESULTS AND DISCUSSION

Effect of Particle Gradation on the SWCC of Fine-Grained Tailings

The fitting parameters and correlation coefficients of the Van Genuchten model at different gradations were obtained as shown in Table 3.

As can be seen from Table 3, the correlation coefficient R^2 values were 0.952, 0.981, and 0.972, respectively, indicating that the Van Genuchten model fits the experimental data determined by filter paper-based method at different gradations. Additionally, the top tailings have maximum fitting parameters of α , n , m value, indicating that the top tailings have better water-holding capacity, more uniform particle size distribution, and smaller porosity than the bottom tailings, which is consistent with screening experimental results.

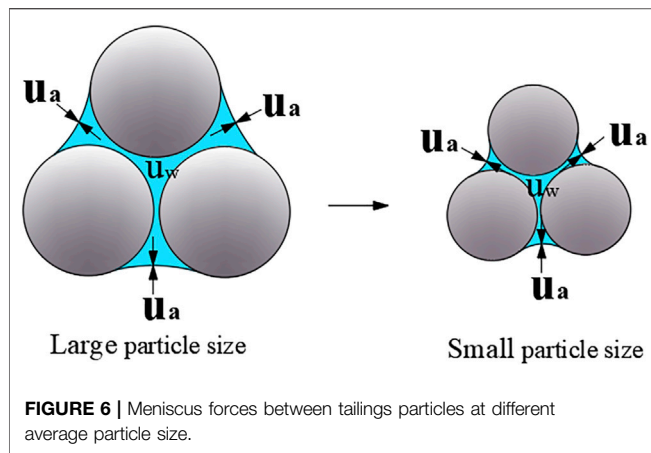


FIGURE 6 | Meniscus forces between tailings particles at different average particle size.

The experimental data and best-fit SWCC of fine-grained tailings at different gradations as shown in **Figure 5**. The matrix suction of fine-grained tailings increased with decreasing volumetric moisture content, and the increasing trend of matrix suction at different gradations is consistent and can be divided into three stages: the slow growth stage (volumetric moisture content more than 20%), stable growth stage (volume moisture content between 10 and 20%), and sharp growth stage (volumetric moisture content less than 10%).

The average particle size and non-uniformity coefficient of each tailings sample are different due to the gravity sedimentation, which affects the water-holding capacity and matrix suction of the fine-grained tailings. From **table 2**, we can see that the top tailings have a minimum average particle size ($d_{60} = 0.089$ mm) and non-uniformity coefficient ($C_u = 2.472$), while the bottom tailings have a maximum average particle size ($d_{60} = 0.121$ mm) and non-uniformity coefficient ($C_u = 2.951$). At the same volumetric moisture content, the matrix suction of top tailings is greater than that of bottom tailings, the matrix suction of top tailings is 18.6% higher than that of bottom tailings under natural volumetric moisture content (14.0%). According to the experimental results of the previous studies (Chen et al., 2018; Zhai et al., 2020), the matrix suction increased with decreasing soil particle size (Negative correlation) and with increasing non-uniformity coefficient (Positive correlation). However, as can be seen from **Figure 5**, experimental results show that tailings (Top tailings) with minor uniformity coefficients have larger matrix suction, indicating that the particle size plays a more important role than the non-uniformity coefficient to affect the matrix suction of fine-grained tailings.

For the unsaturated soil, according to the Young–Laplace equation (Young, 1805; Laplace, 1806), there is the following relationship among the additional pore pressure, the curvature radius of the meniscus, and the surface tension of fluids, as shown in **Eq. (3)**:

$$u_a - u_w = \frac{2T_s}{R_a} \quad (3)$$

where u_a , u_w are the pore air pressure and pore water pressure, $(u_a - u_w)$ is the matrix suction; R_a is the average curvature radius of the meniscus; and T_s is the surface tension of fluids.

TABLE 4 | Fitting parameters of the Van Genuchten model for the SWCC of tailings at different ambient temperature.

Ambient temperature	n	m	α/kPa	$R^2(\text{COD})$
Spring (15 °C)	2.67	0.625	0.118	0.991
Summer (30 °C)	2.7	0.629	0.171	0.989
Autumn (20 °C)	2.63	0.620	0.155	0.983
Winter (5 °C)	2.46	0.593	0.100	0.986

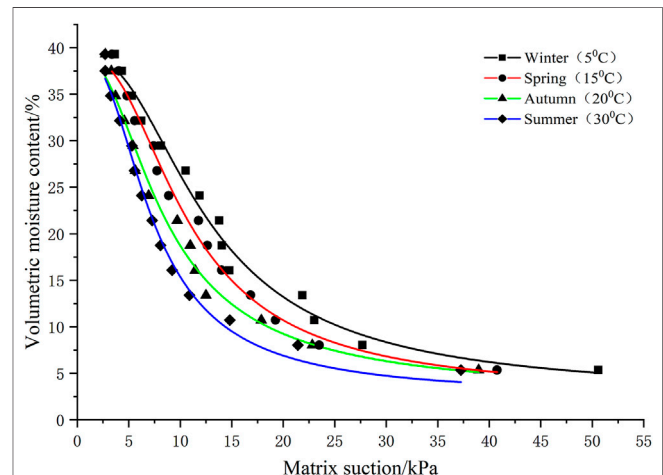


FIGURE 7 | The experimental data and best-fit SWCC of tailings at different temperatures.

At the same volumetric moisture content, the change of particle size will change the curvature radius of the meniscus. The smaller the particle size of fine-grained tailings, the larger the curvature radius of the meniscus. So, the fine-grained tailings with smaller particle sizes have greater matrix suction ($u_a - u_w$) and better water-holding capacity, as shown in **Figure 6**.

Effect of Ambient Temperature on the SWCC of Fine-Grained Tailings

Temperature theoretically affects the matrix suction of soil in direct and indirect aspects, especially in the case of large temperature differences. The local average temperature in Spring (15°C), Summer (30°C), Autumn (20°C), and Winter (5°C) are chosen in this experimental program to analyze the effect of seasonal temperature changes on the SWCC of fine-grained tailings.

The fitting parameters and correlation coefficients of the Van Genuchten model at different ambient temperatures were obtained, as shown in **Table 4**.

As can be seen in **Table 4**, the correlation coefficient R^2 values were 0.991, 0.989, 0.983, and 0.986, indicating that the Van Genuchten model fits the experimental data determined by filter paper-based method at different ambient temperatures. The fitting parameter n, m value showed little change since to the tailings used in the test have the same particle size and

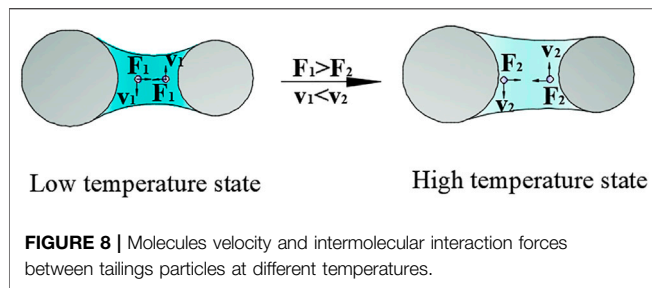
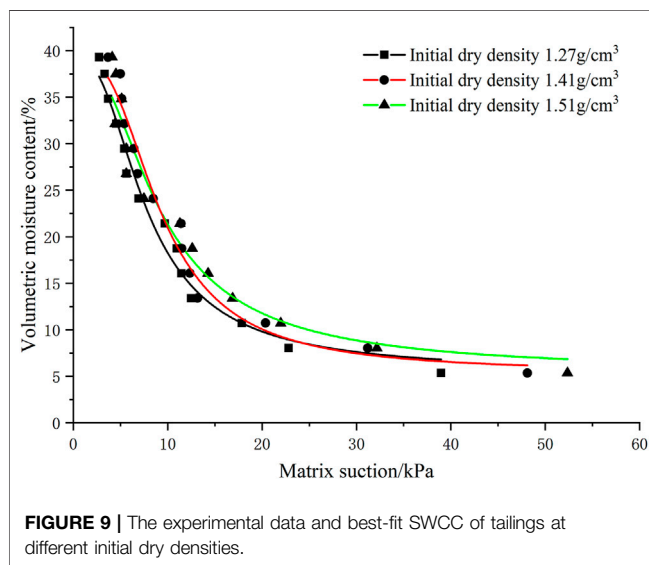


TABLE 5 | Fitting parameters of the Van Genuchten model for the SWCC of tailings at different initial dry densities.

Initial dry density (g/cm ³)	<i>n</i>	<i>m</i>	α /kPa	<i>R</i> ² (COD)
1.27	2.72	0.632	0.160	0.982
1.41	2.51	0.602	0.141	0.951
1.51	2.36	0.576	0.129	0.974



porosity. The fitting parameter α value decreased with decreasing temperature, are minimum in winter and maximum in summer, indicating that a decrease in temperature can improve the water-holding capacity of fine-grained tailings.

As can be seen from **Figure 7**, the ambient temperature has a significant effect on the matrix suction of fine-grained tailings. At the same volumetric moisture content, the lower the ambient temperature, the greater the matrix suction. The matrix suction of the tailings in summer is 38.3% lower than that in winter under the natural volumetric moisture content (14.0%). Therefore, it should be considering the effect of reduced matrix suction of fine-grained tailings on the stability of tailings dams in hot summer.

The influence mechanism of temperature on matrix suction is different from that of particle size. At the same volumetric moisture content, the kinetic energy of liquid molecules increases ($v_1 < v_2$), and the intermolecular interaction force ($F_1 > F_2$) weakens with the increase of temperature, reducing the surface tension of fluids and resulting in a decrease in the matrix suction of fine-grained tailings, as shown in **Figure 8**.

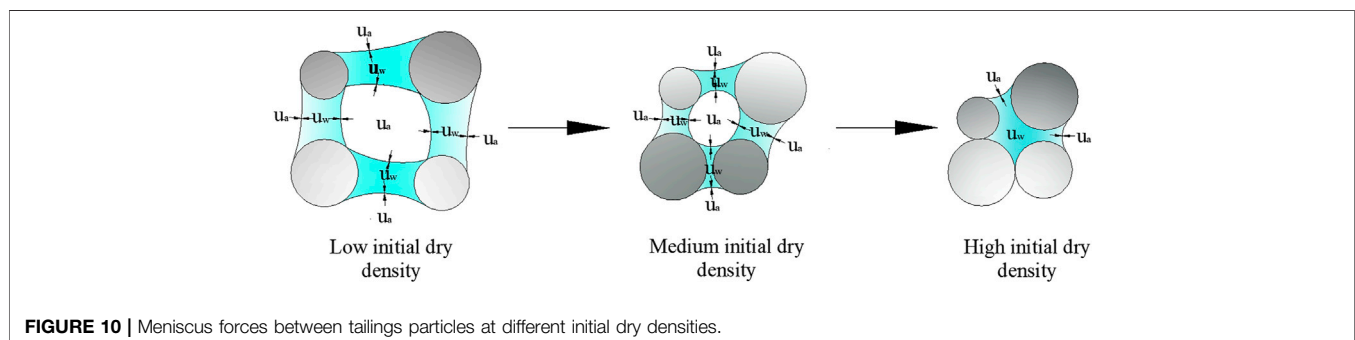
Effect of Initial Dry Density on SWCC of Fine-Grained Tailings

The fitting parameters and correlation coefficients of the Van Genuchten model at different initial dry densities were obtained as shown in **Table 5**.

As can be seen from **Table 5**, the correlation coefficient R^2 values were 0.982, 0.951, and 0.974, indicating that the Van Genuchten model can well-fit the experimental data determined by filter paper-based method at different initial dry densities. The fitting parameter α, n, m value decreased with increasing initial dry density due to the tailings were compacted, indicating that the greater the initial dry density, the smaller the porosity and the better the water-holding capacity of the fine-grained tailings.

As can be seen from **Figure 9**, when the degree of saturation is less than 60%, the matrix suction of the fine-grained tailings increased by increasing the initial dry density: the greater the compaction of the tailings, the greater the matrix suction. When the degree of saturation is greater than 60%, the matrix suction of fine-grained tailings does not vary significantly.

As can be seen from **Figure 10**, when the initial dry density of fine-grained tailings increases, the air between pores and water is compressed, and the spacing distance between particles decreases, resulting in a decrease in the curvature radius of the meniscus and



increase in matrix suction. When the tailings are over compacted, the gravitational water in the pores is extruded, which reduces the contact surface area between the gravitational water and the tailings particles. Instead, the matric suction of the tailings decreases when the saturation degree is greater than 60%.

CONCLUSION

This paper investigated the effects of gradation, temperature, and initial dry density on the SWCC of fine-grained tailings by the laboratory tests and theoretical analysis, and the following conclusions were obtained.

First, the correlation coefficient R^2 value of Van Genuchten model is more than 0.95, and the physical significance of the fitting parameters α , m , and n are also consistent with the experimental results, indicating that the matrix suction is determined by the filter paper-based method was accurate and appropriate.

Second, the top tailings have better water-holding capacity, more uniform particle size distribution, and smaller porosity than the bottom tailings. At the same volumetric moisture content, the matrix suction of top tailings is greater than that of bottom tailings, and the particle size plays a more important role than the non-uniformity coefficient to affect the matrix suction of fine-grained tailings.

Third, at the same volumetric moisture content, the lower the ambient temperature, the greater the matrix suction and water-holding capacity of fine-grained tailings. The matrix suction of the tailings in summer was 38.3% lower than that in winter under the natural volumetric moisture content (14%) because an increase in temperature reduces the surface tension and viscosity of the water.

Finally, when the saturation degree of fine-grained tailings is less than 60%, the greater the initial dry density, the better the water-holding capacity and matrix suction.

REFERENCES

- Ahmed, M. A., Tamer, Y. E., and Mosleh, A. A. (2018). Hysteresis Soil–Water Characteristic Curves of Highly Expansive clay. *Eur. J. Environ. Civil Eng.* 22 (9), 1041–1059. doi:10.1080/19648189.2016.1229232
- ASTM D2216-19 (2019). *Standard Test Methods for Laboratory Determination of Water (Moisture) Content of Soil and Rock by Mass*. West Conshohocken, PA: ASTM.
- ASTM D5298-10 (2010). *Standard Test Method for Measurement of Soil Potential (Suction) Using Filter Paper*. West Conshohocken, PA: ASTM.
- ASTM D6913-04 (2017). *Standard Test Methods for Particle-Size Distribution (Gradation) of Soils Using Sieve Analysis*. West Conshohocken, PA: American Society for Testing Materials.
- ASTM D7263-21 (2021). *Standard Test Methods for Laboratory Determination of Density (Unit Weight) of Soil Specimens*. West Conshohocken, PA: ASTM.
- ASTM D854-14 (2014). *Standard Test Methods for Specific Gravity of Soil Solids by Water Pycnometer*. West Conshohocken, PA: ASTM.
- Bechtold, M., Dettmann, U., Wöhl, L., Durner, W., Piayda, A., and Tiemeyer, B. (2018). Comparing Methods for Measuring Water Retention of Peat Near Permanent Wilting point. *Soil Sci. Soc. America J.* 82 (3), 601–605. doi:10.2136/sssaj2017.10.0372

The research results provide a reference to quantify the effect of gradation, temperature, and initial dry density on the engineering properties of fine-grained tailings. However, there are inevitable differences in the weighing process of the filter paper due to the light weight and high moisture sensitivity of the filter paper. The calibration curve of the filter-paper method has certain limitations for different types of filter paper, which easily leads to certain errors between the measured value and the actual value of the matrix suction. Therefore the focus in subsequent research should be on how to reduce and eliminate the errors caused by these factors.

DATA AVAILABILITY STATEMENT

The raw data supporting the conclusions of this article will be made available by the authors, without undue reservation.

AUTHOR CONTRIBUTIONS

All authors listed have made a substantial, direct, and intellectual contribution to the work and approved it for publication.

FUNDING

This study was supported by the National Natural Science Foundation of China (11875164), Natural Science Foundation of Hunan Province (2019JJ50496, 2021JJ30571), Science and Technology Department Key R and D Plan Project of Hunan Province (2019SK 2011), Scientific Research Project of Education Department of Hunan Province (20B496), and Uranium Tailings Depot Resiliency Engineering Technology Research Center of Hunan Province.

- Birle, E., Heyer, D., and Vogt, N. (2008). Influence of the Initial Water Content and Dry Density on the Soil–Water Retention Curve and the Shrinkage Behavior of a Compacted clay. *Acta Geotech.* 3 (3), 191–200. doi:10.1007/s11440-008-0059-y
- Brooks, R., and Corey, A. (1964). *Hydraulic Properties of Porous media*. Hydrology Paper. Fort Collins, Colorado: Colorado State University.
- Chen, X., Hu, K., Chen, J., and Zhao, W. (2018). Laboratory Investigation of the Effect of Initial Dry Density and Grain Size Distribution on Soil–Water Characteristic Curves of Wide-Grading Gravelly Soil. *Geotech. Geol. Eng.* 36 (2), 885–896. doi:10.1007/s10706-017-0362-1
- ElKeshky, M. M. (2011). *Temperature Effect on the Soil Water Retention Characteristic*. Phoenix, Arizona: Arizona State University.
- Fattah, M. Y., Majeed, Q. G., and Joni, H. H. (2021). Comparison between Methods of Soil Saturation on Determination of the Soil Water Characteristic Curve of Cohesive Soils. *Arab J. Geosci.* 14 (2), 1–10. doi:10.1007/s12517-020-06362-y
- Fredlund, D. G., and Rahardjo, H. (1993). *Soil Mechanics for Unsaturated Soils*. New York: John Wiley & Sons.
- Fredlund, D. G., and Xing, A. (1994). Equations for the Soil–Water Characteristic Curve. *Can. Geotech. J.* 31 (4), 521–532. doi:10.1139/t94-061
- Gallage, C. P. K., and Uchimura, T. (2010). Effects of Dry Density and Grain Size Distribution on Soil–Water Characteristic Curves of Sandy Soils. *Soils and Foundations* 50 (1), 161–172. doi:10.3208/sandf.50.161

- Gardner, W. R. (1958). Mathematics of Isothermal Water Conduction in Unsaturated Soil. Highway Research Board Special Report, Washington, 78–87.
- Heshmati, A. A., and Motahari, M. R. (2015). Modeling the Dependency of Suction Stress Characteristic Curve on Void Ratio in Unsaturated Soils. *KSCE J. Civ Eng.* 19 (1), 91–97. doi:10.1007/s12205-013-1185-0
- Jiang, X., Wu, L., and Wei, Y. (2020). Influence of Fine Content on the Soil-Water Characteristic Curve of Unsaturated Soils. *Geotech Geol. Eng.* 38 (2), 1371–1378. doi:10.1007/s10706-019-01096-5
- Kern, J. S. (1995). Evaluation of Soil Water Retention Models Based on Basic Soil Physical Properties. *Soil Sci. Soc. America J.* 59 (4), 1134–1141. doi:10.2136/sssaj1995.03615995005900040027x
- Lersow, M. (2010). “Safe closure of uranium mill tailings ponds-on basis of long-term stability-proofs linked with an extensive environmental monitoring,” in 6th International Congress on Environmental Geotechnics, New Delhi, India, November 2010. doi:10.13140/RG.2.1.4805.7364
- Li, J. H., Lu, Z., Guo, L. B., and Zhang, L. M. (2017). Experimental Study on Soil-Water Characteristic Curve for Silty clay with Desiccation Cracks. *Eng. Geology.* 218, 70–76. doi:10.1016/j.enggeo.2017.01.004
- Ma, D., Kong, S., Li, Z., Zhang, Q., Wang, Z., and Zhou, Z. (2021). Effect of wetting-drying cycle on hydraulic and mechanical properties of cemented paste backfill of the recycled solid wastes. *Chemosphere* 282 (10), 131163. doi:10.1016/j.chemosphere.2021.131163
- Mahler, C., and Mendes, C. (2005). *Measurement of Suction of Thick Textured Soil Using Filter Paper Method and Equivalent Tensiometer—EQT*. Berlin Heidelberg: Springer.
- Marinho, F. A. M., Take, W. A., and Tarantino, A. (2008). Measurement of Matric Suction Using Tensiometric and axis Translation Techniques. *Geotech Geol. Eng.* 26 (6), 615–631. doi:10.1007/s10706-008-9201-8
- Matlan, S. J., Taha, M. R., and Mukhlisin, M. (2015). Assessment of Model Consistency for Determination of Soil-Water Characteristic Curves. *Arab J. Sci. Eng.* 41 (4), 1233–1240. doi:10.1007/s13369-015-1888-2
- Qiao, X., Ma, S., Pan, G., and Liu, G. (2019). Effects of Temperature Change on the Soil Water Characteristic Curve and a Prediction Model for the Mu Us Bottomland, Northern China. *Water* 11 (6), 1235. doi:10.3390/w11061235
- Tamer, Y. E., Ahmed, M. A., Muawia, D., and Mosleh, A. A. (2017). Effect of Compaction State on the Soil Water Characteristic Curves of Sand-Natural Expansive clay Mixtures. *Eur. J. Environ. Civil Eng.* 21 (3), 289–302. doi:10.1080/19648189.2015.1112844
- Tripathy, S., Tadza, M. Y. M., and Thomas, H. R. (2014). Soil-Water Characteristic Curves of Clays. *Can. Geotech. J.* 51 (8), 869–883. doi:10.1139/cgj-2013-0089
- Van Genuchten, M. T. (1980). A Closed-Form Equation for Predicting the Hydraulic Conductivity of Unsaturated Soils. *Soil Sci. Soc. America J.* 44 (6), 892–898. doi:10.2136/sssaj1980.03615995004400050002x
- Yan, W. M., and Zhang, G. (2015). Soil-Water Characteristics of Compacted sandy and Cemented Soils with and without Vegetation. *Can. Geotech. J.* 52 (9), 1331–1344. doi:10.1139/cgj-2014-0334
- Zeitoun, R., Vandergest, M., Vasava, H. B., Machado, P. V. F., Jordan, S., Parkin, G., et al. (2021). *In-situ* Estimation of Soil Water Retention Curve in silt Loam and Loamy Sand Soils at Different Soil Depths. *Sensors* 21 (2), 447–461. doi:10.3390/s21020447
- Zhai, Q., Rahardjo, H., Satyanaga, A., and Dai, G. (2020). Estimation of the Soil-Water Characteristic Curve from the Grain Size Distribution of Coarse-Grained Soils. *Eng. Geology.* 267, 105502. doi:10.1016/j.enggeo.2020.105502
- Zhang, K., Chanpura, R. A., Mondal, S., Wu, C.-H., Sharma, M. M., Ayoub, J. A., et al. (2015). Particle-Size-Distribution Measurement Techniques and Their Relevance or Irrelevance to Wire-Wrap-Standalone-Screen Selection for Gradual-Formation-Failure Conditions. *SPE Drilling & Completion* 30 (2), 164–174. doi:10.2118/168152-PA

Conflict of Interest: The authors declare that the research was conducted in the absence of any commercial or financial relationships that could be construed as a potential conflict of interest.

Publisher's Note: All claims expressed in this article are solely those of the authors and do not necessarily represent those of their affiliated organizations, or those of the publisher, the editors and the reviewers. Any product that may be evaluated in this article, or claim that may be made by its manufacturer, is not guaranteed or endorsed by the publisher.

Copyright © 2021 Cao, Tian, Gui and Liu. This is an open-access article distributed under the terms of the Creative Commons Attribution License (CC BY). The use, distribution or reproduction in other forums is permitted, provided the original author(s) and the copyright owner(s) are credited and that the original publication in this journal is cited, in accordance with accepted academic practice. No use, distribution or reproduction is permitted which does not comply with these terms.



On-Site Measurement on Compaction Characteristics of Coal Gangue and Surface Subsidence Disaster in Deep Backfilling Mining

Jiaqi Wang^{1,2}, Qiang Zhang^{1,2*}, Wei Yin³, Shengming Qi^{1,2}, Difa Gao^{1,2} and Dan Ma^{1,2*}

¹School of Mines, China University of Mining and Technology, Xuzhou, China, ²State Key Laboratory of Coal Resources and Safe Mining, China University of Mining and Technology, Xuzhou, China, ³The Key Laboratory for Traffic and Transportation Security of Jiangsu Province, Huaiyin Institute of Technology, Huaian, China

OPEN ACCESS

Edited by:

Jie Chen,
Chongqing University, China

Reviewed by:

Qinglei Yu,
Northeastern University, China
Yang Ke,
Anhui University of Science and
Technology, China

*Correspondence:

Qiang Zhang
leafkky@163.com
Dan Ma
dan.ma@cumt.edu.cn

Specialty section:

This article was submitted to
Geohazards and Georisks,
a section of the journal
Frontiers in Earth Science

Received: 13 June 2021

Accepted: 29 September 2021

Published: 20 October 2021

Citation:

Wang J, Zhang Q, Yin W, Qi S, Gao D
and Ma D (2021) On-Site
Measurement on Compaction
Characteristics of Coal Gangue and
Surface Subsidence Disaster in Deep
Backfilling Mining.
Front. Earth Sci. 9:724476.
doi: 10.3389/feart.2021.724476

Gangue is the main backfilling material in solid backfilling mining, and its compaction characteristics determine the overburden control effect and surface subsidence. Under the action of compaction force and overburden pressure, the gangue will be broken, rotated and occluded, resulting in different compaction characteristics of gangue in the field and laboratory. To this end, a laboratory gangue compaction test system was established to test the compaction characteristics of gangue in the laboratory, such as stress-strain, stress bulk density and stress deformation modulus. Based on actual geological conditions of backfilling mining in the Tangshan coal mine, the characteristics of stress deformation modulus of gangue under different inclination angles and mining heights were tested on-site. Through the Beidou satellite CORS system, the surface subsidence of working face F5001 was monitored. The research results show that the stress deformation modulus of gangue measured in the field is slightly less than that measured in the laboratory, and it is maintained at about 27 MPa under the overburden pressure in the on-site measurement. Backfilling technology with an initial compaction force of 2.5MPa can be used to effectively control the surface subsidence, and the maximum subsidence value is only 61 mm.

Keywords: backfilling mining, compaction characteristics of gangue, deformation modulus, compaction force, surface subsidence

INTRODUCTION

As the main energy source in China, coal still plays an irreplaceable role in economic and social development in the short term. However, the ecological environment damage caused by coal mining and ground collapse cannot be ignored (Xie et al., 2012; Xie et al., 2015a; Xie et al., 2015b). The Chinese government attaches great importance to the problems caused by coal mining subsidence and has issued a series of documents on the treatment of subsidence areas caused by coal mining. The control of strata movement and surface collapse in backfilling mining and the implementation of backfilling mining technology in combination with field work is key work of researchers (Zhang and Wang, 2007; Fall et al., 2008; Shukla et al., 2009).

Solid backfilling mining is a relatively mature backfilling technology and has been widely used in mining areas in Northeast, North and West China. Up to now, solid backfilling mining technology

has gone through three stages: gangue dumping backfilling, mechanized solid non-dense backfilling and mechanized solid full-section dense backfilling. In the solid backfilling mining, gangue is used as backfilling material to fill goaf and support overburden (Ma et al., 2021b). In recent years, research on the mechanical properties of solid backfilling materials and the mechanism of controlling strata movement have been widely performed. Through macroscopic mechanical tests, Malusis et al. (Malusis et al., 2009) studied the compression properties of continuously graded gangue, discontinuously graded gangue and single-grain graded gangue under the three-dimensional loading. Based on the compression test of broken gangue, Li et al. (2018) reconstructed the gangue particles through 3D scanning and established the meso numerical model of gangue particle flow. Besides, the effects of particle gradation and loading rate on the compaction characteristics and lateral pressure coefficient of gangue were mainly studied. Fall et al. (2010) carried out the confined compression experiment of gangue, and analyzed the deformation and crushing characteristics of gangue particles at different immersion heights. Chong et al. (2020) tested the compaction characteristics of gangue granular backfilling materials with different particle sizes, and explored the influence of initial particle size of backfilling materials on the control effect of strata. Zhang et al. (2015) investigated the mesostructure, stress-strain relationship, energy dissipation and roof control effect of five common solid backfilling materials (Ma et al., 2021a).

It can be seen that the mechanical properties of gangue, especially the compaction characteristics, are the focus of backfill mining. The compaction characteristics of gangue affect the overburden control effect and surface collapse (Niu et al., 2014; Meng et al., 2016; Wei et al., 2021). In the above studies, all the mechanical properties of gangue were tested in the laboratory. However, the mechanical properties of gangue are dynamic in the stope, and the pressure situation of gangue in the goaf is more complex than that in the laboratory. In the advance of the working face, the gangue filling body will be rotated, slipped, occluded and broken under loads (Ercikdi et al., 2009; Cao et al., 2018; Zhu et al., 2020). Therefore, it is of great significance to study the actual compaction characteristics of gangue in stope.

Based on the geological conditions and gangue in Tangshan Coal Mine in Hebei Province, China, the confined compression test of gangue was carried out by the self-designed bearing-compression device; the compaction characteristics such as bulk density and deformation modulus of the backfilling body were obtained. Subsequently, the optimal axial pressure was obtained from the test, and applied to the working face F5001. The on-site compaction characteristics monitoring scheme was designed to explore the compaction characteristics under different inclination angles and different mining heights in the process of advancing. Through the developed Beidou satellite CORS monitoring system, the surface subsidence was monitored in this study. This study promotes the development of backfilling mining technology in China.

PROJECT OVERVIEW AND BACKFILLING TECHNOLOGY

Project Overview

Tangshan coal mine is located in Lunan District, Tangshan City, Hebei Province, with a minefield of 37.28 km² and a mining area of 55 km². With convenient transportation, it is the sole state-owned super-large coal mine located in the central area of the city in China. Tangshan Mine adopts the progressive development mode of vertically inclined shaft mining in stages. At present, it has seven vertical shafts and 10 mining production areas, and no major fault. The main coal seams are coal seams 5, 8, 9, and 12, with an average thickness of 2.4, 3.7, 3.5, and 6.4 m, respectively.

Recently, the mining area F has been mined in the Tangshan mine; the working face F5001 was the first mining face, and the mining time was from 2016.10.5–2019.9.16. The average thickness of coal seams was 2.2 m, and the average inclination angle of coal seams was 11°, and the buried depth was about 600 m. The main roof was gray fine sandstone with a thickness of 17.5 m; The immediate roof was grey strip medium and fine sandstone, with a thickness of 3.7–6.0 m. The immediate floor was dark gray mudstone with a thickness of 0.4–1.4 m, and the main floor was gray strip fine sandstone with a thickness of 5.2 m. The strike length of the working face was 639.5 m and the inclined length was 66 m. **Figure 1** shows the location of the Tangshan Mine and the layout of the working face F5001.

Backfilling Method and Technology

Backfilling Mining Method in Tangshan Mine

The full cross-section solid mechanized backfilling mining was adopted in the Tangshan Mine (Livaoglu et al., 2011; Mitchell et al., 2011; Dai et al., 2018). The backfilling system included the ground conveying system, vertical feeding system, underground separation system, underground conveying system and backfilling system (Hawkes and Fellers, 1969; Wijewickreme and Vaid, 1993; Yuan and Sun, 2012). The ground conveying system was mainly used to crush and transport gangue backfilling materials on the ground. The vertical feeding system was used to transport the backfilling materials from the ground to the underground (Li and Sheng, 1995; Louréno et al., 1997; Benzaazoua et al., 1999). The underground separation system was used to separate the gangue contained in the underground coal flow. The underground conveying system was used to transport the gangue from various sources to the backfill working face. The function of the backfilling system was used to fill gangue into goaf. **Figure 2** shows the backfilling system of the Tangshan mine (Zhang et al., 2015).

Backfilling Technology in the Working Face F5001

In the process of mining, the inclination angle and mining height of the working face F5001 are constantly changing, and the backfilling technology is relatively complex. The inclined mining is not conducive to the backfilling of working face. To improve the backfilling quality in the inclined mining, the

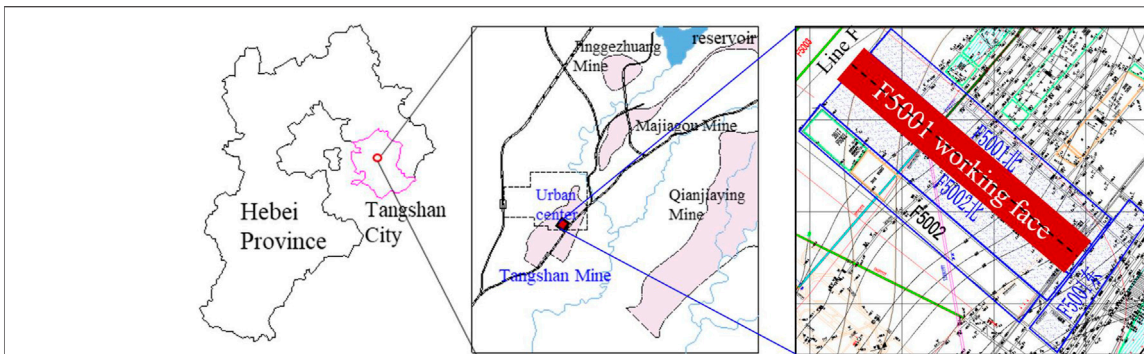


FIGURE 1 | Location of the Tangshan mine and the layout of working face F5001.

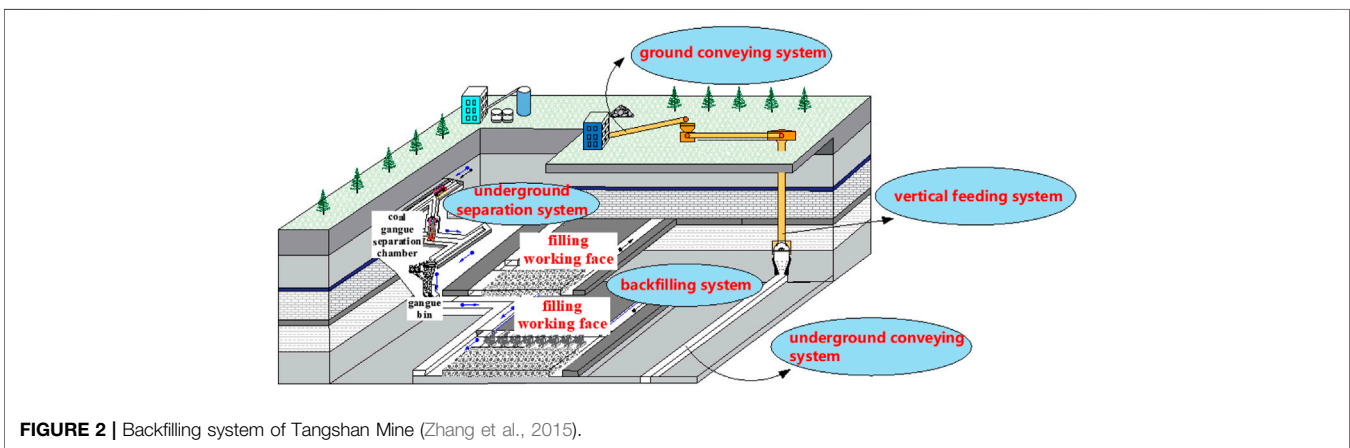


FIGURE 2 | Backfilling system of Tangshan Mine (Zhang et al., 2015).

following points should be ensured: 1) the compaction force should be appropriately increased (Ye et al., 2010; Yanli et al., 2011; Zhou et al., 2016), and the compaction force should no less than 2.5 MPa; 2) a small amount of backfilling materials should be discharged at sections, and the number of compaction and single-hole discharge should be increased to ensure the backfilling body can fully connect with the roof (Chen et al., 2002; Komine, 2004; Latha and Krishna, 2008). It can be seen that compaction force is the key point of backfilling technology research.

VERIFICATION OF LABORATORY GANGUE COMPACTION TEST RESULTS

Materials and Test Systems

The gangue samples were taken from washing gangue and excavated gangue in the mining area F of Tangshan mine. The main lithology of gangue samples was sandy mudstone. Before the test, the gangue samples were crushed. The crusher was used to break the gangue to obtain gangue samples with a particle size of less than 30 mm (Cihangir et al., 2012; Grgic et al., 2013; Han et al., 2016), and then the grading screen was used to grade the original gangue. The grading of particle size was 0–5 mm, 5–10 mm, 10–15 mm, 15–20 mm, 20–25 mm and 25–30 mm, respectively.

The uniaxial loading test system of gangue backfilling material (Komine, 2010; Brzesowsky et al., 2014; Miao et al., 2016) was developed, which was mainly composed of the axial loading system, steel cylinder, data monitoring and acquisition system. The compaction test was carried out on the electro-hydraulic servo universal testing system, which includes the WAW-1000D microcomputer controlled electro-hydraulic servo universal testing machine and the self-made compaction steel cylinder. The maximum loading force provided by the testing machine was 1000 KN. The self-made compaction steel cylinder was composed of the steel cylinder, base, dowel bar and loading plate. The inner diameter of the steel cylinder was 250 mm, the outer diameter was 274 mm, the height was 305 mm, and the wall thickness was 12 mm. The steel cylinder and the base were connected by the flange. The radius of the loading plate was 124 mm and the height was 40 mm, which can realize the uniform stress of the sample in the loading process. **Figure 3** shows gangue samples and the test system.

Test Principle and Scheme

Test Principle

The axial loading force was used to simulate the compaction force in the field (Helwany et al., 1999; Ahmadabadi and Ghanbari, 2009; Yan et al., 2021). After the initial loading stress was applied,

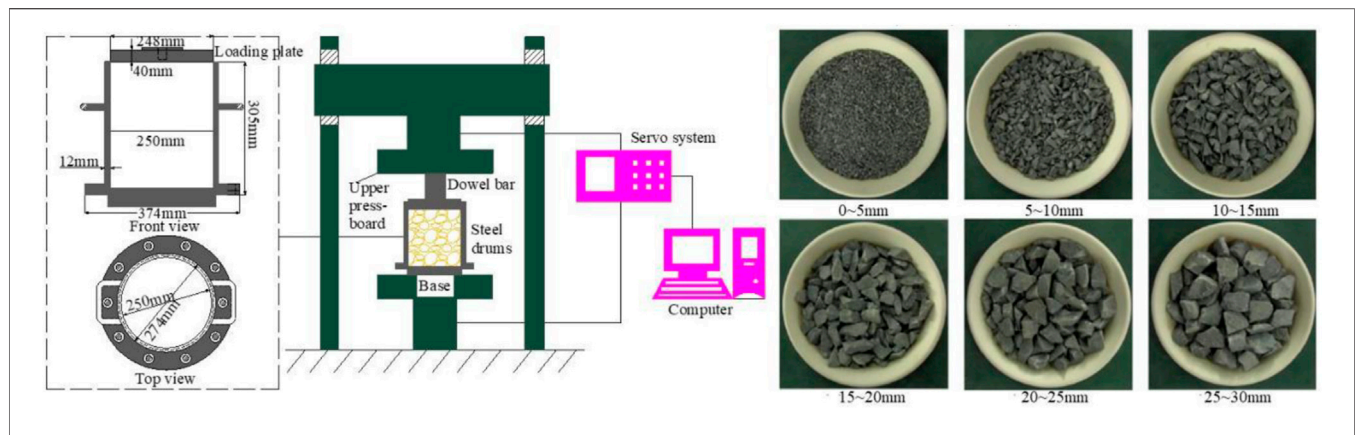


FIGURE 3 | Test system and gangue samples.

a final loading force of 735 kN (15MPa) was applied, and the final compaction deformation of gangue backfilling materials was recorded. The test principle is as follows:

The strain of the sample is:

$$\varepsilon = \frac{\Delta h}{h} \quad (1)$$

where ε is the strain, Δh is the compression deformation and h is the initial loading height before compaction.

The relationship between stress and bulk density is as follows

$$\rho(\sigma) = \frac{\rho_0}{1 - \varepsilon(\sigma)} \quad (2)$$

where ρ_0 is the initial density of gangue, 2.4 t/m³.

There is no fixed parameter to express the stress-strain relationship of gangue, and the deformation modulus of gangue is defined as $E = \sigma/\varepsilon$, and the elastic foundation coefficient of the backfilling body is $k_g = E/h$. During the compaction, the relationship between stress and elastic foundation coefficient is as follows:

$$k_g = \frac{\sigma}{\varepsilon h} \quad (3)$$

Test Scheme

According to the grading of gangue, six graded particle sizes are 0–5, 5–10, 10–15, 15–20, 20–25, and 25–30 mm, which are named as g1, g2, g3, g4, g5 and g6, respectively. The gangue with different particle size was proportioned evenly, i.e., g1: g2: g3: g4: g5: g6 = 1:1: 1:1:1:1:1. The compaction deformation characteristics of six kinds of particle size gangue and uniform graded gangue were tested, and then the compaction and deformation characteristics of seven groups of samples were studied.

Test Results

Stress-Strain Relationship

The stress-strain curve of gangue during compaction is obtained, as shown in Figure 4. The comparison of gangue strain in each stage is shown in Table 1.

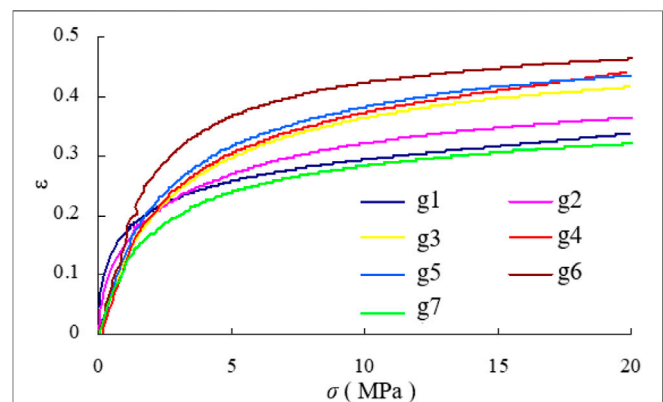


FIGURE 4 | Stress-strain curves of gangue samples.

As shown in Figure 4 and Table 1, the stress-strain curve of the gangue sample generally shows a logarithmic distribution trend. In the initial compaction stage (0–2.5 MPa), the strain increases by 16.6–25.8%, and the gangue sample has a rapid deformation rate. With the gradual increase of axial loading, the gangue sample is compacted gradually, and the strain growth decreases gradually.

Relationship Between Stress and Bulk Density

The stress bulk density curve of gangue samples in the compaction process is obtained, as shown in Figure 5. The variation of gangue bulk density in different stages is shown in Table 2.

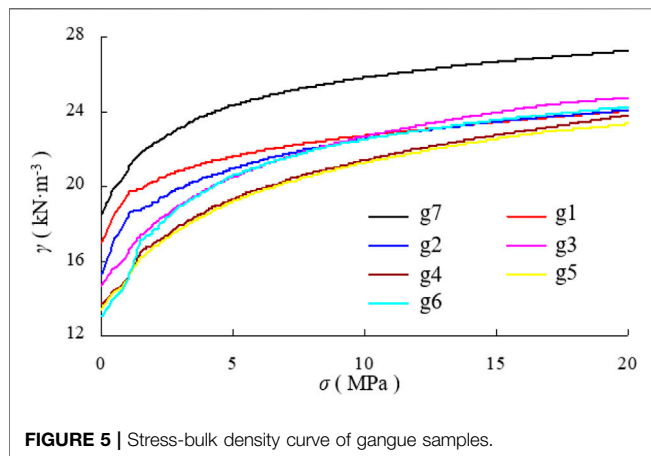
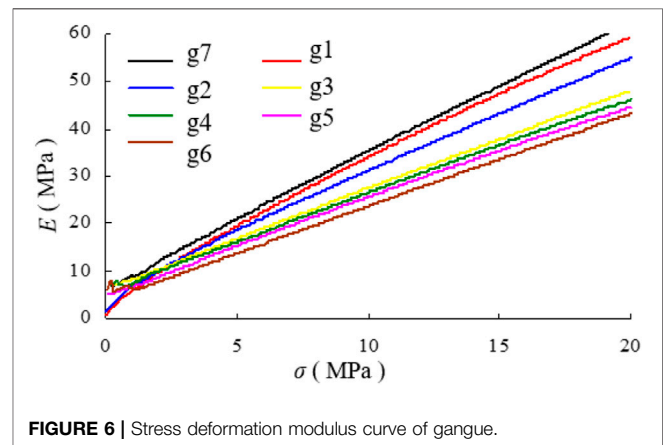
As illustrated in Figure 5 and Table 2, with the increase of the compaction force, the bulk density of the backfilling material increases. The bulk density of the backfilling material is 22.2–17.6 kN m⁻³ under the compaction force of 0–2.5MPa. With the increase of compaction force, the deformation of gangue samples increases gradually. The bulk density increases slowly in the later compaction stage, which is represented by the gentle curve in the later compaction stage.

TABLE 1 | Strain variable of gangue samples at different stages.

	Uniform proportioning (%)	0–50 mm (%)	5–50 mm (%)	10–50 mm (%)	15–50 mm (%)	20–50 mm (%)	25–50 mm (%)
2.5 MPa	16.6	19.7	20.4	20.8	21.3	23.0	25.8
15 MPa	30.6	31.0	34.7	39.0	40.3	41.6	42.4
2.5–15MPa	14.0	11.3	14.3	18.2	19.0	18.6	16.6

TABLE 2 | Variation of bulk density of gangue samples in different stages.

	Uniform proportioning	0–50 mm	5–50 mm	10–50 mm	15–50 mm	20–50 mm	25–50 mm
Original bulk density/(kN m^{-3})	18.5	16.2	15.3	14.7	13.7	13.4	13.0
Bulk density at the 2.5MPa/ kN m^{-3}	22.2	20.3	19.1	17.9	16.9	16.7	17.6
Mass ratio of mining and backfilling after compaction	1.49	1.36	1.28	1.20	1.14	1.12	1.18

**FIGURE 5** | Stress-bulk density curve of gangue samples.**FIGURE 6** | Stress deformation modulus curve of gangue.

Relationship Between Stress and Deformation Modulus

The stress deformation modulus curve of gangue during compaction is shown in **Figure 6**, and the variation of deformation modulus of gangue at different stages is shown in **Table 3**.

As shown in **Figure 6** and **Table 3**, with the increase of pressure σ , the deformation modulus E of gangue samples with different particle sizes increases, and the changing range of E is 0–60 MPa. Compared with the elastic modulus of intact gangue, the order of magnitude of the granular material composed of broken gangue particles is quite different. When the compressive strength reaches 15 MPa, the deformation modulus is about 28–50 MPa.

FIELD TEST ON LONG-TERM COMPACTION CHARACTERISTICS OF GANGUE SAMPLES

According to test results in the laboratory, 2.5 MPa is the optimal compaction force. In the actual backfilling operation of working face F5001, the compaction force of 2.5 MPa was adopted, and the backfilling materials were discharged and backfilled at sections.

Principle and Scheme of Compaction Characteristics in the On-Site Measurement

The mass ratio of mining and backfilling refers to the mass ratio of coal and gangue. Through monitoring the mass ratio of mining and backfilling, the compaction characteristics of gangue are further converted in the Tangshan mine. According to the formula of the mass ratio of mining and backfilling, it is obtained as follows:

$$\frac{1}{c} = \frac{m_c}{m_g} = \frac{v_c \cdot \rho_c}{v_g \cdot \rho_g} = \frac{h_0}{h_0 - \Delta h} \frac{\rho_c}{\rho_g} = \frac{1}{1 - \varepsilon} \frac{\rho_c}{\rho_g} \quad (4)$$

$$E = \frac{\sigma_0}{\varepsilon} \quad (5)$$

TABLE 3 | Variation of deformation modulus of gangue in different stages.

No	Particle size grade	E- σ equation
1	Uniform proportioning	$E = 2.7958\sigma + 6.7557$
2	0–50 mm	$E = 2.8311\sigma + 4.7453$
3	5–50 mm	$E = 2.5159\sigma + 5.4693$
4	10–50 mm	$E = 2.1014\sigma + 6.3100$
5	15–50 mm	$E = 2.0366\sigma + 5.9730$
6	20–50 mm	$E = 2.0098\sigma + 5.1370$
7	25–50 mm	$E = 1.9578\sigma + 4.0882$

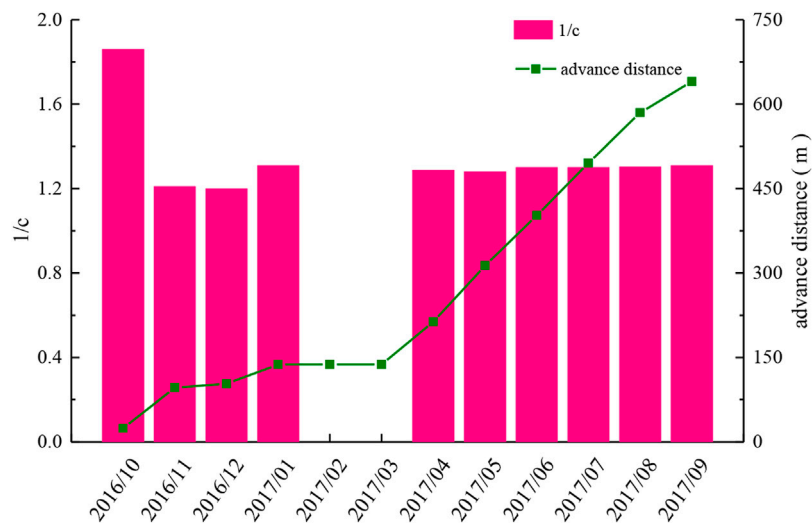


FIGURE 7 | Distribution of mass ratio of mining and backfilling in coal mining.

TABLE 4 | Mass ratio of mining and backfilling and deformation modulus data in coal mining.

Date	2016/10	2016/11	2016/12	2017/1	2017/2	2017/3	2017/4	2017/5	2017/6	2017/7	2017/8	2017/9
Cumulative advancing distance	24	96	103	138	138	138	213	313	403	495	585	640
Mass ratio of mining and backfilling	1.86	1.21	1.2	1.31	0	0	1.29	1.28	1.30	1.30	1.30	1.31
Deformation modulus	21.88	29.03	29.26	27.10	0	0	27.49	27.62	27.26	27.26	27.21	27.10

where c is the mass ratio of mining to backfilling; ϵ is the test strain; ρ_c is the density of coal, $\text{kg}\cdot\text{m}^{-3}$; ρ_g is the density of gangue, $\text{kg}\cdot\text{m}^{-3}$; σ_0 is the vertical stress and E is the deformation modulus.

Due to the change in the inclination angle and mining height during the actual mining process, the angles of -5° , 0° , 10° , 15° , and 20° were used, and the mining heights of 2.2, 2.4, 2.6, 2.8, and 3.0 m were selected. In this way, the mass ratio of mining and backfilling under different advancing distances, inclination angles and mining heights were explored.

On-Site Measurement Results of Compaction Characteristics

On-Site Measurement of Compaction Characteristics of Gangue During Advancing

With the advance in the working face from October 2016 to September 2017, the distribution of mass ratios of the mining and backfilling is shown in **Figure 7**. The deformation modulus data converted from the mass ratio of mining and backfilling is shown in **Table 4**. During this period, 211,439 t gangue was filled and 164,127 t coal was mined.

As shown in **Figure 7** and **Table 4**, during the initial mining in the working face, the roof condition of the goaf is good and more gangue can be filled in the goaf. With the continuous advancement of the working face, the mass ratio of mining and backfilling is stable at about 1.30.

The deformation modulus of the final gangue backfilling body remains at about 27 MPa under the compaction state, which is slightly smaller than the data measured in the laboratory.

Experimental Study on Compaction Characteristics of Gangue Under Different Inclination Angles and Mining Heights

With the change of inclination angles, the distribution of the mass ratio of mining and backfilling is obtained, as shown in **Figure 8**. It can be seen that with the increase of inclination angle, the mining in the working face gradually changes from downward mining to upward mining, and the mass ratio of mining and backfilling gradually increases, which is conducive to backfilling in goaf. However, the deformation modulus of the backfilling body decreases gradually, and the deformation resistance of the backfilling body weakens. Thus, the larger inclination angle in the upward mining is not beneficial to the backfilling.

With the change of mining heights, the distribution of mass ratios of mining and backfilling is shown in **Figure 9**, and the deformation modulus data converted from these mass ratios are obtained. As shown in **Figure 9**, with the increase of mining height, the mass ratio of mining and backfilling first increases and then decreases, indicating that the mining height of 2.6 m is more conducive to backfilling. The deformation modulus of gangue backfilling body is the smallest at the mining height of 2.6 m. It can be concluded that the smaller

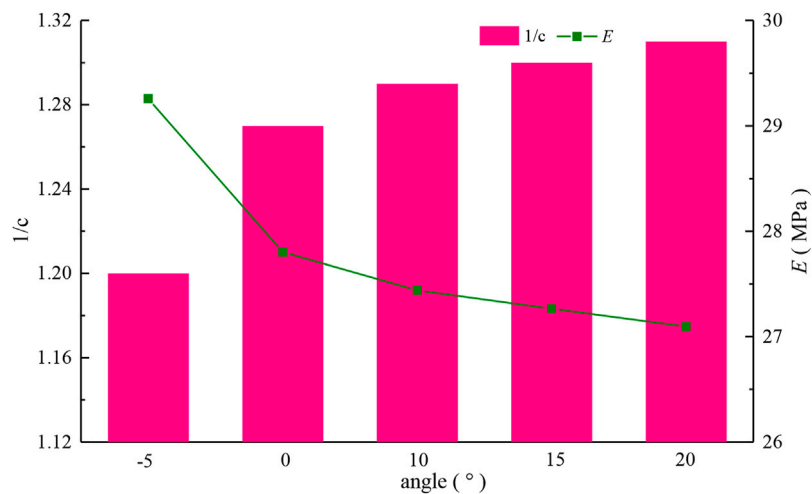


FIGURE 8 | Distribution of the mass ratio of mining and backfilling with the change of inclination angle.

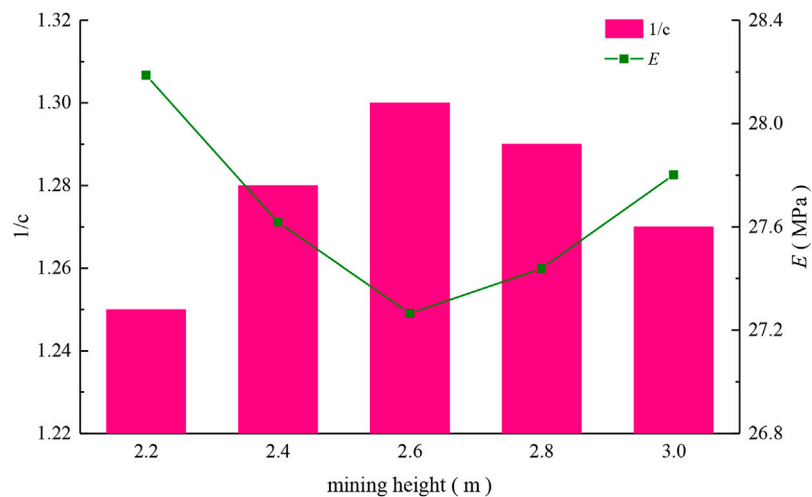


FIGURE 9 | Distribution of mass ratios of mining and backfilling with the change of mining heights.

the deformation resistance of gangue, the more gangue can be filled.

SURFACE SUBSIDENCE MONITORING AND CONTROL EFFECT

Surface Subsidence Monitoring System

The surface subsidence monitoring system includes Beidou satellite navigation system, Beidou satellite reference station and CORS monitoring system (Rollins and Sparks, 2002; Liu et al., 2009; Hla et al., 2021). This system can automatically and accurately monitor the surface subsidence above the working face all day. CORS monitoring system includes data center, reference station, data communication subsystem and user application

subsystem, which greatly improves the accuracy of surface subsidence measurement. The monitoring system is shown in **Figure 10**.

Surface Subsidence Monitoring Scheme

The ground position of working face F5001 crossed Jianshe South Road and Daxue Road, and was adjacent to the mining area railway in the east. A surface observation line F was set on the surface of working face F5001, and a total of 22 measuring points were set along the line to observe the influence of mining on the surface subsidence of working face F5001.

Surface Subsidence Monitoring Results

The surface subsidence test results of the working face F5001 are shown in **Figure 11**.

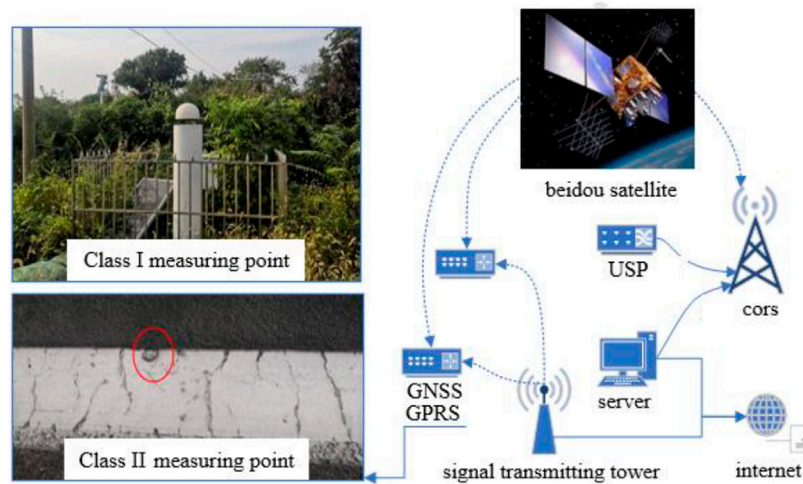


FIGURE 10 | Surface subsidence monitoring system.

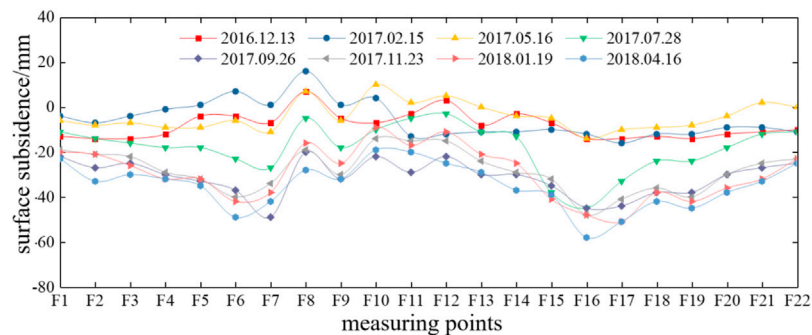


FIGURE 11 | Surface subsidence monitoring results.

From December 2016 to May 2017, the surface subsidence increased slowly, and the subsidence value was less than 20 mm. From May 2017 to July 2017, the surface subsidence increased significantly, but the total subsidence was still in a small range, and the maximum subsidence was 45 mm at the measuring point of F16. In November 2017, the working face was fully mined; in April 2018, the maximum subsidence increased to 61 mm at the measuring point of F12, which was a small increase in 3 months. Therefore, it can be considered that working face F5001 was fully affected by the mining activities in January 2018.

According to the surface subsidence value in the measuring line F of the working face F5001 in April 2018, the surface tilt deformation, curvature deformation, horizontal displacement and horizontal deformation at different measuring points were calculated. The maximum surface tilt deformation value was 1.65 mm/m, which appeared at the measuring point of F12. The maximum curvature deformation value was 0.094 mm/m², which occurred at the measuring point of F17; the maximum deformation value in the horizontal displacement was 16.1 mm, and the maximum horizontal deformation value was 1.25 mm/m, which also occurred at the measuring point of F17.

The maximum surface subsidence value was 61 mm, and the value met the fortification standard of “Regulations for coal pillar setting of buildings, water bodies, railways and main shafts and coal pressed mining” (Ma et al., 2019; Ma et al., 2021a) in 2017. With the advance of the working face, the surface of the ground sank slowly. When the advancing speed of the working face increased, the surface subsidence rate increased, and the curve in **Figure 11** was steeper. In other words, the greater the advancing speed, the greater the sinking speed. After the mining, the surface subsidence rate decreased obviously, even tended to be constant. It indicated that the strata moved slowly and tended to be stable after backfilling mining, which is helpful to the protection of surface buildings.

CONCLUSION

In this study, the uniaxial loading test system of gangue backfilling material was developed, and the basic compaction characteristics of gangue were obtained, such as stress-strain relationship, relationship between stress and bulk density, and relationship

between stress and deformation modulus. The test results show that the initial loading stress of 2.5 MPa can ensure the large deformation characteristics of gangue.

Based on the on-site measurement of the compaction characteristics of the gangue backfilling body in the Tangshan mine, the deformation modulus of the working face with different inclination angles and mining heights was studied. The results show that the field measurement data are consistent with the laboratory test data, and the deformation modulus of the gangue after compaction is close to 27 MPa.

After the backfilling in the working face F5001, the Beidou satellite CORS monitoring system has been used to monitor the surface subsidence for 2 years. The monitoring results show that the surface deformation is effectively controlled, and the maximum surface subsidence is limited to 61 mm.

DATA AVAILABILITY STATEMENT

The original contributions presented in the study are included in the article/Supplementary Material, further inquiries can be directed to the corresponding authors.

REFERENCES

- Ahmadabadi, M., and Ghanbari, A. (2009). New Procedure for Active Earth Pressure Calculation in Retaining walls with Reinforced Cohesive-Frictional Backfill. *Geotextiles and Geomembranes* 27 (6), 456–463. doi:10.1016/j.geotexmem.2009.06.004
- Benzaazoua, M., Ouellet, J., Servant, S., Newman, P., and Verburg, R. (1999). Cementitious Backfill with High Sulfur Content Physical, Chemical, and Mineralogical Characterization. *Cement Concrete Res.* 29 (5), 719–725. doi:10.1016/S0008-8846(99)00023-X
- Brzesowsky, R. H., Hangx, S. J. T., Brantut, N., and Spiers, C. J. (2014). Compaction Creep of Sands Due to Time-Dependent Grain Failure: Effects of Chemical Environment, Applied Stress, and Grain Size. *J. Geophys. Res. Solid Earth* 119 (10), 7521–7541. doi:10.1002/2014JB011277
- Cao, L.-M., Sun, S.-J., Zhang, Y.-Z., Guo, H., and Zhang, Z. (2018). The Research on Characteristics of Hydraulic Support Advancing Control System in Coal Mining Face. *Wireless Pers Commun.* 102, 2667–2680. doi:10.1007/s11277-018-5294-4
- Chen, S. L., Feng, X. T., and Li, S. J. (2002). Effects of Chemical Erosion on Mechanical Behaviors of Xiaolangdi Sandstone. *Rock Soil Mech.* 23 (3), 284–283. doi:10.1007/s11769-002-0073-1
- Chong, Z., Yao, Q., Li, X., and Shivakumar, K. (2020). Acoustic Emission Investigation on Scale Effect and Anisotropy of Jointed Rock Mass by the Discrete Element Method. *Arab J. Geosci.* 13 (9), 1–14. doi:10.1007/s12517-020-05303-z
- Cihangir, F., Ercikdi, B., Kesimal, A., Turan, A., and Deveci, H. (2012). Utilisation of Alkali-Activated Blast Furnace Slag in Paste Backfill of High-Sulphide Mill Tailings: Effect of Binder Type and Dosage. *Minerals Eng.* 30, 33–43. doi:10.1016/j.mineng.2012.01.009
- Dai, G., Sheng, Y., Li, S., and Zhang, Y. (2018). Experimental Study on Mechanical Properties of Anti-Seepage Slurry in Landfill. *Mod. Phys. Lett. B* 32, 1840065. doi:10.1142/S0217984918400651
- Ercikdi, B., Cihangir, F., Kesimal, A., Deveci, H., and Alp, İ. (2009). Utilization of Industrial Waste Products as Pozzolanic Material in Cemented Paste Backfill of High Sulphide Mill Tailings. *J. Hazard. Mater.* 168 (2-3), 848–856. doi:10.1016/j.jhazmat.2009.02.100
- Fall, M., Benzaazoua, M., and Saa, E. G. (2008). Mix Proportioning of Underground Cemented Tailings Backfill. *Tunnelling Underground Space Technol.* 23 (1), 80–90. doi:10.1016/j.tust.2006.08.005
- Fall, M., Célestin, J. C., Pokharel, M., and Touré, M. (2010). A Contribution to Understanding the Effects of Curing Temperature on the Mechanical

AUTHOR CONTRIBUTIONS

JW: Conceptualization, Model investigation, Data curation, Writing—original draft. QZ: Model investigation, Laboratorial investigation, Data curation. WY: Funding acquisition, Writing—review and editing. SQ: Data curation. DG: Laboratorial investigation, Data curation. DM: Conceptualization, Funding acquisition Data curation.

FUNDING

This work is funded by Independent Research Project of the National Natural Science Foundation of China (52174134, 51904110, 51804339, 41977238 and 52122404) and the Fundamental Research Funds for the Central Universities (2021GJZPY12).

ACKNOWLEDGMENTS

Thanks to the staff of Tangshan mine, they worked hard to monitor and got precious measured data.

- Properties of Mine Cemented Tailings Backfill. *Eng. Geology.* 114 (3-4), 397–413. doi:10.1016/j.enggeo.2010.05.016
- Grgic, D., Giraud, A., and Auvray, C. (2013). Impact of Chemical Weathering on Micro/Macro-Mechanical Properties of Oolitic Iron Ore. *Int. J. Rock Mech. Mining Sci.* 64, 236–245. doi:10.1016/j.ijrmms.2013.09.005
- Han, T., Shi, J., and Cao, X. (2016). Fracturing and Damage to Sandstone Under Coupling Effects of Chemical Corrosion and Freeze-Thaw Cycles. *Rock Mech. Rock Eng.* 49 (11), 4245–4255. doi:10.1007/s00603-016-1028-7
- Hawkes, I., and Fellers, G. E. (1969). Theory of the Determination of the Greatest Principal Stress in a Biaxial Stress Field Using Photoelastic Hollow cylinder Inclusions. *Int. J. Rock Mech. Mining Sci. Geomechanics Abstr.* 6 (2), 143–158. doi:10.1016/0148-9062(69)90032-1
- Helwany, S. M. B., Reardon, G., and Wu, J. T. H. (1999). Effects of Backfill on the Performance of Grs Retaining walls. *Geotextiles and Geomembranes* 17 (1), 1–16. doi:10.1016/S0266-1144(98)00021-1
- Komine, H. (2004). Simplified Evaluation on Hydraulic Conductivities of Sand-Bentonite Mixture Backfill. *Appl. Clay Sci.* 26 (1/4), 13–19. doi:10.1016/j.clay.2003.09.006
- Komine, H. (2010). Predicting Hydraulic Conductivity of Sand-Bentonite Mixture Backfill before and after Swelling Deformation for Underground Disposal of Radioactive Wastes. *Eng. Geology.* 114 (3-4), 123–134. doi:10.1016/j.enggeo.2010.04.009
- Latha, G. M., and Krishna, A. M. (2008). Seismic Response of Reinforced Soil Retaining wall Models: Influence of Backfill Relative Density. *Geotextiles and Geomembranes* 26 (4), 335–349. doi:10.1016/j.geotexmem.2007.11.001
- Li, K., and Sheng, P. (1995). Plane Stress Model for Fracture of Ceramics during Laser Cutting. *Int. J. Machine Tools Manufacture* 35 (11), 1493–1506. doi:10.1016/0890-6955(94)00127-6
- Li, H., Guo, G., and Zheng, N. (2018). Influence of Coal Types on Overlying Strata Movement and Deformation in Underground Coal Gasification without Shaft and Prediction Method of Surface Subsidence. *Process Saf. Environ. Prot.* 120, 302–312. doi:10.1016/j.psep.2018.09.023
- Liu, H., Wang, X., and Song, E. (2009). Long-Term Behavior of Grs Retaining walls with Marginal Backfill Soils. *Geotextiles and Geomembranes* 27 (4), 295–307. doi:10.1016/j.geotexmem.2009.01.002
- Liu, H., Zhang, J., Li, B., Zhou, N., Li, D., Zhang, L., et al. (2021). Long Term Leaching Behavior of Arsenic from Cemented Paste Backfill Made of Construction and Demolition Waste: Experimental and Numerical Simulation Studies. *J. Hazard. Mater.* 416, 125813. doi:10.1016/j.jhazmat.2021.125813

- Li, M., Zhang, J.-x., Huang, P., and Gao, R. (2016). Mass Ratio Design Based on Compaction Properties of Backfill Materials. *J. Cent. South. Univ.* 23, 2669–2675. doi:10.1007/s11771-016-3328-1
- Livaoglu, R., Cakir, T., Dogangun, A., and Aytekin, M. (2011). Effects of Backfill on Seismic Behavior of Rectangular Tanks. *Ocean Eng.* 38 (10), 1161–1173. doi:10.1016/j.oceaneng.2011.05.017
- Louréno, P. B., De Borst, R., and Rots, J. G. (1997). A Plane Stress Softening Plasticity Model for Orthotropic Materials. *Int. J. Numer. Methods Eng.* 40 (21), 4033–4057. doi:10.1002/(SICI)1097-0207(19971115)40:21<4033::AID-NME248>3
- Ma, D., Wang, J., Cai, X., Ma, X., Zhang, J., Zhou, Z., et al. (2019). Effects of Height/Diameter Ratio on Failure and Damage Properties of Granite under Coupled Bending and Splitting Deformation. *Eng. Fracture Mech.* 220, 106640. doi:10.1016/j.engfracmech.2019.106640
- Ma, D., Kong, S., Li, Z., Zhang, Q., Wang, Z., and Zhou, Z. (2021a). Effect of Wetting-Drying Cycle on Hydraulic and Mechanical Properties of Cemented Paste Backfill of the Recycled Solid Wastes. *Chemosphere* 282, 131163. doi:10.1016/j.chemosphere.2021.131163
- Ma, D., Zhang, J., Duan, H., Huang, Y., Li, M., Sun, Q., et al. (2021b). Reutilization of Gangue Wastes in Underground Backfilling Mining: Overburden Aquifer Protection. *Chemosphere* 264 (Pt 1), 128400. doi:10.1016/j.chemosphere.2020.128400
- Malusis, M. A., Barben, E. J., and Evans, J. C. (2009). Hydraulic Conductivity and Compressibility of Soil-Bentonite Backfill Amended with Activated Carbon. *J. Geotech. Geoenviron. Eng.* 135 (5), 664–672. doi:10.1061/(ASCE)GT.1943-5606.0000041
- Miao, S., Cai, M., Guo, Q., Wang, P., Liang, M., et al. (2016). Damage Effects and Mechanisms in Granite Treated with Acidic Chemical Solutions. *Int. J. Rock Mech. Mining Sci.* 88, 77–86. doi:10.1016/j.ijrmms.2016.07.002
- Mitchell, R. J., Olsen, R. S., and Smith, J. D. (2011). Model Studies on Cemented Tailings Used in Mine Backfill. *Can. Geotech. J.* 19 (1), 14–28. doi:10.1139/t82-002
- Niu, D. X., Wang, P., Wang, Q., Hua, F. Y., Wang, F., and Cai, Z. H. (2014). Analysis of the Power Plant Security Management Capability Based on the Ism and Ahp. *Adv. Mater. Res.* 960-961, 1477–1482. doi:10.4028/www.scientific.net/AMR.960-961.1477
- Rollins, K. M., and Sparks, A. (2002). Lateral Resistance of Full-Scale Pile Cap with Gravel Backfill. *J. Geotech. Geoenviron. Eng.* 128 (9), 711–723. doi:10.1061/(asce)1090-0241(2002)128:9(711)
- Shukla, S. K., Gupta, S. K., and Sivakugan, N. (2009). Active Earth Pressure on Retaining Wall for C- ϕ Soil Backfill under Seismic Loading Condition. *J. Geotech. Geoenviron. Eng.* 135 (5), 690–696. doi:10.1061/(ASCE)GT.1943-5606.0000003
- Wei, H., Wen, Z., Ba, L., and Gao, Q. (2021). Study on Strength Test and Hydration Mechanism of Phosphogypsum Based Cemented Backfill. *IOP Conf. Ser. Earth Environ. Sci.* 768 (1), 012100. doi:10.1088/1755-1315/768/1/012100
- Wijewickreme, D., and Vaid, Y. P. (1993). Behaviour of Loose Sand under Simultaneous Increase in Stress Ratio and Principal Stress Rotation. *Can. Geotech. J.* 30 (6), 953–964. doi:10.1139/t93-093
- Xie, H. P., Zhou, H. W., Xue, D. J., Wang, H. W., Zhang, R., and Gao, F. (2012). Research and Consideration on Deep Coal Mining and Critical Mining Depth. *J. China Coal Soc.* 37 (37), 535–542. doi:10.1007/s11783-011-0280-z
- Xie, H., Feng, G., Yang, J. U., and University, S. (2015a). Research and Development of Rock Mechanics in Deep Ground Engineering. *Chin. J. Rock Mech. Eng.* 11, 2161–2178. doi:10.13722/j.cnki.jrme.2015.1369
- Xie, H. P., Gao, F., Ju, Y., Gao, M. Z., Zhang, R., and Gao, Y. N. (2015b). Quantitative Definition and Investigation of Deep Mining. *J. China Coal Soc.* 40 (1), 1–10. doi:10.13225/j.cnki.jccs.2014.1690
- Yan, H., Zhang, J., Li, B., and Zhu, C. (2021). Crack Propagation Patterns and Factors Controlling Complex Crack Network Formation in Coal Bodies during Tri-axial Supercritical Carbon Dioxide Fracturing. *Fuel* 286, 119381. doi:10.1016/j.fuel.2020.119381
- Yanli, H., Jixiong, Z., Baifu, A., and Qiang, Z. (2011). Overlying Strata Movement Law in Fully Mechanized Coal Mining and Backfilling Longwall Face by Similar Physical Simulation. *J. Min. Sci.* 47 (5), 618–627. doi:10.1134/S1062739147050108
- Ye, W.-M., Chen, Y.-G., Chen, B., Wang, Q., and Wang, J. (2010). Advances on the Knowledge of the Buffer/backfill Properties of Heavily-Compacted Gmz Bentonite. *Eng. Geology* 116 (1-2), 12–20. doi:10.1016/j.enggeo.2010.06.002
- Yuan, Y., and Sun, H. (2012). A Novel Silica Alumina-Based Backfill Material Composed of Coal Refuse and Fly Ash. *J. Hazard. Mater.* 213-214, 71–82. doi:10.1016/j.jhazmat.2012.01.059
- Zhang, Q.-L., and Wang, X.-M. (2007). Performance of Cemented Coal Gangue Backfill. *J. Cent. South. Univ. Technol.* 14 (2), 216–219. doi:10.1007/s11771-007-0043-y
- Zhang, J., Zhang, Q., Sun, Q., Gao, R., Germain, D., and Abro, S. (2015). Surface Subsidence Control Theory and Application to Backfill Coal Mining Technology. *Environ. Earth Sci.* 74 (2), 1439–1448. doi:10.1007/s12665-015-4133-0
- Zhou, N., Han, X., Zhang, J., and Li, M. (2016). Compressive Deformation and Energy Dissipation of Crushed Coal Gangue. *Powder Technol.* 297, 220–228. doi:10.1016/j.powtec.2016.04.026
- Zhu, C., Yuan, Y., Yuan, C. f., Liu, F. Q., Chen, Z. S., and Wang, S. Z. (2020). Study on the Structural Forms of the Key Strata in the Overburden of a Stope during Periodic Weighting and the Reasonable Working Resistance of the Support. *Energy Sci Eng* 8, 2599–2620. doi:10.1002/ese3.688

Conflict of Interest: The authors declare that the research was conducted in the absence of any commercial or financial relationships that could be construed as a potential conflict of interest.

Publisher's Note: All claims expressed in this article are solely those of the authors and do not necessarily represent those of their affiliated organizations, or those of the publisher, the editors and the reviewers. Any product that may be evaluated in this article, or claim that may be made by its manufacturer, is not guaranteed or endorsed by the publisher.

Copyright © 2021 Wang, Zhang, Yin, Qi, Gao and Ma. This is an open-access article distributed under the terms of the Creative Commons Attribution License (CC BY). The use, distribution or reproduction in other forums is permitted, provided the original author(s) and the copyright owner(s) are credited and that the original publication in this journal is cited, in accordance with accepted academic practice. No use, distribution or reproduction is permitted which does not comply with these terms.



An Object-Oriented Approach for the Recursive Numeration and Visualization of the Key Strata of Coal Mines

Chun Xu^{1,2}, Keping Zhou^{1,2}, Xin Xiong^{1,2*} and Yan Lu³

¹School of Resources and Safety Engineering, Central South University, Changsha, China, ²Hunan Provincial Key Laboratory of Resources Exploitation and Hazard Control for Deep Metal Mines, Central South University, Changsha, China, ³State Key Lab Coal Resources and Safe Min, China University of Mining and Technology, Xuzhou, China

OPEN ACCESS

Edited by:

Jie Chen,
Chongqing University, China

Reviewed by:

Jianwei Cheng,
China University of Mining and
Technology, China
Sun Yunjiang,
China University of Mining and
Technology, China

*Correspondence:

Xin Xiong
xiongxin@csu.edu.cn

Specialty section:

This article was submitted to
Geohazards and Georisks,
a section of the journal
Frontiers in Earth Science

Received: 30 May 2021

Accepted: 29 September 2021

Published: 04 November 2021

Citation:

Xu C, Zhou K, Xiong X and Lu Y (2021)
An Object-Oriented Approach for the
Recursive Numeration and
Visualization of the Key Strata of
Coal Mines.
Front. Earth Sci. 9:717177.
doi: 10.3389/feart.2021.717177

The exploitation and utilization of coal resources have caused serious ecological and environmental problems that are closely related to the movement and destruction of the overlying strata, especially the activities of the overlying key strata (KS). The existing KS calculation methods are characterized by low efficiency and high costs. This study proposes an object-oriented improved recursive algorithm (OORA) model to achieve efficient calculations for KS. An application program was developed and tested with the KS of the Xiadian coal mine, Shanxi, China. The calculation results were basically consistent with field observations, and the calculation depth was increased by 146.05 m. In addition, five typical KS calculation cases were selected for in-depth testing. The calculation time ranged from 0.175–0.225 s, and the calculation time was shortened by approximately three times compared to that with traditional methods. Therefore, it is feasible to apply the model algorithm for KS calculations, and the model provides benefits such as high efficiency and low costs.

Keywords: KS calculation, object-oriented recursive algorithm (OORA), high efficiency and low cost, rock strata control, coal mine

INTRODUCTION

The mining industry, which is driven by human demand for mineral resources, is one of the main causes of current environmental pollution problems and poses a serious threat to the ecological environment system (Gu, 2018). The pollution of groundwater and air in mining areas is closely related to the development of the mining industry (Silva and Lizardi-Jimenez, 2020). Problems, such as the movement and destruction of strata and surface subsidence caused by high-intensity mining, have seriously affected the deterioration of the ecological environment and the destruction of water resources (Lin et al., 2020a; Santana et al., 2020; Zhang et al., 2020; Zhu et al., 2020). During the mining process, the movement and destruction of the overlying rock strata directly reflect the damage done to the environment by mining. With the advancement of the mining face and the gradual expansion of the mining scope, the overlying rock is seriously damaged (Bai et al., 2018; Bai et al., 2019a; Bai et al., 2019b). The breaking of the strata directly destroys the conditions for the occurrence of groundwater, causes the loss and pollution of groundwater, severely damages water resources, and leads to the deterioration of the ecological environment, which will bring extremely adverse effects to sustainable development; furthermore, this will cause mine water inrush accidents,

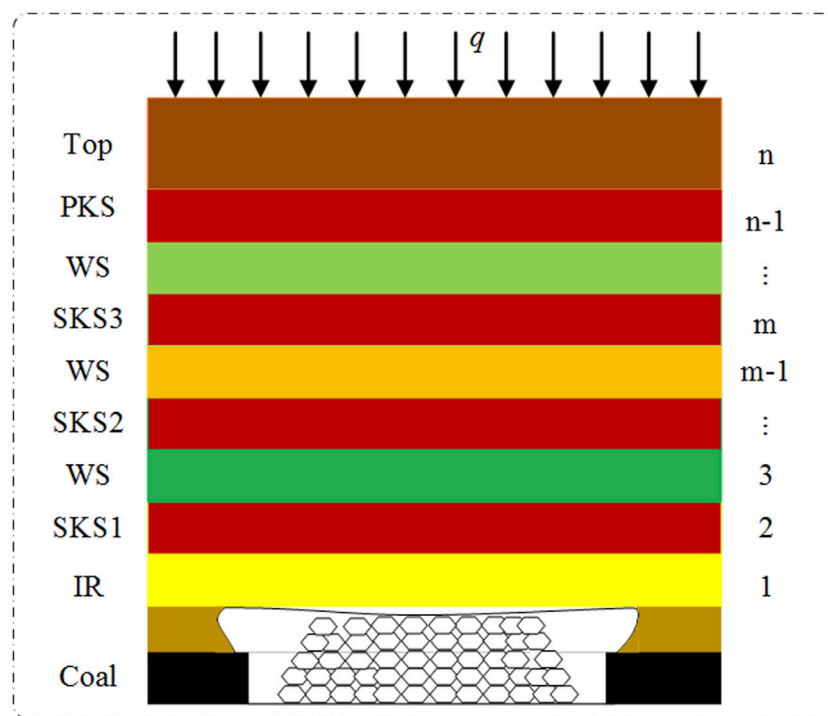


FIGURE 1 | Model of the key strata in the overburden.

causing serious casualties and economic and property losses (Li et al., 2015; Liang et al., 2015; Zhang et al., 2017).

A series of environmental problems induced by coal mining are essentially caused by the movement and destruction of the overburden, and the location and damage of the key strata are closely related to the movement and destruction of the overburden (Ma et al., 2012; Shi and Zhang, 2013; Chen et al., 2015; Jiang et al., 2015; Ma et al., 2018). In coal mines, the overlying strata are composed of strata with different lithologies, thicknesses, strengths, and other characteristics. Therefore, during the mining process, the impact of mining on the strata is different, and the sensitivity and response of strata with different characteristics to the impact of mining are also different (Wu et al., 2009; Zhang et al., 2019; Sun et al., 2020; Wang et al., 2020).

Hard strata may have a greater bearing capacity and weaker sensitivity and may control and support relatively weak strata. Based on the differences in these characteristics, the key strata theory is proposed and successfully applied to field production, which highlights an important direction for the study of mining overburden control (Qian et al., 1996). According to the key strata theory, strata that are hard and thick and have major control over overburden activity are named key strata; the immediate roof (IR) and weak strata (WS) have little effect. As shown in **Figure 1**, the top key stratum (KS) is named the primary KS (PKS) as it plays a major role in controlling the movement and destruction of the overlying strata. Correspondingly, the following KS that controls the partial influence of some overlying strata activities are named the sub-key strata (SKS). On the assumption that the load on the

strata is evenly distributed and the dip angle is horizontal, the criteria for determining the stiffness and strength are proposed. Assuming that the range of strata controlled by the first stratum includes n strata, the load formed by the n strata on the first stratum is $(q_n)_1$ (Xu and Qian, 2000; Xu and Ju, 2011).

$$(q_n)_1 = \frac{E_1 h_1^3 \sum_{i=1}^{n-1} \gamma_i h_i}{\sum_{i=1}^{n-1} E_i h_i^3}, \quad (1)$$

where E is the modulus of the elasticity, γ is the bulk density, h is the thickness, i is the number of strata, and q is the load. These variables correspond to the corresponding rock strata.

If the strata of no. n are still controlled by the first stratum, their load acts on the first stratum. This action should obey inequality $(q_n)_1 > (q_{n-1})_1$; otherwise, it appears that the strata of no. n are not controlled by the first, and the strata of no. n can be considered hard strata. After analyzing each stratum, all hard strata can be searched. Then we regard the strata as a beam model and analyze the advancing distance of the working face that caused the strata to break. The breaking distance (L_i) of each hard rock strata can be calculated by **Eq. 2**.

$$L_i = h_i \sqrt{\frac{2\sigma_i}{q_i}}, \quad (2)$$

where σ is the tensile strength, q is the load, and h is the thickness. The breaking distance of all hard rock strata can be obtained by

calculation, and then the key strata can be determined by analyzing the relationship between the breaking distances. The breaking distance of the key strata should satisfy the inequality $L_i > L_{i-1}$. Otherwise, the load of the previous strata needs to be added to the next strata and recalculated. After a series of calculations and analyses, the key strata can be searched. The identification methods of the key strata mainly includes lithology calculations, ground drilling, and laboratory simulations (Xie and Xu, 2017; Zhu et al., 2017; Li et al., 2018). Key strata recognition software was developed and successfully used in field practice, and the fast calculation efficiency of the software soon showed a huge advantage (Xu et al., 2000).

Inspired by key strata theory, research on mine disaster management, mining safety, water-preserving mining, and green mining has achieved decent practical results, effectively guiding field practice (Cheng et al., 2018; Liang et al., 2019; Gong et al., 2020). Furthermore, a large number of valuable research results on strata control and surface subsidence prediction based on the KS have been obtained, which provides new ideas for solving environmental problems caused by mining (Cheng et al., 2017a; Cheng et al., 2017b; Cheng et al., 2018; Cheng et al., 2020). However, in practical applications, using lithology calculations, laboratory simulations, magnetotelluric (MT) detection methods, etc. to identify the location of the key strata consume considerable resources and time. There is no doubt that using a program for lithology calculation is one of the most efficient and economical methods, but a development of the program requires a computational foundation and certain programming skills, and the actual development process is cumbersome and complicated.

It is necessary to find a high-efficiency, low-cost, easy-to-understand, and implementable method to realize do-it-yourself KS program calculations to meet the increasing amount of research relying on key strata theory.

With the rapid development and popularization of computer technology, the application of computers has gradually penetrated various industries. Emerging technologies such as artificial intelligence, data mining, machine learning, and big data have had huge impacts on many traditional industries. Many traditional industries have made full use of the research results from the development of computer technology to provide new research ideas and solutions for the research of some professional problems (Lin et al., 2018; Ahmed et al., 2020; Lin et al., 2020b; Brykov et al., 2020; Ge et al., 2020; Leng et al., 2020). Under the background of the rapid popularization of computer technology in various areas, basic programming abilities, which makes it possible to write programs by oneself, have become basic skills of universities, research institutions, and even field staff. Designing programs and writing codes through do-it-yourself (DIY) are conducive to a deep understanding of the physical meaning behind the theoretical principles and the way of thinking of previous scholars. Researchers can use black box software and rely on their own abilities to connect theory with practice. Through DIY, humans improve their comprehensive ability to research and analyze problems and maintain an active thinking mode; more importantly, DIY improves the practical abilities (Sarpong et al., 2020; Yoon et al., 2020).

Object-oriented technology connects the objective world with the computer world in a way that is easier for humans to understand. It has the advantages of abstraction, encapsulation, inheritance, and polymorphism, and the design logic is similar to the way of human thinking. Therefore, the logic is simple and easy-to-understand and does not require a solid professional computer background and basic knowledge. Object-oriented technology has become one of the main methods of modern programming (Chen et al., 2020; Lopes et al., 2020; Lv et al., 2020; Prajapati and Chhabra, 2020; Van Hien et al., 2020). Recursion is an algorithm widely used in program design. Its characteristic is that it can transform a large and complex problem into a smaller problem similar to the original problem to solve. Recursion provides a structured, readable, and easily debuggable way of designing algorithms to solve complex problems (Hamouda et al., 2020; Rakic et al., 2020).

According to the above analysis, the key strata have an important influence on mining rock strata control and disaster management. In the current research, the use of programs for lithology calculation still occupies an important position, but there are still some problems in their actual application and promotion.

First, mathematical formulas and related judgment conditions are used for programming. The lack of an overall abstract process of mathematical formulas makes it difficult to fully utilize the advantages of algorithms.

Second, the traditional process-oriented programming method has a complicated logic and is difficult to program. It is difficult to meet the needs of mining staff to develop programs by themselves, which invisibly increases the development costs and application difficulty.

It is necessary to find a high-efficiency, low-cost, easy-to-understand, and implementable method to realize do-it-yourself KS program calculations to meet the increasing research relying on key strata theory. In response to the above problems, we introduced an approach using object-oriented programming techniques and improved recursive algorithm strategies to achieve high-efficiency, low-cost, easy-to-understand, and practical methods to conduct key strata calculation.

First, traditional KS theory is abstractly analyzed, and a flexible and robust algorithm model is established to improve the convenience, efficiency, and accuracy of KS calculations.

Second, object-oriented technology is used to encapsulate the KS algorithm and corresponding functional modules to establish a technical framework with high cohesion and low coupling, which improves the flexibility and maintainability of the system and decreases the difficulty of independent development.

REQUIREMENTS ANALYSIS AND OVERALL RESEARCH FRAMEWORK ESTABLISHMENT

Lithology Data

In the actual study, lithology data are generally stored in a spreadsheet such as an Excel spreadsheet, and its main

TABLE 1 | Format of lithology data.

Number	Lithology	Thickness h (m)	Bulk density γ (kg/m ³)	Elastic modulus E (GPa)	Tensile strength σ (MPa)
1	Sandstone	8.2	2,680	40	3.83
2	Mudstone	3.9	2,200	8	1.2
3	Fine sandstone	2.3	2,660	34	2.75
4	Medium sandstones	5.9	2,680	40	3.45
5	Siltstone	4.6	2,550	37	3.76
6	Mudstone	7.5	2,230	7	1.3

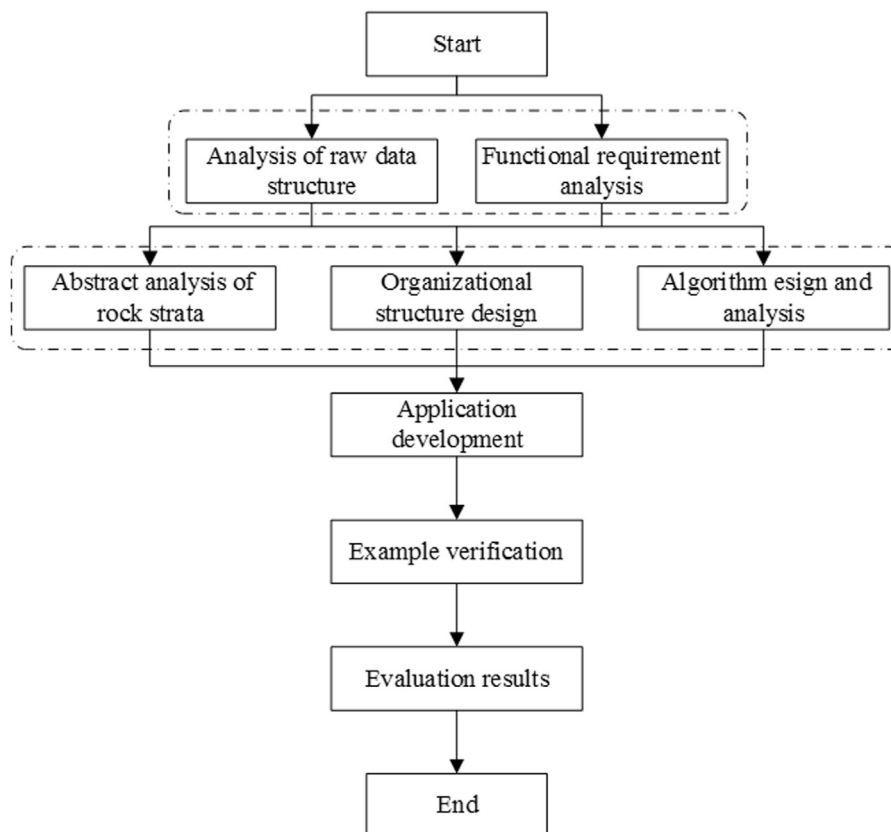


FIGURE 2 | Research framework of KS calculation research.

indicators are the following: number, lithology, thickness (m), bulk density (kg/m³), elastic modulus (GPa), and tensile strength (MPa). The organization format is shown in **Table 1**.

Program Function Analysis

- 1) In order to make a program to have better applicability, in the functional analysis, the user should first design a function to read the traditional spreadsheet data to achieve an import batch data function, avoid repeated manual input, and improve the overall efficiency of the calculation process.
- 2) The data visualization function is an important link in the process of users checking the correctness of data and adjusting parameters. When the data are imported into memory, a

certain carrier should be used to display the data, and the user can check the data by viewing it.

- 3) The iterative calculation function is the core of the entire program. After the data are ready, iterative calculations can be performed. The calculation process is completed in the background, and the calculation results are displayed in real time.
- 4) The parameter adjustment function is the core of improving the efficiency and reducing the time costs. In actual applications, the most troublesome thing is the need to repeatedly adjust the parameters. Therefore, the logic of adjusting parameters must be considered when designing functions. After the parameters are updated, the iterative

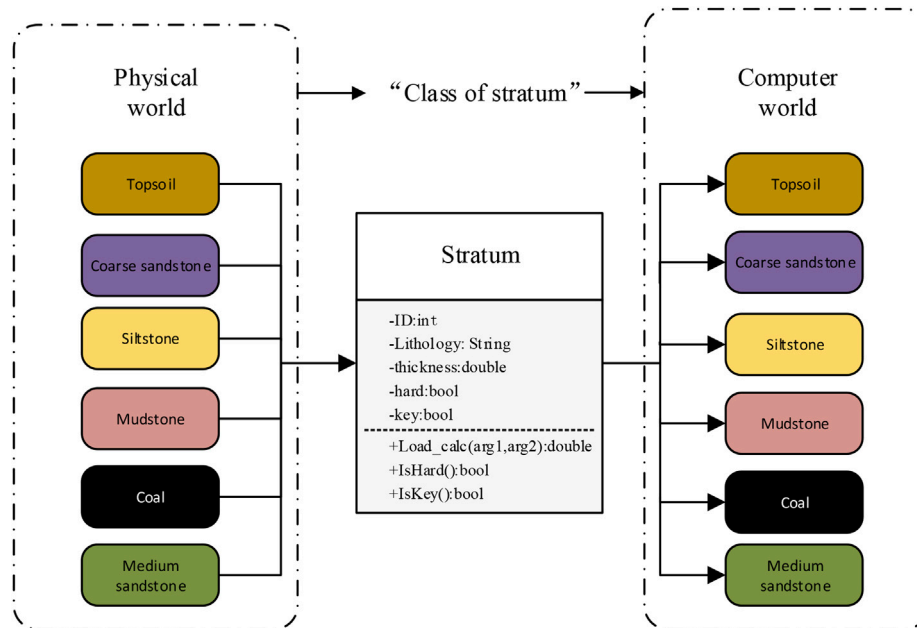


FIGURE 3 | The abstract analysis of rock strata.

calculation function is automatically triggered and the new calculation results are displayed in real time.

- 5) The data export and storage function is the end of the entire process. Users can export and store the calculation results, and then perform other lithology calculations or choose to end the program.

Specific Research Framework of KS Based on an Object-Oriented Recursive Algorithm Model

According to the above analysis, the research framework of the entire program can be preliminarily defined as shown in Figure 2.

ABSTRACT ANALYSIS AND ALGORITHM DESIGN

Abstract Analysis of Strata

The strata in the physical world have different characteristics. After the abstract analysis, the strata class is defined to describe the strata. The parameters of the strata such as the number, lithology, and bulk density are defined as attributes in the class, and the load and fracture of the strata are defined as functions. The objects describing different strata can be obtained by instantiating the strata with different strata parameters. Through the process of abstraction, encapsulation, and instantiation, the strata of the physical world can be mapped into the computer world for expression. The data are all encapsulated inside the object, and an interface is provided for access, which is not only easy to manage but also ensures data security. Through the object-oriented analysis, strata are

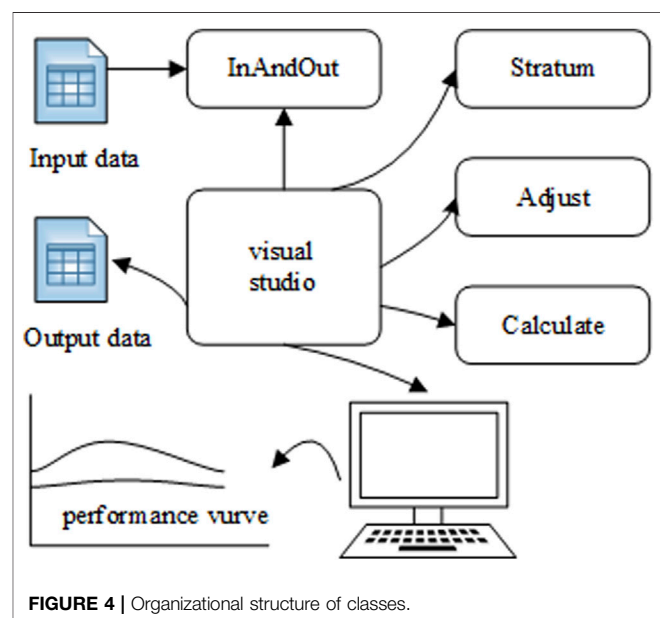


FIGURE 4 | Organizational structure of classes.

transformed from the physical world to the computer world, which not only simplifies the analysis process but also expresses it in a logical way similar to human thinking, which is more conducive to learning and application. Internal functions are defined to simulate the loading and breaking of rock strata and perform function calls and data exchange through message transmission.

Using the rock strata class as a space carrier to map the strata in the physical world into the computer world, the abstract expression of the strata data is related to object-oriented technology, as shown in Figure 3.

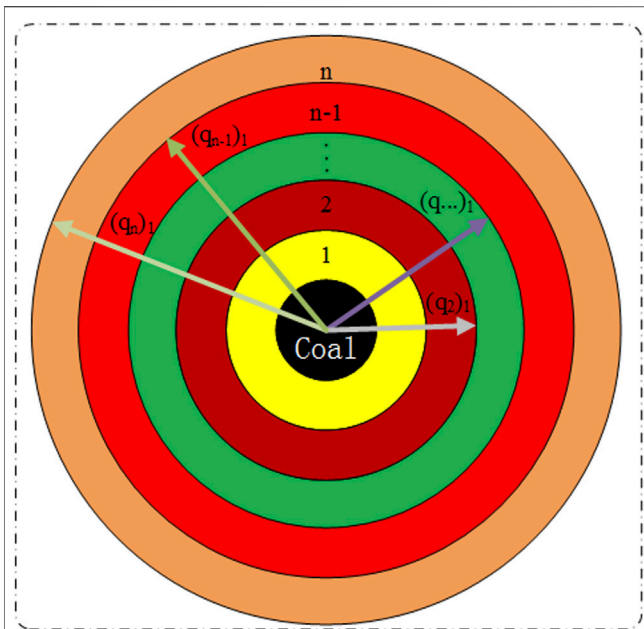


FIGURE 5 | Load condition of stratum no.1.

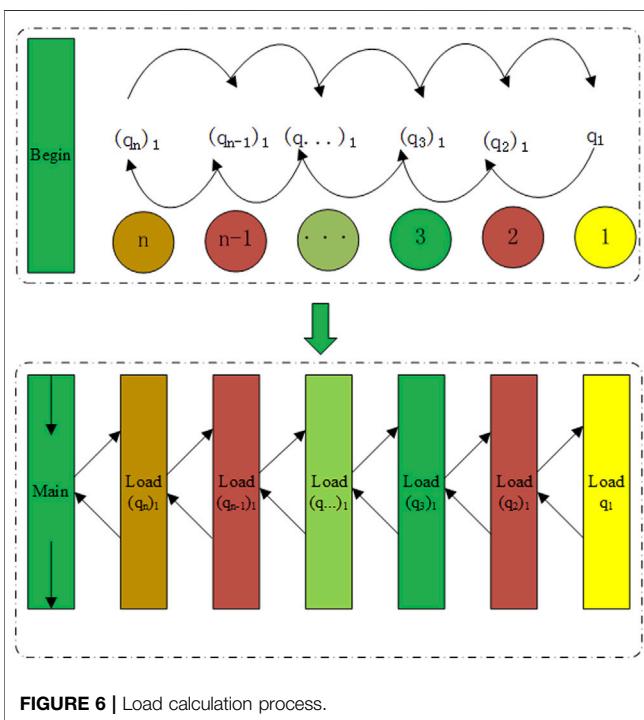


FIGURE 6 | Load calculation process.

Main Class Organization Structure

According to the above analysis, the main classes in program design include strata, input and output, calculation, and parameter adjustment. The C# language was used to define the classes, their attributes, and the methods in the Visual Studio 2015 compilation environment, and the logical calling relationship and organizational structure between classes was defined, as shown in Figure 4.

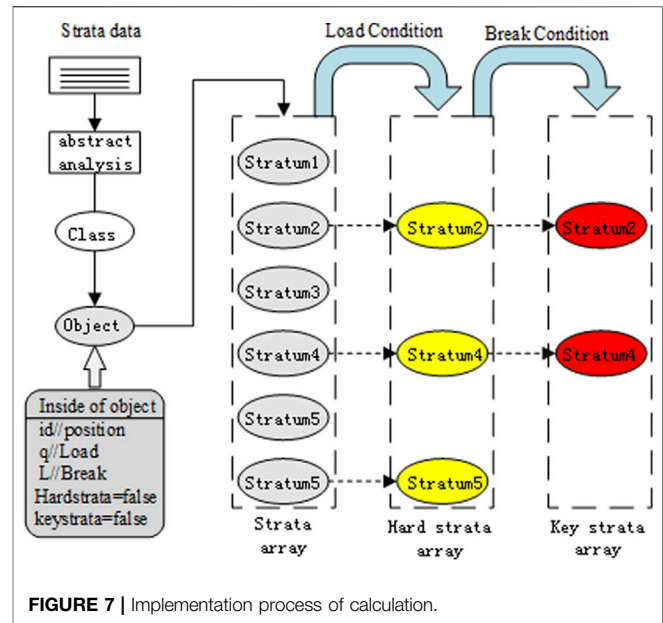


FIGURE 7 | Implementation process of calculation.

Algorithm Design

1) Principle analysis

For different strata positions, the overlying rock load needs to be calculated and then compared. Taking the stratum numbered 1 as an example, the number of load calculations is n , and the load calculation is shown in Figure 5.

When you need to calculate $(q_n)_1$, you need to calculate $(q_{n-1})_1$ first; and when you calculate $(q_{n-1})_1$, you need to calculate $(q_{n-2})_1$. The calculation process is shown in Figure 6.

2) Core algorithm design

The calculation of the load is a recursive calculation process because each recursion has to wait for the return of the following results. As the number of recursions increases, the time complexity and space complexity increase drastically. Therefore, a more efficient tail recursion algorithm is adopted, and the recursive iterative algorithm for the strata is designed according to the results of the above analysis. After the recursive iteration, the load of all the strata can be solved. Then all the hard rock strata in the array can be located according to the load judgment criterion.

After calculating the hard strata, the breaking condition is used to judge the key strata. According to the breaking condition, the judgment function of the key strata is designed. Then an infinite loop is used to traverse the hard rock strata and finally locate the key strata.

The class describing strata is constructed through object-oriented technology, and the strata objects are instantiated with the parameters of the real strata to map the strata in the physical world to the computer world. The recursive algorithm structure is used to decompose the complex strata data and is finally merged to realize the load calculation. Using the load and breaking distance conditions of the key strata theory, the final key strata position calculation can be realized through a simple cycle.

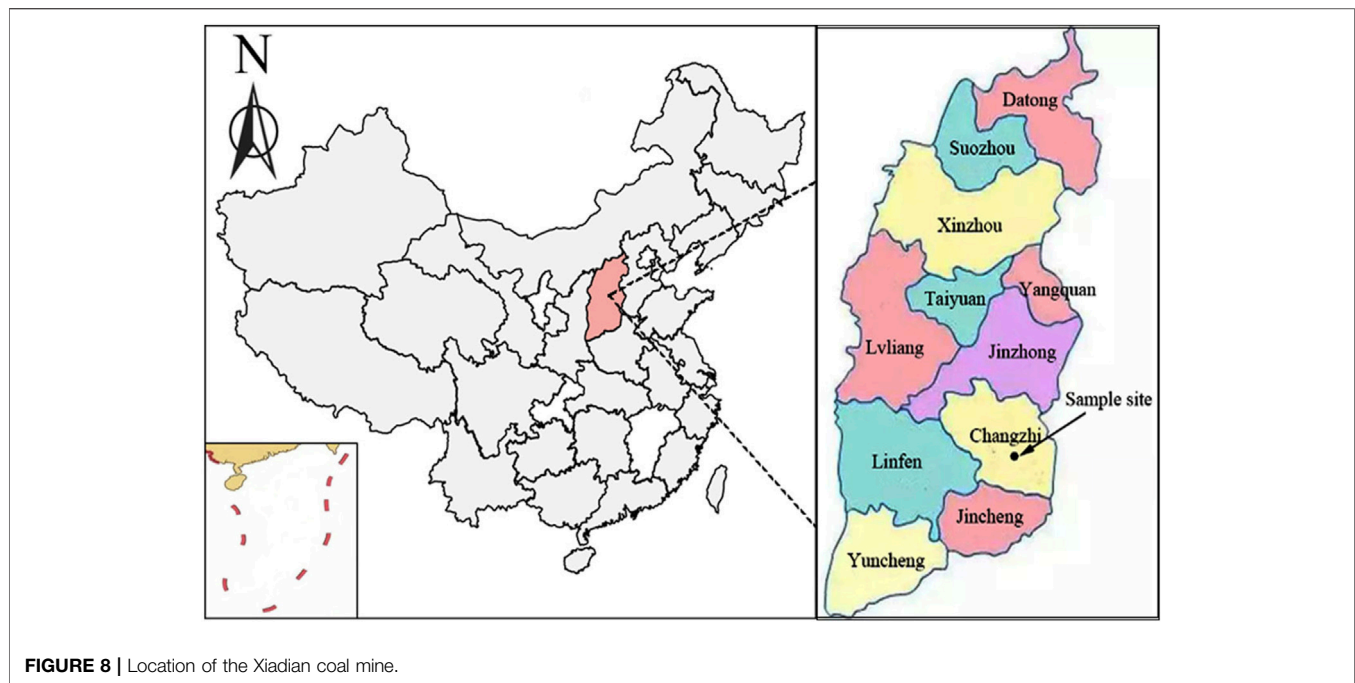


FIGURE 8 | Location of the Xiadian coal mine.

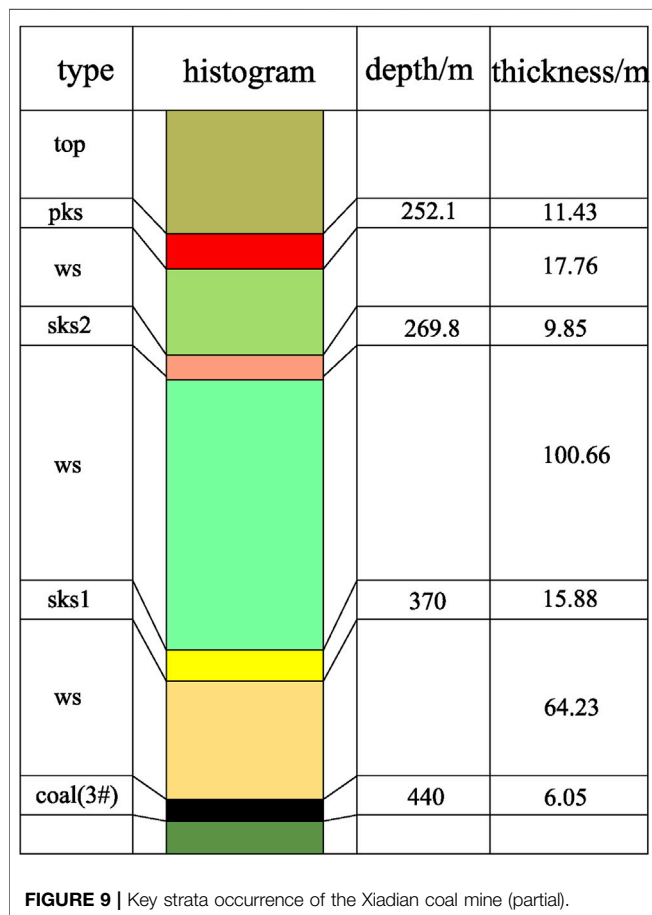


FIGURE 9 | Key strata occurrence of the Xiadian coal mine (partial).

The logic of the entire calculation process is clear and easy-to-understand and practice; the data are completely encapsulated and separated from the calculation, it has higher cohesion and low coupling, and it is more conducive to expansion and debugging. The implementation process is shown in **Figure 7**.

EXPERIMENT AND ANALYSIS

Accuracy Verification

In order to verify the accuracy and efficiency of the program, the Xiadian coal mine in Shanxi Province, China, was chosen as a case study, as shown in **Figure 8**. The key strata occurrence of the Xiadian coal mine is shown in **Figure 9**.

The input function of the program is used to import data in batches and calculate and adjust parameters. The user interacts with the program through the visual interface, and the calculation process is completely shielded from the user. The friendly interactive experience reduces the complicated repetitive calculation work and improves the efficiency of the key strata calculation.

In the verification of the key strata of the Xiadian coal mine, the program response and the calculation process are completely consistent with the design, and the calculation results are basically consistent with the original results, as shown in **Table 2**.

The borehole data of the Xiadian coal mine are calculated and compared with the actual situation of the key strata on-site, as shown in **Figure 10**. The calculation is basically consistent with field practice. The algorithm searches out more strata that meet the iterative conditions, and the calculated search height is increased by 164.05 m, approaching 22 strata.

Table 2 | Comparisons of program calculation and actual practical example.

Number	Lithology	Thickness h (m)	KS of xiadian	Program calculation
1	Sandstone	15.04	NOT	PKS
2	Siltstone	11.43	PKS	SKS
3	Sandstone	9.85	SKS	SKS
4	Siltstone	15.88	SKS	SKS

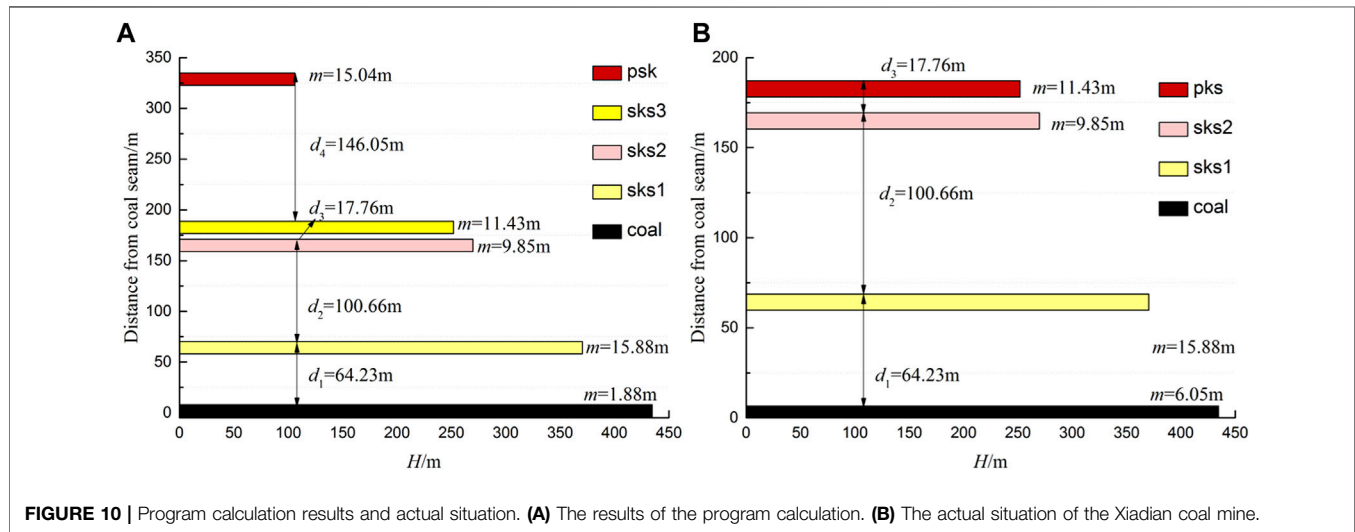


FIGURE 10 | Program calculation results and actual situation. (A) The results of the program calculation. (B) The actual situation of the Xiadian coal mine.

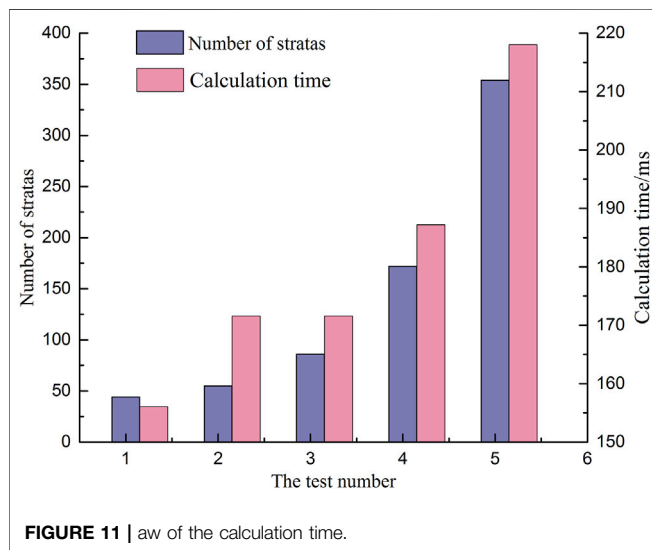


FIGURE 11 | Law of the calculation time.

The reasons for the difference between the calculation results and the field results are as follows.

- 1) The occurrence of KS, shown in **Figure 10**, is a comprehensive conclusion drawn from the theoretical analysis, numerical simulation, field practice, observation, and engineering work experience. This is a further optimization and application in preliminary theoretical calculations.

- 2) The method provided in this study can calculate all solutions stably and quickly; however, it cannot combine the actual mining situation and the working experience of engineers for further optimization analysis.

These are the main reasons why the calculation results are not exactly consistent with the field results. However, the method proposed in this study can calculate all solutions stably and efficiently, reduce the calculation time, improve the calculation efficiency, and assist researchers in making decisions. Therefore, it has a good application value.

Efficiency Analysis

In order to analyze the calculation efficiency and stability of the program, different amounts of strata data are imported for calculation and observation. When the number of strata is less than 100, the calculation time is approximately 175 ms. As the number of strata doubled, the calculation time increased. When the number of rock layers reaches about approximately 350, the calculation time is approximately 218 ms. The results show that the calculation time of the program does not increase drastically as the calculation data capacity increases, indicating that the calculation efficiency of the program will not be significantly reduced due to the increase in the amount of data. Therefore, the do-it-yourself program can complete the calculation task within an acceptable time. The law of the calculation time change is shown in **Figure 11**.

Table 3 | Efficiency comparison results.

Number	Number of stratas	Previous research example		Test of the paper
		Number of KS		Number of KS
1	11	3		3
2	10	8		8
3	14	3		3
4	16	14		14
5	68	61		61

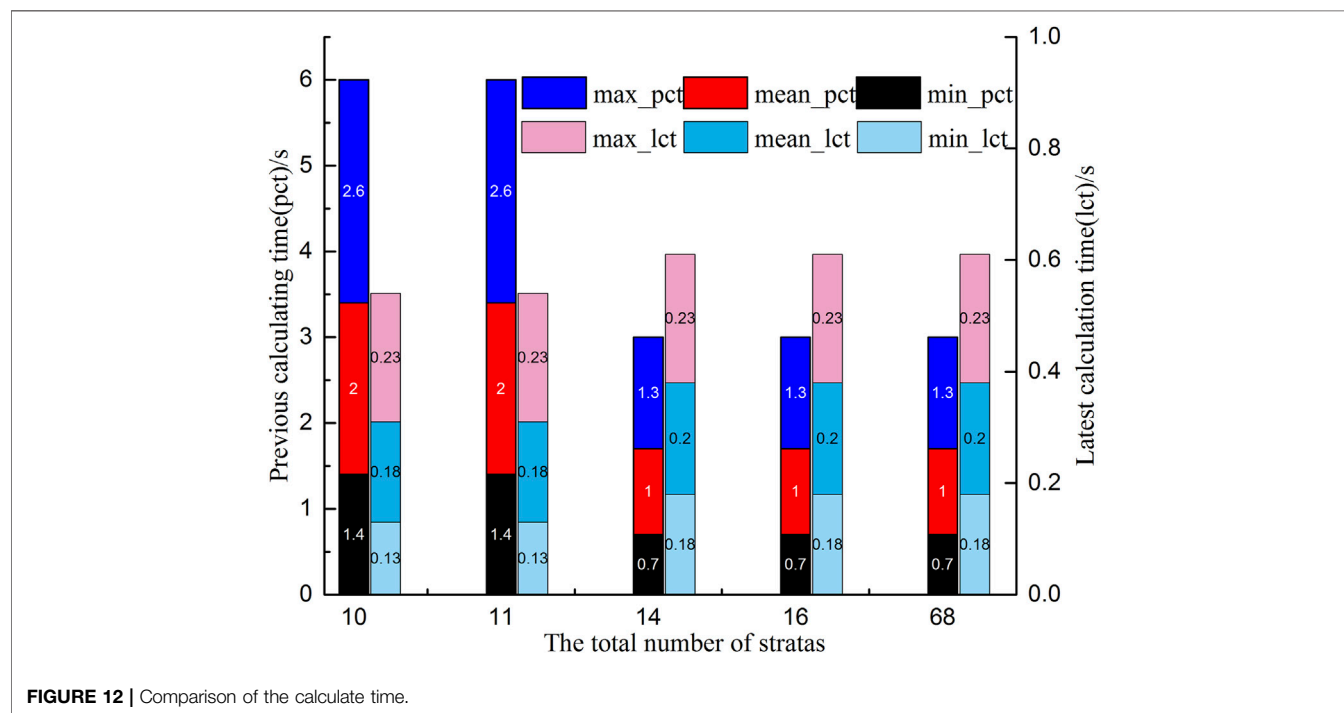


FIGURE 12 | Comparison of the calculate time.

DISCUSSION AND SUGGESTION

Discussion

The calculation of key strata is an important topic of strata movement control in coal mining. In this section, five previous cases were selected for testing, and the calculation efficiency was compared and analyzed to provide a reference for the optimization of the program (Xu and Qian, 2000; Xu and Ju, 2011).

Examples 1–5 are the calculation examples of the key strata. The comparison results in **Table 3** show that the calculation results of the method proposed in this study are basically consistent with previous conclusions. The comparison results of the calculation time are shown in **Figure 12**.

Figure 12 shows that the program designed by the method provided in this study improves the computational efficiency by approximately 5 times in terms of the maximum and average computational time, and by approximately three times in terms of the minimum computational time.

Suggestions

In recent years, problems such as environmental damage, water loss, and mining-out collapse caused by mining have gradually become prominent. On the basis of key strata theory, coal mining has achieved remarkable results in mining design, rock strata control, and post-mining goaf governance; however, there are a number of problems with the key strata calculation. The influence of mining conditions and the working experience of engineers are fuzzy and random, but they have an important influence on the calculation of key strata, which should be further studied and analyzed. The main recommendations are as follows:

- 1) It is necessary to construct a mining influence analysis system, comprehensively evaluate the influence of mining conditions on key strata, and establish a quantifiable influence coefficient to improve the precision of the calculation of key strata.
- 2) It is necessary to develop a fuzzy intelligent algorithm to analyze fuzzy concepts such as work experience, optimize the calculation conclusions of key strata, and improve the auxiliary decision-making ability.

CONCLUSION

Aiming at the problems of complex calculations, a lack of simplified algorithm models, difficult program development, low efficiency, and high costs in traditional KS judgments, this study proposes an object-oriented method combined with an improved recursive algorithm to realize the visual calculation of KS. In addition, object-oriented applications were developed and applied to the Xiadian coal mine, Shanxi, China, which proved the practicability and high efficiency of the method. The main conclusions are as follows:

- 1) The calculation principle of KS is abstractly analyzed, and an improved recursive algorithm structure is adopted to establish an algorithm model with a clear structure and good readability, which provides a clear and concise idea for efficient judgment of KS.
- 2) Object-oriented technology is used to extract and encapsulate the functional modules of KS computing and build a high-cohesion and low-coupling architecture to reduce the technical and time costs of program development.
- 3) The application program has been developed and applied to the Xiadian coal mine. The conclusion shows that the method has the ability to solve the KS stably and efficiently. However, this method makes efficient use of algorithms and program design skills to quickly calculate all solutions. It is difficult to

integrate factors such as on-site working conditions and engineers' experience. The calculation results need further evaluation and analysis. This is also a research direction that needs to be improved in the future.

DATA AVAILABILITY STATEMENT

The original contributions presented in the study are included in the article/Supplementary Material; further inquiries can be directed to the corresponding author.

AUTHOR CONTRIBUTIONS

CX: investigation, data curation, methodology, writing—original draft, algorithm design, and program development. KZ: funding acquisition, supervision, and methodology. XX: conceptualization, investigation, data curation, and writing—review and editing. YL: methodology.

FUNDING

This work was supported by the National Natural Science Foundation of China (Grant No. 51774323).

REFERENCES

- Ahmed, U., Petri, I., Rana, O., Raza, I., and Hussain, S. A. (2020). Federating Cloud Systems for Collaborative Construction and Engineering. *IEEE Access* 8, 79908–79919. doi:10.1109/access.2020.2990233
- Bai, E., Guo, W., Tan, Y., and Yang, D. (2018). The Analysis and Application of Granular Backfill Material to Reduce Surface Subsidence in China's Northwest Coal Mining Area. *Plos One* 13, e0201112. doi:10.1371/journal.pone.0201112
- Bai, E., Guo, W., and Tan, Y. (2019). Negative Externalities of High-Intensity Mining and Disaster Prevention Technology in China. *Bull. Eng. Geol. Environ.* 78, 5219–5235. doi:10.1007/s10064-019-01468-4
- Bai, E. H., Guo, W. B., Zhang, D. S., Tan, Y., Guo, M. J., and Zhao, G. B. (2019). Using the Magnetotelluric Method for Detecting Aquifer Failure Characteristics under High-Intensity Mining of Thick Coal Seams. *Energies* 12, 4397. doi:10.3390/en12224397
- Brykov, M. N., Petryshynets, I., Pruncu, C. I., Efremenko, V. G., Pimenov, D. Y., Giasin, K., et al. (2020). Machine Learning Modelling and Feature Engineering in Seismology Experiment. *Sensors-Basel* 20, 4228. doi:10.3390/s20154228
- Chen, G. L., Rui, X. T., Gu, J. J., Zeng, X. Y., and Liu, X. B. (2020). Development of an Object-Oriented Framework for the Vibration Characteristic Computation of Multibody Systems. *Adv. Eng. Softw.* 148, 102874. doi:10.1016/j.advengsoft.2020.102874
- Chen, L., Zhang, F. W., Yao, H. C., Han, Z. T., Qian, L., Chen, L., et al. (2015). Using of Key Stratum Theory to Study the Structural Development of Roof Aquifer. *Acta Geol. Sin. Engl.* 89 (6), 2091. doi:10.1111/1755-6724.12623
- Cheng, J., Liu, F., and Li, S. (2017). Model for the Prediction of Subsurface Strata Movement Due to Underground Mining. *J. Geophys. Eng.* 14, 1608–1623. doi:10.1088/1742-2140/aa8238
- Cheng, J., Zhang, X., and Ghosh, A. (2017). Explosion Risk Assessment Model for Underground Mine Atmosphere. *J. Fire Sci.* 35 (1), 21–35. doi:10.1177/0734904116676495
- Cheng, J., Zhao, G., Feng, G., and Li, S. (2020). Characterizing Strata Deformation over Coal Pillar System in Longwall Panels by Using Subsurface Subsidence Prediction Model. *Eur. J. Environ. Civil Eng.* 24 (5), 650–669. doi:10.1080/19648189.2017.1415981
- Cheng, J., Zhao, G., and Li, S. (2018). Predicting Underground Strata Movements Model with Considering Key Strata Effects. *Geotech. Geol. Eng.* 36, 621–640. doi:10.1007/s10706-017-0307-8
- Ge, L., Li, D., Huang, Q., Tian, G., Wei, G., and Ahmed, J. (2020). Electrodes Optimization of an Annular Flow Electromagnetic Measurement System for Drilling Engineering. *IEEE Access* 8, 138481–138492. doi:10.1109/access.2020.3011935
- Gong, P. L., Zhao, T., Yetilmezsoy, K., and Yi, K. (2020). Sliding Instability Characteristics and Re-stabilization Mechanism of Key Stratum in Thin-Topsoil SCS Mining: a Computer-Aided Case Study from the Niushan Coal Mine, China. *Environ. Earth Sci.* 79 (1), 1–7. doi:10.1007/s12665-019-8691-4
- Gu, J.-D. (2018). Mining, Pollution and Site Remediation. *Int. Biodeterior. Biodegr.* 128, 1–2. doi:10.1016/j.ibiod.2017.11.006
- Hamouda, S., Edwards, S. H., Elmongui, H. G., Ernst, J. V., and Shaffer, C. A. (2020). BTRecurTutor: a Tutorial for Practicing Recursion in Binary Trees. *Comput. Sci. Educ.* 30, 216–248. doi:10.1080/08993408.2020.1714533
- Jiang, J. Q., Zhang, P. P., Qin, G. P., and Xu, B. (2015). Analysis of Destabilized Fracture and Microseismic Activity of High-Located Main Key Strata. *Rock Soil Mech.* 36 (12), 3567–3576. doi:10.16285/j.rsm.2015.12.029
- Leng, S., Lin, J.-R., Hu, Z.-Z., and Shen, X. (2020). A Hybrid Data Mining Method for Tunnel Engineering Based on Real-Time Monitoring Data from Tunnel Boring Machines. *IEEE Access* 8, 90430–90449. doi:10.1109/access.2020.2994115
- Li, L. P., Zhou, Z. Q., Li, S. C., Xue, Y. G., Xu, Z. H., and Shi, S. S. (2015). An Attribute Synthetic Evaluation System for Risk Assessment of Floor Water Inrush in Coal Mines. *Mine Water Environ.* 34, 288–294. doi:10.1007/s10230-014-0318-0
- Li, Z., Xu, J., Ju, J., Zhu, W., and Xu, J. (2018). The Effects of the Rotational Speed of Vissous Beam Structures Formed by Key Strata on the Ground Pressure of Stopes. *Int. J. Rock Mech. Mining Sci.* 108, 67–79. doi:10.1016/j.ijrmms.2018.04.041
- Liang, D.-x., Jiang, Z.-q., and Guan, Y.-z. (2015). Field Research: Measuring Water Pressure Resistance in a Fault-Induced Fracture Zone. *Mine Water Environ.* 34, 320–328. doi:10.1007/s10230-014-0323-3
- Liang, Y. P., Li, B., and Zou, Q. L. (2019). Movement Type of the First Subordinate Key Stratum and its Influence on Strata Behavior in the Fully

- Mechanized Face with Large Mining Height. *Arab J. Geosci.* 12 (2). doi:10.1007/s12517-018-4208-9
- Lin, G., Jiang, D., Fu, J., Dong, D., Sun, W., and Li, X. (2020). Spatial Relationships of Water Resources with Energy Consumption at Coal Mining Operations in China. *Mine Water Environ.* 39, 407–415. doi:10.1007/s10230-020-00663-0
- Lin, G., Zhoumo, Z., Xinjing, H., Mingze, L., Hao, F., Jian, L., et al. (2020). Low-Cost and High-Efficiency Method for Detecting Vertical Bends of Subsea Pipelines. *IEEE Access* 8, 33926–33933. doi:10.1109/access.2020.2974405
- Lin, Y., Zhou, K., and Li, J. (2018). Prediction of Slope Stability Using Four Supervised Learning Methods. *IEEE Access* 6, 31169–31179. doi:10.1109/access.2018.2843787
- Lopes, M. S., Saldanha, D. L., and Veettil, B. K. (2021). Object-Oriented and Fuzzy Logic Classification Methods for Mapping Reforested Areas with Exotic Species in Rio Canoas State Park–Santa Catarina, Brazil. *Environ. Dev. Sustain.* 23 (1). doi:10.1007/s10668-020-00946-0
- Lv, Z., Liu, T., and Benediktsson, J. A. (2020). Object-Oriented Key Point Vector Distance for Binary Land Cover Change Detection Using VHR Remote Sensing Images. *IEEE Trans. Geosci. Remote Sensing* 58, 6524–6533. doi:10.1109/tgrs.2020.2977248
- Ma, D., Mao, X. B., Li, C., and Du, F. (2012). Boundary Integral Computation of Elastic Water Resisting Key Strata Under the Condition of Discontinuous Load. *Comp. Model. Eng. Sci.* 83 (6), 561–574. doi:10.1016/j.mssp.2011.05.010
- Ma, K., Yin, L. M., Chen, J. T., Chen, M., Wang, Z. Q., and Cui, B. Q. (2018). Theoretical Analysis on Failure of Water-Resisting Key Strata in the Floor by Local High Confined Water in Deep Mining. *Rock Soil Mech.* 39 (9), 3213–3223. doi:10.16285/j.rsm.2017.1176
- Prajapati, A., and Chhabra, J. K. (2020). Information-Theoretic Remodularization of Object-Oriented Software Systems. *Inf. Syst. Front.* 22, 863–880. doi:10.1007/s10796-019-09897-y
- Qian, M. G., Miao, X. X., and Xu, J. L. (1996). Key Strata Theory in Strata Control. *J. China Coal Soc.* 03, 2–7.
- Rakic, G., Toth, M., and Budimac, Z. (2020). Toward Recursion Aware Complexity Metrics. *Inform. Softw. Tech.* 118, 106203. doi:10.1016/j.infsof.2019.106203
- Santana, C. S., Montalván Olivares, D. M., Silva, V. H. C., Luzardo, F. H. M., Velasco, F. G., and de Jesus, R. M. (2020). Assessment of Water Resources Pollution Associated with Mining Activity in a Semi-arid Region. *J. Environ. Manage.* 273, 111148. doi:10.1016/j.jenvman.2020.111148
- Sarpong, D., Ofori, G., Botchie, D., and Clear, F. (2020). Do-it-yourself (DiY) Science: The Proliferation, Relevance and Concerns. *Technol. Forecast. Soc. Change* 158, 120127. doi:10.1016/j.techfore.2020.120127
- Shi, B. Q., and Zhang, J. (2013). Key Protecting Strata Criterion of Water Conservation Mining and its Application. *Construction Urban Plann.* 1–4, 671–674. doi:10.4028/www.scientific.net/amr.671-674.2621
- Silva, V. M., and Lizardi-Jimenez, M. A. (2020). Environmental Problems and the State of Compliance with the Right to a Healthy Environment in a Mining Region of Mexico. *Int. J. Chem. React. Eng.* 18 (7), 228–237. doi:10.1515/ijcre-2019-0179
- Sun, Q., Zhang, J. X., Li, M., and Zhou, N. (2020). Experimental Evaluation of Physical, Mechanical, and Permeability Parameters of Key Aquiclude Strata in a Typical Mining Area of China. *J. Clean. Prod.* 267, 122109. doi:10.1016/j.jclepro.2020.122109
- Van Hien, N., Truong, V., and Bui, N. T. (2020). An Object-Oriented Systems Engineering Point of View to Develop Controllers of Quadrotor Unmanned Aerial Vehicles. *Int. J. Aerospace Eng.* 2020, 1–17. doi:10.1155/2020/8862864
- Wang, Y. G., Guo, W. B., Bai, E. H., and Wang, Y. X. (2020). Key Strata Identification of Overburden Based on Magnetotelluric Detection: A Case Study. *Appl. Sci.-basel* 10, 558. doi:10.3390/app10020558
- Wu, Q., Zhou, W., Wang, J., and Xie, S. (2009). Prediction of Groundwater Inrush into Coal Mines from Aquifers Underlying the Coal Seams in China: Application of Vulnerability index Method to Zhangcun Coal Mine, China. *Environ. Geol.* 57, 1187–1195. doi:10.1007/s00254-008-1415-9
- Xie, J.-L., and Xu, J.-L. (2017). Effect of Key Stratum on the Mining Abutment Pressure of a Coal Seam. *Geosci. J.* 21, 267–276. doi:10.1007/s12303-016-0044-7
- Xu, J. L., and Ju, J. (2011). Structural Morphology of Key Stratum and its Influence on Strata Behaviors in Fully-Mechanized Face with Super-large Mining Height. *J. China Coal Soc.* 30 (8), 1547–1556. doi:10.1007/s12583-011-0163-z
- Xu, J. L., and Qian, M. G. (2000). Method to Distinguish Key Strata in Overburden. *J. China Univ. Mining Technol.* 29, 463–467. doi:10.3321/j.issn:1000-1964.2000.05.005
- Xu, J. L., Wu, P., and Zhu, W. B. (2000). The Computer Realization of the Key Strata Discrimination Method. *Ground Press. Strata Contro* 17, 29–31.
- Yoon, J., Vonortas, N. S., and Han, S. W. (2020). Do-It-Yourself Laboratories and Attitude toward Use: The Effects of Self-Efficacy and the Perception of Security and Privacy. *Technol. Forecast. Soc. Change* 159, 120192. doi:10.1016/j.techfore.2020.120192
- Zhang, T., Gan, Q., Zhao, Y., Zhu, G., Nie, X., Yang, K., et al. (2019). Investigations into Mining-Induced Stress-Fracture-Seepage Field Coupling Effect Considering the Response of Key Stratum and Composite Aquifer. *Rock Mech. Rock Eng.* 52, 4017–4031. doi:10.1007/s00603-019-01811-x
- Zhang, X. G., Lin, J., Liu, J. X., Li, F., and Pang, Z. Z. (2017). Investigation of Hydraulic-Mechanical Properties of Paste Backfill Containing Coal Gangue-Fly Ash and its Application in an Underground Coal Mine. *Energies* 10, 1309. doi:10.3390/en10091309
- Zhang, Y., Cao, S. G., Zhang, N., and Zhao, C. Z. (2020). The Application of Short-wall Block Back Fill Mining to Preserve Surface Water Resources in Northwest China. *J. Clean. Prod.* 261, 121232. doi:10.1016/j.jclepro.2020.121232
- Zhu, D., Chen, T., Zhen, N., and Niu, R. (2020). Monitoring the Effects of Open-Pit Mining on the Eco-Environment Using a Moving Window-Based Remote Sensing Ecological index. *Environ. Sci. Pollut. Res.* 27, 15716–15728. doi:10.1007/s11356-020-08054-2
- Zhu, W., Xu, J., Xu, J., Chen, D., and Shi, J. (2017). Pier-column Backfill Mining Technology for Controlling Surface Subsidence. *Int. J. Rock Mech. Mining Sci.* 96, 58–65. doi:10.1016/j.ijrmms.2017.04.014

Conflict of Interest: The authors declare that the research was conducted in the absence of any commercial or financial relationships that could be construed as a potential conflict of interest.

The reviewer JC declared a shared affiliation with one of the authors, YL, to the handling editor at time of review.

Publisher's Note: All claims expressed in this article are solely those of the authors and do not necessarily represent those of their affiliated organizations, or those of the publisher, the editors, and the reviewers. Any product that may be evaluated in this article, or claim that may be made by its manufacturer, is not guaranteed or endorsed by the publisher.

Copyright © 2021 Xu, Zhou, Xiong and Lu. This is an open-access article distributed under the terms of the Creative Commons Attribution License (CC BY). The use, distribution or reproduction in other forums is permitted, provided the original author(s) and the copyright owner(s) are credited and that the original publication in this journal is cited, in accordance with accepted academic practice. No use, distribution or reproduction is permitted which does not comply with these terms.



Experimental Study on Gangue Backfilling Materials Improved by Soda Residue and Field Measurement of Surface Subsidence

Wei Yin^{1,2*}, Kun Zhang^{1,2}, Shenyang Ouyang³, Xiaomin Bai⁴, Wenjie Sun¹ and Jingru Zhao¹

¹The Key Laboratory for Traffic and Transportation Security of Jiangsu Province, Huaiyin Institute of Technology, Huaian, China,

²Huai'an Zhongbo Traffic Safety Technology Co., Ltd, Huaian, China, ³School of Mines, China University of Mining and Technology, Xuzhou, China, ⁴Faculty of Mechanical and Material Engineering, Huaiyin Institute of Technology, Huaian, China

OPEN ACCESS

Edited by:

Qingsheng Bai,
Freiburg University of Mining and
Technology, Germany

Reviewed by:

Di Wu,
University of Science and Technology
Beijing, China
Mohammed Ashfaq,
National Institute of Technology
Warangal, India

*Correspondence:

Wei Yin
yinweihiyt@163.com

Specialty section:

This article was submitted to
Geohazards and Georisks,
a section of the journal
Frontiers in Earth Science

Received: 26 July 2021

Accepted: 19 October 2021

Published: 23 November 2021

Citation:

Yin W, Zhang K, Ouyang S, Bai X,
Sun W and Zhao J (2021) Experimental
Study on Gangue Backfilling Materials
Improved by Soda Residue and Field
Measurement of Surface Subsidence.
Front. Earth Sci. 9:747675.
doi: 10.3389/feart.2021.747675

In coal mining, the problems of massive discharge of solid waste, environmental pollution, and surface subsidence disaster are urgent to be solved. Based on this engineering background, the feasibility of using solid waste soda residue to improve gangue cemented backfilling material was discussed, and the surface subsidence of the test working face was measured in this study. Besides, the influence of soda residue on the performance of gangue cemented backfilling materials was analyzed through laboratory tests. The experimental results show that 1) as the content of soda residue increases within the range of 0–12%, the slump of the soda residue gangue backfilling material (SRGBM) slurry gradually increases, and the bleeding rate increases. The early strength and later strength of SRGBM increase first and then decrease with the increase in soda residue content. 2) The optimal ratio of the soda residue cemented backfilling material is soda residue: fly ash: lime: cement: gangue = 6%: 34%: 10%: 2.5%: 47.5%. Compared with the reference group, the slump of the material is increased by 12.7%, the bleeding rate is only 3.8%, and the early strength and later strength are increased by 449 and 187%, respectively. 3) The addition of soda residue promotes the hydration reaction of the slurry system of soda residue cemented materials. The coexistence of C-S-H gel and N-A-S-H gel reduces the connectivity of pores and improves the strength of the material. 4) The maximum surface subsidence of the test working face is only 245 mm, and the surface subsidence control effect is good. Therefore, the preparation of SRGBM with soda residue can achieve energy saving and emission reduction, with significant technical, economic, and social benefits, and has good promotion and application value.

Keywords: soda residue, cemented fill mining, transport property, mechanical properties, strength mechanism, surface subsidence

INTRODUCTION

Coal is the basic energy in China. However, the traditional caving mining method causes surface collapse disaster in a large area and solid waste discharge of gangue, which seriously damages the ecological environment of mining areas (Zhang et al., 2020; Ma et al., 2021a). Statistically, about 795 million tons of solid waste gangue is discharged annually in China, and about $6.56 \times 10^8 \text{ m}^2$ of land subsidence is caused (He et al., 2015), which severely restricts the sustainable development of mines

in China. Cemented fill mining has the advantages of surface subsidence reduction, gangue emission reduction, and environmental protection and has become the core technology of green mining systems (Martin And Holger, 2013; Deng et al., 2020; Meng et al., 2017). Cemented backfilling can be divided into low-concentration tailings cemented backfilling, high-concentration full-tailings cemented backfilling (Zhao et al., 2011), high water quick setting tailings cemented backfilling (Guangming et al., 2010), paste cemented backfilling (Zhou et al., 2019), and waste rock cemented backfilling (Li et al., 2020a; Liu et al., 2020; Meng et al., 2020). Backfilling material (Ma et al., 2019a) is the key to cemented backfilling, and the material cost accounts for more than 40% of the backfilling cost (Liu et al., 2021). The gangue-based cemented backfilling mainly composed of gangue and fly ash (solid waste) has been widely applied (Cui and Henghu, 2010; Wang et al., 2019; Ran et al., 2020). Studies on the performance of gangue-based cemented materials (including slump, diffusivity, rheological properties, setting time, compressive strength, shear strength, and material mix proportion) have been widely performed (Li et al., 2020b; Yin et al., 2020a; Yin et al., 2020b). With the development of deep mining (Ma et al., 2021b), the mining environment of high ground stress and high ground temperature is frequently encountered; the proper disposition of bulk solid waste and cost reduction of backfilling materials are urgently required (Zhang et al., 2018). Consequently, higher requirements are put forward for the performance of cemented backfilling materials and cost control of backfilling mining (Ma et al., 2020a).

Soda, renowned as “the mother of chemical industry,” has been widely used in construction, chemical industry, textile, and other industries. The output of soda ash in China ranks first in the world, mainly based on the ammonia-soda process (Song et al., 2019). According to statistics, 0.3–0.6 t solid waste of soda residue is discharged for every 1 t of soda ash produced (Sun et al., 2012). Due to the high alkalinity and high chloride ion content of soda residue, the traditional ground discharge method not only occupies a large number of land resources but also causes soil salinization (Yang et al., 2017a). From the perspective of environmental protection and land resource utilization, the scientific treatment of solid waste soda residue has become a problem faced by salt chemical enterprises (Hulisz and Piernik, 2013; Yang et al., 2017b). Mitchell (Mitchell, 1993) in Japan mixed soda residue with fly ash to make engineering soil for road reclamation. Xu Dong et al. (Xu et al., 2020) used soda residue, slag, steel slag, and desulfurization gypsum as composite cementing materials, tailings sand, and waste rock as aggregates to prepare clinker-free concrete. Yan Shuwang (Yan et al., 2006) mixed soda residue and calcium ash in a certain proportion and made soda residue soil for site backfilling. Morgan (Morgan, 1996) and Huang Lanfen (Lanfen et al., 2014) used the alkalinity of soda residue to improve acid soil. Yang Jiujun (Yang et al., 2010) used soda residue as an admixture to partially replace fly ash for the preparation of building mortar. The above utilization method consumes the solid waste of soda residue to a certain extent. However, due to the low strength of soda residue itself and the existence of chloride in soda residue,

the phenomenon of spreading soda and corrosion of steel bar appears in the engineering (Ma et al., 2020b). Consequently, the existing soda residue treatment methods hardly meet the comprehensive requirements of the project on bearing capacity, anti-deformation, environmental protection, and large-scale treatment at the same time (Ma et al., 2019b).

Research has found that soda residue contains alkalinity (Tian and Li, 2009) and a large number of CaCO_3 , Ca(OH)_2 , and other components, which can be used to improve the performance of cement concrete to a certain extent (Tan et al., 2018). Due to the non-chlorine corrosion of the filling body (no reinforcement is used inside the backfill) and the rising price of fly ash, the technical idea of using soda residue to replace part of fly ash and preparing soda residue gangue backfilling material (SRGBM) is germinated. In this study, the basic characteristics of soda residue, gangue, fly ash, and other raw materials were tested, and SRGBM with different soda residue contents was prepared. The slump, bleeding rate, and uniaxial compressive strength of SRGBM at different ages were analyzed. The influence of soda residue content on the flow performance and mechanical properties of SRGBM was investigated, and the strength formation mechanism of SRGBM was explored. The proposed SRGBM was applied to engineering in the test mine, and the surface subsidence measurement was performed to verify the control effect of SRGBM on the surface subsidence of the mining area. This study provides a reference for the large-scale resource treatment of solid waste soda residue and the development and performance improvement of new cemented backfilling materials.

GANGUE CEMENTED FILL MINING AND PERFORMANCE INDEX

Technical Principle

In the gangue cemented fill mining, gangue is used as an aggregate, and the additives (such as fly ash) and cementing materials (such as cement, lime) are added. Then, water is added in the ground or underground mixing station to obtain paste slurry by mixing. Subsequently, the slurry is transported to the underground goaf by gravity or backfilling pump through the transportation channel such as drilling or pipeline, and then the excess water is removed from the slurry in the goaf (or dehydration is omitted). After the slurry solidifying strength is improved, the slurry is used to support the surrounding rock, fill the goaf, and control the overburden movement and surface deformation. The principle of gangue cemented fill mining technology is shown in **Figure 1**.

Performance Index Analysis of Soda Residue Gangue Backfilling Material

SRGBM is formed by gangue with certain gradation, lime, cement, fly ash, and other materials mixed with water. As the main bearing body of goaf, the cemented backfilling materials go through the flowing state and solidification state of the slurry. The ideal SRGBM needs to have two core indexes of good transport property and mechanical property at the same time. In addition, it should also meet the requirements of wide sources, low cost, and no contaminants in engineering.

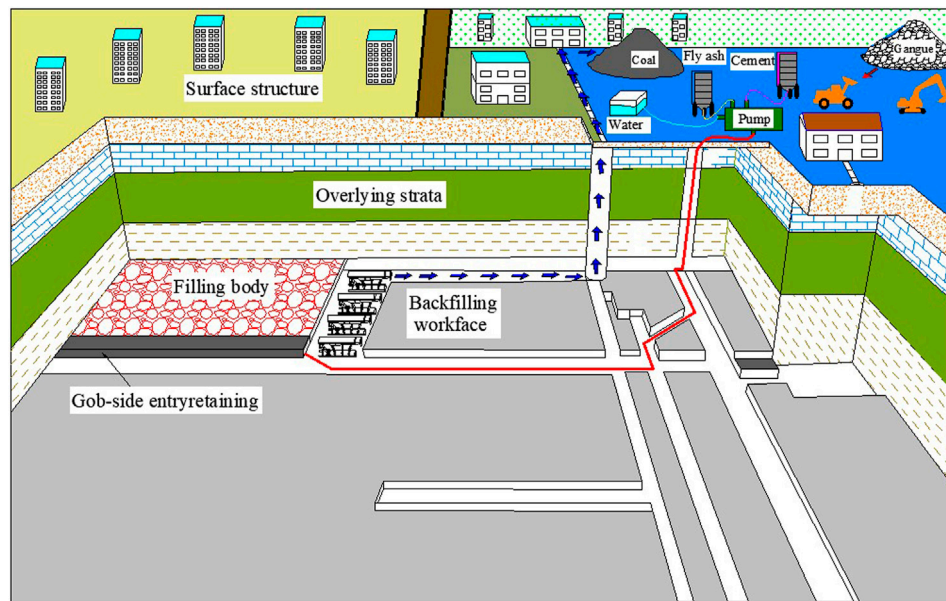


FIGURE 1 | Technical principle of cemented fill mining.

Transport Properties

Slump

The transport property determines the difficulty and effect of transportation of backfilling slurry to the underground goaf. A poor transport property will lead to plugging of the backfilling pipeline. Slump directly reflects the workability, fluidity, and pump ability of cemented backfilling materials (Yu et al., 2016), which is usually used as a direct index to evaluate the transport property of the backfilling slurry. Engineering practice has proved that the slump of the backfilling slurry meeting the transportation requirements should not be less than 100 mm, and it has good transport properties when the slump is 120–200 mm (Shenyang, 2019).

Bleeding Rate

Bleeding rate is another index to measure the transport property of the backfilling slurry, which reflects the water retention and segregation degree of slurry. The larger the bleeding rate, the more serious the slurry segregation and the worse the transport property. Consequently, pipe plugging can be easily caused in the pumping process. Besides, the cement and other fine particles in the slurry can be easily brought out during the bleeding process, which reduces the strength of the material in the later stage (Wang et al., 2014). The practice has shown that the bleeding rate of the backfilling slurry meeting the requirements of transport property should be less than 5% (Shenyang, 2019).

Mechanical Properties

The mechanical properties of the backfilling materials determine the controlling effect of the filling body on the overburden after solidification. The higher the mechanical strength of backfilling materials, the stronger the bearing capacity of the filling body. According to the function of the cemented filling body in

different periods of goaf, the mechanical properties can be divided into early strength and later strength.

Early Strength

During the backfilling mining, cemented backfilling materials must be self-supporting without collapse after backfilling into goaf. Therefore, SRGBM needs to have early strength, that is, the strength required for the filling body to maintain self-supporting at the early stage. Although the early strength requirement is not high, it is of great significance for backfilling mining. The early strength design methods include the empirical formula and Thomas model (Wang, 2019). Considering the actual backfilling technology in a coal mine, the unconfined compressive strength (UCS) of the filling body at the curing age of 1 day is selected as the early strength index. The relationship between the early strength and the backfilling height of the goaf is shown in the following equation:

$$h^2 = k\sigma_z^3, \quad (1)$$

where h is the height of the filling body, m; k is the empirical coefficient of early strength, and $k=600$ generally; and σ_z is the early strength of the cemented filling body, MPa.

Later Strength

With the internal hydration reaction of the cemented backfilling slurry, the strength of the cemented filling body gradually increases and finally tends to be stable. In the goaf, the filling body is used to support the overburden, and the strength at the curing age of 28 days is generally taken as the later strength in the research. In this study, the control of surface subsidence is taken as the backfilling target. If the strength of the filling body needs to control the main key strata of overburden without breaking, then the later strength of the filling body needs to control the weight of

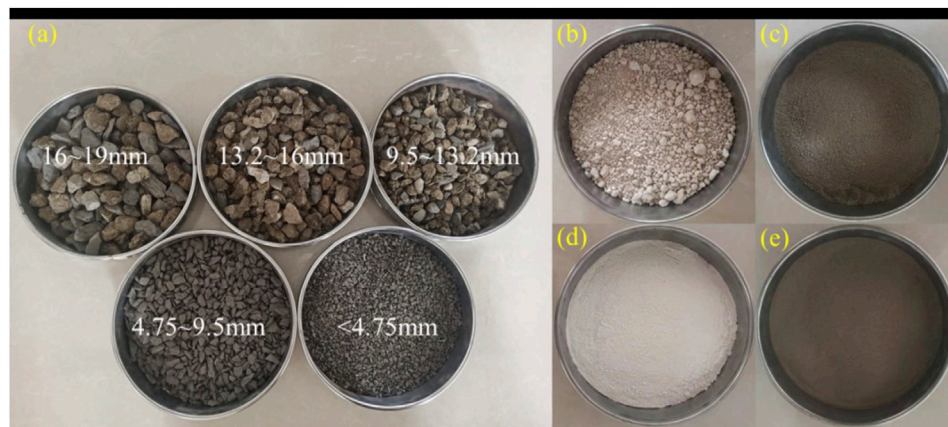


FIGURE 2 | Composition materials of SRGBM: (A) gangue, (B) soda residue, (C) fly ash, (D) lime, and (E) cement.

rock strata between the immediate roof and the main key strata. The later strength calculation is shown in the following equation:

$$\sigma_h = a \sum_{i=1}^n r_i h_i, \quad (2)$$

where σ_h is the later strength of cemented filling body, MPa; n is the number of strata between the direct roof of overburden and the main key strata; h_i is the thickness of the i th layer, m; r_i is the unit weight of the i th layer, MN/m³; and a is the safety factor of later strength, ranging from 1.1 to 1.4.

MATERIALS AND METHODS

Materials

The original gangue-based cemented backfilling material used in the test mine was taken as the reference group. The mix proportion of raw materials in the reference group was gangue: fly ash: cement: lime = 47.5%: 40%: 10%: 2.5%, and the mass concentration of the slurry was 84%. In recent years, there is a supply tension of fly ash in the market, and the price of fly ash is rising gradually. In this study, the technical idea of using soda residue to replace fly ash was proposed. Based on the reference group, SRGBM was prepared by replacing fly ash with soda residue in proportion. **Figure 2** shows the actual photos of raw materials.

Soda Residue

The test soda residue was taken from Huai'an Soda Plant. The fresh soda residue was a gray sticky paste with a pungent smell and strong corrosion. The soda residue was dried by natural air drying, and the moisture content, pH value, liquid plastic limit, UCS, and other basic parameters of the air-dried soda residue were tested according to Test Methods of Soils for Highway Engineering (JTG E40-2007). The chemical composition of soda residue was analyzed by XRF tests. **Table 1** shows basic physical and mechanical parameters and chemical components of soda residue.

The moisture content of soda residue was 89.95%, the pH value was 9.2, and it was alkaline. The plasticity index was 29.53, belonging to high liquid limit clay. The UCS value of soda residue was only 0.20 MPa, indicating the low strength of soda residue. The scanning electron microscope (SEM) was used to scan the internal structure of air-dried soda residue. **Figure 3** shows the internal structure under different magnifications. Based on the analysis, the soda residue was a porous aggregate structure. It was inferred that the material skeleton of soda residue was mainly formed by CaCO₃, and the single-particle size was about 2–5 μm. The particles were cemented with each other to form aggregates. Due to the main point contact of particles, the cementation of the soda residue was weak. The surface of the aggregate structure was rough, and there were many pores of different sizes on the surface and inside of particles, resulting in the high water content and large bearing deformation in a natural state.

Gangue

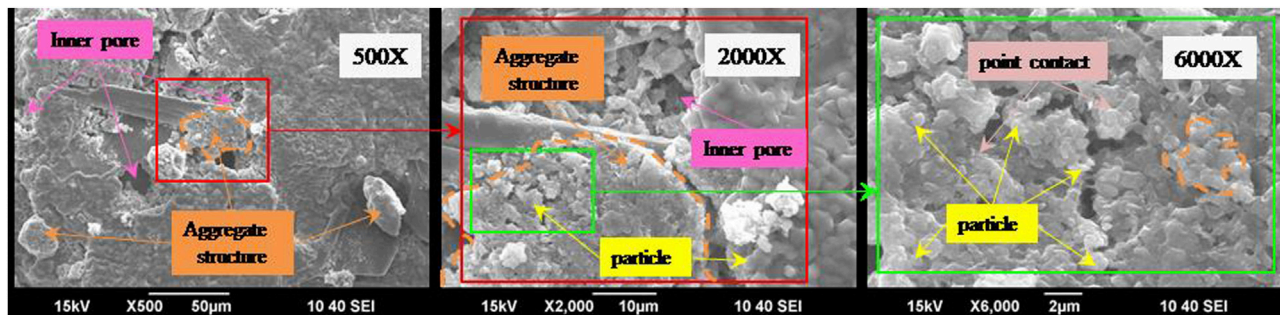
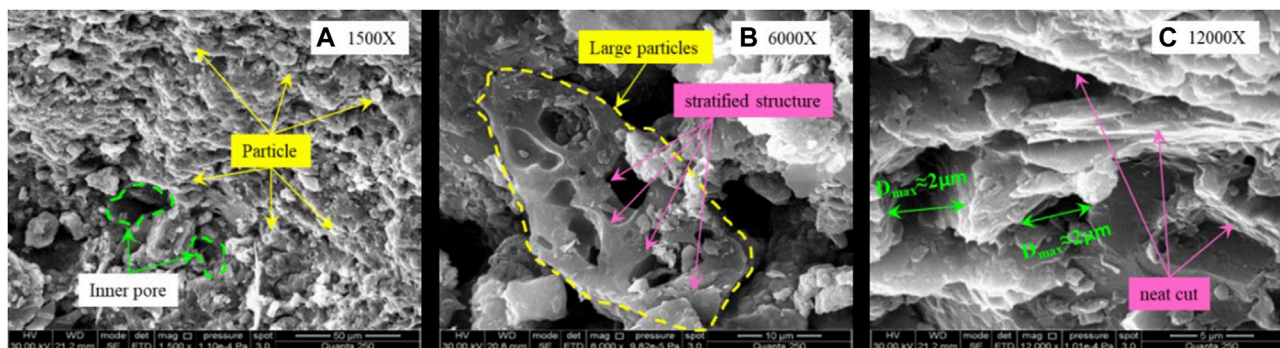
The test gangue was taken from the washing gangue of the coal preparation plant. The natural moisture content of the gangue was 6.7% and the density was 1.9 g/cm³. The gangue was ground into a powder specimen and tested by a D/max-3B X-ray diffractometer. The main components of gangue are quartz and kaolinite, and the total amount of both is more than 70%; there are also some illite and illite/smectite formations, amorphous materials, and a small number of other minerals.

Gangue has a high content of SiO₂ and can act as the material skeleton, contributing to better deformation resistance of backfilling materials. Besides, gangue also contains carbon, aluminum, and Cao, which is easy to react with fly ash. **Figure 4** shows the SEM micrographs of the internal structure of gangue under different resolution conditions.

According to **Figure 4A**, there are many holes on the surface of gangue, the surface joints and fissures are developed, the coarse and fine particles are cemented with each other, there are obvious edges and corners at the end of the particles, and the fracture is flat. After magnification of 6000 times (**Figure 4B**), the micro-layered structure of fractures can be clearly found; the rock specimens are stacked in sheets, and the sheets are

TABLE 1 | Physical and mechanical parameters and chemical composition of soda residue.

Physical and mechanics parameters				Chemical component/%					
No	Item	Value	Unit	No	Compositions	Content	Number	Compositions	Number
1	Moisture content	89.95	%	1	CaO	52.25	6	MgO	2.33
2	PH	9.2	-	2	SO ₃	16.97	7	Al ₂ O ₃	1.76
3	Plastic limit	53.96	%	3	Cl	18.39	8	Fe ₂ O ₃	1.17
4	Liquid limit	83.49	%	4	SiO ₂	4.06	9	K ₂ O	0.15
5	UCS	0.20	MPa	5	NaO ₂	2.46	10	Others	0.46

**FIGURE 3** | SEM micrographs of microstructure inside soda residue at different magnification.**FIGURE 4** | SEM micrographs of gangue at different magnification: (A) 1500x, (B) 6000x, and (C) 12000x.

crisscrossed. After magnification of 12000 times (**Figure 4C**), the microscopic pores are distributed on the surface of gangue, and the diameter of pores is about 2 μm . SEM results show that gangue itself has good density and can be used as an aggregate component of cemented backfilling materials.

Fly Ash

The fly ash used in the test was from the spontaneous combustion coal power plant. According to the analysis, the main oxide components in fly ash are SiO₂, Al₂O₃, Fe₂O₃. The Al₂O₃, and SiO₂, which account for 74% are the favorable component of fly ash activity and are closely related to the later setting and hardening characteristics of cemented backfilling materials (Papadakis, 1999).

According to SEM micrographs of fly ash, fly ash particles have different particle sizes and shapes. There are more particles

with small sizes and fewer particles with large sizes; most of the particle size is 10–20 μm , and the maximum particle size is about 170 μm . It is observed that many pores are evenly distributed on its surface, and there are small flake structures locally.

Cement

The cement used in this test was P.O.32.5 cement produced by China United Cement Company. The apparent density of the cement was 3.1 g/cm³, and 80 μm sieve residual was 6.4%. The analysis shows that there are a lot of tricalcium silicate (C₃S), dicalcium silicate (C₂S), part of tricalcium aluminate (C₃A), and tetracalcium ferroaluminate (C₄AF) in cement. After hydration of cement, calcium silicate hydrate and ettringite with cementing ability can be produced. The results of the mineral composition analysis are shown in **Table 2**.

TABLE 2 | Mineral composition of cement.

Compositions	C ₃ S	C ₂ S	C ₃ A	C ₄ AF	Other
Content (%)	1.5	1.2	25.5	48.8	Rest

Lime

The lime used in this test was quicklime produced by Huihui Industrial Company. Through the analysis, it is found that the main components of lime are calcium oxide and calcium hydroxide, accounting for 70%. Calcium oxide is a kind of nonhydraulic cementing material, which has poor cementing ability in the water environment. The addition of lime can stimulate the activity of fly ash, promote the hydration process of fly ash, and improve the strength of the filling body; Besides, the calcium oxide contained in lime can react with water, consume free water content, and reduce slurry bleeding rate.

Test Scheme

To study the influence of soda residue content on the flow and mechanical properties of SRGBM, five groups of tests (groups A0–A4) were designed. Group A0 was the reference group without soda residue. The specific ratios are available in Chapter 3.1. The amount of soda residue in groups A0–A4 was 0, 3, 6, 9, and 12% respectively, and the corresponding quality of fly ash in each group decreased. Slump and bleeding rate are specific indexes of flow performance. Early strength, middle strength, and later strength are mechanical property indexes in this test, corresponding to the UCS at the curing age of 1, 7, and 28 days. Table 3 shows the test proportioning scheme and monitoring indexes.

Sample Preparation and Test Process

After grinding the soda residue in advance, raw materials in different groups were mixed according to the test scheme. Then, an appropriate amount of tap water was added to stir to form cemented backfilling slurry. The slump and bleeding rate of slurry were tested according to the GB/T 50080–2016 Standard for test method of performance on ordinary fresh concrete. During the bleeding rate test, the water exuded from the surface was sucked by the straw at an interval of 10 min in the first 60 min; after 60 min, the water was sucked every 30 min until there was no more water on the surface. The mechanical properties were tested with a triple die ($7.07 \times 7.07 \times 07$ cm) for mold mounting, and then the mold was removed after 24 h. The mold was cured under the standard curing condition (at the temperature of 20°C and the

humidity of 95%) at the curing age of 1, 7, and 28 days. The WAW-1000D electro-hydraulic servo press was selected to test the UCS of the cemented filling body at different curing ages. The loading speed was set as 1 mm/s. Three specimens were tested at each age, and the average value was taken as the final result. The actual pictures of the test process are shown in Figure 5.

RESULTS AND DISCUSSION

Flow Performance

Slump

Figure 6 shows the slump test results of the SRGBM slurry with different soda residue contents in Groups A0–A4.

As shown in Figure 6, when the soda residue content is 0, 3, 6, 9, and 12%, the slump values of slurry are 110, 115, 124, 135, and 152 mm, respectively. It indicates that the slump value of slurry gradually increases with the increase in soda residue content. Compared with the reference group (Group A0), the increase in the slump value in Groups A1–A4 is 4.5, 12.7, 22.7, and 38.2%, respectively, and the increasing amplitude gradually increases with the increase in soda residue content. The reason is as follows: there is a large number of fine particles of soda residue after grinding and the water content is high, which increases the slump value of slurry and enhances the fluidity of the backfilling material.

Bleeding Rate

Figure 7 shows test results of bleeding and bleeding rate of slurry with different contents of soda residue.

As shown in Figure 7A, the bleeding law of the SRGBM slurry in each group presents two-stage characteristics of rapid bleeding (stage I) and slow bleeding (stage II). In stage I, the speed of bleeding is faster and the bleeding proportion is larger in the whole process, while in stage II, the speed of bleeding is slower and the bleeding proportion is smaller in the whole process. The bleeding proportion of stage I in the reference group (Group A0) is as high as 98% and that of stage I in Group A4 is 91%. With the increase in soda residue content, the final bleeding in stage II increases gradually, but the proportion of bleeding in stage I decreases gradually. It indicates that soda residue can delay the initial bleeding rate of free water, which is conducive to material transportation.

As presented in Figure 7B, when the soda residue contents are 0, 3, 6, 9, and 12%, the bleeding rate of slurry in Groups A0–A4 is 2.4, 3.0, 3.8, 4.7, and 5.3%, respectively. The bleeding rate

TABLE 3 | Test proportioning scheme and monitoring index.

Group	Solids content composition (wt%)					Mass Concentration (%)	Monitoring index				
	Soda residue	Fly ash	Cement	Lime	Gangue		Slump	Bleeding rate	UCS (1 day)	UCS (7 days)	UCS (28 days)
A0	0	40	10	2.5	47.5	84	S ₀	b ₀	σ ₀₁	σ ₀₂	σ ₀₃
A1	3	37	10	2.5	47.5	84	S ₁	b ₁	σ ₁₁	σ ₁₂	σ ₁₃
A2	6	34	10	2.5	47.5	84	S ₂	b ₂	σ ₂₁	σ ₂₂	σ ₂₃
A3	9	31	10	2.5	47.5	84	S ₃	b ₃	σ ₃₁	σ ₃₂	σ ₃₃
A4	12	28	10	2.5	47.5	84	S ₄	b ₄	σ ₄₁	σ ₄₂	σ ₄₃

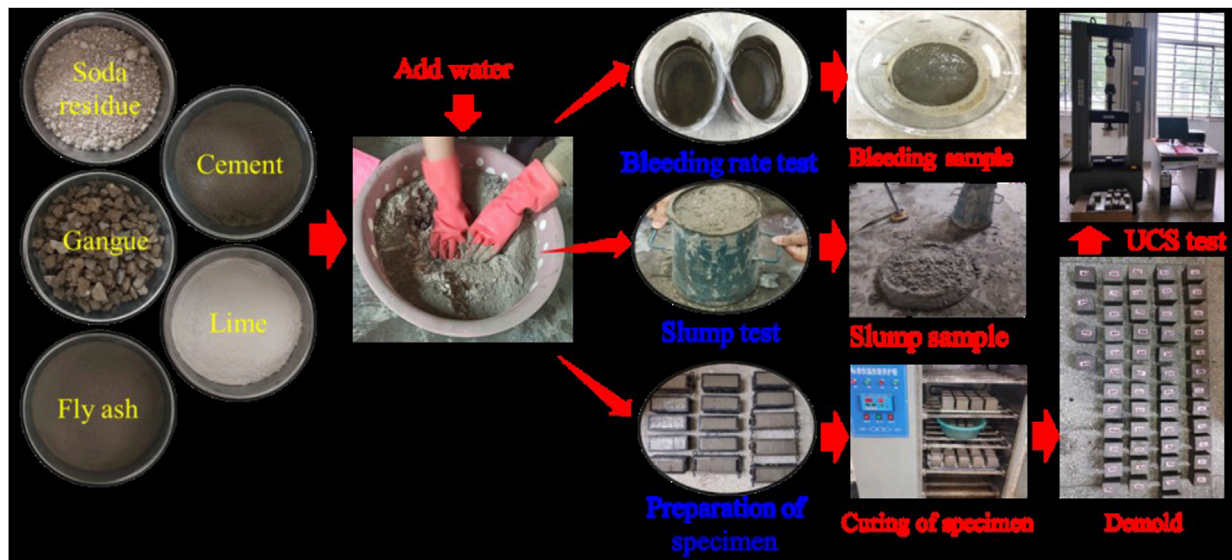


FIGURE 5 | Actual pictures of the test process.

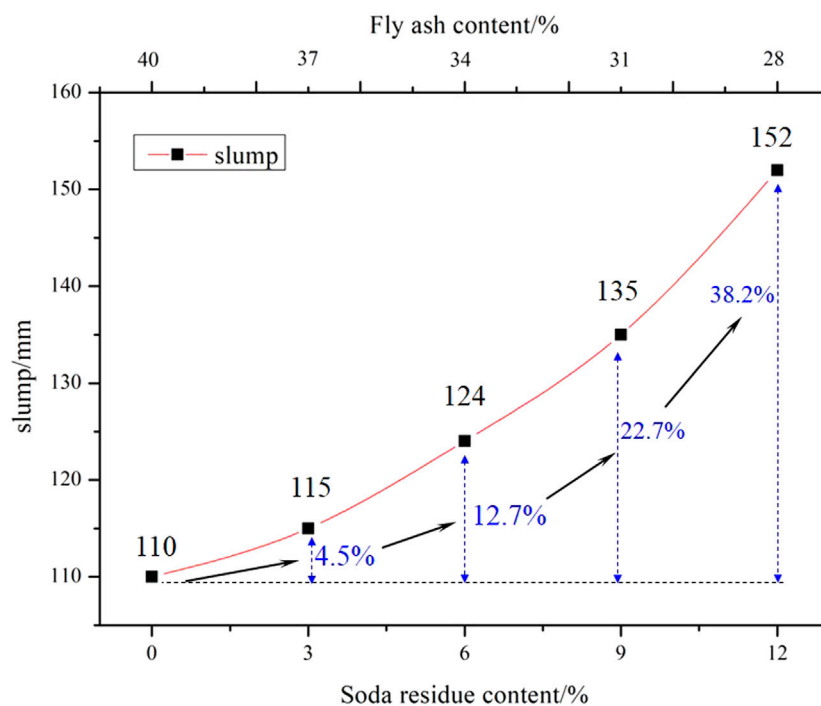


FIGURE 6 | Influence law of slump.

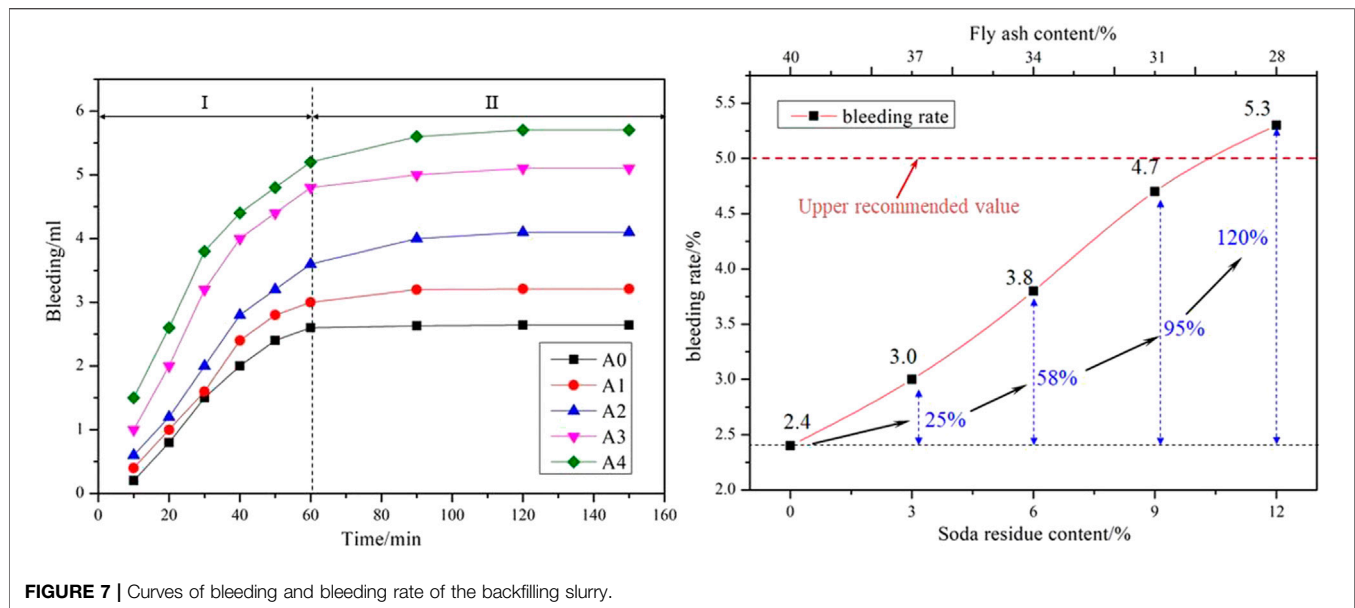
gradually increases with the increase in soda residue content. The increasing amplitude of the bleeding rate of slurry in Groups A1–A4 is 25, 58, 95, and 120%, respectively. This increasing amplitude is significant, and the bleeding rate of slurry in Group A4 is too large, which has exceeded the recommended value. The analysis shows that the water absorption rate of fly ash with the same quality is higher than that of soda residue; the water absorbed by soda residue

is less than the water demand of fly ash; the free water of slurry is more, which leads to the increase in bleeding rate.

Mechanical Properties

Bearing Deformation Characteristics

One specimen was selected from three specimens at different curing ages in Groups A0–A4 and subject to the loading. The



stress–strain curve of SRGBM specimens was drawn, as shown in **Figure 8**.

As shown in **Figure 11**, the strength curves of SRGBM specimens with different soda residue contents and different ages show significant three-stage characteristics, namely, pre-peak bearing area (zone I), post-peak attenuation area (zone II), and residual bearing area (zone III). In zone I, the strength of the specimen almost increases linearly with the increase of load. At the peak point, the specimen is in the ultimate strength, and the bearing capacity is the strongest. Zone I belongs to the strain hardening stage. In zones II and III, with the continuous action of the load, the strength of the specimen decreases rapidly, the bearing capacity becomes weak, the cracks continue to develop and connect, and the residual bearing area shrinks. However, the specimen in zone III does not completely lose the bearing capacity. It indicates that the material still has a certain bearing capacity after failure, but the bearing capacity is weak. Zones II and III belong to the strain-softening stage.

Analysis of Influence Characteristics

The UCS values of SRGBM specimens with different soda residue contents and ages were summarized. To further analyze the influence of soda residue content and curing age on the UCS of SRGBM specimens, the data are plotted as shown in **Figure 9**.

Curing age

As shown in **Figure 9A**, the UCS of SRGBM specimens with different soda residue contents increases gradually with the increase in curing time. The early strength and later strength of SRGBM in Group A2 are the largest, and the average uniaxial UCS of SRGBM at the curing age of 1, 7, and 28 days are 0.74, 3.95, and 12.54 MPa, respectively. The average UCS of the specimen at the curing age of 7 days is 5.3 times of that at the curing age of 1 day; the average UCS of the specimen at the curing age of 28 days is 16.9 times of that at the curing age of 7 days.

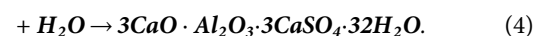
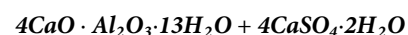
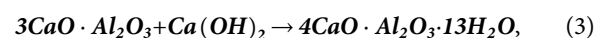
Soda residue content

As shown in **Figure 9B**, the UCS of SRGBM specimens increases first and then decreases with the increase in soda residue content. The strength of SRGBM at different curing ages is the highest at the soda residue content of 6%. Compared with the reference group, the UCS of SRGBM specimens at the curing ages of 1, 7, and 28 days in Group A2 is 5.49, 2.23, and 2.87 times of that in Group A2 (reference group), respectively. Based on the test results, it is suggested that the optimum mix proportion of SRGBM is soda residue: fly ash: lime: cement: gangue = 6%: 34%: 10%: 2.5%: 47.5%, and the slurry concentration is 84 wt%.

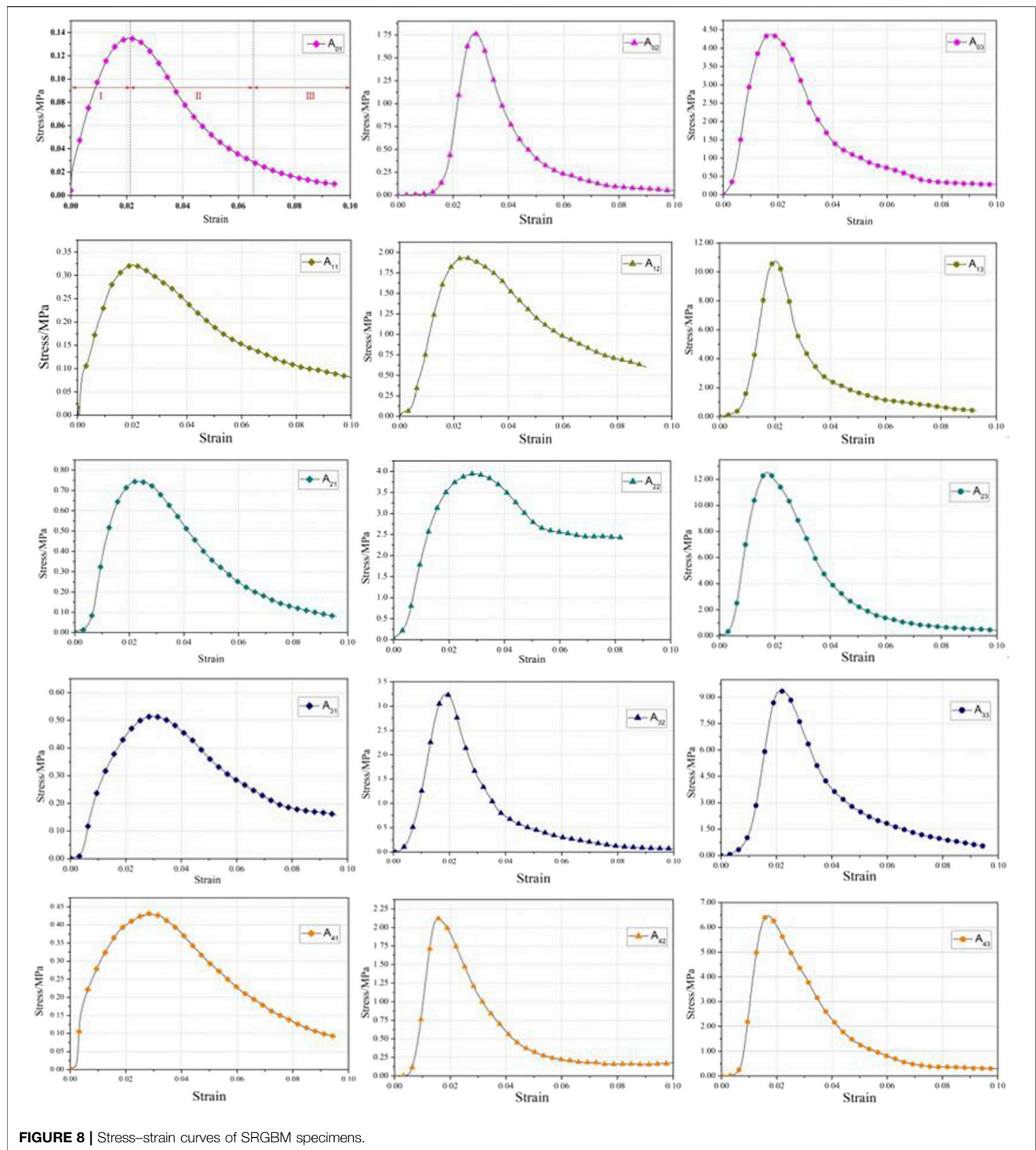
Strength Formation Mechanism

The cured specimen was broken and a small rectangular specimen with a base area of 10 × 10 mm and a height of 2–10 mm was cut from the inside of the specimen. The conductive adhesive was glued to the base and sprayed with gold to improve the electrical conductivity. Finally, the specimen was observed in the electron microscope. **Figure 10** shows the production process and the actual photos of the experiment. **Figure 11** shows the micrographs of SRGBM specimens under different resolution conditions.

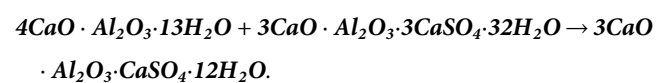
According to the analysis of Chapter 3.1.4, the main components of cement are C_3A and C_4AF . The pH value and temperature of the solution are increased by the CaO in lime and water heating, and then trisulfide hydrated calcium sulfate ($3CaO \cdot Al_2O_3 \cdot 3CaSO_4 \cdot 32H_2O$, known as ettringite, expressed by Aft) is generated by C_3A . The reaction formula is shown in the following equations:



When the gypsum is exhausted, calcium aluminate hydrate (C_4AH_{13}), which is the hydration product of C_3A , reacts with Aft



to form calcium sulphoaluminate hydrate ($3\text{CaO} \cdot \text{Al}_2\text{O}_3 \cdot \text{CaSO}_4 \cdot 12\text{H}_2\text{O}$, expressed as AFm). Both of these hydrates are needle-like crystals and are insoluble in water. The reaction equations are shown in the following equations:



(6)

At the same time, fly ash is activated in the sodane environment of lime, the hydration reaction of cement is very rapid, and the

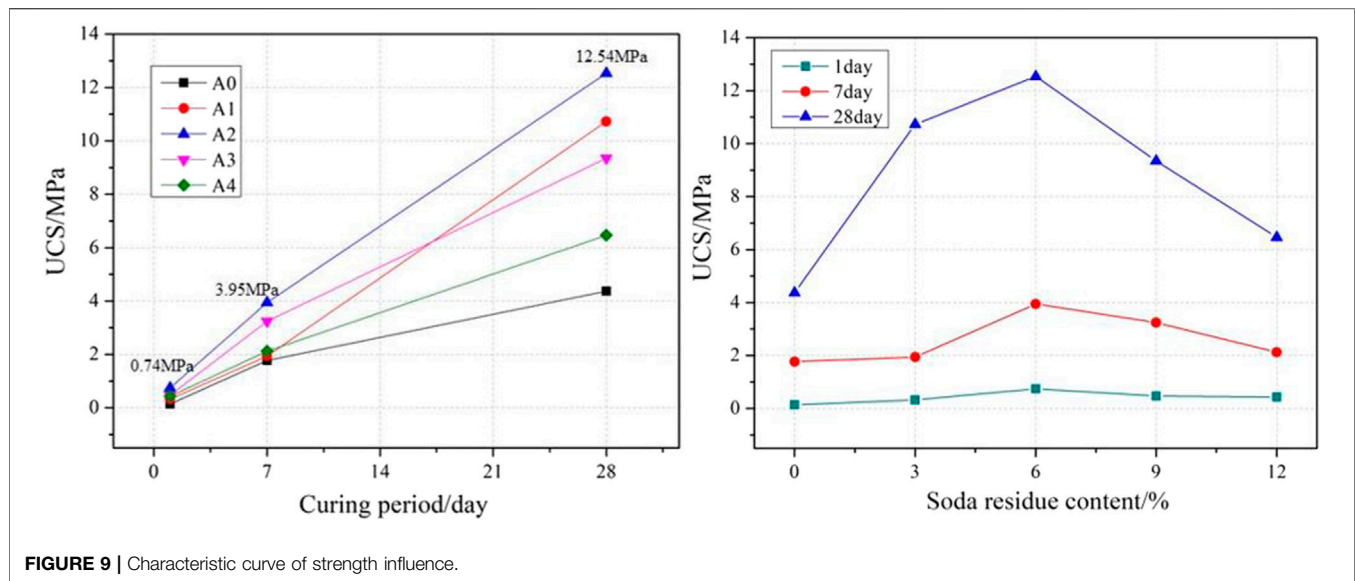


FIGURE 9 | Characteristic curve of strength influence.

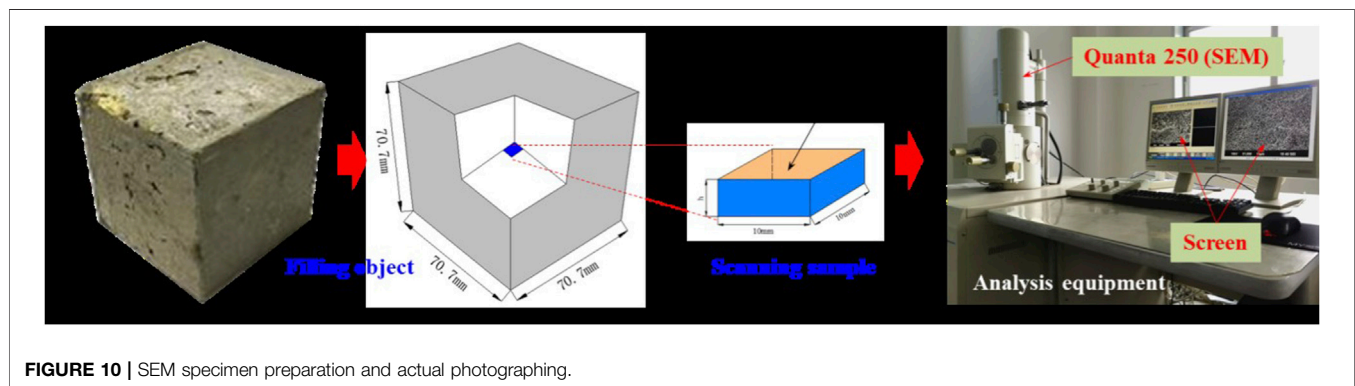


FIGURE 10 | SEM specimen preparation and actual photographing.

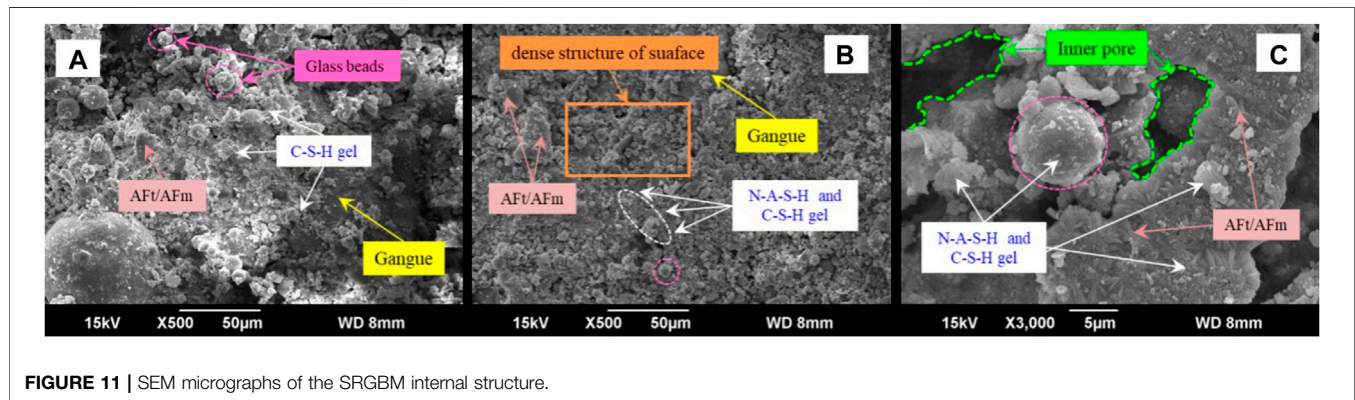


FIGURE 11 | SEM micrographs of the SRGBM internal structure.

released substances make the pH value of the solution further increase. The substances in fly ash have the characteristics of modifying the system structure, such as Ca^{2+} , K^+ , and Na^+ ; silicate or aluminosilicate minerals are also dissolved in the solution. These substances with the ability of modifying the system structure contact with each other to form calcium silicate cement (C-S-H) and calcium aluminate hydrate (C_4AH_{13}). These

hydration products can increase the structural density and strength of cemented backfilling materials and make the materials have a higher bearing capacity.

With the addition of soda residue, the active SiO_2 and Al_2O_3 contained in fly ash are excited by the OH^- contained in soda residue. After the dissolution and re-polymerization with different structures, aluminosilicate cementitious polymer

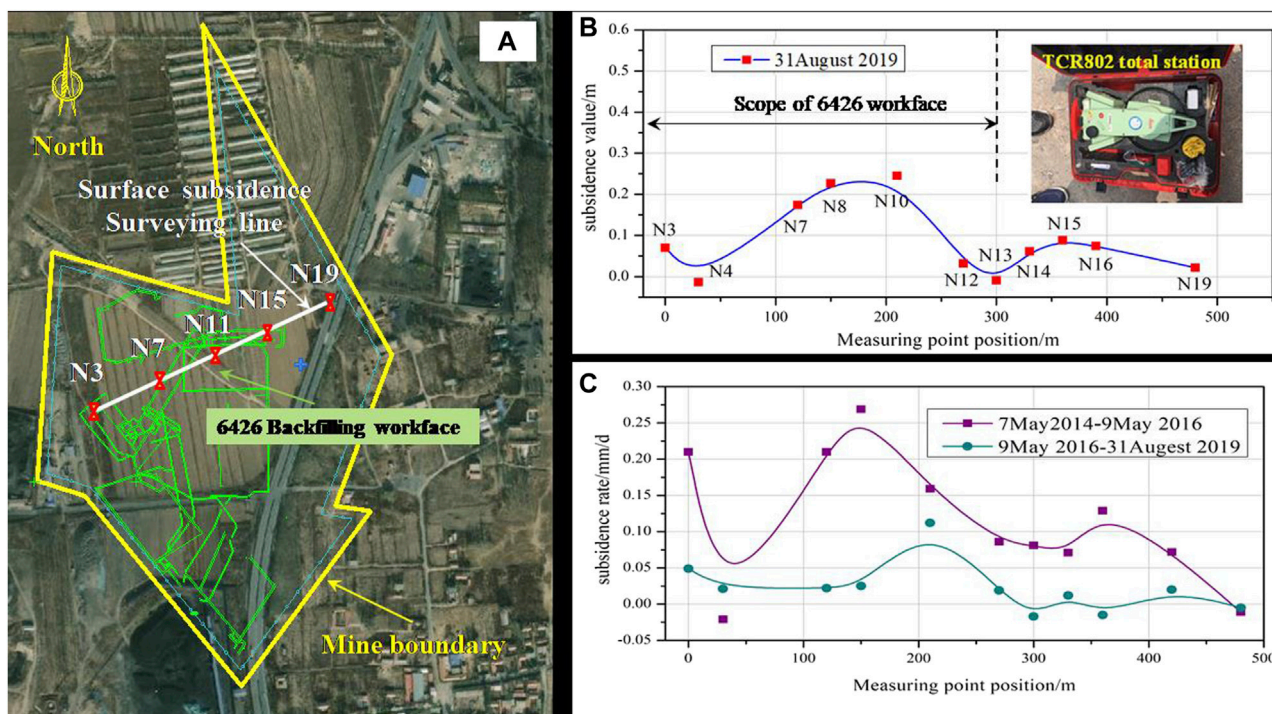
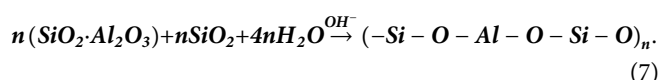


FIGURE 12 | Monitoring scheme and results of surface subsidence.

(N-A-S-H) is formed. N-A-S-H has a stronger cementing performance. In the soda residue cementing slurry system, C-S-H gel and N-A-S-H gel coexist (Liu et al., 2017), which improves the cementing performance of the system, reduces the connectivity of pores, and improves the strength of the material. This is the main reason for the gradual increases in the strength of the material with the increase in soda residue content in the range of 0–6%. The reaction process is shown in the following equation:



With the continuous increase in soda residue content, the degree of soda residue participating in the hydration reaction of materials is weakened, and the surplus soda residue no longer participates in the hydration reaction. The decrease of fly ash content reduces the content of the C-S-H gel polymer and N-A-S-H polymer. Since the strength of soda residue itself is low, the strength of SRGBM shows a downward trend with the continuous increase in soda residue content.

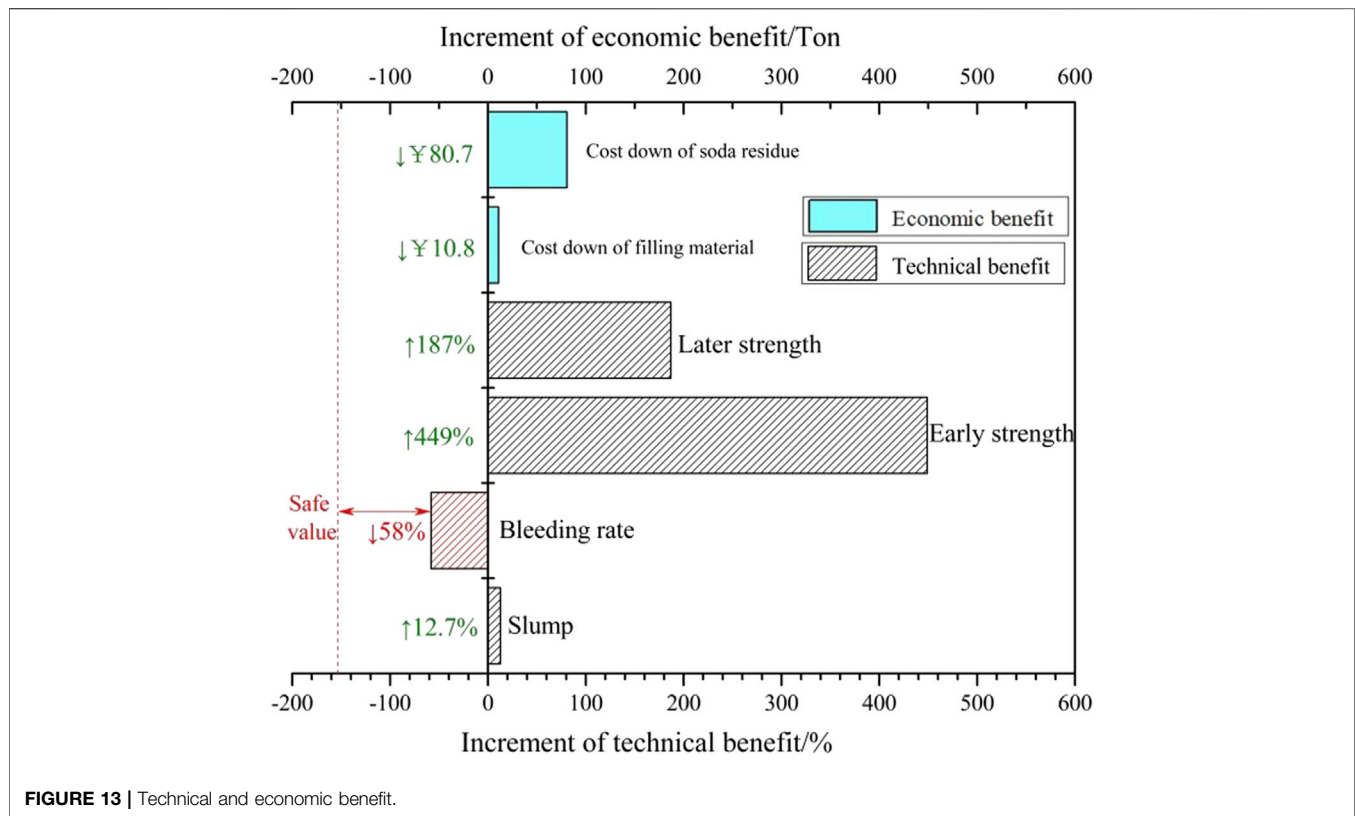
ENGINEERING APPLICATION AND FIELD MEASUREMENT OF SURFACE SUBSIDENCE

Surface Subsidence Observation

The working face 6246 of a mine was selected as the experimental working face of soda residue cemented

backfilling. According to the test results, the material ratio of Group A2 was used. Surface settlement observation points were set on the corresponding surface of the working face. Then, the surface subsidence of the backfilling working face was monitored, and the control effect of SRGBM on the surface subsidence was observed. The survey line was arranged on the north of the coal mine, and the length of the survey line was 480 m. A total of 17 measuring points (N3–N19) were arranged at an interval of 30 m. The monitoring instrument was tested by the Laika TCR802 total station. Below the survey line was the working face 6246. The surface subsidence monitoring lines were monitored on May 7, 2014, May 9, 2016, and August 31, 2019. Some observation points were damaged or lost due to human destruction and natural factors, but there are still 11 observation points in good condition. **Figure 12** presents the surveying scheme and surveying results.

As shown in **Figure 12B**, the maximum surface subsidence from May 7, 2014, to August 31, 2019, is 245 mm, which is located above the working face 6246. According to the subsidence velocity curve, from May 7, 2014, to May 9, 2016, the surface subsidence velocity is faster (the maximum subsidence velocity of measuring point N8 is 0.269 mm/d) than that from May 9, 2016, to August 31, 2019 (the maximum subsidence velocity of N10 is 0.112 mm/d). The measuring points N8 and N10 are, respectively, located above the working face 6246, and the mining of the working face 6246 is completed on December 31, 2015. It can be known that the main reason for the rapid surface subsidence from May 7, 2014, to May 9, 2016, is that



the working face 6246 is in the mining period, and the mining had a severe impact on the overlying rock, which leads to the rapid surface subsidence. During the second observation of the working face 6246, the mining has been completed, and the surface subsidence was slow. In addition, the measuring points N14, N15, and N16 are at the edge of the working face 6241. Combined with the subsidence curves and subsidence speed curves, it can be seen that the surface subsidence is small from May 9, 2016, to August 31, 2019, and the surface subsidence has tended to be stable. In summary, SRGBM has a good control effect on overburden movement and can effectively control the surface subsidence.

Benefit Analysis

The test results show that the effect of soda residue on the transport performance and mechanical properties of SRGBM is significant, and the surface subsidence value of the test mine is small, and the surface subsidence control effect is good. To comprehensively compare and analyze the influence of soda residue on the economic, technical, and social benefits of cemented fill mining, SRGBM with the soda residue content of 6% in Group A2 and SRGBM without soda residue content in Group A0 were taken as the comparison. **Figure 13** shows the specific results of data analysis.

In Group A2, 6% fly ash in Group A0 was replaced by solid waste soda residue. The results show that the performance indexes of specimens in Groups A2 and A0 are significantly improved except for the bleeding rate. The slump of SRGBM

slurry increases by 12.7%. With the increase in slurry bleeding, although the increase in bleeding rate is 58%, the bleeding rate is only 3.8% (less than 5%), which still meets the engineering requirements. The increase in early strength and later strength is 449 and 187%, respectively, and the mechanical properties of SRGBM are greatly improved. According to statistics, the plant price of fly ash and soda is about 150 yuan per ton and 80.7 yuan per ton. Considering the transportation cost of soda residue, the economic benefit of SRGBM is estimated to be 200 yuan per ton of soda residue consumed. At the same time, this technology can achieve energy saving and emission reduction, environmental protection and social benefits and has good application value (Biernacki et al., 2017).

CONCLUSION

- 1) The moisture content of fresh soda residue is 89.95%, and the pH value is 9.2, which is alkaline. The plasticity index of fresh soda residue is 29.53, which belongs to the category of cohesive soil. The UCS of soda residue is only 0.20 MPa. Soda residue is a porous aggregate structure, with many internal interconnected pores, large compression deformation, and weak bearing capacity.
- 2) With the increase in soda residue content within the range of 0–12%, the slump of the SRGBM slurry gradually increases, and the bleeding rate gradually increases, but the proportion

of bleeding in the early rapid bleeding stage (stage I) is gradually smaller. The early strength, middle strength, and later strength of SRGBM increase first and then decrease. The optimum mix proportion of SRGBM is soda residue: fly ash: lime: cement: gangue = 6%: 34%: 10%: 2.5%: 47.5%, and the slurry concentration is 84 wt%.

- 3) Soda residue promotes the hydration reaction of cementing materials in the slurry system, and C-S-H gel and N-A-S-H gel coexist in the slurry system. The N-A-S-H gel has a stronger cementing performance, reduces the connectivity of pores, and improves the strength of materials. However, the excessive addition of soda residue cannot always promote the formation of C-S-H and N-A-S-H. The excessive addition of soda residue can reduce the strength of the material gradually.
- 4) The field measurement of the surface subsidence shows that the maximum subsidence value of the backfilling working face with SRGBM is only 245 mm, and the surface subsidence control effect is good. The statistical data show that compared with the reference group, the slump of SRGBM in Group A2 increases by 12.7%, the bleeding rate is only 3.8%, and the early strength and later strength increase by 449 and 187%, respectively; the economic benefit of 200 yuan is generated by the addition of soda residue per ton. The technical, economic,

and social benefits of soda residue cemented filling materials are remarkable.

DATA AVAILABILITY STATEMENT

WY: Conceptualization, Data curation, Writing—original draft. KZ and SO: Design and complete experiments. XB: Complete the translation and article proofs. JZ: Polish the article and partial data analysis.

AUTHOR CONTRIBUTIONS

All authors listed have made a substantial, direct, and intellectual contribution to the work and approved it for publication.

FUNDING

This work was funded by the National Natural Science Foundation of China (Grant No: 51904110) and the Open Fund for Jiangsu Key Laboratory of Advanced Manufacturing Technology (Grant No: HGAMTL_1714).

REFERENCES

- Biernacki, J. J., Bullard, J. W., Sant, G., Banthia, N., Brown, K., Glasser, F. P., et al. (2017). Cements in the 21st Century: Challenges, Perspectives, and Opportunities. *J. Am. Ceram. Soc.* 100 (100), 2746–2773. doi:10.1111/jace.14948
- Cui, Z., and Henghu, S. N. (2010). The Preparation and Properties of Coal Gangue Based Sia Lite Paste-like Backfill Material[J]. *J. China Coal Soc.* 35 (06), 896–899.
- Deng, X., Yuan, Z., Yu, Li., Liu, H., Feng, J., and Benjamin, W. (2020). Experimental Study on the Mechanical Properties of Microbial Mixed Backfill[J]. *Construct. Build. Mater.* 265, 120643. doi:10.1016/j.conbuildmat.2020.120643
- Guangming, F., Sun, C., Wang, C., and Zhou, Z. (2010). Research on Goaf Filling Methods with Super High-Water Material[J]. *J. China Coal Soc.* 35 (12), 1963–1968. doi:10.13225/j.cnki.jccs.2010.12.004
- He, Y., Ye, X., and Wang, Z. (2015). Consideration on the 13th Five Year Plan of Coal Industry[J]. *Coal Econ. Res.* 35 (01), 6–8+21. doi:10.13202/j.cnki.cer.2015.01.001
- Hulisz, P., and Piernik, A. (2013). Soils Affected by Soda Industry in Inowrocaw[J]. *Techn. Soils of Poland* (7), 125–140.
- Lanfen, H., Li, J., Chen, Z., and Wang, L. (2014). Effect of Combined Application of Alkali Residue and Biomass Ash on Improving Acid Soil[J]. *South China Fruits* 43 (04), 65–67. doi:10.1016/j.still.2016.04.017
- Li, B., Yan, H., Zhang, J., and Zhou, N. (2020a). Compaction Property Prediction of Mixed Gangue Backfill Materials Using Hybrid Intelligence Models: A New Approach[J]. *Constr. Build. Mater.* 247, 118633. doi:10.1016/j.conbuildmat.2020.118633
- Li, D., Wang, D., and Yuan, N. (2020b). Influence of Circulating Fluidized Bed Fly Ash on Properties of Gangue Cemented Filling Materials[J]. *Bull. Chin. Ceram. Soc.* 39 (08), 2401–2407+2432. doi:10.16552/j.cnki.issn1001-1625.2020.08.006
- Liu, C., Zhao, X., Zhu, N., Liu, Y., and Pang, Y. (2017). Mechanical Properties of Fly Ash-Based Geopolymers and Modification Mechanism of Soda Residue[J]. *Bull. Chin. Ceram. Soc.* 36 (02), 679–685+691. doi:10.16552/j.cnki.issn1001-1625.2017.02.046
- Liu, H., Zhang, J., Li, B., Zhou, N., Xiao, X., Li, M., et al. (2020). Environmental Behavior of Construction and Demolition Waste as Recycled Aggregates for Backfilling in Mines: Leaching Toxicity and Surface Subsidence Studies. *J. Hazard. Mater.* 389, 121870. doi:10.1016/j.jhazmat.2019.121870
- Liu, L., Fang, Z., Zhang, B., Wang, M., Qiu, H., and Zhang, X. (2021). Development History and Basic Categories of Mine Backfill Technology[J]. *Metal Mine* 50 (03), 1–10. doi:10.19614/j.cnki.jsks.202103001
- Ma, D., Wang, J., Cai, X., Ma, X., Zhang, J., Zhou, Z., et al. (2019). Effects of Height/diameter Ratio on Failure and Damage Properties of Granite under Coupled Bending and Splitting Deformation. *Eng. Fracture Mech.* 220, 106640. doi:10.1016/j.engfracmech.2019.106640
- Ma, J., Zhang, P., Bai, X., and Arsyad, A. (2019). Experimental on Bearing Capacity of Alkali Slag Foundation[J]. *Sci. Tech. Eng.* 19 (30), 303–309. doi:10.28991/cej-2020-03091623
- Ma, D., Duan, H., Liu, W., Ma, X., and Tao, M. (2020). Water-sediment Two-phase Flow Inrush hazard in Rock Fractures of Overburden Strata during Coal Mining. *Mine Water Environ.* 39, 308–319. doi:10.1007/s10230-020-00687-6
- Ma, D., Duan, H., Zhang, Q., Zhang, J., Li, W., Zhou, Z., et al. (2020). A Numerical Gas Fracturing Model of Coupled thermal, Flowing and Mechanical Effects. *Comput. Mater. Contin.* 65 (3), 2123–2141. doi:10.32604/cmc.2020.011430
- Ma, D., Zhang, J., Duan, H., Huang, Y., Li, M., Sun, Q., et al. (2021). Reutilization of Gangue Wastes in Underground Backfilling Mining: Overburden Aquifer protection. *Chemosphere* 264, 128400. doi:10.1016/j.chemosphere.2020.128400
- Ma, D., Kong, S., Li, Z., Zhang, Q., Wang, Z., and Zhou, Z. (2021). Effect of Wetting-Drying Cycle on Hydraulic and Mechanical Properties of Cemented Paste Backfill of the Recycled Solid Wastes. *Chemosphere* 282, 131163. doi:10.1016/j.chemosphere.2021.131163
- Martin, J., and Holger, W. (2013). Progress in the Research and Application of Coal Mining with Stowing[J]. *Int. J. Mining Sci. Tech.* 23 (1), 7–12. doi:10.1016/j.ijmst.2013.01.002
- Meng, L., Zhang, J., Zhou, N., and Huang, Y. (2017). Effect of Particle Size on the Energy Evolution of Crushed Waste Rock in Coal Mines. *Rock Mech. Rock Eng.* 50 (5), 1347–1354. doi:10.1007/s00603-017-1207-1
- Meng, Li., Zhang, J., Meng, G., Gao, Y., and Li, A. (2020). Testing and Modelling Creep Compression of Waste Rocks for Backfill with Different Lithologies[J]. *Int. J. Rock Mech. Mining Sci.* 125, 104170. doi:10.1016/j.ijrmms.2019.104170
- Mitchell, J. K. (1993). *Foundamentals of Soil Behavior*. John Wiley&Sons Inc. 21, 43–47.
- Morgan, D. R. (1996). Compatibility of concrete Repair Materials System[J]. *Constr. Build. Mater.* 10 (1), 51–61. doi:10.1016/0950-0618(95)00060-7

- Papadakis, V. G. (1999). Effect of Fly Ash on Portland Cement Systems. *Cement Concr. Res.* 29, 1727–1736. doi:10.1016/s0008-8846(99)00153-2
- Ran, H., Guo, Y., Guorui, F., Qi, T., and Du, X. (2020). Creep Properties of Coal Gangue Cemented Backfill Material under Step Loading[J]. *Mining Res. Develop.* 40 (02), 42–47. doi:10.13827/j.cnki.kyyk.2020.02.008
- Shenyang, O. (2019). *Study on Transportation and Mechanical Properties Optimization of Sand-Based Cemented Filling Materials[D]*. XuZhou: China University of Mining and Technology
- Song, Q., Liu, K., Fu, X., and Li, H. (2019). New Technology of Rock Salt Mining by Filling-Water Solution[J]. *China Well Rock Salt* 50 (04), 19–21.
- Sun, S., Zheng, Q., Tang, J., Zhang, G., Zhou, L., and Shang, W. (2012). Experimental Research on Expansive Soil Improved by Soda Residue[J]. *Rock Soil Mech.* 33 (06), 1608–1612. doi:10.16285/j.rsm.2012.06.045
- Tan, A., Lianyu, W., and Wang, Q. (2018). Physical and Mechanical Experimental Study on Improving Weathered Mudstone with Soda Residue[J]. *Bull. Chin. Ceram. Soc.* 37 (08), 2610–2615. doi:10.16552/j.cnki.issn1001-1625.2018.08.044
- Tian, X., and Li, X. (2009). Research on Engineering Utilization of Soda Residue Soil in Tangshan[J]. *Build. Sci.* 25 (07), 77–79+101.
- Wang, T., Wang, Z., Wang, S., Pan, Y., and Kang, Y. (2014). Study on Flowing Features of Mine High Density Cemented Filling Slurry in Pipeline[J]. *Coal Sci. Tech.* 42 (S1), 50–52. doi:10.13199/j.cnki.cst.2014.s1.035
- Wang, C., Liu, Y., Hu, H., Li, Y., and Lu, Y. (2019). Study on Filling Material Ratio and Filling Effect: Taking Coarse Fly Ash and Coal Gangue as the Main Filling Component. *Adv. Civil Eng.* 2019 (1), 1–11. doi:10.1155/2019/2898019
- Wang, M. (2019). Simulation experiment of Coupling Effect between Surrounding Rock and Filling Body in Early Strength Stage[J]. *J. Wuhan Univ. Sci. Tech.* 42 (02), 129–134.
- Xu, D., Wen, N., Wang, Q., Xu, C., and Jiang, Y. (2020). Preparation of Clinker-free concrete by Using Soda Residue Composite Cementitious Material[J]. *J. Harbin Inst. Tech.* 52 (08), 151–160.
- Yan, S., Hou, J., and Liu, R. (2006). Research on Geotechnical Properties and Environmental Effect of Mixture of Soda Waste and Fly Ash[J]. *Rock Soil Mech.* 27 (12), 2305–2308. doi:10.16285/j.rsm.2006.12.042
- Yang, J., Wu, X., Zhang, L., He, C., and Bao, G. (2010). Study on Experimental Preparation of Cement Mortar Incorporating Fly Ash-Soda Residue[J]. *Bull. Chin. Ceram. Soc.* 29 (05), 1211–1216. doi:10.16552/j.cnki.issn1001-1625.2010.05.045
- Yang, Y., Pu, Y., Yan, W., Guo, W., and Wang, H. (2017). Microstructure and Chloride Ion Dissolution Characteristics of Soda Residue[J]. *J. South China Univ. Tech.* 45 (05), 82–89.
- Yang, Y., Pu, Y., Yan, W., Guo, W., and Wang, H. (2017). Experimental Study on the Performance of concrete Using Soda Residue as mineral Admixture[J]. *Concrete* (09), 80–83.
- Yin, L., Wang, H., Guo, H., Li, H., Wang, K., and Wu, H. (2020a). Proportion Optimization and Performance of Filling Materials with Large-Content of Fly Ash [J]. *Mining Res. Develop.* 40 (03), 56–61. doi:10.13827/j.cnki.kyyk.2020.03.013
- Yin, S., Shao, Y., Wu, A., Wang, H., Liu, X., and Wang, Y. (2020b). A Systematic Review of Paste Technology in Metal Mines for Cleaner Production in China. *J. Clean. Prod.* 247, 119590. doi:10.1016/j.jclepro.2019.119590
- Yu, W., Qi, Y., Zhou, Y., Chen, L., Du, H., and Xie, H. (2016). Synergistic Improvement of thermal Transport Properties for Thermoplastic Composites Containing Mixed Alumina and Graphene Fillers[J]. *J. Appl. Polym. Sci.* 133 (13), 4830. doi:10.1002/app.43242
- Zhang, J., Zhang, Q., Ju, F., et al. (2018). Theory and Technique of Greening Mining Integrating Mining, Separating and Back Filling in Deep Coal Resources [J]. *J. China Coal Soc.* 43 (2), 377–389. doi:10.13225/j.cnki.jccs.2017.4102
- Zhang, J., Ju, F., Meng, L. I., et al. (2020). Method of Coal Gangue Separation and Coordinated In-Situ Backfill Mining[J]. *J. China Coal Soc.* 45 (1), 131–140. doi:10.13225/j.cnki.jccs.YG19.1826
- Zhao, K., Wang, X., Liu, H., Wu, C., and Zhang, J. (2011). Experimental Study of Mechanical Behaviors of Cemented Tailings Backfill Roof with Reinforcement [J]. *Rock Soil Mech.* 32 (01), 9–14+20. doi:10.16285/j.rsm.2011.01.001
- Zhou, N., Ma, H., Ouyang, S., Germain, D., and Hou, T. (2019). Influential Factors in Transportation and Mechanical Properties of Aeolian Sand-Based Cemented Filling Material[J]. *Minerals* 9 (2), 116. doi:10.3390/min9020116

Conflicts of Interest: Authors WY and KZ were employed by Huai'an Zhongbo Traffic Safety Technology Co. Ltd.

The remaining authors declare that the research was conducted in the absence of any commercial or financial relationships that could be construed as a potential conflict of interest.

Publisher's Note: All claims expressed in this article are solely those of the authors and do not necessarily represent those of their affiliated organizations, or those of the publisher, the editors and the reviewers. Any product that may be evaluated in this article, or claim that may be made by its manufacturer, is not guaranteed or endorsed by the publisher.

Copyright © 2021 Yin, Zhang, Ouyang, Bai, Sun and Zhao. This is an open-access article distributed under the terms of the Creative Commons Attribution License (CC BY). The use, distribution or reproduction in other forums is permitted, provided the original author(s) and the copyright owner(s) are credited and that the original publication in this journal is cited, in accordance with accepted academic practice. No use, distribution or reproduction is permitted which does not comply with these terms.



Mechanism of Rock Bursts Induced by the Synthetic Action of “Roof Bending and Rock Pillar Prying” in Subvertical Extra-Thick Coal Seams

Zhenhua Wu^{1,2}, Peng-Zhi Pan^{1,2*}, Jianqiang Chen³, Xudong Liu³, Shuting Miao^{1,2} and Peiyang Yu^{1,2}

¹State Key Laboratory of Geomechanics and Geotechnical Engineering, Institute of Rock and Soil Mechanics, Chinese Academy of Sciences, Wuhan, China, ²University of Chinese Academy of Sciences, Beijing, China, ³Shenhua Xinjiang Energy Company Limited, Urumqi, China

OPEN ACCESS

Edited by:

Jie Chen,
Chongqing University, China

Reviewed by:

Xuesheng Liu,
Shandong University of Science and
Technology, China
Mingzhong GAO,
Sichuan University, China
HuaFu Qiu,
Xi'an University of Science and
Technology, China

*Correspondence:

Peng-Zhi Pan
pzpan@whrsm.ac.cn

Specialty section:

This article was submitted to
Geohazards and Georisks,
a section of the journal
Frontiers in Earth Science

Received: 08 July 2021

Accepted: 01 November 2021

Published: 01 December 2021

Citation:

Wu Z, Pan P-Z, Chen J, Liu X, Miao S
and Yu P (2021) Mechanism of Rock
Bursts Induced by the Synthetic Action
of “Roof Bending and Rock Pillar
Prying” in Subvertical Extra-Thick
Coal Seams.
Front. Earth Sci. 9:737995.
doi: 10.3389/feart.2021.737995

When studying the rock burst mechanism in subvertical extra-thick coal seams in the Wudong coal mine in Xinjiang, China, most studies focus on rock pillars, while the effect of the roof on rock bursts is usually ignored. In this paper, a rock burst mechanism in subvertical extra-thick coal seams under the control of a “roof-rock pillar” is proposed. A theoretical analysis is first performed to explain the effect of roof-rock pillar combinations on rock bursts in coal seams. Numerical modeling and microseismic analysis are implemented to further study the mechanism of rock burst. The main conclusions are as follows: 1) During the mining of the B3+6 coal seam, an obvious microseismic concentration phenomenon is found in both the roof and rock pillar of B3+6. The rock bursts exhibited obvious directionality, and its main failure characteristics are floor heave and sidewall heave, but there will also be some failures such as shoulder socket subsidence in some parts. 2) The stress transfer caused by rock pillar prying is the main reason for the large difference in rock burst occurrence near the vertical and extra thick adjacent coal seams under the same mining depth. 3) Under the same cantilever length, the elastic deformation energy of the roof is much greater than that of the rock pillar, which makes it easier to produce high-energy microseismic events. With an increasing mining depth, the roof will become the dominant factor controlling the occurrence of rock bursts. 4) The high-energy event produced by the rock mass fracture near the coal rock interface easily induces rock bursts, while the high-energy event produced by the fracture at the far end of the rock mass is less likely to induce rock burst. 5) Roof deformation extrusion and rock pillar prying provide high static stress conditions for the occurrence of rock bursts in the B3+6 coal seam. The superposition of the dynamic disturbance caused by roof and rock pillar failure and the high static stress of the coal seam is the main cause of rock burst in the B3+6 coal seam.

Keywords: rock bursts, subvertical extra-thick coal seams, adjacent coal seams, roof bending, rock pillar prying

INTRODUCTION

Rock bursts are dangerous phenomena caused by the brittle failure of deep rock and are associated with excavation-induced seismic events (Kaiser and Cai, 2013). The occurrence of rock bursts usually causes significant economic losses, such as equipment damage and construction delays, and even worker injuries (He, 2011; Feng et al., 2012; Mazaira and Konicek, 2015; Lu et al., 2016; Dou et al., 2018; Feng et al., 2019; Naji et al., 2019; Simser, 2019; Wang et al., 2020; Wu et al., 2021a). They are one of the common dynamic instability modes during underground mining and excavation in the hardness, brittleness and integrity surrounding rock strata. In many cases, a rock burst in a coal mine can destroy tunnels hundreds of meters long, causing equipment damage and casualties (Aydan et al., 2002; Zhu et al., 2015; Afraei et al., 2019). The scale and severity of the damage in coal mines are usually greater than those in hard rock engineering.

Steeply inclined coal seams are widely distributed in Xinjiang, Ningxia, and Gansu in China, Asturias in Spain, and Lorraine in France, as well as other coal-producing regions (Diez and Alvarez, 2000; Driad-Lebeau et al., 2005; Heib, 2012; Qi et al., 2019b; He et al., 2020b). The steeply dipping thick coal seam contributes to approximately 17% of the total coal reserve and 10% of the total coal production of China (Duan et al., 2008; Wu et al., 2014). In recent years, as the mining intensity has increased, some areas in the east have suffered from the depletion of coal reserves that have had good conditions for many years. Many mining areas have begun to consider the mining of steep coal seams distributed in the west. However, compared with a gently inclined coal seam, the roof of a steeply inclined coal seam is not located above the stope but at the side of the stope. Therefore, the stress environment of steeply inclined coal seam roofs, the movement characteristics of overburden and the fracture mechanism are obviously different from those of gently inclined coal seams (Unver and Yasitli, 2006; Miao et al., 2011; Lai et al., 2014). The subvertical extra-thick coal seam is a type of coal seam with a large dip angle of 85–90° and is recognized as difficult to mine in academic circles (Lai et al., 2014; Lai et al., 2018). Because of their special characteristics of a high horizontal stress and complex geological conditions, the critical depth for rock bursts is less than that of most coal mines. The mine area of Urumchi has more than 30 steeply dipping coal seams with various thicknesses and spacings. Among them, the south mining area of the Wudong Coal Mine has particularities in addition to the special occurrence of the steeply dipping thick coal seam. In the southern area of the Wudong coal mine, an ultrathick rock pillar occurs between adjacent coal seams of the steeply dipping coal seam group. It has been shown that when the adjacent working face is mined, the complete and hard thick rock layer plays a macrocontrol role on the working face pressure, and the coupling effect of the stress transfer and structural stress of the thick rock layer increases the static load and the accumulation of the coal and rock mass, which provides the force source conditions for a rock burst occurrence (Xu et al., 2015; Liu et al., 2017; Qi et al., 2019a). Under the coupling action of suspended roofs and rock pillars, adjacent mining faces with

the same mining depth may show completely different rock burst behaviors due to the asymmetry of deformation, failure, energy, and stress transfer of the two working faces. Some experts have been investigated the rock burst mechanisms in steeply inclined coal mines with such coal and rock occurrences and mining conditions, and some meaningful results are obtained (Li et al., 2020a; Wu et al., 2021b; He et al., 2021). However, most studies are based on numerical simulation, and lack of relevant theoretical analysis. Therefore, it is of great significance to analyze the mechanism of rock burst with a combination of theoretical analysis and numerical simulation. Compared with gently inclined coal seams, research on the rock burst mechanism of subvertical extra-thick coal seams is immature. Research on subvertical extra-thick coal seams is rarely reported and is still in the exploratory stage.

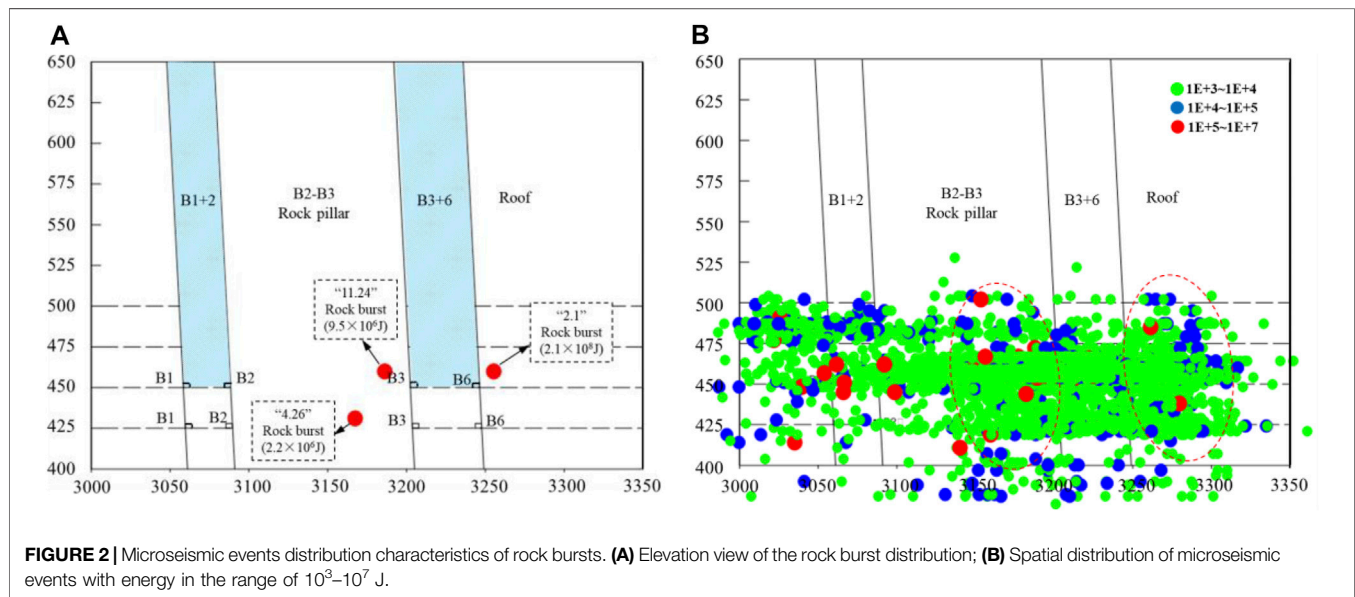
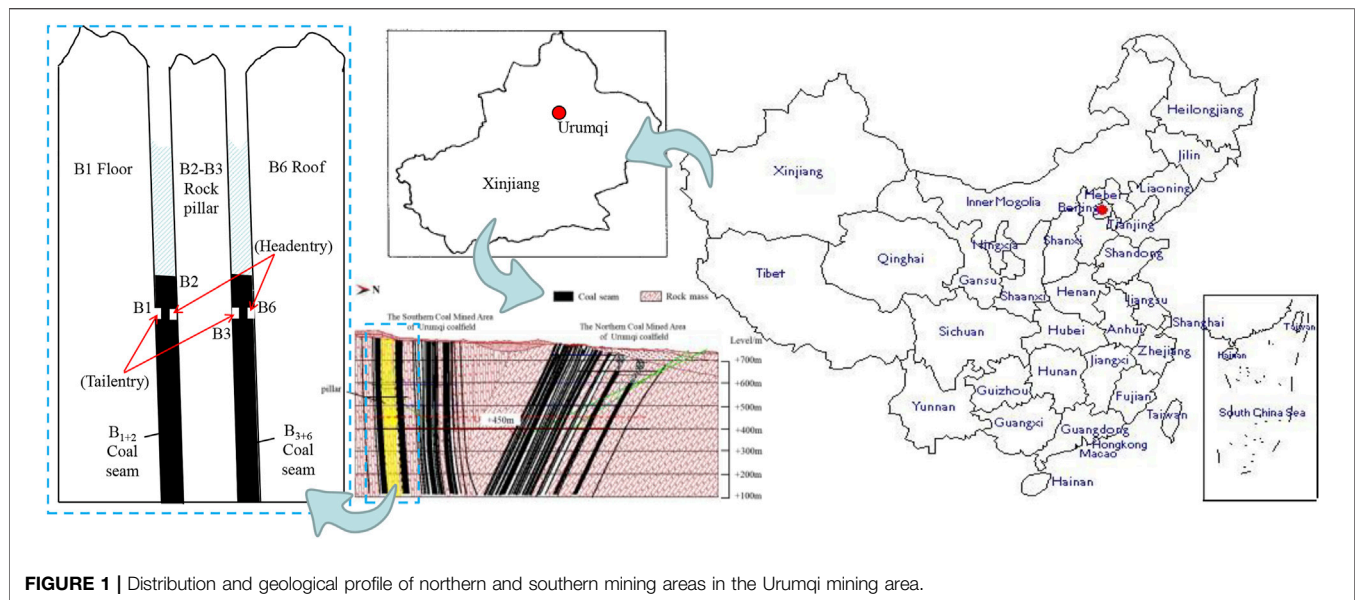
Rock bursts are usually induced by a combination of dynamic and static loads (Cai et al., 2020; Cao et al., 2020). However, the sources of a dynamic load and static stress and the mechanism of a rock burst in the process of mining are still unclear for this special geological structure coal seam. Due to the particularity of the geological structure of subvertical extra-thick coal seams, the occurrence of rock bursts in adjacent coal seams with the same mining depth in the same mining area is different. Currently, some studies are focused on the deformation and failure of roadways under the control of rock pillars. Although the impact of roof on rock burst is considered by some scholars, it is limited to numerical simulations (Li et al., 2020a; He et al., 2021).

In this paper, mechanical models of roof and rock pillar are established based on the Wudong coal mine in Urumqi, Xinjiang. The change law of elastic deformation energy of a roof and rock pillar with an increase in the mining depth and its effect on rock burst in B3+6 coal seam are obtained, and the reason that a rock burst does not occur in the adjacent B1+2 coal seam is explained. Based on numerical modeling and microseismic monitoring, the sources of the dynamic loads and static stress are determined, and the mechanism of rock burst under the joint mining condition of adjacent subvertical extra-thick coal seams is systematically analyzed.

ENGINEERING BACKGROUND

Occurrence Characteristics of Rock Burst and Mining Conditions of the Coal Seam

This study case is located in the Urumqi mining area. Due to the strong geological movement, the dip angles of the north and south wings of the Badaowan syncline are approximately 87° and 45°, respectively. The southern area of the Wudong coal mine is located in the southern wing of the Badaowan syncline. The south mining area of the Wudong coal mine belongs to the near vertical extra-thick coal seam group. The main mining areas are B3+6 and B1+2. To meet the economic benefit requirements, an alternate production mode of two working faces is adopted, among which the B3+6 working face is the first mining face (**Figure 1**), and the tail entry and head entry are arranged along the roof and floor of the coal seam, respectively. The width of the working face is the



thickness of the coal seam, the height of the layer is 25 m, and the mining drawing ratio is approximately 1:7. The coal mine adopts single wing horizontal sublevel fully mechanized top coal caving technology, and the roof is managed by the natural caving method. The average thickness of the B1+2 coal seam is 37.45 m, that of the B3+6 coal seam is 48.87 m, and the strike length of both coal seams is 2,520 m. There are hard and thick rock pillars between the two coal seams, with an average thickness of 100 m. The results of the *in situ* stress test in the south mining area of the Wudong coal mine show that the horizontal stress σ_H is 1.9–2.2 times the vertical stress σ_V when the mining depth exceeds 300 m (Lai et al., 2015), which indicates that the horizontal stress is the main factor leading to the occurrence of rock bursts. According to the statistics of rock burst accidents

in the southern mining area of the Wudong coal mine, the mining depth of the B3+6 coal seam in the southern mining area of the Wudong coal mine is approximately 300 m, which is far less than the critical depth of rock bursts in a gently inclined coal seam.

MS Monitoring System

The Wudong coal seam adopts the ARAMIS M/E MS monitoring system, which is capable of monitoring MS events (with an energy above 100 J, a frequency within 0–150 Hz, and an anti-interference ability lower than 100 dB) across the mine area, and the data can be used to effectively identify the areas at risk of rock burst (Xu et al., 2017). The Wudong coal mine south mining area adopts the joint monitoring of the surface and underground, which increases the positioning accuracy, to a certain extent.

According to field monitoring, three rock bursts occurred in the B3+6 coal seam at the +450 mining level. The occurrence locations of the three rock bursts are shown in **Figure 2A**, and the three events are named 11.24, 2.1, and 4.26 per their occurrence dates.

Field practice shows that microseismic events with energy levels greater than 10^6 J easily cause rock bursts in coal mines. This kind of microseismic event with a high risk of inducing rock bursts is called an “induced shock event” (He et al., 2017). During the mining process of the +450 horizontal coal seam, 22,649 microseismic spontaneous events were monitored, including 23 “induced shock events.” According to a statistical analysis of the distribution of “induced scour events” in the mining process of the B3+6 coal seam, the regional distribution was very obvious, with 62.5% in the rock pillar, 25.0% in the B3+6 coal seam, and 12.5% in the roof of the B3+6 coal seam. According to the microseismic event energy in the range of 10^3 J~ 10^7 J, it can be determined that the microseismic events near the B3+6 coal seam are distributed intensively (**Figure 2B**) (red dotted line area). The distribution of micro earthquakes in the roof of the B3+6 coal seam also has a similar concentration area, and there are obviously more microseismic events in the B3+6 coal seam than in the B1+2 coal seam. This is because the hanging rock pillar and roof bend to one side of the goaf, and the coal body is squeezed by the rock pillar and roof together, resulting in an increase in the coal stress, which is more likely to produce high-energy events in the process of mining.

Description and Analysis of Rock Bursts

The positions of the three rock bursts are in the B3 and B6 roadways of the B3+6 coal seam, while the B1 and B2 roadways of the B1+2 coal seam are not affected at the same mining depth. The rock bursts exhibited obvious directionality. Based on the actual rock burst situation and the analysis of image data, it can be determined that there are obvious floor heave and sidewall heave deformations in B3 and B6, especially at the bottom corner of the south side of B3 where the floor heave deformation is more obvious, as well as a large top subsidence in B6, where the subsidence of the shoulder socket on north side is more

serious. Combined with the damage of the roadway after rock burst and field microseismic monitoring data, it can be determined that there are two main reasons for the rock burst in the B3+6 coal seam:

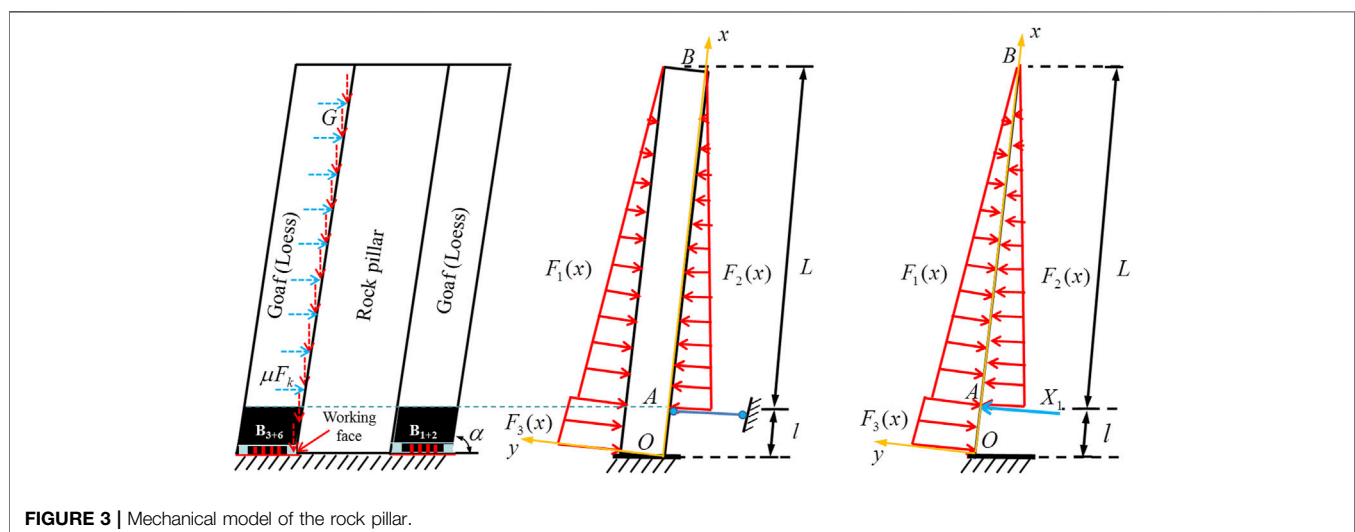
- 1) With a continuous increase in the coal seam mining depth, the rock pillar between coal seams is in a state of suspension. Under the action of an external load and self-weight, the rock pillar moves to the goaf of the B1+2 coal seam and pries B3+6 coal seam to produce a stress transfer. The stress of the B1+2 coal seam transfers to the B3+6 coal seam through the rock pillar, which increases the probability of a rock burst in the B3+6 coal seam. However, the B1+2 coal seam with the same mining depth is not prone to rock bursts due to the release of coal seam stress.
- 2) In addition to the stress transfer of the rock pillar, the B3 + 6 roof is bent and deformed under the action of horizontal tectonic stress and overburden load, which compresses the coal body of the B3+6 coal seam, resulting in a large roof deformation of the roadway (especially B6) when rock burst occurs.

MECHANICAL ANALYSIS OF THE HARD ROOF AND HARD-ROCK PILLAR

According to the analysis above, rock pillar prying and roof bending and extrusion are the main reasons for the rock bursts in the B3+6 coal seam. Therefore, it is necessary to establish mechanical models for roofs and rock pillars in order to analyze the control effect of rock bursts.

Theoretical Analysis of Rock Bursts Induced by Stress Transfer of Hard Rock Pillar

Taking the rock pillar and the coal seams on both sides in as the research object, the mechanical model is established (**Figure 3**). The rock pillar is simplified as a cantilever beam OB for the



mechanical analysis. The cantilever length is L , the length of the constrained part is l , and the angle between the cantilever and the horizontal direction is α . The bottom of the rock pillar extends from the working face to the coal body. Under the joint action of the coal body and the overlying strata, the bottom constraint can be regarded as a fixed constraint. The coordinate system is then established with the bottom end point of the rock pillar as the origin, where x is the upward distance along the surface of the rock pillar. The residual stress μF_k after attenuation of the horizontal tectonic stress, the self-weight of loess and rock pillar, and the component force along the y -axis of the rock pillar are simplified as triangular load $F_1(x)$, and the axial load is ignored (the axial load does not lead to rock pillar bending). $F_3(x)$ is the binding force of the B3+6 coal body on the rock pillar. Combined with the actual conditions of the site, the following two points need to be explained:

- 1) Under actual mining conditions, the fully mechanized caving face is mined from east to west. In the process of mining, with an increasing mining distance, the binding force of coal on the rock mass gradually decreases;
- 2) In this model, B1+2 can alleviate the bending deformation of the rock pillar. To investigate the bending effect of the rock pillar, the force of the B1+2 coal seam on the rock pillar is simplified as a simply supported support, which acts at the junction of the coal seam and loess.

According to the study of *in situ* stress, the horizontal tectonic stress can be estimated according to the vertical stress, where the ratio of the horizontal tectonic stress to vertical stress is a . Assuming that the width of the rock pillar on any section is a unit length, the load on the rock pillar at any section can be deduced as follows:

$$F_1(x) = (L + l - x) \sin \alpha [\mu A \gamma_s \sin \alpha + (\gamma_L + \gamma_p) \cos \alpha] \quad (l \leq x \leq L + l) \quad (1)$$

where μ is the attenuation coefficient of the horizontal tectonic stress; γ_s is the average bulk density of overlying strata on the roof of the B3+6 coal seam; γ_L is the bulk density of backfill loess; γ_p is the bulk density of the rock pillar; and α is the dip angle of the coal seam.

Because the loess is loose, it is inevitable that the compactness of different positions is not consistent in the process of backfill, or the cavity, loess and rock pillar are not fully contacted. If the support effectiveness coefficient f is defined here, then the support force of loess to the rock pillar can be expressed as follows:

$$F_2(x) = \frac{1}{\lambda} f \gamma_L [(L + l) - x] \sin^2 \alpha \quad (l \leq x \leq L + l) \quad (2)$$

where λ is the lateral pressure coefficient, $\lambda = 1/A$; and the value range of the support effectiveness coefficient f is $[0, 1]$. Under the ideal filling condition, $f = 1$, but when the loess has no supporting effect on the rock pillar, $f = 0$.

When the B3+6 coal seam does not start mining, the binding force of the coal seam on the rock pillar is equal to the horizontal *in situ* stress. When the B3+6 coal seam starts mining, the binding

force of the coal seam on the rock pillar is assumed to be k ; then, the binding force of the B3+6 coal seam on the rock pillar can be expressed as:

$$F_3(x) = k A \gamma_s [(L + l) - x] \sin^2 \alpha \quad (0 < x \leq l) \quad (3)$$

where the constraint weakening coefficient $k = 1 - L'/L$, L' is the length of the coal seam that has been mined, and L is the design strike length of the coal seam. When the coal seam is mined out, $k = 0$ (at this time, it is considered that it is the moment when the coal seam is just finished). Because the coal mining height is far less than the suspended length of the rock pillar, it is approximately regarded as a uniform load in a later calculation.

According to the idea of the “geometry, physics, balance” analysis of statically indeterminate problems in material mechanics, the force is taken as the basic unknown quantity, the structural body is analyzed based on automatically satisfying the equilibrium conditions, and the deformation coordination of the cantilever structure is mainly considered. The redundant restraint is removed and the excess reaction force and load are retained. If the load is the same and the excess reaction force is equal to the actual force, then the stress state of the cantilever beam is exactly the same, and the deformation and displacement of the original structure and the basic system are also identical. For j -order statically indeterminate structures, the equation after removing redundant constraints can be written as follows:

$$\begin{cases} \delta_{11}X_1 + \delta_{12}X_2 + \cdots \delta_{1i}X_i + \cdots \delta_{1j}X_j + \Delta_{1P} = 0 \\ \delta_{21}X_1 + \delta_{22}X_2 + \cdots \delta_{2i}X_i + \cdots \delta_{2j}X_j + \Delta_{2P} = 0 \\ \vdots \\ \delta_{i1}X_1 + \delta_{i2}X_2 + \cdots \delta_{ii}X_i + \cdots \delta_{ij}X_j + \Delta_{iP} = 0 \\ \vdots \\ \delta_{j1}X_1 + \delta_{j2}X_2 + \cdots \delta_{ji}X_i + \cdots \delta_{jj}X_j + \Delta_{jP} = 0 \end{cases} \quad (4)$$

where δ_{ij} is the generalized displacement caused by the generalized force at j in the direction of x_i , and Δ_{iP} is the displacement caused by the actual external load in the direction of x_{ij} . δ_{ij} and Δ_{iP} are called the displacement influence coefficient (flexibility coefficient) and the free term, respectively. The calculation method is shown in **Eq. 5** and **Eq. 6**.

$$\delta_{ij} = \sum \int \frac{\bar{M}_i \bar{M}_j}{EI} ds \quad (5)$$

$$\Delta_{iP} = \sum \int \frac{\bar{M}_i M_P}{EI} ds \quad (6)$$

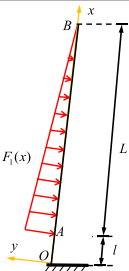
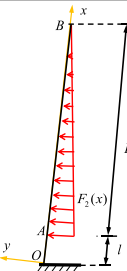


Writing **Eq. 4** as a matrix:

$$[\delta]\{X\} + \{\Delta\} = \{0\} \quad (7)$$

where $[\delta]$ is the structural flexibility matrix, X is the free term matrix of the structure, and Δ is the force matrix to be solved.

The constraint of the B1+2 coal seam on the rock pillar at point A is released, and the constraint reaction force X_1 is applied. The deformation coordination condition is that the deflection at point A is 0. Taking $F_1(x)$, $F_2(x)$, $F_3(x)$, and X_1 into **Eq. 5** and **Eq. 6**, the flexibility coefficient and the free term under different loads

TABLE 1 | Bending moment diagram of the rock pillar's basic structure under different loads.

	M_{F1}	M_{F2}	M_{F3}	M_{X1}
Basic structure				
δ_{ij}	—	—	—	$\frac{\beta}{3EI}$
Δ_{iP}	$-\frac{q_1 L^2 \rho}{12EI}$	$\frac{q_2 L^2 \rho}{12EI}$	$-\frac{q_3 l^2}{8EI}$	—

Notes $q_1 = \mu A \gamma_s L \sin^2 \alpha + (\gamma_L + \gamma_p) L \sin \alpha \cos \alpha$; $q_2 = f \gamma_L \lambda^{-1} L \sin^2 \alpha$; $q_3 = k A \gamma_s L \sin^2 \alpha$.

can be obtained. The results are shown in **Table 1** (only an approximate calculation is made in the table).

The binding force of the B1+2 coal seam on the rock pillar can be obtained by taking the calculation results in **Table 1** into **Eq. 7**.

$$X_1 = \frac{(q_1 - q_2)L^2}{4l} + \frac{3q_3 l}{8} \quad (8)$$

When the local stress conditions and physical and mechanical parameters of loess are known, q_1 and q_2 in **Eq. 8** are constant values. With mining of the B3+6 coal seam, the binding force q_3 of the B3+6 coal seam on the rock pillar gradually decreases. According to Newton's third law, the pressure of the rock pillar on the B1+2 coal seam gradually decreases. In short, the mining of the B3+6 coal seam has a pressure relief effect on the B1+2 coal seam, to a certain extent.

The suspended rock pillar will inevitably bend and deform. Assuming that the bending stiffness of the suspended rock pillar is constant, then the approximate differential equation of the deflection curve of the rock pillar can be expressed as follows:

$$EI\omega = - \int \left[\int M(x) dx \right] dx + C_1 x + C_2 \quad (9)$$

where C_1 and C_2 are integral constants, which are determined by the boundary conditions of the deflection curve of the beam, and $M(x)$ is the bending moment equation of the beam.

The deflection change of the rock pillar's OA section has a direct impact on the mining of the B3+6 coal seam. According to the superposition principle, the deflection curve equation of the rock pillar OA section can be obtained:

$$\omega(x) = \frac{(q_1 - q_2)L^2 x^2}{24EI} (1 - x) + \frac{q_3 x^2}{48EI} (-2x^2 + 5lx - 3l^2) \quad (0 < x \leq l) \quad (10)$$

Because the variation range of the parameters, such as the density of overlying strata and the density of backfill loess, is small, the paper considers that the material parameters at different positions are essentially the same, and the single parameter method is used to analyze the variation of the

deflection of a rock pillar with k in the OA section. According to the field measurement results, the default values of the expression parameters are set as follows: $\gamma_s = 29.82 \text{ KN/m}^3$; $\gamma_p = 24.83 \text{ KN/m}^3$; $\gamma_L = 16.2 \text{ KN/m}^3$; $E = 26.63 \text{ GPa}$; $A = 2$; $\lambda = 0.5$; $f = 0.85$; $\alpha = 87^\circ$; and $k = 0.5$. By substituting the above parameters

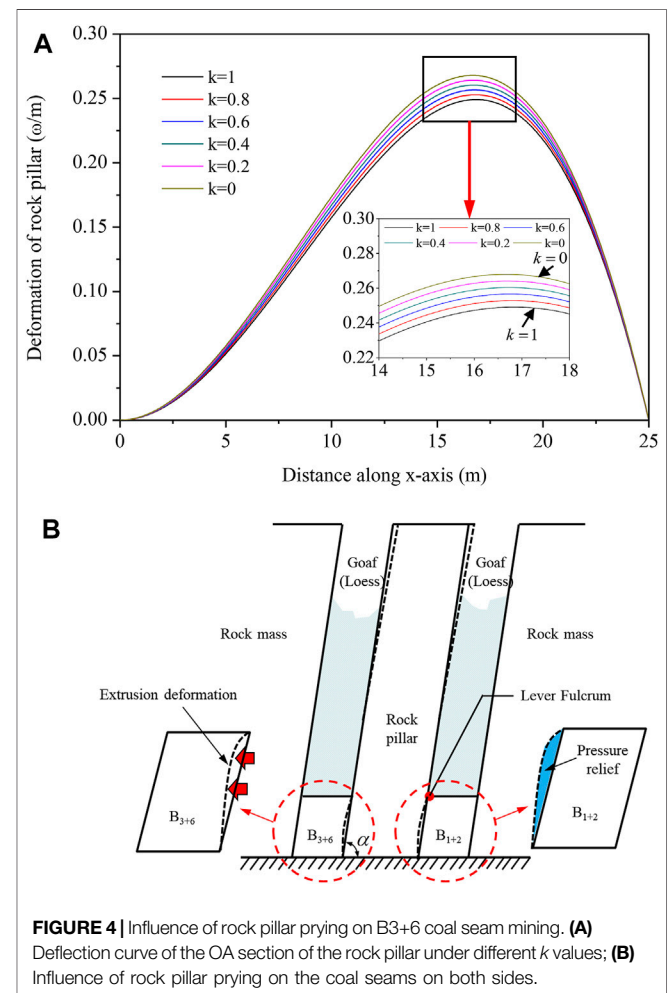


FIGURE 4 | Influence of rock pillar prying on B3+6 coal seam mining. **(A)** Deflection curve of the OA section of the rock pillar under different k values; **(B)** Influence of rock pillar prying on the coal seams on both sides.

into Eq. 10, the deflection curves of the OA section of the rock pillar under different k values are obtained (assuming that the deflection changes to the B3+6 coal seam are positive).

As seen from Figure 4A, with a decrease in the constraint weakening coefficient k , the deformation of the OA section of the rock pillar increases, especially in the range of 12–18 m above the working face, and the rock pillar crowing is more obvious. This is mainly because with the continuous extraction of the coal body in the B3+6 coal seam, the binding force of the coal body on the rock pillar is gradually reduced, and the activation degree of the rock pillar is strengthened, leading to a more obvious prying action. The rock pillar takes the coal body of coal seam B1+2 as the fulcrum and deflects to the goaf of coal seam B1+2, releasing the stress of the coal body of coal seam B1+2. However, the stress of the coal body of coal seam B3+6 increases due to the extrusion effect, which increases the probability of a rock burst (Figure 4B). The stress transfer of the rock pillar caused by prying is the main reason for the difference in rock bursts in adjacent coal seams with the same mining depth.

According to the load distribution, the moment function $M(x)$ along the rock pillar can be calculated, and then the deformation energy of the rock pillar at any position can be obtained. The bending moment at any position of the rock pillar is:

$$M(x) = \begin{cases} \frac{[\mu A \gamma_s - f \gamma_L \lambda^{-1} + (\gamma_L + \gamma_p) \cos \alpha] L^2 \sin^2 \alpha}{4l} \left[(L - 2l)x + 2l^2 - \frac{1}{3} L l \right] \\ + \frac{k A \gamma_s L \sin^2 \alpha}{8} (l - x)(l - 4x) & (0 \leq x \leq l) \\ \frac{(L + l - x) \sin^2 \alpha [\mu A \gamma_s + (\gamma_L + \gamma_p) \cos \alpha - f \gamma_L \lambda^{-1}]}{6} (L + l - x)^2 & (l < x \leq L + l) \end{cases} \quad (11)$$

According to the relationship between the bending moment and the elastic deformation energy, the elastic deformation energy at any x along the rock pillar can be expressed as:

$$U(x) = \begin{cases} \frac{1}{2EI} \left[\frac{[\mu A \gamma_s - f \gamma_L \lambda^{-1} + (\gamma_L + \gamma_p) \cos \alpha] L^2 \sin^2 \alpha}{4l} \left[(L - 2l)x + 2l^2 - \frac{1}{3} L l \right] + \frac{k A \gamma_s L \sin^2 \alpha}{8} (l - x)(l - 4x) \right]^2 & (0 \leq x \leq l) \\ \frac{1}{2EI} \left[\frac{(L + l - x) \sin^2 \alpha [\mu A \gamma_s + (\gamma_L + \gamma_p) \cos \alpha - f \gamma_L \lambda^{-1}]}{6} (L + l - x)^2 \right]^2 & (l < x \leq L + l) \end{cases} \quad (12)$$

Under the condition of different rock pillar suspension lengths L , the variation curve of the elastic deformation energy of the rock pillar along the coordinate axis x direction is shown in Figure 5A.

Figure 5A shows that the elastic deformation energy of the rock pillar increases with an increasing suspended height. At the junction of the coal seam and loess, the elastic deformation energy of the rock pillar reaches its maximum, and the rock pillar is most prone to fracturing. According to the statistical analysis of the high-energy microseismic events ($>10^3$ J) around the +450 mining horizontal pillar in the B3+6 coal seam (Figures 5B–C), it can be determined that 73.2% of the high-energy

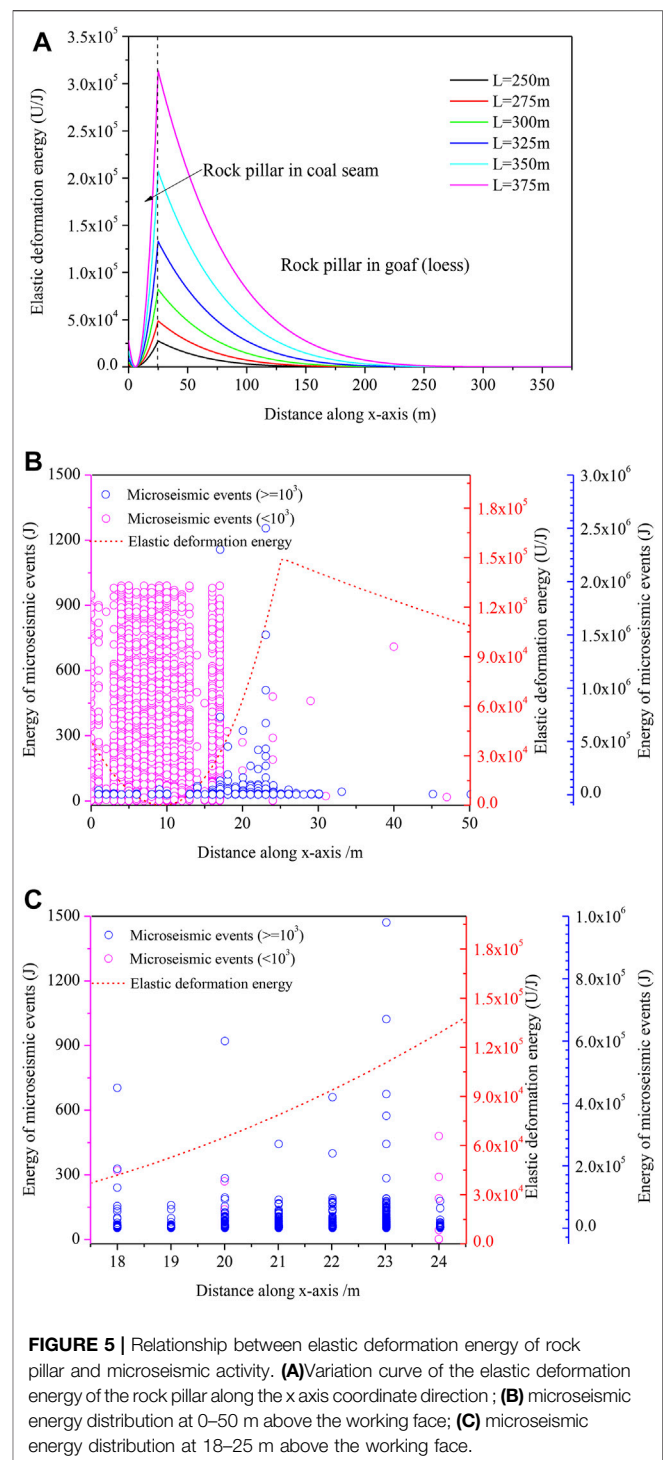


FIGURE 5 | Relationship between elastic deformation energy of rock pillar and microseismic activity. (A) Variation curve of the elastic deformation energy of the rock pillar along the x axis coordinate direction; (B) microseismic energy distribution at 0–50 m above the working face; (C) microseismic energy distribution at 18–25 m above the working face.

events are distributed in the range of 18–25 m above the working face (in particular, the high-energy events are more concentrated at approximately 22–23 m), which indicates that the rock pillar activity is more intense in this area. Because the theoretical calculation results are based on the assumption of idealized conditions, there will be some deviations from the actual conditions, but they are essentially consistent with the field

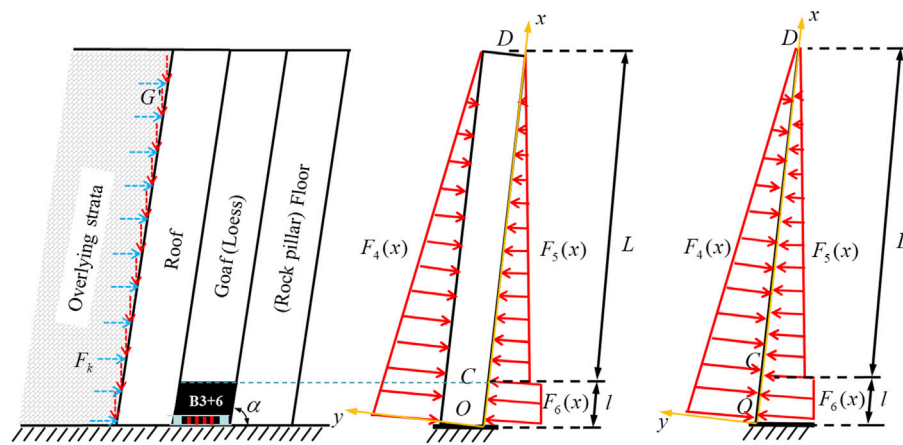


FIGURE 6 | Mechanical model of a rock pillar.

TABLE 2 | Bending moment diagram of the basic roof structure under different loads.

	M_{F4}	M_{F5}	M_{F6}
Basic structure			
δ_{ij}	—	—	$\frac{\beta}{3EI}$
Δ_{ip}	$-\frac{F_4(x)l^2}{12EI} (L + \frac{2}{3}l)^2$	$\frac{q_5 L l^2}{12EI} (L + 2l)$	—

Notes $q_5 = \frac{1}{\lambda} f \gamma_L L \sin^2 \alpha$.

monitoring results. The events near the working face are mainly low-energy position events, which are due to the compression of the rock pillar on the B3+6 coal seam, which leads to an increase in coal mining stress in this area. However, in the process of coal mining the coal body is constantly disturbed by an external load. In this process, a part of the coal body is released without storing high energy, which leads to more low-energy microseismic events.

A large amount of elastic deformation energy is stored in the rock pillar at the interface of the coal seam and loess. When the rock mass breaks a large amount of energy will be released. Because the distance between the fracture position of the rock pillar and coal seam is short, the seismic wave generated after the rock pillar fracture can act on the coal body quickly without great attenuation, resulting in a rapid increase in the coal stress and the superposition of dynamic stress and static stress. Therefore, B3+6 coal seam is prone to rock bursts. However, the elastic deformation energy of the rock pillar in the goaf area is small,

and the rock pillar does not easily break. Even if fracture occurs, the dynamic stress applied to the coal body by seismic wave load disturbance action will be greatly reduced due to the attenuation of the long-distance transmission process. To more intuitively show the variation in the vibration wave load disturbance with distance, it is assumed that the rock pillar breaks at x m away from the coal rock interface, the vibration wave propagates vertically down to the coal body of the B3+6 coal seam along the shortest distance, and the mine earthquake energy is 1×10^6 J. The densities of the coal and rock mass are 1,325 and 2,663 kg/m³, respectively, and the propagation velocities of the S-wave in intact sandstone are 4.2 and 2.4 km/s, respectively. One study (Wang et al., 2018) fitted and analyzed the *in situ* test data of the propagation law of underground vibration waves in coal mines and obtained the relationship between the peak vibration velocity of particles and the energy of mine earthquakes:

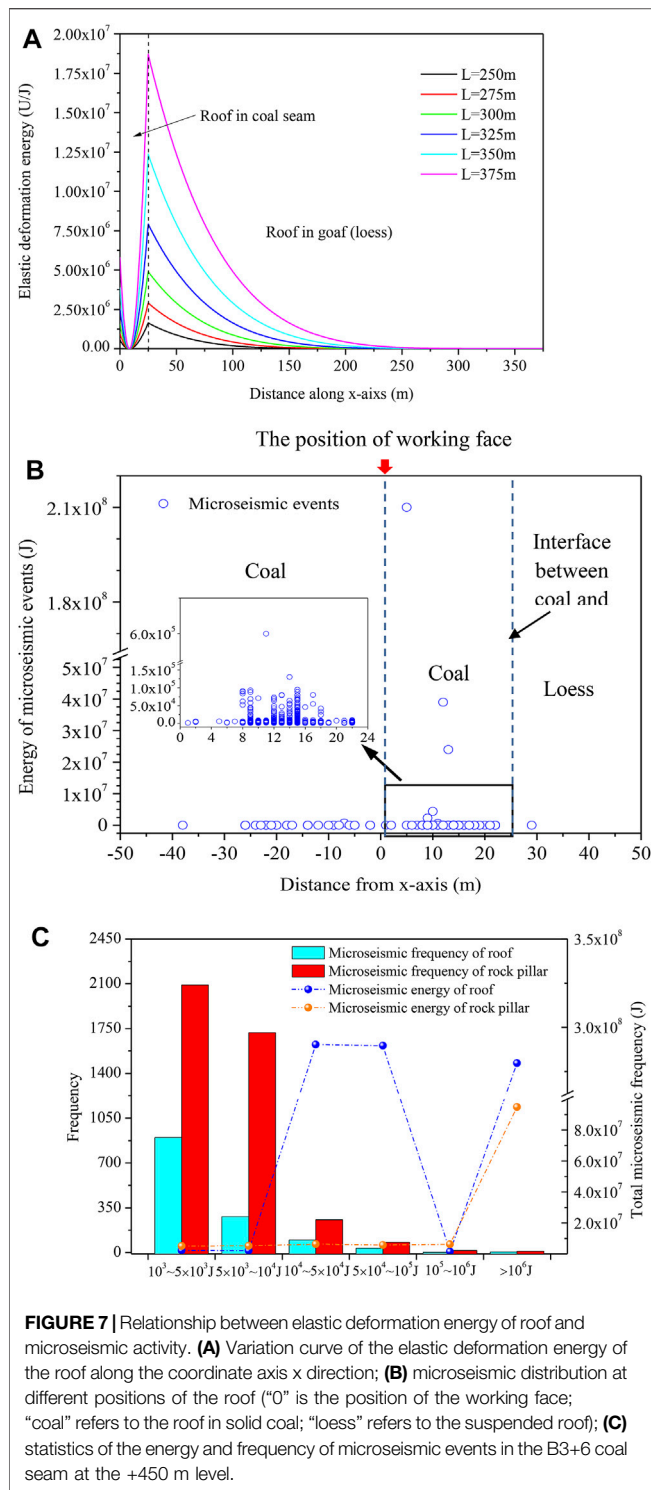
$$V_{pm} = 0.0645 U_k^{0.3566} \quad (13)$$

where V_{pm} is the peak vibration velocity of the particle and U_k is the energy value of the microseismic event.

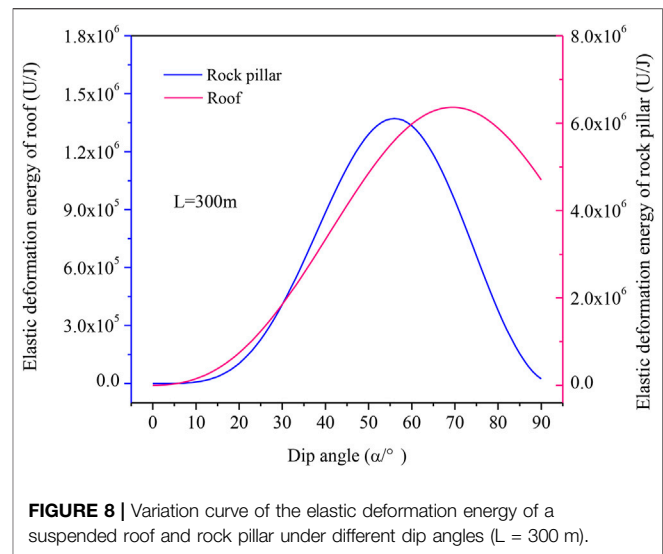
Assuming that coal is an isotropic continuous medium, the dynamic stress caused by the propagation of vibration waves to a specific position of the medium can be expressed as (Dou et al., 2014):

$$\begin{cases} \sigma_{dp} = 0.0645 U_k^{0.3566} \rho_m C_{pm} \prod_{i=1}^n L_i^{-\lambda_i} \\ \tau_{ds} = 0.0645 U_k^{0.3566} \rho_m C_{sm} \prod_{i=1}^n L_i^{-\lambda_i} \end{cases} \quad (14)$$

where σ_{dp} and τ_{ds} are the dynamic stresses produced by the P-wave and S-wave, respectively; ρ_m is the density of the medium at L_m away from the source boundary; C_{pm} and C_{sm} are the wave velocities of the P-wave and S-wave at L_m from the source boundary; L_i is the propagation distance of the seismic wave in the i -th medium, $L_m = \sum_{i=1}^m L_i$; m represents the m -th propagation medium; and λ_i is the attenuation coefficient of the i -th medium.



He and Dou (2012) used a microseismic monitoring system and blasting to obtain the attenuation coefficient $\lambda = 1.526$. According to Eq. 12, the variation curve of the vibration wave generated using a rock pillar fracture with the distance calculated. The result of calculation showed that the initial propagation stage of the vibration wave attenuates the fastest before gradually



weakening and tending to stability. When the propagation distance of the vibration wave is 10 m, the normal stress decreases from 94.5 to 2.8 MPa, and the tangential stress decreases from 26.9 It can be seen that the high-energy events produced by the rock pillar fracture near the coal rock interface very easily induces a rock burst, while the high-energy events produced by the fracture at the far end of the rock pillar have difficulty inducing a rock burst. Combined with the analysis results of the previous paper, as the rock pillar is difficult to fracture as a whole, the rock burst prevention and control in the south mining area of Wudong coal mine should be based on the rock mass blasting pressure relief near the coal rock interface, supplemented by the pressure relief of the remote suspended rock pillar. At the same time, the rock pillar can be artificially fractured on site to reduce the hanging length of the rock pillar.

Mechanical Model and Elastic Deformation Energy Distribution Function of the Roof

The analysis method is the same as that in *Theoretical Analysis of Rock Bursts Induced by Stress Transfer of Hard Rock Pillar*. The roof is simplified as a cantilever beam structure mechanical model, as shown in Figure 6, which comprehensively considers the stress of the rock pillar. The left side of the roof is affected by the horizontal tectonic stress F_k and the gravity load G' of the overburden, which can be simplified as the load $F_4(x)$ perpendicular to the roof. The supporting force of loess on the roof of the B3+6 coal seam goaf is $F_5(x)$, and the force between the left side of the roof and coal seam is $F_6(x)$.

Assuming that the width of the roof on any section is a unit length, the load $F_4(x)$ at any position of the roof can be expressed as

$$F_4(x) = (L + l - x) \sin \alpha (A \gamma_s \sin \alpha + \gamma_R \cos \alpha) \quad (0 \leq x \leq L + l) \quad (15)$$

The supporting force $F_5(x)$ of loess at any section on the right side of the roof can be expressed as

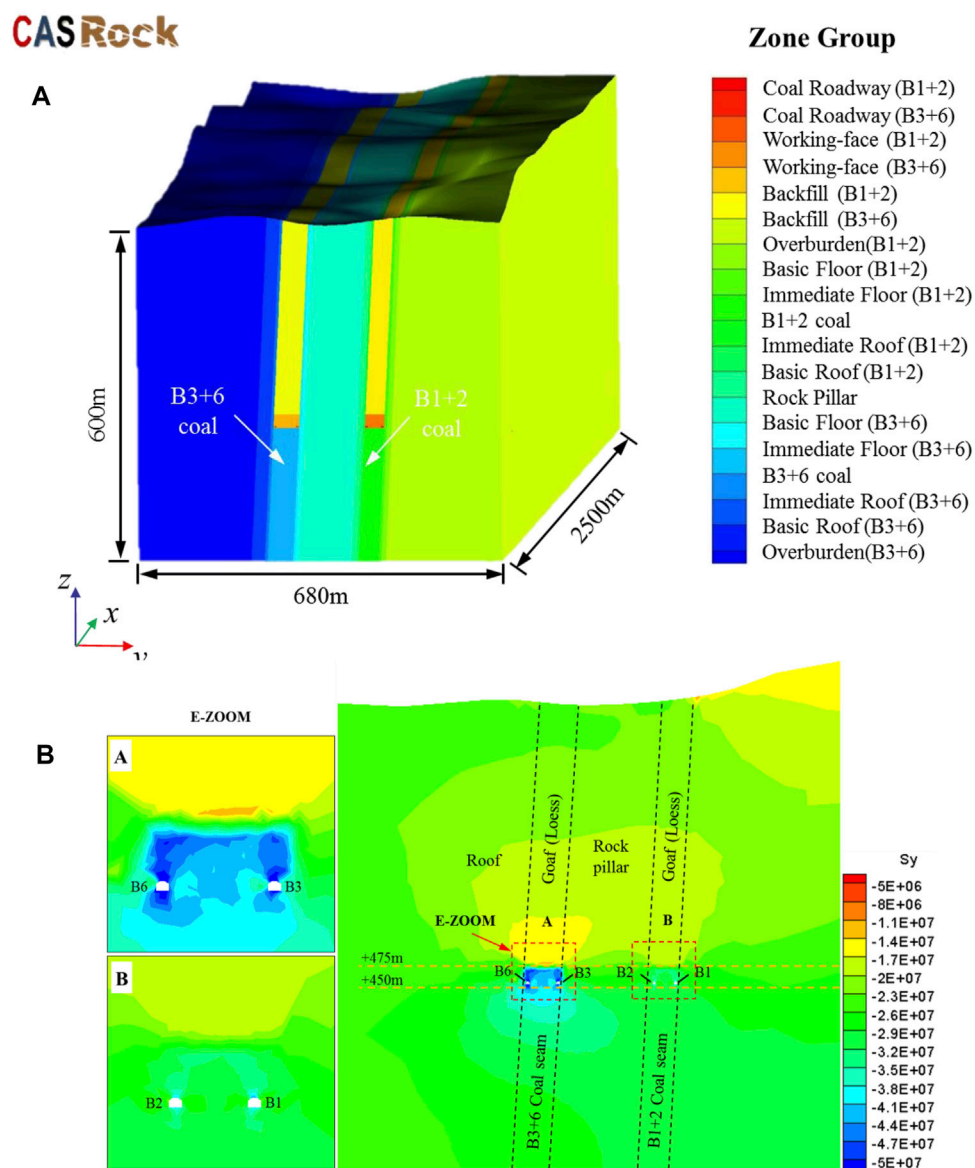


FIGURE 9 | Numerical simulation results of horizontal stress distribution in B3+6 coal seam. **(A)** Numerical calculation model; **(B)** Horizontal stress distribution of the "2.1" rock burst.

TABLE 3 | Measured tectonic stress (He et al., 2020a).

No	Level	σ_H			σ_h			σ_z		
		Stress/MPa	Trend/°	Plunge/°	Stress/MPa	Trend/°	Plunge/°	Stress/MPa	Trend/°	Plunge/°
1#	+475	15.2	158.0	15.6	10.4	70.4	8.6	8.7	188.3	72.1
2#	+475	14.1	157.3	7.8	9.6	69.2	7.8	8.4	189.4	74.8
3#	+450	15.8	158.5	15.9	10.2	76.0	15.0	9.3	193.0	69.4
4#	+450	15.4	160.5	13.6	11.3	76	8.6	9.5	178.7	65.0

σ_H is the maximum horizontal principal stress; σ_h is the minimum horizontal principal stress; and σ_z is the vertical stress.

TABLE 4 | Physical and mechanical property parameters of coal rock in the numerical model of the Wudong coal mine (Mine Safety Technology Branch CCRI, 2017a; Mine Safety Technology Branch CCRI, 2017b; Li et al., 2020a; He et al., 2021).

Stratum	γ KN/m ³	σ_t /MPa	σ_c /MPa	E/GPa	μ	C/MPa	$\Phi/^\circ$
Overburden (B1+2)	29.82	4.25	63.15	29.63	0.22	41.25	37.98
Basic Floor (B1+2)	27.50	3.01	58.11	21.70	0.25	46.57	34.20
Immediate Floor (B1+2)	26.67	4.17	49.63	18.02	0.19	32.46	38.40
B1+2 Coal Working-face (B1+2)	12.84	2.12	15.66	2.04	0.21	25.10	36.80
Immediate roof (B1+2)	20.32	3.77	30.20	26.80	0.21	35.34	33.05
Basic Roof (B1+2)	25.55	3.80	55.91	20.64	0.20	38.22	35.19
Rock Pillar	24.83	4.25	65.82	16.74	0.23	31.17	30.88
Basic Floor (B3+6)	28.87	4.39	61.12	25.91	0.22	37.66	35.10
Immediate Floor (B3+6)	27.74	4.01	57.32	20.39	0.25	33.82	36.25
B3+6 Coal Working-face (B3+6)	12.53	1.68	17.04	3.09	0.19	11.68	38.57
Immediate Roof (B3+6)	24.55	2.89	52.78	22.65	0.24	30.54	30.56
Basic Roof (B3+6)	26.85	3.66	46.90	27.56	0.22	34.22	35.91
Overburden(3+6)	27.46	4.43	58.79	21.37	0.22	21.46	36.50
Backfill (B1+2)	15.00	1.00	10.00	16.00	0.25	5.00	40.00
Backfill (B3+6)	15.00	1.00	10.00	16.00	0.25	5.00	40.00
Coal Roadway (B1+2)	12.84	2.12	15.66	2.04	0.21	25.10	36.80
Coal Roadway (B3+6)	12.53	1.68	17.04	3.09	0.19	11.68	38.57

$$F_5(x) = \frac{1}{\lambda} f \gamma_L \sin^2 \alpha (L + l - x) \quad (l \leq x \leq L + l) \quad (16)$$

If $F_4(x)$, $F_5(x)$ and $F_6(x)$ are brought into Eq. 5 and Eq. 6, the flexibility coefficient and the free term under different loads can be obtained. The uniform load of $F_6(x)$ is equivalent to the concentrated load acting on point C. The calculation results are shown in Table 2 (only approximate calculations are made in the table).

According to Newton's third theorem, the surface load of the roof at any section is

$$F_6(x) = \frac{1}{4l} \left[F_4(x) \left(L + \frac{2}{3}l \right)^2 - q_5 L (L + 2l) \right] \quad (17)$$

According to the load distribution, the bending moment function $M(x)$ at any position along the roof can be calculated

$$M(x) = \begin{cases} (L + l - x) (A \gamma_s \sin^2 \alpha + \gamma_R \sin \alpha \cos \alpha) \left[\frac{1}{6} (L + l - x)^2 - \frac{1}{4l} \left(L + \frac{2}{3}l \right)^2 (l - x) \right] \\ - \frac{f \gamma_L L^3 \lambda^{-1} \sin^2 \alpha}{4l} \left(x - \frac{l}{3} \right) & (0 \leq x \leq l) \\ \frac{(L + l - x)^3 \sin \alpha}{6} (A \gamma_s \sin \alpha + \gamma_R \cos \alpha - f \gamma_L \lambda^{-1} \sin \alpha) & (l < x \leq L + l) \end{cases} \quad (18)$$

According to the relationship between the bending moment and elastic deformation energy, the elastic deformation energy at any position x along the roof can be expressed as

$$U(x) = \begin{cases} \frac{1}{2EI} \left[(L + l - x) (A \gamma_s \sin^2 \alpha + \gamma_R \sin \alpha \cos \alpha) \left[\frac{1}{6} (L + l - x)^2 - \frac{1}{4l} \left(L + \frac{2}{3}l \right)^2 (l - x) \right] \right. \\ \left. - \frac{f \gamma_L L^3 \lambda^{-1} \sin^2 \alpha}{4l} \left(x - \frac{l}{3} \right) \right]^2 & (0 \leq x \leq l) \\ \frac{1}{2EI} \left[\frac{(L + l - x)^3 \sin \alpha}{6} (A \gamma_s \sin \alpha + \gamma_R \cos \alpha - f \gamma_L \lambda^{-1} \sin \alpha) \right]^2 & (l < x \leq L + l) \end{cases} \quad (19)$$

Under the condition of different suspended roof heights H , the variation curve of roof elastic deformation energy along the coordinate axis x direction is shown in Figure 7A.

Figure 7A shows that the elastic deformation energy of the roof increases with an increasing cantilever length. According to the theoretical calculation results, the elastic deformation of the roof at the interface of the B3+6 coal seam and loess can reach a maximum value. However, according to the field monitoring results (Figure 7B), the high-energy microseismic events of the roof are mostly concentrated in the range of 8–16 m above the working face. This is due to the stress transfer of the rock pillar and roof extrusion, the stress concentration area of the B3+6 coal seam being larger than that of the B1+2 coal seam, and the lateral restraint of coal on the roof being weakened, which leads to the downward movement of the bending position of the roof, in practice. Under the same cantilever length, the elastic deformation energy of the roof is much higher than that of the rock pillar. This is because one side of the roof directly bears the horizontal tectonic stress and the overlying load while the other side is in contact with the goaf, and the thickness of the roof

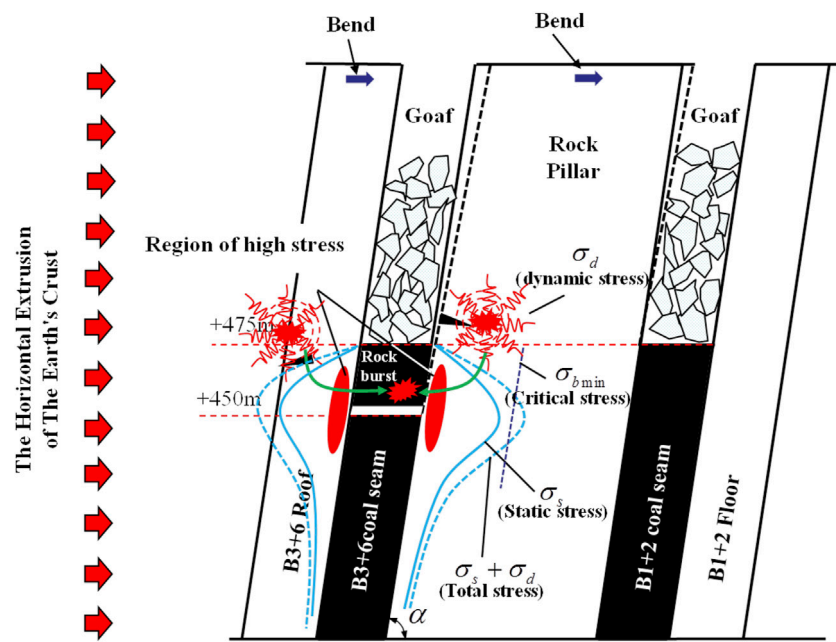


FIGURE 10 | Schematic diagram of the rock burst induced by superposition of the vibration wave load and static load.

is less than 1/2 of the rock pillar with a bending stiffness is far less than that of the rock pillar. Therefore, the roof plate is prone to bending deformation in the direction of the goaf, thus accumulating more elastic deformation energy. Both sides of the rock pillar are goaf, and the horizontal stress is greatly reduced after being attenuated by loess. The horizontal stress acting on the rock pillar is very small, which is mainly due to its own gravity bending. At the same time, the elastic strain energy of the rock pillar is relatively low due to its large thickness and large bending stiffness. Based on the statistics of the energy results of microseismic events in the period from the beginning of mining to the end of mining in B3+6 coal seam at the +450 m level (**Figure 7C**), it is determined that in the range of “ 10^3 – 10^4 J,” the frequency of high-energy microseismic events in the rock pillar is much higher than that in roof, while the sum of microseismic energy of roof in the range of “ 10^4 – 10^5 J” and “ $>10^6$ J” is much higher than that of rock pillar, and there is even a 10^8 J microseismic event. This is because both sides of the rock pillar are close to the working face. In the process of coal mining on both sides, compared with the roof of the B3+6 coal seam, the rock pillar will be more disturbed and release energy continuously. However, only one side of the roof is close to the working face, which is less affected by the mining disturbance, and the roof easily accumulates higher energy. Therefore, to prevent the occurrence of rock bursts in the B3+6 coal seam, roof pressure relief and artificial roof breaking are also important preventive measures. In addition, the lithology of the roof is carbonaceous mudstone. Under the condition of the same mine earthquake energy, the declining trend of the seismic wave generated after a roof fracture with distance must be the same as that of the rock pillar. Therefore, the blasting pressure relief of

the roof at the coal rock junction is also an effective means to prevent rock bursts.

Influence of the Coal Seam Dip Angle on Elastic Deformation Energy

Compared with the gently inclined coal seam, the initial depth of the rock burst in the steeply inclined coal seam is smaller. Therefore, under the same geological conditions, the coal seam dip angle is also an important factor affecting the occurrence of rock bursts. When the length of the suspended roof and rock pillar is fixed, the change curve of the elastic deformation energy with the coal seam dip angle is shown in **Figure 8**. For the roof, the elastic deformation energy first increases and then decreases when the coal seam dip angle changes from 0 to 90° and reaches the maximum value when $\alpha = 69.5^\circ$. Compared with the gently inclined coal seam, the roof of the steeply inclined coal seam has a higher elastic deformation performance. Under the same mining intensity, the rock mass is more prone to fracturing and releasing energy, which also explains why the critical depth of the rock burst in steeply inclined coal seams is much smaller than that in gently inclined coal seams. The change trend of the elastic denaturation energy of the rock pillar is the same as that of the roof. When $\alpha = 56.1^\circ$, the elastic deformation energy of the rock pillar reaches its maximum value, but the elastic deformation energy of the roof is much greater than that of the rock pillar. This is because the goaf of the coal seam weakens the influence of horizontal *in situ* stress, and a large part of the prying force of the rock pillar comes from a gravity action rather than horizontal tectonic force, while the roof is the opposite. The bending of the roof is the result of the joint action of horizontal

tectonic force and the overlying rock mass, and its own gravity is only a small part. At the same time, the bending stiffness of the rock pillar is also greater than that of the roof, so the elastic deformation energy of the roof is much higher than that of the rock pillar under the same cantilever length.

NUMERICAL ANALYSIS

According to the results of field investigation and theoretical analysis above, the occurrence of rock bursts in subvertical extra-thick coal seams are caused by the coupling effect of roof and rock pillar. In order to verify the rationality of this analysis result, numerical analysis on the stress concentration induced by the combination of roof and rock pillar after mining was carried out. A self-developed numerical code, i.e., Cellular Automata Software for engineering the Rockmass fracturing process (CASRock), was used to simulate the stress evolution of the coal seam in the process of mining. CASRock is composed of different modulars, such as EPCA for elasto-brittle-plastic analysis, THM-EPCA for coupled thermo-hydro-mechanical analysis, RDCA for continuum-discontinuum analysis in rock mass etc. (Feng et al., 2006; Pan et al., 2009; Pan et al., 2019; Li et al., 2020b; Feng et al., 2021; Mei et al., 2021). To avoid the interference from other factors, the influence of the geological structure and mining layout is omitted in the modeling. The model is established according to the actual size of the coal seam mining area. The B3+6 coal seam is 48 m wide, the B1+2 coal seam is 37 m wide, the middle pillar is 100 m wide, the vertical direction is 600 m high, the coal seam inclination is 87°, and the coal seam strike direction is 2,500 m long. The tunnel was modeled according to the actual size. The model has a total of 76,465 elements. The actual geological conditions, incorporating thinner and weaker interlayers are simplified (**Figure 9A**). Gravity load is applied in the vertical direction with the gravity acceleration 9.8 m/s². The horizontal to vertical stress ratio is calibrated by field *in situ* stress measurement between levels +450 and +475 m (**Table 3**). The trapezoidal boundary stress conditions are applied and the maximum horizontal principal stress and minimum principal stress at +450 m level are around 15.6 and 10.7 MPa, respectively. After that, all boundaries except top boundary are roller fixed.

The physical and mechanical parameters of the corresponding rock strata in the model are shown in **Table 4**, and the Mohr-Coulomb strength criterion is adopted for the calculation. The mechanical parameters of coal and rock in this paper are taken according to the previous research results (Li et al., 2020a; He et al., 2021) and the technical reports from Wudong Coal Mine (Mine Safety Technology Branch CCRI, 2017a; Mine Safety Technology Branch CCRI, 2017b). In the modeling, backfilled loess and broken coal gangue in the goaf are also considered.

Take the “2.1” rock burst as an example, when a rock burst occurs, the mining level of the B3+6 and B1+2 coal seams is +450 m, and the strike positions of the working face are 1824 and 2,309 m, respectively. The simulated stress distribution is shown in **Figure 9B** (impact appearance position: 1,730 m). It can be seen that the stress of the B3+6 coal seam reaches 45.1 MPa, which is 2.64 times the uniaxial compressive strength of the coal

body and 2.85 times the measured horizontal tectonic stress (mining depth of 365 m). High stress areas are found at the top and bottom of lanes B3 and B6 with the highest stress value 57.6 MPa, while at the top and bottom of lanes B1 and B2, the highest stress is only 41.2 MPa. The numerical results show that under the coupling action of rock pillar and roof, the stress concentration degree of B3+6 coal seam increases obviously, which might be the reason for the frequent occurrence of rock bursts in B3+6 coal seam. This is because the B3+6 coal seam is squeezed by a rock pillar and roof in addition to horizontal tectonic stress. The prying of the rock pillar causes a stress transfer between coal seam B1+2 and coal seam B3+6, which increases the stress of coal seam B3+6. Meanwhile, the bending of the coal seam roof to the goaf further increases the stress of the coal body. The joint action of the rock pillar and roof makes the high stress area near the B3 and B6 roadways more obvious, making it easier to produce an impact appearance.

DISCUSSION

Figure 10 shows a schematic diagram of the rock burst in the B3+6 coal seam under the coupling effect of the rock pillar and roof. The south mining area of the Wudong coal mine adopts horizontal section top coal caving, where the two adjacent coal seams are alternately mined. Due to the large dip angle of the coal seam, the roof does not easily crack. With an increasing mining depth, the stress concentration area of the B3+6 coal seam is produced under the action of the overlying rock mass and the horizontal *in situ* stress. At the same time, the release or weakening of the lateral restraint in the goaf provides deformation space for lateral deformation of the rock pillar between two coal seams. The bending and prying of the rock pillar causes the internal stress of the B3+6 coal body to increase suddenly, but the stress of the B1+2 coal seam is released. The mining stress of the B3+6 coal seam increases rapidly under the joint action of the roof and rock pillar, which provides high static stress conditions for the occurrence of rock bursts. In addition, with the mining of coal the hanging length of the roof and rock pillar of the B3+6 coal seam increases gradually. The fracture sliding of the roof and the local failure of rock pillar produce a stress wave, which makes the coal rock vibrate and rapidly increases the stress of the coal and rock mass, which provides dynamic stress conditions for the occurrence of rock burst, and ultimately leading to the occurrence of rock burst.

With an increase in the coal seam mining depth, the horizontal tectonic stress increases continuously, resulting in a stress increase of the B3+6 coal seam and B1+2 coal seam. When the mining depth is the same, the probability of a rock burst in the two coal seams should be similar. However, due to the special mining method of the near vertical extra thick coal seam, the rock pillar between the two coal seams is suspended and bent to one side of the goaf, which causes the rock pillar pry to squeeze the B3+6 coal seam and release the stress of the B1+2 coal seam (the rock pillar contains the roof of the B1+2 coal seam). At the same time, the bending compression of the roof of the B3+6 coal seam to the goaf further increases the stress of the B3+6 coal seam. Under the superposition of these three conditions, the

B3+6 coal seam is more prone to rock bursts. This is why the B3+6 coal seam is more prone to rock bursts than the B1+2 coal seam at the same mining depth.

CONCLUSION

In this paper, the mechanism of rock burst in subvertical extra-thick coal seams in the Wudong coal mine was studied using analytical and numerical methods. The main conclusions are as follows:

- 1) In the process of mining the B3+6 coal seam, the “inductive impact event” has an obvious regional distribution. A total of 62.5% is distributed in the rock pillar, 25.0% in the B3+6 coal seam, and 12.5% is distributed in the roof of the B3+6 coal seam. The rock pillar and B3+6 coal seam roof fractures are obvious, and the microseismic events in the energy range of 10^3 – 10^7 J have a concentrated distribution.
- 2) The mining of the B3+6 coal seam intensifies the activation of the rock pillar and leads to a more obvious prying action. The rock pillar deflects to the goaf of the B1+2 coal seam, releasing the stress of the B1+2 coal seam and increasing the stress of the B3+6 coal seam. The stress transfer of the rock pillar caused by prying is the main reason that the occurrences of rock bursts in adjacent coal seams with the same mining depth are quite different.
- 3) Mechanical models of the cantilever structure of the roof and rock pillar in subvertical extra-thick coal seams are established, and elastic deformation energy distribution functions are obtained. Under the same cantilever length, the elastic deformation energy of the roof is much greater than that of the rock pillar, which makes it easier to produce high-energy microseismic events. With an increasing mining depth,

the roof will become the dominant factor controlling the occurrence of rock bursts.

- 4) The occurrence of rock bursts in the southern mining area of the Wudong coal mine is caused by the coupling action of the rock pillar prying and roof bending. Roof bending and rock pillar prying provided high static stress conditions for the occurrence of rock bursts in the B3+6 coal seam. The superposition of dynamic disturbance caused by roof and rock pillar failure and the high static stress of the coal seam is the main reason for the occurrence of rock bursts in the B3+6 coal seam.

DATA AVAILABILITY STATEMENT

The original contributions presented in the study are included in the article/supplementary material, further inquiries can be directed to the corresponding author.

AUTHOR CONTRIBUTIONS

ZW: Contribution to the paper: Data collection, Writing-original draft, Visualization. P-ZP: Contribution to the paper: Conceptualization, Supervision, Methodology. JC: Contribution to the paper: Investigation, Data collection. XL: Contribution to the paper: Methodology, Investigation. SM: Contribution to the paper: Validation, Editing. PY: Contribution to the paper: Investigation, Visualization.

FUNDING

This work was supported by National Natural Science Foundation of China (Grant Nos. 52125903, 51621006).

REFERENCES

- Afraei, S., Shahriar, K., and Madani, S. H. (2019). Developing Intelligent Classification Models for Rock Burst Prediction after Recognizing Significant Predictor Variables, Section 1: Literature Review and Data Preprocessing Procedure. *Tunnelling Underground Space Technol.* 83, 324–353. doi:10.1016/j.tust.2018.09.022
- Aydan, O., Genis, M., Akagi, T., and Kawamoto, T. (2002). Assessment of Susceptibility of Rock Bursting in Tunnelling in Hard Rocks. *J. Toyota Coll. Technol.* 35, 391–396. doi:10.1201/9780203746653-67
- Cai, W., Bai, X., Si, G., Cao, W., Gong, S., and Dou, L. (2020). A Monitoring Investigation into Rock Burst Mechanism Based on the Coupled Theory of Static and Dynamic Stresses. *Rock Mech. Rock Eng.* 53, 5451–5471. doi:10.1007/s00603-020-02237-6
- Cao, J., Dou, L., Zhu, G., He, J., Wang, S., and Zhou, K. (2020). Mechanisms of Rock Burst in Horizontal Section Mining of a Steeply Inclined Extra-thick Coal Seam and Prevention Technology. *Energies* 13, 6043. doi:10.3390/en13226043
- Diez, R. R., and Álvarez, J. T. (2000). Hypothesis of the Multiple Subsidence Trough Related to Very Steep and Vertical Coal Seams and its Prediction through Profile Functions. *Geotechnical Geol. Eng.* 18, 289–311. doi:10.1023/a:1016650120053
- Dou, L.-m., Mu, Z.-l., Li, Z.-l., Cao, A.-Y., and Gong, S.-y. (2014). Research Progress of Monitoring, Forecasting, and Prevention of Rockburst in Underground Coal Mining in China. *Int. J. Coal Sci. Technol.* 1, 278–288. doi:10.1007/s40789-014-0044-z
- Dou, L., Cai, W., Cao, A., and Guo, W. (2018). Comprehensive Early Warning of Rock Burst Utilizing Microseismic Multi-Parameter Indices. *Int. J. Mining Sci. Technol.* 28, 767–774. doi:10.1016/j.ijmst.2018.08.007
- Driad-Lebeau, L., Lahaie, F., Al Heib, M., Josien, J. P., Bigarré, P., and Noirel, J. F. (2005). Seismic and Geotechnical Investigations Following a Rockburst in a Complex French Mining District. *Int. J. Coal Geology.* 64, 66–78. doi:10.1016/j.coal.2005.03.017
- Duan, H. M., Hu, X. M., and Wu, S. Z. (2008). Optimized Research on Coal Mining Method of Thin and Medium Steep Inclined Seam [J]. *Coal Sci. Technol.* 2, 16–18. doi:10.13199/j.cst.2008.02.21.duanhm.005
- Feng, G.-L., Feng, X.-T., Chen, B.-R., Xiao, Y.-X., and Zhao, Z.-N. (2019). Effects of Structural Planes on the Microseismicity Associated with Rockburst Development Processes in Deep Tunnels of the Jinping-II Hydropower Station, China. *Tunnelling Underground Space Technol.* 84, 273–280. doi:10.1016/j.tust.2018.11.008
- Feng, X.-T., Pan, P.-Z., and Zhou, H. (2006). Simulation of the Rock Microfracturing Process under Uniaxial Compression Using an Elasto-Plastic Cellular Automaton. *Int. J. Rock Mech. Mining Sci.* 43, 1091–1108. doi:10.1016/j.ijrmms.2006.02.006
- Feng, X., Chen, B., Li, S., Zhang, C., Xiao, Y., Feng, G., et al. (2012). Studies on the Evolution Process of Rockbursts in Deep Tunnels. *J. Rock Mech. Geotechnical Eng.* 4, 289–295. doi:10.3724/sp.j.1235.2012.00289

- Feng, X. T., Pan, P. Z., Wang, Z. F., and Zhang, Y. L. (2021). "Development of Cellular Automata Software for Engineering Rockmass Fracturing Processes," in International Conference of the International Association for Computer Methods and Advances in Geomechanics (Torino, Italy: Springer International Publishing). doi:10.1007/978-3-030-64514-4_4
- Heib, M. A. (2012). Numerical and Geophysical Tools Applied for the Prediction of Mine Induced Seismicity in French Coalmines. *Jig* 03, 834–846. doi:10.4236/jig.2012.324084
- He, J., and Dou, L.-M. (2012). Gradient Principle of Horizontal Stress Inducing Rock Burst in Coal Mine. *J. Cent. South. Univ.* 19, 2926–2932. doi:10.1007/s11771-012-1360-3
- He, J., Dou, L., Gong, S., Li, J., and Ma, Z. (2017). Rock Burst Assessment and Prediction by Dynamic and Static Stress Analysis Based on Micro-seismic Monitoring. *Int. J. Rock Mech. Mining Sci.* 93, 46–53. doi:10.1016/j.jirmms.2017.01.005
- He, M. (2011). Physical Modeling of an Underground Roadway Excavation in Geologically 45° Inclined Rock Using Infrared Thermography. *Eng. Geology*. 121, 165–176. doi:10.1016/j.enggeo.2010.12.001
- He, S., Chen, T., Vennes, I., He, X., Song, D., Chen, J., et al. (2020a). Dynamic Modelling of Seismic Wave Propagation Due to a Remote Seismic Source: A Case Study. *Rock Mech. Rock Eng.* 53, 5177–5201. doi:10.1007/s00603-020-02217-w
- He, S., Song, D., He, X., Chen, J., Ren, T., Li, Z., et al. (2020b). Coupled Mechanism of Compression and Prying-Induced Rock Burst in Steeply Inclined Coal Seams and Principles for its Prevention. *Tunnelling Underground Space Technol.* 98, 103327. doi:10.1016/j.tust.2020.103327
- He, X. Q., Chen, J. Q., Song, D. Z., He, S. Q., Li, Z. L., Zhong, T. P., et al. (2021). Study on Mechanism of Rock Burst and Early Warning of Typical Steeply Inclined Coal Seams. *Coal Sci. Technol.* 49, 13–22. doi:10.13199/j.cnki.cst.2021.06.002
- Kaiser, P. K., and Cai, M. (2013). "Critical Review of Design Principles for Rock Support in Burst-Prone Ground-Time to Rethink," in Seventh International Symposium on Ground Support in Mining & Underground Construction, Perth, WA, October 5–8, 2009. Editors Potvin Y. and Brady B. (Perth, WA: Australian Centre for Geomechanics), 3–38. doi:10.36487/ACG_rep/1304_01_Kaiser
- Lai, X. P., Sun, H., Shan, P. F., Cai, M., Cao, J. T., and Feng, C. (2015). Structure Instability Forecasting and Analysis of Giant Rock Pillars in Steeply Dipping Thick Coal Seams. *Int. J. Minerals, Metall. Mater.* 22, 1223. doi:10.1007/s12613-015-1190-z
- Lai, X. P., Yang, Y. R., Wang, N. B., Shan, P. F., and Zhang, D. S. (2018). Comprehensive Analysis to Temporal-Spatial Variation of Dynamic Instability of Steeply Inclined Coal-Rock Mass. *Chin. J. Rock Mech. Eng.* 37, 583–592. doi:10.13722/j.cnki.jrme.2017.1115
- Lai, X., Shan, P., Cao, J., Sun, H., Suo, Z., and Cui, F. (2014). Hybrid Assessment of Pre-Blasting Weakening to Horizontal Section Top Coal Caving (HSTCC) in Steep and Thick Seams. *Int. J. Mining Sci. Technol.* 24, 31–37. doi:10.1016/j.ijmst.2013.12.006
- Li, D. H., He, X. Q., Chen, J. Q., Song, D. Z., Li, Z. L., He, S. Q., et al. (2020a). Inducing Mechanism of Rockburst Occurring in Steeply-Inclined Coal Seam of Wudong Coal Mine. *J. China Univ. Mining Technol.* 49, 835–843. doi:10.13247/j.cnki.jcmt.001191
- Li, M., Mei, W., Pan, P.-Z., Yan, F., Wu, Z., and Feng, X.-T. (2020b). Modeling Transient Excavation-Induced Dynamic Responses in Rock Mass Using an Elasto-Plastic Cellular Automaton. *Tunnelling Underground Space Technol.* 96, 103183. doi:10.1016/j.tust.2019.103183
- Liu, C., Li, H., Mitri, H., Jiang, D., Li, H., and Feng, J. (2017). Voussoir Beam Model for Lower strong Roof Strata Movement in Longwall Mining - Case Study. *J. Rock Mech. Geotech. Eng.* 9, 1171–1176. doi:10.1016/j.jrmge.2017.07.002
- Lu, C.-P., Liu, G.-J., Zhang, N., Zhao, T.-B., and Liu, Y. (2016). Inversion of Stress Field Evolution Consisting of Static and Dynamic Stresses by Microseismic Velocity Tomography. *Int. J. Rock Mech. Mining Sci.* 87, 8–22. doi:10.1016/j.jirmms.2016.05.008
- Mazaira, A., and Konicek, P. (2015). Intense Rockburst Impacts in Deep Underground Construction and Their Prevention. *Can. Geotech. J.* 52, 1426–1439. doi:10.1139/cgj-2014-0359
- Mei, W., Li, M., Pan, P.-Z., Pan, J., and Liu, K. (2021). Blasting Induced Dynamic Response Analysis in a Rock Tunnel Based on Combined Inversion of Laplace Transform with Elasto-Plastic Cellular Automaton. *Geophys. J. Int.* 225, 699–710. doi:10.1093/gji/ggaa615
- Miao, S. J., Lai, X. P., and Cui, F. (2011). Top Coal Flows in an Excavation Disturbed Zone of High Section Top Coal Caving of an Extremely Steep and Thick Seam. *Mining Sci. Technol.* 21, 99–105. doi:10.1016/j.mstc.2010.12.006
- Mine Safety Technology Branch CCRI (2017a). *Appraisal Report on Bursting Liability of B1 + 2 Coal Seam and its Roof and Floor in Wudong Coal Mine*. Urumqi: Group XECOSE.
- Mine Safety Technology Branch CCRI (2017b). *Appraisal Report on Bursting Liability of B3 + 6 Coal Seam and its Roof and Floor in Wudong Coal Mine*. Urumqi: Group XECOSE.
- Naji, A. M., Emad, M. Z., Rehman, H., and Yoo, H. (2019). Geological and Geomechanical Heterogeneity in Deep Hydropower Tunnels: A Rock Burst Failure Case Study. *Tunnelling Underground Space Technol.* 84, 507–521. doi:10.1016/j.tust.2018.11.009
- Pan, P.-Z., Yan, F., Feng, X.-T., Wu, Z., and Qiu, S. (2019). Modeling of an Excavation-Induced Rock Fracturing Process from Continuity to Discontinuity. *Eng. Anal. Bound. Elem.* 106, 286–299. doi:10.1016/jenganabound.2019.05.014
- Pan, P. Z., Feng, X. T., and Zhou, H. (2009). Failure Evolution Processes of Brittle Rocks Using 3D Cellular Automaton Method. *Rock Soil Mech.* 30, 1471–1476. doi:10.16285/j.rsm.2009.05.054
- Qi, Q. X., Li, Y. Z., Zhao, S. K., Pan, P. Z., and Wei, X. Z. (2019a). Discussion on the Mechanism and Control of Coal Bump Among Mine Group. *J. China Coal Soc.* 44, 141–150. doi:10.13225/j.cnki.jccs.2018.1701
- Qi, Q. X., Li, Y. Z., Zhao, S. K., Zhang, N. B., Zheng, Y. W., Li, H. T., et al. (2019b). Seventy Years Development of Coal Mine Rockburst in China: Establishment and Consideration of Theory and Technology System. *Coal Sci. Technol.* 47, 1–35. doi:10.13199/j.cnki.cst.2019.09.001
- Simser, B. P. (2019). Rockburst Management in Canadian Hard Rock Mines. *J. Rock Mech. Geotechnical Eng.* 11, 1036–1043. doi:10.1016/j.jrmge.2019.07.005
- Unver, B., and Yasitli, N. E. (2006). Modelling of Strata Movement with a Special Reference to Caving Mechanism in Thick Seam Coal Mining. *Int. J. Coal Geology*. 66, 227–252. doi:10.1016/j.coal.2005.05.008
- Wang, H., Shi, R., Deng, D., Jiang, Y., Wang, G., and Gong, W. (2020). Characteristic of Stress Evolution on Fault Surface and Coal Bursts Mechanism during the Extraction of Longwall Face in Yima Mining Area, China. *J. Struct. Geology*. 136, 104071. doi:10.1016/j.jsg.2020.104071
- Wang, Z. Y., Dou, L. M., Wang, G. F., Feng, L. F., Kang, K., Bai, J. Z., et al. (2018). Resisting Impact Mechanical Analysis of an Anchored Roadway Supporting Structure under P-Wave Loading and its Application in Rock Burst Prevention. *Arab. J. Geosci.* 11, 1–18. doi:10.1007/s12517-018-3426-5
- Wu, Y. P., Liu, K. Z., Yun, D. F., Xie, P. S., and Wang, H. W. (2014). Research Progress on the Safe and Efficient Mining Technology of Steeply Dipping Seam. *J. China Coal Soc.* 39, 1611–1618. doi:10.13225/j.cnki.jccs.2014.9039
- Wu, Z. H., Pan, P. Z., Pan, J. F., Wang, Z. F., and Gao, J. M. (2021a). Analysis on Mechanism of Rock Burst and Law of Mine Earthquake Activity in Graben Structural Area. *Rock Soil Mech.* 42, 2225–2238. doi:10.16285/j.rsm.2020.1732
- Wu, Z. H., Pan, P. Z., Zhao, S. K., Liu, X. D., Miao, S. T., and Li, Y. Z. (2021b). Study on the Mechanism of Rock Bursts Caused by "Roof-Rock Pillar" in Mining Steeply-Inclined and its Prevention and Treatment. *J. China Coal Soc.* 46 (S1), 49–62. doi:10.13225/j.cnki.jccs.2020.0916
- Xu, J., Jiang, J., Xu, N., Liu, Q., and Gao, Y. (2017). A New Energy index for Evaluating the Tendency of Rockburst and its Engineering Application. *Eng. Geology*. 230, 46–54. doi:10.1016/j.enggeo.2017.09.015
- Xu, S. M., Li, S. Y., Li, D. X., Zhang, W. P., Lian, J., and Wei, Q. D. (2015). Geological Laws of Rock Burst Occurrence in Yima coalfield. *J. China Coal Soc.* 40, 2015–2020. doi:10.13225/j.cnki.jccs.2015.0715
- Zhu, S., Feng, Y., and Jiang, F. (2015). Determination of Abutment Pressure in Coal Mines with Extremely Thick Alluvium Stratum: A Typical Kind of Rockburst Mines in China. *Rock Mech. Rock Eng.* 49, 1943–1952. doi:10.1007/s00603-015-0868-x

Conflict of Interest: Author JC was employed by the company Shenhua Xinjiang Energy Company Limited.

The remaining authors declare that the research was conducted in the absence of any commercial or financial relationships that could be construed as a potential conflict of interest.

Publisher's Note: All claims expressed in this article are solely those of the authors and do not necessarily represent those of their affiliated organizations, or those of the publisher, the editors and the reviewers. Any product that may be evaluated in

this article, or claim that may be made by its manufacturer, is not guaranteed or endorsed by the publisher.

Copyright © 2021 Wu, Pan, Chen, Liu, Miao and Yu. This is an open-access article distributed under the terms of the Creative Commons Attribution License (CC BY). The use, distribution or reproduction in other forums is permitted, provided the original author(s) and the copyright owner(s) are credited and that the original publication in this journal is cited, in accordance with accepted academic practice. No use, distribution or reproduction is permitted which does not comply with these terms.



Deterioration and Cavity of Surrounding Rocks at the Bottom of Tunnel Under the Combined Action of Heavy-Haul Load and Groundwater: An Experimental Study

Zheng Li^{1,2,3}, Kunping Chen^{4*}, Ziqiang Li^{5,6}, Weiwei Huang⁵ and Xinsheng Wang⁴

¹School of Civil Engineering, Chongqing University, Chongqing, China, ²Chongqing University Industrial Technology Research Institute, Chongqing, China, ³Chongqing City Construction Investment (Group) Co., Ltd., Chongqing, China, ⁴School of Resources and Safety Engineering, Chongqing University, Chongqing, China, ⁵School of Civil Engineering and Architecture, Chongqing University of Science and Technology, Chongqing, China, ⁶Key Laboratory of New Technology for Construction of Cities in Mountain Area, Ministry of Education, Chongqing University, Chongqing, China

OPEN ACCESS

Edited by:

Jie Chen,
Chongqing University, China

Reviewed by:

Wang Tongtao,
Chinese Academy of Sciences (CAS),
China

Shi Xilin,
Institute of Rock and Soil Mechanics
(CAS), China

Junbao Wang,
Xi'an University of Architecture and
Technology, China

*Correspondence:

Kunping Chen
chen.kp@qq.com

Specialty section:

This article was submitted to
Geohazards and Georisks,
a section of the journal
Frontiers in Earth Science

Received: 19 September 2021

Accepted: 15 November 2021

Published: 13 December 2021

Citation:

Li Z, Chen K, Li Z, Huang W and
Wang X (2021) Deterioration and
Cavity of Surrounding Rocks at the
Bottom of Tunnel Under the Combined
Action of Heavy-Haul Load and
Groundwater: An Experimental Study.
Front. Earth Sci. 9:779578.
doi: 10.3389/feart.2021.779578

In China, the first tunnel was built in accordance with the 30-ton heavy-haul railway standard. Based on the change in water and soil pressure obtained from long-term on-site monitoring, the cavity mechanism of the surrounding rock at the bottom of a heavy-haul railway tunnel under rich water conditions was explored in this study. The cavity characteristics and degradation depth of the three types of surrounding rock under different axial loads and hydrodynamic pressures were analyzed through laboratory tests. The structural defects at the bottom of the tunnel and local cracks in the surrounding rock were determined to provide a flow channel for groundwater. The dynamic load of heavy-haul trains causes groundwater to exert high hydrodynamic pressure on the fine cracks. The continuous erosion of the bottom surrounding rock leads to a gradual loss of surrounding rock particles, which would further exacerbate with time. The cohesive soil surrounding rock is noticeably affected by the combined action of heavy-haul load and groundwater in the three types of surrounding rock, and the surrounding rock cavity is characterized by overall hanging. In the simulation experiment, the particle loss of the surrounding rock reached 1,445 g, which is 24.2% higher than that of the pebble soil surrounding rock and 40.8% higher than that of sandy soil surrounding rock. The findings of this study could be helpful for developing methods for defect prediction and treatment of heavy-haul railway tunnels.

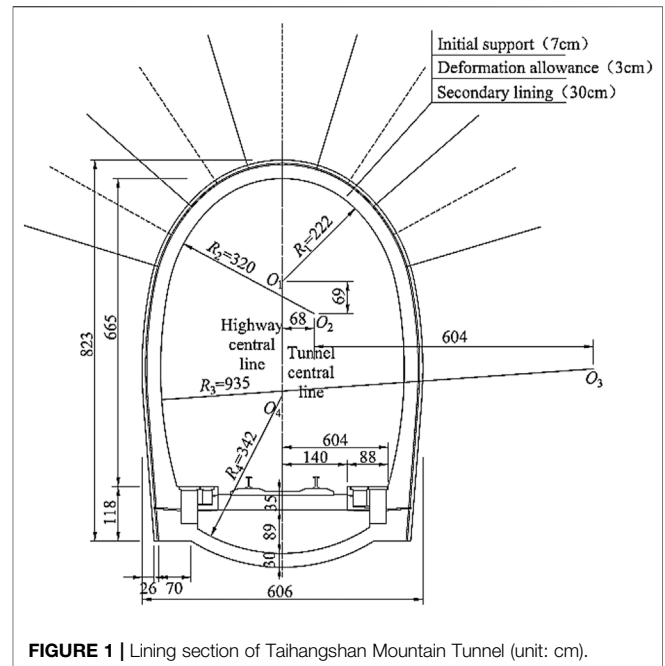
Keywords: heavy-haul railway tunnel, field test, train load-groundwater, laboratory test, tunnel bottom cavity

INTRODUCTION

At present, heavy-haul railway transportation has become one of the major means of transportation of global trade goods. Owing to their large volume, low cost, and high efficiency, heavy-haul railways have been widely promoted and used worldwide. In addition, the characteristics of heavy-haul railways, such as large axle loads, large total weights, high traffic densities, and large traffic volumes, have a significant dynamic impact on the structure of the bottom of a tunnel, greatly reducing the

operation state and service life of the tunnel structure. When the heavy-haul railway tunnel is built within a surrounding rock environment with groundwater development, the damage to the structure of the tunnel bottom is more severe under high frequency and large axle loads (Hong, 2000; Zou et al., 2016; Wu et al., 2017). Through the investigation of diseases of heavy-haul railway tunnels in service, it was found that these diseases are mainly concentrated to the bottom of the tunnel structure, for example, the deterioration of and cavity formation in the surrounding rock of the tunnel bottom, sinking of the basement, and mud pumping (Li, 2018; Lazorenko et al., 2019; Singh, 2019; Li et al., 2021). According to the disease situation, the train load is one of the major factors affecting the damage to the bottom of a heavy-haul railway tunnel. Combined with the effect of groundwater, the diseases of a tunnel bottom will further increase and endanger the safety of tunnel operation. Therefore, the evolution law of such diseases must be studied in the case of heavy-haul railway tunnels under the coupling effect of train load and groundwater.

At present, research on the formation and development of diseases of the bottom of heavy-haul railway tunnels under the coupling effect of train load and groundwater has achieved certain results. In the field investigation of heavy-haul railway tunnel diseases, the study by Mandal and Singh (2009) shows that when the tunnel is located in weak surrounding rock, the tunnel structure is strongly squeezed under large geological tectonic stress. Li Ziqiang (Li et al., 2019) determined that the diseases to the tunnel bottom are mainly manifested as basement surrounding rock cavities, especially under the combined action of groundwater and train load. Based on the plastic damage constitutive model of concrete, Ding Zude (Ding et al., 2012) found that the dynamic response and damage to the bottom structure of the tunnel increased with an increase in the cavity distance after the cavity occurred at the bottom of the tunnel. Based on the structural dynamics theory, Fan Xiangxi (Fan et al., 2018) analyzed the dynamic response of the tunnel structure under a train dynamic load and the change in the surrounding rock seepage field. Their results showed that the train dynamic load can significantly improve the water pressure of water-rich tunnels without considering the influence of waterproofing and drainage methods. Jia Chaojun (Jia et al., 2020) derived the damage evolution law of brittle rock surrounding rock under water-force coupling based on an elastic-plastic damage model. Joo and Shin (Joo and Shin, 2013) confirmed the relationship between pore water pressure and inflow rate. Su Haijian (Su, 2015) proposed a numerical method for calculating the degradation effect of surrounding rock under groundwater. Gao Liping (Gao et al., 2020) established a three-dimensional model of train load-tunnel-surrounding rock with an axle load of 300 kN, and divided the different degrees of the tunnel basement cavity into four grades: safety, alertness, danger, and extreme danger. Zhang Dongmei (Zhang et al., 2003) established a viscoelastic rheological model of a soft soil tunnel based on the Terzaghi consolidation theory and obtained tunnel settlement characteristics and settlement stability time. Liu Xinrong (Liu et al., 2012) studied the interaction between water and rock and found that the deterioration of rock was



mainly caused by the coupling of seepage and stress. Khamitov et al. (Khamitov et al., 2021) established a contact bond model to determine the damage range and discrete particle trajectory of weakly cemented sandstone during perforation and sand production. Wang Nianyi (Wang et al., 2016a) analyzed and summarized the variation law of water and soil pressure of heavy-haul railway tunnels under train loads and found that the dynamic influence of water and soil pressure of the surrounding rock of the tunnel base was mainly concentrated in the arch bottom and below the track. In summary, the surrounding rock cavity at the bottom of a heavy-haul railway tunnel is mainly caused by defects in the surrounding rock, train load, and groundwater. However, owing to the lack of field measured data, most of the research results are based on qualitative research of theoretical analysis and numerical simulation, and differ considerably from each other.

In this study, based on the engineering of the Taihangshan tunnel of the Wali line, according to the measured data of contact pressure and water pressure on the surface of the surrounding rock at the bottom of the tunnel, the phenomenon of surrounding rock degradation and cavity was explored. Combined with the actual conditions at the site, a laboratory test was conducted to explore the evolution law of the surrounding rock under the coupling effect of train load and groundwater, and the scope and degree of the cavity are quantitatively analyzed.

FIELD LONG-TERM MONITORING

Engineering Situation

This study is based on the Taihang Mountain Tunnel of Wali Railway, which is the first railway built according to the standard

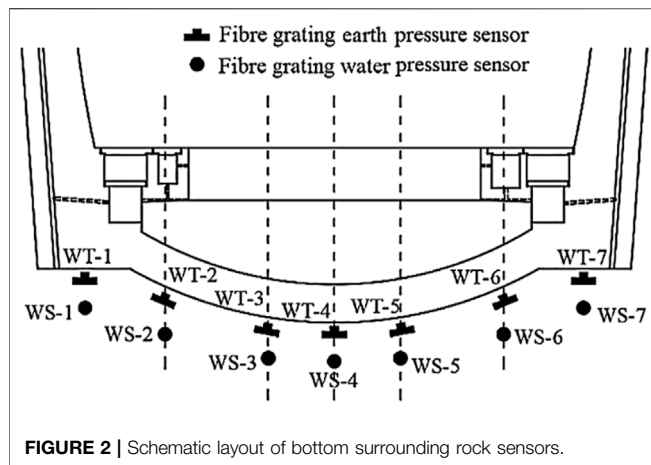


FIGURE 2 | Schematic layout of bottom surrounding rock sensors.

300-kN heavy-haul railway in China. Taihang Mountain is the third double-hole, single-line heavy-haul railway tunnel in China. A ballastless slab track structure is adopted in the tunnel. Curves were set in the inlet and outlet sections, and the remaining sections are straight lines. The length of the left tunnel is 18.125 km (DK 578 + 875–DK 597 + 000), and the right tunnel is 18.108 km (DYK 578 + 865–DYK 596 + 973). The actual axle load of the heavy-haul train in the Taihang Mountain Tunnel is 300 kN, the designed speed is 120 km/h, and the actual opening speed is 80 km/h. The daily traffic includes approximately 16 heavy-haul trains, with annual traffic exceeding 40 million tons. The hydrogeological conditions of the section where the tunnel is located are complex, and groundwater is developed in some mileages. The lining is illustrated in **Figure 1**.

Detection Scheme

Measuring Point Arrangement

To measure the distribution and variation in the water pressure and contact pressure of the surrounding rock of the tunnel basement under the long-term load of the heavy-haul train, the measuring points, as shown in **Figure 2**, were symmetrically arranged on the surface of the bottom surrounding rock, arch foot, bottom of the side ditch, bottom of the track, and center of the line (Goh et al., 2018; Zhang et al., 2020a). The geological condition of the sensor buried section is class V surrounding rock, and the buried depth is 872 m.

In the long-term monitoring process of the Taihang Mountain Tunnel, the measuring range of the soil pressure gauge (WT-1–WT-7) on the surrounding rock surface was 2 MPa, and the measuring range of the water pressure gauge (WS-1–WS-7) was

700 kPa. The sampling frequency was 100 Hz, that is, the sampling time interval was 0.01 s.

Test Sensors

In view of the complex hydrogeological conditions of the Taihang Mountain Tunnel, it is necessary to meet the requirements of strong anti-interference, long-term durability, and stable test data when selecting test sensors. Therefore, the long-term monitoring employed in this study uses fiber grating water and soil pressure sensors.

REMOTE MEASUREMENT RESULTS

Because the tunnel structure is statically indeterminate, it is bound to accumulate stress on the surrounding rock of the tunnel bottom under the action of high-frequency reciprocating trains during operation. This cumulative effect also directly affects the long-term change in the contact and water pressures of the surrounding rock at the bottom.

Long-Term Variation in Contact Pressure of the Bottom Rocks

To systematically study the variation law of the contact pressure of the surrounding rock at the bottom, the long-term variation law of the contact pressure of the rock was divided into four characteristic stages (before operation, 1 month, 6 months, and 1 year) according to the measured data analysis, as shown in **Table 1** and **Figure 3**.

As shown, the surrounding rock at the bottom of the Taihang Mountain tunnel is only disturbed by the construction stage before operating the tunnel. The surrounding rock at the bottom shows that the contact pressure distribution at each measuring point is uniform, with the maximum contact pressure of 51.419 kPa below the left rail. For a single-track railway tunnel, the transverse distribution of the base contact pressure should theoretically be symmetrical. However, because of factors, such as site construction methods and geological conditions, the inverted arch structure and the bottom surrounding rock cannot be fully fitted, resulting in a transverse distribution of the contact pressure.

After 1 month of operation, the contact pressure of each measuring point in the bottom surrounding rock increased, and the maximum contact pressure below the left rail was still 61.445 kPa. This phenomenon indicates damage between the inverted arch structure below the left rail and the bottom surrounding rock and implies a small deviation in the position

TABLE 1 | Contact pressure of surrounding rock of Taihangshan tunnel basement (kPa).

Traffic state	Left arch foot	Bottom of left ditch	Left track	Arch bottom	Right track	Bottom of right ditch	Right arch foot
Before operation	23.524	30.118	51.419	36.410	37.670	48.901	21.651
One month	28.324	38.181	61.445	57.345	53.465	50.657	24.310
Six months	40.563	89.129	84.129	72.997	62.766	73.806	23.245
One year	78.486	142.505	113.944	137.812	93.169	122.846	32.444

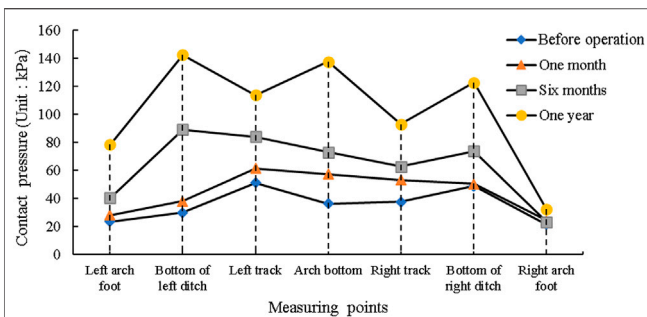


FIGURE 3 | Contact pressure of surrounding rock at the bottom of Taihangshan tunnel (unit: kPa).

of the earth pressure sensor. Under the load of a heavy-haul train, reciprocating rolling aggravates the damage to form a local cavity, resulting in an increase in the contact pressure.

After 6 months of operation, the contact pressure at the bottom of the left ditch on the surrounding rock surface increased to a maximum of 89.129 kPa. The increase in contact pressure at the adjacent positions of the left rail measuring point (the bottom of the left ditch and the arch bottom) was 195.9% and 100.5%, respectively. This phenomenon shows that with the increase in operation time, the damage cavity range of the surrounding rock at the tunnel bottom gradually expands to the adjacent measuring points.

After 1 year of operation, the measuring points at the bottom of the left ditch and arch bottom increased most obviously. The contact pressure at the bottom of the left ditch increased from 30.118 to 142.505 kPa, with an increase of 373.16%. The arch bottom measuring point increased by 278.5% from 36.410 to 137.812 kPa. The long-term effect of the contact pressure on the surface of the bottom surrounding rock is not the same after opening; however, the overall increment of the left is significantly higher than that of the right. According to this development law, it is easy to cause instability in the basement structure and affect the operation safety.

Long-Term Variation of Water Pressure in Bottom Rock

The uneven distribution of contact pressure was caused by groundwater erosion on the surrounding rock under heavy-haul train loads. To clarify the change in water pressure, the long-term change in hydrodynamic pressure was divided into four stages (before operation, 1 month, 6 months, and 1 year) and

analyzed. The hydrodynamic pressures are listed in **Table 2; Figure 4**.

As shown, the maximum hydrodynamic pressure of the Taihangshan tunnel before operation is 111.765 kPa, which is located below the left track. The main reason for the large water pressure at this measuring point is that during the construction stage, the empty slag of the base surrounding rock is not completely cleared during the inverted arch pouring, resulting in a large gap between the surrounding rock and inverted arch structure, and thus allowing space for groundwater to seep in and cause high hydrodynamic pressure owing to the disturbance of the construction on the surrounding rock.

After 1 month of operation, the water pressure at each measuring point increased. The local cavity beneath the left rail and the combined action of heavy-haul train load and groundwater make the water pressure at this position the maximum, which is 184.804 kPa. The maximum increase in the water pressure at the arch bottom is 143.2%.

After half a year of operation, under the long-term action of heavy-haul train load and groundwater, the surrounding rock damage under the track was intensified, and the cavity was developed. The maximum water pressure at this location on the lateral distribution was 239.804 kPa.

After 1 year of operation, the water pressure at the left rail measuring point increased from 111.765 to 250.931 kPa. With an increase in the cavity range, the hydrodynamic pressure of the adjacent measuring points, namely, the bottom of the left ditch and the arch bottom, also increased continuously. The largest increase was the increase in the arch bottom measuring point by 243.4%.

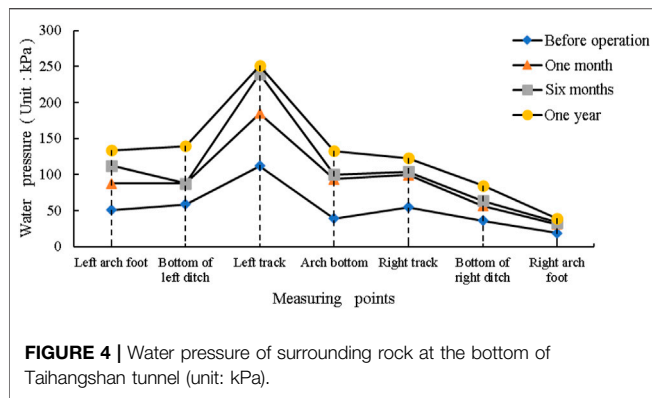
According to the analysis of the variation in water pressure at each measuring point, the dynamic water pressure increases with the increase in the degree of cavity, indicating that the load of the heavy-haul train intensifies the erosion of groundwater on the surrounding rock, expanding the surrounding rock gap, and intensifying the accumulation of groundwater. In view of the flow of water to places with low terrain, this phenomenon is the most obvious at the bottom of the surrounding rock arch for the single-track railway tunnel.

LABORATORY TEST DESIGN OF BOTTOM SURROUNDING ROCK CAVITY

According to the analysis results of the contact pressure and water pressure of the surrounding rock at the base of the Taihang Mountain Tunnel, after the heavy-haul railway tunnel

TABLE 2 | Water pressure of surrounding rock of Taihangshan tunnel basement (kPa).

Traffic state	Left arch foot	Bottom of left ditch	Left track	Arch bottom	Right track	Bottom of right ditch	Right arch foot
Before operation	50.673	58.605	111.765	38.528	54.694	36.000	18.605
One month	87.420	88.257	184.804	93.714	99.587	56.530	30.620
Six months	112.358	87.623	239.804	100.173	104.070	63.289	33.470
One year	133.453	139.389	250.931	132.294	122.523	84.622	38.625

**TABLE 3 |** Dynamic similarity constants of laboratory tests.

Physical quantity	Similitude parameter
Geometrical dimension L /m	$C_L = 20$
Pressure P /kPa	$C_P = 20$
Quality density C_p /Kg · m ⁻³	$C_p = 1$
Elastic modulus C_{Ed} /Pa	$C_{Ed} = 20$
Poisson ratio μ_d	$C_{\mu d} = 1$
Vibration (loading) frequency ω (1/s)	$C_\omega = C_L^{1/2} = 4.47$
Gravity g /m·s ⁻²	$C_g = 1$
Duration of input vibration T /s	$C_T = C_L^{-1/2} = 0.224$
Dynamic response stress σ_d /Pa	$C_{\sigma d} = C_L = 20$
Dynamic response line displacement S_d /m	$C_{Sd} = C_L = 20$
Dynamic response deformation ε_d	$C_{\varepsilon d} = 1$
Physical quantity	Similitude parameter
Dynamic response acceleration a /m·s ⁻²	$C_a = 1$
Dynamic response pore water pressure u /Pa	$C_u = C_L = 20$

TABLE 4 | Dynamic similarity constants of model tests.

Test parameters	Dynamic similarity constant
Permeability coefficient k /m·s ⁻¹	$C_k = 1$
Flow velocity v /m·s ⁻¹	$C_v = C_k = 1$
Water head height H /m	$C_H = C_L = 20$
Seepage quantity Q /m ³ ·s ⁻¹	$C_Q = C_L^2 C_k = 400$

was put into use, with an increase in operation time, the bottom surrounding rock was damaged and deteriorated under the influence of groundwater and large axle load; this affected the operational safety of the tunnel structure. It was predicted that the deterioration of the bottom surrounding rock was due to the erosion of the surrounding rock by groundwater and the loss of surrounding rock particles, resulting in cavities and cracks.

Based on the measured water–soil pressure, a laboratory test was established to simulate the cavity characteristics and formation mechanism of three types of surrounding rock: pebble soil, clay soil, and sandy soil. Among them, the cavity mechanism of the bottom structure of the heavy-haul railway tunnel was qualitatively obtained by studying the defect location, defect degree, soil pressure value of the bottom surrounding rock, and the degree of soil particle loss.

Principle of Experimental Design

Based on the similarity theorem, the geometric similarity ratio between the test model and prototype was 1:20, the similarity ratio of mass density was 1:1, and the similarity ratio of the elastic modulus of the surrounding rock and concrete inverted arch plate was 1:20. The bottom structure of Taihang Mountain adopts plain concrete; that is, the reinforcement is not conducted using the bottom structure model. The similarity constants of other physical quantities derived from the π theorem are listed in Table 3.

According to the seepage mechanics of the rock mass, the water movement along the rock gap obeys Darcy's law. The similarity constants of the fluids can be obtained by dimensional analysis, as shown in Table 4.

Test Materials and Simulation Devices

Test Material Parameters

The similar materials of the surrounding rock in this laboratory test were simulated by class V surrounding rock. Based on the physical and mechanical parameters of the Code for the design of railway tunnels (Ministry of Railways (200, 2005) class V, surrounding rock, and the actual situation of the Taihangshan tunnel surrounding rock, the range of physical and mechanical parameters of similar materials in the laboratory test of the surrounding rock was determined, as shown in Table 5.

To study the cavity characteristics and degree of degradation of various types of surrounding rocks, three representative soil surrounding rocks, namely, pebble soil, clay soil, and sandy soil, with high observability in a relatively short period of time, were selected for the study in a laboratory.

The tunnel bottom structure adopts a simplified model, and the inverted arch filling and inverted arch structure were regarded as the overall structure and prefabricated with gypsum. The inverted arch of the Taihang Mountain Tunnel was filled with C20 concrete, and C30 concrete was used as the inverted arch structure. Therefore, the concrete label of the tunnel bottom structure in this laboratory test was regarded as C25 for the simulation. According to the literature (*Similarity Theory and Structural Model Test*) (Yang, 2005; Wu et al., 2013; Wang et al.,

TABLE 5 | Physical and mechanical parameters of Class V surrounding rock prototype and similar materials.

Class V	Unit weight γ (kN/m ³)	Deformation modulus E (MPa)	Poisson ratio ν	Internal friction angle φ (°)	Cohesion C (kPa)
Prototype materials	17–20	1,000–2000	0.35–0.45	20–27	50–200
Similar materials	17–20	50–100	0.35–0.45	20–27	2.5–10

TABLE 6 | Comparison of concrete materials of tunnel basement structure.

Mechanical parameter	Prototype value (C25)	Model values
Uniaxial compressive strength	17	0.85
Elastic modulus	29.5	1.475

2016b; Zheng et al., 2017) and previous production experience, the mixture ratio of water, gypsum, and diatomite was determined as 1:0.8:0.2. The mechanical parameters of the concrete prototype and model are listed in **Table 6**.

Training the Simulation Device

The vibration motor 100 W belt governor was selected for the simulation, and the maximum excitation force could reach 130 kg. According to the dynamic load of a 300-kN heavy-haul train obtained by the excitation test, combined with the dynamic similarity ratio of the laboratory test, the excitation force was increased by 10 times as that applied to the surface of the tunnel bottom structure at 100 kPa.

Model Equipment

The self-designed test box was used for testing, and the test box was made of an organic glass plate to facilitate changes in the surrounding rock model and real-time measurement records (Zhang et al., 2020b). A consolidated flume was set on both sides of the main test box, and the water conveyance channel was set on the side wall of the flume to form a connecting device in the main test box, which provides water supply between the tunnel bottom structural model and the bottom surrounding rock. The size of the main test box was 30 cm × 30 cm × 40 cm, and the size of the two sides of the flume was 10 cm × 10 cm × 40 cm. The material similar to the tunnel bottom structure and a device with simulation of train were set inside the test box, as shown in **Figure 5**.

As shown in **Figure 5**, 1–8 structures are as follows: 1, main test box; 2, left flume; 3, right flume; 4, train load simulation device (exciter); 5, material similar to bottom surrounding rock; 6, material similar to tunnel bottom structure; 7, test water

storage; and 8, test bench; 9, water conveyance pipeline. The test bench was used to offset the dynamic effect of the exciter, as a detachable structure, and it cannot be set.

Test Conditions

This laboratory simulation test was mainly conducted to study the cavity characteristics and formation mechanism of three types of surrounding rocks under the combined action of heavy-haul train load and groundwater. The simulation opening time was 1 year, and the test time was approximately 118 h. The test conditions are listed in **Table 7**.

LABORATORY TEST RESULTS

In this laboratory test, the characteristics and formation mechanism of the cavity and degradation of the surrounding rock at the tunnel bottom under the combined action of heavy-haul train and groundwater were simulated for three types of surrounding rocks: pebble soil, clay soil, and sandy soil. Heavy-haul train load will further promote the erosion of groundwater on the surrounding rock, and under the same conditions of cavity, different types of surrounding rocks form and their distribution range is different.

Surrounding Rock of Pebble Soil

The laboratory test results of the pebble soil surrounding the rock under water-rich conditions are shown in **Figure 6**.

As shown in **Figure 6**, before the water-rich excitation test, the surface of the surrounding rock of the pebble soil was uniform, and there was no obvious bump phenomenon. After water-rich excitation, the grooves in the middle line were visible, and pebbles sank further owing to their weight. The mud sand was affected by the excitation force and the outlet of the flume, which gathered at the top of the surrounding rock and flowed into the groove to form a catchment area. Under the action of excitation, the light mud sand in the surrounding rock of pebble soil flowed out from the outlet of the flume, and approximately 941 g of fine particles was lost after excitation.

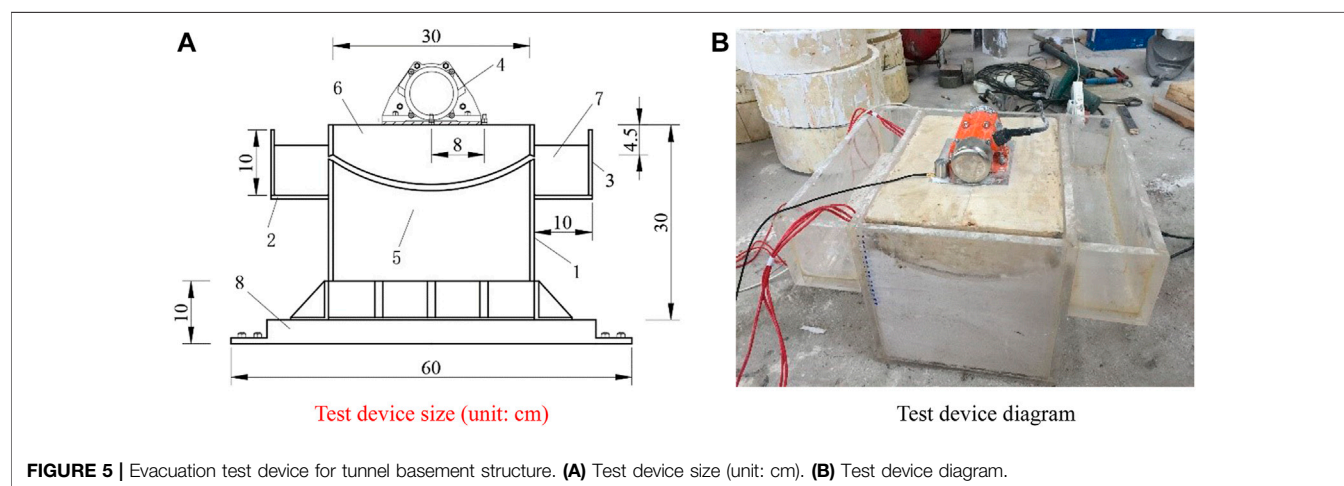


TABLE 7 | Test conditions.

Serial number	Tunnel bottom structure type	Rock condition	Hydrographic condition	Excitation times /10,000 times
1	Invert structure	Pebble soil	Water-rich	2.53×10^3
2		Clay soil		
3		Sandy soil		

**FIGURE 6** | Excitation of water-rich surrounding rock of pebble soil.**FIGURE 7** | Excitation of water-rich surrounding rock of clay soil.

Clay Soil Surrounding Rock

The laboratory test results of the clay surrounding rock under water-rich conditions are shown in **Figure 7**.

As observed, the surrounding rock morphology of clay soil before water-rich excitation is basically consistent with that of the anhydrous condition, and the clay property between particles of clay soil surrounding rock under water-rich conditions is enhanced, and the whole cohesive soil is stable and homogeneous. After water-rich excitation, owing to the lack of large-sized aggregates in the clay surrounding rock, the surrounding rock gradually changes from plasticity to flow plasticity under excitation. Because the plasticity of the surrounding rock weakens the active pore water between the surrounding rock particles and carries more clay particles, the cavity phenomenon is most obvious at the opening of the flume on the side of the test box owing to the high flow velocity. After excitation under water-rich conditions, the clay particles lost approximately 1,415 g.

Sandy Surrounding Rock

The laboratory test results of the sandy soil surrounding rock under water-rich conditions are shown in **Figure 8**.

As observed, the integrity of the sandy soil surrounding rock before water-rich excitation is good, and the distribution of surrounding rock particles on the surface of the bottom surrounding rock is relatively uniform without obvious defects. After water-rich excitation, the soil particles on the surface of the sandy soil surrounding the rock are no longer evenly distributed and appear uneven. Under the action of dynamic load, groundwater scours the bottom surrounding rock, and soil particles enter the flume on both sides through the water channels, thus forming a number of water channels on the surface of the sandy soil surrounding rock, thereby accelerating the formation of the cavity surrounding the rock.

There are three hard soil blocks with obvious uplift at the interface between the inverted arch structure and sandy soil surrounding the rock, and they are distributed along the corresponding positions of the two sides of the track. The main reason for the formation of the soil block is that under the combined action of heavy-haul train load and groundwater, the compactness of the sandy soil surrounding the rock is different in different regions after water erosion. The loose soil particles are eroded by water erosion, and an area with a large consolidation strength is gradually formed. After water-rich

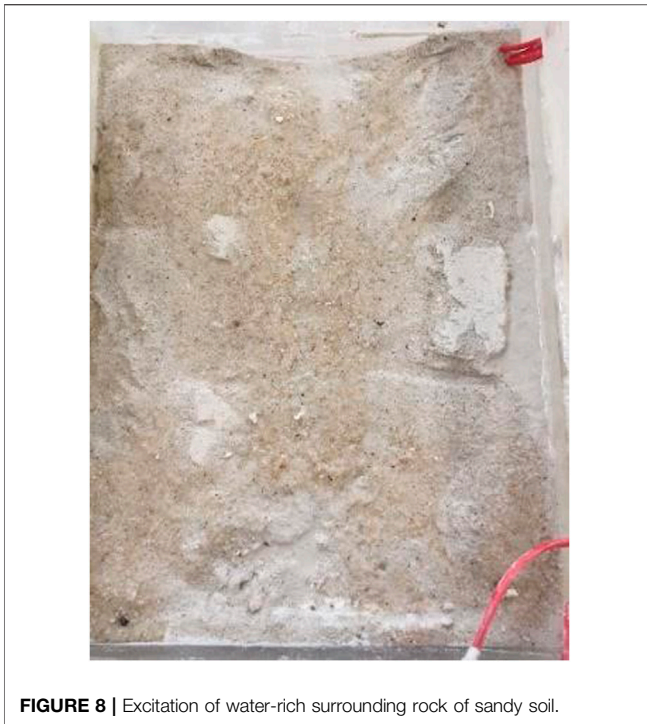


FIGURE 8 | Excitation of water-rich surrounding rock of sandy soil.

excitation, the weight loss of the sandy soil particles is approximately 858 g.

Comprehensive Analysis of Laboratory Test Results

Under the condition of rich water, after the long-term action of heavy-haul train simulation load, the tunnel bottom structure of sandy soil surrounding the rock is characterized by large hanging area. The cavity characteristics of the tunnel bottom structure in the clay surrounding the rock are characterized by a large hanging area with a partial uplift soil block. The cavity characteristics of the tunnel bottom structure of the pebble soil surrounding rock are shown as local cavities. It can be seen that the cavity characteristics of the tunnel bottom structure are mainly determined by the surrounding rock properties.

Under water-rich conditions, the cavity characteristics of different surrounding rocks are different after the heavy-haul train simulates the long-term load, and different degrees of particle loss occur. Among them, the loss of clay surrounding the rock is the most significant, reaching 1,415 g, which is 50.3% higher than that of the pebble soil surrounding rock and 64.9% higher than that of the sandy soil surrounding rock, which directly affects the range and depth of cavity deterioration of the bottom surrounding rock.

CONCLUSION

Based on the measured data of water and soil pressure in the Taihang Mountain tunnel, this study investigated the mechanism

of the structural cavity at the bottom of the tunnel, and discussed the cavity characteristics and degradation depth of pebble soil, clay soil, and sandy soil under the combined action of heavy-haul trains and groundwater. The following conclusions can be drawn.

- 1) For a heavy-haul railway tunnel under water-rich conditions, the objective defects of the bottom surrounding rock after the completion of construction continue to develop and deteriorate under the combined action of groundwater and train load. Thus, the soil and water pressures of the bottom surrounding rock continue to increase with the increase in the operation time, resulting in the instability of the tunnel base and affecting the operation safety.
- 2) Laboratory tests showed that the cavity characteristics of different surrounding rocks differ from each other. The cavity characteristics of the pebble soil surrounding rock are mainly characterized by small-scale local cavities, while that of the clay soil surrounding rock are overall hanging, and sandy soil surrounding rock are convex with local soil blocks.
- 3) Under the same test conditions, among the three typical types of surrounding rock, the clay soil surrounding rock had the largest particle loss of 1,310 g, which was 64.9% higher than that of 941 g of the pebble soil surrounding rock and 50.3% higher than that of 858 g of the sandy soil surrounding rock. Special attention should be paid to the deterioration and damage of the bottom surrounding rock in the weak surrounding rock area with rich water environment.
- 4) In the design and construction process of heavy-haul railway tunnels, especially in the condition of rich water, in addition to the safety of the bottom structure under a train impact load, it is also necessary to compare and select the design scheme of the bottom structure according to geological and groundwater conditions. In the construction process, more attention should be paid to the treatment of the bottom slag to improve the construction quality.

DATA AVAILABILITY STATEMENT

The original contributions presented in the study are included in the article/Supplementary Material, further inquiries can be directed to the corresponding author.

AUTHOR CONTRIBUTIONS

ZL: Overall thinking and thesis writing. KC: Data analysis, paper modification, and coloring. ZL: Experimental design. WH: Literature research and data analysis. XW: Data collation.

FUNDING

The constructive comments and suggestions made by the Open-end Fund of Key Laboratory of New Technology for Construction of Cities in Mountain Area (LNTCCMA-20210108), the

Chongqing Talent Plan (CQYC2020058263), Chongqing Natural Science Fund General Project (cstc2020jcyj-msxmX0904), Chongqing Talents : Exceptional Young Talents Project

(cstc2021ycjh-bgzxm0246), China Postdoctoral Science Foundation- General Project (2021M693739), the National Natural Science Foundation of China (5108098).

REFERENCES

- Ding, Z., Peng, L., Huang, J., and Shi, C. (2012). Traffic Safety Analysis of Railway Tunnel under the Condition of Base Void. *J. railways* (09), 104–110. doi:10.3969/j.issn.1001-8360.2012.09.018
- Fan, X., Yang, J., Ma, Y., Miao, D., and Ma, T. (2018). Dynamic Analysis of Fushui Tunnel under Train Vibration Load under Different waterproof and Drainage Methods. *J. Railway Sci. Eng.* 15 (11), 187–194. doi:10.19713/j.cnki.43-1423/u.2018.11.022
- Khamitov, F., Minh, N. H., and Yong, Z. (2021). Coupled CFD–DEM Numerical Modelling of Perforation Damage and Sand Production in Weak sandstone Formation. *Geo. Eng. Env.* 28, 100255. doi:10.1016/j.gete.2021.100255
- Gao, L., Luo, J., and Wang, L. (2020). Analysis on Vibration Characteristics and Life Prediction of Inverted Arch under the Condition of Base Void. *J. civil Eng.* 53 (S1), 348–354. doi:10.15951/j.tmgxcb.2020.s1.055
- Goh, A. T. C., Zhang, W., Zhang, Y., Xiao, Y., and Xiang, Y. (2018). Determination of Earth Pressure Balance Tunnel-Related Maximum Surface Settlement: a Multivariate Adaptive Regression Splines Approach. *Bull. Eng. Geol. Environ.* 77, 489–500. doi:10.1007/s10064-016-0937-8
- Hong, L. (2000). An Overview of Foreign Heavy Haul Railway. *Railway Eng. J.* (4), 32–34. doi:10.3969/j.issn.1006-2106.2000.04.009
- Jia, C., Wang, Y., Gong, C., Lei, M., and Shi, C. (2020). Study on Constitutive Model of Tunnel Surrounding Rock under Water Force Coupling. *J. underground Space Eng.* 16 (126(S1)), 106–113.
- Joo, E. J., and Shin, J. H. (2013). Relationship between Water Pressure and Inflow Rate in Underwater Tunnels and Buried Pipes. *Géotechnique* 64 (3), 226–231. doi:10.1680/geot.12.p.185
- Lazorenko, G., Kasprzhitskii, A., Khakiev, Z., and Yavna, V. (2019). Dynamic Behavior and Stability of Soil Foundation in Heavy Haul Railway Tracks: A Review. *Construction building Mater.* 205, 111–136. doi:10.1016/j.conbuildmat.2019.01.184
- Li, Z., Huang, W., Xu, Z., Tang, X., Wang, M., Yu, L., et al. (2021). Analysis of the Mechanical Characteristics of Different Track Bed Types in Heavy-Haul Railway Tunnels. *Math. Probl. Eng.* 2021 (2), 1–11. doi:10.1155/2021/5527073
- Li, Z. (2018). *Dynamic Characteristics and Design Method of Heavy Haul Railway Tunnel Structure*. Chengdu: Southwest Jiaotong University.
- Li, Z., Wang, N., Yu, Li., and Xu, Z. (2019). Study on Damage Mechanism of Surrounding Rock at the Bottom of Heavy Haul Railway Tunnel. *J. railways* 41 (07), 162–170. doi:10.3969/j.issn.1001-8360.2019.07.021
- Liu, X., Fu, Y., Zheng, Y., and Liang, N. (2012). Study on the Influence of Water Rock Interaction on Rock Degradation. *J. underground Space Eng.* (01), 77–82. doi:10.3969/j.issn.1673-0836.2012.01.013
- Mandal, S. K., and Singh, M. M. (2009). Evaluating Extent and Causes of Overbreak in Tunnels. *Tunnelling Underground Space Tech.* 24 (1), 22–36. doi:10.1016/j.tust.2008.01.007
- Ministry of Railways (2005). *TB10003-2005 Code for Design on Tunnel of Railway*. Beijing: China Railway Publishing House.
- Singh, M. (2019). Subgrade Instability and Fluidisation under Cyclic Railway Loading. Philosophy thesis. Wollongong(Australia): University of Wollongong.
- Su, H. (2015). *Seepage Evolution Mechanism and Engineering Application of Deep Jointed Rock Mass*. Xuzhou: China University of mining and technology.
- Wang, K., Li, S., Zhang, Q., Zhang, X., Li, L., Zhang, Q., et al. (2016). Development and Application of New Similar Materials for Fluid - Solid Coupling Model Test. *Geotechnics* 37 (09), 2521–2533.
- Wang, N., Luo, Y., Li, Z., et al. (2016). Dynamic Study on Water and Soil Pressure of Surrounding Rock at the Base of Heavy Haul Railway Tunnel. *Hydrogeology Engineering Geology*. 43 (4), 96–102. doi:10.16030/j.cnki.issn.1000-3665.2016.04.16
- Wu, B., Zhu, H., Xu, Q., and Ming, J. (2013). Experimental Study on Similar Materials of Grade IV Weak Surrounding Rock. *Geotechnics* 34 (S1), 109–116.
- Wu, Q., Li, Z., Yu, Li., Huayang, Y., and Wang, M. (2017). Experimental Study on Long-Term Dynamic Characteristics of Base Structure of Heavy Haul Railway Tunnel. *Vibration and impact* 36 (10), 127–133. 167. doi:10.13465/j.cnki.jvs.2017.10.021
- Yang, J. (2005). *Similarity Theory and Structural Model Test*. Wuchang: Wuhan University of Technology Press.
- Zhang, D., Huang, H., and Wang, J. (2003). Coupling Analysis of Viscoelastic Rheology and Consolidation of Long-Term Ground Settlement of Soft Soil Tunnel. *J. rock Mech. Eng.* 22 (0z1), 2359–2362. doi:10.3321/j.issn:1000-6915.2003.z1.049
- Zhang, W., Zhong, H., Zeng, Z. K., Wu, D. F., and Zhang, Y. (2020). Visualization and Digitization of Model Tunnel Deformation via Transparent Soil Testing Technique. *Underground Space* 2020 (1). doi:10.1016/j.undsp.2020.05.004
- Zhang, W. G., Li, H. R., Wu, C. Z., Li, Y. Q., Liu, Z. Q., and Liu, H. L. (2020). Soft Computing Approach for Prediction of Surface Settlement Induced by Earth Pressure Balance Shield Tunneling. *Underground Space* 6, 353–363. doi:10.1016/j.undsp.2019.12.003
- Zheng, L., He, C., Gao, X., Yang, S., Luo, Y., and Yang, W. (2017). Development and Application of Similar Materials for Rock Tunnel Seepage Model Test. *J. Harbin Inst. Tech.* 49 (09), 33–39. doi:10.11918/j.issn.0367-6234.201607075
- Zou, W., Zhang, M., Liu, Y., and Ma, W. (2016). 30t Axle Load of Heavy Haul Railway Tunnel Basement Structure Stress Distribution and Dynamic Response. *China Railway Sci.* 37 (05), 50–57. doi:10.3969/j.issn.1001-4632.2016.05.07

Conflict of Interest: The handling editor declared a shared affiliation with with the authors (ZL, KC, ZL, WH, XW) at time of review.

Author ZL was employed by the company Chongqing City Construction Investment (Group) Co., Ltd.

The remaining authors declare that the research was conducted in the absence of any commercial or financial relationships that could be construed as a potential conflict of interest.

Publisher's Note: All claims expressed in this article are solely those of the authors and do not necessarily represent those of their affiliated organizations, or those of the publisher, the editors, and the reviewers. Any product that may be evaluated in this article, or claim that may be made by its manufacturer, is not guaranteed or endorsed by the publisher.

Copyright © 2021 Li, Chen, Li, Huang and Wang. This is an open-access article distributed under the terms of the Creative Commons Attribution License (CC BY). The use, distribution or reproduction in other forums is permitted, provided the original author(s) and the copyright owner(s) are credited and that the original publication in this journal is cited, in accordance with accepted academic practice. No use, distribution or reproduction is permitted which does not comply with these terms.



Tailings Dam Break: The Influence of Slurry with Different Concentrations Downstream

Xuanyi Chen¹, Xiaofei Jing^{1*}, Yulong Chen^{2*}, Changshu Pan^{3*} and Wensong Wang⁴

¹School of Safety Engineering, Chongqing University of Science and Technology, Chongqing, China, ²School of Energy and Mining Engineering, China University of Mining and Technology-Beijing, Beijing, China, ³Chongqing GaoXin Engineering Survey and Design Institute Ltd., Co., Chongqing, China, ⁴School of Resources and Safety Engineering, Chongqing University, Chongqing, China

OPEN ACCESS

Edited by:

Jie Chen,
Chongqing University, China

Reviewed by:

Yulong Cui,
Anhui University of Science and
Technology, China
Huafu Qiu,
Xi'an University of Science and
Technology, China
Zhihong Zhao,
Tsinghua University, China

*Correspondence:

Xiaofei Jing
xfjing@cqust.edu.cn
Yulong Chen
chenyulong@cumt.edu.cn
Changshu Pan
pcsqs@163.com

Specialty section:

This article was submitted to
Geohazards and Georisks,
a section of the journal
Frontiers in Earth Science

Received: 16 June 2021

Accepted: 15 November 2021

Published: 24 December 2021

Citation:

Chen X, Jing X, Chen Y, Pan C and
Wang W (2021) Tailings Dam Break:
The Influence of Slurry with Different
Concentrations Downstream.
Front. Earth Sci. 9:726336.
doi: 10.3389/feart.2021.726336

The risk of tailings dam-break disaster is dependent on the type of slurry and its flow characteristics. The flow characteristics of slurry surging from tailings dams collapse are directly influenced by grain size, breach width, slurry concentration, and surface roughness of the gully. Among these parameters, slurry concentration plays the most critical role, but there are few studies on it. This paper focuses on the flow characteristics of slurry with different concentrations, and a series of flume experiments were carried out to obtain the flow characteristics of inundated height, impact force, and velocity in 30%, 40%, 50%, and 60% concentrations. The study confirms that the concentration of slurry has a significant influence on the flow characteristics. Through the experimental study, it is observed that, with the decreasing of slurry concentration, the impact force and velocity of slurry increased in varying degrees; on the contrary, the flow height elevated with the slurry concentration decreasing. The main reason is that the higher the slurry concentration, the higher the static yield stress and viscosity—in varying degrees. The results can provide a detailed understanding of the slurry concentration influence on the flow characteristics, which guides the evacuation time and height downstream.

Keywords: tailings dam, dam break, slurry concentration, flow characteristic, model experimental

INTRODUCTION

Tailings are generated from mineral processing operations. The release of tailings to an open environment causes serious safety and environmental issues. The tailings are generally retained in the tailings storage facility (TSF) for reuse purposes. Once the TSF breaks, it causes flooding, which pollutes the environment; moreover, the slurry causes serious loss of life and property downstream.

TSF is a unique industrial structure and also a dangerous source of artificial debris flow with high potential energy (Tang et al., 2012; Detzel, 2016). In recent years, accidents of TSF caused by heavy rainfall or earthquakes have occurred frequently, resulting in loss of lives and property (Moxon, 1999; Jing et al., 2019). Therefore, it is necessary to conduct an in-depth study to improve the prevention and mitigation of TSF disasters. Previous research on tailings dams mainly focuses on environmental pollution, stability analysis, and the mechanical properties of tailings (Nelson, 1977; Finn, 1993; Rico et al., 2008; Yu et al., 2014; Bhuiyan, 2016). Wijewickreme and Lu study the mechanical properties of tailings through indoor geotechnical tests (Wijewickreme et al., 2005; Lu et al., 2019). Proskin analyzes the stability of the tailings dam under a freeze–thaw condition by examining the influence of the freeze–thaw cycle on the permeability of fine tailings (Proskin et al.,

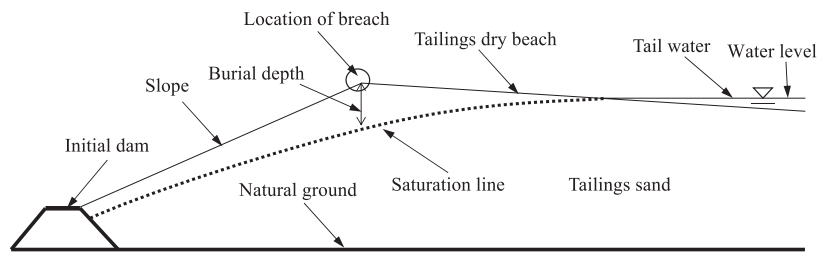


FIGURE 1 | Cross-section diagram of tailings dam.

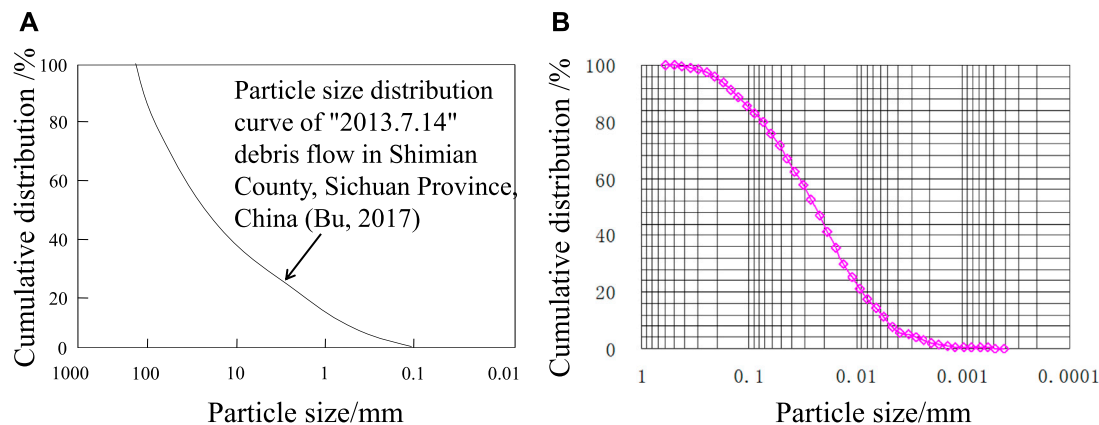


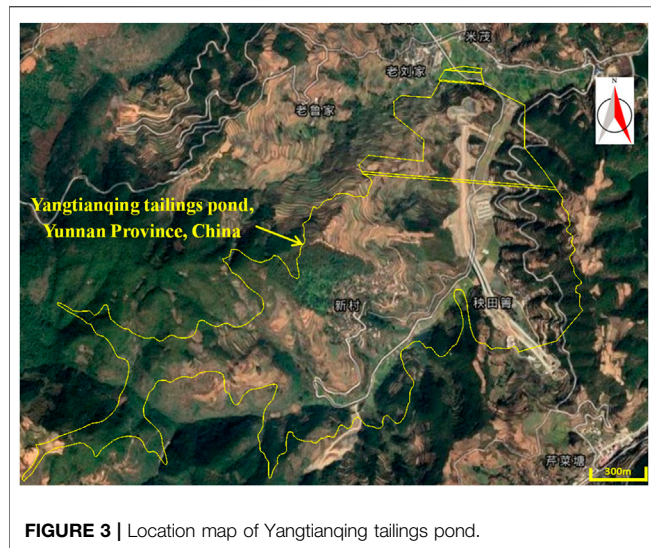
FIGURE 2 | The grain-size distribution curve of debris flow and slurry, (A) debris flow, (B) slurry.

2010). Li, Dong, and Yu analyze the stability of the dam body based on the fluid–solid coupling theory and a numerical simulation analysis method (Dong et al., 2011; Li et al., 2012; Yu et al., 2013). They find that the burial depth of the saturation line is too shallow (**Figure 1**), which is the main reason for the local instability of the dam. Jing (Jing et al., 2019) studies the overtopping failure process of a reinforced tailings dam using a small-scale model test, which finds that the reinforcement layers could improve the anti-erosion capability of the tailings dam. However, these studies are limited to the dam body and do not take into account the flow characteristics of slurry after a dam break. Once a tailings dam breaks, the slurry causes catastrophic damage downstream.

For this reason, Yin, Zhou, Jing, and Wang study the slurry resulting from a dam break with different dam heights and tailings particle sizes (Yin et al., 2010; Jing et al., 2012; Zhou et al., 2013; Wang et al., 2018). They analyze the disaster chain of a dam break according to disaster system theory and describe the evolution process of a dam-break disaster. Jeyapalan (Jeyapalan et al., 2000) and Kwak (Kwak et al., 2005) study the flow characteristics of slurry resulting from a tailings dam break through a series of flume tests and predicted the possible impact range. Jing (Jing et al., 2019) studies the effect of particle size on the flow characteristics of dam-break fluid with laboratory model tests, which observed that the flow height decreased with the particle size increasing, and the

impact force and velocity decreased with the particle size decreasing. The flow characteristics of slurry are similar to those of natural debris flows. The particle size of debris flow is widely distributed, ranging from a few millimeters of clay to a few meters of stone as shown in **Figure 2A** (Bu et al., 2017). However, the particle size of slurry is about 0.1 mm with a uniform material source as shown in **Figure 2B**. The flow characteristics of slurry and debris flow are similar; therefore, the research results of a natural debris flow can be used as a reference to analyze tailings dam-break fluid. For natural debris flows, Chen et al. (2021), and Jeong (2010) study the impact characteristics of debris flows using different particle sizes, slurry viscosities, and solid-phase ratios with similar model tests (Chen et al., 2021; Jeong, 2010; He et al., 2014). It is believed that the average impact force of fluid increases with the slurry viscosity, solid-phase ratio, and particle size increasing.

The flow characteristics of slurry surging from tailings dams collapse are directly influenced by grain size, breach width, slurry concentration, and surface roughness of the gully. Among these parameters, slurry concentration plays the most critical role, but there are few studies on it. To explore the flow characteristics of slurry with different concentrations, a detailed study is undertaken. The Yangtianqing tailings pond (in Yunnan Province, China) is used for this purpose. The location map of the Yangtianqing tailings pond is shown in **Figure 3**. A scaled-down version of the pond is developed in the laboratory for the



dam-break tests. The tests are carried out for a range of slurry concentrations using an experimental simulation test device for a dam break (SSTDDDB). The flow characteristics of slurry with different concentrations resulting from a tailings dam break through a series of flume tests predicted the possible impact

range. The results provide a detailed understanding of the slurry concentration influence on the flow characteristic, which guides the evacuation time and height downstream.

EXPERIMENTAL SETUP

Terms

Understanding and analyzing the flow characteristics of slurry are the focus of the present work; a few terms which are used frequently in the paper are defined. These terms set the context for the readers:

TSF: tailing storage facilities.

Slurry: Mass concentration of tailings, which includes fluid along with sediment.

Tailings: Products of the mineral after ore-dressing practice; its useful mineral content is very low, so it cannot be used in production.

Flow height: The liquid level height from the bottom of the flume as shown in **Figure 8**.

Beneficiation technology: The beneficiation technology is the same as mineral processing technology. It refers to the separation of useful minerals from ores by mineral processing equipment based on the difference of physical and chemical properties.

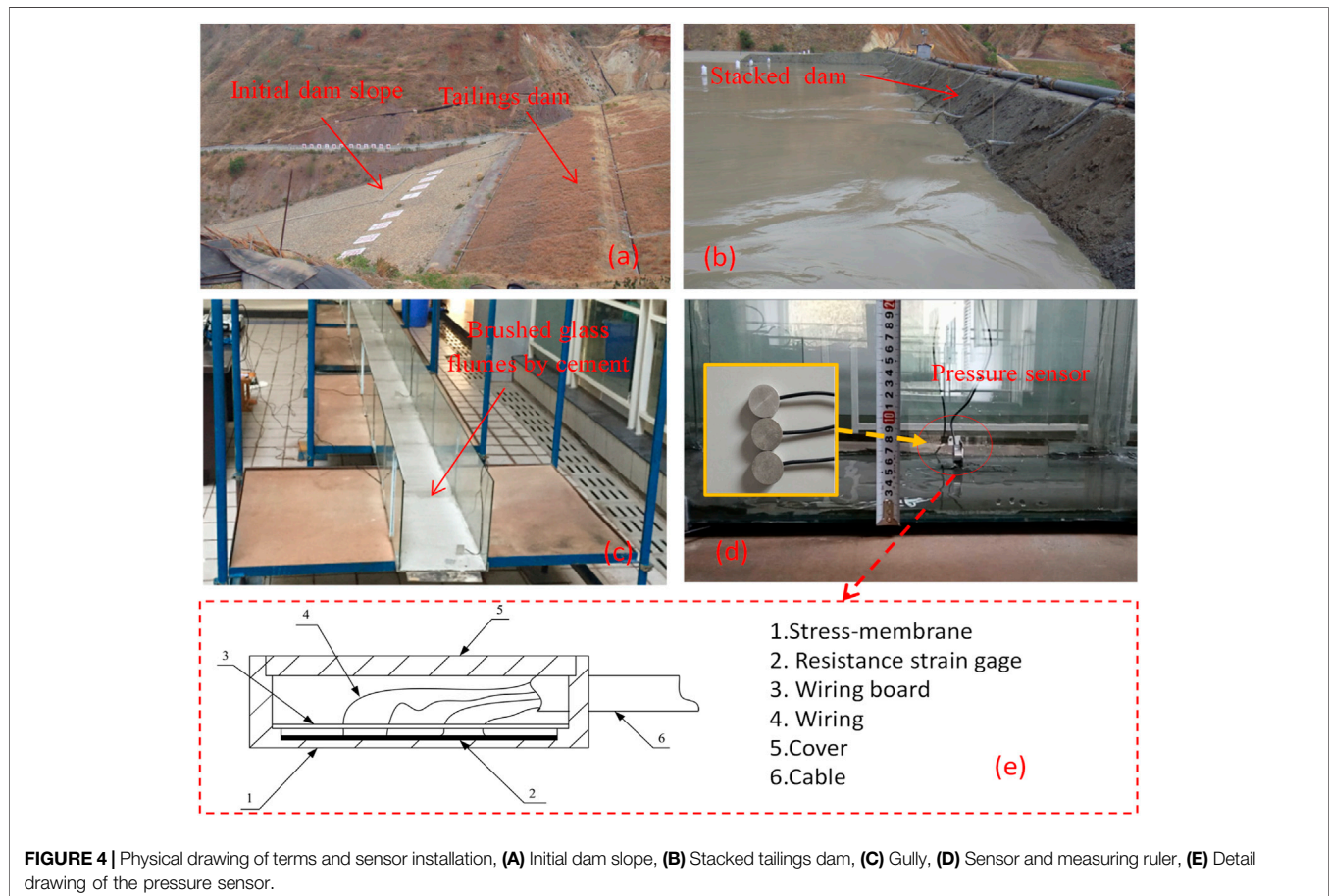


TABLE 1 | Physical and mechanical index of tailings.

Index	Tailings		
	1#	2#	3#
Plastic limit (W_p /%)	13.2	12.8	13.5
Liquid limit (W_L /%)	20.7	21.0	19.7
Plasticity index I_p	7.6	7.2	6.2
Compression modulus (MPa)	13.87	14.38	14.29
Compressibility (MPa^{-1})	0.142	0.135	0.137
Permeability coefficient ($\text{cm}\cdot\text{s}^{-1}$)	1.46e-04	1.53e-04	1.51e-04
Cohesion (kPa)	6.8	7.0	6.4
Internal friction angle (φ /°)	28.4	28.1	28.5
Specific gravity G_s	2.83	2.84	2.81

Slope: The slope with a certain angle as shown in **Figure 4A**.

Tailings Dam: The structure of intercepting tailwater in the tailings pond. As shown in **Figure 4B**, the dam consists of two slopes and one platform.

Gully: The flow pathway of tailings is brushed glass flumes by cement as shown in **Figure 4C**; the sensor in the gully is shown in **Figure 4D**, and the detailed drawing of the pressure sensor is shown in **Figure 4E**.

Experimental Material

The experimental materials are tailings from the Yangtianqing tailings pond in Yunnan Province, China. We randomly divided the tailings sand into three parts and carried out particle size analysis and triaxial tests. We obtained the particle size distribution of tailings by the Microtrac S3500 tri-laser particle size analyzer (Measurement range: 0.02–2,800 μm , Microtrac Inc., United States) as shown in **Figure 2B**. Cumulative distribution refers to the proportion smaller than a certain particle size. The physical and mechanical properties of tailings are obtained by a triaxial test as shown in **Table 1**.

In China, more than 80% of tailings impoundments are built using the upstream method with a thickening of 20%–30% because it is considered to be more economic (Zheng, 2017). High-density thickened tailings (HDTT) discharge can save a lot of water resources, reduce environmental pollution, and improve the utilization of the reservoir. Therefore, more and more HDTT discharge was considered in recent years. The TSF design considered discharge of tailings at 62% solids of Sierra Gorda Sociedad Contractual Minera (SCM), Chile (Engels et al., 2018). So, the four common types of slurry with mass concentrations of 30%, 40%, 50%, and 60% were used for experimental research. The test conditions are shown in **Table 2**.

TABLE 2 | The test conditions.

Dam height (cm)	Slurry concentration (%)	Gully gradient (%)	Bed roughness (μm)
30	30	2.0	Roughness by cement 0.012
30	40	2.0	
30	50	2.0	
30	60	2.0	

Experimental Apparatus

Based on the geometric size of the Yangtianqing tailings pond, an SSTDDDB is developed in the ratio of 1:400. The kinematic similarity ratio is 1:20. The experimental apparatus (SSTDDDB) consists of a reservoir area, downstream gully, slurry mixing system, gate (simulated dam), measurement device for impact force and velocity, flow monitoring system, and slope adjustment device. The panorama of the experimental apparatus (SSTDDDB) is demonstrated in **Figure 5A**. The impact force-measuring device is composed of the pressure sensor (Type: BX-2, Range: 0–10kPa \pm 0.5%F.S, Dandong city electronic instrument factory, Liaoning, China), sensor support plate, dynamic strain gauge, and computer as illustrated in **Figure 5B**. **Figure 6** shows the schematic of the gate device and gate lifting device. The highest sampling frequency of the dynamic strain gauge is 1 kHz, and the sampling frequency is 5 Hz. The pressure sensor is fixed on the sensor support plate, and the height from the bottom of the gully is 2 cm. The pressure sensor and measuring rulers are installed at 2 and 4 m away from the dam. To thoroughly explore the flow characteristics of slurry in the downstream gully, the gully is constructed of transparent toughened glass.

The internal dimension of the tailings pond is 200 \times 60 \times 50 cm (length \times width \times height). The dimension of the gully is 400 \times 30 \times 40 cm (length \times width \times height). According to the actual topography of the Yangtianqing tailings dam in China, the slope ratio of the gully is set to be 2%, the floor is roughened with cement, and the bed roughness of the gully is calculated by Manning's formula (i.e., $V_c = \frac{1}{n_c} R^{2/3} I^{1/2}$) and corrected by empirical judgment (Li et al., 2005). Here, n_c is the bed roughness of the gully, V_c is the velocity of slurry at one section, R is the hydraulic radius, and I is the gradient of the gully. Flow characteristics of fluids are monitored using measuring rulers and high-resolution cameras (Sony/HDR-CX680, Camera resolution: 1920 \times 1080/50p, Sony (China) Co., Ltd., Beijing, China). The installation of the measuring rulers is shown in **Figure 4D**, and the real-time height of the slurry is recorded through the measuring rulers and video. To measure the impact force of the fluid, pressure sensors are arranged at 2.0 and 4.0 m away from the dam layout. Experimental monitoring points and the equipment layout are depicted in **Figure 7**.

Experimental Procedures

(1) After the slope ratio of the gully is set to be 2%, the pressure sensor, dynamic strain gauge, and computer are connected and the impact force-measuring device is benchmarked so that the data is zero at the start. Moreover, the digital camera is placed in the research section ($S_1 = 2\text{ m}$, $S_2 = 4\text{ m}$).

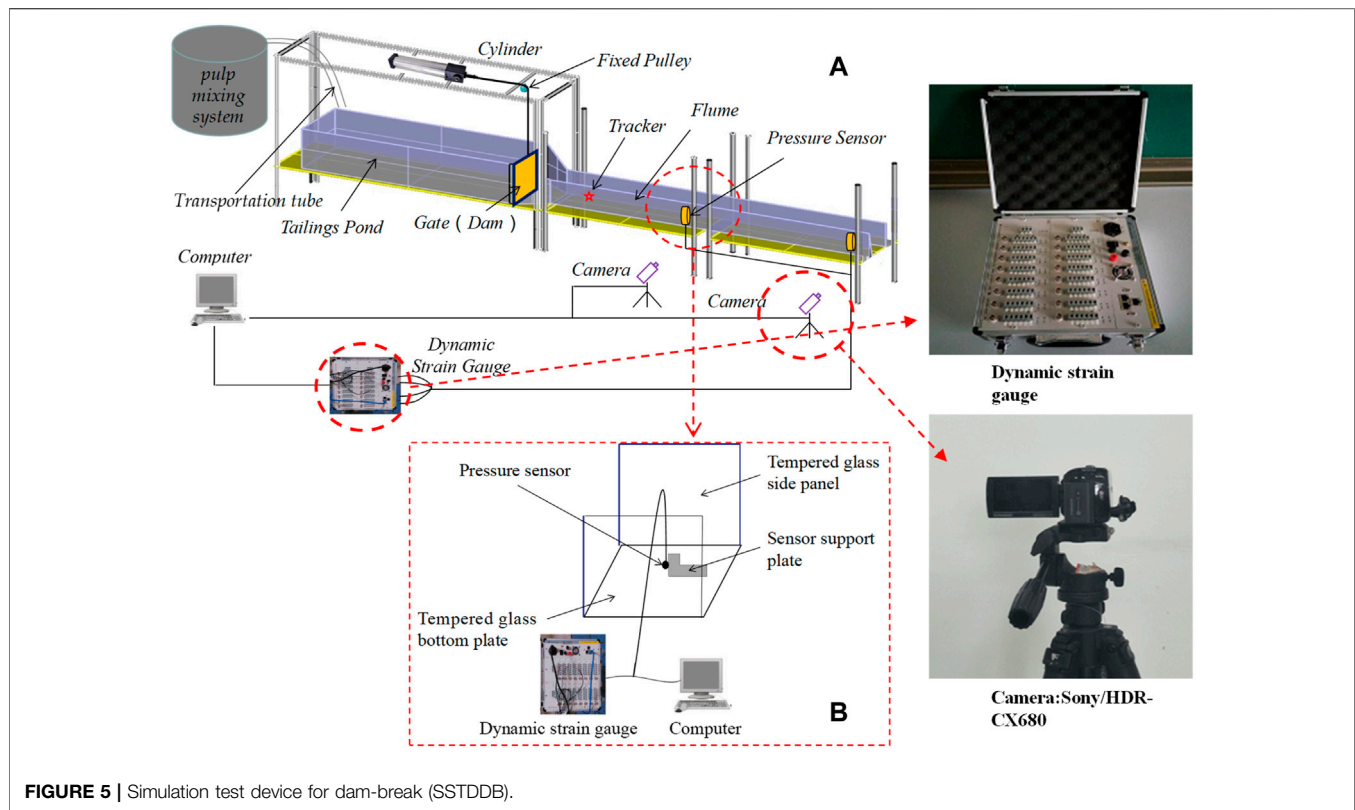


FIGURE 5 | Simulation test device for dam-break (SSTDDB).

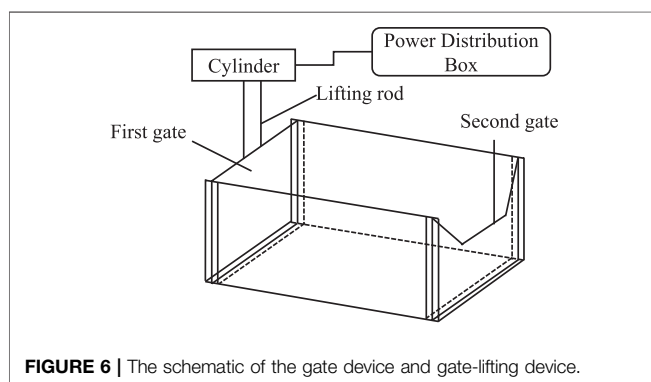


FIGURE 6 | The schematic of the gate device and gate-lifting device.

(2) Then, the slurry is prepared by the slurry mixing system to concentrations of 30%, 40%, 50%, and 60%. The slurry is conveyed to the tailings pond through the conveying pipeline. At the same time, the slurry in the area is stirred to create a uniform suspension. The initial filling height in the tailings pond is 30 cm as shown in **Figure 7**. After the slurry surface is stable, the gate is completely opened in 0.5 s by the cylinder to simulate the instantaneous dam break of the tailings pond.

(3) The impact force, flow height, and velocity (using a displacement tracer method) of slurry are collected by pressure sensors, high-resolution cameras, computers, and measuring rulers.

(4) Each concentration test was performed three times, and the average value was taken as the data analysis value. The scale recommended by previous research (Jing, 2011) (flow height,

impact force and time, 1:400, 1:557.3, and 1:20, respectively) is used for the flow height, impact force, and the time to reach the peak velocity.

The whole experimental procedure is shown in **Figure 8**.

RESULTS AND ANALYSIS

Analysis of Flow Characteristics

The flow height of the slurry at sections S_1 and S_2 were recorded by two high-resolution cameras placed $S_1 = 2$ m and $S_2 = 4$ m away from the dam toe. The flow pattern diagram of slurry with different concentrations after 4.0 s at section S_1 is shown in **Figure 9**. It shows that the concentration of slurry has a significant effect on the flow pattern. The slurry is fluctuant at $S_1 = 2$ m and $S_2 = 4$ m; the flow pattern of slurry becomes flattered with the slurry concentration decreasing, which indicates that the flow pattern of slurry is a nonconstant flow. The flow height is monitored by measuring rulers and high-resolution cameras (Sony/HDR-CX680, Camera resolution: $1920 \times 1080/50p$, Sony (China) Co., Ltd., Beijing, China) in real time. The flow height with different concentrations at sections S_1 and S_2 is illustrated in **Figure 10**.

By analyzing the submerged peak of section S_1 , it is found that the curve of flow height includes two peaks; the first peak is 11.9, 13, 14, and 14.8 cm, and the second peak is 9.7, 10.8, 12, and 13 cm for slurry concentrations of 30%, 40%, 50%, and 60%, respectively. It also shows a submerged peak increase with a slurry concentration in the S_1 and S_2 sections. The main reason is the

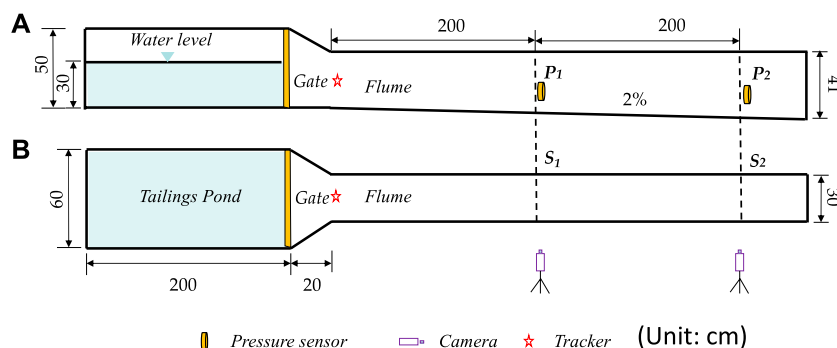


FIGURE 7 | Monitoring points distribution, (A) lateral view, (B) top view.

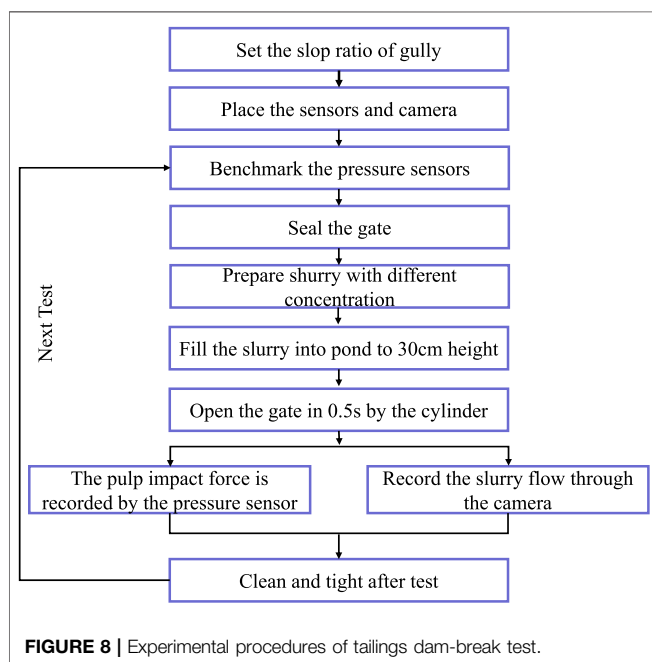


FIGURE 8 | Experimental procedures of tailings dam-break test.

viscosity of slurry increases with increasing concentrations of slurry, which can enhance the friction force between slurry and gully; the flow height increased significantly at the S_1 and S_2 sections.

When the slurry concentration is 60%, in section S_1 , the first peak reaches 14.8 cm at 2.1 s, and the second peak reaches 13 cm at 3.3 s. As M. Rico (M Rico., 2008) says, the slurry resulting from dam break forms a lower viscosity “water stream” at the front and a higher viscosity “slurry” at the back. The water stream moves faster because of its low viscosity. Therefore, the first peak is formed by a water stream with lower viscosity, and the second peak is formed by slurry with higher viscosity. The flow of slurry in any section can be divided into three stages: stage (A) rapid increase; stage (B) rapid reduction; stage (C) slow decline. The graph of flow height presents a triangular shape, and the conclusion is consistent with that in reference (Xie, 1992). It can also be observed from Figure 10 that the slurry with higher

concentration can take less time to reach the same section. It means the evacuation time downstream can increase.

Variation in an Impact Force of the Slurry

The impact force of the slurry is obtained by pressure sensors at sections S_1 and S_2 , respectively, and is shown in Figure 11 (the coordinate origin is the time when the slurry reaches S_1 and S_2). As illustrated in Figure 11, there are two peaks in the graph of impact force. In section S_1 , the graph shows that the first peak reaches 6.5 kPa at 1.0 s, and the second peak reaches 5.7 kPa at 2.1 s when the slurry concentration is 30%. The main reason is that, when the tailings dam collapses, the water stream with a lower concentration is the first to flow, followed by the slurry with a higher concentration. After the slurry reaches S_1 , the water stream first hits the pressure sensor. Because the concentration of the water stream is lower, its velocity is higher, so it produces the largest impact force peak, and then the first peak is formed. As the water stream flows away, the impact force gradually decreases, the slurry with its higher concentration hits the pressure sensor at this time. Because the sand in the slurry generates additional force on the sensor, the impact force increases, and the second peak is formed. The overall trend of the impact force graph is similar with different slurry concentrations. The impact force graph can be divided into three stages: stage (A), rapid increase; stage (B), rapid reduction; stage (C), slow decline.

As depicted in Figure 11A, the first peak value of impact force produced by slurry with 30%, 40%, 50%, and 60% concentration at sections S_1 is 6.5 kPa (equivalent to 3.62 MPa on site), 5.7 kPa (equal to 3.18 MPa on site), 3.9 kPa (equal to 2.17 MPa on site), and 3.3 kPa (equivalent to 1.84 MPa on site), respectively. It shows that the impact force of slurry decreases with the concentration increasing. The main reason is the viscosity of slurry increases with increasing the concentration of slurry, which can decrease the flow velocity. According to the relationship between flow velocity and impact force (Xie, 1992), it is observed that impact force is positively correlated with fluid velocity and also with the size of solid substances carried in the fluid. Therefore, liquid concentration is closely related to the impact force on buildings downstream. Figure 11 demonstrates that all the impact force curves reach the peak value within 2.0 s

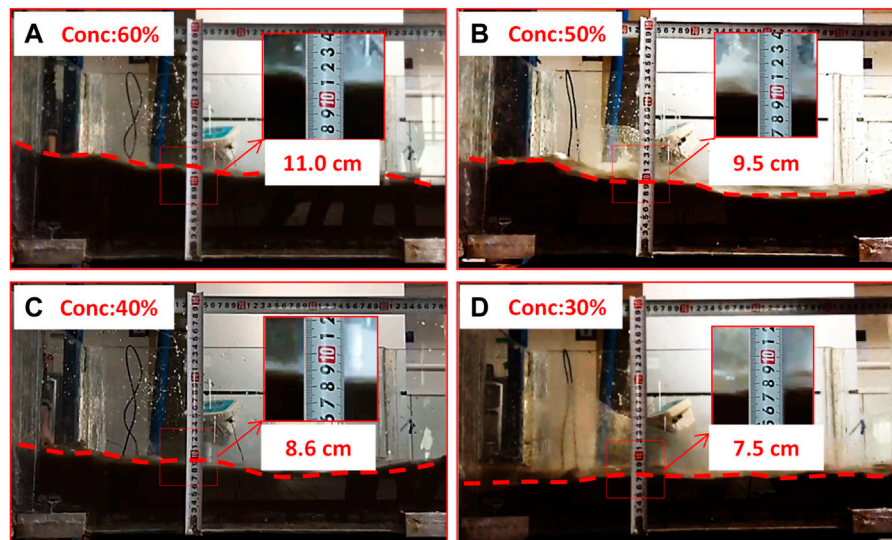


FIGURE 9 | Flow pattern of slurry with different concentration at section S_1 (2.0 m). (A) 60%, (B) 50%, (C) 40%, (D) 30%. ($t = 4.0$ s).

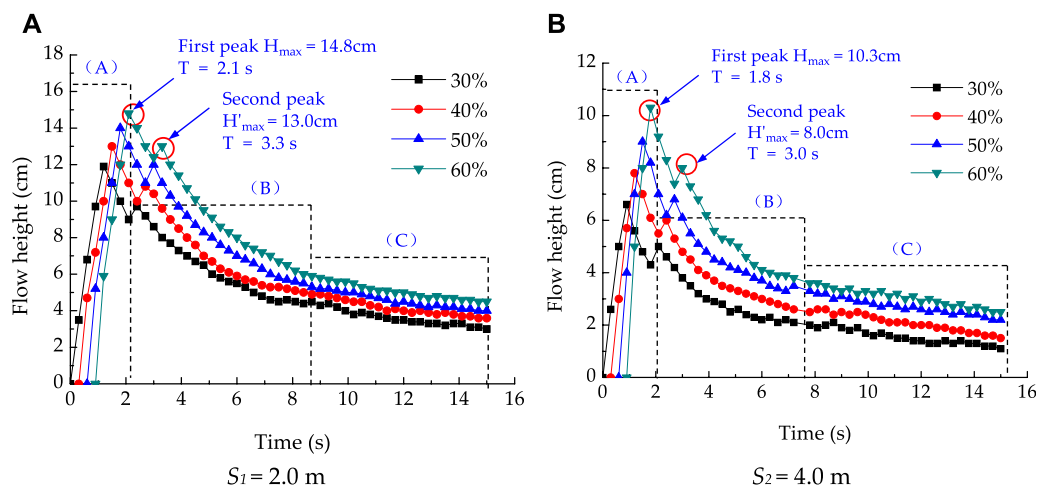


FIGURE 10 | Flow height of slurry at sections S_1 (2.0 m) and S_2 (4.0 m) and away from the dam toe. Stage (A) rapid increase; Stage (B) rapid reduction; Stage (C) slow decline.

TABLE 3 | Front velocity at different sections for the four different slurry concentrations.

Slurry concentration (%)	Front velocity V (m s ⁻¹)	
	$S_1 = 2.0$ m	$S_2 = 4.0$ m
30	3.61	3.22
40	3.30	2.94
50	3.00	2.61
60	2.77	2.20

(equivalent to 40.0 s on site) with a rapid increase in front and a gentle decrease in back. This demonstrates that the growth rate of the impact force is much faster than the decrease rate.

Variation in the Velocity of the Slurry

The displacement tracer points are used to record the velocity of the slurry. The tracker and camera record the velocity at two sections S_1 and S_2 . The front velocities at different monitoring points are explained in Table 3. The flow velocity curves of slurry with different concentrations at sections S_1 and S_2 are shown in Figure 12. (The coordinate origin is the front time of slurry reaching sections S_1 and S_2 .) It is observed that the front velocities of slurry with 30%, 40%, 50%, and 60% slurry concentrations at section S_1 are 3.61, 3.3, 3.0, and 2.77 m/s, respectively. This demonstrates that the velocity of the slurry decreases with the increasing concentration. The higher the concentration, the longer time it takes for the slurry to reach downstream. The time for 60% concentration to reach section S_1 is 0.5 s longer than

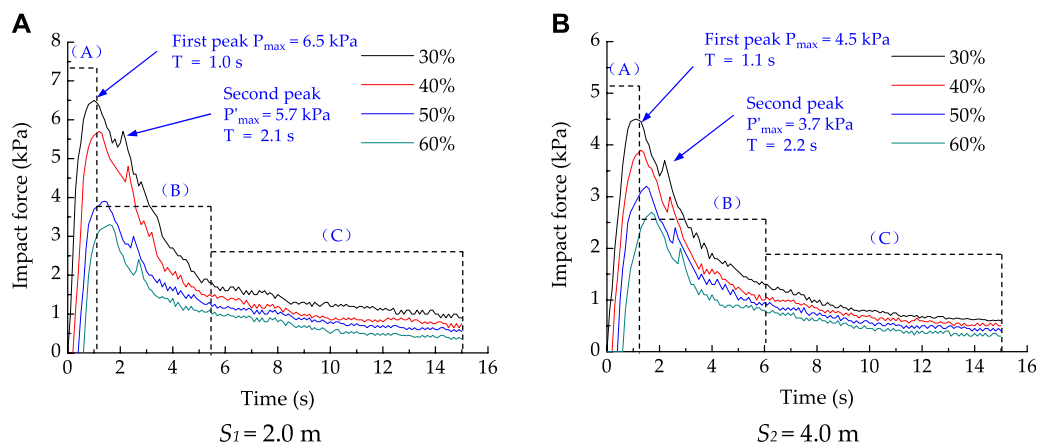


FIGURE 11 | The impact force of slurry at sections S_1 and S_2 (2.0 and 4.0 m away from the dam toe). Stage (A) rapid increase stage; Stage (B) rapid reduction stage; Stage (C) slow reduction stage.

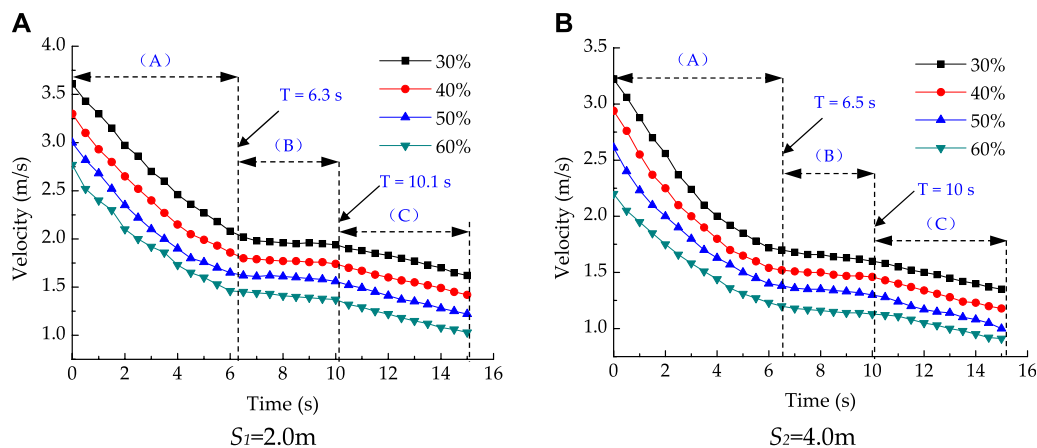


FIGURE 12 | Velocity curve of slurry at section S_1 and S_2 (2.0 and 4.0 m away from the dam toe). The coordinate origin is the initial time of slurry reaching sections S_1 and S_2 . Stage (A) Rapid reduction stage; Stage (B) Stable stage; Stage (C) Slow reduction stage.

the 30% concentration, which is equivalent to an increase of 10 s at the actual site. It can extend the evacuation time in the event of a dam-break accident.

Figure 12 also shows that the instantaneous velocity of slurry decreases with increasing the concentration. The reason is that the concentration can increase the viscosity of the slurry, which makes the slurry consume more energy in the flow process. The velocity curve of the slurry resulting from a dam break can be divided into three stages: stage (A) rapid reduction; stage (B) constant; stage (C) slow decline. Stage (A), rapid reduction in the leading section, is the initial stage when the dam break slurry reaches the characteristic sections. When the slurry reaches downstream, the speed at the front of the slurry is higher, and then it decreases rapidly, lasting about 6.0 s. For stage (B), the stable stage (dragon body), the velocity remains at the stable stage relatively. However, the average duration of velocity is distinctive respectively in different

sections. In stage (C), slow reduction (dragon tail), as the flow of slurry from upstream decreases gradually and the energy of slurry from the dragon tail decreases slowly, the velocity of slurry decreases steadily until all slurry flows out of the gully.

DISCUSSION

TSF is a unique processing subsystem of a mining and mineral processing facility. The slurry resulting from a dam break is hazardous and may cause serious safety and environmental impact. The slurry concentration determines the viscosity and affects the energy conversion of the slurry in the downstream movement. There are thousands of TSFs in China, and the deposit methods of each tailings pond is different; the concentration of tailing disposal is also different. Therefore,

the study of disaster damage from different slurry concentrations is significant. Then, the results can provide a detailed understanding of the flow characteristic by slurry concentration influence, which guides the evacuation time and height downstream.

Through the experimental study, it is observed that, with the decrease of slurry concentration, the impact force and velocity of slurry increase in varying degrees; on the contrary, the flow height is elevated with the slurry concentration decreasing. The main reason is that the higher the slurry concentration, the higher the static yield stress and viscosity are in varying degrees. The reduction of static yield stress and viscosity indicate that the resistance of slurry during movement decreases, and the slurry moves farther. According to the formula $\Delta H = \tau_0 / \gamma_C \cdot I$ (where H is the adhesive thickness, τ_0 is the static yield stress of the slurry, γ_C is the bulk density of the slurry, and I is the longitudinal slope of the groove) (Jing, 2011), it is known that the flow height of the slurry (H) decreases with the decreasing of the static yield stress (τ_0). As the static yield stress of the slurry has a nonlinear relationship with the concentration, it can be inferred that the flow height of the slurry varies nonlinearly with the change of concentration, which is also confirmed by the test results.

From the point of energy, before the tailings dam breaks, the slurry has a certain gravitational potential energy. The total energy of the slurry resulting from a dam break is derived from the total gravitational potential energy. The gravitational potential energy of the slurry is gradually transformed into kinetic energy after the dam break. As the concentration decreases, the viscosity of the slurry decreases gradually, making the substances in the slurry loose instead of gathering together, thus reducing the interaction between the materials, so the flow rate of slurry increases with the slurry concentration decreasing. A faster velocity leads to a tremendous conversion rate from potential to kinetic energy after the dam break, making the retained potential energy smaller in the limited space, and a lower flow height is generated downstream. According to research (Wu et al., 1990), the impact force of the flowing sand is proportional to the square of the velocity. Therefore, the impact force of slurry resulting from a dam break increases with the slurry concentration decreasing.

The experimental study finds that, at section S_1 , the impact range of the 30% concentration slurry was 0–6.5 kPa, whereas that of 60% concentration slurry was 0–3.3 kPa as shown in **Figure 11**. This shows that the fluctuation of the impact force of the low concentration is more intense. This phenomenon is consistent with Liu's research on debris flow (Liu et al., 2019). As Liu says, when low-density debris flow interacts with obstacles, the maximum impact force mainly comes from the impact of particles in the fluid and obstacles, which exist throughout the impact process. When high-density debris flow interacts with obstacles, the maximum impact force appears when they just touch the obstacles, and the main contributor of the impact force is the high-viscosity "viscous body" composed of particles and water. Moreover, the fluid with a higher viscosity has a smaller flow velocity (Liu et al., 2019), so the fluctuation of the impact force of the low-concentration slurry is more intense.

After the tailings dam breaks, the slurry causes huge damage downstream; therefore, we can build a diversion channel or other

structures downstream and build energy dissipation structures in the diversion channel, thereby reducing the damage degree of fluid (Kim et al., 2018). For example, Chen (Chen et al., 2015) built an energy dissipation structure by digging pits in the channel. The energy dissipation structure can reduce the debris flow velocity to the original 0.43 to 0.63 times. The establishment of a flexible net barrier is also a good energy dissipation measure. After the fluid impacts the flexible net barriers, its energy is greatly reduced. The degree of reduction depends on both the material textures and mesh sizes (Huo et al., 2018; Yuan et al., 2019). Therefore, it is suggested to build a flexible net barrier downstream or dig pits in the diversion channel to reduce the damage degree of dam break.

CONCLUSION

- (1) The curve of flow height and impact force of slurry downstream includes two peaks. The first peak is formed by the front water stream with lower viscosity, and the second peak is formed by slurry with a higher viscosity. At section S_1 (2.0 m from dam), the peak heights and impact force are 11.9, 13, 14, 14.8 cm and 6.5, 5.7, 3.9, and 3.3 kPa for slurry concentrations of 30%, 40%, 50%, and 60%, respectively. It is observed that the front velocities of slurry with 30%, 40%, 50%, and 60% concentrations at section S_1 are 3.61, 3.3, 3.0, and 2.77 m/s.
- (2) The curve of flow height and impact force can be divided into three stages: rapid increase, rapid decline, and slow decline. The velocity curve can also be divided into three stages: rapid decline, stable, and slow decline.
- (3) Through the experimental study, it is observed that, with the decreasing of slurry concentration, the impact force and velocity of slurry increased in varying degrees; on the contrary, the flow height elevated with the slurry concentration decreasing. The main reason is that the higher the slurry concentration, the higher the static yield stress and viscosity—in varying degrees.

The results provide a detailed understanding of the slurry concentration influence on the flow characteristics, which guides the evacuation time and height downstream.

DATA AVAILABILITY STATEMENT

The original contributions presented in the study are included in the article/supplementary material, further inquiries can be directed to the corresponding authors.

AUTHOR CONTRIBUTIONS

Conceptualization, XJ; Methodology, CP; Validation, YC, XX, and WW; Writing—Original Draft Preparation, XJ and CP; Writing—Review and Editing, XJ.

FUNDING

This research is funded by the National Natural Science Foundation of China (Grants Nos. 51974051, 51804051, and 51804222), the Natural Science Foundation project of Chongqing Science and Technology Commission (No. cstc2018jcyjAX0231), the Chongqing Special Postdoctoral Science Foundation (Grant No. XmT2018017), the Post-Funded

REFERENCES

- Bu, X., Tang, C., and Qu, Y. P. (2017). Grain-size Distribution and Structure Dimension of "7. 4" Giant Debris Flow Deposition in Shimian County, Sichuan Province, China. *J. Disaster Prev. Mitigation Eng.* 37 (6), 1016–1022.
- Chen, Y., Zuo, J., Liu, D., Li, Y., and Wang, Z., (2021). Experimental and Numerical Study of Coal-Rock Bimaterial Composite Bodies Under Triaxial Compression. *Int. J. Coal Sci. Technol.* 8, 908–924. doi:10.1007/s40789-021-00409-5
- Chen, J., Chen, X., Li, Y., and Wang, F. (2015). An Experimental Study of Dilute Debris Flow Characteristics in a Drainage Channel with an Energy Dissipation Structure. *Eng. Geology*. 193, 224–230. doi:10.1016/j.enggeo.2015.05.004
- Dong, L., Zhao, G., and Gong, F. (2011). *Interval Analysis Model of Tailings Dam Seismic Stability and its Application*, 42. Journal of Central South University, 164–169.
- Engels, J., Gonzalez, H., Aedo, G., and McPhail, G. I. (2018). "Implementation of Spigot Discharge Systems for High-Density Tailings at Sierra Gorda Sociedad Contractual Minera, Chile," in *Proceedings of the 21st International Seminar on Paste and Thickened Tailings*. Editors R. J. Jewell and A. B. Fourie (Perth: Australian Centre for Geomechanics), 389–400. doi:10.36487/acg_rep/1805_32_engels
- Finn, W. (1993). Seismic Stabilization of St. Joe State Park Tailings Dam. *Proc. Geotechnical Pract. Dam Rehabil.*, 25–28.
- He, X., Tang, H., and Chen, H. (2014). Experimental Study on Impacting Characteristics of Debris Flow Considering Different Slurry Viscosities, Solid-phase Ratios, and Grain Diameters. *Chin. J. Geotechnical Eng.* 36 (5), 977–982. doi:10.11779/CJGE201405024
- Huo, M., Zhou, J.-w., Yang, X.-g., and Zhou, H.-w. (2018). Dynamical Evolution Properties of Debris Flows Controlled by Different Mesh-Sized Flexible Net Barriers. *Arab J. Geosci.* 11, 465–477. doi:10.1007/s12517-018-3786-x
- Jeong, S. W. (2010). Grain Size Dependent Rheology on the Mobility of Debris Flows. *Geosci. J.* 14, 359–369. doi:10.1007/s12303-010-0036-y
- Jeyapalan, J. K., Duncan, J. M., and Seed, H. B. (2000). Investigation of Flow Failures of Tailings Dams. *J. geotechnical Eng.* 109, 172–189.
- Jing, X., Chen, Y., Pan, C., Yin, T., Wang, W., and Fan, X. (2019). Erosion Failure of a Soil Slope by Heavy Rain: Laboratory Investigation and Modified GA Model of Soil Slope Failure. *Ijeph* 16 (6), 1075–1085. doi:10.3390/ijeph16061075
- Jing, X., Chen, Y., Xie, D., Williams, D. J., Wu, S., Wang, W., et al. (2019). The Effect of Grain Size on the Hydrodynamics of Mudflow Surge from a Tailings Dam-Break. *Appl. Sci.* 9 (12), 2474. doi:10.3390/app9122474
- Jing, X. F. (2011). *Study on Sediment Flow Characteristics and Disaster Prevention of Tailings Dam Break*. Chongqing: Chongqing University.
- Jing, X., Yin, G., and Wei, Z. (2012). Study of Tailings Dam-Break Surges with Floating Pulp in the Model experiment in Different Collapse gates. *Rock Soil Mech.* 33, 745–752. doi:10.1007/s11783-011-0280-z
- Jing, X., Chen, Y., Williams, D., Serna, M., and Zheng, H. (2019). Overtopping Failure of a Reinforced Tailings Dam: Laboratory Investigation and Forecasting Model of Dam Failure. *Water* 11 (2), 315–330. doi:10.3390/w11020315
- Kim, M.-I., Kwak, J.-H., and Kim, B.-S. (2018). Assessment of Dynamic Impact Force of Debris Flow in Mountain Torrent Based on Characteristics of Debris Flowflow in Mountain Torrent Based on Projects of Chongqing University of Science and Technology (No. ckhqzz2008005), the Key Technological Projects for Prevention and Control of Major Accidents in Safety Production (Chongqing-0009-2018AQ, Chongqing-0006-2018AQ, Chongqing-0004-2017AQ). the Self-made Equipment Foundation of Chongqing University of Science and Technology (No. ZZSB2019013), the Scientific and Technological Research Program of Chongqing Municipal Education Commission (KJZD-K201901501).
- Characteristics of Debris Flow. *Environ. Earth Sci.* 77, 538–552. doi:10.1007/s12665-018-7707-9
- Kwak, M., James, D. F., and Klein, K. A. (2005). Flow Behaviour of Tailings Paste for Surface Disposal. *Int. J. mineral Process.* 77, 139–153. doi:10.1016/j.minpro.2005.06.001
- Li, Q., Zhang, L., and Qi, Q. (2012). Instability Characteristics and Stability Analysis of a Tailings Dam Based on Fluid-Solid Coupling Theory. *Rock Soil Mech.* 33, 243–250. doi:10.16058/j.issn.1005-0930.2017.03.012
- Liu, D., You, Y., and Du, J. (2019). Spatio-temporal Distribution of the Impact Force of Debris Flow. *Advaced Eng. Sci.* 51 (3), 17–25.
- Lu, X., Zhou, W., and Ding, X. (2019). *Ensemble Learning Regression for Estimating the Unconfined Compressive Strength of Cemented Paste Backfill*. IEEE Access, 2918177. doi:10.15961/j.jsuese.201801042
- Moxon, S. (1999). Failing Again. *Int. Water Power Dam Construction* 51, 16–21.
- Nelson, J. (1977). *Parameters Affection Stability of Tailings Dams*. Ann Arbor: Proc of the Conf on Geotech Pmct for Disposal of Solid Water Mater, 440–460.
- Proskin, S., Sego, D., and Alostaz, M. (2010). Freeze-thaw and Consolidation Tests on Suncor Mature fine Tailings (MFT). *Cold Regions Sci. Techn.* 63, 110–120. doi:10.1016/j.coldregions.2010.05.007
- Rico, M., Benito, G., and Diez-Herrero, A. (2008). Floods from Tailings Dam Failures. *J. Hazard. Mater.* 154, 79–87. doi:10.1016/j.jhazmat.2007.09.110
- Tang, L., Li, Z., Zhao, Y., Qin, J., and Lin, L. (2012). Life Cycle Oriented Hazards Identification for Tailings Facility. *Proced. Eng.* 43, 282–287. doi:10.1016/j.proeng.2012.08.048
- Wang, K., Yang, P., Hudson-Edwards, K., Lyu, W., Yang, C., and Jing, X. (2018). Integration of DSM and SPH to Model Tailings Dam Failure Run-Out Slurry Routing across 3D Real Terrain. *Water* 10 (8), 1087–1101. doi:10.3390/w10081087
- Wijewickreme, D., Sanin, M. V., and Greenaway, G. R. (2005). Cyclic Shear Response of fine-grained Mine Tailings. *Can. Geotech. J.* 42, 1408–1421. doi:10.1139/t05-058
- Wu, J., Kang, Z., and Tian, L. (1990). *Observing Study of Debris Flow in Jiangjiagou*. Yunnan Province. Beijing: Science Press.
- Xie, R. Z. (1992). *Hydraulics of Dam-Break*. Jinan: Shandong Science and Technology Press.
- Yin, G., Jing, X., and Wei, Z. (2010). Experimental Study of the Similar Simulation of Tailings Dam-Break. *Chin. J. Rock Mech. Eng.* 29, 3830–3838.
- Yu, G., and Song, C. (2014). Review of New Progress in Tailing Dam Safety in Foreign Research and Current State with the Development Trend in China. *Chin. J. Rock Mech. Eng.* 33, 3238–3248.
- Yu, S., Shao, L., and Liu, S. (2013). Stability Analysis of Tailings Dam Based on Finite Element Limit Equilibrium Method. *Rock Soil Mech.* 34, 1185–1190.
- Yuan, D., Liu, J., You, Y., Zhang, G., Wang, D., and Lin, Z. (2019). Experimental Study on the Performance Characteristics of Viscous Debris Flows with a Grid-type Dam for Debris Flow Hazards Mitigation. *Bull. Eng. Geol. Environ.* 78, 5763–5774. doi:10.1007/s10064-019-01524-z
- Zheng, B. (2017). *Research on the Basic Issues for Upstream Method of High Thickened Tailings and Stability Analysis of Tailings Dam [D]*. Chongqing: Chongqing University.
- Zhou, K., Liu, F., and Hu, J. (2013). Research of Tailings Dam-Break Disaster Chain and Chain-Cutting Disaster Mitigation Control Technology. *J. Catastrophology* 28, 24–29. doi:10.3969/j.issn.1000-811X.2013.03.006

Conflict of Interest: WW was employed by Chongqing GaoXin Engineering Survey and Design Institute Ltd., Co.

The remaining authors declare that the research was conducted in the absence of any commercial or financial relationships that could be construed as a potential conflict of interest.

The handling editor declared a shared affiliation with one of the authors (WW) at time of review.

Publisher's Note: All claims expressed in this article are solely those of the authors and do not necessarily represent those of their affiliated organizations, or those of the publisher, the editors and the reviewers. Any product that may be evaluated in

this article, or claim that may be made by its manufacturer, is not guaranteed or endorsed by the publisher.

Copyright © 2021 Chen, Jing, Chen, Pan and Wang. This is an open-access article distributed under the terms of the Creative Commons Attribution License (CC BY). The use, distribution or reproduction in other forums is permitted, provided the original author(s) and the copyright owner(s) are credited and that the original publication in this journal is cited, in accordance with accepted academic practice. No use, distribution or reproduction is permitted which does not comply with these terms.



Rainfall Infiltration Process of a Rock Slope with Considering the Heterogeneity of Saturated Hydraulic Conductivity

Qingqing Zhang, Laigui Wang and Huabin Zhang*

Mechanical and Engineering College of Liaoning Technical University, Fuxin, China

OPEN ACCESS

Edited by:

Wei Liu,
Chongqing University, China

Reviewed by:

Shibin Tang,
Dalian University of Technology, China
Kang Zhao,
Jiangxi University of Science and
Technology, China
Kaizong Xia,
Institute of Rock and Soil Mechanics
(CAS), China

*Correspondence:

Huabin Zhang
lgd_zhb@163.com

Specialty section:

This article was submitted to
Geohazards and Georisks,
a section of the journal
Frontiers in Earth Science

Received: 28 October 2021

Accepted: 29 November 2021

Published: 03 January 2022

Citation:

Zhang Q, Wang L and Zhang H (2022)
Rainfall Infiltration Process of a Rock
Slope with Considering the
Heterogeneity of Saturated
Hydraulic Conductivity.
Front. Earth Sci. 9:804005.
doi: 10.3389/feart.2021.804005

In order to analyze the effects of rainfall events on the stability of an open-pit rock slope, with considering the spatial variability of saturated hydraulic conductivity, based on the unsaturated seepage theory and the random field theory, modified functions of the unit saturation, the hydraulic conductivity (k), and the shear strength parameters are established for unsaturated slope, by using FISH and the non-intrusive stochastic method. A saturated-unsaturated seepage random field model is proposed. And then the impacts of the rainfall intensity, the rainfall duration, and the spatial variability of saturated hydraulic conductivity (k_s) on the infiltration process and stability of the unsaturated rock slope are analyzed. The results show that the proposed model can estimate rainfall infiltration of rock slope accurately. Rainfall mainly affects the seepage field in the shallow layer of the slope, where a transient saturated zone can be formed. With the development of the rainfall duration, the weight of the rock mass increased, the matric suction reduced, the negative pore pressure, the degree of saturation, and the infiltration depth of the rock slope increased, and the water in the slope root connects with the initial water table gradually, the unsaturated zone shrinks, which causes the safety factor of the model decreases, but the trend of change slows down gradually. As the rainfall intensity strengthened, the infiltration depth increased and the safety factor of the slope reduced, while the changing rate increases first and then decreases. Increasing the correlation length of k can reduce the infiltration depth and safety factor of the slope. Increasing the variation coefficient of k will increase the infiltration depth, while the safety factor of the slope decreases. The infiltration depth and safety factor of the slope are most affected by rainfall duration, but its sensitivity to the variability coefficient of k will be strengthened when the rainfall intensity exceeds the infiltration capacity. This conclusion can provide reference significance for the risk estimation of slope geological hazards, which are induced by the rainfall infiltration.

Keywords: rock slope, random field, unsaturated seepage, rainfall infiltration, FISH

INTRODUCTION

The impact of water on the safety and stability of slope is not ignorable, the rock mass of a slope generally contains a large amount of groundwater, and, what is more, it is eroded by seasonal rainfall. In recent years, the global climate anomalies, for example, extreme rainfall, may lead to frequent occurrence of various geological disasters on slope. Rainfall events affect the seepage of a slope differently, short-term rainfall can form a transient saturation zone in the shallow layer of a slope, and a continuous rainfall can even raise the groundwater level. Rainfall infiltration is a continuous and dynamic process, and the physical composition, sedimentary feature, and complex geological processes on the rock and soil mass have significant differences. It is necessary to comprehensively analyze the effect of rainfall infiltration on the seepage field and stability of rock slope with considering its natural spatial variability.

Many scholars, both foreign and domestic, expended significant research on the infiltration of water into soil; some of them take into account the natural spatial heterogeneity of hydraulic soil properties, from the late 1970s. Horton (1939) defined the infiltration capacity (IC) of soil as a hyetograph separation rate, and put forward that if the rainfall intensity exceeds the IC, a portion of the rainfall will runoff the soil surface. Santoso et al. (2011) analyzed the probability of slope failure induced by rainfall with considering the spatial variability of hydraulic conductivity. Based on the limit equilibrium method and finite element method, Collins and Znidarcic (2004) studied the mechanism of rainfall-induced landslides, and then analyzed the slope stability under multiple rainfall conditions. Chu-Agor et al. (2008), Huang and Jia (2007), and Oh and Vanapalli (2010) analyzed the influence of rainfall infiltration on the shear strength and stability of a slope. Considering the shear strength changes with the matric suction, Cho and Lee (2001) carried out a two-dimensional flow-deformation coupled model to analyze the stability of a soil slope under rainfall infiltration. Morbidelli et al. (2018) reviewed the research on infiltration models, such as models established by Green, Ampt, Horton, Philip, Brutsaert, Parlange, etc., and put forward that the natural spatial variability of soil hydraulic characteristics and that of rainfall make the estimate of infiltration has further challenges. Cai et al. (2020) developed a coupled hydro mechanical model of unsaturated soil considering the effect of the microscopic pore structure, and analyzed the effects of rainfall intensity and rainfall duration on the pore pressure, fluid velocity, and displacement of the unsaturated soil slope. Some scholars adopt the saturated-unsaturated seepage theory to analyze the rainfall infiltration process of rock slope (Qin et al., 2003; Rong et al., 2005; Liu and Xu 2017; Pan et al., 2020; Zhang et al., 2021). Huang and Qi (2002) discussed the effect of unsaturated soil's suction on slope stability, suggested a modified model and applied it to an open pit mine slope, and analyzed some basic laws of suction on slope stability. Based on the unsaturated soil theory, Xu et al. (2005) analyzed the stability of unsaturated soil slope under rainfall infiltration. Introducing a fluid-mechanical interaction model based on continuous porous media theory and mixture theory, Xie et al. (2019) applying FISH language to program, studied the

saturated-unsaturated seepage with FLAC3D. Jiang et al. (2014) studied the unsaturated seepage module and seepage calculation algorithm used in FLAC3D platform, based on that analyzed the unsaturated seepage of slope under rainfall condition. Fu et al. (2014) carried out the numerical simulation on the safety factor variation on an embankment slope of Six River highway in Guangxi, and analyzed the slope stability during continuous rainfall. Li et al. (2012) proposed a modified adjusting element permeability method to correct the permeability of unsaturated zone strictly, after calculation, an exact continuous smooth seepage surface and saturated-unsaturated seepage of a slope are obtained. Hu et al. (2017) investigated the effect of spatial variability of the shear strength parameters on the stability of completely decomposed granite slopes under intense rainfall infiltration. Based on the Monte Carlo method, Qin et al. (2017) established a reliability analysis model of bedrock laminar slope with considering the variability of k_s of slope soil, analyzed the failure probability of Zhang jia wan landslide under different variation coefficients of k_s and different rainfall intensities. Jiang et al. (2014) developed a modified Green-Ampt model to determine the distribution of moisture content of soils and the wetting front depth within the slope under different rainfall durations, and investigated the failure mechanism of the infinite slope considering the interaction of the spatial variability of multiple soil parameters and the rainfall infiltration. And some scholars considered the randomness of the geotechnical properties of rock and soil when studying the rainfall infiltration process and slope landslides induced by rainfall (Wang et al., 2019; Chen et al., 2020; Hamrouni et al., 2020; Han et al., 2020; Liu and Wang, 2021).

The above references mostly considered the rainfall infiltration process of soil slopes and/or the effects of the spatial variability of slope soil parameters on slope stability. While the surface of an open-pit mine rock slope is mainly composed of a mixture of soil and rock, coupled with the seasonal rainfall effect and the natural spatial variability of the slope rock and soil, which greatly increases the risk of geological disasters, even if the open-pit mine ceased operation, the risks are still greatly. Based on the above researches, the non-intrusive stochastic method was realized in this paper by using FISH and MATLAB, which can be used to simulating the unsaturated seepage stochastic field, and the numerical realization of a saturated-unsaturated seepage random field was carried out by adopting the seepage coupling function module in FLAC3D. Then, the seepage field and stability of a rock slope under different rainfall intensity and rainfall duration was analyzed, with considering the variability of k of rock slope. The result can provide technical support for further study on the risk assessment of geological disasters of open-pit mines slope that induced by extreme rainfall.

SATURATED-UNSATURATED SEEPAGE RANDOM FIELD

Saturated-Unsaturated Seepage Theory

The upper-layer of a rock slope, which is above the water table, is unsaturated. Water entry into the shallow layer of a slope during

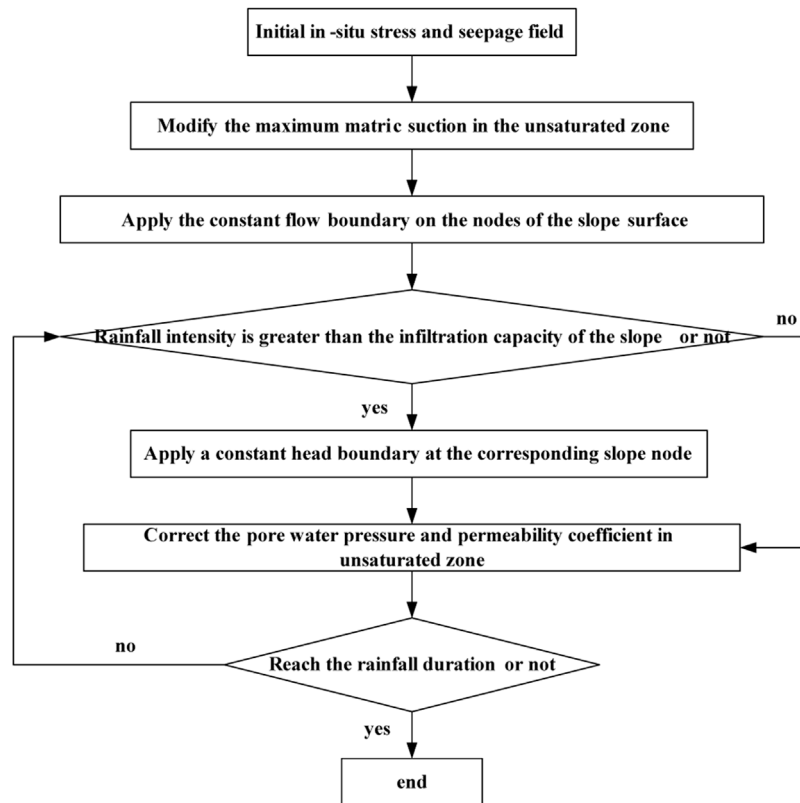


FIGURE 1 | Schematic diagram of saturated-unsaturated seepage procedure.

the rainfall process changes the initial water content of the slope, and the matric suction changes with it too. The matric suction is one of the important parameters reflecting unsaturated soil mechanics. Between the degree of saturation or the value of k of the unsaturated seepage zone and the matric suction, there exists a functional relation (Guo et al., 2005). According to the soil water characteristic curve (SWCC), many scholars are committed to fitting the empirical formula, such as Liakopoulos, Alonso, Van Genuchten (1980), and so on. Alonso et al. (1995) put forward the relationship between liquid permeability and matric suction, and then the hydraulic conductivity can be obtained as a function of matric suction.

$$\begin{cases} s = s_r + \frac{(1 - s_r)a_s}{a_s + (b_s p_c)^n} \\ k_w = \frac{a_k k_s}{a_k + (b_k p_c)^c} \end{cases} \quad (1)$$

where s_r is the residual degree of saturation, which is dimensionless, and p_c is the matric suction, the unit is kPa. Parameters a_s , b_s , a_k , b_k , and c are the model parameters. k_s is the hydraulic conductivity of saturated soil (the unit is cm/s).

Therefore, according to (1), the unit saturation and k of unsaturated soil can be determined by user-defined functions in FLAC3D. In the unsaturated zone, the value of saturation and pore water pressure at the zone gridpoint changes with the

development of rainfall duration; what is more, the value at the unit changes with it. Therefore, it is necessary to correct the degree of saturation and the value of k at the unit at each time step in calculation. In addition, it is necessary to modify the strength criterion to analyze the slope stability. Bishop proposed the shear strength of unsaturated rock mass in 1960, and Fredlund and Rahardio (1997) put forward the revised formula in 1978.

$$\tau_f = c' + (\sigma - u_a) \tan \varphi' + (u_a - u_w) \tan \varphi^b \quad (2)$$

$$c^* = c' + (u_a - u_w) \tan \varphi^b \quad (3)$$

where $u_a - u_w$ is the matric suction of the potential failure surface (the unit is kPa), u_a is the pore-air pressure, and u_w is the pore-water pressure (the unit is kPa). c' , φ' , are the effective cohesion and friction angle, and φ^b is an angle defining the increase in shear strength for an increase in matric suction. The cohesion can be corrected according to (3), when calculating the safety factor via FLAC3D.

Verification of Saturated-Unsaturated Seepage Filed Model

Figure 1 shows the schematic diagram for developing the saturated-unsaturated seepage procedure. In order to verify the accuracy of the development program of the modified algorithm

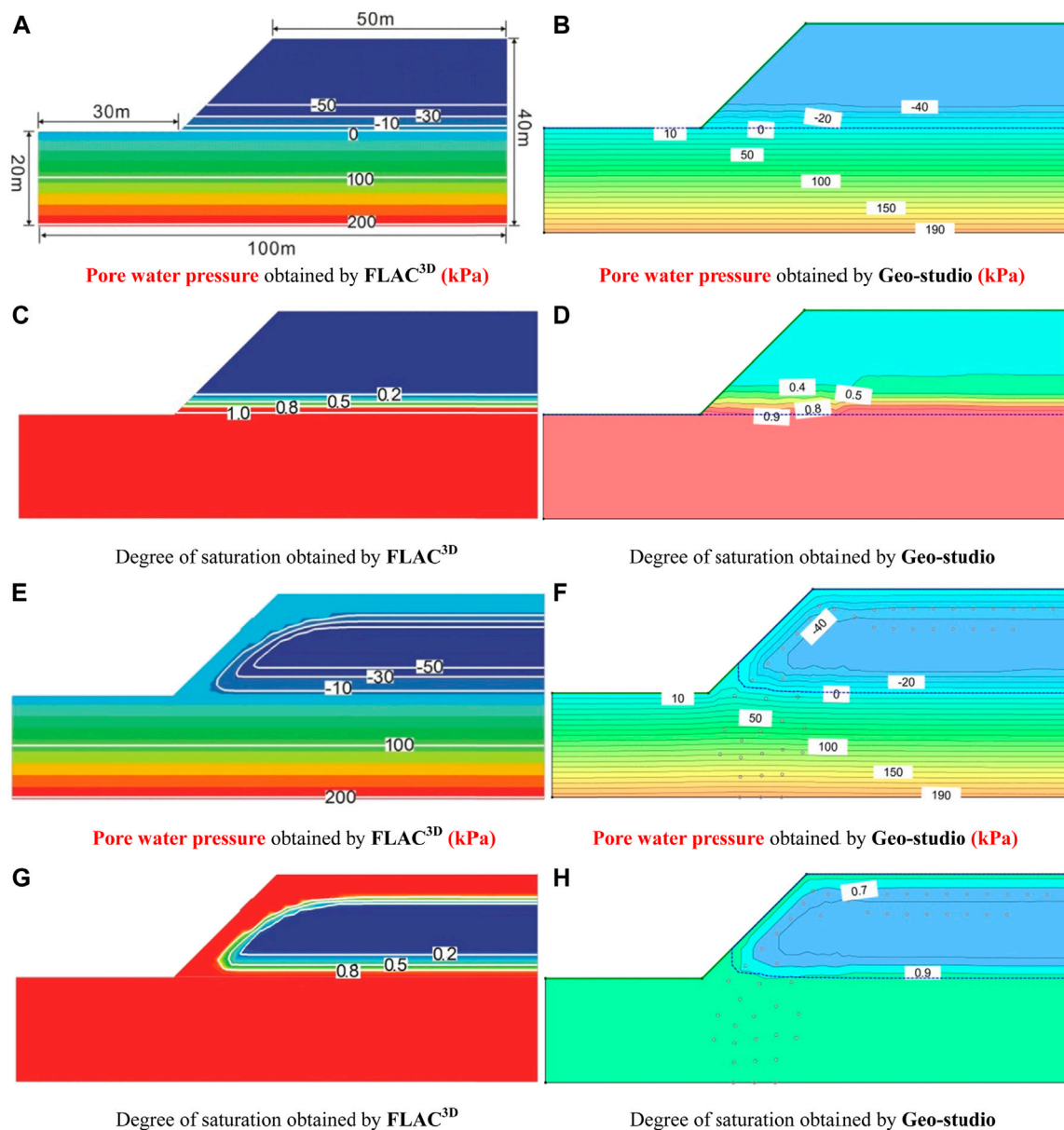
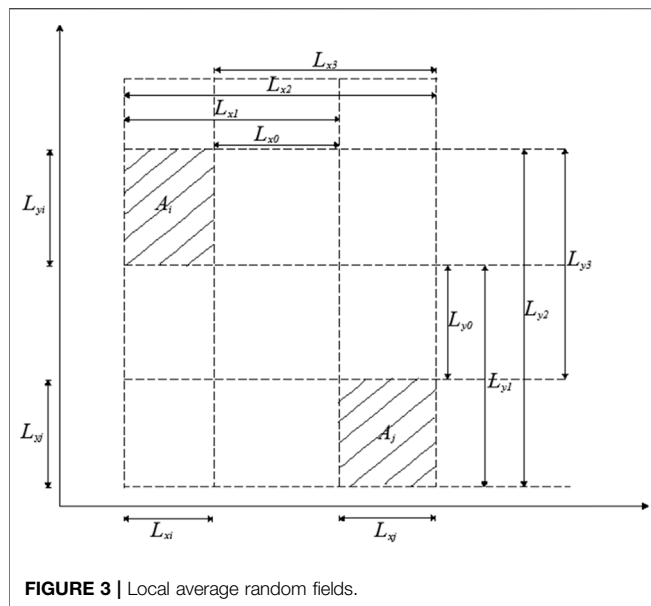


FIGURE 2 | Distributions of pore water pressure and saturation under different conditions obtained by using FLAC3D and Geo-studio: (A) Pore water pressure before raining, (B) Pore water pressure before raining, (C) Degree of saturation before raining obtained, (D) Degree of saturation before raining, (E) Pore water pressure after rainfall last 84 h, (F) Pore water pressure after rainfall last 84 h, (G) Degree of saturation after rainfall last 84 h, (H) Degree of saturation after rainfall last 84 h.

for the seepage field in FLAC3D, the results in this paper were compared with that of the reference (Xie et al., 2019) and the results were obtained using the SEEP/W module of GEO-Studio. **Figure 2A** shows the simple model for a homogeneous rock slope, the height of the model is 40 m and the length is 100 m, the height of the slope is 20 m, and the angle is 45°. The initial water level is horizontal and below the ground, so the water table is at the height of 20 m, and a zero flux condition is imposed at the bottom, the front, and back of the model. The left and right boundaries of the model represent a constant head boundary below the water table. The surface of the model is free. In

addition, the water pressure on the slope surface is not considered, so the zero pressure head boundary is applied when the slope surface exhibits transient saturation. And the softening effect on the rock mass under rainfall is ignored. The initial groundwater level of the slope is at $h = 20$ m, and the value of k_s is set to 5.56×10^{-6} m/s. The maximum value of the matric suction in the unsaturated zone is 50 kPa. The rainfall intensity is 5×10^{-5} m/s, the rainfall durations selected is 84 h, and the mechanical parameters of the rock slope are consistent with the reference (Xie et al., 2019). The simulation results shown in **Figure 2** are basically consistent with the results get in reference



(Xie et al., 2019) and the laws obtained by GEO-Studio, which indicate the correctness of the development program. It can be seen from **Figure 2**, at the end of 84 h continuous rainfall events, the wetting front depth increased, and the pore water pressure at the slope surface rises to a stable value of zero, and the rock mass in the up-layer of the slope exhibits a transient saturation. As the rainfall continues, the transient saturated zone formed in the shallow layer of the slope expands gradually, and the range of the unsaturated zone decreases.

RANDOM FIELD FOR HYDRAULIC CONDUCTIVITY OF THE ROCK SLOPE

The Non-invasive Stochastic Method for Random Field

Many scholars have adopted the random field theory in geotechnical engineering to characterize the natural spatial variability of k_s (Cho 2014; Yang et al., 2018; Nguyen and Likitlersuang 2019; Jiang et al., 2020; Zhang et al., 2021). In addition, the non-invasive stochastic method is more simple and easier to implement than the traditional stochastic finite elements method (such as perturbed stochastic finite element method PSFEM, Neumann stochastic finite element method NSFEM and spectral stochastic finite element method SSFEM) (Wang and Xu, 2014; Zhang et al., 2020). Discretizing the random field and determining the covariance matrix are the core issue of a random field realization. Methods to discretize the random field include the center of discrete method, local average method, interpolation function method, weighted integral method, and random field orthogonal expansion method. The local average method is relatively simple and widely used, and **Figure 3** detailed the mathematical method that can be used to discretize the random field. The random field is divided into units through mesh generation, and then the statistical characteristics of these

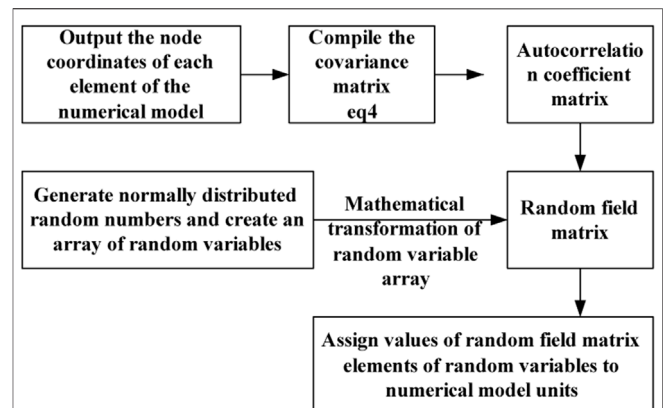
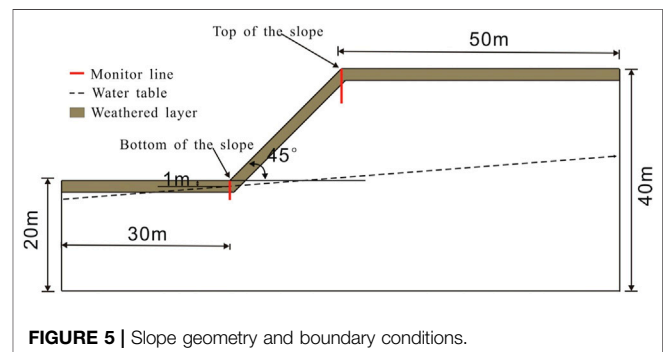


FIGURE 4 | Schematic diagram of program development for non-intrusive stochastic method.



units can be described approximately by the mean, variance, and covariance of stochastic variables (Vanmarcke, 2010).

The elements of the covariance matrix can be got according to Eq. 4, and then the elements of the correlation coefficient matrix M can be obtained according to $\rho(E_i, E_j) = \frac{\text{Cov}(E_i, E_j)}{\sqrt{D(E_i)D(E_j)}}$.

$$\begin{aligned} \text{Cov}(E_i, E_j) &= \frac{\sigma^2}{4A_i A_j} \sum_{k=0}^3 \sum_{l=0}^3 (-1)^{k+l} (L_{xk} L_{yl})^2 \Gamma(L_{xk} L_{yl}) \\ &= \frac{\sigma^2}{4A_i A_j} \sum_{k=0}^3 \sum_{l=0}^3 (-1)^{k+l} (L_{xk} L_{yl})^2 \Gamma(L_{xk}) \Gamma(L_{yl}) \end{aligned} \quad (4)$$

where, E_i, E_j mean the i th and j th unit in the random field. $D(E_i), D(E_j)$ are the variance of the random variable. A_i, A_j represent the area of a rectangular unit at different positions in the x and y -direction of the local average units; the edges of the unit are parallel to the coordinate axis. L_{xk}, L_{yl} ($k = 0, 1, 2, 3; l = 0, 1, 2, 3$) indicate the distance between the edge of different rectangular units in the x and y -direction, respectively. For example, the distances from the left side of A_i to the left and right sides of A_j are denoted as L_{x1} and L_{x2} , respectively; the distances from the right side of A_i to the left and right sides of A_j are denoted as L_{x0} and L_{x3} , respectively; and the distances from the upper and lower sides of A_i to the sides of A_j are detailed in **Figure 3**. $\Gamma(L_{xk})$ is the variation reduction function, which can be expressed as the

TABLE 1 | Mechanics parameters of the model.

Elastic modulus of salt rock E	1.2 GPa
Poisson ratio of salt rock μ	0.28
Effective cohesion c'	150 kPa
Effective friction angle φ'	30°
Tensile strength σ_t	0.2 MPa
Density ρ	2500 Kg m ⁻³
hydraulic conductivity k_s	1 × 10 ⁻⁴ cm/s
Parameters of Eq. 1a	$a_s = 1, b_s = 5 \times 10^{-5}, n = 3.5$
Parameters of Eq. 1b	$a_k = 1000, b_k = 0.01, c = 1.7$
Porosity of the rock n	0.2975
Residual degree of saturation S_r	0.08
Angle defining the increase in shear strength for an Increase in matric suction φ^b	15°

attenuation of the variance of random variable in the local average process of the random field, that is, the relationship between the changing of the local average range and the degree of variation reduction. The variation reduction function can be established by the correlation function which is shown in Eq. 5 as a triangular form.

$$\Gamma(T) = \begin{cases} 1 - \frac{T}{3\theta} & T \leq \theta \\ \frac{\theta}{T} \left(1 - \frac{T}{3\theta}\right) & T > \theta \end{cases} \quad (5)$$

where $\theta = \delta$, δ is the correlation length, the unit is m.

According to Eqs 4, 6, mathematical transformation for the random variable k can be carried out *via* using Matlab, and then a random field model can be obtained, which has same units with the numerical model.

$$\bar{Y} = \mu + \sigma L_1 Y L_2 \quad (6)$$

where \bar{Y} , μ , and σ represent the column vector of the random field, the mean value, and the standard deviation of k , respectively. L_1 is the conjugate transpose form of the triangular matrix obtained by the Cholesky decomposition of the autocorrelation coefficient matrix. Y is the column vector of the random variable k . L_2 is the upper triangular matrix obtained by the Cholesky decomposition of the cross-correlation matrix.

In order to analyze the impact of the variability of k on the seepage characteristic of a rock slope, this paper refers to the non-intrusive stochastic method proposed by Dou et al., 2016, and Figure 4 details the development flow chart of the method. The value of k of the rock slope is smaller than that of the soil, referring to the locale data of an open-pit mine coal rock slope, and the k_s of the rock slope is set to 1 × 10⁻⁴ cm/s. According to the flow chart shown in Figure 4, a k_s random field of the model can be obtained firstly, and then update the value of k in the unsaturated zone according to Figure 3. In addition, considering the weathering effect on the slope surface, which caused a significantly increases in the value of k , take the layer within 2 m from the slope surface as the weathered layer, in which the value of k is magnified by 10 times.

Simplified Model

To analyze the seepage and stability of the slope under rainfall infiltration, it is necessary to form a simplified steady-state seepage field as the initial condition for the transient seepage calculation. Figure 5 shows the numerical model. A saturated hydraulic conductivity random field can be generated, when the value of random variable k is assigned to each unit of the model. The displacements of the bottom boundary and the normal displacements of the left and right boundaries of the model are fixed. In addition, the other boundaries are free. And then

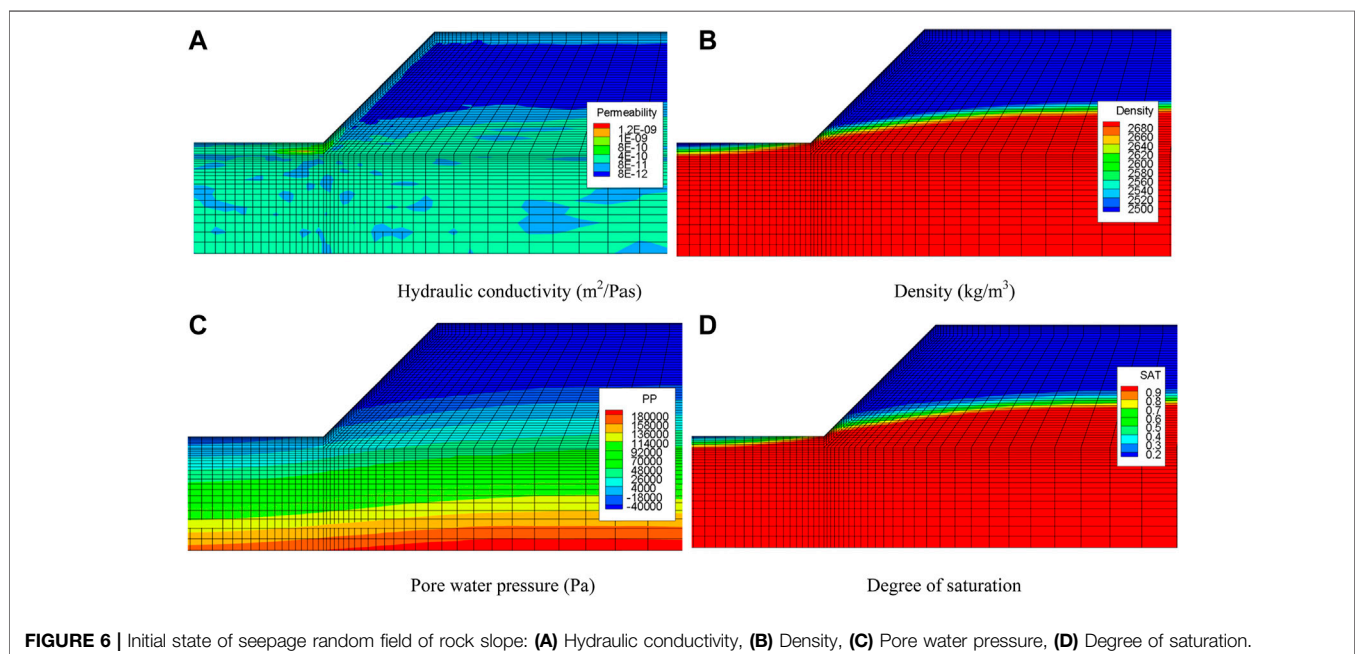


FIGURE 6 | Initial state of seepage random field of rock slope: (A) Hydraulic conductivity, (B) Density, (C) Pore water pressure, (D) Degree of saturation.

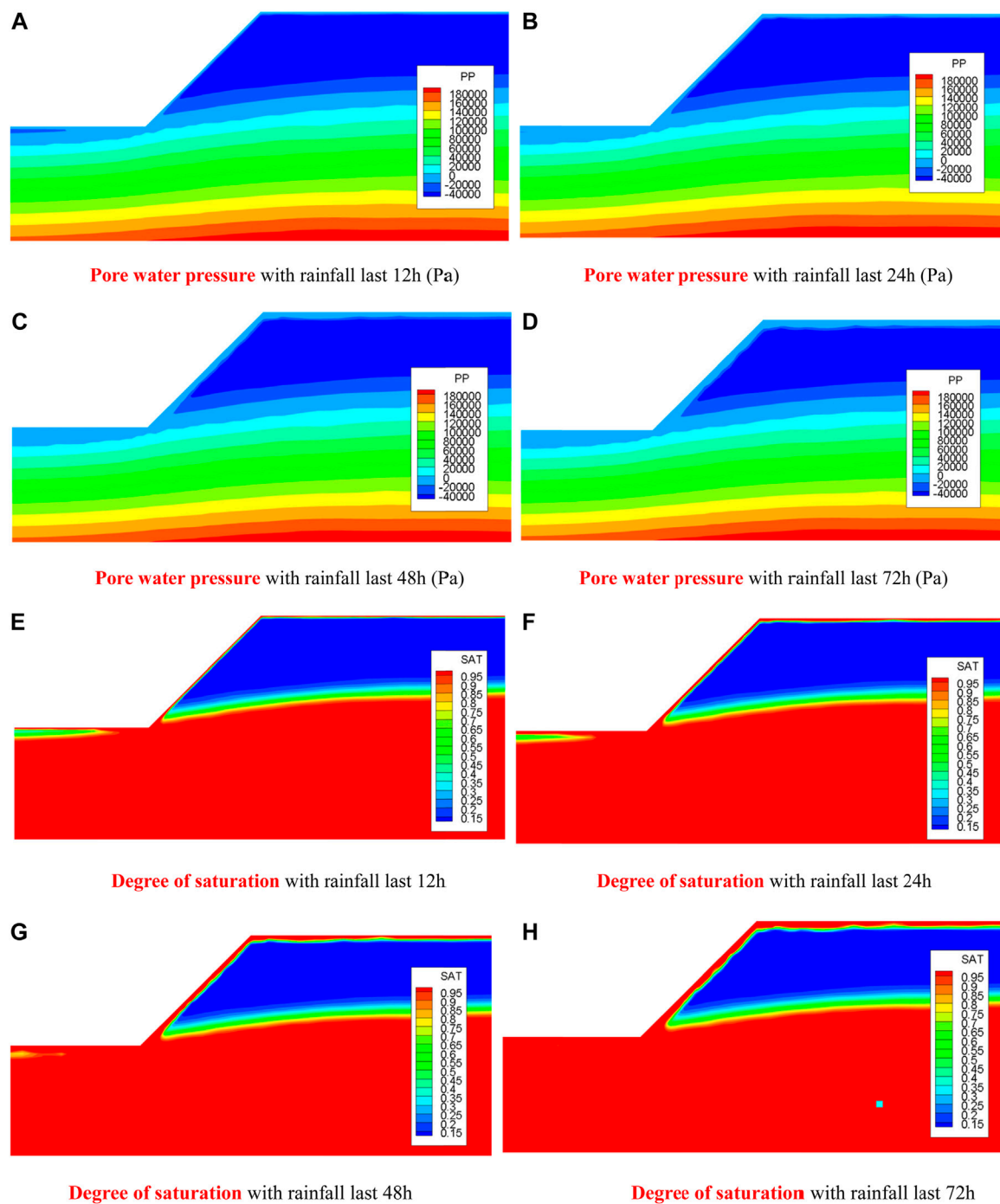


FIGURE 7 | Pore water pressure and saturation under different rainfall duration: **(A)** Pore water pressure with rainfall last 12h (Pa), **(B)** Pore water pressure with rainfall last 24 h (Pa), **(C)** Pore water pressure with rainfall last 48 h (Pa), **(D)** Pore water pressure with rainfall last 72 h (Pa), **(E)** Degree of saturation with rainfall last 12 h, **(F)** Degree of saturation with rainfall last 24 h, **(G)** Degree of saturation with rainfall last 48 h, **(H)** Degree of saturation with rainfall last 72 h.

the initial water table is set, the water table on the left side is at $h = 18$ m, and that on the right is at $h = 25$ m. Firstly, carrying out the balance calculation of the initial *in situ* stress field and the saturated-unsaturated seepage field, and then modifying the unsaturated seepage field, the steady seepage field can be

obtained. Secondly, apply constant rainfall intensity on the slope surface.

The pore water pressure at the model node changed constantly when the rainfall boundary is applied, which means the matric suction of the model is changed. According to Eq. 1, the

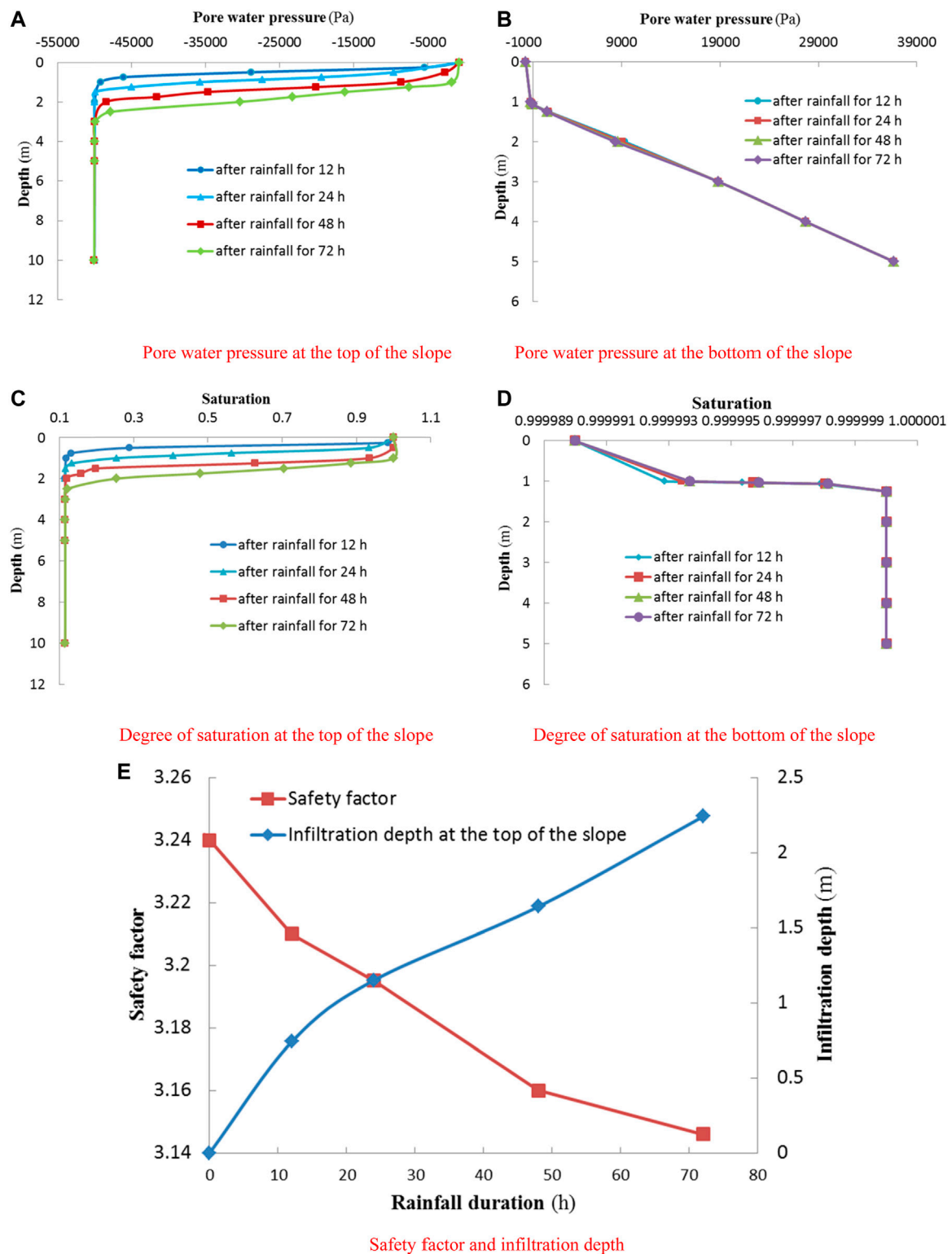


FIGURE 8 | The seepage and stability of the slope with the development of rainfall duration: **(A)** Pore water pressure at the top of the slope, **(B)** Pore water pressure at the bottom of the slope, **(C)** Degree of saturation at the top of the slope, **(D)** Degree of saturation at the bottom of the slope, **(E)** Safety factor and infiltration depth.

saturation is a function of pore water pressure, and the value of saturation at the model node can be obtained. In addition, the value of the unit saturation can be calculated. What is more, the pore water pressure at the unit should be modified with its changing value at the model node, and then the value of k at the unit can be acquired according to Eq. 1. So the value of k and saturation should be modified at each time step in calculation. While the rainfall intensity is greater than the infiltration capacity of the slope, the boundary on the slope surface becomes a constant head condition. Finally, according to Eq. 3, the unit cohesion of the model is corrected, and the safety factor of the rock slope under rainfall infiltration can be got by using the strength reduction method. The initial safety factor of the slope is 3.24, indicating that the rock slope is safety. The mechanical parameters E , μ , c , ϕ , σ_r , ρ and k_s are determined from the laboratory test results of rock slope in an open-pit mine in China, which has ceased excavating. Other parameters are determined combining previous studies (Xie et al., 2019). The mechanical parameters of rock mass are detailed in Table 1.

Initial Conditions

Based on the non-invasive method and the simplified model, the realization of the random field is shown in Figure 6A, the variation coefficient of k_s is set to 0.45, the horizontal correlation length is 60 m, and the vertical is 6 m. The maximum value of the matric suction is 50 kPa. Different colors in Figure 6A represent different values of k , the darker the color, the smaller the value of k . The value of k distributed randomly ranges from 1.0689×10^{-12} to $1.127 \times 10^{-9} \text{ m}^2/\text{Pa}\cdot\text{s}$ (it is necessary to convert the unit of k from m/s to $\text{m}^2/\text{Pa}\cdot\text{s}$ for calculation) (Liu et al., 2020). There is a nonlinear relationship between the value of k and the matric suction of unit in the unsaturated zone: the larger the matric suction, the smaller the value of k . The value of k of the unit in unsaturated zone is corrected according to Eq. 1. The value of k decreases rapidly with the increase of matric suction, so the value in the unsaturated zone is obviously smaller than that in the saturated zone (except for the superficial weathered layer). Figures 6B–D show the initial density, the pore water pressure, and the saturation distribution of the rock slope, respectively. Density, pore water pressure, and saturation have undergone major changes above and below the water table. The zero pore water pressure line is defined as the water table. The rock below the groundwater level is saturated, and the density and saturation of the rock mass are large, and the pore water pressure is positive. But, the rock above the groundwater level is unsaturated, where the density, the saturation, and the negative pore water pressure all transition to a minimum value rapidly.

RAINFALL INFILTRATION CHARACTERISTICS AND STABILITY OF THE ROCK SLOPE

Influence of Rainfall Duration

Figures 7A–D show the pore water pressure inside the rock slope with the rainfall last different times, 12, 24, 48 and 72 h, when the rainfall intensity is 7.2 mm/h. Figures 7E–H show the degree of

saturation. It can be seen from Figure 7 that rainfall events have an important impact on the unsaturated zone of the slope. The negative pore water pressure in the unsaturated zone changes greatly with the development of rainfall duration. With the extension of the rainfall, the more water penetrates into the slope, the greater the impact on the negative pore water pressure. As the rainfall intensity exceeds the infiltration capacity of the soil, only a portion of it can infiltrate while the remaining quantity runoff the slope surface at the beginning of the rainfall, and the surface of the slope enters a transient saturation rapidly. Under the action of gravity and hydraulic gradient, rainwater moves continuously from the slope surface to the inside of the slope, and the infiltration depth will first increase rapidly and then slowly, and the range of transient saturation expands continuously. The transient saturation connects with the water table at the bottom of the slope, and then raises the water level. The unsaturated zone, between the top of the slope and the water table, shrinks gradually, and the negative pore water pressure of the rock mass in the unsaturated zone increase continuously, while the matric suction decreases. Figures 7E–H show that the changes of saturation is basically consistent with that of pore water pressure of the rock slope suffering continuous rainfall.

In order to analyze the rainfall infiltration in the shallow layer of the slope, monitoring points within 10 and 5 m away from the slope surface at the top and bottom of the slope are selected, and the location is detailed in Figure 5 and the negative pore water pressure and the degree of saturation at the monitoring points are compared. Figures 8A–D show the curves of pore water pressure and saturation within different distances to the slope surface at the top and bottom of the slope at the end of different continuous rainfall events. With the distance away from the slope surface, the rainfall effect on the slope decreases gradually until there is no change. With the development of rainfall duration, negative pore water pressure and saturation have similar changes in time and spatial. The negative pore water pressure increases gradually from -50 kPa to approximately 0 kPa , and the saturation changes from 0.08 to approximately 1, which is a dynamic process. The negative pore water pressure on the slope surface and the points near the surface rises sharply and reaches the peak value 0 kPa earliest. But with the distance away from the slope surface, the rising trend slows down gradually. The rainfall infiltration has a certain hysteresis. The vertical distance from the surface at the slope root to the water table is only 1 m, and considering the impact of rainfall infiltration and surface runoff, the transient saturation zone at the slope root connected with the groundwater soon after the rainfall begins, and the groundwater level raises quickly. The transient saturation zone of the upper layer expanded gradually with the continuous rainfall, and the infiltration depth at the end of 24, 48, and 72 h rainfall duration are 1.15, 1.64, and 2.24 m in sequence, and the relationship between the infiltration depth and the rainfall duration is shown in Figure 8E.

The transient saturation caused by rainfall events has an important impact on the safety and stability of the slope. The

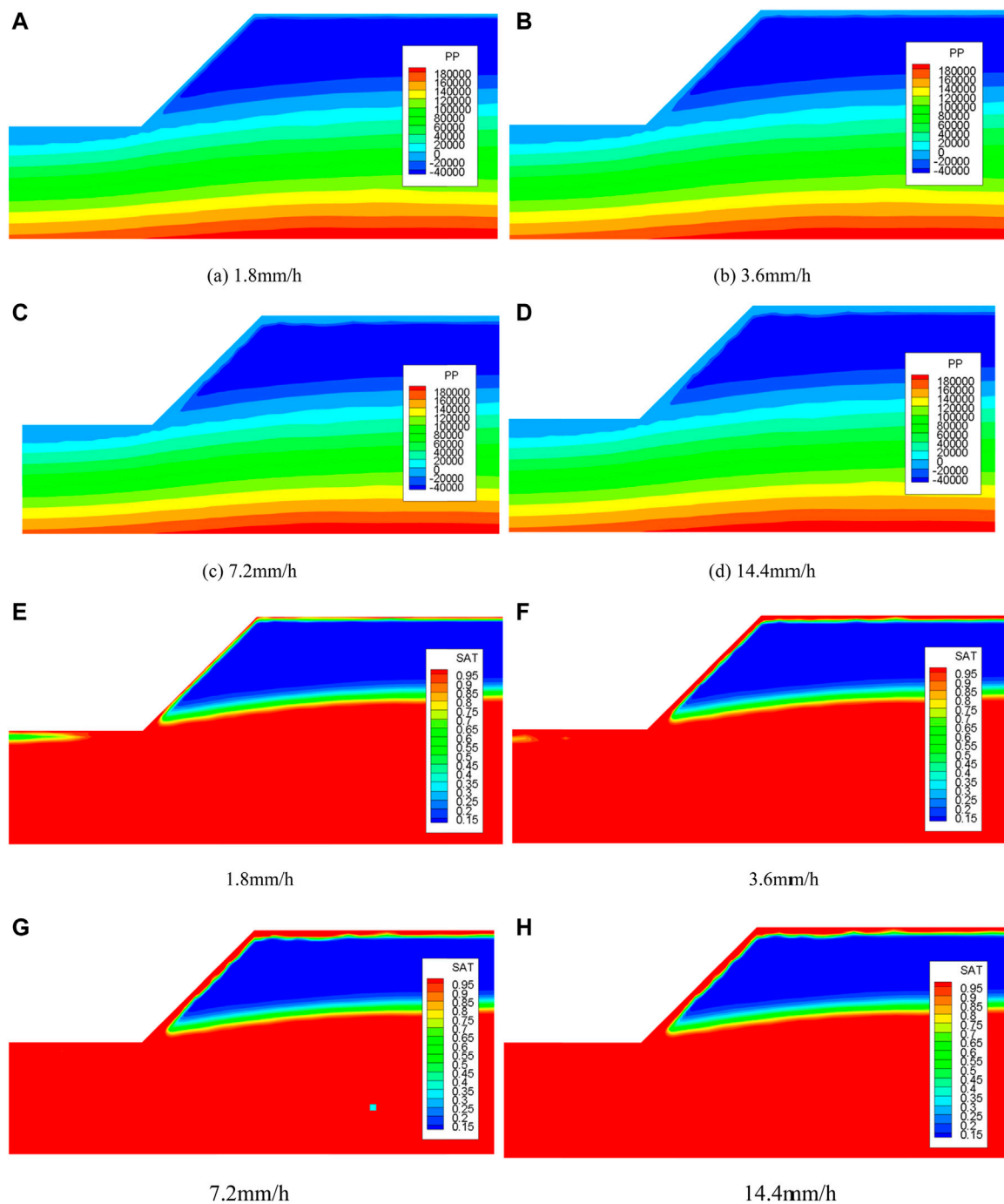


FIGURE 9 | Pore water pressure and saturation under different rainfall intensity: (A) Pore water pressure, (B) Pore water pressure, (C) Pore water pressure, (D) Pore water pressure, (E) Degree of saturation, (F) Degree of saturation, (G) Degree of saturation, (H) Degree of saturation.

safety factor is an important parameter for evaluating the stability of a slope: the greater the safety factor, the more safety the slope (Zhang et al., 2021). The safety factor of the slope changes with the development of rainfall duration, and the changing rules are detailed in Figure 8E. It can be seen from the figure that the safety factor at the initial stage of rainfall is relatively large, and it decreases linearly as the rainfall continues. The safety factors are 3.195, 3.160, and

3.146 at the end of 24, 48, and 72 h rainfall duration, respectively. As the rainwater infiltrates into the slope, the internal water content of the slope changes, and a transient saturation zone appears at the shallow layer of the slope, which increases the weight of the rock mass, reduces the matric suction, and deteriorates the shear strength of the slope. Eventually, the anti-sliding ability of the slope is reduced, and its safety factor is reduced.

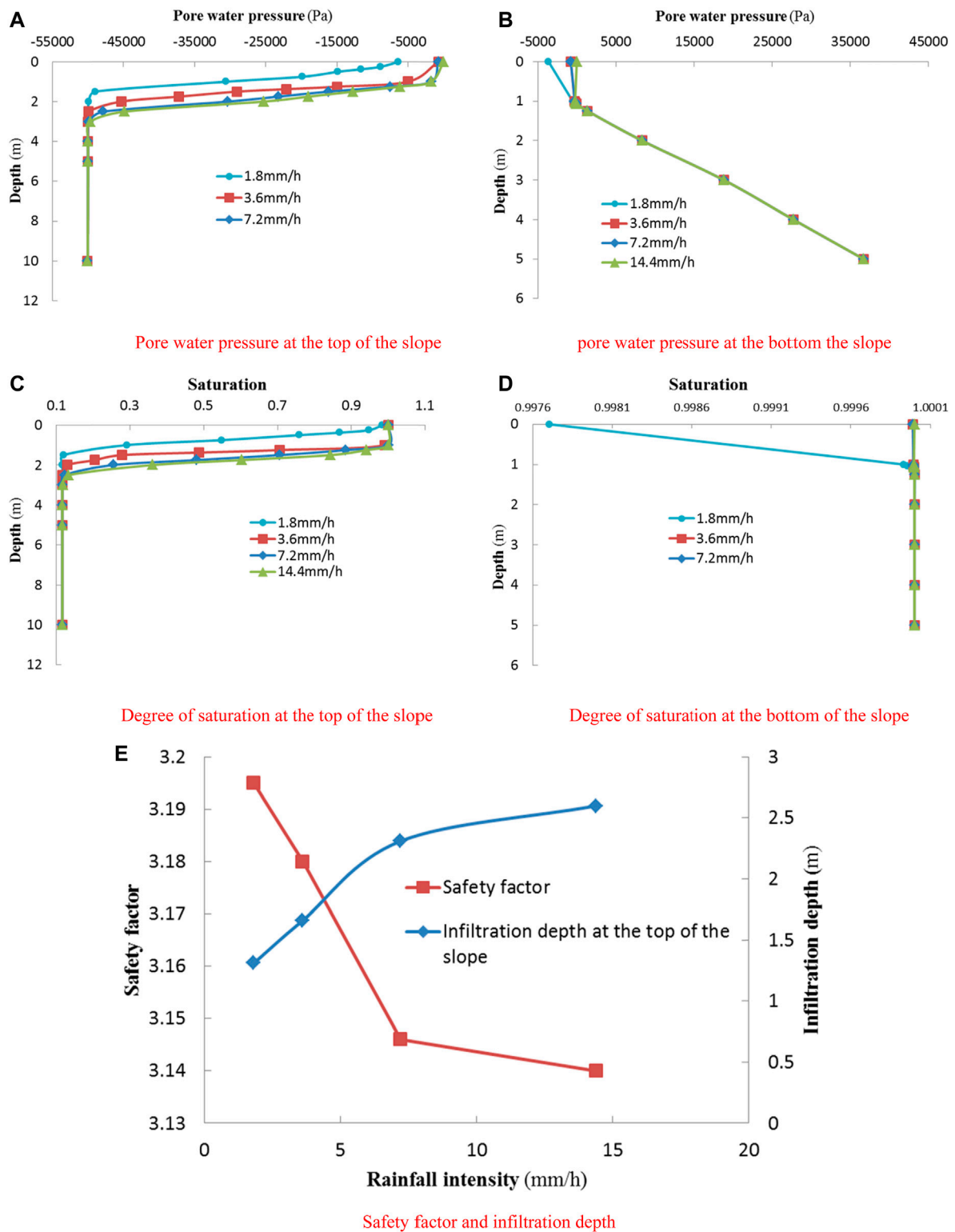


FIGURE 10 | Distribution of pore water pressure and degree of saturation under different rainfall intensities: **(A)** Pore water pressure at the top of the slope, **(B)** Pore water pressure at the bottom of the slope, **(C)** Degree of saturation at the top of the slope, **(D)** Degree of saturation at the bottom of the slope, **(E)** Safety factor and infiltration depth.

TABLE 2 | Ratios setting in different calculation conditions.

Case No	x/x^*				
	Variable coefficient ratio	Horizontal correlation length ratio	Vertical correlation length ratio	Rainfall duration ratio	Rainfall intensity ratio
1	1.31	1	1	1	1
2	1.49	1	1	1	1
3	1.64	1	1	1	1
4	1	0.75	1	1	1
5	1	0.50	1	1	1
0.6	1	0.25	1	1	1
7	1	1	0.83	1	1
8	1	1	0.67	1	1
9	1	1	0.50	1	1
10	1	1	1	0.17	1
11	1	1	1	0.33	1
12	1	1	1	0.67	1
13	1	1	1	1	0.25
14	1	1	1	1	0.50
15	1	1	1	1	2.00

Influence of Rainfall Intensity

Based on the same seepage random field conditions, the impact of rainfall intensity on the rainfall infiltration process of the slope is calculated. Considering four different rainfall intensities, with the rainfall last 3 days, the pore water pressure and the degree of saturation of the unsaturated zone and the slope stability are analyzed. Referring to the rainfall classification standards issued by the National Meteorological department, the rainfall intensities considered for analysis are 1.8 mm/h (heavy rain), 3.6 mm/h (torrential rain), 7.2 mm/h (downpour), and 14.4 mm/h (heavy downpour).

Figures 9A–D show the negative pore water pressure of the rock slope at the end of 72 h continuous rainfall under different rainfall intensities, 1.8, 3.6, 7.2, and 14.4 mm/h. **Figures 9E–H** show the saturation. It can be seen from **Figure 9** that, at the end of 72 h continuous rainfall under different rainfall intensities, a transient saturated zone can be formed in the shallow layer of the slope, and it will be connected with the initial groundwater at the slope root, and then raising the groundwater level. The pore water pressure and saturation in the transient saturation zone change greatly with the rainfall intensity. The greater the rainfall intensity, the more water penetrates into the slope, and the seepage field of the slope is affected more significantly. With the rainfall intensity increases, the range of the transient saturated zone enlarged, and the depth of infiltration becomes deeper, which means the range of the unsaturated zone decreased.

Figures 10A–D show the pore water pressure and saturation at the top and bottom of the slope under different rainfall intensities. The impact of rainfall intensity on the seepage field weakened gradually with the distance away from the slope surface, and the infiltration depth was within 1.31–2.6 m. As the rainfall intensity changes, the negative pore water pressure and saturation exhibits similar characteristic in spatial. The negative pore water pressure and saturation at the slope surface and the points close to the surface increased sharply, and are closer to the peak value. But its rate of increase decrease gradually. Increasing the rainfall intensity will increase the negative pore water pressure and saturation at one

point, while the rainfall intensity reaches the downpour level, the change extend will decrease because of the limitation of infiltration capacity. At the end of 72 h continuous rainfall, under different rainfall intensities, heavy rain, torrential rain, downpour, and heavy downpour, the maximum infiltration depth is 1.31, 1.66, 2.31, and 2.6 m, respectively.

Figure 10E shows the relationship between the slope safety factor and the rainfall intensity. It can be seen from **Figure 10E** that when the rainfall intensity is heavy rain, the safety factor is relatively large. When the rainfall intensity is heavy rain, torrential rain, downpour, and heavy downpour, the safety factors of the slope are 3.195, 3.180, 3.146, and 3.140, respectively. With the increases of rainfall intensity, the volume of water infiltrates into the slope increased. Then, the weight of the transient saturation zone becomes larger, and the impact on the matric suction of the rock and soil becomes greater. The infiltration depth is rapidly increased, so the safety factor of the slope is rapidly reduced. While the rainfall intensity reaches the torrential level or above, that is, it overcomes the infiltration capacity of the slope, the rainwater cannot fully penetrates into the slope, and part of the water will runoff the slope surface. Therefore, the rising rate of the infiltration depth and the rate of decline of the safety factor will slow down.

Influence of the Variability of Hydraulic Conductivity

The physical and mechanical properties of rock and soil of the rock slope has obvious natural spatial variability, and the sensitivity analysis method (Jiang et al., 2014) can be used to study the influence of variability of rock parameters on the seepage and stability of the slope. Jiang et al., 2020 proposed that although the mechanical parameters of soil exhibit variability, there also exist certain correlations between different points of the model. For example, the horizontal correlation length and the vertical represent the fluctuation range of the correlation of rock mass in the horizontal and vertical directions, respectively. The main

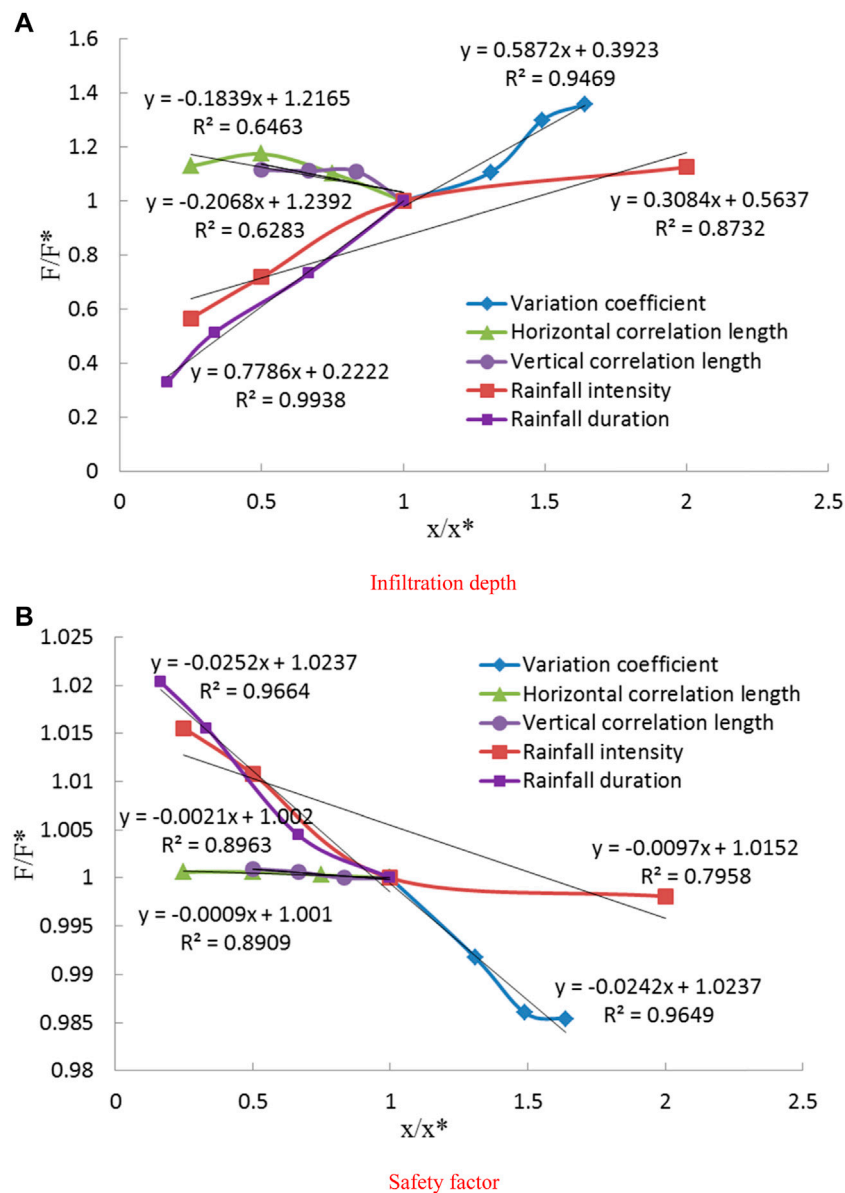


FIGURE 11 | Sensitivity comparison of different impact factors: (A) Infiltration depth, (B) Safety factor.

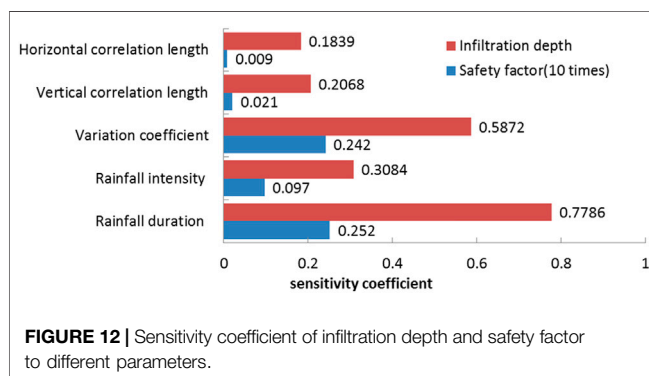


FIGURE 12 | Sensitivity coefficient of infiltration depth and safety factor to different parameters.

parameters reflecting the variability of k include the variation coefficient, the horizontal correlation length, and the vertical. The single factor sensitivity analysis method is used to deal with the above factors. A base case is established, where the rainfall intensity is set to 7.2 mm/h, rainfall duration is 72 h, and the variation coefficient and the horizontal and the vertical correlation length of k is 0.45, 60, and 6 m, respectively. In addition, in accordance with the statistics on the variability and the autocorrelation length of geotechnical parameters at China and abroad, the horizontal correlation length ranges from 10 to 75 m, while the vertical is significantly smaller and ranges from 0.1 to 8 m (Jiang et al., 2014). So comparison cases are established, and the calculation conditions are detailed in **Table 2**, where x represents the value of the rainfall intensity, rainfall duration,

variation coefficient of k , and horizontal or vertical correlation length in a comparison case, and x^* represents the value of parameters in the base case; a total of 15 numerical simulations are carried out. According to the numerical results of different cases, the relationship between impact factors and infiltration depth or safety factor can be obtained, which are shown in **Figure 11**. Taking x/x^* as the X -axis, and taking F/F^* as the Y -axis, F represents the infiltration depth or safety factor of a comparison case, and F^* represents the corresponding results of the base case. The absolute value of the curve slope is defined as the sensitivity coefficient, which reflects the influence degree of various factors on the seepage of the model (Wu et al., 2010). The larger the sensitivity coefficient is, the greater the impact of the factor on the seepage of the slope.

It can be seen from **Figure 11** that the effects of various factors on the slope seepage and stability are significantly different. The increase in rainfall intensity, rainfall duration, and variation coefficient can lead to an increase in the infiltration depth, while an increase in horizontal and/or vertical length will result in a reduction in the infiltration depth. The impact of various factors on the safety factor of the slope exhibit a same trend, and increasing the value of the influence factor will cause decrease of the safety factor. When the rainfall intensity is smaller than the infiltration capacity of the rock and soil, the slope of the curve referring to the rainfall intensity and rainfall duration is larger than that of the variability of k_s , that is, the infiltration process of the rock slope is more sensitive to the rainfall intensity and/or duration. While the rainfall intensity reaches the downpour level or above, the impact degree of rainfall events on the infiltration depth and safety factor is slowed down, even lower than the impact of the variability of k . This is mainly due to the high rainfall intensity, which results in the water forms runoff on the slope surface, and then the impact of rainfall intensity on the seepage and stability of the slope is alleviated. Considering the variability of k , the slope is most affected by the variation coefficient of k , followed by the vertical correlation distance, while the least sensitive to the horizontal correlation length, which is mainly related to the geological sedimentation history of the rock layer. **Figure 12** shows the sensitivity of the slope to various factors, and the order of the sensitivity is: rainfall duration, variation coefficient of k , rainfall intensity, vertical correlation length of k , and horizontal correlation length.

CONCLUSION

1) Based on the unsaturated theory, a program for the saturated-unsaturated seepage of a rock slope under rainfall infiltration is established. Comparing the results of this paper with previous research and results obtained *via* Geo-studio, the correctness of the development program is verified.

2) The spatial variability of saturated hydraulic conductivity (k_s) has great impact on rainfall infiltration process. According to the local average random field theory, the spatial variability of k_s can be described with parameters such as variation coefficient and correlation length. The variance reduction function is used to obtain the connection between the variability of points and space. The non-invasive realization of the random field k_s of rock mass is carried out by adopting MATLAB; on this basis, the numerical

simulation of the seepage random field of the slope suffering rainfall is carried out. The dynamic seepage characteristic is obtained with considering both the variability of k_s and the rainfall infiltration.

3) Rainfall infiltration has a great impact on the shallow layer of the rock slope, and the infiltration process leads to an increase in the value of pore water pressure and the degree of saturation in the unsaturated zone of the slope. A transient saturated zone appears in the upper layer of the slope, and it connects with the initial groundwater level at the slope root firstly. With the increasing of rainfall duration and/or rainfall intensity, both the negative pore water pressure and the degree of saturation in the transient saturation zone all increased. The infiltration depth is positively associated with the rainfall too; while the rainfall intensity reaches the downpour level, the increase rate of the infiltration depth slows down.

4) Rainfall infiltration is a dynamic process from surface to inside of the slope, from shallow to deep. Water penetrates into the slope gradually with the continuous of the rainfall. This process increases the weight of the shallow layer of the slope and causes the reduction of the matric suction, which makes the shear strength of the slope reduced. Then the safety factor of the slope decreases with the increase of rainfall duration, rainfall intensity, variation coefficient, and/or relative length. When the rainfall intensity reaches the downpour level, the deceleration rate slows down.

5) Considering the variability of the k_s , the seepage of the slope is most sensitive to the variation coefficient, followed by the vertical correlation length, while it is least sensitive to the horizontal length. Compared with the variability of the k_s , the seepage field is more sensitive to rainfall duration and rainfall intensity. However, when the rainfall intensity reaches the downpour level, the impact of the variation coefficient of k_s is greater than the rainfall intensity. For practical engineering, it is necessary to consider both the spatial variability of saturated hydraulic conductivity and the unsaturated seepage characteristics of rock slopes.

DATA AVAILABILITY STATEMENT

The raw data supporting the conclusions of this article will be made available by the authors, without undue reservation.

AUTHOR CONTRIBUTIONS

QZ contributed significantly to analysis and manuscript preparation; LW helped perform the analysis with constructive discussions; HZ performed the data analyses and wrote the manuscript.

FUNDING

This study was supported by the National Key R&D Program of China (grant no. 2017YFC1503102), National Natural Science Foundation of China (grant no. 51504124), and Scientific Research Project of Education Department of Liaoning Province (grant no. LJKZ0335).

REFERENCES

- Alonso, E., Gens, A., Lloret, A., and Delahaye, C. (1995). "Effect of Rain Infiltration on the Stability of Slopes," in Proceedings of the International Conference on Unsaturated Soils, Paris, 241–249.
- Cai, G., Li, M., Han, B., Di, K., Liu, Q., and Li, J. (2020). Numerical Analysis of Unsaturated Soil Slopes Under Rainfall Infiltration Based on the Modified Glasgow Coupled Model. *Adv. Civil Eng.* 2020, 1–13. doi:10.1155/2020/8865179
- Chen, J., Liu, P., Xu, Q., and Li, J. (2020). Seismic Analysis of Hardfill Dams Considering Spatial Variability of Material Parameters. *Eng. Structures* 211, 110439. doi:10.1016/j.engstruct.2020.110439
- Cho, S. E., and Lee, S. R. (2001). Instability of Unsaturated Soil Slopes Due to Infiltration. *Comput. Geotechnics* 28 (3), 185–208. doi:10.1016/s0266-352x(00)00027-6
- Cho, S. E. (2014). Probabilistic Stability Analysis of Rainfall-Induced Landslides Considering Spatial Variability of Permeability. *Eng. Geology* 171, 11–20. doi:10.1016/j.enggeo.2013.12.015
- Chu-Agor, M. L., Fox, G. A., Cancienne, R. M., and Wilson, G. V. (2008). Seepage Caused Tension Failures and Erosion Undercutting of Hill Slopes. *J. Hydrol.* 359 (3–4), 247–259. doi:10.1016/j.jhydrol.2008.07.005
- Collins, B. D., and Znidarcic, D. (2004). Stability Analyses of Rainfall Induced Landslides. *J. Geotech. Geoenviron. Eng.* 130 (4), 362–372. doi:10.1061/(asce)1090-0241(2004)130:4(362)
- Dou, H.-Q., Han, T.-C., and Gong, X.-N. (2016). Reliability Analysis of Slope Stability Considering Variability of Soil Saturated Hydraulic Conductivity under Rainfall Infiltration. *Rock Soil Mech.* 37 (4), 1144–1152. doi:10.16285/j.rsm.2016.04.029
- Fredlund, D. G., and Rahardio, H. (1997/1997). *Mechanics of Unsaturated Soils [M]. Translated by Chen Zhongyi*. Beijing: China Construction Industry Press.
- Fu, H.-Y., Wu, Y., He, Z.-M., and Shi, Z.-N. (2014). Embankment Slope Stability Safety Factor Variation of Coarse Grained Soil under Continuous Rainfall. *J. Changsha Univ. Sci. Technol. (Natural Science)* (2), 48–53. doi:10.3969/j.issn.1672-9331.2014.02.009
- Guo, X., Zhao, C., and Yu, W. (2005). Stability Analysis of Unsaturated Soil Slope and its Progress. *China Saf. Sci. J.* 15 (1), 14–18. doi:10.3969/j.issn.1003-3033.2005.01.004
- Hamrouni, A., Dias, D., and Sbartaï, B. (2020). Soil Spatial Variability Impact on the Behavior of a Reinforced Earth Wall. *Front. Struct. Civil Eng.* 14, 518–531. doi:10.1007/s11709-020-0611-x
- Han, T., Liu, L., and Li, G. (2020). The Influence of Horizontal Variability of Hydraulic Conductivity on Slope Stability Under Heavy Rainfall. *Water* 12 (9), 2567. doi:10.3390/w12092567
- Horton, R. E. (1939). Analysis of Runoff-Plat Experiments with Varying Infiltration-Capacity. *Trans. AGU* 20 (4), 693. doi:10.1029/tr020i004p00693
- Hu, J., Zhang, J., Chen, H., Wang, H., and Zheng, W. (2017). Stability of Completely Decomposed Granite Slopes under Intense Rainfall Infiltration Based on the Random Field Theory. *South. Energ. Construction* 4 (03), 107–114. doi:10.16516/j.gedi.issn2095-8676.2017.03.020
- Huang, M., and Jia, C. Q. (2007). Strength Reduction FEM in Stability Analysis of Soil Slopes Subjected to Transient Unsaturated Seepage. *Chin. J. Rock Mech. Eng.* 36 (1–2), 93–101. doi:10.1016/j.compgeo.2008.03.006
- Huang, R., and Qi, G. (2002). The Effect of Unsaturated Soil Suction on Slope Stability. *J. Eng. Geology* 10 (4), 343–348. doi:10.3969/j.issn.1004-9665.2002.04.002
- Jiang, S., Li, D., and Zhou, C. (2014). Slope Reliability Analysis Considering Effect of Autocorrelation Functions. *China Saf. Sci. J.* 36 (03), 508–518. doi:10.11779/CJGE201403014
- Jiang, S.-H., Liu, X., and Huang, J. (2020). Non-intrusive Reliability Analysis of Unsaturated Embankment Slopes Accounting for Spatial Variabilities of Soil Hydraulic and Shear Strength Parameters. *Eng. Comput.* doi:10.1007/s00366-020-01108-6
- Jiang, Z., Zeng, L., Fu, H., and Xiong, X. (2014). Dynamic Stability Analysis of Soft Rock Slope Due to Extremely Prolonged Rainfall[J]. *China J. Highw. Transport* 27 (2), 27–34. doi:10.3969/j.issn.1001-7372.2014.02.004
- Jiang, Z.-M., Xiao-hu, X., and Zeng, L. (2014). Unsaturated Seepage Analysis of Slope Under Rainfall Condition Based on FLAC3D. *Rock Soil Mech.* 35 (03), 855–861. doi:10.16285/j.rsm.2014.03.016
- Li, Y., Wu, J., and Kun, L. (2012). Saturated-unsaturated Seepage Analysis Based on FLAC3D. *Rock Soil Mech.* 33 (02), 617–622. doi:10.16285/j.rsm.2012.02.001
- Liu, W., Zhang, Z., Fan, J., Jiang, D., Li, Z., and Chen, J. (2020). Research on Gas Leakage and Collapse in the Cavern Roof of Underground Natural Gas Storage in Thinly Bedded Salt Rocks. *J. Energ. Storage* 31, 101669. doi:10.1016/j.est.2020.101669
- Liu, X., and Wang, Y. (2021). Probabilistic Simulation of Entire Process of Rainfall-Induced Landslides Using Random Finite Element and Material Point Methods with Hydro-Mechanical Coupling. *Comput. Geotechnics* 132, 103989. doi:10.1016/j.compgeo.2020.103989
- Liu, X., and Xu, M. (2017). The Unsaturated Hydromechanical Coupling Model of Rock Slope Considering Rainfall Infiltration Using DDA. *Geofluids* 2017, 1–15. doi:10.1155/2017/1513421
- Morbidei, R., Corradini, C., Saltalippi, C., Flammini, A., Dari, J., and Govindaraju, R. (2018). Rainfall Infiltration Modeling: A Review. *Water* 10 (12), 1873. doi:10.3390/w10121873
- Nguyen, T. S., and Likitlersuang, S. (2019). Reliability Analysis of Unsaturated Soil Slope Stability Under Infiltration Considering Hydraulic and Shear Strength Parameters. *Bull. Eng. Geology. Environ.* 78, 5727–5743. doi:10.1007/s10064-019-01513-2
- Oh, W. T., and Vanapalli, S. K. (2010). Influence of Rain Infiltration on the Stability of Compacted Soil Slopes. *Comput. Geotechnics* 37 (5), 649–657. doi:10.1016/j.compgeo.2010.04.003
- Pan, Y., Wu, G., Zhao, Z., and He, L. (2020). Analysis of Rock Slope Stability Under Rainfall Conditions Considering the Water-Induced Weakening of Rock. *Comput. Geotechnics* 128, 103806. doi:10.1016/j.compgeo.2020.103806
- Qin, G., Huang, R., Su, B., Hu, Y., and Zhan, M. (2003). Numeric Simulation on Rainfall Infiltration on Rock Slope. *Chin. J. Rock Mech. Eng.* 22 (4), 625–629. doi:10.3321/j.issn.1000-6915.2003.04.023
- Qin, X., Liu, D., Song, Q., Wu, Y., Zhang, Y., and Ye, Y. (2017). Reliability Analysis of Bedrock Laminar Slope Stability Considering Variability of Saturated Hydraulic Conductivity of Soil Under Heavy Rainfall. *Chin. J. Geotechnical Eng.* 39 (6), 1065–1073. doi:10.11779/CJGE201706012
- Rong, G., Zhang, W., and Zhou, C.-B. (2005). Numerical Analysis of Saturated-Unsaturated Seepage Problem of Rock Slope Under Rainfall Infiltration. *Rock Soil Mech.* 26 (10), 1545–1550. doi:10.16285/j.rsm.2005.10.005
- Santoso, A. M., Phoon, K. K., and Quek, S. T. (2011). Effects of Soil Spatial Variability on Rainfall-Induced Landslides. *Comput. Structures* 89 (11–12), 893–900. doi:10.1016/j.compstruc.2011.02.016
- Van Genuchten, M. T. (1980). A Closed-form Equation for Predicting the Hydraulic Conductivity of Unsaturated Soils. *Soil Sci. Soc. America J.* 44 (5), 892–898. doi:10.2136/sssaj1980.03615995004400050002x
- Vanmarcke, E. H. (2010). *Random Fields: Analysis and Synthesis (Revised and Expanded)*. New Edn. Singapore: World Scientific Publishing Co. Pte. Ltd.
- Wang, L., and Xu, Q. (2014). Analysis of Three Dimensional Random Seepage Field Based on Monte Carlo Stochastic Finite Element Method. *Rock Soil Mech.* 35 (01), 287–292. doi:10.16285/j.rsm.2014.01.002
- Wang, L., Wu, C., Li, Y., Liu, H., Zhang, W., and Chen, X. (2019). Probabilistic Risk Assessment of Unsaturated Slope Failure Considering Spatial Variability of Hydraulic Parameters. *KSCE J. Civ. Eng.* 23 (12), 5032–5040. doi:10.1007/s12205-019-0884-6
- Wu, Z., Wang, S., Tang, H., and Ge, X. (2010). A New Sensitivity Analysis Approach for Slope Stability-Reliability Analysis Method. *Chin. J. Rock Mech. Eng.* 29 (10), 2050–2055.

- Xie, Q., Tian, D.-L., Jin-hui, L., Jian-hua, Z., and Zhi-bin, Z. (2019). Simulation of Seepage Flow on Soil Slope and Special Stress-Correction Technique. *Rock Soil Mech.* 40 (03), 879–892. doi:10.16285/j.rsm.2017.1827
- Xiong, Z. A., Wei, L., Jiang, D., Qiao, W., Liu, E., Zhang, F., et al. (2020). Investigation on the Influences of Interlayer Contents on Stability and Usability of Energy Storage Caverns in Bedded Rock Salt. *Energy* 231, 120968. doi:10.1016/j.energy.2021.120968
- Xu, H., Zhu, Y., Cai, Y., and Zhu, F. (2005). Stability Analysis of Unsaturated Soil Slopes Under Rainfall Infiltration. *Rock Soil Mech.* 26 (12), 1957–1962. doi:10.3969/j.issn.1000-7598.2005.12.019
- Yang, H.-Q., Zhang, L., Xue, J., Zhang, J., and Li, X. (2018). Unsaturated Soil Slope Characterization with Karhunen–Loève and Polynomial Chaos via Bayesian Approach. *Eng. Comput.* 35, 337–350. doi:10.1007/s00366-018-0610-x
- Zhang, G., Lu, G., Xia, C., Wu, L., Xu, Z., Bai, Y., et al. (2021). A Sensitivity Analysis of the Anisotropy of Hydraulic Conductivity to the Seepage, Deformation and Stability of Anti-dipping Layered Rock Slopes: A Case Study of the Pulang Area in Southwestern China. *Geotechnical Geol. Eng.* doi:10.1007/s10706-021-01910-z
- Zhang, Q., Wang, L., Zhang, H., Ran, L., and Guo, z. (2020). Non-intrusive Random Analysis on Reliability of Weak Layers Bench Slope. *J. Saf. Sci. Technol.* 16 (11), 33–39. doi:10.11731/j.issn.1673-193x.2020.11.005
- Zhang, W.-G., Meng, F.-S., Chen, F.-Y., and Liu, H.-L. (2021). Effects of Spatial Variability of Weak Layer and Seismic Randomness on Rock Slope Stability and Reliability Analysis. *Soil Dyn. Earthquake Eng.* 146 (2021), 106735. doi:10.1016/j.soildyn.2021.106735

Conflict of Interest: The authors declare that the research was conducted in the absence of any commercial or financial relationships that could be construed as a potential conflict of interest.

Publisher's Note: All claims expressed in this article are solely those of the authors and do not necessarily represent those of their affiliated organizations, or those of the publisher, the editors and the reviewers. Any product that may be evaluated in this article, or claim that may be made by its manufacturer, is not guaranteed or endorsed by the publisher.

Copyright © 2022 Zhang, Wang and Zhang. This is an open-access article distributed under the terms of the Creative Commons Attribution License (CC BY). The use, distribution or reproduction in other forums is permitted, provided the original author(s) and the copyright owner(s) are credited and that the original publication in this journal is cited, in accordance with accepted academic practice. No use, distribution or reproduction is permitted which does not comply with these terms.



Study on Mechanical Problems of Complex Rock Mass by Composite Material Micromechanics Methods: A Literature Review

Junzhao He^{1,2}, Yunan Li^{1*}, Yuling Jin³, Anming Wang^{4*}, Yumin Zhang⁴, Jinchao Jia⁴, Hei Song² and Dong Liang²

¹China University of Geosciences, Wuhan, China, ²Henan Geological and Mineral Resources Construction Engineering (Group) Co. Ltd, Zhengzhou, China, ³Institute of Geodesy and Geomatics, Henan Bureau of Geology and Mineral Resources, Zhengzhou, China, ⁴North China University of Water Conservancy and Electric Power, Zhengzhou, China

OPEN ACCESS

Edited by:

Wei Liu,
Chongqing University, China

Reviewed by:

Jinyang Fan,
Chongqing University, China
Guimin Zhang,
China University of Mining and
Technology, China
Yintong Guo,
Institute of Rock and Soil Mechanics
(CAS), China

*Correspondence:

Yunan Li
liyunan@cug.edu.cn
Anming Wang
wam992001@163.com

Specialty section:

This article was submitted to
Geohazards and Georisks,
a section of the journal
Frontiers in Earth Science

Received: 03 November 2021

Accepted: 02 December 2021

Published: 13 January 2022

Citation:

He J, Li Y, Jin Y, Wang A, Zhang Y,
Jia J, Song H and Liang D (2022) Study
on Mechanical Problems of Complex
Rock Mass by Composite Material
Micromechanics Methods: A
Literature Review.
Front. Earth Sci. 9:808161.
doi: 10.3389/feart.2021.808161

The mechanical analysis of complex rock mass is a difficult problem, which often occurs in scientific research and practical engineering. Many achievements have been made in the study of rock mass composite problems by composite material micromechanics method, but it has not been well summarized so far. This paper summarizes in detail the research status of complex rock mass problems by composite material micromechanics method at home and abroad, including the application of the Eshelby equivalent inclusion theory and self-consistent model in rock mass composite problems, and the application of the homogenization method in jointed rock mass and other rock mass composite problems such as anchored rock mass, layered rock mass, and salt rock mass with impurities. It is proposed that the structural similarity and mechanical analysis similarity should be satisfied when the composite material micromechanics method is used to study the complex rock mass. Finally, the problems that need to be further studied are put forward. The research results provide a valuable reference for the study of complex rock mass by the composite material micromechanics method.

Keywords: complex rock mass, composite material micromechanics method, Eshelby equivalent inclusion theory, self-consistent model, homogenization method

INTRODUCTION

As a very complex structure, the rock contains defects such as the holes, stratification, schistosity, joints, weak structural planes, and interlayer. In addition, micro-structures, micro-cracks, or multiphase inclusions are also formed in the microstructure, and the mineral crystals that make up rocks also bear a variety of forms. The spatial distribution, geometric size, and internal filling type of these defects have a great influence on the physical and mechanical properties of rock materials (Chen and Li, 1992). Therefore, the study of the evolution law of cracks or defects under various external factors such as force, temperature, and moisture has important significance for some special rock mass structures such as fissure rock mass, jointed rock mass, weak interlayer rock mass, and impurity rock mass.

In the early days, the elastic mechanics method was used to analyze the rock materials. Subsequently, plastic mechanics, fracture damage mechanics, explosive mechanics, statistical mechanics, computational mechanics, and computer technology are increasingly applied for rock

mechanics. However, rock is a kind of complex geological material, and the discipline of rock mechanics and engineering should not only develop its theories, technologies, and methods from other basic disciplines but also carry out multidisciplinary cross-collaboration (She and Peng, 2014). The composite mechanics is a science of specializing in mechanical behavior under different material combinations based on theoretical mechanics, material mechanics, elasticity mechanics, plasticity mechanics, etc.

Based on the idea of applying composite material mechanical methods to study the rock mechanics, as early as 1956, Einstein (Einstein, 1956) was apparently the first to attempt such work, followed by Hashin (Hashin and Shtrikman, 1963). After that, a great number of scholars (Salamon, 1968; Eshelby, 1957; Li et al., 2006a; Abou-ChakraGue' et al., 2008) have studied the mechanical problems of complex rock mass by composite material micromechanics methods. In 1979, Chinese Professor Wang Jingtao (Wang, 1979) pointed out that it is meaningful to deal with the problems of rock mechanics by using the basic principles and composite material micromechanics methods, and it can more realistically reflect the mechanical properties of rock mass. In 1990, Professor Zhao Pinglao (Zhao and Zeng, 1990) believed that studying rock mechanics by the composite material mechanics methods would be a favorite new idea to promote the rapid development of rock mechanics.

This article mainly summarizes the application of composite material micromechanics methods in the field of rock mechanics, and analyzes and discusses the relevant problems in order to provide relevant researchers with a more comprehensive understanding of the research status in this field and promote the further application of composite material micromechanics methods to the research of geotechnical engineering problems.

BASIC THEORY OF COMPOSITE MATERIAL MECHANICS AND ITS APPLICATION IN ROCK MECHANICS

The theoretical research methods of mechanical properties of composite materials are mainly divided into macro-mechanical methods and micro-mechanical methods (Qin and Yang, 2006). In the macro-mechanics theory of composites, the composites are regarded as macro-homogeneous media, and the internal reinforcing phase and matrix are regarded as a whole without considering the interaction between internal components, and the micromechanics is to establish the quantitative relationship among the macro properties, composition properties, and microstructure of composites (Du and Wang, 1998).

As early as 1957, Eshelby (Eshelby, 1957; Eshelby, 1959) put forward Eshelby's equivalent inclusion theory based on a large number of studies. Subsequently, more mature micro-mechanics theories have been put forward, such as the Mori Tanaka method (Mori and Tanaka, 1973), self consistent theory (Hill, 1965a; Budiansky, 1973), and generalized self consistent theory (Christensen and Lo, 1979).

The homogenization method (Benssousan et al., 1978; Cioranescu and Paulin, 1979; Sanchez-Palencia, 1980) developed in the 1970s is used as an alternative method to find the effective characteristics of equivalent homogenized materials. The representative volume element method, the multi-scale progressive homogenization method, and the homogenization method based on inclusion theory are the main contents of the homogenization method.

Eshelby Equivalent Inclusion Theory and Its Application

Eshelby uses Green's function method of three-dimensional elastic problems to obtain the explicit solution of the ellipsoidal inclusion problem, and also analyzes the elastic stress field around the inclusion (Eshelby, 1957; Eshelby, 1959). More research work has been carried out in the field of rock mechanics. On the one hand, scholars used Eshelby's equivalent inclusion theory to study the application of rock macro-equivalent elastic modulus (Hu et al., 2013; Xiao and Huang, 2013; Nguyen et al., 2016), rock rheology, and reinforcement engineering (Xiao and Huang, 2013). At the same time, the change of the rock meso-structure is studied by Eshelby inclusion theory and meso-damage mechanics (Bai, 2016).

Pensee (Vincent and Kondo, 2003) and Zhu (Zhu et al., 2008) combined Eshelby's inclusion theory and energy method to obtain the damage model of brittle materials. Zhu (2006) used the Eshelby inclusion problem solution to construct the thermodynamic framework of the micromechanical damage model, and by considering the elastic strain (ϵ^m) of matrix and the inelastic strain (ϵ^c) caused by crack, the general form of representative volume element free energy is obtained, as shown in Eq. 1:

$$W = \frac{1}{2} (\epsilon - \epsilon^c) : C^m : (\epsilon - \epsilon^c) + \frac{1}{2} \epsilon^c : C^b : \epsilon^c, \quad (1)$$

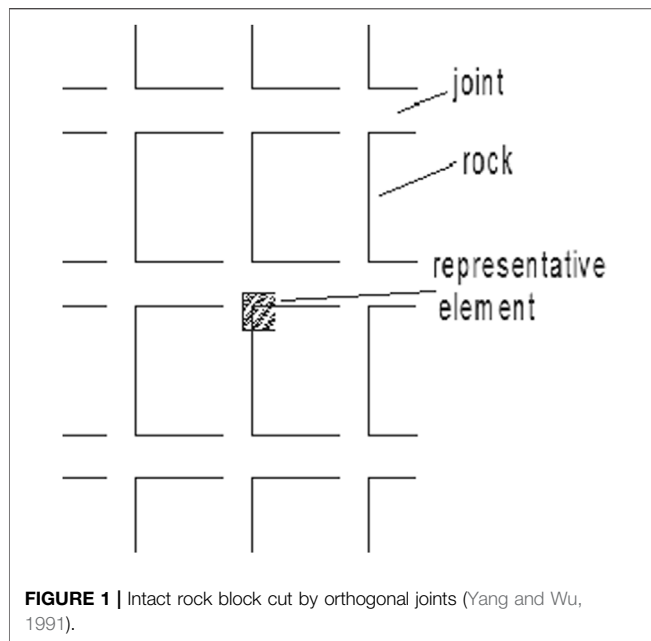
where : C^m is the matrix modulus, which is the fourth-order effective elastic tensor.

Chen et al. (2011) established the meso-damage mechanics model of rock under the condition of thermal mechanical coupling by using the M-T method and Taylor method.

The above is the case of meso-damage mechanics studied by inclusion theory. Within the framework of macro-damage mechanics, Weilide (Lide et al., 2004a; Lide et al., 2004b) used the Eshelby equivalent inclusion method to establish the elastic-plastic constitutive relationship of rock mass considering the plastic deformation of damaged rock. However, because the Eshelby theoretical solution is not applicable to the case of large inclusion proportion, the model simulation results are quite different from the test results in the later stage.

Self-Consistent Model and Its Application

The basic idea of the self-consistent method is to obtain the average strain in the inclusion phase from the self-consistent model under uniform boundary conditions, so as to obtain the



effective elastic stiffness tensor. In view of the defects in the application of the self-consistent method to the calculation of equivalent modulus of multiphase (inclusion) composites (Zheng et al., 2010), Kerner (Kerner, 1956) proposed a generalized autonomous model. The prediction results of the generalized self-consistent model are more reasonable than those of the self-consistent model (Christensen, 1990). In general, the application of the self-consistent method in rock mechanics is not much. In order to consider the influence of the interaction between microcracks in rock on rock damage, Wen Jianhua and Zhou Cuiying (Wen et al., 2011) studied the damage effect of rock materials based on the generalized self-consistent theory, and established a damage constitutive model reflecting the development and change of rock micro-cracks under load. Wang et al. (2015) developed a self-consistent model for the elastic contact of rough surfaces to account for the asperity interaction through Boussinesq's solution.

The Homogenization Method and Its Application

The homogenization theory can be applied in many areas of physics and engineering, having finely heterogeneous continuous media, like heat transfer or fluid flow in porous media, or, for example, electromagnetism in composites (Hassani and Hinton, 1998). The homogenization method has also been widely used in the field of rock mechanics, such as joint rock mass, anchored rock mass, and layered rock mass.

Jointed Rock Mass

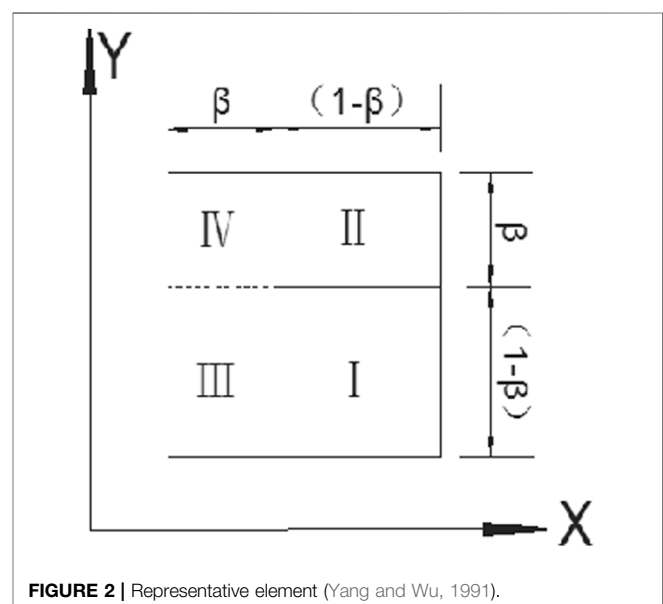
Joints have a profound impact on the mechanical properties of rock mass structures. The purpose of studying the mechanical properties of jointed rock mass is to study its macro rock mass properties. For a single jointed rock mass, the joint model can be

directly established. For example, Goodman joint element (Goodman et al., 1968) can be easily introduced into numerical analysis. However, the problems of joint set and discontinuity plane are often encountered in practical rock engineering. When analyzing this kind of rock mass, it is very difficult to establish a separate joint element for numerical analysis (Zhang et al., 2012).

Therefore, scholars equalize jointed rock mass into generalized composite materials, regard joints as matrix materials in composite materials, and regard rock mass as an inclusion material in composite materials. Appropriate representative units are selected to equivalent jointed rock into homogeneous rock materials. Typical representative units are shown in Figures 1, 2. In representative units, the constitutive relations of rock mass and joints are given. The macroscopic equivalent mechanical parameters and constitutive model of jointed rock mass can be obtained by using the coordination conditions between macro and meso stress-strain and the meso-mechanical method [Zhang Wu et al. (Zhang and Zhang, 1987); Yang Haitian et al. (Yang and Wu, 1991)], such as the elastic constants and joint occurrence parameters of jointed material and complete rock mass (Zhang and Zhang, 1987), and the composite creep model of jointed rock mass (Yang and Wu, 1991; Maghous et al., 20212021).

It should be noted that there are many forms of joints in practical engineering. Researchers also use the composite meso homogenization method to obtain the macro equivalent constitutive models and parameters of these joints, such as stepped jointed rock mass (Singh, 1973); unidirectional, bidirectional, and multidirectional jointed rock mass (Zhang and Zhang, 1987); oblique jointed rock mass (Niu and Yang, 2007a); and layered jointed rock mass (Huang et al., 2010).

In another case, scholars assume that jointed rock mass has meso-periodic characteristics. First, according to the principle of



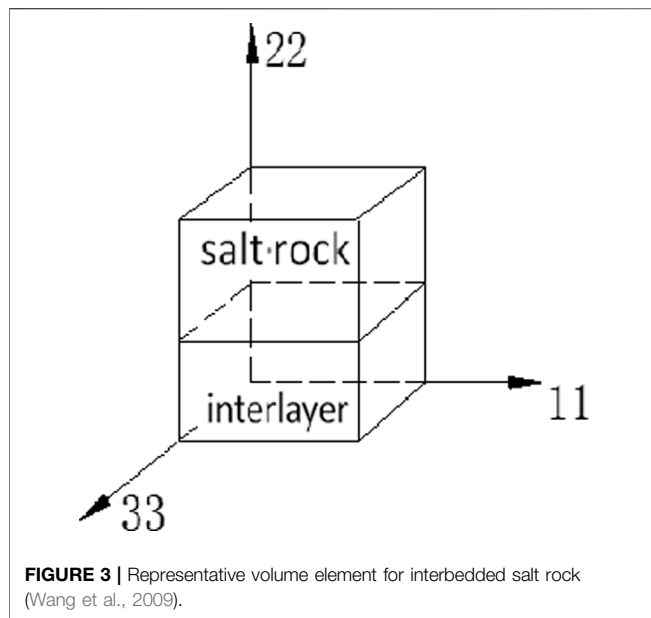


FIGURE 3 | Representative volume element for interbedded salt rock (Wang et al., 2009).

virtual displacement within the range of linear elasticity (Niu and Yang, 2007b; Ren and Xu, 2008), as shown in Eq. 2:

$$\int_{\Omega} E_{ijkl} \frac{\partial \mu_k^e}{\partial \chi_i} \frac{\partial v_i}{\partial \chi_j} d\Omega = \int_{\Omega} f_i^e v_i d\Omega + \int_{\Gamma_t} t_i v_i d\Gamma, \quad (2)$$

where f_i^e is the volume force, t_i represents the external load acting on the boundary, Γ_t , μ^e is the real displacement, and v_i is any virtual displacement satisfying the boundary conditions, $i, j, k \in \{1, 2, 3\}$.

Then, the displacement and stress of a point in the macro-structure are expanded into a small parameter progressive expansion about the meso-structure scale. Combined with the perturbation technology, a series of control equations are obtained. According to these equations, the equivalent material parameters of homogenized jointed rock mass can be solved, as shown in Eq. 3, so as to convert the meso-heterogeneous jointed rock mass into homogeneous material (Ren and Xu, 2008).

$$E_{ijkl}^H = \frac{1}{|Y|} \int_Y \left(E_{ijkl} - E_{ijpm} \frac{\partial \chi_p^{kl}}{\partial y_m} \right) dY. \quad (3)$$

Anchored Rock Mass

The mechanical and homogenization methods for composite materials have also been applied to anchored rock mass. The rock mass support system was regarded as a kind of composite materials composed of rock mass (matrix), anchor (reinforcing material), and mortar (bonding material) (Li et al., 2006b), and then the micromechanical elastic constant calculation model for rock mass was established by using composite material mechanical methods. As a further study, the layered rock mass—anchor support system (Li et al., 2006a)—was regarded as a kind of unidirectional composite reinforcement material composed of layered rock mass (matrix material), anchor rod (fiber material), and mortar (carrier material). The relationship

between the mechanical properties of the equivalent composite material and each component was quantitatively analyzed.

Layered Rock Mass

The layered rock mass mentioned here refers to the interbedded rock mass, which is composed of at least two lithologic units with different engineering behaviors and properties. This layered rock mass often presents the structure of alternating layers of hard rock and soft rock with different thicknesses (Zhang et al., 2021). Because this layered rock mass shows high anisotropy and heterogeneity, it is very important to determine the mechanical properties of layered rock mass for the selection of eigenvalues for design and stability analysis in such engineering construction (Liu et al., 2019; Zhang et al., 2019; Liu et al., 2020a).

In the experimental study, layered composite rock samples were often used to carry out the relevant tests (Liang et al. (Liang et al., 2007)). It is clear that complex samples have more complex mechanical parameters or strength characteristics than a single rock sample. The homogenization method is often used for the heterogeneous medium when establishing the constitutive model; that is, the rock mass of various thicknesses is generalized as an equivalent homogeneous medium by using the representative elements. The complex representation element, as shown in Figure 3, is commonly found, and it can be taken as plane strain problems or spatial problems. Of course, the correct mixing rate is chosen according to the structural characteristics of the rock strata, such as the strain coordination principle and the multiphase mixture principle (Fan et al., 1999; Haj-Ali and Muliana, 2003; Haj-Ali and Muliana, 2004). The mixing rate is the bridge between the microscopic volume and the macroscopic volume for the homogenization method, by which the equivalent elasticity, elastic-plastic, and viscous constitutive model of the layered rock mass can be finally obtained. For example, the macro-equivalent elastic, elasto-plastic, and non-linear creep constitutive models of interbedded salt rock mass were established by the Yang Chunhe research group (Chun-he and Yin-ping, 2005; Li and Yang, 2006; Wang et al., 2009). Zhao Pinglao (Zhao and Zeng, 1990) has studied the constitutive relations of layered rock mass by means of composite material mechanical methods. Liu Kaixue et al. (Liu, 1990) have established the viscoelastic model of interbedded and jointed rock mass.

Two-Step Homogenization Method and Its Application

In recent years, the two-step homogenization method has been applied to solve the multi-scale problem of heterogeneous materials (Nguyen et al., 2011; Shen et al., 2012; Bikong et al., 2015; Zhao et al., 2019). WQ Shen and JF Shao (Shen et al., 2012; Zhao et al., 2019) have regarded clay rock as a complex of linear elastic mineral particles embedded in the pore clay matrix, and the clay matrix was considered to be made up of the solid phase and spherical micro-pores. As shown in Figure 4, the clay solid phase and spherical micro-pores are subjected to the first homogenization on the microscopic scale, and the macroscopic homogeneous stress-strain relationship of the clay matrix is obtained. On the basis of the first homogenization, the second homogenization of clay matrix and mineral particles is carried out on the microscopic

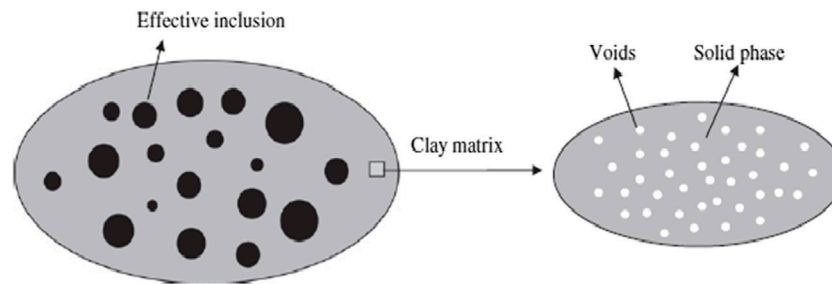


FIGURE 4 | Basic principle program of the two-step homogenization method (Shen et al., 2012).

scale, and the micromechanical model of clay rock is established to evaluate its macroscopic plastic properties.

However, the application of the homogenization method and the establishment of representative elements are always greatly related to the structural characteristics of rock mass. Unlike the jointed rock mass, the isotropic porous rock materials or geo-materials are, in the microstructure scale, composed of nearly spherical grains surrounded by a matrix. Such kinds of materials are encountered in geo-mechanics, such as concretes and some rocks (limestone, ironore, clay rock, etc.). Because this material has the particles in the matrix, the composite material mechanical methods are used well in the homogenization process, such as the Mori Tanaka Scheme (Mori and Tanaka, 1973), Hill's incremental method (Hill, 1965a; Hill, 1965b), and J.F. Shao method (Shen et al., 2012; Bikong et al., 2015; Zhao et al., 2019).

STUDY ON OTHER COMPOSITE GEOTECHNICAL PROBLEMS WITH COMPOSITE MATERIAL MICROMECHANICAL PRINCIPLES

Composite subgrade and composite soil are common treatment ways for subgrade in geotechnical engineering. It is usually composed of two or more kinds of component materials: one is the soil (matrix) of continuous distribution and the other is a pile or geo-synthetics (reinforcements) surrounded by the soil. Because of the non-uniform structure of composite soil, it is difficult to understand its nature. Ye Guanbao (Ye et al., 2002) proposed a micro-mechanical view of composite subgrade where the core task is to establish a quantitative relationship between the macroscopic performance of composite subgrade and its component performance and its meso-structure, and reveal the response law and essence of composite subgrade under certain working conditions.

Based on the micromechanical homogenization method, many scholars (Ye et al., 2002; Wang et al., 2002; Lu, 2013) predict the equivalent elastic parameters of pile-soil composite foundation. In other similar studies, Ren et al. (2009) considered the geo-grid and soil as generalized composite materials and established a numerical calculation model to predict the elastic equivalent constitutive parameters.

STUDY ON MECHANICAL PROBLEMS OF IMPURITY SALT ROCK MASS BY COMPOSITE MATERIAL MECHANICAL PRINCIPLE

Impurity salt rock mass belongs to the concept of rock mass. In addition to pure salt rock, it also contains other common symbiotic mineral components, such as gypsum, anhydrite, glauberite, and other impurities (Ding, 2010). Impurities have a great impact on the overall mechanical properties of impurity salt rock mass (Liu et al., 2020b).

By the light of the composite material mechanical principle, the impurity salt rock mass was considered as the particle-reinforced composite material. In addition, the targeted research into the impurity salt rock mass by composite material micromechanical principles may present two types of mechanical analysis models to evaluate the properties of the impurity salt rock mass.

On the one hand, the impurity salt rock mass is regarded as a homogeneous medium, and the continuum constitutive model is deduced with the continuous stress-strain field. From the microscopic viewpoint, the impurity salt rock mass is a non-uniform material composed of different impurities and salt layers. However, from the macroscopic viewpoint, it should be regarded as a uniform material. Therefore, the representative elements can be used for impurity salt rock mass, and the stress-strain relationship of each component of the representative elements can be used to establish the macroscopic equivalent stress-strain relationship of the impurity salt rock mass. The purpose of the micro-mechanical study on composite materials is to establish the quantitative relationship among the macroscopic composite properties, the component properties, and micro-structure. The impurity salt rock mass is considered as a particle-reinforced composite material, and the macroscopic and micro-mechanical properties of the impurity salt rock mass can be analyzed by the composite material micromechanical principles.

On the other hand, the impurity salt rock mass itself has obvious structural features. It is a kind of multiphase material (salt rock matrix, impurity-enhanced phase, and interfacial phase). Due to the difference in mechanical properties among the different phases, the various phases will interact with each

other under external load. The impurity salt rock mass is regarded as an inhomogeneous medium, and the micromechanical finite element method of composite materials, with consideration of different microstructure and composition, can be used to study the internal micro-stress field, displacement field, and overall mechanical properties of the impurity salt rock mass, in terms of the different contents, sizes, shapes, and mechanical properties of impurities. Furthermore, the properties and damage of impurity salt rock mass depend on the properties of salt rock compositions and impurities as well as the micro-structure characteristics such as impurity volume, impurity fraction, impurity shape, impurity size, impurity distribution, and interface phase features. Therefore, the key to revealing the effect of the microscopic characteristics of impurity salt rock mass on its performance depends on how to forecast and analyze its performance and reveal its nature of damage and destruction by micromechanical method.

DISCUSSION ON THE KEY PROBLEMS OF ROCK MECHANICS BY COMPOSITE MATERIAL MICROMECHANICAL METHODS

Similarity of Structural Composition Between Complex Rock Mass and Composite Materials

According to the research literature works above, the authors believe that the similarity in the structural composition must exist between rock mass and composite materials when studying rock mechanics issues by composite material mechanical methods.

In the composite materials faculty, composite materials are defined as new materials composed of two or more components. Essentially, the different components were optimized by the most suitable microscopic structure to produce composite materials in order to meet the practical needs of different industries.

As the research object of geotechnical engineering, the natural rock mass is itself a kind of natural geological material. As the literature (Peng, 2010) describes, the difference between the rock mass and other materials mainly lies in the structure, and the material structure is closely related to its scale. Rock is a non-homogeneous material composed of particles, voids, fissures, and cement. Heterogeneity has a significant effect on the strength and deformation of rock. It can be seen that the idea on rock is just the opposite of that on composite material, but with consistent essence.

In terms of material composition, the composite model (Liu et al., 2011) of the composite material is divided into two types: macro-composite and micro-composite. Macro-composite refers mainly to the overlap between two or more layers of different materials (also known as lamination), such as aluminum alloy sheet and carbon fiber or glass fiber composite sheet stack. A microscopic composite, such as a particle-reinforced, fiber-reinforced, or polymer-based composite material, means that one or more fine materials are uniformly dispersed in another

continuous material. Therefore, as mentioned in the literature (Chen and Li, 1992), rock is a kind of a complex material which can be considered to contain two components: the matrix and the defects or micro-cracks in the matrix. In addition, there are also rock mass with cements, impurity particles, and weak interlayer, which are commonly referred to as soft and hard interbedded rock mass, interbedded salt rock mass, or impurity salt rock mass. Obviously, from the composition viewpoint, the complex structure of rock mass is also very similar to that of composite materials. **Figure 5** shows the micro-structural model of two-phase composite materials, which are very similar to those of common geotechnical engineering objects such as columnar jointed rock mass, composite foundation, interbedded rock mass, and impurity salt rock mass.

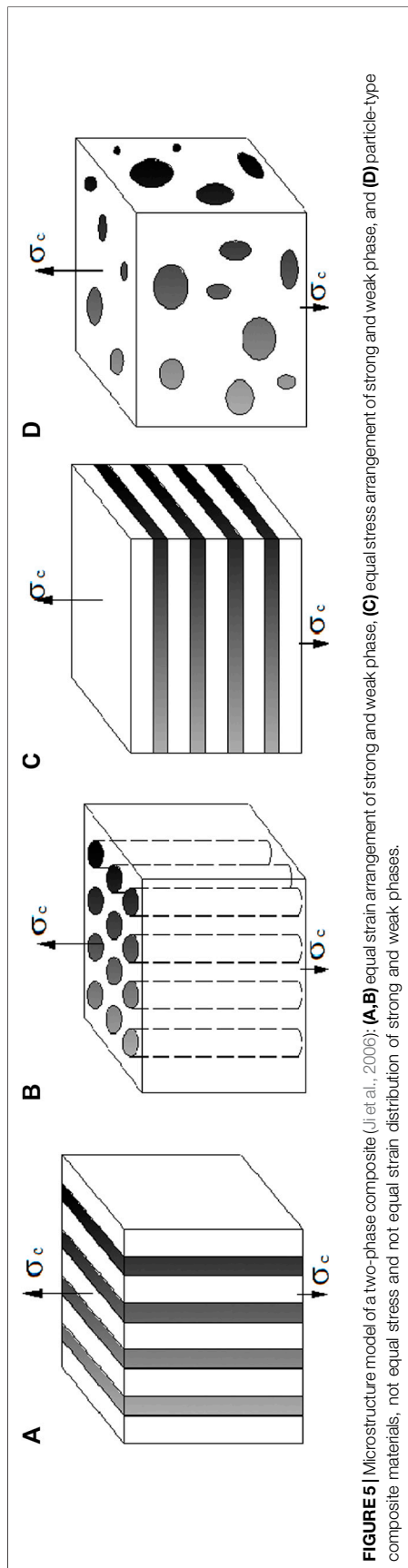
Similarity in Mechanical Analysis Between Complex Rock Mass and Composite Materials

Fan et al. (1995) considered that any material capable of two levels of analysis and calculation can be called composite material. Composite material mechanics is a two-level mechanics theory, which is embodied in the establishment of the conversion between two levels of mechanics, namely, between micro-mechanics and macro-mechanics. In addition, the mechanical properties and damage laws of composite materials depend on the component properties and micro-structure features such as volume fraction, distribution, shape, and interfacial properties of the enhanced phase. It can be seen that the mechanical analysis of composite materials focuses on the influence of micro-structural features on the macroscopic properties from the qualitative viewpoint and on the relationship between microscopic mechanics and macroscopic mechanics from the quantitative viewpoint. The macroscopic stress-strain relationship of the composite is deduced by the stress-strain relationship, the volume fraction of microscopic materials, and Eq. 4 (Belayachi et al., 2012).

$$\overline{\sigma}_{ij} = \frac{1}{V} \int_V \sigma_{ij} dV \quad \overline{\varepsilon}_{ij} = \frac{1}{V} \int_V \varepsilon_{ij} dV, \quad (4)$$

where $\overline{\sigma}_{ij}$ and $\overline{\varepsilon}_{ij}$ are the macroscopic average components of the stresses and strains over the whole volume V of the unit cell, respectively.

From the viewpoint of rock mass mechanics, Ji et al. (2006) believed that the difference in rock types lies mainly in the differences in the volume fraction of rock-forming minerals. As long as the physical and mechanical properties and volume fraction of the main rock-forming minerals are determined, the physical and mechanical properties of any type of composite multi-mineral rock can be calculated by using the correct mixing law. Therefore, it is the key to establishing the correct mixing law. Obviously, this view is consistent with the transition relationship between micromechanics and macroscopic mechanics in the quantitative analysis of composite materials. In addition, Gaofeng and Wei (2005) compared composite materials with rock blocks. The similarity between composite materials and rock



blocks is that there is a clear interface between the two materials, and the no-embedding criterion is satisfied at the interface. The difference is that the displacement of the composite material is continuous at the interface, with the existence of tensile stress and compressive stress, but the rock blocks, when contacting, are only under compressive pressure with continuous displacement, without tensile stress, and detach under tension.

Bolt support systems can be regarded as special composite materials (Li et al., 2006a). From the point of view of composite material, a bolt is a reinforcement material, and rock mass is the matrix material in a composite material. From the point of view of mechanics, bolt reinforcement of surrounding rock improves the mechanical properties of rock mass. Similarly, salt rock mass containing impurities can be regarded as particle reinforced composites (Wang et al., 2011), in which impurities are regarded as the “reinforcing phase” in composites and salt rock is regarded as the “matrix phase.” From the point of view of the mechanical mechanism, the “reinforcement and creep inhibition” of impurities on the salt rock layer is essentially consistent with the “reinforcement and creep inhibition” of particles on the matrix.

DISCUSSION AND OUTLOOK

In summary, scholars in the world have carried out fruitful research work in the study on rock mechanics using composite material micromechanics methods. The authors believe that the following aspects should be mainly concerned in the future study:

Mechanical Properties of Interface

The combination of the rocks in the underground rock mass is quite different at the boundary (Tan et al., 1994). The calculated stress, strain, and strength at the boundary with cohesion are obviously different from those without cohesion. One of the most important problems in composite materials composed of grains surrounded by a matrix with a strong contrast of stiffness between them, such as concrete materials and also rock–composite materials, is the interphase zone or interfacial transition zone (ITZ) between grain and matrix. Therefore, more rock mechanical experiments and microscopic experiments should be carried out to understand the mechanical properties and bonding action of the interface; study the interface stress transfer, interface damage, and slip mechanisms; and explore the effect of interface performance on the macro-mechanical and micro-mechanical properties.

Macro-Failure Criteria

Due to the physical combination and structural characteristics, the composite materials are totally different from homogeneous materials in the failure mode. Uniform materials fail macroscopically and evenly as a whole, but composite materials fail in the weakest section among the reinforcement, matrix, and interface. The failure form and law of composite materials are related

not only to the stress state but also to the component performance and combination situation.

Similar to composite materials, relative displacement and stress transfer will occur among the phases of the complex rock mass when the external load changes. Thus, the mechanical response, deformation, and destruction of complex rock mass result from the micro-effects among internal components and represent the macroscopic group behavior. Therefore, the macroscopic deformation and failure mechanisms should be researched in terms of the micro-structure level, which is also the major problem in studying the macroscopic failure criterion of rock complex mechanics.

Multiphase Complex of Geotechnical Engineering

Guo (2000) proposed the concept of multiphase materials which have a wide range of material composition and microstructure, with clear micro-structure direction, organizational diversity, anisotropy, and scale effect, compared to the two-phase composite materials. Thus, the multiphase materials demonstrate more complicated mechanical behavior. For example, the anchoring rock and soil in geotechnical complexes can be regarded as three-phase composite materials composed of the bolt (cable), cement slurry, and rock (soil), which can be further studied by means of composite material micromechanical methods.

Combination Between Digital Image Processing Technique and Finite Element Method

As known by all, the microscopic behavior detection methods, such as scanning electron microscopy (SEM), transmission electron microscopy (TEM), electron backscatter diffraction (EBSD), neutron diffraction, and digital image technology, cannot provide microscopic information about stress and strain, and the pure finite element model cannot reflect the real microscopic characteristics and microscopic compositions of materials.

Next, the rock samples can be sliced by using digital image processing technology (Yue et al., 2004; Kang et al., 2007; Yan et al., 2017) in combination with the meso-experimental research method of composite material, and the real two-dimensional microstructure of the rock samples can be obtained through the digital image of a scanning electron microscope. Then the microstructure is imported into the finite element software for meshing, which can more truly

reflect the shape and distribution of particles in rock mass and obtain more accurate calculation results.

CONCLUSION

It is of great practical significance to study the mechanical problems of complex rock mass by using composite material micromechanics methods. This article summarizes in detail the application of the composite micromechanics method, Eshelby inclusion theory, and self-consistent model, especially the homogenization method, in the combination of jointed rock mass, anchored rock mass, layered rock mass, and complex salt rock mass. On this basis, the author believes that when the composite material micromechanics methods are used to study the composite problem of rock mass, the complex rock mass should be similar to the composite material in structure and consistent with the composite material in mechanical analysis. In the next step, the mechanical properties of the composite rock mass interface, failure criteria, multiphase geotechnical composite problems, and the combination of digital image processing technology and finite element method can be studied by using or drawing lessons from the mechanical method of composite materials.

AUTHOR CONTRIBUTIONS

JH has made contributions to the conception of the study, the geological characteristics of the rock mass structure, anchored rock mass and the composite foundation, and revised, discussed, and wrote the part of the first draft. YL contributed to the conception of this study. YJ, HS, and DL provided technical advice on rock mass structure and geology. AW wrote the part of the first draft. AW, YZ, and JJ polished the first draft. All authors contributed to the revision, reading, and approval of the first draft.

FUNDING

This research was financed by “Intelligent monitoring, simulation, control, and early warning of urban geological disasters based on geological big data” (u1711266), a key project jointly funded by NSFC and Guangdong Province. Jia Tao, Wu Jiaqi, Hao Shun, and Xing Jiangpeng et al. took part in the study, and sincere gratitude is expressed to them.

REFERENCES

- Abou-ChakraGue', A., Cormery, F., Shao, J.-F., and Kondo, D. (2008). A Micromechanical Model of Elastoplastic and Damage Behavior of a Cohesive Geomaterial. *Int. J. Sol. Structures* 45, 1406–1429. doi:10.1016/j.ijsolstr.2007.09.025
- Bai, J. (2016). Study of Equivalent Elastic Modulus of Sand Gravel Soil with Eshelby Tensor and Mori-Tanaka Equivalent Method. *Shanxi Architecture* 42 (8), 81–83. (in Chinese). doi:10.13719/j.cnki.cn14-1279/tu.2012.01.143
- Belayachi, N., Do, D. P., and Hoxha, D. (2012). A Note on the Numerical Homogenisation of the Mechanical Behaviour of an Argillaceous Rock. *Comput. Geotechnics* 41, 70–78. doi:10.1016/j.compgeo.2011.11.007

- Benssousan, A., Lions, J. L., and Papanicoulau, G. (1978). *Asymptotic Analysis for Periodic Structures*. North Holland: Amsterdam.
- Bikong, C., Hoxha, D., and Shao, J. F. (2015). A Micro-macro Model for Time-dependent Behavior of Clayey Rocks Due to Anisotropic Propagation of Microcracks. *Int. J. Plasticity* 69, 73–88. doi:10.1016/j.iijplas.2015.02.001
- Budiansky, B. (1973). On the Elastic Moduli of Some Heterogeneous Materials. *J. Mech. Phys. Solids* 13, 223–227. doi:10.1016/0022-5096(65)90011-6
- Chen, L., and Li, C. (1992). Constitutive Relation of Rock. *Prog. Mech.* 22 (2), 173–181. (in Chinese). doi:10.13245/j.hust.1990.05.009
- Chen, Y., Li, D., Rong, G., Jiang, Q., and Zhou, C. (2011). A Micromechanical Model for Damage and thermal Conductivity of Brittle Rocks. *Chin. J. Rock Mech. Eng.* 30 (10), 1959–1969. (in Chinese).
- Christensen, R. M. (1990). A Critical Evaluation for a Class of Micro-mechanics Models. *J. Mech. Phys. Sol.* 38 (3), 379–404. doi:10.1016/0022-5096(90)90005-o
- Christensen, R. M., and Lo, K. H. (1979). Solutions for Effective Shear Properties in Three Phase Sphere and cylinder Models. *J. Mech. Phys. Sol.* 27 (4), 315–330. doi:10.1016/0022-5096(79)90032-2
- Chun-he, Y., and Yin-ping, L. I. (2005). The Expanded Cosserat Medium Constitutive Model for Laminated Salt Rock. *Chin. J. Rock Mech. Eng.* 24 (23), 4226–4232. (in Chinese). doi:10.3321/j.issn:1000-6915.2005.23.005
- Cioranescu, D., and Paulin, J. S. J. (1979). Homogenization in Open Sets with Holes. *J. Math. Anal. Appl.* 71, 590–607. doi:10.1016/0022-247x(79)90211-7
- Ding, G. (2010). *Salt Hole Underground Gas Storage*. Beijing: Petroleum Industry Press. (in Chinese).
- Du, S., and Wang, B. (1998). *Composite Materials Mesoscopic Mechanics*. Beijing: Science Press. (in Chinese).
- Einstein, A. (1956). *Investigations on the Theory of Brownian Motion*. New York: Dover Pubns., 36–62.
- Eshelby, J. D. (1957). The Determination of the Elastic Field of an Ellipsoidal Inclusion and Related Problems. *Proc. R. Soc. Scr. A* 241, 376–396. doi:10.1098/rspa.1957.0133
- Eshelby, J. D. (1959). The Elastic Field outside an Ellipsoidal Inclusion. *Proc. Roy. Soc. London* 252, 561–569. doi:10.1098/rspa.1959.0173
- Fan, F., Wang, Z., Xing, J., and Huang, X. (1995). Research on Several Basic Issues of Composite Material Mechanics. *J. south China Univ. Technol. (natural Sci. edition)* 23 (4), 1–6. doi:10.3321/j.issn:1000-565X.1995.04.001
- Fan, J., Gao, Z., and Liu, T. (1999). The Micro/macro Mechanic Analysis of PD3 Pearlitic Steel with Layered Microstructures. *J. Chongqing Univ.* 22 (5), 37–46. (in Chinese). doi:10.11835/j.issn.1000-582X.1999.05.008
- Gaofeng, W., and Wei, F. (2005). Three-dimensional Numerical Manifold Method and its Application in Composite Materials. *J. Appl. Mech.* 22 (3), 351–356. (in Chinese). doi:10.3969/j.issn.1000-4939.2005.03.005
- Goodman, R. E., Taylor, R. L., and Brekke, T. L. (1968). A Model for the Mechanics of Jointed Rock. *J. Soil Mech. Found. Div.* 94(3):637–659. doi:10.1061/jsfeaq.0001133
- Guo, J. (2000). From Composite Materials to Multiphase Materials. *Chin. J. Mater. Res.* 14 (2), 123–126. (in Chinese). doi:10.3321/j.issn:1005-3093.2000.02.002
- Haj-Ali, R. M., and Muliana, A. H. (2003). A Micromechanical Constitutive Framework for the Nonlinear Viscoelastic Behavior of Pultruded Composite Materials. *Int. J. Sol. Structures* 40, 1037–1057. doi:10.1016/S0020-7683(02)00663-7
- Haj-Ali, R. M., and Muliana, A. H. (2004). A Multi-Scale Constitutive Formulation for the Nonlinear Viscoelastic Analysis of Laminated Composite Materials and Structures. *Int. J. Sol. Structures* 41, 3461–3490. doi:10.1016/j.jisolsolstr.2004.02.008
- Hashin, Z., and Shtrikman, S. (1963). A Variational Approach to the Theory of the Elastic Behaviour of Multiphase Materials. *J. Mech. Phys. Sol.* 11, 127–140. doi:10.1016/0022-5096(63)90060-7
- Hassani, B., and Hinton, E. (1998). A Review of Homogenization and Topology Optimization I-Homogenization Theory for media with Periodic Structure. *Comput. Structures* 69, 707–717. doi:10.1016/S0045-7949(98)00131-x
- Hill, R. (1965a). A Self-Consistent Mechanics of Composite Materials. *J. Mech. Phys. Sol.* 13, 213–222. doi:10.1016/0022-5096(65)90010-4
- Hill, R. (1965b). Continuum Micro-mechanics of Elastoplastic Polycrystals. *J. Mech. Phys. Sol.* 13, 89–101. doi:10.1016/0022-5096(65)90023-2
- Hu, M., Xu, G., and Hu, S. (2013). *Study of Equivalent Elastic Modulus of Sand Gravel Soil with Eshelby Tensor and Mori-Tanaka Equivalent Method*, 34, 1437–1442. (in Chinese).
- Huang, S., Xu, J., Ding, X., and Aiqing, W. (2010). Study of Layered Rock Mass Composite Model Based on Characteristic of Structural Plane and its Application. *Chin. J. Rock Mech. Eng.* 29 (4), 743–756. (in Chinese).
- Ji, S., Wang, Q., Xia, B., and Xu, Z. (2006). Generalized Mixed Law and its Application in Geomaterial Rheology. *Acta Petrologica Sinica* 22 (7), 2067–2080.
- Kang, J., Ososkov, Y., Embury, J., and Wilkinson, D. (2007). Digital Image Correlation Studies for Microscopic Strain Distribution and Damage in Dual Phase Steels. *Scripta Materialia* 56 (11), 999–1002. doi:10.1016/j.scriptamat.2007.01.031
- Kerner, E. H. (1956). The Elastic and Thermoelastic Properties of Composite media. *Proc. Phys.* 69, 801–808. doi:10.1088/0370-1301/69/8/305
- Li, X., Song, G., Chen, X., and Yang, W. (2006). Research on the Composite Material Mechanical Properties of Anchoring Rock Mass. *J. Wuhan Univ. Tech.* 28 (4), 79–82. (in Chinese). doi:10.3321/j.issn:1671-4431.2006.04.023
- Li, X., Wang, T., Song, G., Yunhua, C., and Hang Chengliang, Z. (2006). Study on Composite Anchoring Theory and Numerical Simulation Test on Layered Rocks. *Chin. J. Rock Mech. Eng.* 25 (2), 3654–3660. (in Chinese). doi:10.3321/j.issn:1000-6915.2006.22.050
- Li, Y., and Yang, C. (2006). Three-dimensional Expanded Cosserat Medium Constitutive Model for Laminated Salt Rock. *Rock Soil Mech.* 27 (4), 509–513. (in Chinese). doi:10.16285/j.rsm.2006.04.001
- Liang, W., Yang, C., Zhao, Y., Dusseault, M. B., and Liu, J. (2007). Experimental Investigation of Mechanical Properties of Bedded Salt Rock. *Int. J. Rock Mech. Mining Sci.* 44, 400–411. doi:10.1016/j.ijrmms.2006.09.007
- Lide, W., Xu, W., Yang, C., and Yang, S. (2004). Study on Elastic Constitutive Model of Rock with Statistucal Damage[J]. *Chin. J. Rock Mech. Eng.* 23 (12), 1971–1975. (in Chinese). doi:10.3321/j.issn:1000-6915.2004.12.00
- Lide, W., Yang, C., and Xu, W. (2004). Study on Statistical Seepage Model and Statistical Damage Constitutive Model of Rock. *Rock Soil Mech.* 25 (10), 1527–1536. (in Chinese). doi:10.16285/j.rsm.2004.10.00
- Liu, K. (1990). Viscoelastic Model of Layered Rock Mass and Jointed Rock Mass. *J. Shaanxi Inst. Machinery* 6, 292–307. (in Chinese). doi:10.19322/j.cnki.issn.1006-4710.1990.04.009
- Liu, W., Yu, Y., and Gao, L. (2011). *Composites*. Harbin: Harbin Institute of Technology Press. (in Chinese).
- Liu, W., Zhang, X., Fan, J., Zuo, J., Zhang, Z., and Chen, J. (2020). Study on the Mechanical Properties of Man-Made Salt Rock Samples with Impurities. *J. Nat. Gas Sci. Eng.* 84, 103683. doi:10.1016/j.jngse.2020.103683
- Liu, W., Zhang, Z., Chen, J., Fan, J., Jiang, D., Jjk, D., et al. (2019). Physical Simulation of Construction and Control of Two Butted-Well Horizontal Cavern Energy Storage Using Large Molded Rock Salt Specimens. *Energy* 185, 682–694. doi:10.1016/j.energy.2019.07.014
- Liu, W., Zhang, Z., Fan, J., Jiang, D., Li, Z., and Chen, J. (2020). Research on Gas Leakage and Collapse in the Cavern Roof of Underground Natural Gas Storage in Thinly Bedded Salt Rocks. *J. Energ. Storage* 31, 101669. doi:10.1016/j.est.2020.101669
- Lu, Y. (2013). *Application of Asymptotic Homogenization Method in Settlement Calculation of Biaxial Reinforced concrete Composite Foundation*. Master's thesis. Xiangtan: Xiangtan University. (in Chinese).
- Maghous, S., Barros de Aguiar, C., and Rossi, R. (2021/2021). Micromechanical Approach to Effective Viscoelastic Behavior of Jointed Rocks. *Int. J. Rock Mech. Mining Sci.* 139, 104581. doi:10.1016/j.ijrmms.2020.104581
- Mori, T., and Tanaka, K. (1973). Average Stress in Matrix and Average Elastic Energy of Materials with Misfitting Inclusions. *Acta Metallurgica* 21, 571–574. doi:10.1016/0001-6160(73)90064-3
- Nguyen, B. N., Hou, Z., Bacon, D. H., Murray, C. J., and White, M. D. (2016). Three-dimensional Modeling of the Reactive Transport of CO₂ and its Impact on Geomechanical Properties of Reservoir Rocks and Seals. *Int. J. Greenhouse Gas Control* 46, 100–115. doi:10.1016/j.jggc.2016.01.004
- Nguyen, N. B., Giraud, A., and Grgic, D. (2011). A Composite Sphere Assemblage Model for Porous Oolitic Rocks. *Int. J. Rock Mech. Mining Sci.* 48, 909–921. doi:10.1016/j.ijrmms.2011.05.003
- Niu, B., and Yang, H. (2007). Homogenization-based Investigation on Constitutive Relationship of Oblique Joint Rock. *Chin. J. Geotechnical Eng.* 29 (5), 773–778.

- Niu, B., and Yang, H. (2007). Study on Composite Constitutive Relation of Skew Jointed Rock Mass Based on Homogenization Method. *J. Geotechnical Eng.* 29 (5), 773–778. (in Chinese). doi:10.3321/j.issn:1000-4548.2007.05.024
- Peng, C. (2010). “Rock Mass Generalized Multi-Layer Structure Model,” in *Doctoral Dissertation* (Hangzhou: Zhejiang University). (in Chinese).
- Qin, Q., and Yang, Q. (2006). *Macro-meso Theory of Multi-Field Coupling Behavior of Non-uniform Material*. Beijing: Higher Education Press. (in Chinese).
- Ren, Q., and Xu, W. (2008). Homogenization-based Method for Predicting Effective Elastic Properties of Jointed Rock. *Eng. Mech.* 25 (4), 75–92.
- Ren, Y., Yang, H., Niu, B., and Yan, J. (2009). Study on Equivalent Constitutive Relation of Geogrid Based on Homogenization Method. *Dalian Univ. Tech.* 49 (3), 317–321. (in Chinese).
- Salamon, M. D. G. (1968). Elastic Moduli of a Stratified Rock Mass. *Int. J. Rock Mech. & Mining Sci.* 5, 519–527. doi:10.1016/0148-9062(68)90039-9
- Sanchez-Palencia, E. (1980). *Non-homogenous media and Vibration Theory*, 127. New York, NY: Lecture Notes in Physics.
- She, S., and Peng, L. (2014). Some Progress and Challenges of Rock Engineering in China. *Chin. J. Rock Mech. Eng.* 33 (3), 433–457. (in Chinese). doi:10.13722/j.cnki.jrme.2014.03.001
- Shen, W. Q., Shao, J. F., Kondo, D., and Gatmiri, B. (2012). A Micro-macro Model for Clayey Rocks with a Plastic Compressible Porous Matrix. *Int. J. Plasticity* 36, 64–85. doi:10.1016/j.iijplas.2012.03.006
- Singh, B. (1973). Continuum Characterization of Jointed Rock Masses. *Int. J. Rock Mech. Mining Sci. Geomechanics Abstr.* 10, 311–335. doi:10.1016/0148-9062(73)90041-7
- Tan, X., Xian, X., Zheng, D., and Zhao, Y. (1994). *Composite Rock Mechanics Theory and Application*. Beijing: Coal Industry Press. (in Chinese).
- Vincent, P., and Kondo, D. (2003). Micromechanics of Anisotropic Brittle Damage: Comparative Analysis between a Stress Based and a Strain Based Formulation. *Mech. Mater.* 35, 747–761. doi:10.1016/s0167-6636(02)00203-x
- Wang, A., Yang, C., Chen, J., Huang, Z., and Li, Y. (2009). Nonlinear Creep Constitutive Model of Layered Rock Salt. *J. Rock Mech. Eng.* 28 (1), 2708–2714. (in Chinese). doi:10.3321/j.issn:1000-6915.2009.z1.018
- Wang, A., Yang, C., Chen, J., Zhang, X., and Huang, Z. (2011). “Composite Material Method for Studying Mechanical and Deformation Properties of Layered Salt Rock,” in *Proceeding of the 3rd International Conference on Heterogeneous Material Mechanics*, 421–424. (in Chinese).
- Wang, G. F., Long, J. M., and Feng, X. Q. (2015). A Self-Consistent Model for the Elastic Contact of Rough Surfaces. *Acta Mech.* 226, 285–293. doi:10.1007/s00707-014-1177-2
- Wang, J. (1979). Propagation of Cylindrical Wave in Stratified Rock Mass. *Rock Soil Mech.* (2), 73–80. (in Chinese). doi:10.16285/j.rsm.1979.02.005
- Wang, J. G., Leung, C. F., and Ichikawa, Y. (2002). A Simplified Homogenisation Method for Composite Soils. *Comput. Geotechnics* 29, 477–500. doi:10.1016/s0266-352x(02)00004-6
- Wen, J., Zhou, C., and Peng, M. (2011). On Statistical Damage Constitutive Model for Rock Based on General Self-Consistent Theory. *Subgrade Eng.* (4), 1–3. (in Chinese). doi:10.3969/j.issn.1003-8825.2011.04.001
- Xiao, C., and Huang, S. (2013). *The Application of Eshelby's Theory on Rock Mechanics Discussion*, 34, 1437–1442. (in Chinese). 5
- Yan, L., Meng, Q.-x., Xu, W.-y., Wang, H.-l., Zhang, Q., Zhang, J.-c., et al. (2017). A Numerical Method for Analyzing the Permeability of Heterogeneous Geomaterials Based on Digital Image Processing. *J. Zhejiang Univ. Sci. A* 18 (2), 124–137. (in Chinese). doi:10.1631/jzus.A1500335
- Yang, H., and Wu, R. (1991). A Composite Creep Model of Biorthogonal Joint Jointed Rock Mass. *Dalian Univ. Tech.* 31 (3), 267–273. (in Chinese).
- Ye, G., Lan, H., Xu, C., Chen, J., Bai, H., and Gao, Y. (2002). Microscopic Mechanical Properties of Composite Foundation. *Rock Soil Mech.* 23, 48–51. (in Chinese). doi:10.3969/j.issn.1000-7598.2002.z1.01310.16285/j.rsm.2002.s1.041
- Yue, Z., Chen, S., Zheng, H., and Tan, G. (2004). Digital Image Proceeding Based on Finite Element Method for Geomaterials. *Chin. J. rock Mech. Eng.* 23 (6), 889–897. (in Chinese). doi:10.3321/j.issn:1000-6915.2006.10.002
- Zhang, H., Zhu, J., Liu, Y., Xu, B., and Wang, X. (2012). Strength Properties of Jointed Rock Masses Based on the Homogenization Method. *Acta Mechanica Solida Sinica* 25 (2), 177–185. (in Chinese). doi:10.1016/s0894-9166(12)60018-4
- Zhang, W., and Zhang, X. (1987). Elastic Model of the Rock Mass. *Chin. J. Geotechnical Eng.* 9 (4), 33–44. (in Chinese). doi:10.3321/j.issn:1000-4548.1987.04.004
- Zhang, X., Liu, W., Jiang, D., Qiao, W., Liu, E., Zhang, N., et al. (2021). Investigation on the Influences of Interlayer Contents on Stability and Usability of Energy Storage Caverns in Bedded Rock Salt. *Energy* 231, 120968. doi:10.1016/j.energy.2021.120968
- Zhang, Z., Jiang, D., Liu, W., Chen, J., Li, E., Fan, J., et al. (2019). Study on the Mechanism of Roof Collapse and Leakage of Horizontal Cavern in Thinly Bedded Salt Rocks. *Environ. Earth Sci.* 78 (10), 292. doi:10.1007/s12665-019-8292-2
- Zhao, L.-Y., Shao, J.-F., Zhu, Q.-Z., Liu, Z.-B., and Yurtdas, I. (2019). Homogenization of Rock-like Materials with Plastic Matrix Based on an Incremental Variational Principle. *Int. J. Plasticity* 123, 145–164. doi:10.1016/j.iijplas.2019.07.015
- Zhao, P., and Zeng, Y. (1990). Composite Model of Layered Rock Mass. *J. Lanzhou Univ. (Natural Sci. Edition)* 26 (2), 114–118. (in Chinese). doi:10.13885/j.issn.0455-2059.1990.02.020
- Zheng, X., Zheng, X., and Duan, L. (2010). Progress of Multiscale Methods in the Mechanical Analysis of Composites[J]. *Adv. Mech.* 40 (1), 41–56. (in Chinese). doi:10.6052/1000-0992-2010-1-J2008-104
- Zhu, Q. (2006). *Applications of Homogenization Approaches to 3D Damage Modelling of Quasi-Brittle Materials: formulation, Valilotions and Numerical Implantations*. Lille: Lille:Universite, des Sciences et Technologies de Lille.
- Zhu, Q., Kondo, D., Shao, J., and Pensee, V. (2008). Micromechanical Modelling of Anisotropic Damage in Brittle Rocks and Application. *Int. J. Rock Mech. Mining Sci.* 45, 467–477. doi:10.1016/j.ijrmms.2007.07.014

Conflict of Interest: Authors JH, HS, and DL were employed by the company Henan Geological and Mineral Resources Construction Engineering (Group) Co. Ltd.

The remaining authors declare that the research was conducted in the absence of any commercial or financial relationships that could be construed as a potential conflict of interest.

Publisher's Note: All claims expressed in this article are solely those of the authors and do not necessarily represent those of their affiliated organizations, or those of the publisher, the editors, and the reviewers. Any product that may be evaluated in this article, or claim that may be made by its manufacturer, is not guaranteed or endorsed by the publisher.

Copyright © 2022 He, Li, Jin, Wang, Zhang, Jia, Song and Liang. This is an open-access article distributed under the terms of the Creative Commons Attribution License (CC BY). The use, distribution or reproduction in other forums is permitted, provided the original author(s) and the copyright owner(s) are credited and that the original publication in this journal is cited, in accordance with accepted academic practice. No use, distribution or reproduction is permitted which does not comply with these terms.



Regional Characteristics of Porosity and Permeability of Dahebian Syncline Coal and Its Application

Fuping Zhao^{1,2,3} and Yuanlong Wei^{2,3*}

¹School of Resources and Geosciences, China University of Mining and Technology, Xuzhou, China, ²Key Laboratory of Unconventional Natural Gas Evaluation and Development in Complex Tectonic Areas, Ministry of Natural Resources, Guiyang, China, ³Guizhou Research Institute of Oil and Gas Exploration and Development Engineering, Guiyang, China

OPEN ACCESS

Edited by:

Jie Chen,
Chongqing University, China

Reviewed by:

Jinyang Fan,
Chongqing University, China
Huabin Zhang,
Liaoning Technical University, China
Xianjie Hao,
China University of Mining and
Technology, China

*Correspondence:

Yuanlong Wei
yuanlongwei1988@126.com

Specialty section:

This article was submitted to
Geohazards and Georisks,
a section of the journal
Frontiers in Earth Science

Received: 25 November 2021

Accepted: 08 December 2021

Published: 27 January 2022

Citation:

Zhao F and Wei Y (2022) Regional
Characteristics of Porosity and
Permeability of Dahebian Syncline Coal
and Its Application.
Front. Earth Sci. 9:822322.
doi: 10.3389/feart.2021.822322

In order to study the basic properties of coal seam thus to provide reference for coalbed methane (CBM) production, the porosity and permeability of coal from DH and WJZ regions of Dahebian syncline in Liupanshui Coalfield were systematically studied. The results shows that the porosity and permeability of coal samples in DH region are between 7.4–10.1% and 0.01 mD~0.04 mD respectively. The permeability is obviously anisotropic, and it is distributed in a U-shape along bedding angle. The porosity and permeability in the WJZ region are between 12.4–24.85% and 0.3 mD–4.8 mD, but the correlation of permeability and bedding angle is not obvious. There are many primary cracks in coal matrix of WJZ region, while the coal of DH region is relatively complete. As a result, the porosity and permeability of WJZ coal samples are much higher than that of DH coal samples. With the change of confining pressure, obvious change has taken place in the permeability of coal in the two regions. When the confining pressure decreases from 2 to 8 MPa, the permeability loss rate of coal samples is close to 80%. The internal mechanism of the permeability loss is related to crack closure and plastic deformation caused by confining pressure. In contrast, the porosity and permeability of coal in WJZ region are much higher than those in DH region, which indicates that the permeability of the same coal seam in the same structural will have great differences and inhomogeneities. Therefore, the WJZ region is the preferred area, which can be included in the preferential exploitation plan of CBM. In addition, for the typical syncline gas reservoir in Liupanshui Coalfield, it is necessary to consider the block division according to the porosity and permeability indexes, and select the optimal block and give priority to development of CBM. Furthermore, we should pay attention to the difference and adaptability of CBM development in different regions.

Keywords: permeability, porosity, primary cracks, effect of confining pressure, intersection angle between bedding

INTRODUCTION

Natural gas is an important clean energy, which is of great significance for reducing carbon emissions, haze and acid rain hazards (Aguilera, 2014; Nduagu and Gates, 2016; Shen et al., 2016). At present, the annual consumption of natural gas in China has reached 300 billion m³, and it is expected to reach 500 billion m³ by 2030 (Liang et al., 2019; Liu et al., 2020a). Natural gas exploration and development (Wang et al., 2021), pipeline transportation (Liu et al., 2019a; Liu et al.,

2020b), storage (Liu et al., 2019b; Zhang et al., 2019; Liu et al., 2020c; Liu et al., 2020d; Wan et al., 2021; Zhang et al., 2021) and peak shaving (Lin and Wang, 2012; Qiao et al., 2019; Qiao et al., 2020) have become important deployment and research work in the energy field of China. However, China's conventional natural gas reserves are limited and its dependence on foreign countries is too high at present, which has become an important bottleneck restricting the future development of China's natural gas (Wang and Lin, 2014). The total resources of unconventional natural gas (coal-bed methane, shale gas and tight gas) in China reach over 190 trillion m³, more than 5 times of the total geological reserves of conventional natural gas (Zheng et al., 2018). Therefore, in order to realize the large-scale utilization of natural gas in the future, it is particularly important to speed up the exploration and development of unconventional natural gas. However, compared with conventional natural gas reservoirs, unconventional natural gas reservoirs are generally characterized by low porosity and low permeability, so it is difficult to effectively form commercial industrial exploitation with the existing exploitation technologies (Zhou, 2015). Taking CBM resources as an example, the geological reserves of shallow CBM in China below 2,000 m are 368,10 billion m³ (Li et al., 2015). However, because most coal seams in China are soft and low permeability reservoirs, the surface and underground exploitation of CBM is not satisfactory (Regan and Chao, 2014; Tao et al., 2018; Men et al., 2021).

Since the "11th Five-Year Plan", the central government and local governments have issued a series of support policies such as "Effective development and utilization of coalbed methane", but the long-term development was not satisfactory. In the "12th Five-Year Plan" period, the output of CBM should reach 30 billion m³, including 16 billion m³ above ground and 14 billion m³ below ground. By 2015, both goals had failed, and only 4.4 billion m³ was extracted from the surfaces. During the "13th Five-Year Plan" period, the output of surface extraction was about 6 billion m³, while the target was 10 billion m³, just over half of which. In the beginning of the "13th Five-Year Plan", the China's CBM production was mainly concentrated in Jincheng and Liulin, Shanxi province, and the total utilization rate of China's resources was less than 0.1%. So far, the situation has not improved significantly (Wang et al., 2019).

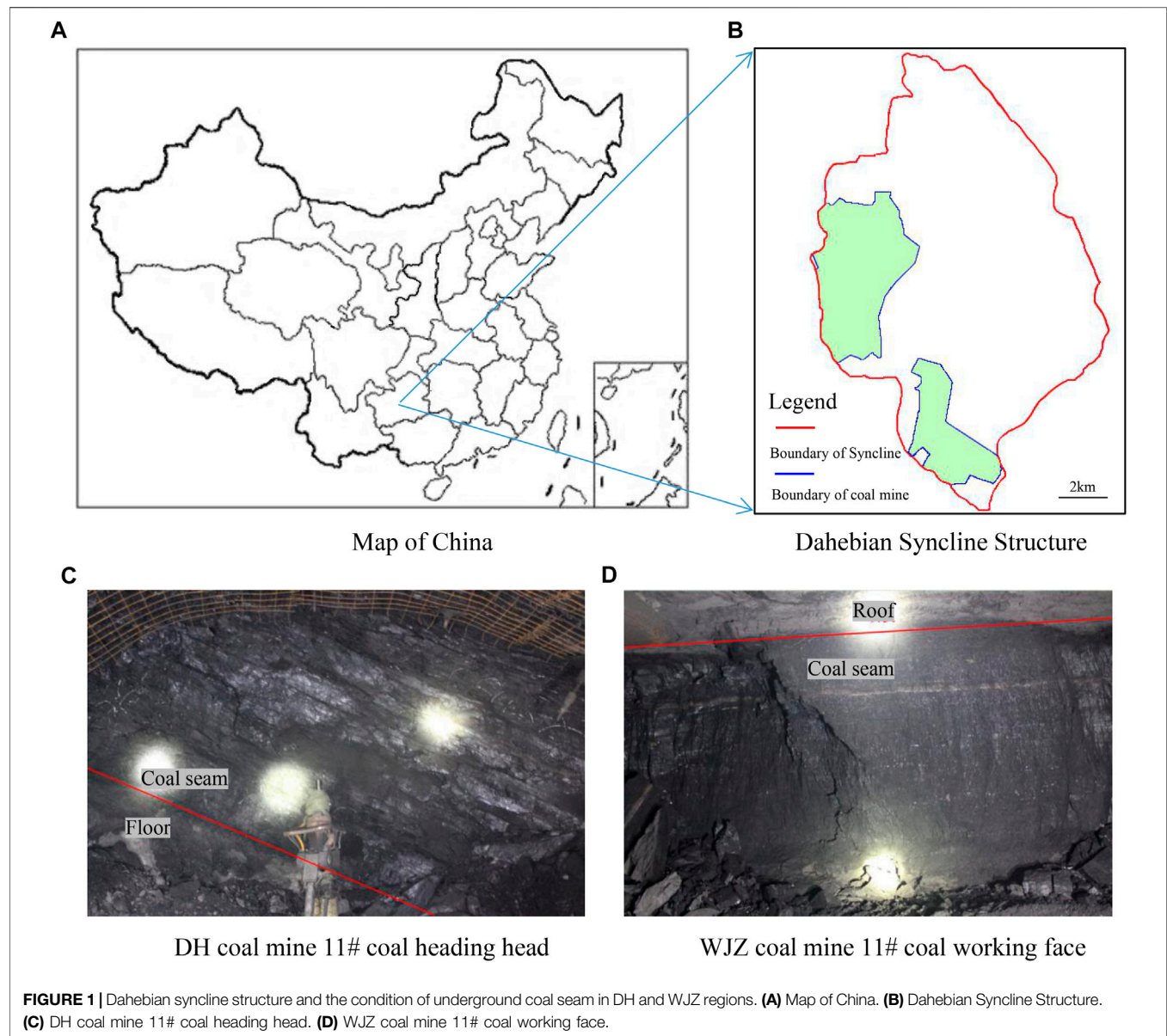
Guizhou Province is the province with the richest coal resources in South China, and its resource reserves exceed the sum of the fourteen provinces in South China. As an important energy supply base in South China, Guizhou Province plays an important role in ensuring energy security in South China. CBM is a semi-natural resource of coal mines, and the reserves of CBM in Guizhou Province are also very large. According to the shallow buried depth of 2000m, the total amount of CBM resources in Guizhou Province is 3,151 billion m³, accounting for about 10% of the total CBM resources in China, ranking the third in China, only after that of Xinjiang and Shanxi (Huang et al., 2010; Zhou et al., 2015). Therefore, most mines in the west of Guizhou Province belong to high gas mines, and gas safety accidents occur frequently (Zhong et al., 2016). Coal methane, like a sword hanging on miners' heads, which directly affects miners' life safety, and it is a big worry for the development of coal

industry in Guizhou province. Therefore, realizing the safe and efficient exploitation of CBM resources in Guizhou Province can not only greatly alleviate the safety situation of coal mining in Guizhou Province, but also obtain a large amount of clean energy-CBM (methane as its main component), which is of great significance for improving the energy structure of Guizhou Province, which lacks gas and oil.

However, compared to other types of rock (Li et al., 2021a; Li et al., 2021b), coal have low strength. And compared with the coal seam conditions in Qinshui Basin, Shanxi Province, the coal reservoir conditions in Guizhou Province are more complex, and the exploitation is more difficult. Coal reservoirs in Guizhou Province have special conditions, such as high *in-situ* stress, low permeability and low water-content, and are composed of several thin-medium-thick coal seams (Yi et al., 2007). However, there are a few studies on the mechanical and physical properties of this kinds of coal reservoirs, which needs further improving. The geological conditions of CBM in Guizhou province are complex, and the mainstream CBM development technologies at home and abroad can not adopt to the complex geological conditions in Guizhou Province, which leads to the unsatisfactory gas production effect of most CBM extraction wells in Guizhou Province.

The characteristics and evolution of porosity and permeability of coal seam are the important basis for evaluating the recoverable potential of CBM and formulating corresponding development plans. In order to realize the efficient exploitation of CBM, scientific understanding of the porosity and permeability characteristics of coal seam is an important prerequisite. Scholars at home and abroad have made extensive research on the characteristics of porosity and permeability of coal reservoirs (Yang et al., 2019; Xue et al., 2020). For example, Ayers pointed out that the coal lithotypes rich in vitrinite tend to have an increased cleavage frequency, so they have a correspondingly higher grades than those with lower vitrinite (Ayers, 2002). Liu et al. studied the anisotropic characteristics of cubic coal sample under triaxial stress state (Liu et al., 2019c). Liu and Rutqvist put forward a new permeability model of coal, which can reflect the influences of internal swelling stress and fracture-matrix interaction (Liu and Rutqvist, 2010; Meng et al., 2011). Meng et al. studied the relationship between the permeability evolution process of coal and *in-situ* stress, pore pressure by using coal sample obtained from the southern Qinshui basin (Meng et al., 2011). Nie et al. studied the pore structure characteristics of different ranks by gas adsorption and SEM methods (Nie et al., 2015; Liu and He, 2017). Li et al. (Li et al., 2020) studied the mechanism of temperature and pore pressure on the evolution of coal permeability by taking the raw coal of Qianbei Coalfield, Guizhou Province as the research object. Yang et al. studied the anisotropic permeability of coal sample under cyclic load (Yang et al., 2018).

From the above research, it can be seen that the characteristics of porosity and permeability of coal have always been the focus of research in this field. Generally speaking, the characteristics of porosity and permeability of coal reservoirs are greatly affected by coal rank, stress state, temperature and so on. The porosity and permeability characteristics of coal reservoirs usually have great



anisotropy and regional differences. However, these studies mainly focus on the coalfields in the north China, such as the Qinshui coalfield, while there are few reports devoted to Liupanshui Coalfield in Guizhou Province. In particular, the research on the characteristics of porosity and permeability of the syncline gas-controlled coal reservoir in Liupanshui Coalfield is even more scarce. Therefore, in this study, the pore and permeability characteristics of typical coal in the Dahebian syncline area of Liupanshui Coalfield were studied in order to fill the research gap in this field and provide sufficient basis for the exploration and development of CBM and the improvement of the suitable technology.

In this paper, the coal of two typical regions of Dabebian Syncline with typical syncline gas-controlling structure in Liupanshui Coalfield, Guizhou Province was selected as the research object. A series of porosity tests and permeability

evolution law studies were carried out for the underground raw coal cores in two typical areas (DH region and WJZ region) in the Dahebian Syncline region. The purpose is to provide theoretical reference and basic data for CBM reservoir evaluation, desert spot screening, and rationale exploitation design of CBM in Liupanshui Coalfield and similar coal seams.

TESTING SCHEME

Region and Coring

The Liupanshui Coalfield is the most representative coalfield in Guizhou Province. The study area is named as Dahebian syncline, which is one secondary geo-structure in Liupanshui Coalfield. This syncline covers an area of about 50 km², which is high in the west, and lower in the east, with its major axis in the north-south



FIGURE 2 | Coal cores and samples for porosity and permeability testing. **(A)** Raw coal cores **(B)** Sample preparation process by using wire cutting technology **(C)** Coal samples containing different intersection angles (50×100 mm).

direction, and its minor axis in the east-west direction. And the position, shape, and boundary of Dahebian syncline are shown in **Figures 1A, B**. The regional distribution of methane content in coal seams in Liupanshui Coalfield is directly related to the scale of single syncline and the depth of “Depression”, and it has typical syncline gas-controlling structural characteristics. And there are dozens of coal seams with thick-to-medium thickness. Dahebian syncline is a typical syncline controlling gas structure in Liupanshui area, and it is also the preferred block for CBM exploration and development in Guizhou Province.

The study on the porosity and permeability characteristics of Dahebian syncline coal seam and its evolution law is of great representative significance to the mining of the whole Liupanshui Coalfield and even the coal seam with syncline gas-controlling structure in other coalfields of Guizhou Province. This study takes No.11 coal seam in DH and WJZ regions as the research object, with a depth of about 800 m, and a layer thickness ranging from 1.77 to 5.7 m. This coal seam has the

largest thickness and the highest gas content in this syncline, so it is chosen as the research target. As can be seen from **Figures 1C, D**, they belong to the same coal seam, but the apparent morphology of the coal seam is still different, which may be related to the tectonic evolution and stress conditions in different regions. At the same time, it is found that the coal exhibits strong bedding characteristics. Therefore, the influence of intersection angle should be fully considered when testing permeability.

Coal Sample Preparation

All coal cores are taken from underground coal mining face in the No.11 coal seam of DH and WJZ regions. The blocks with well integrity and low cracks are selected, and the large blocks with the size over 300 mm × 300 mm × 300 mm are obtained with crowbars, and transported to the surface (**Figures 2A**), and then packaged and transported to the laboratory. Because the cores contain many fissures and has low strength, so as to reduce the damage to the coal structure, all the samples in this study are

processed by wire cutting (**Figures 2B**). Considering the obvious bedding characteristics of coal, five intersection angles of 0°, 30°, 45°, 60° and 90° are considered in sample preparation, which is defined as the intersection angle between the axis direction of sample and the bedding plane of coal seam. The influence of intersection angles on the permeability will be studied to reveal the anisotropy of permeability, which provides an important reference for the subsequent well-stability analysis and hydraulic fracturing designing.

Typical coal samples (50 mm × 100 mm, cylinder-shape) proceeding containing different intersection angles are shown in **Figures 2C**: the first row is the coal from the DH region. The coal samples have obvious bedding, good integrity, hard texture and a few initial cracks; the second row presents the coal from WJZ region, with many cracks and no obvious bedding, the integrity of which is worse than that of DH coal samples. This also fully shows that although they are in the same syncline tectonic area and the same coal seam, the structural characteristics of coal still show great differences with the different regional locations, which increases the difficulty in forming a unified coal-bed methane development technology.

Testing Principle and Scheme

1) Porosity test

In this experiment, the gas expansion method is used to measure the porosity of rock samples, which is an indirect method. The measuring principle is Boyle-Mariotte's specific law: $P_1V_1 = P_2V_2$. First, open the valve of nitrogen bottle, under a certain pressure P_1 , and expand the gas into a standard chamber whose initial pressure equals the standard atmospheric pressure. The standard chamber has a volume of V_1 . measure the balance pressure at this moment. Then, open the valve to connect the standard chamber with the core holder. The core holder has a volume of V_2 . After reaching a new pressure balance, measure the new balance pressure of P_2 . after then, the gas volume in the system is $V_1 + V_2 - V_s$.

According to Boyle-Mariotte's law:

$$P_1V_1 = P_2V_2, \quad (1)$$

$$V_s = V_1 + V_2 - \frac{V_1P_1}{P_2}, \quad (2)$$

The definition of porosity is:

$$\varphi = (V_f - V_s)/V_f = 1 - V_s/V_f, \quad (3)$$

Where: V_f , the total volume of the appearance of the rock, the unit is cm^3 ; V_s , is the volume of solid phase in cm^3 .

Substitute **Eqs 1, 2** into **Eq. 3** to obtain:

$$\varphi = 1 - [P_2(V_1 + V_2) - V_1P_1]/P_2V_f \quad (4)$$

The gas source is provided by the laboratory, including nitrogen, methane, carbon dioxide and helium. Considering the development of micro-pores in coal, the permeable gas medium is helium in this study. The corresponding program has been compiled from the test system, which only needs to input

the basic information of the sample, and the result can be read directly after the pressure becomes stable.

2) Routine permeability testing.

The permeability is measured by the steady-state method: first, an initial fluid pressure difference is applied to both ends of the rock, and the fluid will flow across the rock. After reaching a steady state, the measured flow rate and pressure difference are substituted into the Darcy seepage formula, and finally the corresponding permeability is calculated. The basic principle of the steady-state permeability measurement is Darcy's law, that is:

$$Q = \frac{kA(h_2 - h_1)}{l} \quad (5)$$

Where: Q , unit seepage flow, unit m^3/s ; K , permeability, unit m^2 ; A , Core cross-sectional area (m^2); core length, unit m ; $h_2 - h_1$: Total head loss, unit m .

According to the actual needs of the research, liquid such as brine or gas such as nitrogen can be chosen as the permeation medium, and in some cases, mixed-phase fluid can also be used. When using gas as the permeation medium, the comprehensibility of the gas must be considered, and the calculation formula is as follows:

$$K_g = \frac{2P_0Q_g\mu_g l}{A(P_{in}^2 - P_{out}^2)} \quad (6A)$$

Where, K_g , gas measurement permeability, unit m^2 ; μ_g , gas dynamic viscosity coefficient, in $\text{Pa}\cdot\text{s}$; P_0 , atmospheric pressure value, unit MPa ; Q_g , gas flow rate, unit m^3/s ; l , length of core in m ; P_{in} , inlet end fluid pressure, unit MPa ; P_{out} , the fluid pressure at the outlet, unit MPa . In the oil and gas field, D (Darcy) or mD (mild Darcy) is often used as the permeability unit, $1\text{um}^2 = 1 \times 10^{-12} \text{m}^2 = 1\text{D} = 10^3\text{mD}$.

Porosity and permeability tests are carried out on the LW-1 porosity and permeability tester (Liu et al., 2020c), which was jointly developed by the State Key Laboratory of Coal Mine Disaster Dynamics and Control at Chongqing University and Jiangsu Tuochuang Science and Technology Co., Ltd. It can be used for porosity test by gas expansion, steady-state permeability test and unsteady-state permeability test. This device can fully meet the test requirements, which was shown in **Figure 3**.

3) Sample information.

See **Table 1** for the test scheme. It mainly includes porosity, conventional permeability, and permeability tests at different confining/inlet pressures.

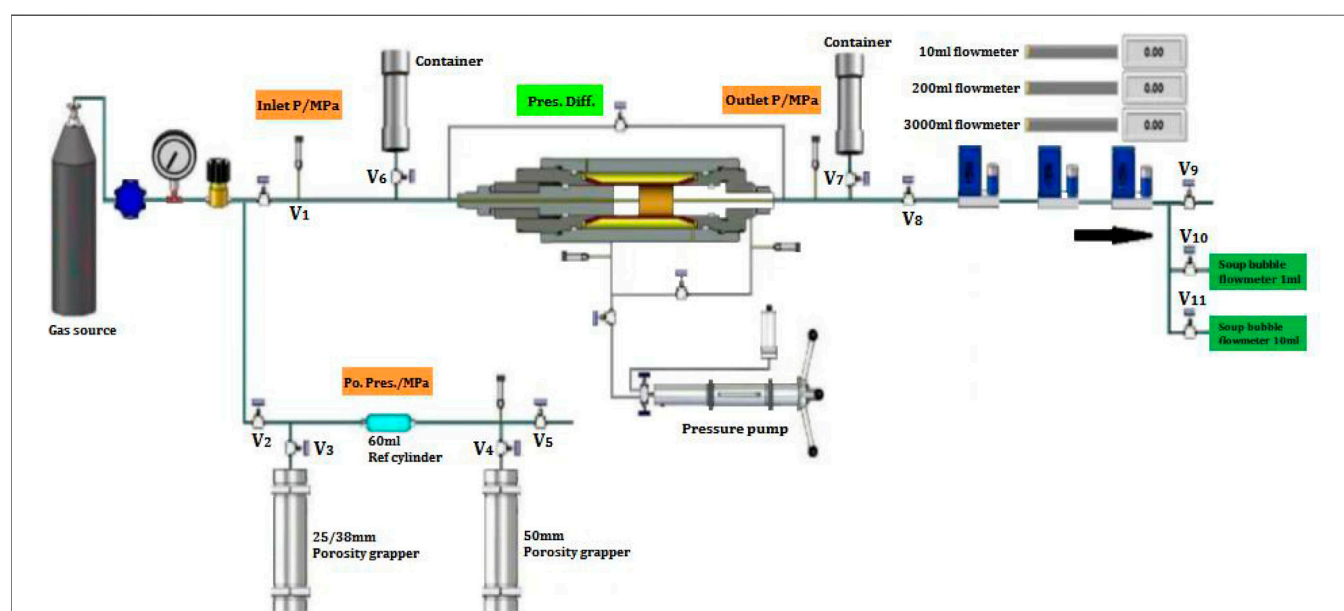
PORE AND PERMEABILITY TESTING

Results in DH Region

Figures 4A shows the test results of coal porosity in DH region. The porosity fluctuates between 7.38 and 11.22%, with an average value of 9.03%. It can be said that the porosity of DH region is

TABLE 1 | Porosity and permeability testing scheme.

Content	Coal zone	Types of coal sample	Quantity
Porosity	DH region	5 types of intersection angle	14
	WJZ region	5 types of intersection angle	12
Permeability	DH region	5 types of intersection angle	12
	WJZ region	5 types of intersection angle	13
Permeability under different pressure	DH region	Confining pressure: 4 types	4
		Gas pressure: 3 types	
		Intersection angle: 0°, 90°	
		Intersection angle: 0°, 45°, 60°, 90°	
	WJZ region	Confining pressure: 4 types	10
		Gas pressure: 3 types	
		Intersection angle: 0°, 45°, 60°, 90°	

**FIGURE 3** | Flow chart of rock porosity and permeability testing equipment.

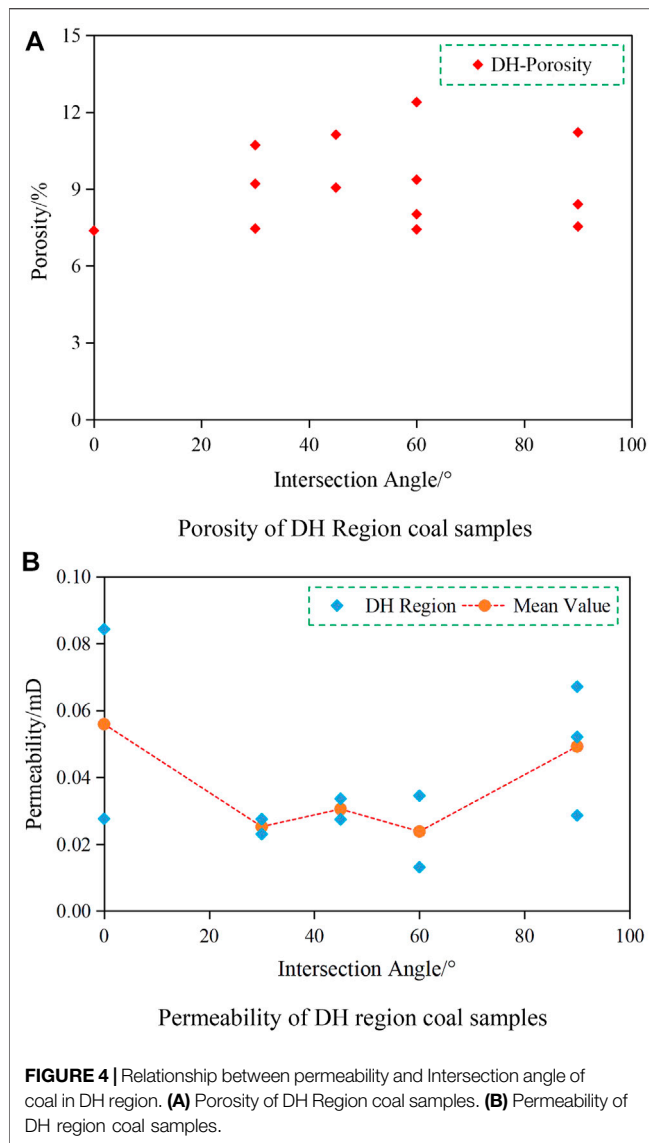
good, which is beneficial to the exploitation of CBM in this area. **Figures 4B** shows the testing results of coal permeability in DH region. The permeability of coal sample in DH region ranges from 0.0131 mD to 6.5797 mD. It should be noted that the permeability of 6.5797 mD corresponds to the sample containing a penetrating crack. If this sample is excluded, the permeability of DH coal is between 0.0131 mD and 0.0843 mD, with an average value of 0.0381 mD. It can be seen that, the permeability of coal in DH region is very poor, which belongs to low permeability coal seam.

Without artificial stimulation measures such as hydraulic fracturing, it is difficult to obtain effective exploitation and utilization of CBM. At the same time, it shows that the existence of cracks will increase the permeability of coal by over than two orders of magnitude. Therefore, it is necessary to pay close attention to the development of primary cracks in coal seams, and find potential favorable regions for the CBM extraction. In addition, it can also be seen in **Figures 4B** that the permeability of DH coal has obvious angle effect. The permeability of 0° sample (permeating along bedding

direction) is the highest, while that of the middle angle samples (30°, 45° and 60°) is the lowest, indicating that the permeability through matrix is slightly poor.

Pore and Permeability Test Results in WJZ Region

The porosity test results of WJZ coal are shown in **Figure 5A** as follows: the porosity ranges from 7.06 to 24.75%, with an average value of 18.67%. It can be said that the porosity of WJZ coal is high and good. **Figure 5B** shows the permeability results of the WJZ coal testing. Permeability ranges from 0.175 mD to 5.21 mD, with an average value of 1.36 mD. It can be said that the WJZ coal has good permeability, which is helpful for realizing the development of CBM directly or through simple reservoir reconstruction. Combined with **Figure 5**, it can be seen that there are many primary cracks in the WJZ coal, which may be an important reason for its good permeability. Due to the existence of a large number of primary cracks, the influence of bedding is



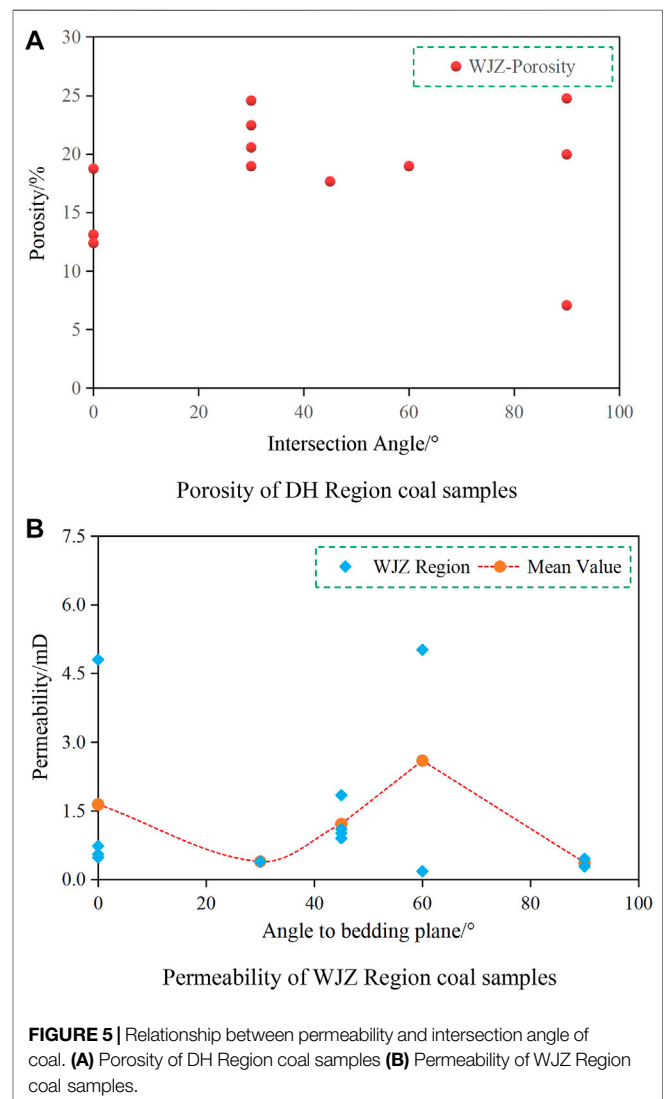
weakened, so the relationship between the permeability and intersection angle of WJZ coal is not obvious. In addition, it is found that the permeability of WJZ coal is only several times higher than that of the same group of samples even if the coal contains perforating fractures, while the permeability of DH coal with perforated fracture has no significant difference. Considering the good porosity and permeability characteristics of WJZ coal, it is necessary to pay close attention to the recoverable potential of this region, and evaluate whether this region belongs to the preferential exploitation block of CBM.

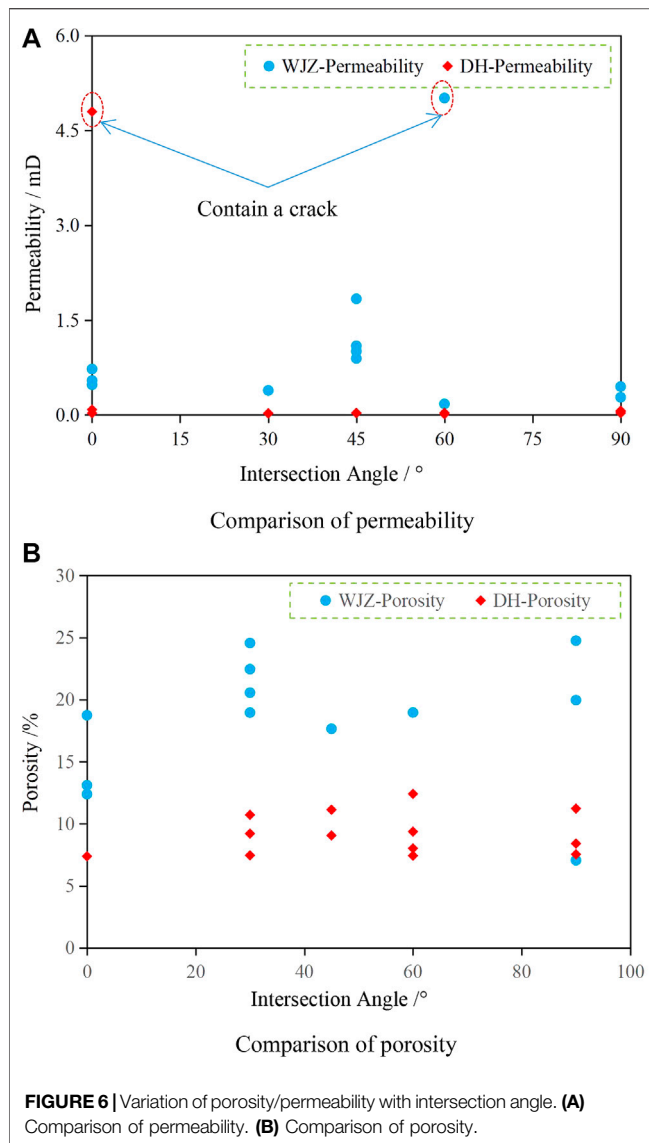
Comparison of Regional Results

DH region and WJZ region belong to two blocks in the same synclinal structure, and the coal cores used here belong to the same stratum. However, according to the above tests and analysis, there are obvious differences between them. **Figure 6** shows the

comparison results of porosity and permeability between these two regions.

The comparison shows that: 1) Due to the integrity of coal structure, the permeability of coal in DH region is as low as the order of 10^{-2} mD, which belongs to the difficult-to-exploit coal seam. However, once there is a crack, the permeability will increase sharply. 2) The coal has good permeability, which is a favorable condition for methane exploitation. At the mD level, more attention should be paid to its exploitable potential and it should be included in the priority area of methane development. 3) The porosity of WJZ coal is almost twice that of coal in DH region, and the primary cracks are much more developed. From the perspective of CBM exploitation, the WJZ region should be given priority. 4) The comparative results fully show that even if the plane distance between the two study regions are very close, only 8 km, and the coal cores are taken from the same coal seam, the characteristics of porosity and permeability are quite different. Therefore, even in the same coalfield, some priority blocks should be founded and exploited first. In addition, it is necessary to further study the porosity and permeability





characteristics of coal, and to find the development technology suitable for each region.

The comparison shows: 1) Because of the integrity of coal structure, the permeability of coal rock in DH region is low, which is in the order of 10^{-2} mD, and without reservoir reconstruction, it is difficult to exploit CBM in this region. However, once there are cracks, the permeability will increase rapidly. 2) The permeability of WJZ coal is almost twice that of the DH coal, with extremely developed cracks. From the perspective of CBM exploitation, WJZ region should be given priority. 3) The comparison results fully show that even if the distance of the same coal seam in the same structural area is as close as 8 km, the characteristics of porosity and permeability are quite different. Therefore, the exploitation of CBM in Liupanshui Coalfield must consider the priority regions, such as the WJZ region in Dahebian Syncline.

INFLUENCE OF CRACKS AND PRESSURE

Influence of Cracks

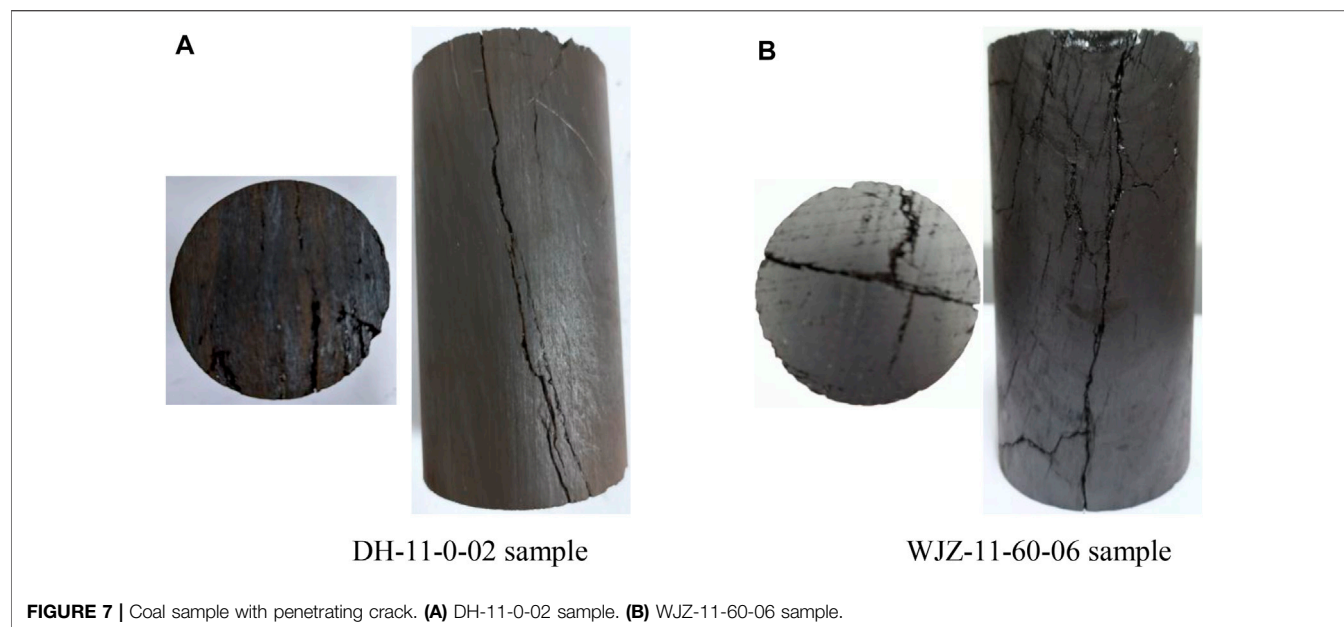
Through the above research, it is found that the permeability test result of individual sample is much higher than other samples in the same group. For example, the permeability of DH-11-02 sample in DH region is as high as 6.5795 mD, which is 117.6 times of the permeability of coals in the same coal seam with the same intersection angle, and 172.8 times of the average permeability of all samples in the same coal seam. After observation, it is found that there is a crack connecting bedding on the surface of sample, as shown in **Figure 7**. The crack runs through the upper and lower ends of the sample, is almost parallel to the bedding, and bends locally, which is a typical bedding tensile fracture. Because of the existence of such crack, the permeability of the coal is increased by more than two orders of magnitude.

Meanwhile, the permeability of some coal samples in WJZ region is obviously higher than that of the same group. For example, the permeability of WHZ-11-60-06 sample is as high as 5.01 mD, which is 8.63 times that of coal with the same intersection angle. This sample has an intersection angle of 60° to the coal seam bedding, but there is a crack on the side penetrating through the sample. The crack surface has a small opening and a relatively straight crack, which is characterized by shear crack. According to the analysis, the intersection angle of 60° is not the dominant direction of seepage migration, but it is this kind of crack that leads to the increase in permeability.

From the above comparison, it can be seen that the integrity of coal in DH region is better, and there are few cracks on the surface of the samples. However, once cracks appear, the increase in permeability is very obvious. From the observation of the sample, most of the cracks are tensile cracks along the bedding direction. However, in WJZ region, the integrity of coal is poor, and there are many primary cracks with poor regularity. These cracks should be formed along with the later tectonic process, including shear cracks and tensile cracks. Due to the existence of primary cracks, the permeability of WJZ coal samples is much higher than that of the DH coal samples. Therefore, when exploring and developing CBM in the WJZ region, the crisscrossing crack-network is a favorable factor for CBM extraction.

Influence of Pressure Condition

In the third part, the conventional permeability tests were carried out when the confining pressure was only 2.5 MPa. However, in the underground space, with the change of coal seam depth and CBM extraction depth, the stress state of coal will change. At present, the depth of coal seam is generally over 300 m, and the reservoir pressure of the coal seam is much higher than 2.5 MPa. Therefore, it is still necessary to study the permeability of coal under different confining pressures and different gas pressure, so as to provide a basis for coal permeability evaluation and CBM extraction designing under the condition of field stress state. The fourth-level confining pressure is 2/4/6/8 MPa and the third-level inlet pressure is 0.4/0.6/0.8 MPa.



1) Coal in DH region

Four coal samples in DH region were tested. The results show that with the increase of confining pressure, the permeability of coal shows a downward trend, indicating that the increase of confining pressure would lead to the compaction of coal, thus leading to the decrease of permeability.

The test results show that when the confining pressure increases from 2 to 8 MPa, the permeability of the three intact DH coal samples decreases by 75–93%, indicating that the confining pressure has a great influence on the permeability. When the confining pressure is in the range of 2–4 MPa, the permeability decreases rapidly, and then the decreasing trend slows down. When the confining pressure reaches 8 MPa, the permeability is basically stable, so no higher confining pressure test will be conducted. The influence of inlet pressure on permeability is still not clear. Taking DH-11-0-05 sample (intersection angle = 0°) as an example, the permeability increases with the increase of inlet pressure. However, DH-11-90-01 sample (intersection angle = 0°), the permeability decreases with the increase of inlet pressure. The testing results of three representative samples are selected as shown in **Figure 8**.

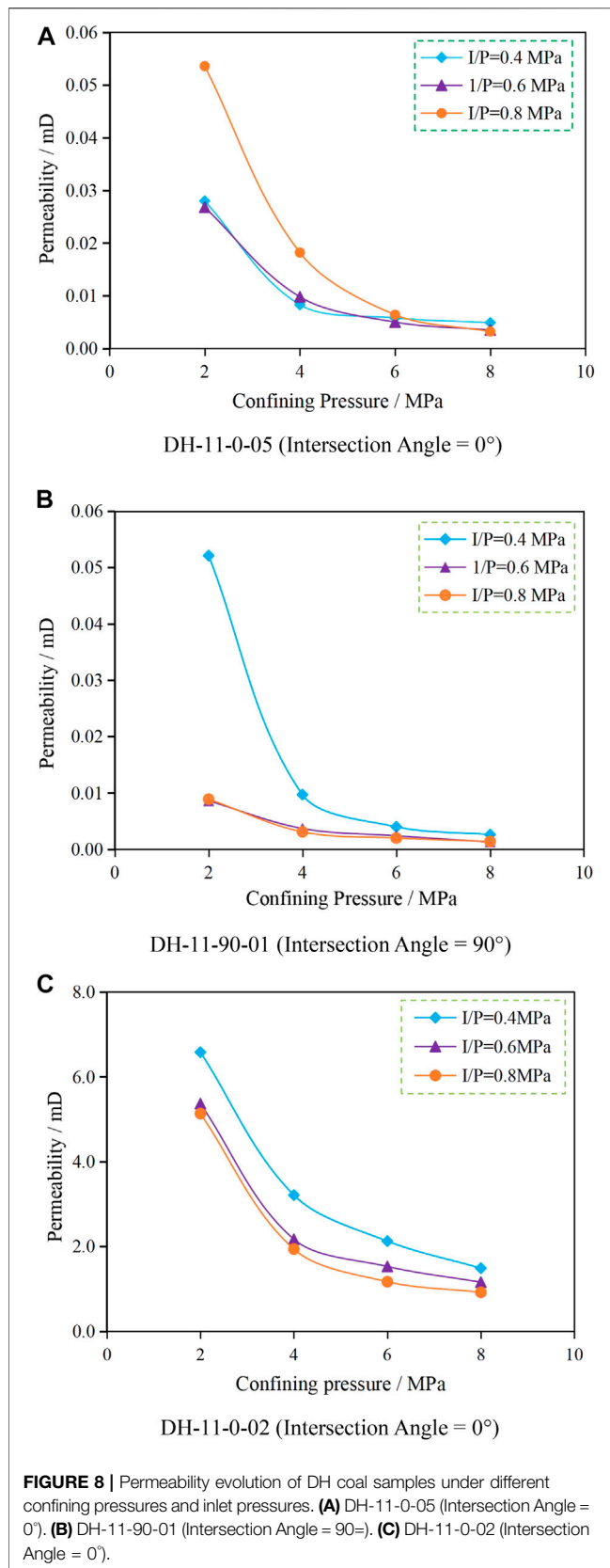
2) Coal in WJZ region

This paper studies the permeability evolution of coal in WJZ region under different confining pressures and inlet pressures. The results show that the confining pressure has a significant influence on the permeability of WJZ coal mass. When the confining pressure is increased from 2 to 8 MPa, the permeability decreases by 51.51–94.21%. Among them, the 60° sample (WJZ-11-6-06) shows the smallest decrease, only 47.43%. The 90° sample (WJZ-7-45-04) has the highest decrease rate, which is 13.74%. It should be noted that samples with intersection angles of 0°, 45° and 90° have the

same decreasing trend and similar decreasing amplitude (13.74–19.91%). There are several penetrating cracks in the sample WJZ-11-60-06, but with the increase of confining pressure, the decrease of permeability is limited, which indicates that the confining pressure only leads to partial closure of the crack. This further indicates that even under the action of underground stress, this crack are still the main channel for gas seepage. The inlet gas pressure shows the similar influence on the permeability of WJZ coal is basically the same. Under the same confining pressure, the higher the inlet pressure, the smaller the decrease of permeability. However, compared with confining pressure, the effect of the inlet pressure is very limited. See **Figure 9** for the representative permeability test results under different confining pressures in the WJZ region.

From the above analysis, it can be seen from the above analysis that the confining pressure has a very significant impact on permeability. However, it is also found that after the first test (confining pressure 2–4–6–8 MPa) and the second test (confining pressure 2–4–6–8 MPa), the inlet pressure increased from 0.4 to 0.6 MPa (average pressure increased from 0.25 to 0.35 MPa), and the permeability is lower than that of the first test. It seems that the inlet pressure causes the decrease in permeability. However, from the third round tests results (Confining pressure 2–4–6–8 MPa, Inlet gas pressure 0.8 MPa), it can be seen that the “Permeability-Confining pressure” curves of the seven samples in the second and third rounds are basically coincidental. This does not explain the influence of inlet pressure on coal permeability. As a matter of fact, this phenomenon has an important influence on the field applications.

Generally speaking, from the external conditions, permeability is related to confining pressure, permeation gas pressure and gas type (Meng et al., 2017; Liu et al., 2020c). But from the internal



mechanism, these factors essentially lead to the change of pore structure in rock matrix, which reflects the interaction between gas and pore structure, thus leading to the difference of permeability. The Kozeny-Carman equation is a famous theoretical formula for the response of permeability to pore structure and permeability channel characteristics inside rocks, and its revised formula is as follows (Kleinberg et al., 2003; Schneider et al., 2011):

$$K = \frac{\phi}{v\tau(A/V)_{\text{grain}}^2}, \quad (6B)$$

Where: v is the shape coefficient, dimensionless; $(A/V)_{\text{grain}}$ is the specific surface area of grain per unit volume, mm^{-1} ; K is the absolute permeability of porous rock, $10^{-3}\mu\text{m}^2$; ϕ is the effective porosity of rock, %; τ is tortuosity, dimensionless.

It can be seen from **Eq.6A** that the porosity, specific surface area and tortuosity are all important factors affecting permeability. For coal sample, the internal porosity will inevitably decrease when subjected to external force. In the process of rock compression, the micro-pores and cracks are closed, and the total volume decreases, but the total surface area of particles remains unchanged, so $(A/V)_{\text{grain}}$ increases instead. The change in tortuosity was not significant. Generally speaking, the larger the confining pressure, the smaller the numerator and the bigger the denominator in **Eq.6B**. As a result, permeability is reduced. In addition, according to the research of Liu et al. (Liu et al., 2015; Fan et al., 2019; Fan et al., 2020), rocks with flat pores and cracks are more easier to close under pressure. Especially, in the process of increasing confining pressure, the smallest pore throat tends to close at first, so the permeability decreases rapidly in the early stage. Even if the confining pressure is increased, the permeability can not be reduced further. This explains why the permeability is almost unchanged when the confining pressure reaches 8 MPa. However, for samples with perforated cracks, because of the large crack size, the “closing pressure” required for complete crack closure will be very high. Therefore, when the confining pressure is 8 MPa, the decreasing trend of permeability is unchanged.

It should be pointed out that both the DH coal and WJZ coal have low strength and belongs to soft rock. After the first test (Confining pressure is 2–4–6–8 MPa), irreversible plastic deformation occurs in rock matrix (Liu et al., 2015). After entering the second and third tests (confining pressure 2–4–6–8 MPa), the porosity, specific surface area and tortuosity of the rock appear new situations due to the appearance of plastic deformation. Therefore, the “Permeability-Confining pressure” curves of the second round and third round are basically close, but there are also a significant difference from those of the first round. Hydro-fracturing and methane extraction is a process of loading and unloading, which inevitably leads to plastic deformation in coal. Therefore, the permeability of the coal reservoir is likely to be reduced and thus affect the productivity. In this study, the influence of plastic deformation under loading on permeability is only studied by conventional permeability test. In the follow-up study, according

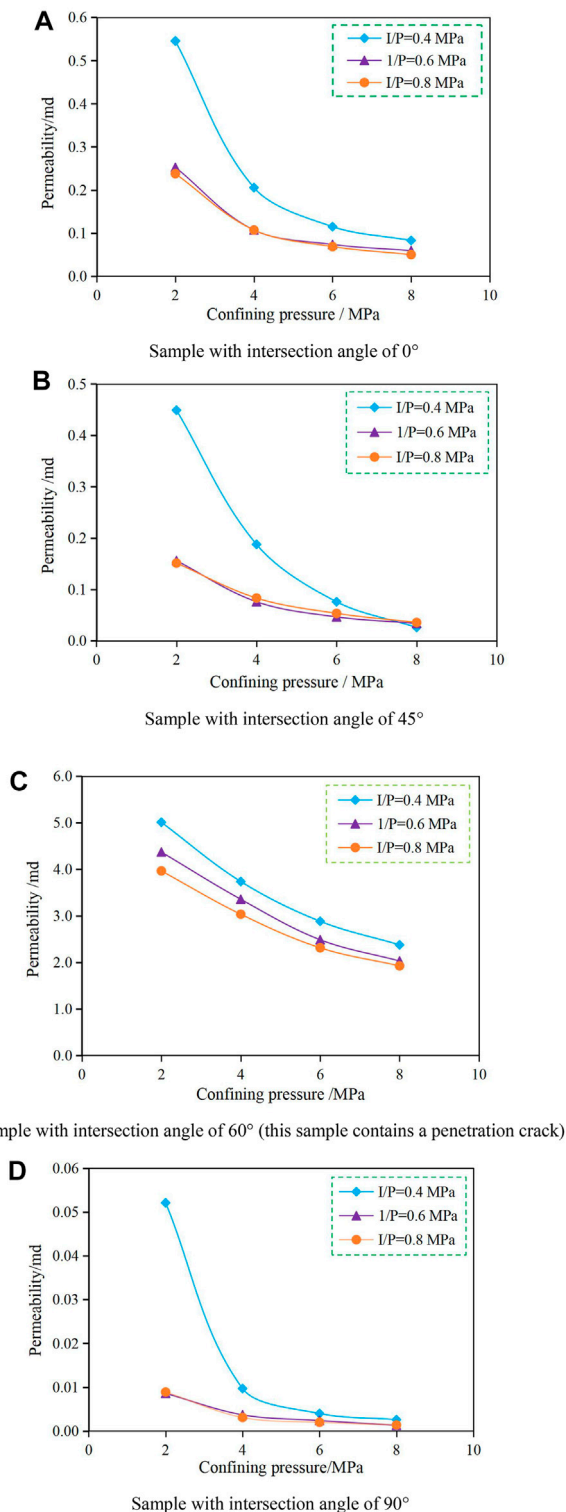


FIGURE 9 | Permeability evolution of WJZ coal samples under different confining pressures and inlet gas pressures. (A) Sample with intersection angle of 0° (B) Sample with intersection angle of 45° (C) Sample with intersection angle of 60° (this sample contains a penetration crack) (D) Sample with intersection angle of 90°.

to the actual stress of coal and the loading and unloading situation of confining pressure, the downward trend of coal permeability will be further quantified, which will provide a favorable basis for on-site CBM extraction.

DISCUSSION AND APPLICATION

The coal samples used in this study were obtained from two different blocks of the same coal seam in Dahebian syncline. The plane distance of the coring point is only 8 km, but the porosity and permeability of the coal are quite different. This fully shows that there are obvious differences in physical and mechanical properties of coal in Liupanshui Coalfield. Therefore, even within the same structural area, it is necessary to understand the differences of coal in different blocks, which is the basis for further implementation of CBM exploitation plan.

In the previous exploitation of coal bed methane in Guizhou Province, the harvest was not great, and the commercial exploitation efficiency of coal bed methane has not yet been achieved. However, according to this study, this is mainly due to the complex coal structure, complex of coal occurrence environment, huge heterogeneity, and regional differences of coal in Guizhou Province. At the same time, the preliminary research work is still insufficient. If the characteristics of porosity and permeability of coal seam are not fully understood, the drilling work may be blind. Therefore, it is difficult to obtain commercial CBM extraction. There are still many blocks with high porosity, good permeability and developed primary fractures in coal seams in Guizhou Province (Figure 10). Although these blocks may be isolated in distribution, they may be the best places for methane extraction.

From the Dahebian Syncline, the anisotropy and heterogeneity of coal in different areas are very obvious. Especially, the coals in the WJZ region are characterized by high porosity and relatively good permeability. These are the best regions for CBM exploitation, and should be listed as the first exploitation areas. Therefore, in the follow-up studies, even for different areas of the same structural area, it is necessary to explore the optimal blocks, find the areas with high porosity and high permeability (relative), and establish the optimal methane extraction areas. Zhou et al. (Zhou et al., 2009) studied the regional tectonic characteristics of Dahebian syncline. They pointed out that the proportion of reserve faults in WJZ regions is about 18%, and the argillaceous caprock in WJZ region accounts for 35.3%, while the sandstone only accounts for 32.2%. However, in the DH region, the proportion of normal faults in the DH region is as high as 96.9%. And the argillaceous caprock in DH region is as low as 3.57%, but the sandstone accounts for 69%. As a result, due to the higher proportion of reserve faults and tighter caprock, the coal seam in WJZ coal seams have subjected to structural compression, and the stress concentration becomes more obvious in this region. As a result, the integrity of coal seam in WJZ region has been weakened or even destroyed. Therefore, the coal in WJZ region have lower integrity

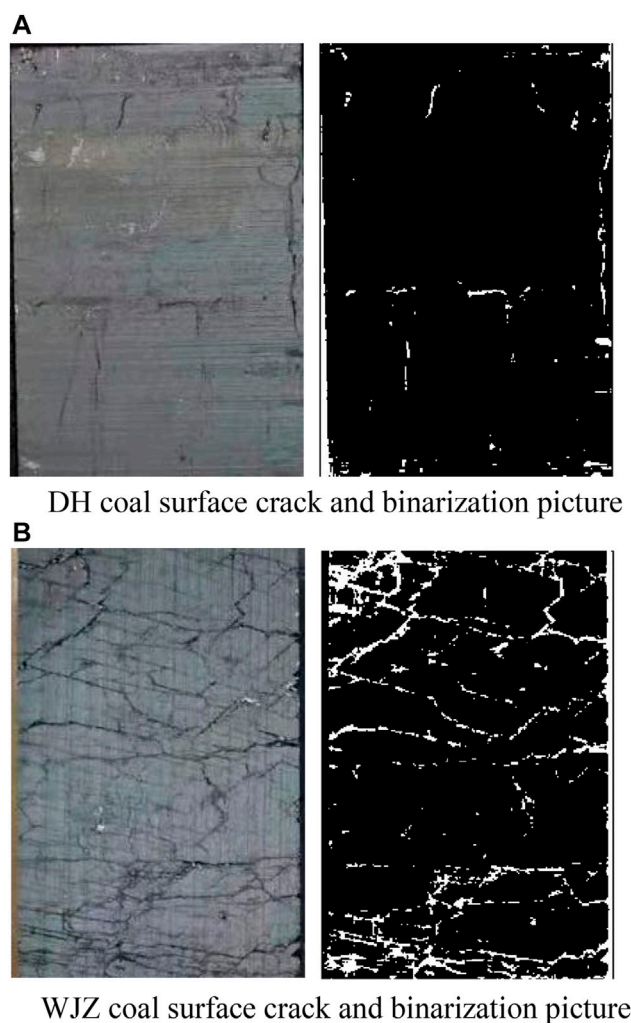


FIGURE 10 | Primary fractures and binarization of WJZ coal (size 50 mm × 75 mm). **(A)** DH coal surface crack and binarization picture **(B)** WJZ coal surface crack and binarization picture.

but greater porosity and permeability than those of the DH region.

Due to the great differences in coal petro-physical properties, the methane extraction methods and technical parameters in different regions should also be different. Therefore, the implementation of the specific technologies of blocks may be a better method for CBM exploitation in Guizhou Province. In addition, Guizhou Province may not be suitable for the formation of a unified and standardized CBM exploitation method. It is suggested to study the relationship between the favorable blocks with high porosity and permeability, so as to provide some guidance for the selection of the favorable blocks from a macroscopic perspective.

CONCLUSIONS AND PROSPECTS

The porosity and permeability of underground coal samples in two blocks of No.11 coal seam in Dahebian Syncline of

Liupanshui Coalfield were systematically tested and studied, and the following conclusions and suggestions are drawn.

- 1) The porosity of coal samples in DH region is 7.4–10.1%, with an average value of 9.2%. The range of permeability k ranges from 0.01 to 0.08 mD, with an average value of 0.04 mD. The permeability of DH coal samples has obvious bedding effects. The DH coal samples has good integrity and poor connectivity of matrix, so it still mainly depends on fracturing to increase productivity.
- 2) The porosity of the coal samples in WJZ region ranges from 7.06 to 24.8%, with an average of 18.67%. The permeability is between 0.2mD and 5.2mD, with an average of 1.4 mD. There is no obvious relationship between permeability and intersection angle. WJZ coal mass has good porosity and permeability, which is expected to be the optimal choice block for CBM development in the Dahebian Syncline.

- 3) Relatively speaking, the porosity of WJZ coal is twice that of DH coal, and the permeability is 1–2 orders of magnitude higher than that of DH coal. With the increase of confining pressure, the permeability of coal decreases rapidly, but there is a “Compaction confining pressure”. When this value is exceeded, the permeability will remain basically stable. In addition, with the occurrence of plastic deformation (irrecoverable deformation), the permeability of coal will be greatly decreased. The porosity and permeability of the same coal seam in different positions are quite different, which shows that the coal at different blocks have obvious heterogeneity and differences. Therefore, we should pay close attention to the differences in exploration and development so as to adopt appropriate technology.
- 4) Generally speaking, when there are cracks in the coal, the permeability will increase greatly. In contrast, the integrity of coal in DH region is better, and the porosity and permeability are lower, while WJZ coal contains more primary cracks, which has higher porosity and permeability. Therefore, when developing CBM similar to the Dahebian Syncline, it is suggested to choose the first desert area and give priority to CBM development, and pay attention to the application of appropriate technology in different blocks to gradually promote the commercialization and scale of CBM development.

Dahebian Syncline, a representative syncline in Liupanshui Coalfield, has the characteristics of strong porosity-permeability heterogeneity and regional particularity, which must be paid

special attention to in the future exploration and development. It also shows that there are still many high permeability blocks in the coalfield. How to grasp the structural characteristics and occurrence characteristics of these desert areas will provide important guidance for the establishment of commercial CBM base in the next step, which is also the research direction for our further study.

DATA AVAILABILITY STATEMENT

The original contributions presented in the study are included in the article/Supplementary Material, further inquiries can be directed to the corresponding author.

AUTHOR CONTRIBUTIONS

FZ organized and wrote this paper, YW proposed the idea and did the experiments and analysis.

FUNDING

This research was supported by the Guizhou Provincial Geological Exploration Fund (Grant no. 208-9912-JBN-UTS0) and by the Fundamental Research Funds for the Central Universities (Grant no. 2021CDJQY-030).

REFERENCES

- Aguilera, R. F. (2014). The Role of Natural Gas in a Low Carbon Asia Pacific. *Appl. Energ.* 113, 1795–1800. doi:10.1016/j.apenergy.2013.07.048
- Ayers, W. B. (2002). Coalbed Gas Systems, Resources, and Production and a Review of Contrasting Cases from the San Juan and Powder River Basins. *AAPG Bull.* 86 (11), 1853–1890. doi:10.1306/61eeddaa-173e-11d7-8645000102c1865d
- Fan, J., Jiang, D., Liu, W., Wu, F., Chen, J., and Daemen, J. (2019). Discontinuous Fatigue of Salt Rock with Low-Stress Intervals. *Int. J. Rock Mech. Mining Sci.* 115, 77–86. doi:10.1016/j.ijrmms.2019.01.013
- Fan, J., Liu, W., Jiang, D., Chen, J., Tiedeu, W. N., and Daemen, J. J. K. (2020). Time Interval Effect in Triaxial Discontinuous Cyclic Compression Tests and Simulations for the Residual Stress in Rock Salt. *Rock Mech. Rock Eng.* 53, 4061–4076. doi:10.1007/s00603-020-02150-y
- Huang, H., Sang, S., Yi, T., Xu, H., Li, L., and Li, J. (2010). Analysis of Coal Resource Effective Supply Ability Based on Grey Clustering in Guizhou Province. *Coal Geology. China* 22 (2), 19–23. doi:10.3969/issn.1674-1803.2010.02.05
- Kleinberg, R. L., Flaum, C., Griffin, D. D., Brewer, P. G., Malby, G. E., Peltzer, E. T., et al. (2003). Deep Sea NMR: Methane Hydrate Growth Habit in Porous Media and its Relationship to Hydraulic Permeability, Deposit Accumulation, and Submarine Slope Stability. *J. Geophys. Research-Solid Earth* 108 (B10), 2508. doi:10.1029/2003jb002389
- Li, B., Ren, C., Wang, Z., Li, J., Yang, K., and Xu, J. (2020). Experimental Study on Damage and the Permeability Evolution Process of Methane-Containing Coal under Different Temperature Conditions. *J. Pet. Sci. Eng.* 184, 106509. doi:10.1016/j.petrol.2019.106509
- Li, S., Tang, D., Pan, Z., Xu, H., and Guo, L. (2015). Evaluation of Coalbed Methane Potential of Different Reservoirs in Western Guizhou and Eastern Yunnan, China. *Fuel* 139, 257–267. doi:10.1016/j.fuel.2014.08.054
- Li, X., Peng, K., Peng, J., and Xu, H. (2021). Effect of Cyclic Wetting-Drying Treatment on Strength and Failure Behavior of Two Quartz-Rich Sandstones under Direct Shear. *Rock Mech. Rock Eng.* 54, 5953–5960. doi:10.1007/s00603-021-02583-z
- Li, X., Wang, Y., Yang, S., Jun, X., and Zhao, K. (2021). Research Progress in the Mining Technology of the Slowly Inclined, Thin to Medium Thick Phosphate Rock Transition from Open-Pit to Underground Mine. *Appl. Maths. Nonlinear Sci.* 6 (1), 319–334. doi:10.2478/amns.2021.2.00017
- Liang, T., Chai, J., Zhang, Y.-J., Zhang, Z. G., and Zhang, Z. (2019). Refined Analysis and Prediction of Natural Gas Consumption in China. *J. Manage. Sci. Eng.* 4 (2), 91–104. doi:10.1016/j.jmse.2019.07.001
- Lin, B., and Wang, T. (2012). Forecasting Natural Gas Supply in China: Production Peak and Import Trends. *Energy Policy* 49, 225–233. doi:10.1016/j.enpol.2012.05.074
- Liu, E., Guo, B., Lv, L., Qiao, W., and Azimi, M. (2020). Numerical Simulation and Simplified Calculation Method for Heat Exchange Performance of Dry Air Cooler in Natural Gas Pipeline Compressor Station. *Energy Sci Eng* 8 (6), 2256–2270. doi:10.1002/ese3.661
- Liu, E., Lv, L., Yi, Y., and Xie, P. (2019). Research on the Steady Operation Optimization Model of Natural Gas Pipeline Considering the Combined Operation of Air Coolers and Compressors. *IEEE Access* 7, 83251–83265. doi:10.1109/access.2019.2924515
- Liu, H.-H., and Rutqvist, J. (2010). A New Coal-Permeability Model: Internal Swelling Stress and Fracture-Matrix Interaction. *Transp Porous Med.* 82 (1), 157–171. doi:10.1007/s11242-009-9442-x
- Liu, W., Li, Y., Yang, C., Daemen, J. J. K., Yang, Y., and Zhang, G. (2015). Permeability Characteristics of Mudstone Cap Rock and Interlayers in Bedded Salt Formations and Tightness Assessment for Underground Gas Storage Caverns. *Eng. Geology* 193, 212–223. doi:10.1016/j.enggeo.2015.04.010
- Liu, W., Zhang, X., Fan, J., Li, Y., and Wang, L. (2020). Evaluation of Potential for Salt Cavern Gas Storage and Integration of Brine Extraction: Cavern Utilization, Yangtze River delta Region. *Nat. Resour. Res.* 29 (5), 3275–3290. doi:10.1007/s11053-020-09640-4

- Liu, W., Zhang, X., Fan, J., Zuo, J., Zhang, Z., and Chen, J. (2020). Study on the Mechanical Properties of Man-Made Salt Rock Samples with Impurities. *J. Nat. Gas Sci. Eng.* 84, 103683. doi:10.1016/j.jngse.2020.103683
- Liu, W., Zhang, Z., Chen, J., Fan, J., Jiang, D., Jjk, D., et al. (2019). Physical Simulation of Construction and Control of Two Butted-Well Horizontal Cavern Energy Storage Using Large Molded Rock Salt Specimens. *Energy* 185, 682–694. doi:10.1016/j.energy.2019.07.014
- Liu, W., Zhang, Z., Fan, J., Jiang, D., Li, Z., and Chen, J. (2020). Research on Gas Leakage and Collapse in the Cavern Roof of Underground Natural Gas Storage in Thinly Bedded Salt Rocks. *J. Energy Storage* 31, 101669. doi:10.1016/j.est.2020.101669
- Liu, X., and He, X. (2017). Effect of Pore Characteristics on Coalbed Methane Adsorption in Middle-High Rank Coals. *Adsorption* 23 (1), 3–12. doi:10.1007/s10450-016-9811-z
- Liu, Y., Yin, G., Li, M., Zhang, D., Deng, B., Liu, C., et al. (2019). Anisotropic Mechanical Properties and the Permeability Evolution of Cubic Coal under True Triaxial Stress Paths. *Rock Mech. Rock Eng.* 52 (8), 2505–2521. doi:10.1007/s00603-019-01748-1
- Men, X. Y., Tao, S., Liu, Z. X., Tian, W. G., and Chen, S. D. (2021). Experimental Study on Gas Mass Transfer Process in a Heterogeneous Coal Reservoir. *Fuel Process. Technol.* 216, 106779.
- Meng, T., You, Y., Chen, J., and Hu, Y. (2017). Investigation on the Permeability Evolution of gypsum Interlayer under High Temperature and Triaxial Pressure. *Rock Mech. Rock Eng.* 50 (8), 2059–2069. doi:10.1007/s00603-017-1222-2
- Meng, Z., Zhang, J., and Wang, R. (2011). In-Situ Stress, Pore Pressure and Stress-dependent Permeability in the Southern Qinshui Basin. *Int. J. Rock Mech. Mining Sci.* 48 (1), 122–131. doi:10.1016/j.ijrmms.2010.10.003
- Nduagu, E. I., and Gates, I. D. (2016). Economic Assessment of Natural Gas Decarbonization Technology for Carbon Emissions Reduction of Bitumen Recovery from Oil Sands. *Int. J. Greenhouse Gas Control.* 55, 153–165. doi:10.1016/j.ijggc.2016.10.011
- Nie, B., Liu, X., Yang, L., Meng, J., and Li, X. (2015). Pore Structure Characterization of Different Rank Coals Using Gas Adsorption and Scanning Electron Microscopy. *Fuel* 158, 908–917. doi:10.1016/j.fuel.2015.06.050
- Qiao, W., Huang, K., Azimi, M., and Han, S. (2019). A Novel Hybrid Prediction Model for Hourly Gas Consumption in Supply Side Based on Improved Whale Optimization Algorithm and Relevance Vector Machine. *IEEE ACCESS* 7, 88218–88230. doi:10.1109/access.2019.2918156
- Qiao, W., Yang, Z., Kang, Z., and Pan, Z. (2020). Short-Term Natural Gas Consumption Prediction Based on Volterra Adaptive Filter and Improved Whale Optimization Algorithm. *Eng. Appl. Artif. Intelligence* 87, 103323. doi:10.1016/j.engappai.2019.103323
- Regan, T., and Chao, Z. (2014). Twenty Five Years of Coal Bed Methane Development in China. *The J. World Energy. L. Business* 7 (5), 423–447. doi:10.1093/jwelb/jwu030
- Schneider, J., Flemings, P. B., Day-Stirrat, R. J., and Germaine, J. T. (2011). Insights into Pore-Scale Controls on Mudstone Permeability through Resedimentation Experiments. *Geology* 39 (11), 1011–1014. doi:10.1130/g32475.1
- Shen, X., Tu, Y., Wang, J., and Chen, J. (2016). Strategic Direction and Policy Suggestions on Promoting Utilization of Natural Gas in China. *Int. Pet. Econ.* 24 (10), 69–78. doi:10.3969/j.issn.1004-7298.2016.10.010
- Tao, S., Chen, S., Tang, D., Zhao, X., Xu, H., and Li, S. (2018). Material Composition, Pore Structure and Adsorption Capacity of Low-Rank Coals Around the First Coalification Jump: A Case of Eastern Junggar Basin, China. *Fuel* 211, 804–815. doi:10.1016/j.fuel.2017.09.087
- Wan, J., Peng, T., Yuan, G., Ban, F., Jurado, M. J., and Xia, Y. (2021). Influence of Tubing/oil-Blanket Lifting on Construction and Geometries of Two-Well-Horizontal Salt Caverns. *Tunnelling Underground Space Technol.* 108, 103688. doi:10.1016/j.tust.2020.103688
- Wang, X., Liu, Y., Wang, F., and Li, H. (2019). Study on CBM Industrial Policy Status Quo in China. *Coal Geol. China* 31 (12), 102–107. doi:10.3969/j.issn.1674-1803.2019.12.20
- Wang, L., Guo, Y., Zhou, J., Yang, H., Yang, C., and Xiao, J. (2021). Rock Mechanical Characteristics of Deep marine Shale in Southern China, a Case Study in Dingshan Block. *J. Pet. Sci. Eng.* 204, 108699. doi:10.1016/j.petrol.2021.108699
- Wang, T., and Lin, B. (2014). Impacts of Unconventional Gas Development on China's Natural Gas Production and Import. *Renew. Sustain. Energy. Rev.* 39, 546–554. doi:10.1016/j.rser.2014.07.103
- Xue, Y., Teng, T., Dang, F., Ma, Z., Wang, S., and Xue, H. (2020). Productivity Analysis of Fractured wells in Reservoir of Hydrogen and Carbon Based on Dual-Porosity Medium Model. *Int. J. Hydrogen Energy.* 45 (39), 20240–20249. doi:10.1016/j.ijhydene.2019.11.146
- Yang, D. S., Qi, X. Y., Chen, W. Z., Wang, S. G., and Yang, J. P. (2018). Anisotropic Permeability of Coal Subjected to Cyclic Loading and Unloading. *Int. J. Geomech.* 18 (8), 04018093. doi:10.1061/(asce)gm.1943-5622.0001229
- Yang, Z., Qin, Y., Yi, T., Tang, J., Zhang, Z., and Wu, C. (2019). Analysis of Multi-Coalbed CBM Development Methods in Western Guizhou, China. *Geosci. J.* 23 (2), 315–325. doi:10.1007/s12303-018-0037-9
- Yi, T., Zhang, J., and Li, X. (2007). Development Geology Assessment on Coalbed Methane in Panguan Syncline of Liupanshui Coal Field. *Nat. Gas Industry* 27 (5), 29–31.
- Zhang, X., Liu, W., Jiang, D., Qiao, W., Liu, E., Zhang, N., et al. (2021). Investigation on the Influences of Interlayer Contents on Stability and Usability of Energy Storage Caverns in Bedded Rock Salt. *Energy* 231, 120968. doi:10.1016/j.energy.2021.120968
- Zhang, Z., Jiang, D., Liu, W., Chen, J., Li, E., Fan, J., et al. (2019). Study on the Mechanism of Roof Collapse and Leakage of Horizontal Cavern in Thinly Bedded Salt Rocks. *Environ. Earth Sci.* 78 (10), 292. doi:10.1007/s12665-019-8292-2
- Zheng, M., Li, J., Wu, X., Wang, S., Guo, Q., Yu, J., et al. (2018). China's Conventional and Unconventional Natural Gas Resources: Potential and Exploration Targets. *J. Nat. Gas Geosci.* 3 (6), 295–309. doi:10.1016/j.jnggs.2018.11.007
- Zhong, D., Liu, Y., Kang, X., and Gao, L. (2016). Analysis and the Prevention Advice of Gas Accidents of Guizhou Province Coal Mines 2007–2015. *Coal Eng.* 48 (11), 69–72.
- Zhou, P., Liu, W., and Li, W. (2009). Effect of Dahebian Syncline on Coal and Gas Outburst. *J. Mining Saf. Eng.* 26 (1), 55–59.
- Zhou, S. (2015). Briefly Introduce of Coal Bed Methane Resources Estimation. *Acta Geologica Sinica - English Edition* 89 (s1), 230. doi:10.1111/1755-6724.12304_4
- Zhou, X., Sang, S., Jin, J., Sun, H., and Hou, D. (2015). Study on Estimation Methods of Abandoned Mine Methane Resources in Coal Resources-Exhausted Mines. *China Coalbed Methane* 15 (1), 3–6.

Conflict of Interest: The authors declare that the research was conducted in the absence of any commercial or financial relationships that could be construed as a potential conflict of interest.

Publisher's Note: All claims expressed in this article are solely those of the authors and do not necessarily represent those of their affiliated organizations, or those of the publisher, the editors and the reviewers. Any product that may be evaluated in this article, or claim that may be made by its manufacturer, is not guaranteed or endorsed by the publisher.

Copyright © 2022 Zhao and Wei. This is an open-access article distributed under the terms of the Creative Commons Attribution License (CC BY). The use, distribution or reproduction in other forums is permitted, provided the original author(s) and the copyright owner(s) are credited and that the original publication in this journal is cited, in accordance with accepted academic practice. No use, distribution or reproduction is permitted which does not comply with these terms.



Experimental Study on Strength and Permeability Characteristics of Cemented Rock-Tailings Backfill

Huafu Qiu^{1,2}, Fushun Zhang^{1,2}, Weibo Sun^{1,2}, Lang Liu^{1,2*}, Yujiao Zhao^{1,2} and Chao Huan^{1,2}

¹School of Energy Engineering, Xi'an University of Science and Technology, Xi'an, China, ²Key Laboratory of Western Mines and Hazards Prevention, Ministry of Education of China, Xi'an, China

OPEN ACCESS

Edited by:

Jie Chen,
Chongqing University, China

Reviewed by:

Guimin Zhang,
China University of Mining and
Technology, China
Junbao Wang,
Xi'an University of Architecture and
Technology, China
Jinyang Fan,
Chongqing University, China

*Correspondence:

Lang Liu
csuliulang@163.com

Specialty section:

This article was submitted to
Geohazards and Georisks,
a section of the journal
Frontiers in Earth Science

Received: 27 October 2021

Accepted: 10 January 2022

Published: 14 February 2022

Citation:

Qiu H, Zhang F, Sun W, Liu L, Zhao Y
and Huan C (2022) Experimental Study
on Strength and Permeability
Characteristics of Cemented Rock-
Tailings Backfill.
Front. Earth Sci. 10:802818.
doi: 10.3389/feart.2022.802818

To study the strength and permeability characteristics of cemented tailings backfill with different cement–sand ratios and different waste rock contents, uniaxial compression strength test and permeability test were carried out respectively. The porosity of cemented tailings backfills after solidification was observed by scanning electron microscope. The effects of cement–sand ratio and waste rock content on the internal porosity and overall permeability of cemented tailings backfill were studied. The test results showed that the cement–sand ratio and waste rock content have certain effects on the strength and permeability of the backfill body. When the cement–sand ratio was fixed, the uniaxial compressive strength and permeability of the backfill body increased first and then decreased with the increase of waste rock content. When the waste rock content was 10%, the uniaxial compressive strength of the backfill body reached the maximum, and when the waste rock content was 30%, the permeability reached the maximum. Due to the increase of the area of waste rock particles in the cross-section, the area of gas passing rapidly decreased, resulting in the decrease of the permeability growth rate. When the waste stone content was fixed, with the decrease of cement–sand ratio, due to the decrease of cementitious materials, more micro-cracks were produced in the curing process of backfill body, resulting in the decrease of uniaxial compressive strength and the increase of permeability.

Keywords: cemented tailings backfill, waste rock, uniaxial compression strength, permeability, scanning electron microscope

1 INTRODUCTION

Backfill mining is an important development direction for safe and green mining in China. The use of solid waste generated in the mining process to fill the goaf can effectively control the deformation and damage of the surrounding rock in the goaf, and prevent the surface subsidence, which can not only ensure the safety of stope but also make full use of the solid waste of mines. It has significant advantages in safe mining, solid waste treatment, environmental protection, and so on (Zhang et al., 2018; Qi and Fourie, 2019; Qi, 2020; Yin et al., 2019; Dong et al., 2019; Liu JG et al., 2020). As the main unit of backfill mining, cement tailings backfill took the solid waste generated in the process of mining as aggregate and cement as cementing material. According to a certain ratio, water was added to fully mix into an appropriate concentration of paste, which was sent into the mine through the pipeline. After solidification, it can be used as an artificial pillar to bear the ground stress in the stope; therefore, its mechanical stability was crucial to the safety of the stope (Zhang et al., 2011a; Zhang

et al., 2011b; Lin et al., 2013; Hong et al., 2021; Li et al., 2021b; Li et al., 2021c). In addition, the backfill is a porous medium, and the permeation characteristic is also an important quality index of the backfill (Wang et al., 2009). Permeability refers to the degree of difficulty of gas, liquid, or ion permeating, diffusing, or migrating into the specimen under the action of gradient such as pressure concentration. The pores in the backfill are the main path of the permeable medium, the transmission speed of harmful substances in the backfill is directly determined by the permeability, and this kind of permeable medium will have a certain influence on the performance of backfill body. Therefore, permeability is a key judgment index of the durability of the backfill (Yang and Zhu, 2003; Liu et al., 2005; Deng et al., 2006; Shi et al., 2021). The material of the backfill is mostly mine solid waste, and the tailings from the concentrator are mainly used as the aggregate. In the process of mineral processing, agents are usually added, so there will be excessive pollution substances in the tailings. Tailings particles produced by metal mines may contain radioactive components and heavy metal ions such as lead, copper, and zinc ions (Yuan and Xu, 2004; Xu et al., 2008; Zhong et al., 2020; Yao et al., 2021). Therefore, the permeability characteristics of the backfill will be related to whether these harmful substances will flow out with the water seepage of the backfill, resulting in the pollution of the underground environment and even underground water. The permeation characteristics of the backfill are studied to understand its change rule, to better design and prepare the environment-friendly and high-durability underground backfill artificial pillar.

Chen et al. (2019) conducted experiments on the permeability characteristics of coal rocks filled with pulverized coal with different air pressures and different crack widths, and studied the variation law of the permeability of coal rocks filled with pulverized coal with different particle sizes under the influence of pressure and crack widths. Wang et al. (2010) combined electron microscope photos of artificial sediment filling pores of the rock fracture and rock seepage experiments, and discussed the sediment particles' influence law of fractured rock permeability characteristics; they concluded that rock permeability under the effect of sediment particles significantly decreased, and when sediment particles migrated into the fracture after balance, rock permeability increased gradually and tends to be stable. Qiu et al. (2020) and Qiu et al. (2021) studied the microstructure characteristics of the cemented rock-tailings backfill and its influence on the strength. Wu et al. (2015) studied the influence of different initial temperatures of backfill, cement-sand mass ratio, and curing temperature on the seepage characteristics of backfill through numerical simulation, and concluded that the permeability of backfill decreases with the increase of curing temperature and cement-sand mass ratio. Wang and Xu (2018) carried out constant head permeability test and variable head permeability test for filling materials with different cement-sand ratios and different cement-cement agents. They studied cement-sand ratio, cement-cement composition, and permeability variation characteristics of filling slurry after gradually solidifying, and discussed the influence relationship between the permeability of backfill and the content of cementing material. Scholars have studied the strength

characteristics of rock materials and reported relevant results (Fan et al., 2019; Zhu et al., 2019; Fan et al., 2020; Li et al., 2021a). Scholars have studied the permeability characteristics of rock materials and reported the experimental results of influencing factors (Chao et al., 2017; Zhang et al., 2020; Liu et al., 2020a; Liu et al., 2020b). But so far, there are few research reports on the permeability characteristics of cemented tailings backfill. Permeability characteristics of the backfill are aggregate composition, cement-sand ratio, and other factors; considering the impact of filling strength on the stability of feature, waste rock added to the aggregate particles can effectively improve the strength of backfill and better meet the needs of the filling (Fu et al., 2014; Ge et al., 2014; Lu et al., 2017), and the addition of waste rock particles has a certain influence on the infiltration characteristics of backfill. Therefore, this article conducted gas permeability tests on cemented tailings backfill with different cement-sand ratios and different waste rock contents, and analyzed the influence of cement-sand ratios and waste rock contents on the permeability characteristics of backfill.

2 EXPERIMENTAL PROGRAMS AND METHODS

All tests mainly included backfill specimen preparation, UCS test, permeability test, and SEM test. The overall process of the test is shown in **Figure 1**.

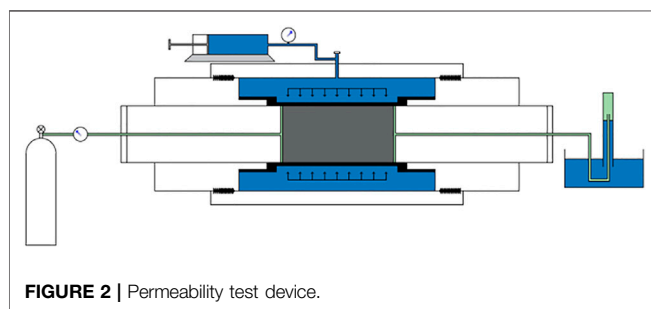
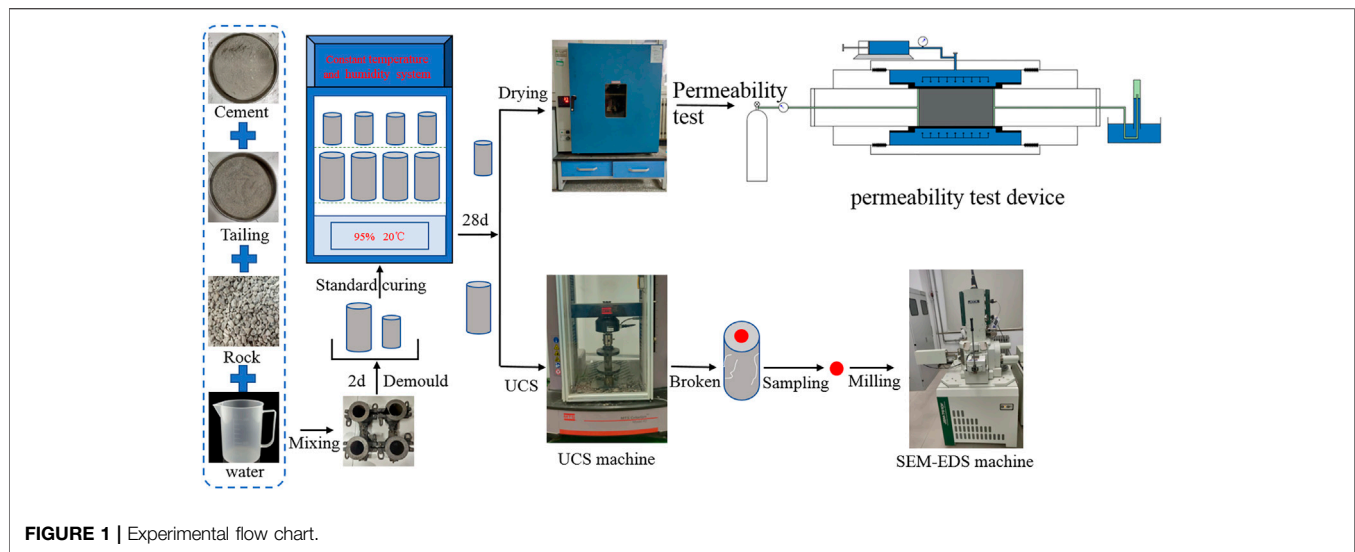
2.1 Specimen Preparation

Tailings from a mine in Shaanxi Province and waste rock particles with a particle size of 3–5 mm were selected as aggregate, and ordinary Portland cement was used as cementing material. Cemented tailings backfill with different proportions were prepared according to a certain proportion. The cement-sand ratios are 1:4, 1:6, and 1:8; the waste rock contents are 0%, 10%, 20%, 30%, and 40%; and the material concentration is 76%. According to the designed material ratio, quantitative tailing, waste rock, and cement were weighed and mixed fully, and water was added quantitatively to mix them evenly. The samples were loaded into the cylindrical cast-iron test mold three times. After standing for 48 h, the surface of the specimen was scraped flat and demolded.

According to the requirements of two test systems for specimen size, 15 cylindrical specimens with a diameter of 50 mm and a height of 100 mm were prepared for the uniaxial compressive strength test, and 15 cylindrical specimens with a diameter of 25 mm and a height of 50 mm were prepared for the permeability test. The specimens were marked and placed into the curing box with constant temperature and humidity for curing (temperature of the curing box was $20 \pm 1^\circ\text{C}$, the humidity was $95 \pm 1\%$). When the curing period reached 28 days, the waste rock cemented tailings backfill specimen was taken out.

2.2 Uniaxial Compression Strength Test

A standard specimen ($\phi 50 \text{ mm} \times 100 \text{ mm}$) with a curing period of 28 days was taken out, and both ends of the specimen were polished to ensure that the two ends of the specimen were smooth



and flat. After treatment, the specimens were subjected to the uniaxial compression strength test. The uniaxial press was used as MTS rock mechanical loading system in the test, and the constant displacement loading mode with a loading rate of 1 mm/min was used to load the specimens until they were destroyed.

2.3 Permeability Test

2.3.1 Permeability Test Device

This experiment using the gas penetration testing device is shown in **Figure 2**. The whole device was composed of three parts: the left side inlet section; a black rubber middle holster package part for hydraulic confining pressure region into the specimen by its surrounding space with water, fully squeezing the rubber holster package backfill specimen and providing the confining pressure; and the right end tank that adopts the inverted cylinder method for gas collection and recording. The permeation medium selected in this experiment was nitrogen.

2.3.2 Air Tightness Inspection

Before the test, the prepared test piece was put in to check the whole device, first turning the confining pressure push water knob for pressurization, observing whether the confining pressure gauge is stable, checking whether there is water leakage at both ends, and determining whether there is rupture damage inside the device's black rubber leather. Then the nitrogen cylinder knob was opened

to check the unblocked test pipeline and airtightness. It is important to ensure that the black rubber plant holster is not ruptured, and the pipe flow is steady and airtight according to the strength of the specimens; to set the test gas inlet pressure in the process of choosing the appropriate confining pressure, the confining pressure should be greater than the test air inlet pressure to ensure that there will be no damage to the specimen during the test and that there is enough tightness.

2.3.3 Specimen Preparation

The small specimens ($\phi 25 \text{ mm} \times 50 \text{ mm}$) were taken out from the curing box for grinding to ensure the flatness of both ends of the specimen and the smoothness of the cylinder to avoid gas passing through the specimen and affecting the accuracy of permeability due to the uneven contact surface or the loose wrapping of the black rubber sleeve around the specimen in the test process. The polished specimens were placed in a drying oven for drying for 24 h to ensure that all specimens were fully dried.

2.3.4 Test Steps

According to the uniaxial compression strength test, the minimum uniaxial compressive strength of the backfill specimen was 0.684 MPa. To ensure that the specimen in the test process will not be destroyed and affect the test results, the confining pressure was set to 0.8 MPa and the air inlet pressure was set to 0.1 MPa. Before the test, the diameter and length of the dried specimen were measured and recorded with Vernier calipers. After the measurement, the specimen was put into the device for permeability test in accordance with the marked order. After placing the specimen in the center of the device, the water injection knob was slowly rotated to adjust the confining pressure to 0.8 MPa. After the confining pressure was stabilized, the cylinder was opened to adjust the inlet pressure and slowly adjust the inlet pressure to 0.1 MPa. After the pressure gauge was stable, the outlet pipe was inserted into the measuring cylinder in the water tank for gas collection, and timing was started. Then 10 ml of gas was collected through the measuring cylinder, the time consumed was

TABLE 1 | Permeability test data of samples with different waste rock contents with cement–sand ratio of 1:4.

No	Backfill length (mm)	Backfill diameter (mm)	Time (s)	Flow rate (mm ³ /s)	Permeability (md)	Average value
Q1	4.983	2.504	27.37	0.490918017	4.32242503	4.310190499
	4.983	2.504	27.46	0.48972415	4.308258306	
	4.983	2.504	27.37	0.491877309	4.32242503	
	4.983	2.504	27.62	0.490439772	4.28330098	
	4.983	2.504	27.42	0.492599243	4.314543147	
Q2	5.006	2.498	15.70	0.641320288	7.606525991	7.554918172
	5.006	2.498	15.74	0.639690503	7.587195556	
	5.006	2.498	15.72	0.640504359	7.596848477	
	5.006	2.498	15.96	0.630872714	7.482610154	
	5.006	2.498	15.92	0.632457822	7.501410682	
Q3	4.958	2.459	13.82	0.728562122	8.83204861	8.844898813
	4.958	2.459	13.76	0.731738991	8.87056045	
	4.958	2.459	13.85	0.726984009	8.812917819	
	4.958	2.459	13.77	0.731207591	8.864118503	
	4.958	2.459	13.80	0.729618009	8.844848681	
Q4	4.952	2.47	11.78	0.854730774	10.25702627	10.23981506
	4.952	2.47	11.73	0.858374128	10.30074761	
	4.952	2.47	11.86	0.848965305	10.18783891	
	4.952	2.47	11.78	0.854730774	10.25702627	
	4.952	2.47	11.85	0.849681732	10.19643624	
Q5	4.988	2.849	16.64	0.605091858	7.202833212	7.11643458
	4.988	2.849	17.19	0.585731735	6.97237607	
	4.988	2.849	16.80	0.599329079	7.1342348	
	4.988	2.849	16.78	0.600043416	7.14273806	
	4.988	2.849	16.81	0.598972547	7.129990758	

recorded, and the permeability of the backfill specimen was calculated with the following calculation formula:

$$K = \frac{Q \times L \times \mu}{\Delta P \times A} \quad (1)$$

where Q —the flow rate of permeable medium through specimen per unit time (cm³/s), μ —the viscosity of the permeable medium (Pa·s), L —length of specimen (cm), ΔP —the pressure difference of the permeable medium before and after passing the specimen (MPa), and A —the cross-sectional area through which the permeable medium passes (cm²).

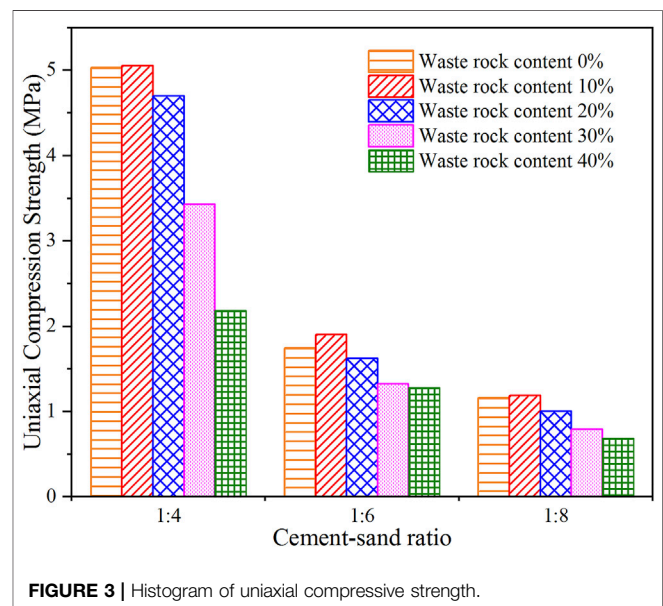
2.3.5 Data Results

Due to the length of the article, **Table 1** shows the data of permeability test for waste rock content with a cement–sand ratio of 1:4. As can be seen from the table, the lowest permeability of the sample with a 1:4 cement–sand ratio of whole tailings was 4.31 md. With the increase of waste rock content, the permeability of the sample gradually increased. When the waste rock content reached 30%, the permeability was 10.24 md, which was the highest value. When waste rock particles were added to 40%, it was found that the permeability decreased at this time.

3 RESULTS AND DISCUSSION

3.1 Uniaxial Compression Strength Characteristics

The histogram of uniaxial compressive strength of backfill was drawn, as shown in **Figure 3**. It can be seen from the figure that,

**FIGURE 3** | Histogram of uniaxial compressive strength.

with the increase of waste rock content, the uniaxial compressive strength of the three cement–sand ratios of backfill body increased first and then decreased. Among the five waste rock content ratios designed, the strength of backfill body reached the highest when the waste rock content reached 10%. With the decreased of cement–sand ratio, the strength of the backfill decreased gradually.

When the cement–sand ratio was constant, adding a small amount of waste stone particles with large particle size can reduce

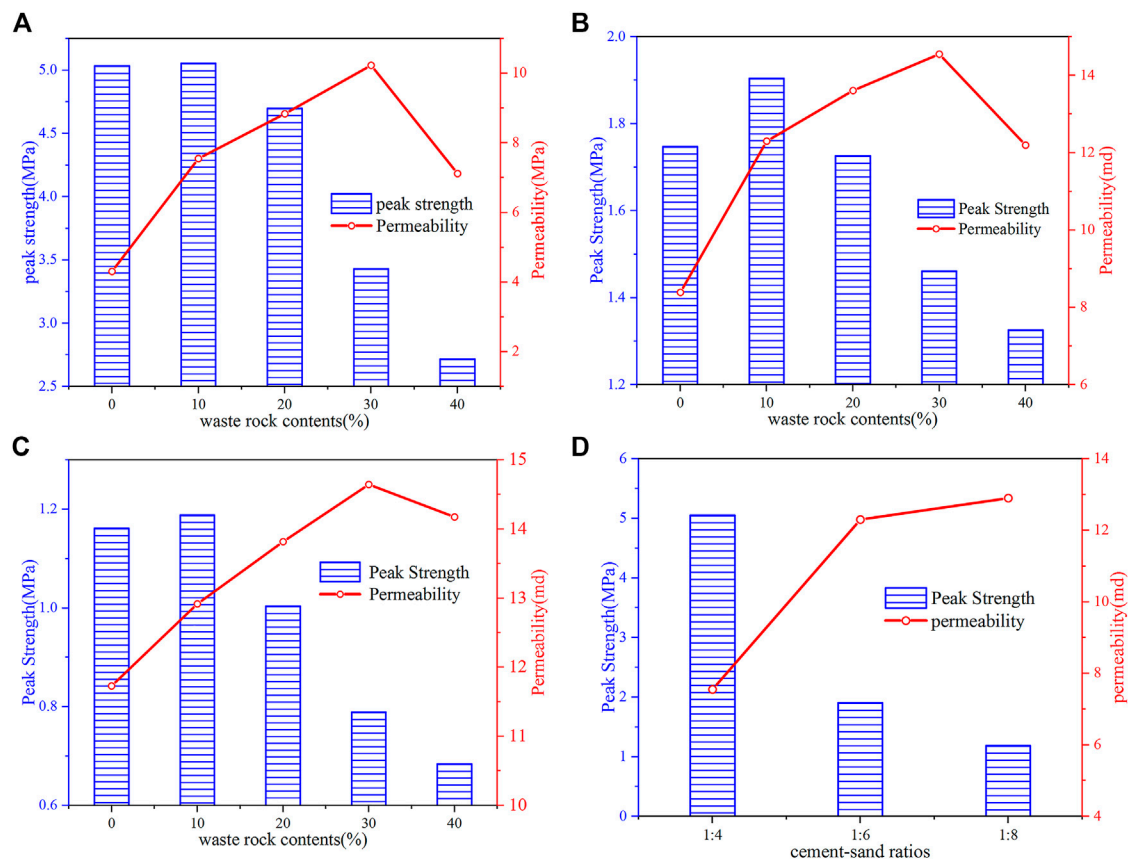


FIGURE 4 | Strength histogram and permeability curve: (A) cement-sand ratio 1:4; (B) cement-sand ratio 1:6; (C) cement-sand ratio 1:8; (D) waste rock content 10%.

the specific surface area of aggregate. In contrast, the content of cementitious materials per unit area increased, and the gelation effect was improved. Moreover, the waste rock particles fully wrapped by cement can prevent the propagation and coalescence of cracks in the specimen under uniaxial compression, effectively inhibiting the growth of cracks in the backfill body during uniaxial compression, thereby improving its uniaxial compressive strength.

The waste rock particles continue to increase due to the increase of large particle aggregates; cement cannot fully cover all waste stone particles because after solidification, there were more primary pores, thus forming a low strength area. In the process of uniaxial compression strength test, the region was more prone to cracks, and more likely to expand, resulting in the decrease of uniaxial compressive strength of the backfill body.

When the waste stone content of the backfill body was constant, the uniaxial compressive strength and stability of the backfill body decreased significantly with the continuous decrease of the cement-sand ratio. The smaller the cement-sand ratio, the more direct is the decrease of the cement content in the slurry. The gelling effect of the backfill body in the curing process was decreased, and the uniaxial compressive strength decreased after curing.

3.2 Permeability Characteristics

3.2.1 Influence of Waste Rock Content on Permeability Characteristics

The uniaxial compressive strength and permeability of backfill with different waste rock contents and cement-sand ratios were drawn, as shown in Figure 4. According to Figure 4, the permeability variation curve of backfill body was analyzed by referring to the uniaxial compressive strength histogram. When the cement-sand ratio of the backfill body was fixed, the permeability of the three cement-sand ratios of backfill body changed in a similar trend with the increase of waste rock content, which all increased first and then decreased with the increase of waste rock content in the specimen.

The surface of the dirt particles was smoother and the waste rock particle size was larger when adding a certain amount of waste rock filling pulp after particles, filling materials in the process of solidification, and backfilling particles with waste rock particles formed between contact cementation or pore type cementation; backfilling of cementation effect between the particle and dirt particles was reduced, and the specimen within the pore content increased. In the permeability test, these pores greatly shorten the permeability path of the permeable gas in the backfill body, resulting in the improvement of the gas

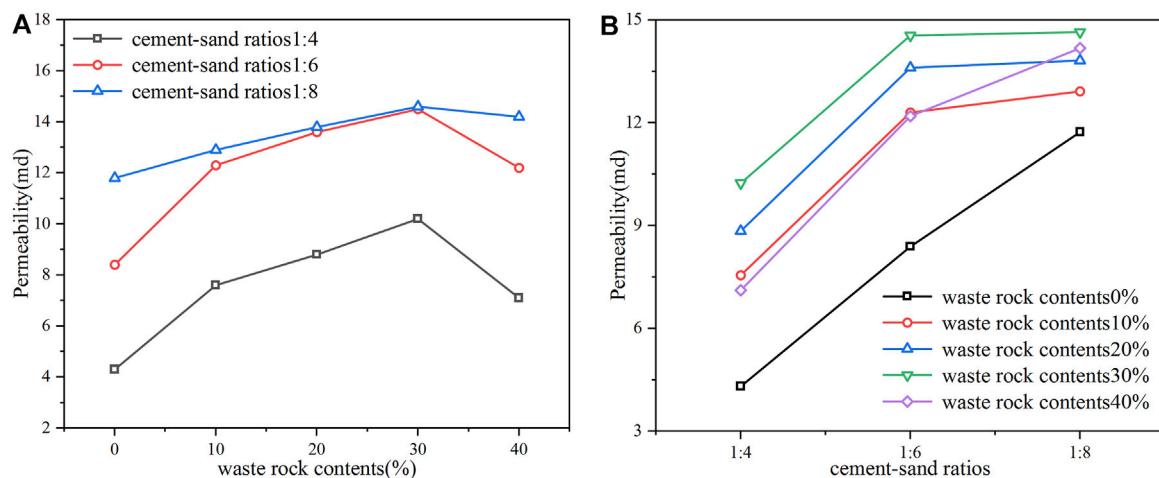


FIGURE 5 | Permeability fluctuation curve: **(A)** different waste rock contents; **(B)** different cement-sand ratios.

permeability of the whole specimen. As the waste rock content continues to increase, the tailings particles and cementing materials between waste rock particles become less and less, and the pores formed between waste rock particles became more and more, and the permeability of backfill body became more and more.

When the waste rock content was too much, the waste rock particles occupy a large area in the cross-section of the backfill body, and the cross-sectional area of the cemented tailings for rapid passage of gas decreases. Moreover, the permeability of waste rock particles was far less than that of whole tailings cemented backfill, and there were more waste rock particles that need to be permeated by gas per unit area, leading to a decrease in the permeability of the backfill body. However, waste rock particles lead to a large increase in primary pores inside the backfill body, so the permeability was still higher than that of whole tailings.

3.2.2 Influence of the Change of the Material Ratio on Permeability Characteristics

Dot-line diagrams with different waste rock contents and different lime-sand permeabilities were drawn, as shown in **Figure 5**. It can be seen from **Figure 5A** that the permeability growth rate of the backfill body decreased with the increase of the waste rock content.

This was due to the increase of waste rock particles in the backfill body, resulting in more primary pores that formed during the solidification process, which promotes the increase of the permeability of the backfill body. However, as waste rock particles increase, the area occupied by waste rock particles in the cross-section increases, and the cross-sectional area of the tailings cemented part through which gas can pass quickly decreases, which had a certain inhibitory effect on the increase in permeability. Under the combined effect of the two, the growth rate of the permeability of the backfill body showed a downward trend.

Observing **Figure 5B**, it can be found that when the content of waste rock was the same, with the decrease of cement-sand ratio, the increase rate of permeability of backfill body decreases. After adding waste rock particles, when the cement-sand ratio decreased from 1:6 to 1:8, the permeability change rate of the specimen decreased obviously.

With the decrease of cement-sand ratio, the cement content in the backfill body decreased directly. The decrease of cement content made it insufficient to completely encapsulate the granular aggregate, and the cementing effect decreases, resulting in more primary pores in the curing process. In the case of whole tailings, the permeability of backfill body was directly affected by cement content. After the waste rock particles were added, the content of primary pores was greater. However, due to the waste rock particles occupying a certain cross-sectional area in the backfill body, the area available for rapid passage of gas in the cross-sectional area was reduced, so it had a certain inhibitory effect on gas permeability. Under the dual effect of the increased of primary pores and waste rock particles, the increase rate of permeability of the backfill body decreased.

4 SCANNING ELECTRON MICROSCOPY ANALYSIS

The schematic diagram of the internal pores and cracks of the cemented rock-tailings backfill with different cement-sand ratios was drawn, as shown in **Figure 6**. When the cement-sand ratio was 1:4, the cement content in the backfill body was sufficient, and the larger waste rock particles can be fully wrapped. Only a few small pores were generated during the curing process; with the decrease of cement-sand ratio, the cement content in the backfill body was less and less, the wrapping effect on the larger waste rock particles was gradually weakened, and it was easy to form larger pores or even micro-cracks during the curing process. The pores and micro-cracks in the backfill body greatly shorten

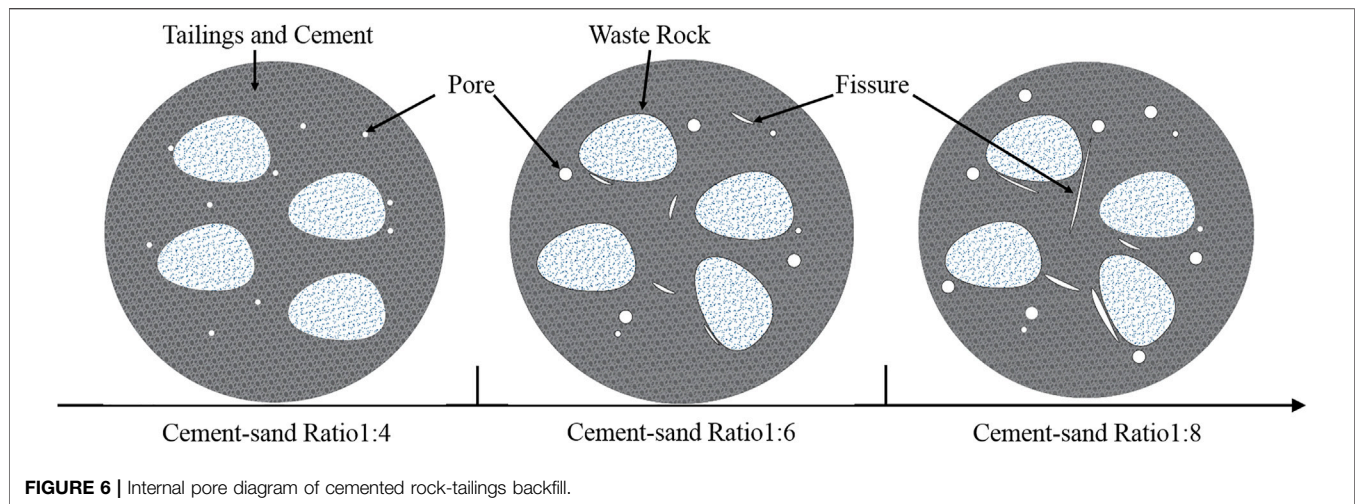


FIGURE 6 | Internal pore diagram of cemented rock-tailings backfill.

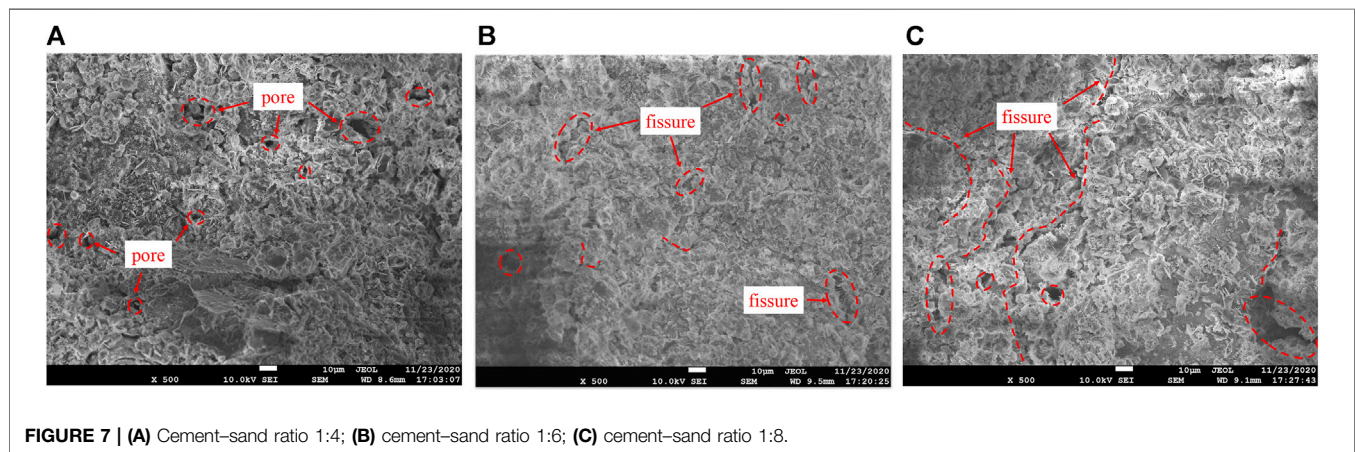


FIGURE 7 | (A) Cement-sand ratio 1:4; (B) cement-sand ratio 1:6; (C) cement-sand ratio 1:8.

the gas penetration path, which was the main influencing factor of its permeability change. To explore the changes of pore structure in the backfill body of this test, the microstructure was observed by scanning electron microscopy.

The backfill body specimens with different cement-sand ratios of 10% waste rock content were placed in alcohol solution to inhibit hydration. A small sample was cut from the core and scanned by scanning electron microscope. The pore condition was observed at $\times 500$ magnification when taking images. The existence of pores in the specimen was observed by photographs as shown in **Figure 7**.

It can be seen from **Figure 7A** that when the cement-sand ratio was 1:4, the pore diameter and the number of solidified backfill bodies were small, and there were only individual larger pores; when the cement content was reduced to 1:6, it can be seen from **Figure 7B** that there were not only larger diameter pore structures in the backfill body but also individual banded cracks; when the cement content was further reduced to 1:8, it can be seen from **Figure 7C** that the internal pore structure of the backfill body was greater, and the diameter was larger. There were long strip cracks, and some cracks were even connected.

When the cement-sand ratio was 1:4, the cement content in the filling material was greater, which can fully cover the aggregate particles, and the overall cementing effect was better in the curing process, so the internal pores were fewer, and the permeability of the backfill body was also low.

When the cement-sand ratio was 1:6, due to the decrease of the cement content of the cementitious material, it was not enough to fully encapsulate the tailings particles, and the overall cementing effect decreases. Contact cementation begins to form between particles, and cracks begin to appear in the curing process. The formation of pore structure and micro-cracks in the backfill body greatly improved the permeability of the specimen.

When the cement-sand ratio was 1:8, the further reduction of the cementitious material makes the granular tailings of the backfill body unable to be wrapped by the cementitious material in the curing process. During the curing process, the contact cementation or pore cementation was formed between the aggregate particles, and the aggregate particles cannot be closely connected, resulting in the further increase of the original pores and micro-cracks in the curing process of the backfill body. These cracks greatly shorten the gas permeability path inside the filling material, and the gas permeability of the backfill body was improved.

5 CONCLUSION

In this paper, backfill samples with different lime–sand ratios and waste stone contents were designed and obtained. The strength and permeability characteristics of the backfill were studied by uniaxial compression and gas permeability tests. The microstructure was observed and analyzed by SEM test, and the formation of pores in the backfill was observed to explain its permeability characteristics. Based on the results and discussion, the following conclusions were summarized.

- 1) When the cement–sand ratio was constant, the uniaxial compressive strength of backfill increased first and then decreased with the increase of waste rock content. Adding an appropriate amount of waste rock particles reduced the specific surface area of solid materials in the backfill body, increased the cement content per unit area, and improved the strength of the backfill body. When the amount of waste rock was too large, the cementation between waste rock particles was weakened and the strength was decreased.
- 2) When the waste rock content was constant, the uniaxial compressive strength of backfill body increased with the increase of cement–sand ratio. The larger the cement–sand ratio was, the higher the cement content in the backfill was, and the aggregate particles can be fully coated, the cementation effect was good, and the uniaxial compressive strength was greater.
- 3) When the cement–sand ratio was constant, with the increase of waste rock content, more micro-cracks were formed in the solidification process of backfill, which greatly shorten the permeability path of permeable medium in backfill, and the permeability increased gradually. With the increase of waste rock content in backfill, the number of waste rock particles per unit cross-sectional area increased, which inhibited gas permeability, so the permeability begins to decrease.
- 4) The increase of waste rock particles will reduce the growth rate of permeability. The increase of waste rock content led to the increase of primary porosity, which led to the increase of permeability. When the waste rock content was too large, the area of waste rock on the cross-section increased, and the area of gas fast passage decreased, which inhibited the increase of permeability.
- 5) The primary porosity in the backfill body was the main influencing factor of its permeability. Through SEM test, due to the decrease of cement–sand ratio, the cementation effect of backfill decreased, the content of primary pores increased, and the permeability increased.

DATA AVAILABILITY STATEMENT

The raw data supporting the conclusion of this article will be made available by the authors, without undue reservation.

AUTHOR CONTRIBUTIONS

HQ: methodology, conceptualization, supervision, writing—original draft. FZ: methodology, writing—review and editing, data curation. WS: validation, resources. LL: investigation, formal analysis. YZ: validation, formal analysis. CH: review and editing.

FUNDING

This work was supported and financed by the Natural Science Fund (Nos. 51904225, 52074212, 52004207, 52104148), the Natural Science Foundation of Shaanxi Province (No. 2020JQ-748), and Scientific Research Project of Youth Innovation Team Construction of Shaanxi Provincial Department of Education (No. 21JP077), all of which are greatly appreciated.

REFERENCES

- Chao, Z. M., Wang, H. L., Xu, W. Y., Yang, L. L., and Zhao, K. (2017). Variation of Permeability and Porosity of Sandstones with Different Degrees of Saturation under Stresses. *Chin. J. Rock Mech. Eng.* 36 (003), 665–680. doi:10.13722/j.cnki.jrme.2016.0063
- Chen, J. G., Zheng, Z. S., and Zhang, L. (2019). Seepage Characteristics of Fractures in Coal Rock Filled with Pulverized Coal under Confining Pressure. *Saf. Coal Mines* 50 (12), 14–17. doi:10.13347/j.cnki.mkaq.2019.12.004
- Deng, D. Q., Yao, Z. L., and Yang, Y. Y. (2006). Study on Permeability of High-Density Slurry Material of Cement-Tailing Backfill. *Nonferrous Met.* 058 (002), 87–90. doi:10.3969/j.issn.2095-1744.2006.02.023
- Dong, L., Tong, X., Li, X., Zhou, J., Wang, S., and Liu, B. (2019). Some Developments and New Insights of Environmental Problems and Deep Mining Strategy for Cleaner Production in Mines. *J. Clean. Prod.* 210, 1562–1578. doi:10.1016/j.jclepro.2018.10.291
- Fan, J., Jiang, D., Liu, W., Wu, F., Chen, J., and Daemen, J. (2019). Discontinuous Fatigue of Salt Rock with Low-Stress Intervals. *Int. J. Rock Mech. Mining Sci.* 115 (3), 77–86. doi:10.1016/j.ijrmms.2019.01.013
- Fan, J., Liu, W., Jiang, D., Chen, J., Tiedeu, W. N., and Daemen, J. J. K. (2020). Time Interval Effect in Triaxial Discontinuous Cyclic Compression Tests and Simulations for the Residual Stress in Rock Salt. *Rock Mech. Rock Eng.* 53, 4061–4076. doi:10.1007/s00603-020-02150-y
- Fu, J. X., Du, C. F., and Song, W. D. (2014). Strength Sensitivity and Failure Mechanism of Full Tailings Cemented Backfills. *J. Univ. Sci. Techn. Beijing* 36 (9), 1149–1157. doi:10.13374/j.issn1001-053x.2014.09.004
- Ge, H. Y., Chen, C., Li, H. B., Wang, S., Zhou, J., and Jing, B. X. (2014). Experiment on the Law of Strength Increasing of Ultrafine Tailings Filling Body. *Mod. Mining* 7, 10–13. doi:10.3969/j.issn.1674-6082.2014.07.004
- Hong, W., Sun, G. H., and Liang, S. B. (2021). Study on Synergetic Mechanism of Ore Pillar-Filling Body System. *Metal Mine* 03, 40–45. doi:10.19614/j.cnki.jsks.202103006
- Li, X., Peng, K., Peng, J., and Hou, D. (2021a). Effect of thermal Damage on Mechanical Behavior of a fine-grained sandstone. *Arab. J. Geosci.* 14, 1212. doi:10.1007/s12517-021-07607-0
- Li, X., Yang, S., Wang, Y., Nie, W., and Liu, Z. (2021b). Macro-micro Response Characteristics of Surrounding Rock and Overlying Strata towards the Transition from Open-Pit to Underground Mining. *Geofluids* 2021, 1–18. doi:10.1155/2021/5582218
- Li, X., Liu, Z., and Yang, S. (2021c). Similar Physical Modeling of Roof Stress and Subsidence in Room and Pillar Mining of a Gently Inclined Medium-Thick Phosphate Rock. *Adv. Civil Eng.* 2021, 1–17. doi:10.1155/2021/6686981
- Lin, M., Su, C. Z., and Zhou, X. C. (2013). Stability Analysis on the Cemented Filling Body in Deep Mining Area. *Morden Mining* 29 (1), 42–44. doi:10.3969/j.issn.1674-6082.2013.01.012

- Liu, Z. Y., Sun, W., and Zhou, X. G. (2005). Research on Rapid Testing Method for Gas Diffusion Coefficient of concrete. *Concrete* 11, 3–5. doi:10.3969/j.issn.1002-3550.2005.11.001
- Liu, W., Zhang, X., Fan, J., Zuo, J., Zhang, Z., and Chen, J. (2020a). Study on the Mechanical Properties of Man-Made Salt Rock Samples with Impurities. *J. Nat. Gas Sci. Eng.* 84, 103683. doi:10.1016/j.jngse.2020.103683
- Liu, W., Zhang, Z., Fan, J., Jiang, D., Li, Z., and Chen, J. (2020b). Research on Gas Leakage and Collapse in the Cavern Roof of Underground Natural Gas Storage in Thinly Bedded Salt Rocks. *J. Energ. Storage* 31, 101669. doi:10.1016/j.est.2020.101669
- Liu JG, J. G., Li, X. W., and He, T. (2020). Application Status and prospect of Backfill Mining in Chinese Coal Mines. *J. China Coal Soc.* 45 (1), 141–150. doi:10.13225/j.cnki.jccs.YG19.1063
- Lu, H. J., Liang, P., Gan, D. Q., and Zhang, S. L. (2017). Research on Flow Sedimentation Law of Filling Slurry and Mechanical Characteristics of Backfill Body. *Rock Soil Mech.* 38 (Suppl. 1), 263–270. doi:10.16285/j.rsm.2017.S1.032
- Qi, C., and Fourie, A. (2019). Cemented Paste Backfill for mineral Tailings Management: Review and Future Perspectives. *Minerals Eng.* 144, 106025. doi:10.1016/j.mineng.2019.106025
- Qi, C.-c. (2020). Big Data Management in the Mining Industry. *Int. J. Miner Metall. Mater.* 27, 131–139. doi:10.1007/s12613-019-1937-z
- Qiu, H., Zhang, F., Liu, L., Hou, D., and Tu, B. (2020). Influencing Factors on Strength of Waste Rock Tailing Cemented Backfill. *Geofluids* 2020, 1–7. doi:10.1155/2020/8847623
- Qiu, H., Zhang, F., Liu, L., Huan, C., Hou, D., and Kang, W. (2022). Experimental Study on Acoustic Emission Characteristics of Cemented Rock-Tailings Backfill. *Constr. Build. Mater.* 315, 125278. doi:10.1016/j.conbuildmat.2021.125278
- Shi, J. S., Qian, R. S., Zhang, Y. S., Chen, Y. D., Qian, J. J., and Liu, Z. Y. (2021). Advances in Gas Permeability Test Methods and its Relationships with Durability for Cementitious Materials. *Mater. Rep.* 35 (1), 10. doi:10.11896/cldb.20040016
- Wang, W. N., and Xu, Z. H. (2018). Experimental Research on the Permeability of Cemented Backfill Body. *Mining Res. Develop.* 38 (07), 56–60. doi:10.13827/j.cnki.kyyk.2018.07.012
- Wang, P., Chen, S. E., Chen, Z. Q., and Mao, X. B. (2009). Dynamic Response of Carbon Dioxide Diffusion and Reaction in Porous Cementitious Back-Filling Material. *J. Mining Saf. Eng.* 36 (02), 381–387. doi:10.13545/j.cnki.jmse.2019.02.022
- Wang, G. L., Liu, W. Q., and Tao, Y. (2010). Experimental Study of Permeability in Fractured Sandstone with Sediment Particles. *Mech. Eng.* 32 (5), 14–17. doi:10.6052/1000-0992-lxysj2010-050
- Wu, D., Sun, G. H., and Huang, G. (2015). Experimental and Simulation Study on Seepage Characteristics of Cemented Tailings Backfill. *J. Cent. South Univ.* 46 (03), 1050–1057. doi:10.11817/j.issn.1672-7207.2015.03.036
- Xu, X. C., Xie, Q. Q., Chen, F., Wang, J., and Wu, W. T. (2008). Acid Mine Drainage and Heavy Metal Pollution from Solid Waste in the Tongling Mines, China. *Acta Geol. Sin.* 01, 150–157. doi:10.3321/j.issn:1000-9515.2008.01.015
- Yang, Q. R., and Zhu, B. R. (2003). Testing Methods on the Permeability and Influence Factors of Permeability of Concrete. *Low Temperature Architect. Techn.* 05, 9–12. doi:10.3969/j.issn.1001-6864.2003.05.003
- Yao, H. H., Cai, L. B., Liu, W., Qin, W. Q., Jiao, F., and Yang, C. R. (2021). Current Status and Development of Comprehensive Utilization of Waste Rock in Metal Mines in China. *Chin. J. Nonferrous Met.* 31 (06), 1649–1660. doi:10.11817/j.ysxb.1004.0609.2021-35986
- Yin, S., Shao, Y., Wu, A., Wang, H., Liu, X., and Wang, Y. (2020). A Systematic Review of Paste Technology in Metal Mines for Cleaner Production in China. *J. Clean. Prod.* 247, 119590. doi:10.1016/j.jclepro.2019.119590
- Yuan, X. L., and Xu, K. C. (2004). Advances in Solid Waste Treatment and Disposal Technology for China's Metal Mines. *Metal Mine* 06, 46–49+60. doi:10.3321/j.issn:1001-1250.2004.06.014
- Zhang, J., Zhang, Q., Huang, Y., Liu, J., Zhou, N., and Zan, D. (2011a). Strata Movement Controlling Effect of Waste and Fly Ash Backfillings in Fully Mechanized Coal Mining with Backfilling Face. *Mining Sci. Techn. (China)* 21 (005), 721–726. doi:10.1016/j.mstc.2011.03.003
- Zhang, J., Zhou, N., Huang, Y., and Zhang, Q. (2011b). Impact Law of the Bulk Ratio of Backfilling Body to Overlying Strata Movement in Fully Mechanized Backfilling Mining. *J. Min Sci.* 47 (1), 73–84. doi:10.1134/S1062739147010096
- Zhang, J. X., Zhang, Q., Ju, F., Zhou, N., Li, M., and Sun, Q. (2018). Theory and Technique of Greening Mining Integrating Mining, Separating and Backfilling Indep Coal Resources. *J. China Coal Soc.* 43 (2), 377–389. doi:10.13225/j.cnki.jccs.2017.4102
- Zhang, P. S., Hou, J. Q., Zhao, C. Y., and Li, T. H. (2020). Experimental Study on Seepage Characteristics of Red sandstone with Different Confining Pressure and Different Damage Degree. *Chin. J. Rock Mech. Eng.* 39 (12), 2405–2415. doi:10.13722/j.cnki.jrme.2020.0266
- Zhong, X., Chen, Z., Li, Y., Ding, K., Liu, W., Liu, Y., et al. (2020). Factors Influencing Heavy Metal Availability and Risk Assessment of Soils at Typical Metal Mines in Eastern China. *J. Hazard. Mater.* 400, 123289. doi:10.1016/j.jhazmat.2020.123289
- Zhu, M. B., Cheng, J. Y., Cui, W. X., and Yue, H. (2019). Comprehensive Prediction of Coal Seam Thickness by Using In-Seam Seismic Surveys and Bayesian Kriging. *Acta Geophys.* 67 (4), 825–836. doi:10.1007/s11600-019-00298-y

Conflict of Interest: The authors declare that the research was conducted in the absence of any commercial or financial relationships that could be construed as a potential conflict of interest.

Publisher's Note: All claims expressed in this article are solely those of the authors and do not necessarily represent those of their affiliated organizations, or those of the publisher, the editors, and the reviewers. Any product that may be evaluated in this article, or claim that may be made by its manufacturer, is not guaranteed or endorsed by the publisher.

Copyright © 2022 Qiu, Zhang, Sun, Liu, Zhao and Huan. This is an open-access article distributed under the terms of the Creative Commons Attribution License (CC BY). The use, distribution or reproduction in other forums is permitted, provided the original author(s) and the copyright owner(s) are credited and that the original publication in this journal is cited, in accordance with accepted academic practice. No use, distribution or reproduction is permitted which does not comply with these terms.



Study on Mechanical Properties of Shale Under Different Loading Rates

Yuanlong Wei^{1,2}, Lingyun Zhao^{1,2*}, Tao Yuan³ and Wei Liu^{3*}

¹Key Laboratory of Unconventional Natural Gas Evaluation and Development in Complex Tectonic Areas, Ministry of Natural Resources, Guiyang, China, ²Guizhou Research Institute of Oil and Gas Exploration and Development Engineering, Guiyang, China, ³Department of Mining Engineering, Chongqing University, Chongqing, China

OPEN ACCESS

Edited by:

Jie Chen,
Chongqing University, China

Reviewed by:

Tianshou Ma,
Southwest Petroleum University,
China
Huafu Qiu,
Xi'an University of Science and
Technology, China
Shi Xilin,
Institute of Rock and Soil Mechanics
(CAS), China

*Correspondence:

Lingyun Zhao
517543239@qq.com
Wei Liu
guarenliuwei@126.com

Specialty section:

This article was submitted to
Geohazards and Georisks,
a section of the journal
Frontiers in Earth Science

Received: 15 November 2021

Accepted: 03 December 2021

Published: 15 February 2022

Citation:

Wei Y, Zhao L, Yuan T and Liu W (2022)
Study on Mechanical Properties of
Shale Under Different Loading Rates.
Front. Earth Sci. 9:815616.
doi: 10.3389/feart.2021.815616

In the process of shale gas development, different drilling, hydro-fracturing, and pumping speeds will produce different productivity effects. This reflects the effect of the loading rate of rock mechanics. Therefore, it is of great scientific significance to study the deformation and failure characteristics of shale under different loading rates. In order to reveal the loading rate effect of the Longmaxi shale, a series of laboratory experiments were carried out, including scanning electron microscope, XRD, and uniaxial compression tests at different loading rates. The results show that 1) the peak strength and elastic modulus of shale increase with the increase in the loading rate, but Poisson's ratio has no obvious rule with the increase in the loading rate. In contrast, the loading rate causes the peak strength to vary by about 20%, which is larger than that of the elastic modulus. 2) The loading rate has a significant influence on shale failure. A higher loading rate will lead to severe damage but with simple cracks, whereas a lower loading rate will lead to complex damage of cracks. With the decrease in the strain rate, the length of the failure crack increases greatly. Therefore, a lower strain rate is helpful to form more broken fragments in the shale matrix. 3) By analyzing the relationship between elastic strain energy/dissipated energy and the loading rate, it is found that the elastic strain rate has a preliminary increasing and then a decreasing trend with the loading rate, but the dissipated energy has a decreasing trend with the loading rate. A higher loading rate is helpful to increase the brittleness of the shale, but a lower loading rate is beneficial to forming more cracks and a greater degree of fracture in the shale matrix. The effect of the loading rate on the mechanical properties and fracture properties of the shale is discussed. It is suggested that the lower hydro-fracturing rate is useful for generating more complex crack networks in the shale reservoirs.

Keywords: shale gas, loading rate, deformation characteristics, dissipated energy, fracture characteristics

INTRODUCTION

Natural gas is a type of clean and quality energy (Qiao et al., 2020a), and the consumption of natural gas in China has continuously increased in the past 2 decades (Zhang X et al., 2021; Qiao et al., 2020b). As a matter of fact, the conventional gas reserves of China are very limited (Shuai et al., 2021). Up until now, more than 45% of natural gas production depends on foreign export (Liu et al., 2020). However, China is rich in unconventional gas reserves, especially the shale gas reserves (Song et al., 2019). In recent years, shale gas has become a new hot spot in global oil and gas exploration (Zhiltsov and Zonn, 2016). Because of the need of economic and social development, China must vigorously promote the exploration and development of shale gas. (Figure 1 shows a diagram of hydro-fracture

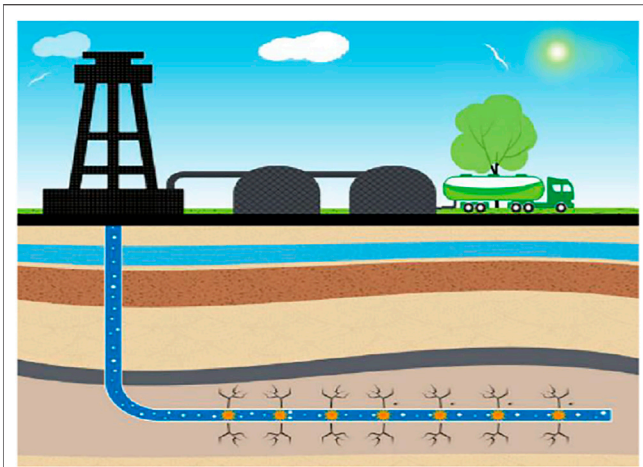


FIGURE 1 | Schematic diagram for shale hydro-fracture.

in a shale reservoir.) Huge shale gas reserves provide a reliable source for the development and upgrading of China's economy (Zhao et al., 2015; Yang et al., 2020; Zhang et al., 2020).

A shale gas reservoir is an unconventional natural gas reservoir in the shale formation; its prospective reserves have far exceeded those of conventional natural gas, and it is an important development direction of clean energy in the future (National Development and Reform Commission and Ministry of Finance, 2012). Until 2020, the total shale gas production of China has exceeded 20 billion m³, and four commercial shale gas production bases were founded; thus, shale gas has become an important portion for the gas production increase in China. Taking the Sichuan Basin as an example, the sedimentary environment, geochemical characteristics, reservoir characteristics, natural gas enrichment degree, and resource potential of three different types of shale in China are introduced (Zou et al., 2010). The mechanical properties of shale are an important aspect that affects the formulation of shale development schemes and production effects. Therefore, the study on the influence of the loading rate on mechanical properties of shale is of great guiding significance for shale gas development.

In recent years, the research on the mechanical properties of shale is also an important trend. For example, Xie et al. (2020) studied the influence of the loading rate on shale fracture behavior under dynamic and static loading conditions and found that the crack propagation rate and fracture toughness were positively correlated with the loading rate. Wang et al. (2018) studied the geotechnical engineering characteristics of red shale and revealed the unfavorable factors of its geological environment. Li et al. (2017) conducted a series of uniaxial compression tests on coal, shale, and tight sandstone and established a constitutive model of micro-damage of various rocks based on power function distribution, Weibull distribution, and Gaussian distribution. Wen et al. (2014) established a chemical-mechanical coupling model for the wall stability of hard and brittle shale shaft lining. Liang et al. (2011) put forward the optimization method for studying the sweet spot area of shale gas exploration. Wei et al. (2015a) and Wei et al. (2015b) carried out uniaxial and triaxial cyclic loading tests on shale and revealed the

deformation and fracture characteristics of shale. Hou et al. (2016) and Rybacki et al. (2016) put forward a new evaluation model for the brittleness of shale, in which the brittleness drop coefficient R can reflect the difficulty of brittle failure, and the stress landing coefficient P and softening modulus M can represent the brittleness strength. Heng et al. (2019) revealed the non-planar propagation of hydraulic fractures in shale through laboratory experiments and numerical research. Li et al. (2021) studied the thermal damage effect of fine grained granite. However, most of the current research studies focus mainly on the deformation and fracture characteristics, and the strain rate effect has not been deeply studied (Liu et al., 2014).

In fact, the loading rate effects of rock mass are a notable issue in the field of rock mechanics and rock engineering. Liang et al. Changyu et al. (2012) discussed the rate-dependent effect and energy mechanism of rocks through uniaxial compression tests. Guo et al. (2012) revealed the influence of the strain rate and cyclic load on the deformation and strength of rock salt. Song et al. (Yao and Yue (2021) studied the dynamic response of Beishan granite and found that with the increase in the loading rate, its dynamic fracture toughness increased. Zhao et al. (2020) studied the energy evolution of granite under different loading rates and proved that the elastic strain energy absorbed by rocks in the elastic stage is mainly stored in the form of elastic energy. Gautam et al. (2016) studied the strain rate and thermal damage of Dholpur sandstone at high temperature. Zhang X et al. (2021) studied the tensile strength and peak tensile strain of red sandstone under different loading rates through direct tensile tests. Chen et al. (2020) studied the deformation and mechanical properties of concrete under different loading conditions and used the acoustic emission technology as the observation technology. According to the aforementioned literature, it is concluded that the mechanical tests under different loading rates are helpful to understand the changing process of the mechanical properties of rocks. However, at present, there is little research on shale loading effects, which cannot support theoretical research and field application. Therefore, it is highly necessary to study the deformation characteristics of shale under different strain rates.

In this study, uniaxial compression tests were carried out on shale of Longmaxi Formation of lower Silurian in Enshi City, Hubei Province. During the loading process, experimental data of axial stress, axial strain, circumferential strain, and volumetric strain were collected. The deformation and fracture characteristics and stress characteristics of shale under different loading rates were analyzed, and the relationship between elastic energy and loading rate was also analyzed. The fracture characteristics under different strain rates were revealed emphatically. Finally, combined with the related background of shale gas development, its application was explored and discussed, which can provide guidance for shale gas development.

SAMPLE PREPARATION AND EXPERIMENT EQUIPMENT

Collection of Shale Samples

All the shale cores were collected from the newly excavated shale of Longmaxi Formation of lower Silurian in Enshi City, Hubei

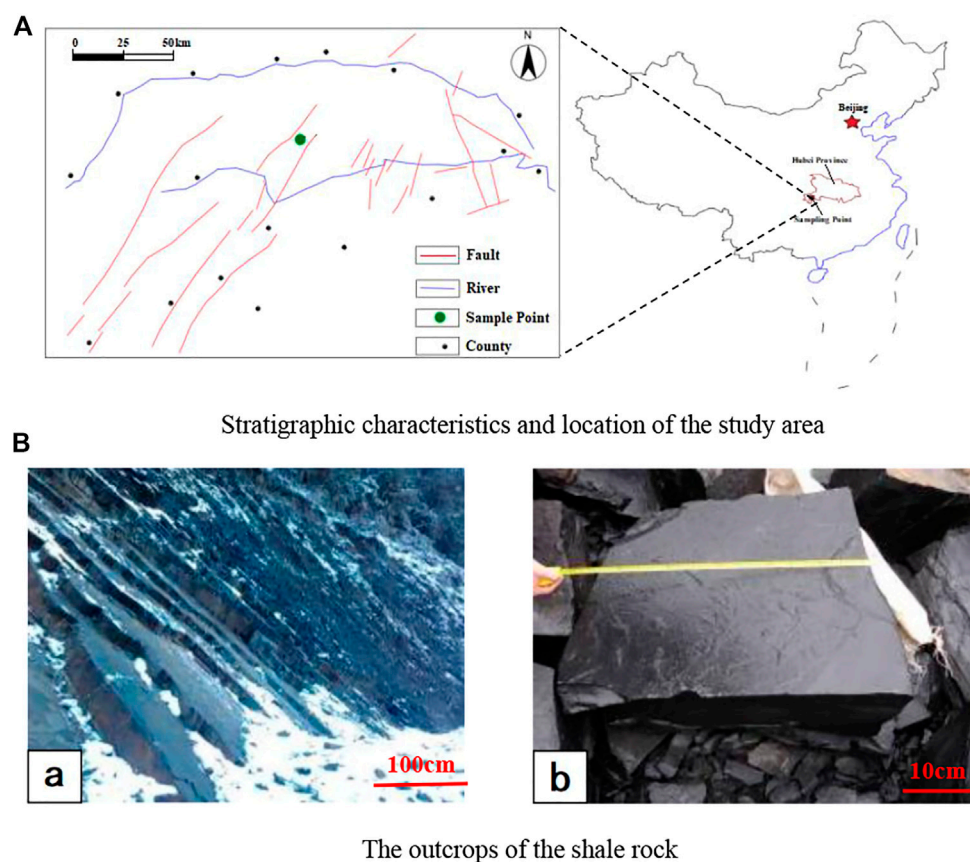


FIGURE 2 | Location shale and outcrops of shale cores. **(A)** Stratigraphic characteristics and location of the study area. **(B)** Outcrops of the shale rock



FIGURE 3 | Representative samples of the study (diameter = 5 cm, length = 10 cm).

Province of China. The geological characteristics of coring position are shown in **Figure 2**, including the main rivers and faults. Large-sized shale cores were obtained on site and then transported to the laboratory for sample preparation. In order to reduce the individual differences among samples, the samples used for testing were taken from the same core (**Figure 2**). The process of sample preparation was carried out strictly according to the requirements of the International

Rock Mechanics Test Regulations. All the samples had a height of 100 mm, a diameter of 50 mm, and an aspect ratio of 2:1. The axis of the samples was perpendicular to the standard cylinder of the bedding plane, and the parallelism between the upper and lower end faces was controlled within 0.02 mm. A total of 15 samples were produced, and each loading rate consisted of three samples. See **Figure 3** and **Table 1** for details of samples.

TABLE 1 | Sample information and loading conditions.

Sample number	Length (mm)	Diameter (mm)	Loading rate (mm/s)
V-90-17	99.57	48.35	0.00011
V-90-18	100	50	
V-90-19	99.8	48.3	
V-90-3	99.61	48.31	0.0005
V-90-4	99.5	48.17	
V-90-5	99.65	48.1	
V-90-6	99.55	48.03	0.0011
V-90-14	99.81	48.61	
V-90-16	99.6	48.33	
V-90-10	99.46	48.32	0.00275
V-90-12	99.56	49.14	
V-90-13	99.53	48.34	
V-90-7	99.42	48.41	0.01
V-90-8	99.48	48.01	
V-90-9	99.42	48.44	

Mineral composition and meso-structure are two aspects that influence the physical and mechanical properties of rock mass. Therefore, during the process of sample preparation, the small samples used for XRD and SEM tests were also prepared. The experiments were carried out in the XRD laboratory of the China University of Geosciences (Wuhan), and the equipment was a German Bruker AXS D8-Focus X-ray diffractometer. In order to ensure the uniformity of the shale samples and also avoid the mechanical property deviation that covers the deviation of the loading rate, the samples with obvious gap and vein filling were eliminated.

Test Program

The uniaxial compression tests of shale samples were carried out on an MTS 815.03 rock rigid press test system in the Wuhan Institute of Rock and Soil Mechanics, Chinese Academy of Sciences. During the process of testing, the system can automatically collect and record the axial load, axial displacement, and circumferential displacement of the sample, and the loading mode was the displacement control mode. In this

study, as the displacement control mode was used, the loading rate referred to displacement within unit time during loading. Five different loading rates were designed, which were 0.00011 mm/s, 0.0005 mm/s, 0.0011 mm/s, 0.00275 mm/s, and 0.01 mm/s, respectively. The uniaxial compression test was carried out on 16 shale samples (Table 1). In order to reduce the error caused by data contingency, each test of loading rate consisted of three shale samples. The testing device and sample installation are shown in Figure 4.

ANALYSIS OF EXPERIMENTAL RESULTS

Mineral Composition

The sedimentary environment of shale reservoirs can be divided into marine sediments, marine–terrestrial transitional sediments, and continental sediments. Due to the different sedimentary environments and models, the mineral composition, bedding structure, and internal pore/crack development of shale reservoirs also show great differences. At present, commercial development of shale gas in China is limited to marine strata in the Sichuan Basin and its periphery; the exploration and development of marine–terrestrial transitional shale have not made great progress and are still in the early evaluation stage (Liu et al., 2014). This also fully illustrates the influence and restriction of the sedimentary environment on mining. The greatest influence of sedimentary environment is the reservoir characteristics of shale, which further affects the subsequent gas-bearing characteristics and subsequent production capacity. Shale reservoir characteristics mainly depend on mineral composition, bedding structure, macro-/micro-pore structure, fracture/microfracture development degree, and other factors, especially on mineral composition and meso- and micro-view structures. Different reservoir characteristics, corresponding brittleness characteristics, bedding and microfracture development characteristics, and hydraulic characteristics will have great differences (Xiao et al., 2021), which will have a significant impact on the fracturing effect of

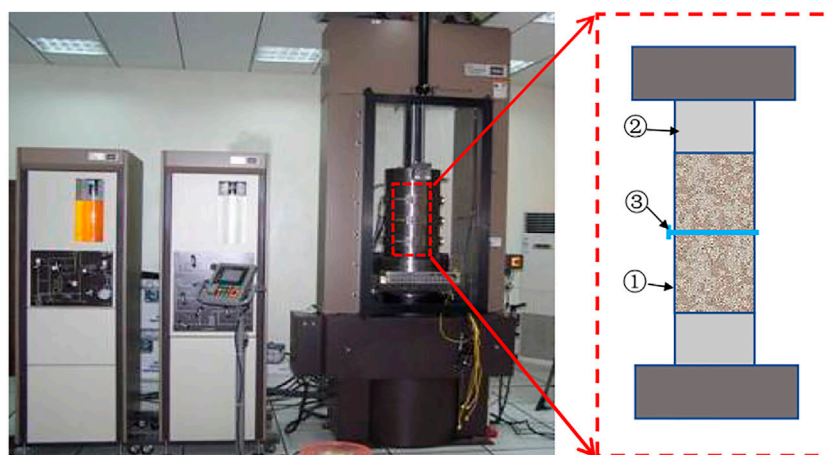
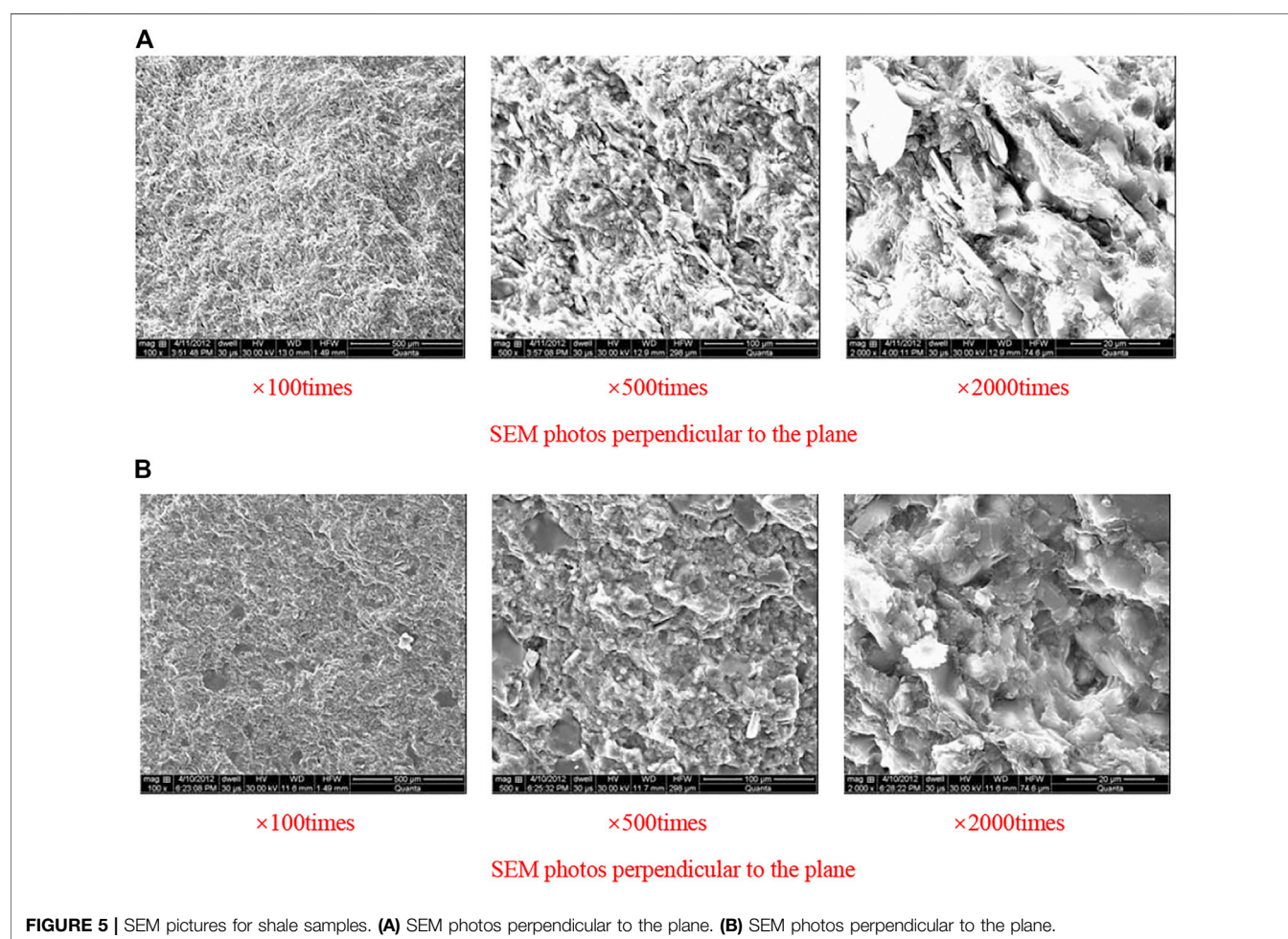
**FIGURE 4** | Testing device of MTS 815 (① shale sample; ② pressure head; ③ circumferential strain gauge).

TABLE 2 | Mineral composition information of shale samples (BM-brittle materials).

Number	Quartz/%	Albite/%	Orthoclase/%	Calcite/%	Chlorite/%	Illite/%	Pyrite/%
MAO-1	27.33	11.96	11.51	1.03	6.02	37.50	4.65
MAO-2	31.39	10.01	6.06	1.89	6.52	40.32	3.80
MAO-3	27.80	11.85	7.11	0.83	3.43	45.30	3.7
MAO-4	27.95	12.23	5.42	0	7.56	42.76	4.08
Average	28.62	11.51	7.53	0.94	5.88	41.47	4.06
BI	48.59						



shale gas wells. Therefore, classifying shale according to its mineral composition, microstructure, and mechanical properties has important engineering application significance.

In this study, the mineral composition of shale samples was analyzed. The samples were scanned using a SEM, and mineral analysis was done by X-ray diffraction for semi-quantitative analysis of the core phase. Detailed information of the mineral composition content and each element content is given in **Table 2**. Generally speaking, quartz, albite, potash feldspar, and calcite can be regarded as brittle minerals. The brittle mineral content of the shale cores is about 48.6%, and it is a group of shale samples with good fracturability.

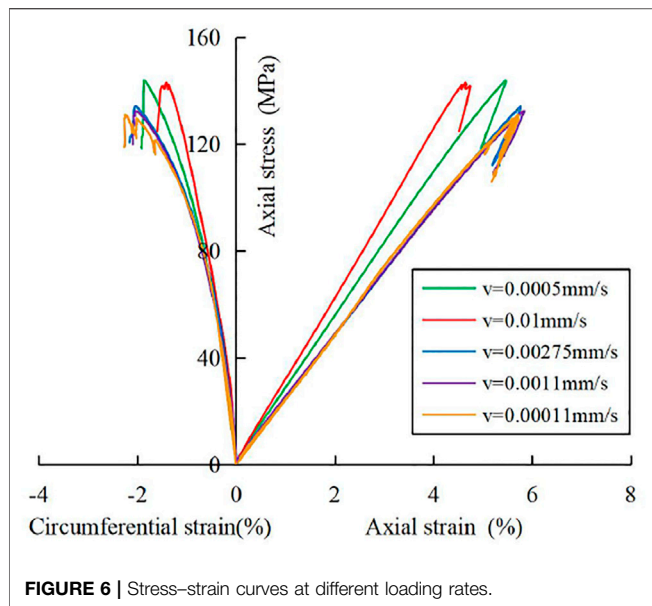
The brittleness index is defined as follows:

$$BI = BMC(\%) \quad (1)$$

where BI is the brittleness index, and BMC refers to the brittle mineral contents of the shale cores.

SEM Testing Results

The shale samples were also tested by using the SEM. The observation directions are vertical and parallel to the bedding plane. The typical SEM photos of two groups of shale samples are shown later. **Figure 5A** shows the photos perpendicular to the



bedding plane, and **Figure 5B** shows the photos parallel to the bedding plane. The magnification of the samples is 100 times, 500 times, and 2000 times, respectively. From **Figure 5**, it is found that the shale sample has a very compact matrix, and the minerals are arranged in a layer along the direction perpendicular to the bedding plane. After magnifying 2000 times, numerous micropores are found among mineral mass, and the micropores and micro-fissures have long aspects. Along the direction parallel to the bedding plane, the matrix structure is dense, and the micropores and micro-fissures have short aspects. The SEM photos evidently reveal the anisotropy of the shale in the point of view of micro-observation.

Stress-Strain Relationship Under Different Loading Rates

By calculating the uniaxial compression testing data of shale samples, the stress-strain curves of shale under different loading rates are obtained. As is shown in **Figure 6**, the axial strain is on the right side of the vertical coordinate, while the circumferential strain is on the left side.

For the stress-strain curves for each group of loading rates, we selected the curves close to the average value of the curves under the same loading rate and drew them together. As shown in **Figure 6**, with the increase in the loading rate, the elastic modulus of the sample also increases. As the loading rate increases, the peak strength of the sample also increases. Shale is a type of hard and brittle rock with obvious elastic characteristics, that is, the stress-strain curve is usually very straight. It can be seen from **Figure 6** that when the linear stage (elastic stage) continues to exceed 2/3 of the peak strength, the curve gradually deflects slightly and the slope decreases slightly. This also shows that the micro-cracks in the sample begin to gradually initiate, propagate gradually, and gradually weaken the stiffness of the sample, but the degree is

still far less than the state that leads to the formation of macro-cracks. The decrease in stiffness is not as obvious as that of soft rock; the peak value drops slowly, and then suddenly, brittle fracture occurs. The lower the loading rate, the more sufficient will be the time for the sample to adjust itself, and then the more obvious the phenomenon of stress falling and rising, and the more will be the time of fluctuation. The circumferential strain is also influenced by the loading rate, as can be seen from the left part of the curve in **Figure 6**; the circumferential strain is also increased with the decrease in the loading rate. A lower loading rate allows more time for lateral deformation, so the circumferential strain has a negative relationship with the loading rate. To sum up, regardless of whether the loading rate is high or low, the axial stress of the specimen decreases rapidly after reaching the peak strength, and the characteristics of hard and brittle failure of the samples are extremely remarkable.

As shown in **Figure 6**, the compaction of cracks or fissures of shale samples is short or almost no. The reason for this result is that the bedding direction of the core is the horizontal direction of the rock sample, and there are almost no developed micro-cracks in the shale matrix, which leads to a very short initial compaction stage in the loading process. In the stage of elastic deformation, the axial deformation of the sample is dominant, but the circumferential deformation is small. When the shale sample enters the stage of stable failure and unstable failure, both the circumferential deformation rate and the axial deformation rate increase. With the change in the strain rate, there is a good corresponding relationship between the axial deformation and circumferential deformation, that is, with the increase in the loading rate, both axial deformation and circumferential deformation reach the peak strain rapidly and steadily.

Experimental Results

Considering the difference in mechanical response characteristics of rock mass under different loading rates, the loading rate used in this test is 0.00011 mm/s–0.01 mm/s, and there is only static load in the loading process. The static load is defined as the loading rate less than 1.07 mm/s, and when the loading rate is greater than 1.07 mm/s, it falls into the category of dynamic load (Zhou, 1990). Different loading rate is an important index to reflect the response of elastic modulus, peak strength, and Poisson's ratio of the rock samples. It should be considered in the design of the rock compression experiment. Based on the aforementioned experimental data, **Table 3** is obtained. The peak strength, Poisson's ratio, and elastic modulus are discussed as follows:

Peak Strength

In order to further clarify the changed rule of peak strength with loading rate, the relationship curve between peak strength and loading rate is drawn, as shown in **Figure 7**. It can be seen that with the increase in the loading rate, the peak strength is positively correlated with the loading rate. The variation range of peak strength is 118.817–140.515 MPa, and the average value is 126.45 MPa. With the increase in the

TABLE 3 | Uniaxial compression test results of shale samples.

Shale sample number	Loading rate (mm/s)	Peak strength (MPa)	Elastic modulus (GPa)	Poisson's ratio
V-90-17	0.00011	121.586	21.795	0.322
V-90-18		103.996	15.834	0.345
V-90-19		130.870	26.564	0.258
Average		118.817	21.398	0.308
V-90-3	0.0005	105.968	21.503	0.242
V-90-4		143.691	27.291	0.296
V-90-5		114.701	20.372	0.295
Average		121.453	23.055	0.278
V-90-14	0.0011	132.403	23.505	0.287
V-90-15		128.870	28.024	0.263
V-90-16		109.148	22.934	0.284
Average		123.474	24.821	0.278
V-90-10	0.00275	128.265	22.392	0.314
V-90-12		122.991	18.541	0.34
V-90-13		134.150	23.670	0.2925
Average		128.468	21.534	0.316
V-90-7	0.01	142.971	23.339	0.323
V-90-8		141.622	30.958	0.292
V-90-9		136.954	22.888	0.296
Average		140.515	25.728	0.303

loading rate, the peak strength also tends to increase, showing a fluctuation range of -6.11% – 11.04% . The fitting curve is obtained by fitting with polynomial, where $R^2 = 0.9668$, and the fitting polynomial given in Eq. 2:

$$\sigma_p = 2056.2u_t + 120.6 \quad (2)$$

where σ_p is the peak strength (MPa) and u_t is the corresponding loading rate (mm/s).

According to the test results of peak strength, it can be seen that the loading rate has a certain influence on the peak strength, that is, the loading rate improves the peak strength of shale to a certain extent, and with the increase in the loading rate, the growth rate of the peak strength increases slightly. Therefore, the negative value of the fluctuation range is -6.11% , and the positive value is 11.04% .

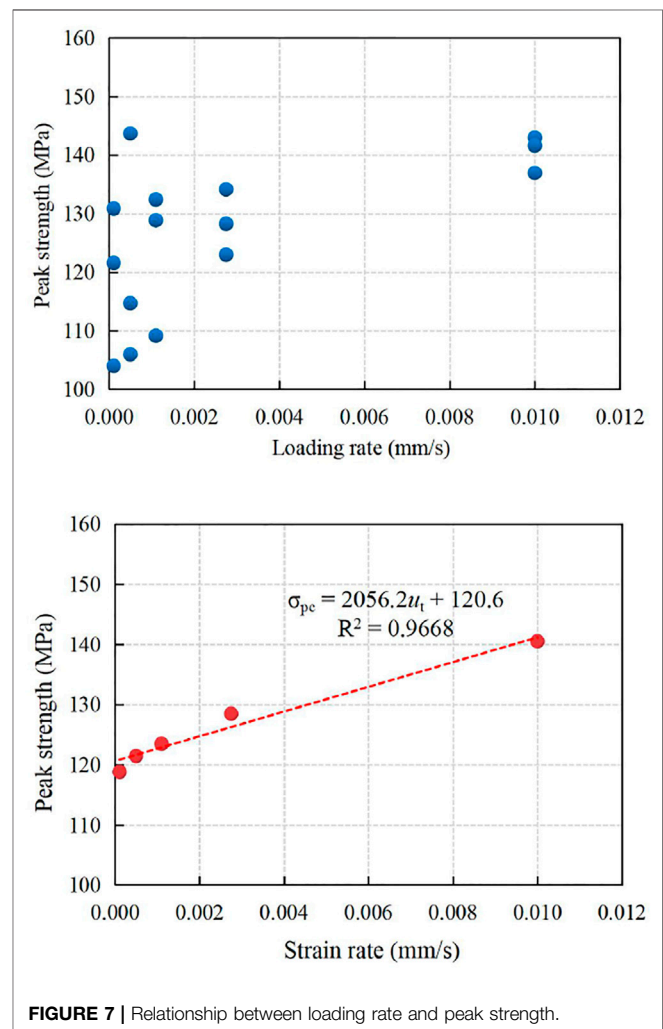
Elastic Modulus and Poisson's Ratio

According to the data in Figure 8, the elastic modulus is calculated and its average value ranges from 21.398 to 25.728 GPa, with an average of 23.550 GPa. With the increase in the loading rate, the elastic modulus also shows a certain increasing trend, with a fluctuation range from -9.14% to $+9.25\%$ around the average value. The relationship between peak strength and loading rate can be fitted by the following curves:

$$E = 0.9196 \ln(u_t) + 29.809 \quad (R^2 = 0.9847) \quad (3)$$

where E is the modulus under each loading rate.

It can be seen that the influence of the loading rate also leads to the increase in the elastic modulus. According to the data fitting, the relationship between the loading rate and elastic modulus accords with logarithmic function. In the stage of low loading rate, the elastic modulus increases

**FIGURE 7 |** Relationship between loading rate and peak strength.

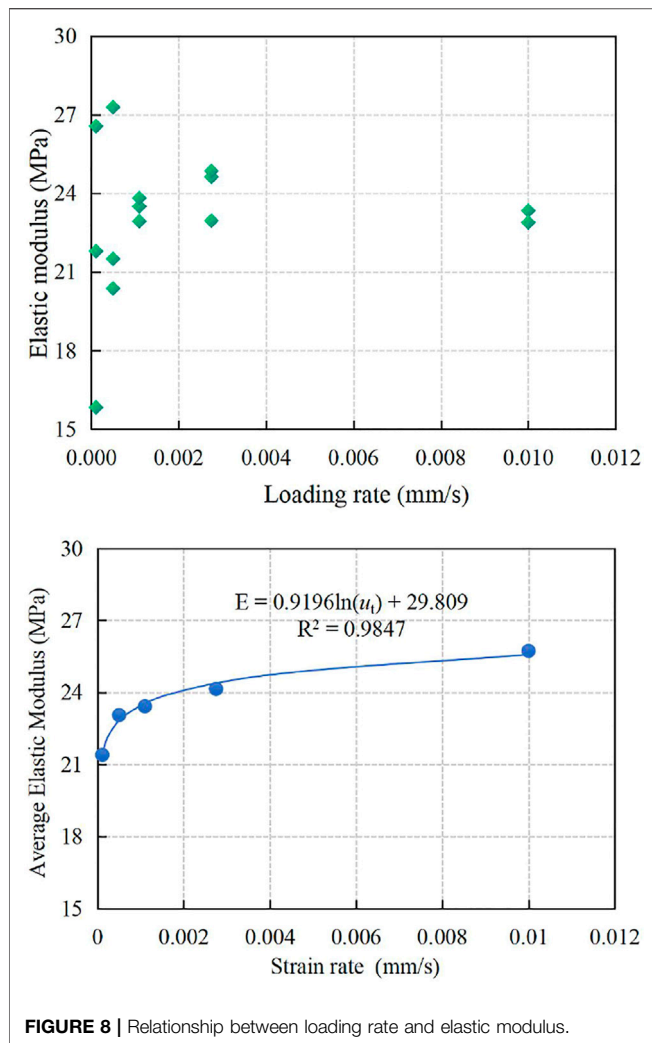


FIGURE 8 | Relationship between loading rate and elastic modulus.

rapidly with the increase in the loading rate and then slows down gradually. Relatively speaking, the elastic modulus fluctuates uniformly around the average value. By comparison, both the peak strength and elastic modulus increase with the increase in the loading rate. Because of high strength and brittleness of shale, in the loading rate of 0.0001–0.01 mm/s, the peak strength and elastic modulus will fluctuate by nearly 20%. Therefore, the change in mechanical properties caused by loading rate should still be considered in wellbore stability analysis, fracturing design, and shale-related engineering in practical projects.

As shown in Figure 9, Poisson's ratio changed from 0.242 to 0.345, with an average of 0.296. In analysis, the relationship between the loading rate and Poisson's ratio is not obvious, and the fluctuation range of Poisson's ratio is very small with the loading rates. Therefore, it can be inferred that the influence of loading rate on Poisson's ratio of shale is not significant, so it is suggested to adopt the average Poisson's ratio for practical engineering.

FRACTURE CHARACTERISTICS AND ENERGY ANALYSIS

Fracture Characteristics

The loading rate has non-negligible influences on the mechanical parameters of shale, which further affects the failure morphologies of the shale samples. Figure 10 shows the photos of shale samples after fracture with loading rates of 0.01 mm/s, 0.00275 mm/s, 0.0011 mm/s, 0.0005 mm/s, and 0.00011 mm/s, respectively. For each loading rate, it consists of two pictures: one is the sample photo after failure and the other is the failure surface (a half circle lateral surface). Apparently, it can be seen that the loading rate has a significant influence on the fracture morphology of the shale samples. The length of all the cracks is also calculated by using image processing technology. The results show that the total lengths of the cracks are 225.2, 304.1, 563.2, 492.4, and 807.5 mm, respectively, for the loading rate from high to low (0.01 mm/s–0.0001 mm/s).

It can be seen from Figure 10 that at a higher loading rate, a single crack develops to failure, and when the sample reaches the peak strength, the sample is split into larger blocks. The failure crack has a large aperture, which implies that a large amount of

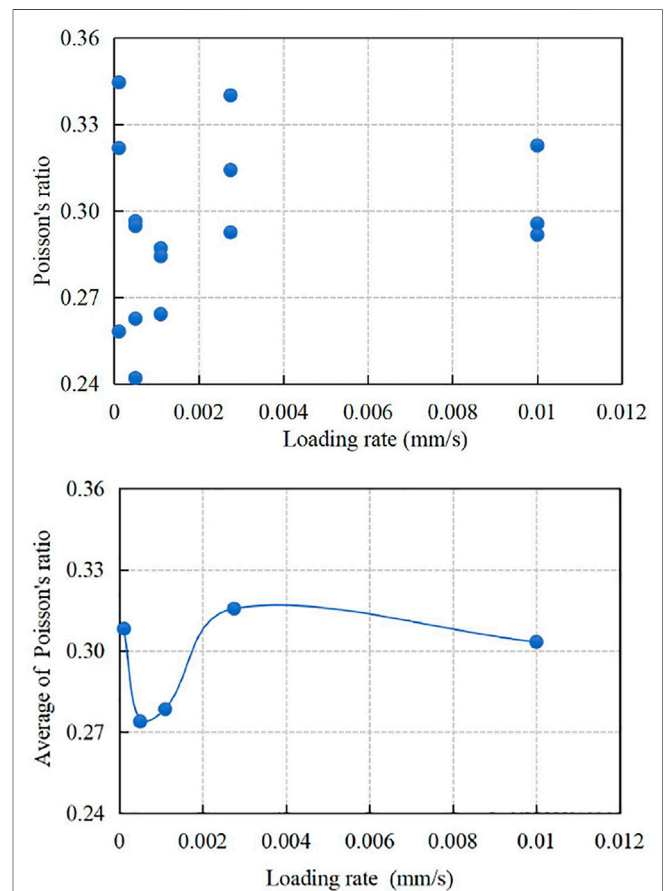


FIGURE 9 | Relationship between loading rate and Poisson's ratio.

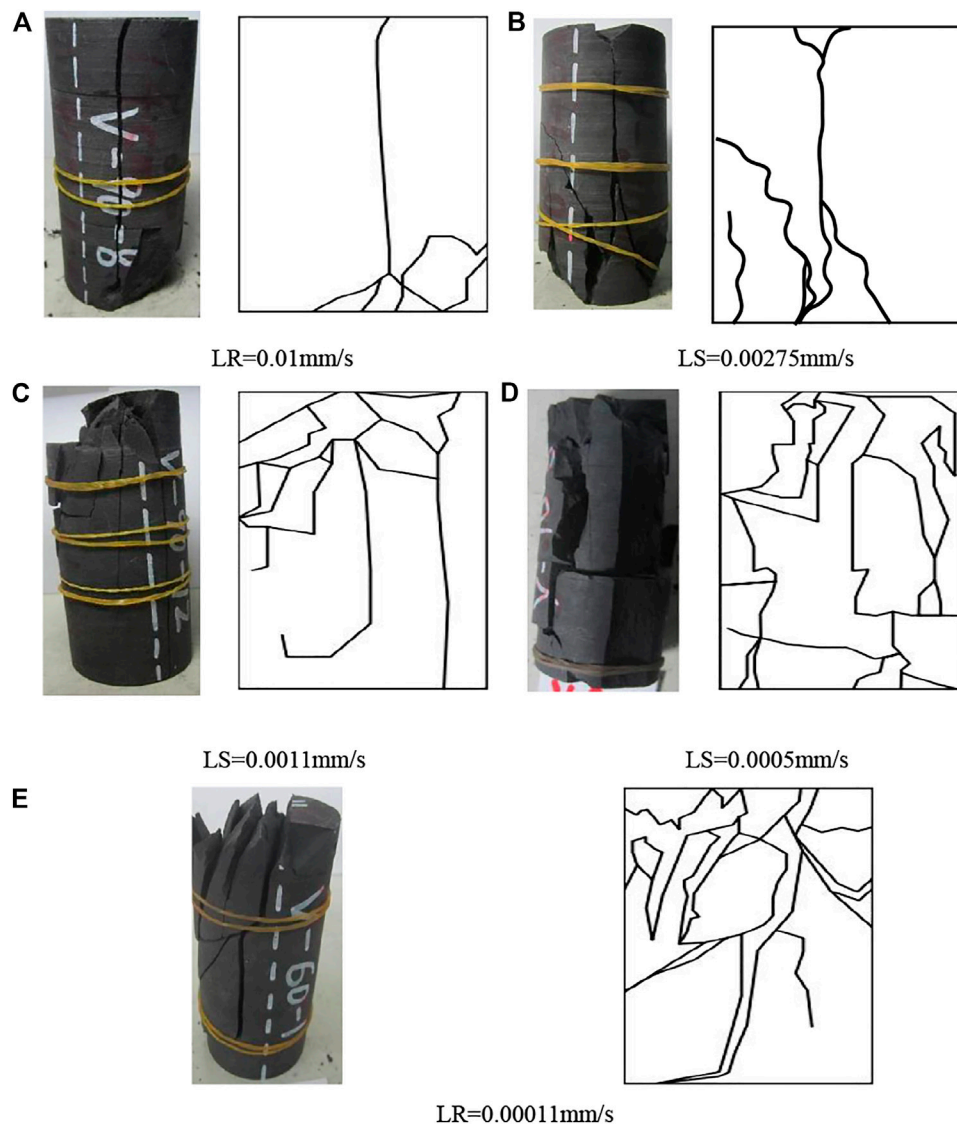


FIGURE 10 | Failure modes and schematic diagrams at different loading rates (LR is short for loading rate, all the samples have a diameter of 5 cm and a length of 10 cm). **(A)** LR=0.01 mm/s. **(B)** LS=0.00275 mm/s. **(C)** LS=0.0011 mm/s. **(D)** LS=0.0005 mm/s. **(E)** LR=0.00011 mm/s

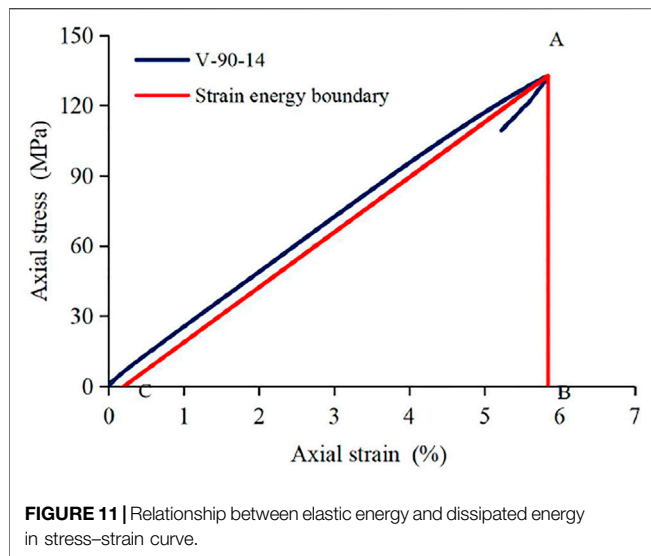
energy is released. In addition, rock powder appears on the failure surface, which indicates that serious friction occurred on the failure surface before failure. Therefore, at a higher loading rate, it can be deduced that the crack initiation, propagation, and penetration time of the shale sample are very short. Moreover, it is observed that the cracks started from the upper end and then quickly destroyed the whole sample; most of the inclined sections appeared in the lower half of the rock sample.

With the decrease in the loading rate, the rock sample is no longer broken by a single crack but by a large number of fragments. When the loading rate is low, it can be clearly observed that the surface cracks of rock samples gradually initiate and penetrate, and brittle failure occurs after the peak value, but the broken pieces are not dispersed. These phenomena

can be explained as follows: at a low loading rate, the deformation and crack development of rock samples have enough reaction time, and there is enough time to adjust the free structure so that the overall damage appears more uniform; after the damage, the rock samples appear as a dense crisscrossing crack distribution phenomenon.

Relationship Between Loading Rate and Elastic Energy

During the deformation and failure of rock samples, the initiation, propagation, and cut-through of micro-cracks will occur. The sample needs to absorb energy from the outside to produce new fracture surfaces. The relative sliding friction



between fracture surfaces will dissipate energy, that is, the process of deformation and failure of rock sample is a process of energy absorption and dissipation (Li et al., 2019). In this study, the instability and failure processes of shale sample are analyzed from an energy point of view. According to the law of thermodynamics, energy dissipation is the essential attribute of rock deformation and failure, which reflects the continuous development, weakening, and ultimate strength loss of the micro-defects in the rock matrix. Therefore, energy dissipation is directly related to the destruction and loss of strength, and the amount of energy dissipation reflects the attenuation of original strength. According to the first law of thermodynamics, we can draw a conclusion as follows:

$$W = W^d + W^e \quad (4)$$

where W is the total energy absorbed by the rock sample during the loading process, W^d refers to the released dissipated energy (unrecoverable energy), and W^e is the recoverable elastic strain energy.

Figure 10 shows the stress-strain curve (V-90-14) of shale sample V-90-14. During uniaxial loading of the shale sample, the deformation and failure processes can be divided into four stages: the compaction stage, the linear elastic stage, the yielding stage, and the post-destruction stage. In the whole process of the rock sample loading test, the deformation of rock samples can be divided into recoverable elastic deformation and unrecoverable plastic deformation. The energies absorbed and dissipated by the rock samples at different stages are closely related to the failure mode of the rock samples. The relationship between the elastic strain energy W^e and dissipated energy W^d per unit volume is shown in **Figure 11**. In this figure, the total input energy W is the total area under the stress-strain curve. The dissipative energy is the area of curved, AOC, surface in the figure, which is used to induce internal damage and plastic deformation of the rock matrix. The area of

triangle ABC in the figure represents the elastic strain energy released by the rock sample unit after unloading. After the external force is eliminated, the energy can restore the deformation of the rock mass to a certain extent. From a thermodynamic point of view, as long as certain conditions are met, energy dissipation is unidirectional and energy release is reversible. Energy dissipation is an essential attribute of deformation and failure of the rock samples, which reflects the continuous development, weakening, and ultimate strength loss of micro-defects in rock samples. Therefore, energy dissipation is directly related to the destruction and loss of strength of rock samples, and the dissipation reflects the attenuation of the original strength of rock samples.

According to the aforementioned analysis, the energy W absorbed by the rock samples under the uniaxial condition is the total area included in the stress-strain curve of the rock samples, which can be obtained by integrating the stress-strain curve. Considering the unknown curve equation, it is difficult to calculate using the integral method, so the definite integral method is adopted to solve (Changyu et al., 2012):

$$W = \int \sigma_1 d\epsilon_1 = \sum_{n=1}^n 1/2 (\sigma_{k+1} + \sigma_k) (\epsilon_{k+1} - \epsilon_k) \quad (5)$$

where σ_k is the stress value under a certain stress state and W is the total energy absorbed by the rock sample at the state of stress value σ_k , with a unit of MJ/m^3 .

The elastic energy of rock sample under the peak strength state is expressed as follows:

$$W^e = 1/2 \cdot \sigma_{\max} \cdot (\epsilon_{\max} - b) \quad (6)$$

where W^e (elastic energy) is the area of right triangle ABC in the figure, σ_{\max} is the peak strength, ϵ_{\max} is the axial strain corresponding to the peak strength, and b is the intercept of line AC on the axial strain axis.

The line AC in the figure is given as follows:

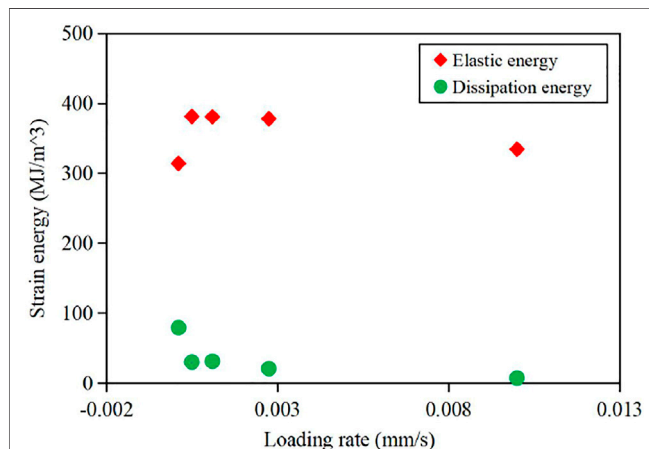
$$\sigma = E_i \epsilon \quad (7)$$

where E_i is generally replaced by the initial elastic modulus of the sample (Changyu et al., 2012). That elastic energy is the area of triangle ABC in **Figure 11**. The curve closest to the average value at each loading rate is selected, and the strain energy of each shale sample under each loading rate when it is loaded to the peak strength is calculated. The calculated results are shown in **Table 4**.

The data in **Table 4** are plotted in the coordinate system, and the trend line of strain energy is shown in **Figure 12**. It can be clearly seen that within the range of the loading rate in this study, with the increase in loading rate, the elastic strain energy W^e absorbed by the rock sample increases first and then decreases, and the peak of the elastic strain energy appears when the loading rate is about 0.0005 mm/s . With the increase in the loading rate, the dissipated energy W^d absorbed by the sample decreases. Fatigue damage and new plastic deformation caused by interfacial friction between cracks during compression are a reflection of dissipated

TABLE 4 | Energy values of samples under peak strength at different loading rates.

Loading rate (mm/s)	Elastic energy W^e (MJ/m ³)	Dissipative energy W^D (MJ/m ³)	Total energy W (MJ/m ³)
0.01	334.3078	7.2210	341.5289
0.00275	377.8769	20.7454	398.6223
0.0011	380.6543	31.2136	411.8678
0.0005	381.1503	30.1490	411.2993
0.00011	313.9827	79.2177	393.2004

**FIGURE 12 |** Relationship between elastic energy, dissipative energy, and loading rate.

energy. The higher the dissipated energy, the more cracks and greater the fracturing degree will occur in the sample. Therefore, in the point of view of the dissipative energy, a lower loading rate is helpful to produce more cracks and greater degree of fracture in the shale matrix.

In the process of uniaxial compression, when the shale sample reaches the peak strength, the elastic strain energy is suddenly released, resulting in complete crushing of the rock matrix immediately, and the consumed fracture energy is close to 0 (Changyu et al., 2012). Therefore, the elastic strain energy absorbed by the sample before the peak value represents the brittleness of the sample to some extent. In other words, the greater the elastic strain energy absorbed by the sample at the peak, the stronger will be the brittleness of the sample. Brittleness is reflected by the number of cracks and the fracturing effect. From this, it can be seen that with the increase in the loading rate, the absorbed elastic strain energy, the number of cracks, and the fracture degree of the sample all show a downward trend, that is, with the decrease of loading rate, the rock samples show stronger brittleness.

DISCUSSION AND APPLICATION

From the previous analysis, it can be seen that the response characteristics of loading rate to peak strength, elastic modulus,

and elastic energy of rock sample are obvious. A comprehensive understanding of various parameters of rock mass is the need of extensive engineering design. Determining the characteristics of mechanical parameters of shale can provide effective and reliable technical references for the design of the shale gas development project. In the process of shale gas development and utilization, most researchers mainly pay attention to the influence of shale fracture characteristics on shale gas production efficiency. Shale is a special reservoir with the functions of production, storage, and covering. For rock mass like shale, the structure is compact, the permeability is low, and the micropores are developed. Therefore, shale has always been regarded as caprock, and it has not received enough attention in the past. With the increasing demand for energy and the gradual depletion of conventional oil and gas resources, we have to turn our attention to shale gas production, although it is difficult to be exploited. According to existing research results, apart from the loading rate, the bedding direction is also one main factor that affects the mechanical properties of shale. A large number of studies have shown that shale is easier to crack in the bedding direction than in the vertical bedding direction.

In the process of shale gas exploitation, it is the most effective way to produce shale gas by fracturing to produce dense, crisscrossing high-density fracture networks. The research results in this study show that the higher the loading rate, the greater will be the total energy absorbed by the sample. The fracture characteristic is that the larger the crack blocks, the fewer will be the cracks. Although the samples absorb more energy at a higher loading rate, most of the energy is used for the kinetic energy of the rock mass. Due to the relatively small number of cracks produced under a high loading rate, the production efficiency in shale gas development will not be ideal. However, when the loading rate is low, the energy absorbed by the rock sample is small. The fracture characteristics are that there are many cracks, the cracks are fully developed, and most of the absorbed energy is fully utilized in the crack development. Therefore, in shale gas development and utilization projects, a low loading rate can often improve the efficiency of shale gas exploitation.

CONCLUSION

- 1) During the uniaxial compression test of shale, different loading rates have an obvious response to the mechanical characteristics and deformation characteristics of rock

samples. The peak strength of rock samples increases with the increase in loading rate, and it has a good linear relationship. The elastic modulus and Poisson's ratio fluctuate with the loading rate.

- 2) In the process of compression, rock sample failure also has four basic stages: the compaction stage, the linear elastic stage, the yielding stage, and the post-destruction stage. Due to the physical properties of rock samples and sampling angle, the compaction time is very short. With the increase in the loading rate, the axial and circumferential deformation of rock samples can rapidly and stably reach the peak strain.
- 3) At high loading rates, shale is broken into pieces, but cracks are less developed; at low loading rates, vertical and horizontal fracture networks are formed. Under a lower loading rate, longer cracks will be formed. Therefore, in the process of hydraulic fracturing, the lower fracturing speed is conducive to the formation of crisscrossing fine fracture networks in the reservoir, which is also beneficial to improve the productivity of shale gas.
- 4) With the increase in the loading rate, the elastic energy, the dissipated energy, and the total energy of the rock samples all decrease. As the loading rate decreases, the dissipative energy and elastic energy absorbed by the rock samples increase. At a lower loading rate, the rock samples are accompanied by stronger brittleness, fully developed

cracks, and a higher macroscopic fracture degree, that is, more and more cracks develop and more fracture surfaces are generated.

DATA AVAILABILITY STATEMENT

The original contributions presented in the study are included in the article/Supplementary Material; further inquiries can be directed to the corresponding author.

AUTHOR CONTRIBUTIONS

YW wrote the manuscript, LZ is the supervisor of the manuscript and project, TY did editing work, and WL designed the research structure and revised the manuscript.

FUNDING

This research was supported by the Guizhou Provincial Geological Exploration Fund (Grant No. 208-9912-JBN-UTS0) and the Fundamental Research Funds for the Central Universities (Grant No. 2021CDJQY-030).

REFERENCES

- Changyu, L., Xiao, L., Wang, S., Li, S., He, J., and Ma, C. (2012). Experimental Investigation on Rate-Dependent Stress-Strain Characteristics and Energy Mechanism of Rock under Uniaxial Compression. *Chin. J. Rock Mech. Eng.* 31 (09), 1831–1838. doi:10.3969/j.issn.1000-6915.2012.02.003
- Chen, C., Fan, X., and Chen, X. (2020). Experimental Investigation of concrete Fracture Behavior with Different Loading Rates Based on Acoustic Emission. *Construction Building Mater.* 237, 117472. doi:10.1016/j.conbuildmat.2019.117472
- Gautam, P. K., Verma, A. K., Jha, M. K., Sarkar, K., Singh, T. N., and Bajpai, R. K. (2016). Study of Strain Rate and thermal Damage of Dholpur sandstone at Elevated Temperature. *Rock Mech. Rock Eng.* 49, 3805–3815. doi:10.1007/s00603-016-0965-5
- Guo, Y., Yang, C., and Mao, H. (2012). Mechanical Properties of Jintan Mine Rock Salt under Complex Stress Paths. *Int. J. Rock Mech. Mining Sci.* 56, 54–61. doi:10.1016/j.ijrmms.2012.07.025
- Heng, S., Liu, X., Li, X., Zhang, X., and Yang, C. (2019). Experimental and Numerical Study on the Non-Planar Propagation of Hydraulic Fractures in Shale. *J. Pet. Sci. Eng.* 179, 410–426. doi:10.1016/j.petrol.2019.04.054
- Hou, Z., Yang, C., Wang, L., and Xu, F. (2016). Evaluation Method of Shale Brittleness Based on Indoor Experiments. *J. Northeast. Univ. (Natural Science)* 37 (10), 1496–1500. doi:10.3969/j.issn.1005-3026.2016.10.027
- Li, S., Chen, G., Shuang, H., Lin, H., and Zhao, P. (2019). Experimental Study on Effect of Loading Rate and Initial Damage on Energy Evolution of sandstone. *J. Mining Saf. Eng.* 36 (2), 373–380.
- Li, X., Peng, K., Peng, J., and Hou, D. (2021). Effect of thermal Damage on Mechanical Behavior of a Fine-Grained Sandstone. *Arab J. Geosci.* 14, 1212. doi:10.1007/s12517-021-07607-0
- Li, Y., Jia, D., Rui, Z., Peng, J., Fu, C., and Zhang, J. (2017). Evaluation Method of Rock Brittleness Based on Statistical Constitutive Relations for Rock Damage. *J. Pet. Sci. Eng.* 153, 123–132. doi:10.1016/j.petrol.2017.03.041
- Liang, X., Ye, X., Zhang, J., and Shu, H. (2011). Reservoir Forming Conditions and Favorable Exploration Zones of Shale Gas in the Weixin Sag, Dianqianbei Depression. *Pet. Exploration Development Online* 38 (6), 225–230. doi:10.1016/S1876-3804(12)60004-4
- Liu, J., Liu, W., Yang, C., and Liang, H. (2014). Experimental Research on Effects of Strain Rate on Mechanical Properties of Shale. *Rock Soil Mech.* 35 (11), 3093–3100.
- Liu, W., Zhang, Z., Fan, J., Jiang, D., Li, Z., and Chen, J. (2020). Research on Gas Leakage and Collapse in the Cavern Roof of Underground Natural Gas Storage in Thinly Bedded Salt Rocks. *J. Energ. Storage* 31, 101669. doi:10.1016/j.est.2020.101669
- National Development and Reform Commission, Ministry of Finance (2012). *Ministry of Land and Resources and Energy Bureau. Shale Gas Development Plan 2011-2015*. Beijing: China Planning Press.
- Qiao, W., Moayed, H., and Foong, L. K. (2020a). Nature-inspired Hybrid Techniques of IWO, DA, ES, GA, and ICA, Validated Through a K-fold Validation Process Predicting Monthly Natural Gas Consumption. *Energy and Buildings* 217, 110023. doi:10.1016/j.enbuild.2020.110023
- Qiao, W., Yang, Z., Kang, Z., and Pan, Z. (2020b). Short-term Natural Gas Consumption Prediction Based on Volterra Adaptive Filter and Improved Whale Optimization Algorithm. *Eng. Appl. Artif. Intelligence* 87, 103323. doi:10.1016/j.engappai.2019.103323
- Rybacki, E., Meier, T., and Dresen, G. (2016). What Controls the Mechanical Properties of Shale Rocks? - Part II: Brittleness. *J. Pet. Sci. Eng.* 144, 39–58. doi:10.1016/j.petrol.2016.02.022
- Shuai, H., Li, X., Zhang, X., and Li, Z. (2021). Mechanisms for the Control of the Complex Propagation Behaviour of Hydraulic Fractures in Shale. *J. Pet. Sci. Eng.* 200 (6), 108417. doi:10.1016/j.petrol.2021.108417
- Song, X., Guo, Y., Zhang, J., Sun, N., Shen, G., Chang, X., et al. (2019). Fracturing with Carbon Dioxide: from Microscopic Mechanism to Reservoir Application. *Joule* 3 (8), 1913–1926. doi:10.1016/j.joule.2019.05.004
- Wang, D.-y., Li, X.-b., Peng, K., Ma, C.-d., Zhang, Z.-y., and Liu, X.-q. (2018). Geotechnical Characterization of Red Shale and its Indication for Ground Control in Deep Underground Mining. *J. Cent. South. Univ.* 25 (12), 2979–2991. doi:10.1007/s11771-018-3968-4
- Wei, Y., Yang, C., Guo, Y., Liu, W., Wang, L., and Heng, S. (2015a). Experimental Investigation on Deformation and Fracture Characteristics of Brittle Shale with Natural Cracks Uniaxial Cyclic Loading. *Rock Soil Mech.* 36 (06), 1649–1658. doi:10.16285/j.rsm.2015.06.017

- Wei, Y., Yang, C., Guo, Y., Liu, W., Wang, L., and Xu, J. (2015b). Experimental Research on Deformation and Fracture Characteristics of Shale under Cyclic Loading. *Chin. J. Geotechnical Eng.* 37 (12), 2262–2270. doi:10.11779/CJGE201512016
- Wen, H., Chen, M., Jin, Y., Wang, K., Xia, Y., Dong, J., et al. (2014). A Chemo-Mechanical Coupling Model of Deviated Borehole Stability in Hard Brittle Shale. *Pet. Exploration Development* 41 (6), 817–823. doi:10.1016/s1876-3804(14)60099-9
- Xiao, D., Lu, S., Shao, M., Zhou, N., Zhao, R., and Peng, Y. (2021). Comparison of marine and continental Shale Gas Reservoirs and Their Gas-Bearing Properties in China: the Examples of the Longmaxi and Shahezi Shales. *Energy Fuels* 35 (5), 4029–4043. doi:10.1021/acs.energyfuels.0c04245
- Xie, Q., Li, S.-x., Liu, X.-l., Gong, F.-q., and Li, X.-b. (2020). Effect of Loading Rate on Fracture Behaviors of Shale under Mode I Loading. *J. Cent. South. Univ.* 27 (10), 3118–3132. doi:10.1007/s11771-020-4533-5
- Yang, L. A., Ma, T. S., Hao, W. C., and Chen, P. B. (2020). Investigation on Mechanical Behaviors of Shale Cap Rock for Geological Energy Storage by Linking Macroscopic to Mesoscopic Failures. *J. Energ. Storage* 29, 101326. doi:10.1016/j.est.2020.101326
- Yao, S., and Yue, Z. (2021). Experimental Study on Dynamic Fracture Behaviors of Beishan NSCB and CCNSCB Granite Specimens under Different Loading Rates. *Soil Dyn. Earthquake Eng.* 141, 106512. doi:10.1016/j.soildyn.2020.106512
- Zhang, Q., Fan, X., Chen, P., Ma, T., and Zeng, F. (2020). Geomechanical Behaviors of Shale after Water Absorption Considering the Combined Effect of Anisotropy and Hydration. *Eng. Geology* 269, 105547. doi:10.1016/j.enggeo.2020.105547
- Zhang, X., Liu, W., Jiang, D., Qiao, W., Liu, E., Zhang, N., et al. (2021). Investigation on the Influences of Interlayer Contents on Stability and Usability of Energy Storage Caverns in Bedded Rock Salt. *Energy* 231, 120968. doi:10.1016/j.energy.2021.120968
- Zhang, Y., Zhang, Q.-Y., Zhou, X.-Y., and Xiang, W. (2021). Direct Tensile Tests of Red sandstone under Different Loading Rates with the Self-Developed Centering Device. *Geotech. Geol. Eng.* 39, 709–718. doi:10.1007/s10706-020-01515-y
- Zhao, J., Liu, C., Yang, H., and Li, Y. (2015). Strategic Questions about China's Shale Gas Development. *Environ. Earth Sci.* 73 (10), 6059–6068. doi:10.1007/s12665-015-4092-5
- Zhao, K., Yu, X., Zhou, Y., Wang, Q., Wang, J., and Hao, J. (2020). Energy Evolution of Brittle Granite Under Different Loading Rates. *Int. J. Rock Mech. Mining Sci.* 132 (7), 104392. doi:10.1016/j.ijrmms.2020.104392
- Zhil'tsov, S. S., and Zonn, I. S. (2016). *Shale Gas Production in the USA*. Moscow, Russia: Shale Gas: Ecology, Politics, Economy.
- Zhou, W. (1990). *Advanced Rock Mechanics*. Beijing: China Water Conservancy and Hydropower Press, pp219.
- Zou, C., Dong, D., Wang, S., Li, J., Li, X., Wang, Y., et al. (2010). Geological Characteristics and Resource Potential of Shale Gas in China. *Pet. Exploration Development* 37 (6), 641–653. doi:10.1016/s1876-3804(11)60001-3

Conflict of Interest: The authors declare that the research was conducted in the absence of any commercial or financial relationships that could be construed as a potential conflict of interest.

The handling editor declared a shared affiliation with the authors TY and WL at the time of review.

Publisher's Note: All claims expressed in this article are solely those of the authors and do not necessarily represent those of their affiliated organizations, or those of the publisher, the editors, and the reviewers. Any product that may be evaluated in this article, or claim that may be made by its manufacturer, is not guaranteed or endorsed by the publisher.

Copyright © 2022 Wei, Zhao, Yuan and Liu. This is an open-access article distributed under the terms of the Creative Commons Attribution License (CC BY). The use, distribution or reproduction in other forums is permitted, provided the original author(s) and the copyright owner(s) are credited and that the original publication in this journal is cited, in accordance with accepted academic practice. No use, distribution or reproduction is permitted which does not comply with these terms.



Influence of Crack Spacing/Layer Thickness Value on Reflection Crack Propagation Mechanism Under Low Temperatures

Chunyan Bao^{1,2,3,4}, Qi Liu^{1,2}, Yingjie Xia^{5*}, Yi Cui⁶, Zongyong Cao³, Yidong Qian³, Minghao Liu⁷, Chaoqian Mu⁵ and Hongliang Wang³

¹College of Civil Engineering, Shaoxing University, Shaoxing, China, ²Collaborative Innovation Center for Prevention and Control of Mountain Geological Hazards of Zhejiang Province, Shaoxing, China, ³Huahui Engineering Design Group Corporation Ltd., Shaoxing, China, ⁴Center of Rock Mechanics and Geohazards of Shaoxing University, Shaoxing, China, ⁵State Key Laboratory of Coastal and Offshore Engineering, Dalian University of Technology, Dalian, China, ⁶China Huaneng Zhalainguoer Coal Industry Co. Ltd., Hulunbuir, China, ⁷State Key Laboratory of Frozen Soil Engineering, Cold and Arid Regions Environmental and Engineering Research Institute, Chinese Academy of Sciences, Lanzhou, China

OPEN ACCESS

Edited by:

Jie Chen,
Chongqing University, China

Reviewed by:

Hui Li,
Xi'an Jiaotong University, China
Jin Jiaxu,
Liaoning Technical University, China
Fanzhen Meng,
Qingdao University of Technology,
China

*Correspondence:

Yingjie Xia
xiayingjie@dlut.edu.cn

Specialty section:

This article was submitted to
Environmental Informatics and Remote
Sensing,
a section of the journal
Frontiers in Earth Science

Received: 08 November 2021

Accepted: 28 December 2021

Published: 16 February 2022

Citation:

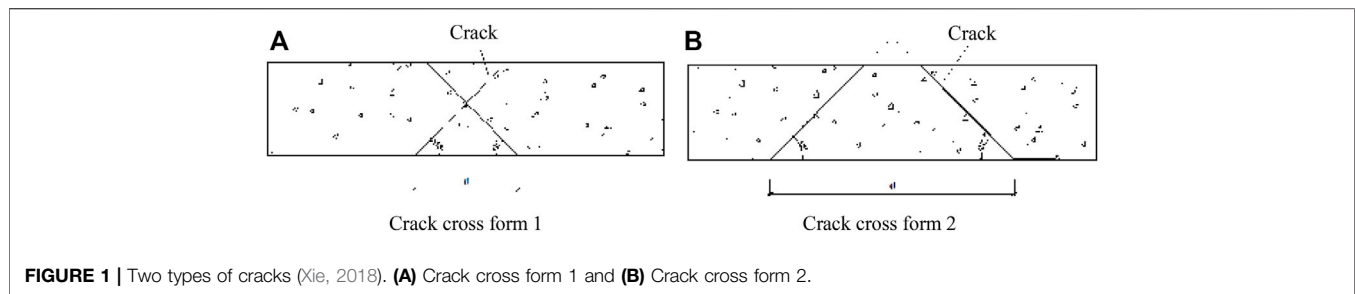
Bao C, Liu Q, Xia Y, Cui Y, Cao Z,
Qian Y, Liu M, Mu C and Wang H
(2022) Influence of Crack Spacing/
Layer Thickness Value on Reflection
Crack Propagation Mechanism Under
Low Temperatures.
Front. Earth Sci. 9:810964.
doi: 10.3389/feart.2021.810964

The damage of asphalt concrete pavement (AC pavement) structure caused by reflection crack is an urgent problem in many areas of China, especially in cold regions of China, so it is necessary to study how to reduce the reflective cracking and prevent the AC pavement structures cracking. The acoustic emission (AE) information is fetched in this paper to study the AE characteristics of pavement structures and the crack propagation law inside the system. On the above basis, cracks with crack spacing/layer thickness values of 1.25, 2.5, 3.75, and 5 were prefabricated in the foundation course by the numerical simulation method. The models with different foundation course crack spacing were calculated by Realistic Failure Process Analysis finite element software. The influence of varying crack spacing on the propagation mechanism of reflective cracks in the foundation course structure was studied. The results show that the AC pavement structure has prominent AE characteristics. The faster the cooling rate is, the more serious the damage to the AC pavement surface is. In addition, with the increase of crack spacing/layer thickness value, the stress level between cracks increases continuously. Most of the stress will make the cracks expand toward the foundation course structure, and only a tiny part of stress is used to form reflective cracks. In practical engineering, it is suggested to increase the crack resistance of foundation course materials and preset some small spacing cracks in the large spacing cracks in the foundation course.

Keywords: value of S/T, mechanism, reflective crack, low temperature effect, asphalt pavement, crack propagation

INTRODUCTION

In southwestern China, the Qinghai-Tibet Plateau and its surrounding areas are mainly alpine regions with a wide area (Liang et al., 2020; Duan et al., 2021). The asphalt concrete (AC) pavement structure is fatal in cold areas with significant temperature differences between winter and summer and seasonal freeze-thaw alternation. Low-temperature cracks are a significant disease of the pavement structure (Wei et al., 2020; Wei et al., 2021). Relevant studies have pointed out an internal relationship between the acoustic emission (AE) of AC pavement structures and the damage



location of pavement structures (Li and Marasteanu, 2011; Wei et al., 2019; Yang et al., 2021b). So far, AE technology has been widely used in concrete materials and concrete bridges, and many AE analyses have been carried out (Nair and Cai, 2010; Behnia et al., 2014; Jiao et al., 2020), as well as the use of AE to study the cracking of mixtures (Li et al., 2006; Behnia et al., 2018; Xu et al., 2018; Yang et al., 2021a). AE was also used to evaluate the related subjects (Hill et al., 2013; Sun et al., 2017; Jiao et al., 2019b; Cai et al., 2021). In recent years, AE detection methods have also been used to characterize AC materials (Jiao et al., 2019a; Qiu et al., 2020). For example, Seo and Kim (2008) applied AE technology to study AC materials' damage and healing characteristics and proved that cumulative AE energy could be a feasible AE parameter to identify fatigue damage and healing in the AC. Hakimzadeh et al. (2017) mainly studied three different asphalt mixtures' internal crack damage characteristics under low temperatures. Hakimzadeh et al. (2017) found that the AE of asphalt mixtures corresponding to three other asphalt binders could be used as a good indicator of low-temperature cracking performance. The research discussed earlier shows that the experience of AE technology in the application of AC materials has been relatively mature and has achieved specific results.

In addition, reflective cracks have long been a severe problem in the process of AC pavement renovation. Reflective cracks will also cause cracks in the AC pavement overlay, affecting the service life of AC pavement (Hu et al., 2010). Qisen and Zheng (1990) applied fracture mechanics to study the reflective cracking of semirigid foundation course in AC pavement and concluded that the shear stress perpendicular to the pavement direction is the main reason for forming reflective cracks. Xie (2018) studied the distribution of cracks on AC pavement overlay pavement surface deflection. When the inclination angle is 45° and the crack spacing increases from 200 to 600 mm, two different forms of cracks will be formed in the cement concrete slab, as shown in **Figure 1**. It is also found that when the intersection point of cracks is located in a concrete slab, the unevenness of bending and settling of the whole structure becomes more evident with the increase of crack spacing. This phenomenon also reflects that the crack spacing d value affects the overall structural stability (d value is also the S value of this paper) (Xie, 2018).

Brown et al. (2001), through experiments and the establishment of a theoretical model, grid steel in the appropriate application can improve the crack resistance and

rutting resistance of the AC layer. Khodaii et al. (2009) using geosynthetic materials laid on a third of the cover can effectively reduce the probability of reflection cracks, providing a more excellent service life. Kim et al. (1999) carried out experiments on the overlay and found that some modified asphalt mixtures and reinforced asphalt mixtures can effectively prevent crack propagation. Tsai et al. (2010) calibrated the model based on mechanical principles. Through this model, hot mix asphalt can virtually reproduce the growth and severity of reflection cracks in field observation. Bai et al. (2000) used the finite element method to study that the spacing of cracks in layered materials is usually proportional to the thickness of the crack layer. Morris et al. (1982) used the finite element program to analyze the stress value near the crack of the pavement structure after cracking and found that the main reason for reflection crack is the displacement difference of foundation course after cracking. Dave and Buttlar (2010) used finite element software to study the reflective cracks of AC pavement under temperature load.

Zhang and Guan (2001) calculated the temperature field of AC pavement surface under a wide range of cooling and analyzed the influence of different crack widths and cooling rates on temperature stress. Liu et al. (2011) used a three-dimensional finite element model to study the distribution of the stress intensity factor value of foundation course cracks in AC pavement structures in a large temperature difference area. Wang and Zhong (2019) used the extended finite element method to study AC pavement's reflection crack propagation mechanism under combined temperature and mobile traffic loads. Based on ABAQUS finite element software and extended finite element method, Hou et al. (2021) analyzed the propagation process of reflection cracks and proved that properly reducing the elastic modulus of the stress absorbing layer could improve antireflection performance cracks. Wang (2012) believes that eliminating reflective cracks is neither feasible nor economical. It should be considered whether it can delay the expansion of reflective cracks.

In this paper, Realistic Failure Process Analysis (RFPA) will be used for numerical simulation. As for the authenticity of RFPA, Chinese researcher Changxu used RFPA to verify Bai's proposal that elastic modulus of the material in uniform medium and prefabricated crack depth would have an essential impact on crack propagation. In addition, Professor Tang Chunan used RFPA to study the change of stress distribution of equal-spacing cracks with crack spacing/layer thickness (S/T) under axial tensile action on a typical three-layer material model and found that the

results are in good agreement with Bai results. At the same time, Tang Shibin used an RFPA temperature plate to verify the correctness of concrete temperature conduction characteristics and concrete temperature crack formation, simulated the pavement cracking problem, and achieved good simulation results. So, it is feasible to use an RFPA temperature plate to study the reflection crack propagation process of AC pavement structure under the action of low temperature.

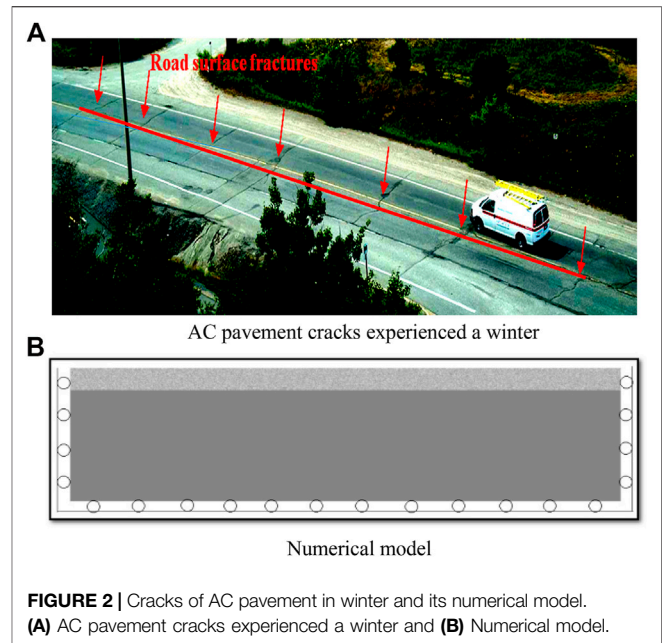
Nowadays, research on applying AE technology in the overall structure of AC pavements is scarce. This paper uses the numerical simulation method to explore the AE of AC pavement structures. This paper attempts to examine the application of AE detection technology in pavement structure detection, which is realized by the RFPA analysis system. AE characteristics of pavement structure and internal crack propagation law are studied. On this basis, we need to further explore AC pavement reflection cracks. At present, research on reflection cracks mainly focuses on the mechanism of temperature shrinkage cracks. However, there is little research on the influence of crack spacing based on the propagation of reflective cracks. Therefore, this paper studies the effect of different S/T values on the propagation of reflective cracks (S/T represents the ratio of crack spacing to surface thickness). The model with different foundation course crack spacing is calculated using RFPA finite element software to determine whether different foundation course crack spacing influences the overall pavement structure. At the same time, according to the results, some preventive measures are provided to provide corresponding guidance for the prevention and control of AC pavement in the future.

Numerical Test Process of Low-Temperature Asphalt Concrete Pavement Acoustic Emission

This section uses an RFPA analysis system to study the AE characteristics of pavement structure and the law of crack propagation inside the structure. This basis paves the way for further exploration of AC pavement reflection cracks below. The low-temperature performance of AC pavement mainly depends on the low-temperature performance of the asphalt binder. The low-temperature performance of asphalt binder plays a 90% role in the low-temperature crack resistance of the whole asphalt pavement materials. Road AC pavement needs to be tested all year round of the four seasons, and the properties of asphalt are soft in summer and brittle in winter, which is opposite to the people's expectations. Typically, when the temperature changes from 70 to -40°C , the asphalt material changes from Newtonian liquid to nearly Hookean elastomer. Under the action of low temperature, the behavior of asphalt is close to elastic brittleness. Therefore, the crack of asphalt at low temperature should be mainly studied under the action of a low-temperature environment.

Numerical Model and Boundary Conditions

The AC pavement structure is a continuous layered structure. To simulate the AC pavement structure under the



actual low-temperature state, the AC pavement structure is simplified as a double-layer model, as seen in Figure 2A. Therefore, this chapter selected the red line section in Figure 2A as the research object, simplifying the AC pavement into a double-layer model, shown in Figure 2B. The model's width is 5,000 mm, and the thickness is 1,200 mm. Furthermore, the thickness of the top layer is 200 mm, and the cell is $40 \times 1,000$; the bottom layer is 1,000 mm, and the cell number is $200 \times 1,000$. The model is fixed at the left and right sides and lower and free upper boundary. According to the meteorological data, the low-temperature region is in China (Shen et al., 2011). The cooling in the cold areas is divided into three periods. The cooling rates are reduced by approximately 1, 2, and 4°C per hour, respectively, and the lowest temperature is also below -30°C . Therefore, this paper uses these parameters. We set the top layer temperature from 0 to -40°C , and we lowered the temperature to -40°C in the following three ways: the first cooling condition is temperature reduced by 1°C per step, the second by 2°C per step, and the third by 4°C per step. The initial temperature of the lower layer of the model is 20°C . The mechanical parameters of model materials are shown in Table 1. The variable coefficient represents the unevenness of AC. In the surface layer, the variable coefficient is smaller than that of the foundation course.

Figure 3 shows the relationship between the cooling step–tensile stress change curve and the cooling step–AE number change curve within the structure with the decrease of temperature during the damage and failure of AC pavement structure under three cooling rates. The cooling step– σ –emission number is carried out below. It can be observed that the data can be divided into several distinct stages with specific characteristics under three cooling rates.

As shown in Figure 3, cooling condition 1 means 1°C per step, cooling condition 2 means 2°C per step, and cooling condition 3

TABLE 1 | Material mechanical properties.

	Inhomogeneity coefficient <i>m</i>	Modulus of elasticity <i>E</i> /MPa	Intensity <i>σ</i> /MPa	Thermal expansion coefficient/°C	Thermal conductivity <i>W</i> /(<i>m</i> °C)	Poisson ratio
Surface	3	1,200	150	2×10^{-5}	10	0.25
Subbase	10	100	20	1×10^{-5}	1	0.25

AE characteristic of AC pavement damage under low temperature.

means 4°C per step. The results of numerical experiments show that the micro-crack process of AC pavement can be divided into three stages:

- 1) Linear deformation stage. In the initial cooling stage, AE occurs in the structure of AC pavement with a decrease in temperature. However, the energy released is less in the early stages of the three load steps. The relationship between the three load steps and σ is linear in the initial stage.
- 2) The macroscopic failure stage of crack formation, propagation, and penetration. The number of AE events in the AC pavement structure increases sharply when the cooling condition is 1/2/3. When the loading step reaches 20/13/7, the load step- σ curve reaches the maximum value, and the number of AE comes at the peak time. This shows that with the increase of cooling rate, the peak value of AE number and pavement structure damage occur earlier.
- 3) At the late stage of macroscopic rupture. The AE frequency of the three cooling conditions is different from that of the initial stage. Also, the energy released is much less than that of the initial loading stage. In addition, the number of AE in the AC pavement structure is relatively stable and trimmed after the corresponding load step.

The process of crack and damage of AC pavement structure is a process of brittleness and toughness transformation in the whole process of AE. There is a critical transition temperature for toughness and brittleness. In general, the AC pavement structure has viscoelastic properties at room temperature. Due to the decreasing temperature, the upper layer continues to shrink, the tensile stress increases, and the lower layer stress cannot be recovered, which leads to the relative embrittlement of the AC pavement structure. Without the original characteristics, the AC pavement structure was destroyed before the ultimate strength was reached when the temperature reached the rupture point, which led to the appearance of various cracks. In addition, the AE curve in **Figure 3** shows a basic pattern of foreshock-main shock-aftershock similar to the law of seismic activity, and the initial temperature drop shows a linear way. Also, the stress drop after the mainshock is apparent, showing strong brittleness.

Final Failure Mode of Asphalt Concrete Pavement Structure Under Three Cooling Conditions

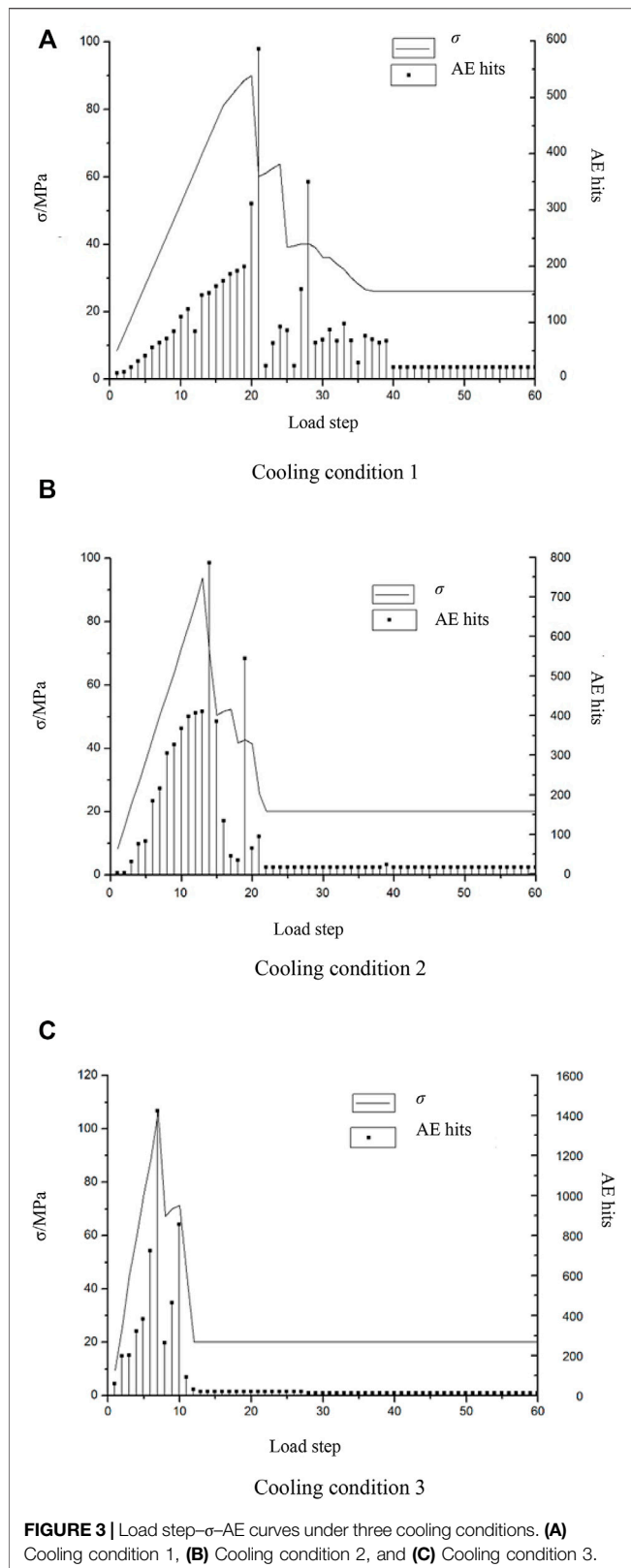
Figure 4 shows the final instability and failure mode diagram of the AC pavement structure under three different cooling rates.

Figure 4 shows the final instability and failure mode with the AE result of AC pavement structure under these three cooling conditions. It can be seen from **Figure 4** in the case of the cooling conditions 1, 2, and 3, respectively. The number of AE cracks in the AC pavement structure is 4, 4, and 6, as the boundary constraint effect may mainly cause the cracks that appear at both ends of the model. So, the number of damages caused by cooling may be 3, 4, and 5. Some of these rupture zones extend to the foundation course. With the increase of cooling rate, the number of AE fracture bands increases, and the crack propagation deepens. With the growth of the cooling rate, the number of AE fracture zones increases, and the crack propagation deepens. This phenomenon is because, with the growth of cooling rate, AE rupture points of AC pavement surface accumulate, connect, and expand earlier, resulting in shrinkage deformation. At this point, combined with the interlayer binding force of the lower layer, the stress generated between layers increases, and thus the interlayer peeling increases, so the crack increases. At the same time, it can be found through observation that the speed of temperature reduction is a crucial factor affecting the number and depth of cracks.

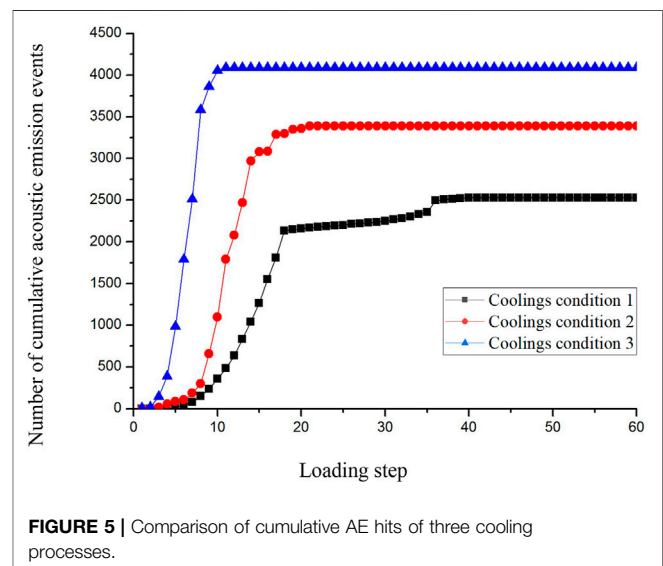
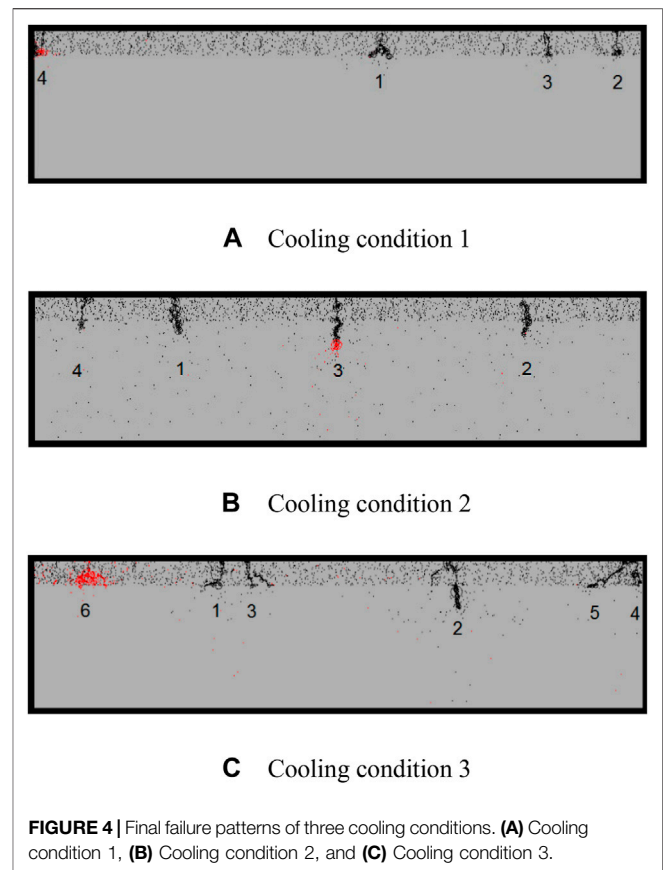
In addition, by collecting the cumulative AE hits of the final damage under three cooling conditions (as shown in **Figure 5**, it can be seen that the cumulative AE inside the AC concrete pavement structure increases with the loading step, wherein, when AC pavement temperature of cooling condition 3, cumulative AE hits of the road surface are the largest, that is, the damage degree is the most serious. On the other hand, we found that the cumulative AE hits of the AC pavement structure under different cooling conditions are within a broad range. When getting to the content, the AE hits of the AC pavement structure will erupt and result in ultimate instability. Therefore, the AE source can be judged by the received AE signal, and then, the damage magnitude and state of the structure can be evaluated. In the future, if conditions permit, a large number of indoor and outdoor experiments could be carried out to obtain a more accurate range before the AE burst, and a more profound study should be done into the relationship between the AE information and the degree of damage and damage inside the AC pavement structure.

Crack Formation and Saturation Process

Because there are many evolution diagrams of AE spatial distribution under different cooling conditions, process change diagrams that can highlight the acoustical emission characteristics of each stage in cooling condition 2 (**Figure 6**) and cooling condition 3 (**Figure 7**) are selected as the



representatives of the AC pavement damage development process. The saturation process refers to the crack propagation gradually reaching its maximum, and crack propagation with the



four stages, and finally got saturation, no longer apparent crack propagation.

1) **Figure 6** temperature loading conditions: the initial temperature is 0°C, each step cools 2°C. Different sizes of red circles and black circles in the model represent AE, red

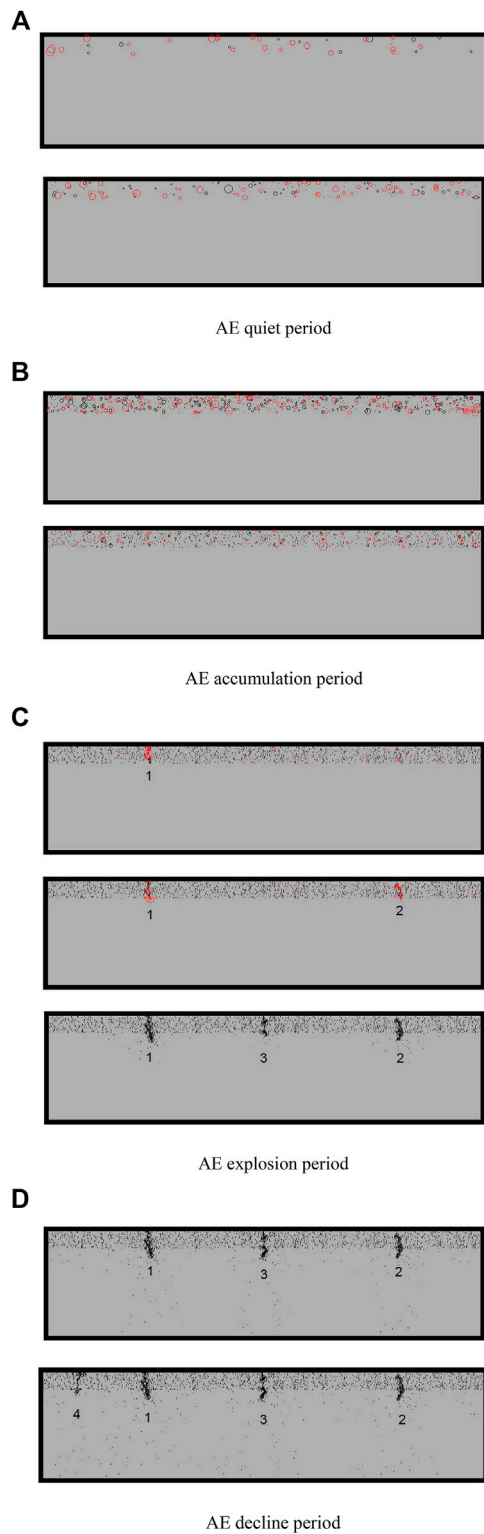


FIGURE 6 | AE evolution with cooling down 2°C per step. **(A)** AE quiet period, **(B)** AE accumulation period, **(C)** AE explosion period, and **(D)** AE decline period.

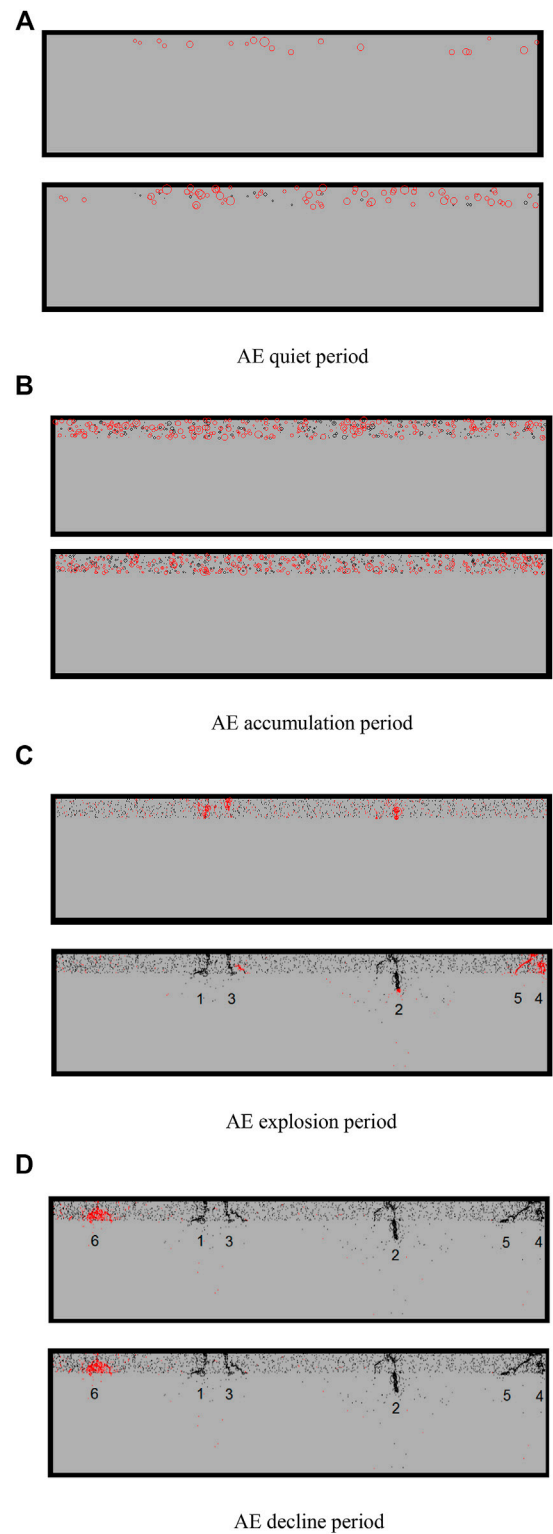


FIGURE 7 | Sample AE evolution with cooling down 4°C per step. **(A)** AE quiet period, **(B)** AE accumulation period, **(C)** AE explosion period, and **(D)** AE decline period.

circles represent tensile failure, and black circles represent final failure. The circle's position represents the rupture point of the AC pavement structure model. Also, the circle's size means the energy's size (the same to discussions later). The specific evolution process is shown in the following figure:

First, (A) Quiet period: In the early cooling stage, a minimal number of red circles appear on the AC pavement. These circles first appear at the top of the pavement surface and then appear inside the cover. These small circles represent a small number of AE, indicating that the AC pavement structure has begun to appear as a phenomenon of AE.

Secondly, (B) the development period is also called the uniform random development stage. With the decrease in temperature, the model's black circle and red circle of AE increased significantly. These AE circles gradually evolved into minor points filled with the upper surface of the AC pavement structure. This phenomenon is because some elements on the upper surface generate tensile stress due to temperature stress under the action of tensile stress. The dislocation and displacement of lattices occur in the model, resulting in AE on the surface of the AC pavement structure. At this stage, AE is independent and has no mutual influence.

Again, (C) the outbreak period is also called the micro-crack nonuniform development stage. It is the most important of the four stages. At this stage, the number of AE increased significantly. Most of the previous circles developed into rupture points, accounting for most of the total. Some rupture points continued to create locally, forming large black and red spots. At the same time, some of the scattered AE crack points in the specimen are connected and superimposed with each other. Finally, the auricular emission crack points gather together first, appear as a red crack zone, and then become a black crack zone, which is presented in the form of cracks 1, 2, and 3 in the left and right of the pavement surface. These cracks will block the shrinkage of adjacent areas, reduce the strength of the AC pavement structure, and continuously reduce the service function.

Finally, (D) the fallback period is called the micro-crack bureau breaking development stage. At this stage, the mutual penetration of AE crack points is increasing. From the original AE crack zones 1, 2, and 3, new AE crack zones are continuously inserted and extended to the grassroots. Finally, there are four AE rupture zones on the AC pavement, which appear in the specimen's surface and the foundation course of the model.

2) **Figure 7** shows the evolution process of the spatial distribution of AE inside AC pavement structure when the temperature is reduced by 4°C in each step. Similar to **Figure 6**, the characteristics of each stage are not repeated.

As shown in **Figure 7**, six AE rupture bands appeared in the sample model with 4°C cooling per step. Compared with the spatial distribution evolution process of AE in **Figure 5**, it can be found that with the increase of cooling rate, the number of AE generated in the model increases, and the interlayer stripping

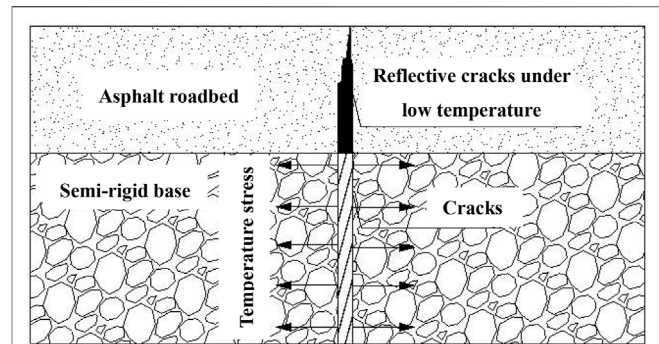


FIGURE 8 | Reflective crack from temperature changes.

phenomenon is more prominent, that is, the damage to the pavement is more serious.

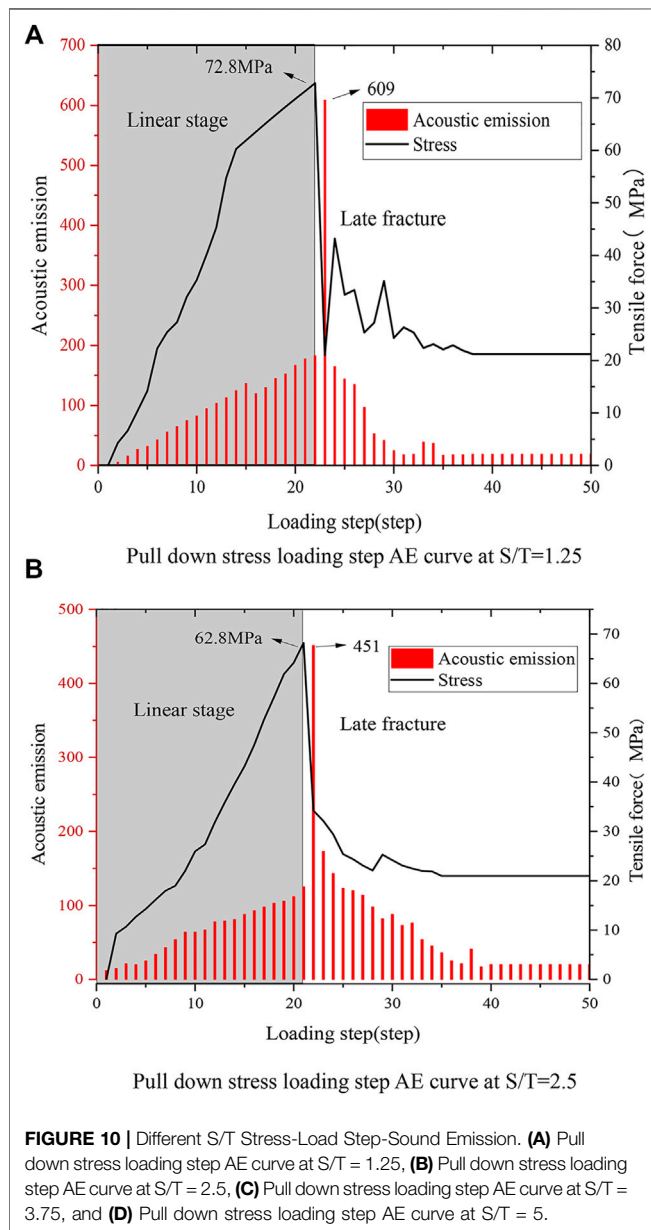
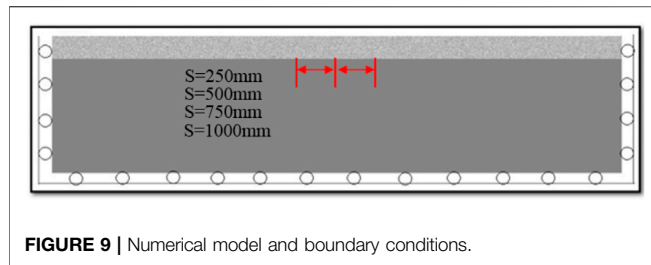
From the above research, it can be seen that under cooling conditions 2 and 3, the cracks extend to the foundation course. Only the surface layer will be excavated and repaved when the pavement is renovated. The gaps in the foundation course will cause reflection cracks on the repaved surface layer, resulting in damage to the surface layer, as shown in **Figure 8**. This is inevitable. Therefore, how to reduce the probability of reflective cracking and reduce the damage to AC pavement structures are very important.

At present, most of the research on reflective cracks focuses on the cracking mechanism of temperature shrinkage cracks. The previous study of Xie (2018) showed that crack spacing affects the stability of the overall structure to a certain extent (this crack spacing is S in this paper). In addition, Chang et al. (2005) pointed out that the stress distribution in the layered model will change due to the prefabricated cracks with different S/T values. Because the asphalt pavement is also a layered model, is this phenomenon possible in the asphalt model? Therefore, the influences of different S/T values on reflection crack propagation (S/T represents the ratio of crack spacing to surface thickness) are studied later to find ways to reduce the probability of reflection crack formation and reduce the damage degree of the asphalt pavement structure. Because the surface thickness T of AC pavement is also an important influencing factor, the influence of different S/T values on the propagation of reflective cracks is studied later.

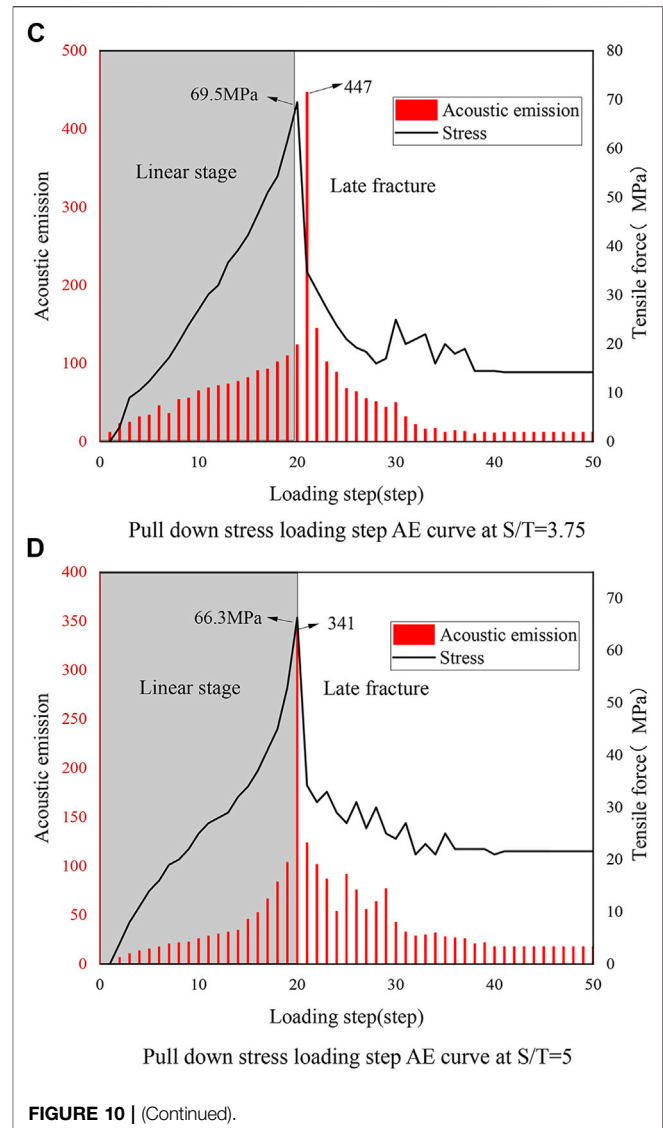
NUMERICAL EXPERIMENT PROCESS OF REFLECTION CRACK PROPAGATION MECHANISM UNDER DIFFERENT CRACK SPACING/LAYER THICKNESS

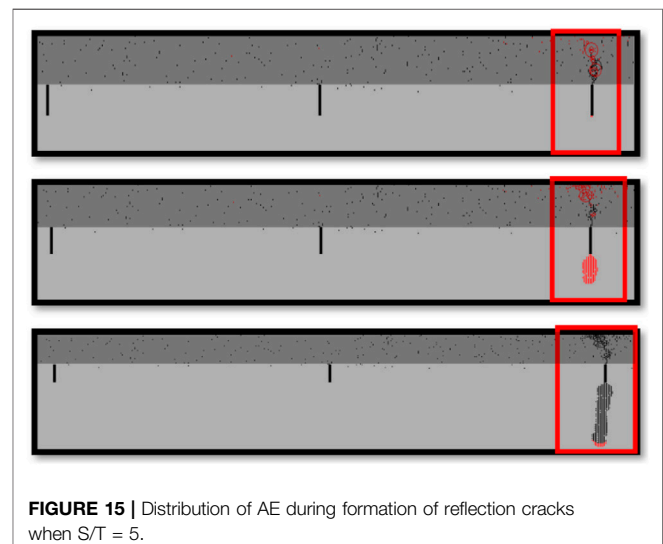
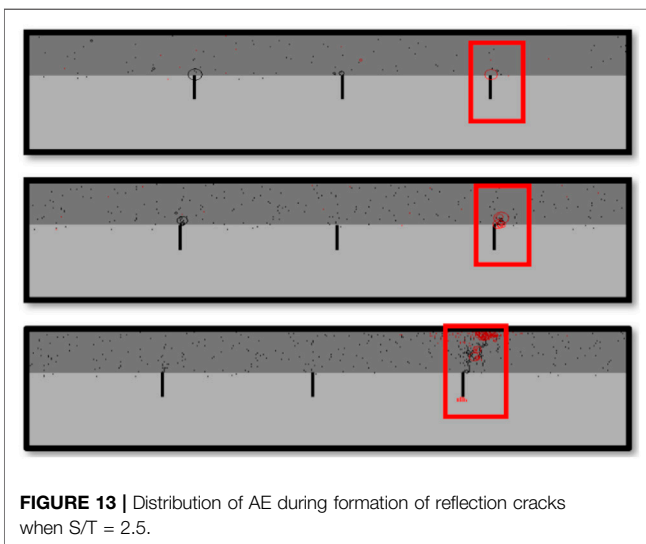
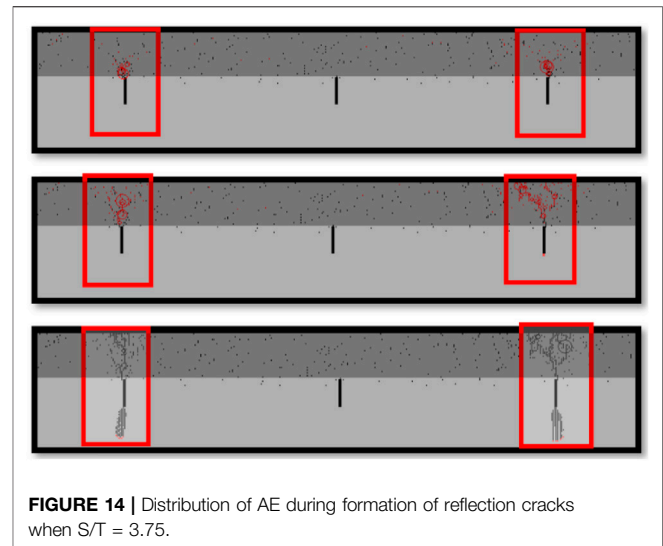
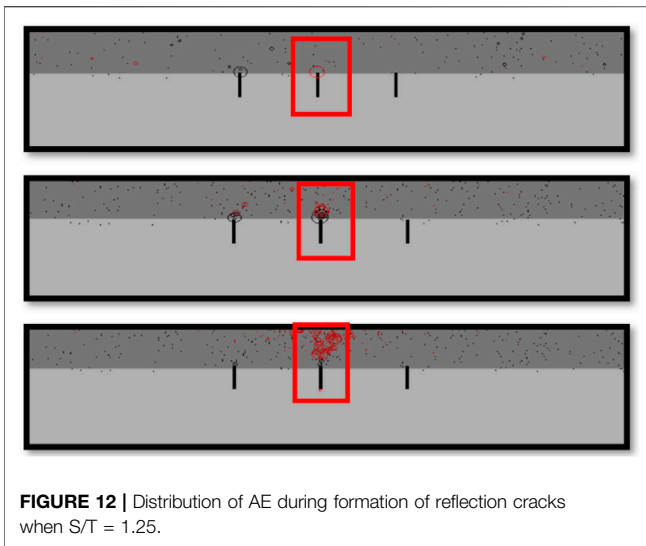
Numerical Model and Boundary Conditions

Three cracks with equal spacing and the same depth are present on the upper surface of the AC pavement structure foundation course. Also, the middle crack is located in the center of the model. The preset crack spacing is 250, 500, 750, and 1,000 mm, so the corresponding S/T values are 1.25, 2.5, 3.75, and 5,



respectively. The actual length of the prefabricated model is 5 m; the thickness is 1.2 m. Also, the double-layer structure model is adopted. The thickness of the superstructure is 200 mm, and the number of cells is $40 \times 1,000$. The thickness of the lower structure





is 1,000 mm, and cells are $200 \times 1,000$. The model's left and right boundary and lower boundary are fixed, and the upper surface is accessible. The corresponding model is shown in **Figure 9**. The mechanical parameters of the materials are shown in **Table 1**.

Stress and Acoustic Emission Analysis

As shown in **Figure 10**, the curves of horizontal stress and AE with the change of loading step under four S/T conditions are shown. The entire simulation process can be divided into three stages:

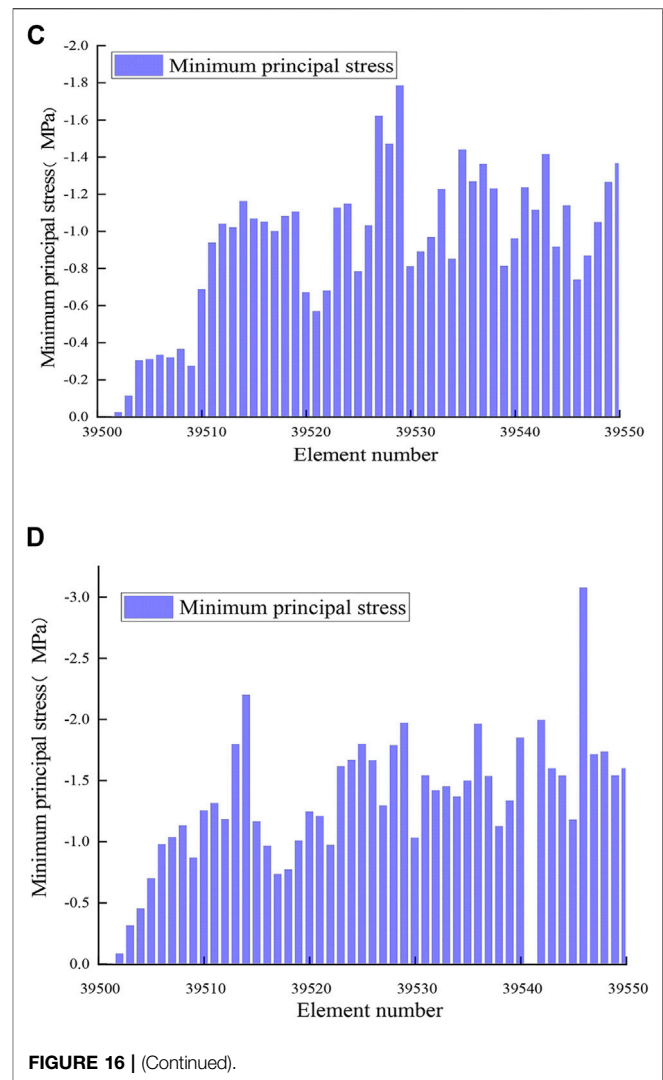
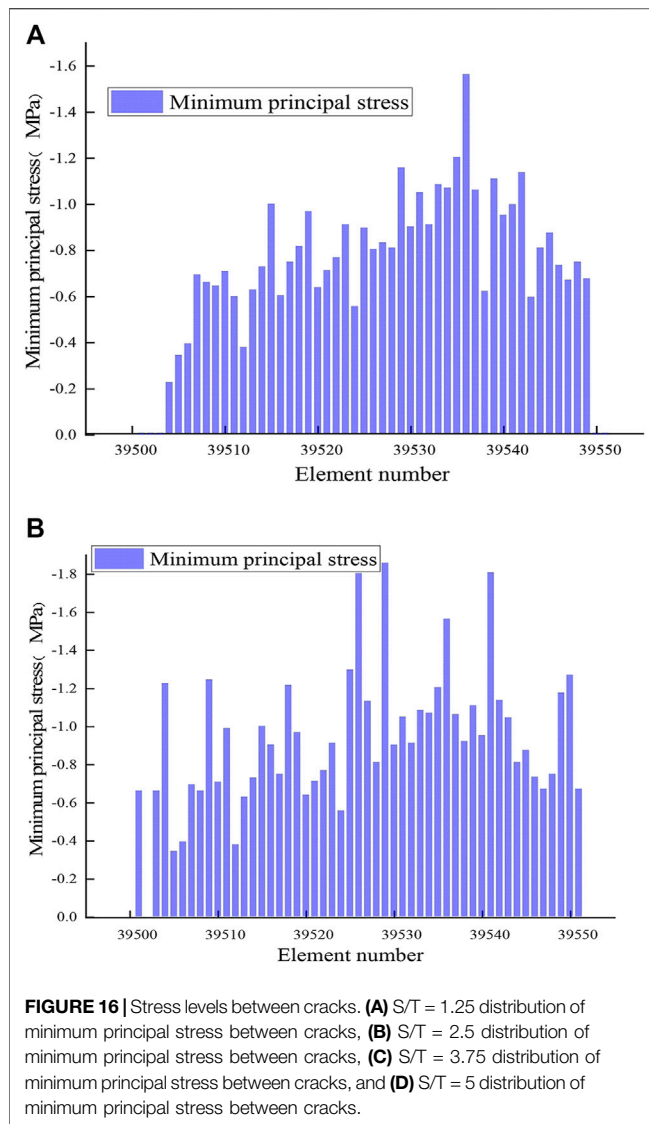
- 1) The linear stage, which occurs before the explosive growth of AE. The stress level of the whole structure and the number of AE show a linear growth trend.
- 2) Reflective crack formation, development, and penetration stage. At this stage, the AE and stress levels peaked. The comparison

of images shows that the external loading temperature during the formation and development of reflective cracks under different S/T ratios was significantly different. Under four conditions, the temperatures of reflection cracks in the model are -23 , -22 , -21 , and -20°C . At this time, the stress peaks of each model are 72.8, 62.8, 69.5, and 66.3 MPa, and the AE peak also has a noticeable difference.

- 3) In the later crack stage, many stress and AE levels drop after the model's failure under four conditions. Also, the trend is almost the same; the final stress falls back to approximately 20 MPa.

Cumulative Acoustic Emission Analysis

Figure 11 shows the cumulative AE curve of the whole model under four S/T values. It can be seen under the four conditions when the loading step is 20 steps. The cumulative AE of the



overall structure has explosive growth, and then, the increase is slow. Finally, with the stop of temperature loading, the overall cumulative number of AE has reached a fixed level. It can be seen from the figure that with the increase of crack spacing, the cumulative amount of AE of the whole pavement structure will decrease. The cumulative number of AE of the system when $S/T = 1.25$ is much larger than that of the form when $S/T = 5$, which shows that the damage degree of the whole pavement structure will decrease with the increase of crack spacing.

Combined with the conclusions discussed earlier, the pavement is more easily damaged with increased crack spacing. We can draw a particular initial determination that the overall AC pavement structure is more prone to damage with increased crack spacing in the foundation course under the uniform cooling effect. However, the degree of injury is lower than when the crack space is small. Also, the life of the overall pavement structure will also be extended accordingly.

Acoustic Emission Analysis Under Different S/T Conditions

To intuitively observe the formation process of reflection cracks under four S/T conditions, this section follows the formation and expansion process of reflection cracks in AC pavement structure under each state by AE module in finite element software to determine the occurrence time and expansion mode of reflection cracks.

They are prefabricated with S/T values of 1.25, 2.5, 3.75, and 5 crack models for numerical simulation, obtained in different S/T values of the AE distribution model. The diagram mentioned later shows the distribution of AE selected in the process of AC pavement structure failure (Figures 12–15).

It can be seen that when $S/T = 1.25$, reflected cracks appeared at the prefabricated crack position in the central part of the model foundation course. At first, AE seemed at the crack's tip and gradually expanded to the AC pavement surface layer. Finally, the reflected shots penetrated the surface structure, destroying the pavement structure.

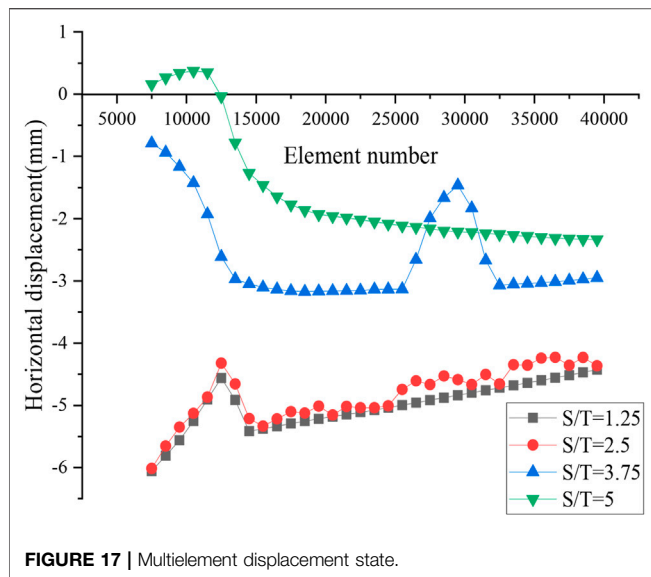


FIGURE 17 | Multielement displacement state.

At $S/T = 2.5$, the reflection cracks appear in the right area of the central position. Also, the failure area is more significant than that at $S/T = 1.25$. When $S/T = 3.75$, many AE phenomena appeared on both sides of the central part of the structural model at first. Also, two reflection cracks appeared in the final failure state of the AC pavement structure. It is evident that after the reflection cracks appeared, the trials expanded to the foundation course. Finally, it formed two shots in the ground, and the depth was almost the same. When $S/T = 5$, a reflection crack appears in the AC pavement structure after uniform cooling and is located in the right area of the model. At the same time, this crack also continues to expand toward the foundation course with the decrease in temperature. The expansion depth is more profound than $S/T = 3.75$, and the damage to the floor is more serious. Finally, the number of micro-cracks in the AC pavement surface under four conditions shows that the AC pavement surface will decrease with increased space.

In summary, we can analyze the AE distribution map under four different spacing of preset cracks. With the increase of preset crack spacing, the damage degree of the AC pavement surface layer in the AC pavement structure will decrease. Still, the increase in preset crack spacing will lead to the expansion of cracks in the foundation course, and the depth will increase with the increase in space. In this case, the damage degree of the road structure foundation course will grow.

Cumulative Acoustic Emission Analysis

To better analyze the reasons for the difference in the overall damage of AC pavement caused by preset crack spacing, this section analyses the stress level between four crack spacing and the changing state of the displacement at the crack—Figure 16 analysis of minimum principal stress state between cracks under four S/T conditions.

Figure 16 shows the minimum principal stress level between cracks under different S/T spaces. It can be seen from the figure

that the curve is more compact with the increase in S/T value because the number of units selected is also increased with the rise of crack space. Overall, the minimum principal stress between cracks under the four S/T values is a state of less than zero. Therefore, the main force between cracks is the tensile force, the point where the minimum principal stress is zero in the image. This is due to the unit's failure due to the tensile stress, which has lost its born capacity. Specifically, when the S/T value is 1.25, the peak value of horizontal tensile stress between cracks is 1.6 MPa, and the overall level between shots is concentrated near 0.8 MPa. When the S/T value is 2.5, the peak stress between cracks is 1.8 MPa, and the stress level of the whole unit between cracks is approximately 1.2 MPa. When the S/T value is 3.75, the horizontal stress peak between cracks reaches approximately 2 MPa, and the overall stress level between shots is approximately 1.5 MPa. Finally, when the S/T value comes 5, the stress peak between the cracks has reached 3 MPa. Also, the overall stress level between the crack shots is approximately 2 MPa; the stress state is precarious, and the fluctuation range is extensive.

The analysis shows that with the increase of crack spacing, the horizontal tensile stress level between cracks will also appear to be an inevitable increase. The peak stress between attempts at $S/T = 5$ is twice that of attempts at $S/T = 1.25$. Therefore, by analyzing the stress level between shots, it can be concluded that the horizontal tensile stress between cracks will increase with the increase of crack spacing in the foundation course. This also explains why the degree of AC pavement structure increases with the preset crack space. Due to the high level of horizontal stress between cracks, it is more likely to have a micro-crack at the intersection of the surface and the foundation course. In addition, the high level of tensile stress between cracks will put the overall structure in a high-stress state for a long time. Micro-crack will gradually develop and evolve and progressively expand to the surface layer to form reflective cracks. In addition, the high-stress state will also make cracks develop downward along with the pavement foundation course structure. Therefore, the foundation course structure will also suffer a certain degree of damage.

Internal Multielement Displacement State Analysis

To better observe the propagation state of reflection cracks under different S/T values, the horizontal displacement state at the formation of reflection cracks under four S/T values was analyzed. Figure 17 is a multielement horizontal displacement analysis of the reflection cracks in the surface layer under four S/T conditions, where the positive and negative displacements represent the direction.

It can be seen from Figure 17 that when $S/T = 1.25$, the horizontal displacement at the formation of the reflection crack is approximately 5.5 mm. When $S/T = 2.5$, the overall curve and the curve trend of $S/T = 1.25$ are consistent and above $S/T = 1.25$. When $S/T = 3.5$, the horizontal displacement is approximately 3 mm. Finally, when $S/T = 5$, the horizontal displacement is approximately 2 mm. In summary, with the increase of S/T value, the horizontal displacement formed in the surface layer shows a

decreasing state. With the rise of the S/T value, the width of the reflective cracks in the surface structure decreases. Also, the damage degree of the surface layer in the overall pavement structure is also low.

CONCLUSION

Based on the temperature version of RFPA software, this paper mainly studies the AE damage process of AC pavement structure under a low-temperature environment, analyzes the auditory emission characteristic information in detail, and studies the propagation mechanism of reflection cracks under cooling mode for four models with different S/T values. The main conclusions are as follows:

- 1) The numerical test process reproduces the AE damage process of the AC pavement structure. This clearly shows that the instability of the AC pavement structure is not completed instantly. The internal fracturing points of the system are superimposed, gathered, and penetrated to form cracks. The instability of the AC pavement structure starts as the micro-cracks expand and penetrate. This process demonstrates that AE technology can detect the location of the crack and predict the location of crack propagation.
- 2) It is found that the development process of AE of AC pavement structure is summarized into four development stages: quiet period, development period, outbreak period, and fallback period. Moreover, different locations have different characteristics. In a low-temperature environment, the greater the temperature reduction rate, the earlier AE burst time and failure in AC pavement structure will occur. This shows that the speed of temperature reduction is a crucial factor affecting the structural damage of AC pavement.
- 3) By observing the change curve of the load–stress–AE number of the AC pavement structure. It can be observed that the AE amplitude change shows a primary mode of the foreshock–main shock–aftershock type similar to the seismic activity law. The temperature at the beginning of temperature reduction showed linearity. The stress drop after the mainshock was significant, offering a solid brittleness.
- 4) The crack generated by the AC pavement structure under temperature is divided into two cases. One is that the surface is expanded with the change of temperature. The other is gradually developed from the middle layer of the surface layer. It shows that under the influence of a low-temperature environment, the cracks appearing in pavement structure are manifested on the road surface and hidden inside, which becomes a hidden danger of engineering. Therefore, AE monitoring is critical.
- 5) Through the study of the cumulative AE, it is found that the AE of the entire structure shows a downward trend with the increase of S/T value, indicating that although the rise of preset crack spacing will make pavement structure more vulnerable to damage, the damage degree of overall surface

structure is low. The AE distribution analysis of the model found that with the increase of S/T value, the number of reflective cracks in the surface layer will increase. Also, the gaps will gradually expand to the foundation course, causing significant damage to the overall AC pavement structure.

- 6) The stress level between cracks and the multielement displacement state at the reflection crack is analyzed. It is concluded that with the increase of preset crack spacing, the overall stress level between shots will increase, and the width of reflection crack in the surface decreases. I am finally combined with the AE distribution of the whole structure. The reasons for the failure difference of the entire system under different S/T conditions are analyzed. With the increase of crack spacing, the stress level between cracks will increase, but it is mainly used to expand trials in the foundation course, and only a tiny part of the stress is used to develop to the surface layer structure to form reflective cracks.

Based on the conclusions discussed earlier, this paper proposes corresponding prevention measures to guide engineering practice:

- 1) According to the conclusion of this paper, in the actual construction process, some small spacing cracks can be present in the large spacing cracks in a foundation course. The reduction of spacing can slow down the frequency of reflection cracks in some ways and avoid cracks extending to the foundation course structure.
- 2) Before overlaying the AC pavement surface, if there is a relatively concentrated crack area on the base surface, asphalt material can be overlaid, such as using an asphalt mixture with extensive low-temperature penetration to better protect the surface structure.

DATA AVAILABILITY STATEMENT

The original contributions presented in the study are included in the article/supplementary material, further inquiries can be directed to the corresponding author.

AUTHOR CONTRIBUTIONS

All authors listed have made a substantial, direct, and intellectual contribution to the work and approved it for publication.

FUNDING

The work presented in this paper was supported by the Open Research Fund of Collaborative Innovation Center for Prevention and Control of Mountain Geological Hazards of Zhejiang Province (PCMGH-2016-Z-04).

REFERENCES

- Bai, T., Pollard, D. D., and Gao, H. (2000). Explanation for Fracture Spacing in Layered Materials. *Nature* 403 (6771), 753–756. doi:10.1038/35001550
- Behnia, A., Chai, H. K., and Shiotani, T. (2014). Advanced Structural Health Monitoring of concrete Structures with the Aid of Acoustic Emission. *Construction Building Mater.* 65, 282–302. doi:10.1016/j.conbuildmat.2014.04.103
- Behnia, B., Buttlar, W., and Reis, H. (2018). Evaluation of Low-Temperature Cracking Performance of Asphalt Pavements Using Acoustic Emission: A Review. *Appl. Sci.* 8 (2), 306. doi:10.3390/app8020306
- Brown, S. F., Thom, N. H., and Sanders, P. J. (2001). *A Study of Grid Reinforced Asphalt to Combat Reflection Cracking (With Discussion)*. Clearwater Beach, Florida. Asphalt Paving Technology 2001. Conference presentation] <https://trid.trb.org/view/720140>.
- Cai, X., Shi, C., Chen, X., and Yang, J. (2021). Identification of Damage Mechanisms during Splitting Test on SFP at Different Temperatures Based on Acoustic Emission. *Construction Building Mater.* 270, 121391. doi:10.1016/j.conbuildmat.2020.121391
- Chang, X., Zhong, H., Tang, C., Zhang, Y., and Zhang, J. (2005). Numerical Research on Fracture Saturation for Layered Rock Stratum. *Chin. J. rock Mech. Eng.* 024 (A01), 5151–5156. Available at: <https://kns.cnki.net/kcms/detail/detail.aspx?FileName=ZGYJ200508002024&DbName=CPFD2006>
- Dave, E. V., and Buttlar, W. G. (2010). Thermal Reflective Cracking of Asphalt concrete Overlays. *Int. J. Pavement Eng.* 11 (6), 477–488. doi:10.1080/10298430903578911
- Duan, R., Huang, G., Li, Y., Zheng, R., Wang, G., Xin, B., et al. (2021). Ensemble Temperature and Precipitation Projection for Multi-Factorial Interactive Effects of GCMs and SSPs: Application to China. *Front. Environ. Sci.* 9, 382. doi:10.3389/fenvs.2021.742326
- Hakimzadeh, S., Behnia, B., Buttlar, W. G., and Reis, H. (2017). Implementation of Nondestructive Testing and Mechanical Performance Approaches to Assess Low Temperature Fracture Properties of Asphalt Binders. *Int. J. Pavement Res. Techn.* 10 (3), 219–227. doi:10.1016/j.ijprt.2017.01.005
- Hill, B., Behnia, B., Buttlar, W. G., and Reis, H. (2013). Evaluation of Warm Mix Asphalt Mixtures Containing Reclaimed Asphalt Pavement through Mechanical Performance Tests and an Acoustic Emission Approach. *J. Mater. Civ. Eng.* 25 (12), 1887–1897. doi:10.1061/(ASCE)MT.1943-5533.0000757
- Hou, F., Li, T., Li, X., Li, Y., and Guo, M. (2021). Research on the Anti-reflective Cracking Performance of a Full-Depth Asphalt Pavement. *Sustainability* 13 (17), 9499. doi:10.3390/su13179499
- Hu, S., Zhou, F., and Scullion, T. (2010). Reflection Cracking-Based Asphalt Overlay Thickness Design and Analysis Tool. *Transportation Res. Rec.* 2155 (1), 12–23. doi:10.3141/2155-02
- Jiao, Y., Fu, L., Shan, W., and Liu, S. (2019a). Damage Fracture Characterization of Pervious Asphalt Considering Temperature Effect Based on Acoustic Emission Parameters. *Eng. Fracture Mech.* 210, 147–159. doi:10.1016/j.engfracmech.2018.10.007
- Jiao, Y., Zhang, L., Guo, Q., Guo, M., and Zhang, Y. (2020). Acoustic Emission-Based Reinforcement Evaluation of Basalt and Steel Fibers on Low-Temperature Fracture Resistance of Asphalt Concrete. *J. Mater. Civ. Eng.* 32 (5), 04020104. doi:10.1061/(ASCE)MT.1943-5533.0003118
- Jiao, Y., Zhang, Y., Zhang, M., Fu, L., and Zhang, L. (2019b). Investigation of Fracture Modes in Pervious Asphalt under Splitting and Compression Based on Acoustic Emission Monitoring. *Eng. Fracture Mech.* 211, 209–220. doi:10.1016/j.engfracmech.2019.02.025
- Khodaii, A., Fallah, S., and Moghadas Nejad, F. (2009). Effects of Geosynthetics on Reduction of Reflection Cracking in Asphalt Overlays. *Geotextiles and Geomembranes* 27 (1), 1–8. doi:10.1016/j.geotextmem.2008.05.007
- Kim, K. W., Doh, Y. S., and Lim, S. (1999). Mode I Reflection Cracking Resistance of Strengthened Asphalt Concretes. *Construction Building Mater.* 13 (5), 243–251. doi:10.1016/s0950-0618(99)00032-x
- Li, X., and Marasteanu, M. O. (2011). Investigation of Low Temperature Cracking in Asphalt Mixtures by Acoustic Emission. *Road Mater. pavement Des.* 7 (4), 491–512. doi:10.1080/14680629.2006.9690048
- Li, X., Marasteanu, M. O., Iverson, N., and Labuz, J. F. (2006). Observation of Crack Propagation in Asphalt Mixtures with Acoustic Emission. *Transportation Res. Rec.* 1970 (1), 171–177. doi:10.1177/0361198106197000118
- Liang, M., Xu, J., Chan, J. C. L., Wu, L., and Xu, X. (2020). Changing Relationship between Tibetan Plateau Temperature and South China Sea Summer Monsoon Precipitation. *Front. Environ. Sci.* 8. doi:10.3389/fenvs.2020.583466
- Liu, J. Q., Chen, C. C., Wang, B. S., and Hao, N. (2011). The Fatigue Fracture Analysis of Semi-rigid Base-Course Asphalt Pavement under the Temperature Effect. *J. Xi'an Univ. Techn.* doi:10.19322/j.cnki.ISSN.1006-4710.2011.03.024
- Morris, G. R., Chen, N. J., and Di Vito, J. A. (1982). “Application of Asphalt-Rubber on New Highway Pavement Construction,” in Paper presented at the 61st annual meeting of the Transportation Board.
- Nair, A., and Cai, C. S. (2010). Acoustic Emission Monitoring of Bridges: Review and Case Studies. *Eng. structures* 32 (6), 1704–1714. doi:10.1016/j.engstruct.2010.02.020
- Qisen, J. Z. J., and Zheng, J. L. (1990). Finite Elements Analysis of Reflection Crack and Stress Intensity Factors in Half Rigid Pavements [J]. *Chin. J. Geotechnical Eng.* 12 (3), 22–30.
- Qiu, X., Xu, J., Xu, W., Xiao, S., Wang, F., and Yuan, J. (2020). Characterization of Fatigue Damage Mechanism of Asphalt Mixtures with Acoustic Emission. *Construction Building Mater.* 240, 117961. doi:10.1016/j.conbuildmat.2019.117961
- Seo, Y., and Kim, Y. R. (2008). Using Acoustic Emission to Monitor Fatigue Damage and Healing in Asphalt Concrete. *KSCE J. Civ Eng.* 12 (4), 237–243. doi:10.1007/s12205-008-0237-3
- Shen, Z. W., Shao, X. S., and Wang, N. X. (2011). Prediction Model of Measured Temperature Field of Asphalt Pavement in Cold Region. *J. China Foreign Highw.* 31 (6), 129–133. doi:10.14048/j.issn.1671-2579.2011.06.043
- Sun, Z., Behnia, B., Buttlar, W. G., and Reis, H. (2017). Assessment of Low-Temperature Cracking in Asphalt Materials Using an Acoustic Emission Approach. *J. Test. Eval.* 45 (6), 20160579–20161958. doi:10.1520/Jte20160579
- Tsai, F.-L., Lytton, R. L., and Lee, S. (2010). Prediction of Reflection Cracking in Hot-Mix Asphalt Overlays. *Transportation Res. Rec.* 2155 (1), 43–54. doi:10.3141/2155-05
- Wang, J. (2012). “Analysis the Control Techniques of Reflection Crack on Asphalt Overlay of Old Cement concrete Pavement,” in Paper presented at the Applied Mechanics and Materials, Beijing, September 26, 2012.
- Wang, X., and Zhong, Y. (2019). Reflective Crack in Semi-rigid Base Asphalt Pavement under Temperature-Traffic Coupled Dynamics Using XFEM. *Construction Building Mater.* 214, 280–289. doi:10.1016/j.conbuildmat.2019.04.125
- Wei, H., Hu, B., Wang, F., Zheng, J., Jin, J., and Liu, C. (2020). Temporal-spatial Evolution Characteristics of Acoustic Emission in Asphalt concrete Cracking Process under Low Temperature. *Construction Building Mater.* 248, 118632. doi:10.1016/j.conbuildmat.2020.118632
- Wei, H., Li, J., Wang, F., Zheng, J., Tao, Y., and Zhang, Y. (2021). Numerical Investigation on Fracture Evolution of Asphalt Mixture Compared with Acoustic Emission. *Int. J. Pavement Eng.* 1–11. doi:10.1080/10298436.2021.1902524
- Wei, J., Zhu, W., Guan, K., Zhou, J., and Song, J.-J. (2019). An Acoustic Emission Data-Driven Model to Simulate Rock Failure Process. *Rock Mech. Rock Eng.* 53 (4), 1605–1621. doi:10.1007/s00603-019-01994-3
- Xie, W. K. (2018). *Research on the Influence of Slice-Cracks Technology on Mechanical Behavior of Asphalt Overlay on Existing Cement Concrete Pavement*. [dissertation/doctoral thesis]. Xian: Xi'an University of architecture and technology.
- Xu, J., Fu, Z., Han, Q., Lacidogna, G., and Carpinteri, A. (2018). Micro-cracking Monitoring and Fracture Evaluation for Crumb Rubber concrete Based on

- Acoustic Emission Techniques. *Struct. Health Monit.* 17 (4), 946–958. doi:10.1177/1475921717730538
- Yang, K., He, Z., Li, D., Xu, H., and Kong, L. (2021a). Experimental Study on Basalt Fiber Crack Resistance of Asphalt Concrete Based on Acoustic Emission. *Materials* 14 (15), 4096. doi:10.3390/ma14154096
- Yang, K., Li, D., He, Z., Zhou, H., and Li, J. (2021b). Study on Acoustic Emission Characteristics of Low-Temperature Asphalt Concrete Cracking Damage. *Materials* 14 (4), 881. doi:10.3390/ma14040881
- Zhang, J. L., and Guan, H. X. (2001). A Finite Element Analysis Based on thermal Viscoelasticity Theory of Reflective Crack Resulting from Low Temperature Shrinkage. *China J. Highw. Transport* 14 (3), 1–5. doi:10.19721/j.cnki.1001-7372.2001.03.001

Conflict of Interest: Authors CB, ZC, and YQ were employed by the Huahui Engineering Design Group Corporation Ltd. Author YC was employed by the China Huaneng Zhalainguo Coal Industry Co. Ltd.

The remaining authors declare that the research was conducted in the absence of any commercial or financial relationships that could be construed as a potential conflict of interest.

Publisher's Note: All claims expressed in this article are solely those of the authors and do not necessarily represent those of their affiliated organizations or those of the publisher, the editors, and the reviewers. Any product that may be evaluated in this article, or claim that may be made by its manufacturer, is not guaranteed or endorsed by the publisher.

Copyright © 2022 Bao, Liu, Xia, Cui, Cao, Qian, Liu, Mu and Wang. This is an open-access article distributed under the terms of the Creative Commons Attribution License (CC BY). The use, distribution or reproduction in other forums is permitted, provided the original author(s) and the copyright owner(s) are credited and that the original publication in this journal is cited, in accordance with accepted academic practice. No use, distribution or reproduction is permitted which does not comply with these terms.



Research on Deformation and Fracture Characteristics of the Fractured Rock Mass Under Coupling of Heavy Rainfall Infiltration and Mining Unloading

Menglai Wang^{1,2}, Xiaoshuang Li^{3,4,5}, Shun Yang^{2,6*}, Lin Teng⁵, Qiusong Chen⁷ and Song Jiang⁸

¹Yunnan Phosphating Group Co. LTD, Kunming, China, ²School of Resources and Safety Engineering, Chongqing University, Chongqing, China, ³State Key Laboratory of Safety and Health for Metal Mines, Sinosteel Maanshan General Institute of Mining Research Co. LTD, Maanshan, China, ⁴Key Laboratory of Rock Mechanics and Geohazards of Zhejiang Province, Shaoxing, China, ⁵College of Civil Engineering, Qilu Institute of Technology, Jinan, China, ⁶School of Resources and Environmental Engineering, Jiangxi University of Science and Technology, Ganzhou, China, ⁷School of Resources and Safety Engineering, Central South University, Changsha, China, ⁸School of Resources Engineering, Xi'an University of Architecture and Technology, Xi'an, China

OPEN ACCESS

Edited by:

Jie Chen,
Chongqing University, China

Reviewed by:

Chun Zhu,
Hohai University, China
Chunyang Zhang,
Wuhan University of Technology,
China
Yingchun Li,
Dalian University of Technology, China

*Correspondence:

Shun Yang
yangshun0820@163.com

Specialty section:

This article was submitted to
Geohazards and Georisks,
a section of the journal
Frontiers in Earth Science

Received: 09 October 2021

Accepted: 23 December 2021

Published: 16 February 2022

Citation:

Wang M, Li X, Yang S, Teng L, Chen Q
and Jiang S (2022) Research on
Deformation and Fracture
Characteristics of the Fractured Rock
Mass Under Coupling of Heavy Rainfall
Infiltration and Mining Unloading.
Front. Earth Sci. 9:792038.
doi: 10.3389/feart.2021.792038

The present study used PFC numerical software to examine the mechanical properties and fracture propagation characteristics of the fractured rock mass under coupling of heavy rainfall infiltration and mining unloading. Based on the engineering background of the Dexing mine, the pore water pressure is set to 0, 0.5, 1.0, 1.5, and 2.0 mpa, the true triaxial lateral unloading rate is 0.3 mpa/level and 0.6 mpa/level, and the water content state of rock is dry, natural, and saturated. Then, the true triaxial compression numerical simulation test is carried out, and the results showed that with the increase of the water content, the rock compaction stage increases, the elastic stage shortens, and the yield stage becomes more obvious. The faster the unloading rate is, the greater the influence on the rock strain is. After unloading, the stress jump point appears and the strain increase rate becomes larger, the volume of the rock increases and occurs as large s in the unloading direction, and finally it leads to severe brittle failure of the rock. With the increase of rock pore water pressure, the compressive strength and the peak strain of the rock decrease, and the pore water pressure accelerates the process of rock failure.

Keywords: rainfall infiltration, mining unloading, fractured rock mass, fracture propagation characteristics, numerical simulation

1 INTRODUCTION

Since the 21st century, with the rapid development of modern mine technology, the scale and depth of mine rock mass projects have been continuing to grow rapidly. Large-scale high-steep rock slopes with a vertical depth of more than 400 m and a slope angle of more than 40° continue to emerge (Chen and Jing, 2016; Li X. S et al., 2021; Li et al., 2021). The long-term stability of high and steep rock slopes under complex geological and external disturbance environments has become a major problem for large-scale mines to convert from open-pit to underground mining. In China, the geological structure of Jiangxi Province is complex, and the long-term strong tectonic movement has fully developed the primary faults, joints, and fractures in the rock mass (Pu et al., 2019; Ji et al., 2020; Shuai, 2021; Liu et al., 2020a;

Song et al., 2020; Du et al., 2021; Li et al., 2021a, Li et al., 2021b). Affected by open blasting, mechanical excavation, and weathering, a large number of secondary fissures have been generated inside the high-steep rock slope, which further aggravates the fracture and instability of the rock mass. In this area, the geological disasters induced by heavy rainfall are becoming more and more serious (Bai and Elsworth, 2020; Rutqvist and Stephansson, 2003; Lee and Cho, 2002; Li et al., 2020; Li L. K et al., 2021; Li et al., 2019; Li et al., 2021a; Li et al., 2021b; Li et al., 2021c; Song et al., 2021; Wang et al., 2021; Zhong et al., 2021). The mine slope rock mass has undergone the two-stage compound mining unloading effect after open-pit and underground mining. This nonsynchronous correspondence between time and space makes the failure mechanism of the slope under compound mining unloading more complicated. Therefore, in-depth research on the deformation and fracture characteristics of fractured rock masses under the coupling of heavy rainfall infiltration and mining unloading can ensure the safety and stability of mine slopes (Vandamme and Roegiers, 1990; Shao and Rudnicki, 2000; Tang et al., 2016; Liu et al., 2020b; Yao et al., 2020; Zhang et al., 2020; Deng et al., 2021; Liu et al., 2021; Zuo et al., 2021).

In the research of the fracture mechanism of the fractured rock mass, Giffith (1921) proposed the fracture criterion–energy criterion and the relationship between fracture toughness and crack size for brittle material crack size, in which the theory of fracture mechanics has been quickly applied and developed. However, this criterion cannot explain the singular solution of the stress at the crack tip of brittle materials. Griffith, (1924); Irwin (1957) revised Giffith's theory to promote the further development of brittle rock linear elastic fracture mechanics. Erdogan and Sih (1963) proposed the theory of maximum stress resistance based on compound cracks in actual engineering, and they put forward the theory of strain energy density of mixed cracks in 1973. In addition, some scholars have proposed the failure criterion based on the tensile strain of brittle hard work. For example, Stacy (1981) believed that the prerequisite for rock fracture when the brittle hard rock cracked under compressive load was that the tensile strain of the brittle rock was greater than the maximum tensile strain threshold of the rock and derived the tensile strain judgment criterion. In the field of research on the fracture mechanism of the fractured rock mass under the coupling of hydraulic and mechanical effects, Kou et al. (2019) conducted a hydraulic coupling test on prefabricated 45° single-crack specimens, which showed that the peak strength of the specimen decreased with the increase of water pressure, and the deviator stress after the peak decreased. As the confining pressure increases, the peak strength increases, and the degree of post-peak strain-softening gradually increases. Valko and Economides (1994) and Souley et al. (2001) used the DMM model and CDM model to simulate the hydraulic fracturing process of rocks. Shao et al. (2005) and Yuan and Harrison (2006) used DMM/CDM and CDM/SM hybrid models to study the crack failure laws and permeability characteristics of the samples.

Nowadays, most scholars focus on the study of the crack criterion based on the maximum circumferential stress criterion (MTS) (Lin et al., 2018), the theory of the maximum energy

release rate, and the theory of the strain energy density factor (S) (Liu et al., 2019; Jia-jun et al., 2020; Li et al., 2021d). Among them, the large-circumferential stress criterion is simple in form and can better predict the crack characteristics. But, this criterion ignores T-stress. For rock brittle materials, not only tensile failure but also shear failure affects the growth of cracks. The crack tip will also have N stress perpendicular to the crack surface (Zhao et al., 2012; Cheng and Zhou, 2015; Wei et al., 2017; Zhao et al., 2018; Guo et al., 2019; Liu et al., 2019; Li H. F et al., 2021; Wang and Zhao, 2021). Therefore, it is necessary to focus on studying the law of crack propagation after crack initiation. This research takes the open-pit to underground mining in the Dexing copper mine as the engineering background. Through geological investigations, on-site sampling, and indoor physical experiments, PFC numerical simulations were carried out for rocks under different water-bearing conditions, buried depths, fracture distribution, loading and unloading methods, and pore water pressure. In-depth analysis of the mechanical properties and crack propagation characteristics of the fractured rock mass of high and steep rock slopes was carried out under the coupling of heavy rainfall infiltration and mining unloading. It can provide necessary theoretical support for open-pit slope mining and underground surrounding rock support.

2 ENGINEERING BACKGROUND

As shown in **Figure 1A**, the copper mine is located in Dexing City, Jiangxi Province, China. The copper factory mining area has the characteristics of mountainous microclimates such as warm climate, abundant rainfall, sufficient sunlight, large temperature difference between day and night, and long frost-free period. The working area is full of precipitation, and the annual average rainfall is 2250 mm. The rainy season is from March to July each year, and the precipitation accounts for about 70% of the annual precipitation. The average water period is from August to November, and the dry season is from December to February of the following year. In addition, the study area is a low mountain and hilly landform, with large undulations, high in the east and low in the west. The microtopography is mostly mountain valleys, forests, and farmland. Due to the artificial excavation of the mountain, an artificial slope with a height of about 548 m and a length of about 400 m is formed. The slope occurrence is 144°–152° in trend, 234°–242° inclination, 41°–42° inclination, and the copper mining area is about 4.8 square kilometers (red curve) (**Figure 1(a1)**). The artificial platform on the surface of the slope is covered by a 0.5–2.5 m thick artificial filling. The lower part of the slope is the mining area and transportation road. The strike and inclination of the fault have the characteristics of relaxation and wavy. The fault structure in the study area (H-H' section) is well developed and has multiple phases. According to the occurrence and nature of the faults, the faults in the Huangniuqian slope area can be divided into EW faults, NNW faults, NWW faults, and NNE faults (**Figure 1(a2)**).

1) EW faults

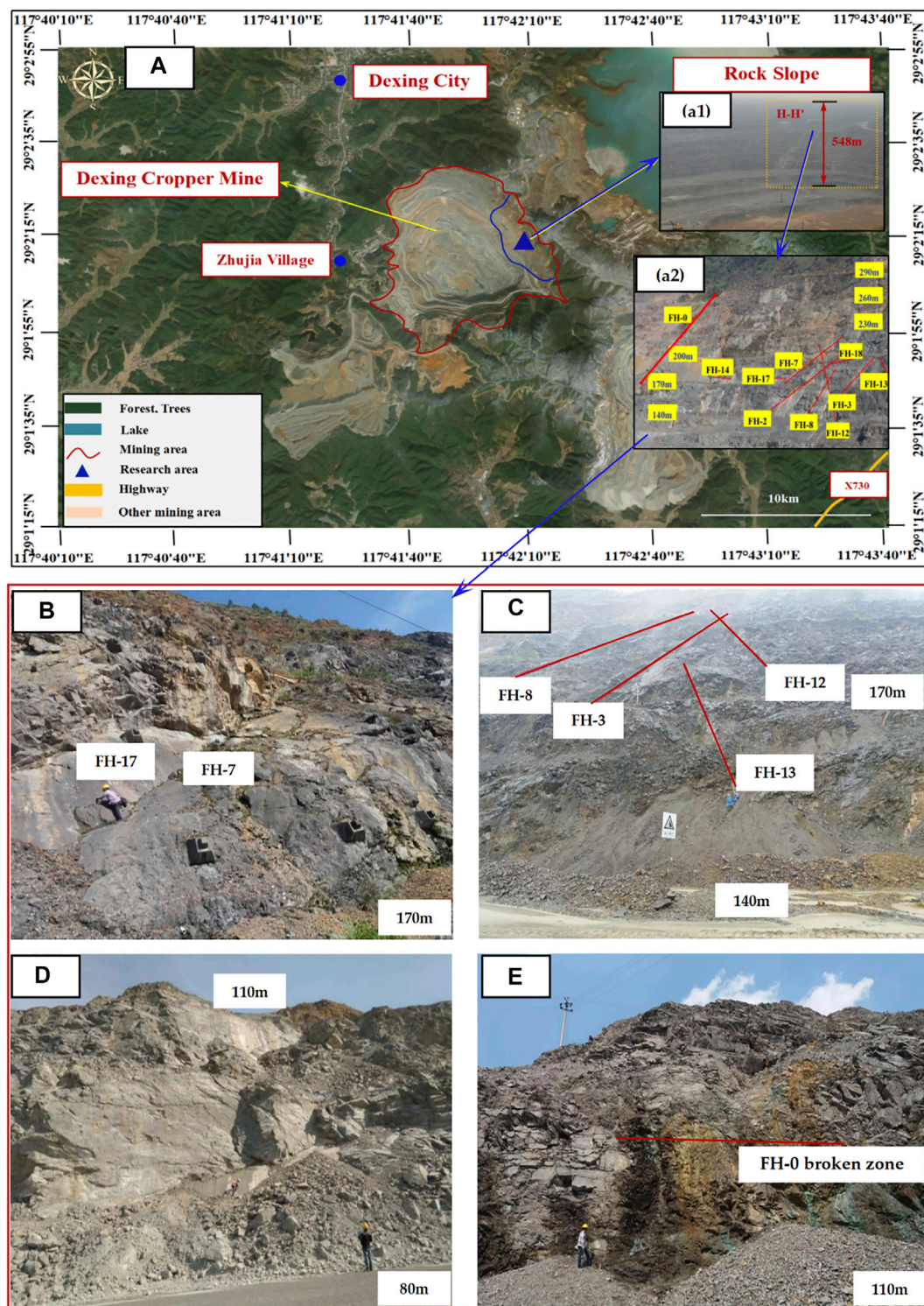


FIGURE 1 | (A) Geographical location and topographic map of Dexing copper mine; **(B)** fault of FH-7 and FH-17; **(C)** fault of FH-3, FH-8, FH-12, and FH-13; **(D)** FH-14 fault (the lower part is an 80-m platform, and the upper part is a 110-m platform); **(E)** FH-0 regional fault broken zone.

As shown in **Figure 1B**, the EW fault is the main fault distributed on the Huangniuqian slope. It has different scales, longer extension, and characteristics of group appearance.

There are 0.3–0.5 m thick compressive fault breccias and cements locally. It is the original rock cuttings and rock dust, and some cements have been schistosified. In

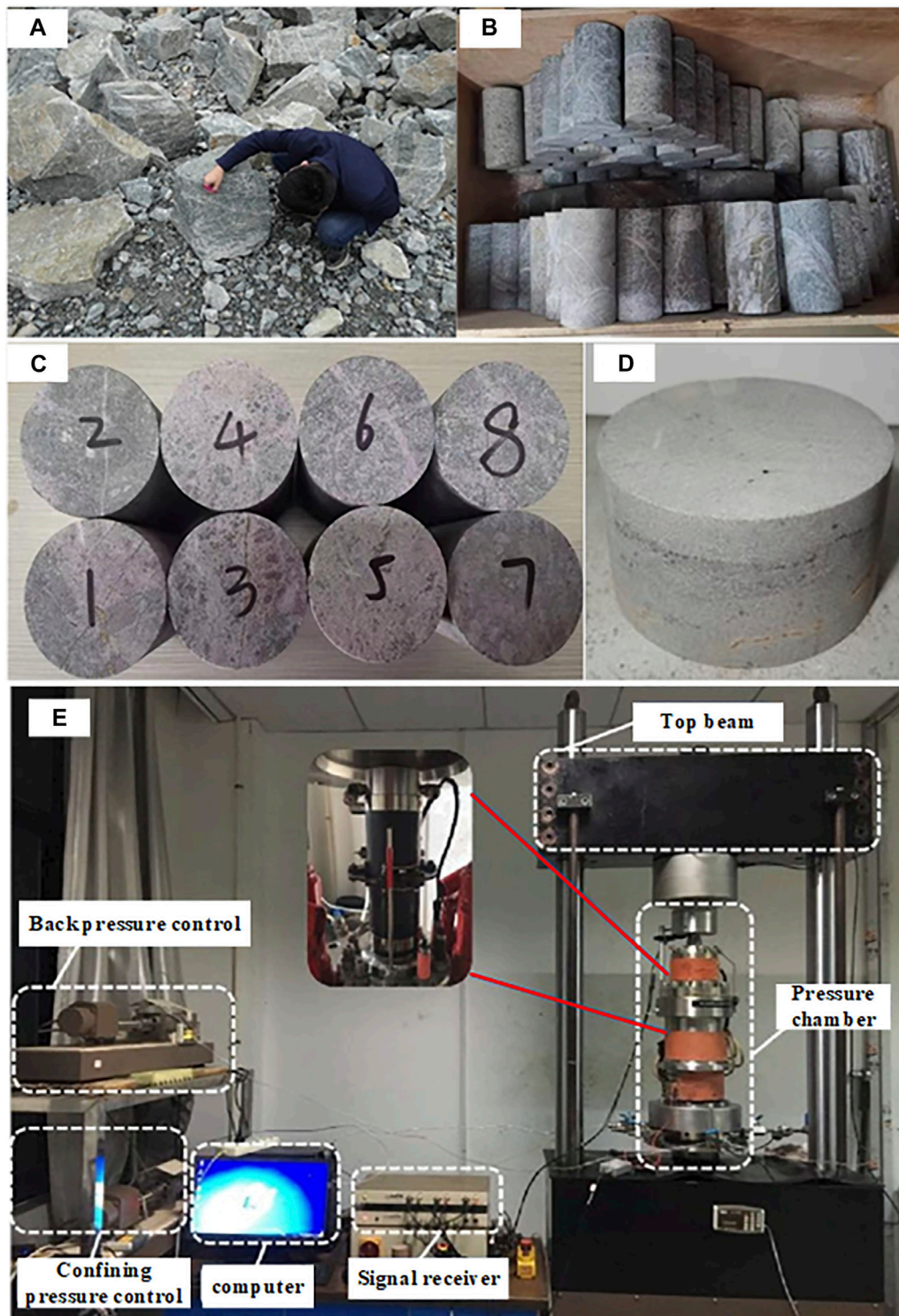


FIGURE 2 | (A) On-site sampling; (B) on-site rock samples; (C) standard cylindrical specimen; (D) standard Brazil split specimen; (E) GDS-VIS uniaxial and triaxial compression machine.

TABLE 1 | Rock mechanical parameters at the sampling point.

Sampling position	Compressive strength σ (Mpa)	Tensile strength T (Mpa)	Elastic modulus E (Gpa)	Cohesion C (Mpa)	Friction angle Φ (°)	Poisson's ratio μ
ZK11	43.95	4.494	11.16	12.9822	28.02	0.236
ZK12	48.26	5.212	14.23	14.5733	28.82	0.205
ZK13	63.97	6.239	15.21	19.3386	28.32	0.163

addition, the larger faults in this group are FH-1 (regional fault), FH-2, and FH-7.

2) NNW faults

The NNW faults include FH-10, FH-11, FH-12, and FH-13. This group of faults obliquely intersects with the slope and is easily deformed and damaged by the wedge-shaped body with the EW-direction fault. For example, the 170 m platform slope is damaged by the wedge-shaped body cut by the FH-12 and FH-3 faults (**Figure 1C**).

3) NWW faults

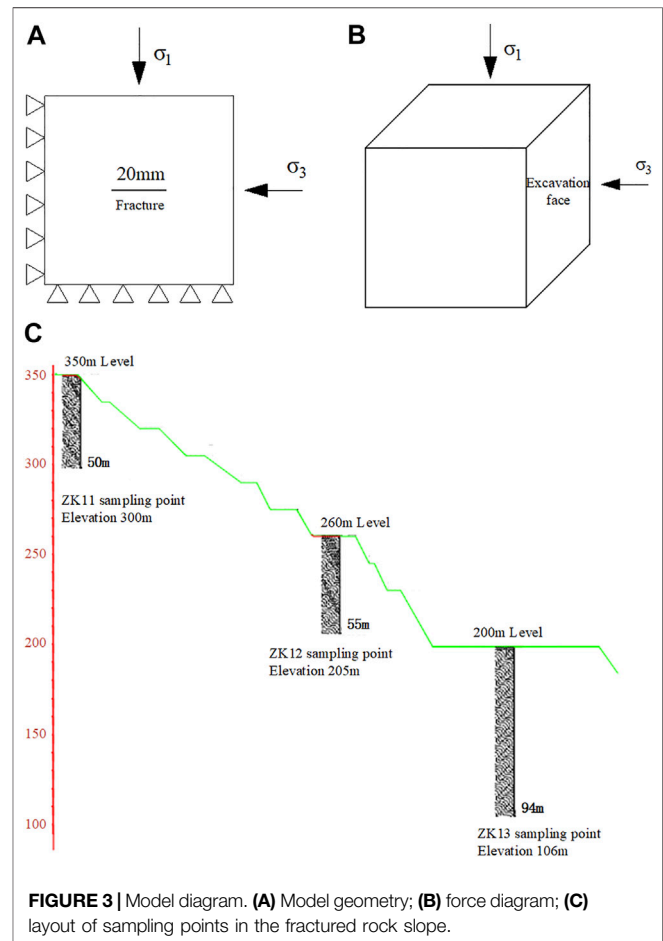
As shown in **Figure 1D**, the strike of the NWW-trending fault is basically the same as that of the Huangniuqian pit slope, and it is one of the main factors affecting the stability of the Huangniuqian slope. The fault planes of this group are usually large and smooth, with an extension length of more than 100 m, and there are 20–30 m wide (densely developed joints) fracture zones on both sides.

4) NNE faults

The NNE faults mainly include FH-0, which is a regional fault (**Figure 1E**). Based on the results of joint statistics, it can be seen that the dominant joints developed in the Huangniuqian slope rock mass are basically consistent with the production and installation of the main faults. Therefore, this joint has a certain genetic relationship with the fault, and its developed dominant joint makes the rock mass of the slope mainly show a fragmented mosaic structure.

3 PHYSICAL MECHANICS TEST

The test sample adopts the original mine slope (**Figure 2A**). Through on-site exploration and geological data analysis, several circular sampling regions (diameter about 2.00 m) with uniform texture and relatively complete rock mass were delineated at the Huangniuqian slope. In the process of drilling the surrounding rock of the rock mass slope, we took at least five relatively complete undisturbed samples from each sampling region (**Figure 2B**). As shown in **Figures 2C,D**, the obtained rock samples are processed in the laboratory into cylindrical standard specimens with a diameter and height of 50 mm \times 100 mm or 50 mm \times 25 mm, then the uniaxial and triaxial compression experiment of rock are carried out by GDS-VIS



as shown in **Figure 2E**, and finally, the rock mechanical parameters at sampling point were obtained as shown in **Table 1** below.

4 NUMERICAL SIMULATION

At present, the study of joint crack propagation and penetration is mainly carried out under loading conditions, but in the study of the transition from open-pit to underground mining, it will cause a lot of unloading of the rock mass; moreover, the tensile stress may appear in the local area, and the damage to the rock mass is large. In this chapter, different loading and unloading schemes are used to carry out numerical simulation tests on the fractured rock mass to study its mechanical and failure characteristics.

4.1 Excavation Unloading Stress Path

4.1.1 Fractured Rock Mass Model

The size of the true triaxial simulation specimen is 70 mm × 70 mm × 70 mm cube, and the parallel bond model is usually used when PFC simulates the high bond strength and the bending moment load of rock, while the plane joint model is used in the meso-structural plane (Shi et al., 2018). The fracture through the whole model in the strike direction and the model geometry are shown in **Figure 3A**.

4.1.2 The Loading and Unloading Stress Path

The excavation of the open-pit and underground chamber can be simplified as the plane strain problem. In general, the redistribution of stress increases in the vertical direction and decreases in the excavation direction (Huang et al., 2007; Liu and Li, 2020; Yang et al., 2021). In this research, it can be simplified as follows: stress is applied on the top face and the side face of the rock, and the other face is fixed. As shown in **Figure 3B**, σ_1 is the stress on the top surface, and σ_3 is the stress on the lateral excavation surface. The values of σ_1 and σ_3 are changed to simulate the stress change during excavation unloading. The loading and unloading schemes are divided into two groups as follows:

Plan A: Loading and unloading are carried out simultaneously; the first step is to pressurize at the same time to σ_3 in the axial and horizontal directions, and the second step is to continue pressurizing in the axial direction until σ_1 reaches the stable state; the first two steps are to simulate the stress state of rock in the rock stratum. The third step is to load and unload σ_1 at 0.10 Mpa/level and σ_3 at 0.05 Mpa/level which is to simulate the stress change process of the underground rock mass after the deep open pit mining is transferred to underground mining. In the fourth step, if the specimen is damaged before the unloading of the excavation face is completed, the lateral pressure is released immediately and the specimen is unloaded to 0 Mpa; if the unloading is completed and the specimen is not destroyed, the axial stress will continue to be applied until the specimen is completely destroyed.

Plan B: This plan is the contrast to plan A, where the axial stress is invariable and the lateral surface unload takes place. The simulation process is also divided into four steps. Compared with the unloading plan A, only the third step is different. The third step of plan B is that the axial stress will remain unchanged after reaching the initial *in situ* stress (preset value), the excavation surface will be unloaded at 0.15 Mpa/level, and proceed to the next level of unloading after equilibrium.

4.2 Simulation Program

As shown in **Figure 3C**, the model parameters are determined by PFC calibration tests on the samples taken from three boreholes according to the depth of the high and steep rock slope in Dexing mine and the fractured rock mass in underground mining.

In order to compare the mechanical properties and failure characteristics of the rock mass with fractures under different unloading rates, two groups of different unloading conditions are set. Also, three sets of initial stress levels (σ_1 and σ_3 take three sets of values, that is, three drill-hole sampling points) are selected

according to a representative set of pore water pressure measured in site and the distribution characteristics of typical fractured rock mass, under the condition that the specimen is saturated with water, the pore water pressure and the initial fracture distribution of the specimen are certain, and the unloading stress is adopted by plan A and plan B. Six groups of tests were carried out to systematically analyze the stress–strain curve trend, macro-mechanical parameters, and fracture evolution characteristics of the samples. The schedule of the loading and unloading comparison test is listed in **Table 2**.

4.3 Physical and Mechanical Parameters of the Rock

The key of particle flow code (PFC) to simulate the mechanical behavior of materials is to generate the initial model (Zhang et al., 2021; Xu and Xu, 2021; Wang et al., 2021). First, the PFC servo system is used to adjust the packing density, size, and contact precision of the model particles to the ideal state and make them in the state of force equilibrium (Tian et al., 2021; Sarfarazi et al., 2021). After the initial model is generated, in order to make the macroscopic and microscopic mechanical properties of the specimen correspond to each other, the calibration test is carried out according to the stress–strain curves of the specimen measured under uniaxial compression, and the microscopic parameters are adjusted repeatedly by PFC. The calibration curves of experiment and simulation are shown in **Figure 4**.

Through calibration, the final determination of the dry, natural, and saturated specimen PFC microscopic parameters is listed in **Table 3**.

5 ANALYSIS OF NUMERICAL SIMULATION RESULTS

5.1 Deformation Characteristics Under Vertical Loading and Lateral Unloading Conditions

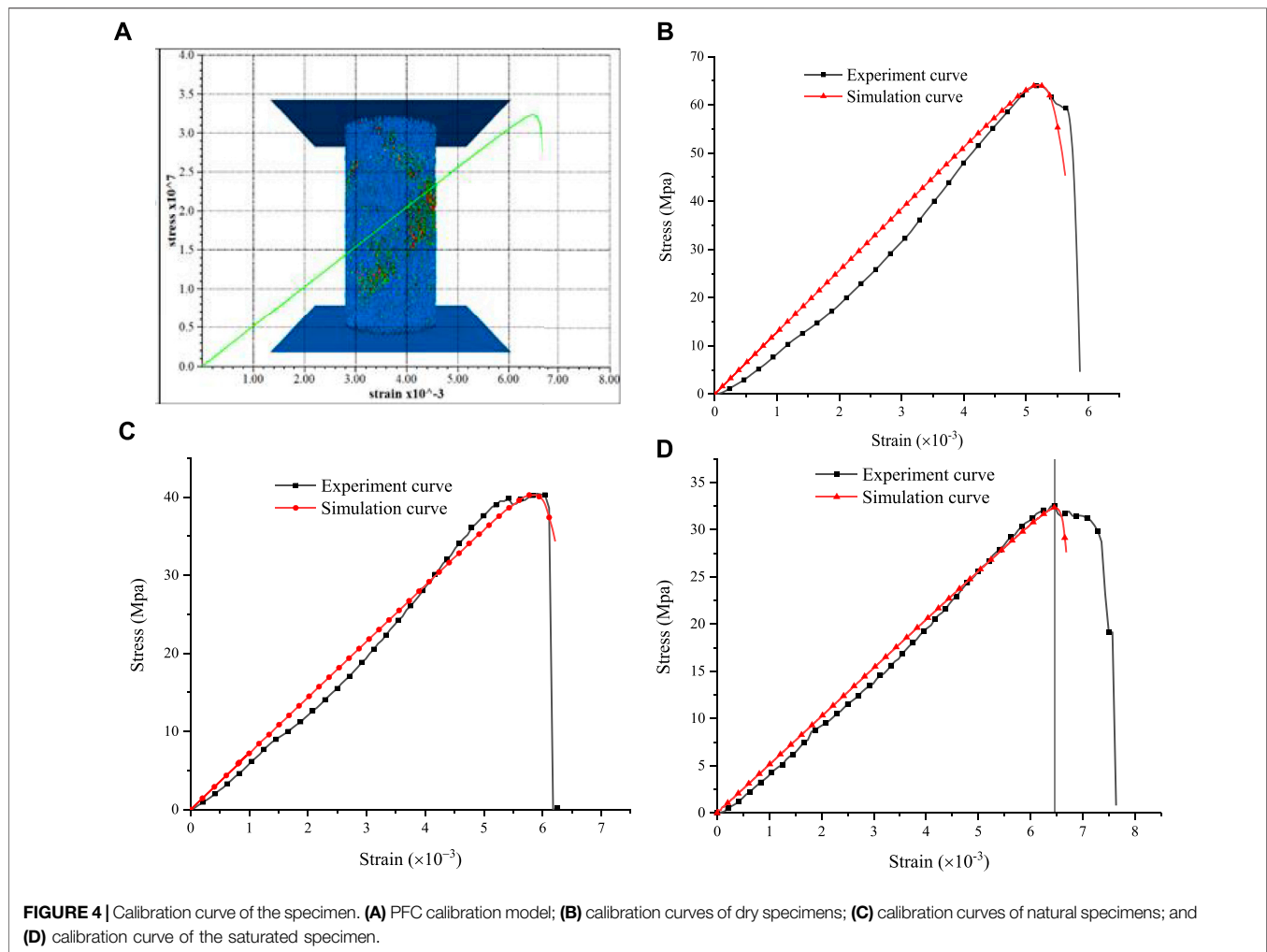
5.1.1 Vertical Loading and Lateral Unloading Plan A

As shown in **Figure 5** below, **Figures 5A–C** show the deformation characteristics of the rock mass under excavation at different depths under the condition of single fracture. The axial stress σ_1 and horizontal stress σ_3 take three sets of values, respectively, for loading and unloading. Phase I is the loading and unloading at the same time, axial loading and unloading in the horizontal direction, which is the third and most important step of plan A, and Phase II is the lateral unloading complete and continuing loading in the axial direction, which is step four in plan A. **Figure 5D** is a comparison of three sets of values obtained under different conditions.

The typical stress–strain curve from **Figure 5** shows that the larger the initial *in situ* stress (that is, the larger the value of σ_1 and σ_3), the smaller the peak axial strain from 3.48 to 3.21‰ and the lower the ductility of rock mass and the more brittle failure, as shown in **Figure 5C**. The specimen has been destroyed before

TABLE 2 | Schedule of the loading and unloading comparison test.

Group	Scheme	Initial vertical stress σ_1 (Mpa)	Initial horizontal stress σ_3 (Mpa)	Axial loading	Horizontal unloading
1	A1	4	2.4	0.5 Mpa/level	0.3 Mpa/level
2	A2	5	3.0	0.5 Mpa/level	0.3 Mpa/level
3	A3	6	4.2	0.5 Mpa/level	0.3 Mpa/level
4	B1	4	2.4	Constant (σ_1)	0.6 Mpa/level
5	B2	5	3.0	Constant (σ_1)	0.6 Mpa/level
6	B3	6	4.2	Constant (σ_1)	0.6 Mpa/level

**TABLE 3 |** Microscopic parameter table of PFC for the specimen.

Hydrous state	Parallel bond modulus (Gpa)	Tangential bond strength (Mpa)	Normal bond strength (Mpa)	Angle of friction (°)	Contact stiffness ratio	Particle density (kg/cm ³)
Dry	7.60	19.34	14.97	28.32	2.1	2,750
Natural	3.95	10.67	9.09	28.32	2.1	2,750
Saturated	3.04	9.09	9.05	28.32	2.1	2,750

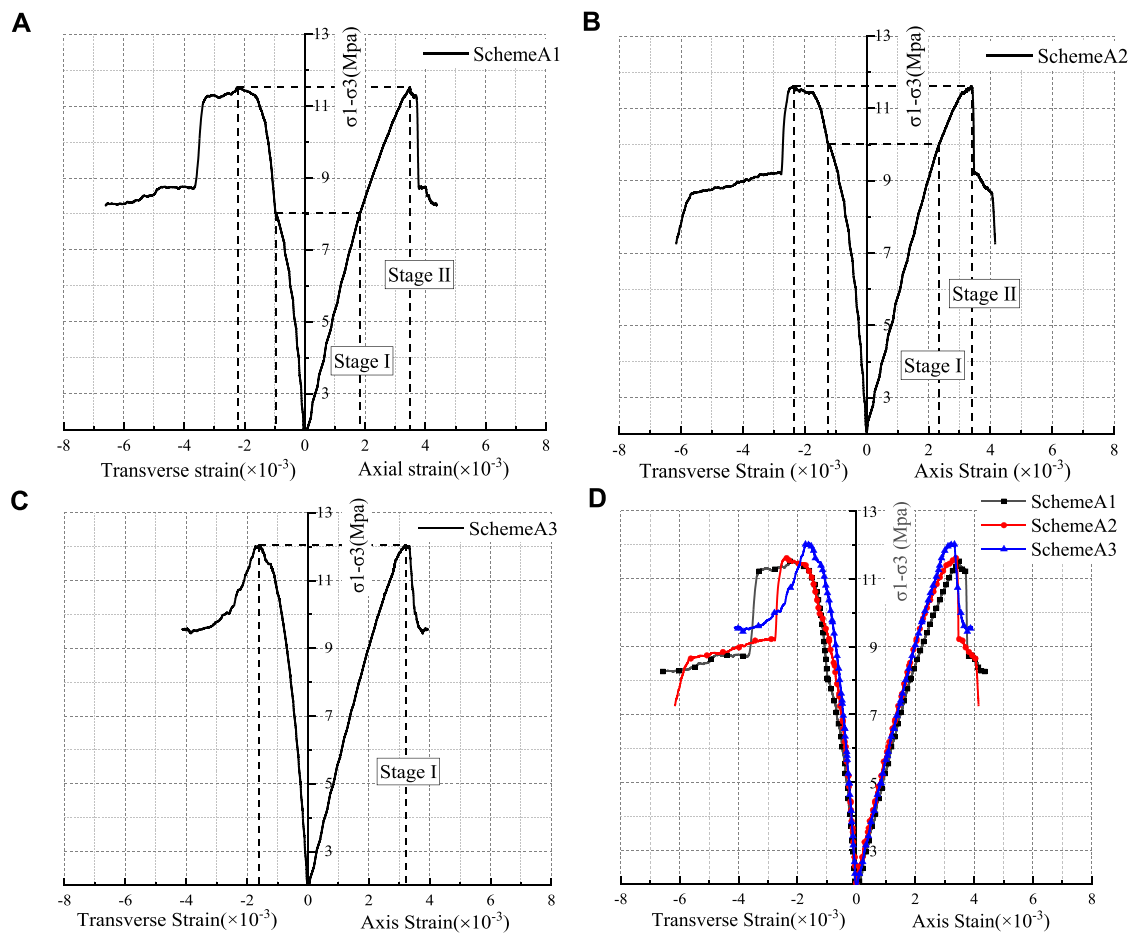


FIGURE 5 | Deformation characteristics of the rock mass under different depth and plan A. **(A)** Loading scheme A1; **(B)** loading scheme A2; **(C)** loading scheme A3; and **(D)** comparative curves.

Stage I is completed, which indicates that the surrounding rock may be destroyed before the unloading of the excavation face is completed during the deep excavation of underground mining. According to the post-peak curve, the process of axial stress decreases from the peak strength to the residual strength, the axial strain σ_1 is small, and the larger the *in situ* stress is, the smaller the axial strain is during the drop process. It shows that the brittleness is more obvious with the increase of mining depth. The failure of the fractured rock mass is accelerated by the excavation of open face. In the loading and unloading test, the failure of the specimen in the axial loading test is mainly due to compression deformation, and the failure of the specimen in the unloading test is mainly due to the strong dilatancy along the unloading direction.

5.1.2 Vertical Loading and Lateral Unloading Plan B

Figure 6 shows the deformation characteristics of the rock mass under excavation at different depths under the condition of plan B.

The typical stress–strain curve from **Figure 6** shows that the deeper the fractured rock mass is, on the basis of the same mining technology, the longer the unloading time of rock mass is. But once unloading is completed, the increase of

stress is larger, and the rock mass will reach the peak strength more quickly.

It can be obtained from the comparative analysis of plan A and plan B that the faster the unloading rate is, the greater the influence is on the axial and transverse strain of the rock mass. When the unloading is completed, there will be a stress jump point and the increasing rate will be faster. The results show that the specimen deforms strongly in the unloading direction, and the dilatancy and the brittle failure are obvious.

5.2 Fracture Propagation Characteristics Under Vertical Loading and Lateral Unloading Conditions

5.2.1 Vertical Loading and Lateral Unloading Plan A

The simulation results of fracture propagation of the specimen under plan A and the sketch drawings are shown in **Figures 7A,B**. As can be seen from the drawings, the length of the preformed fracture is 20 mm, and the secondary airfoil-type tension cracks appear at the tip of the precast cracks. Because of the long precast cracks, a crack also appears in the middle of the precast cracks and extends toward the

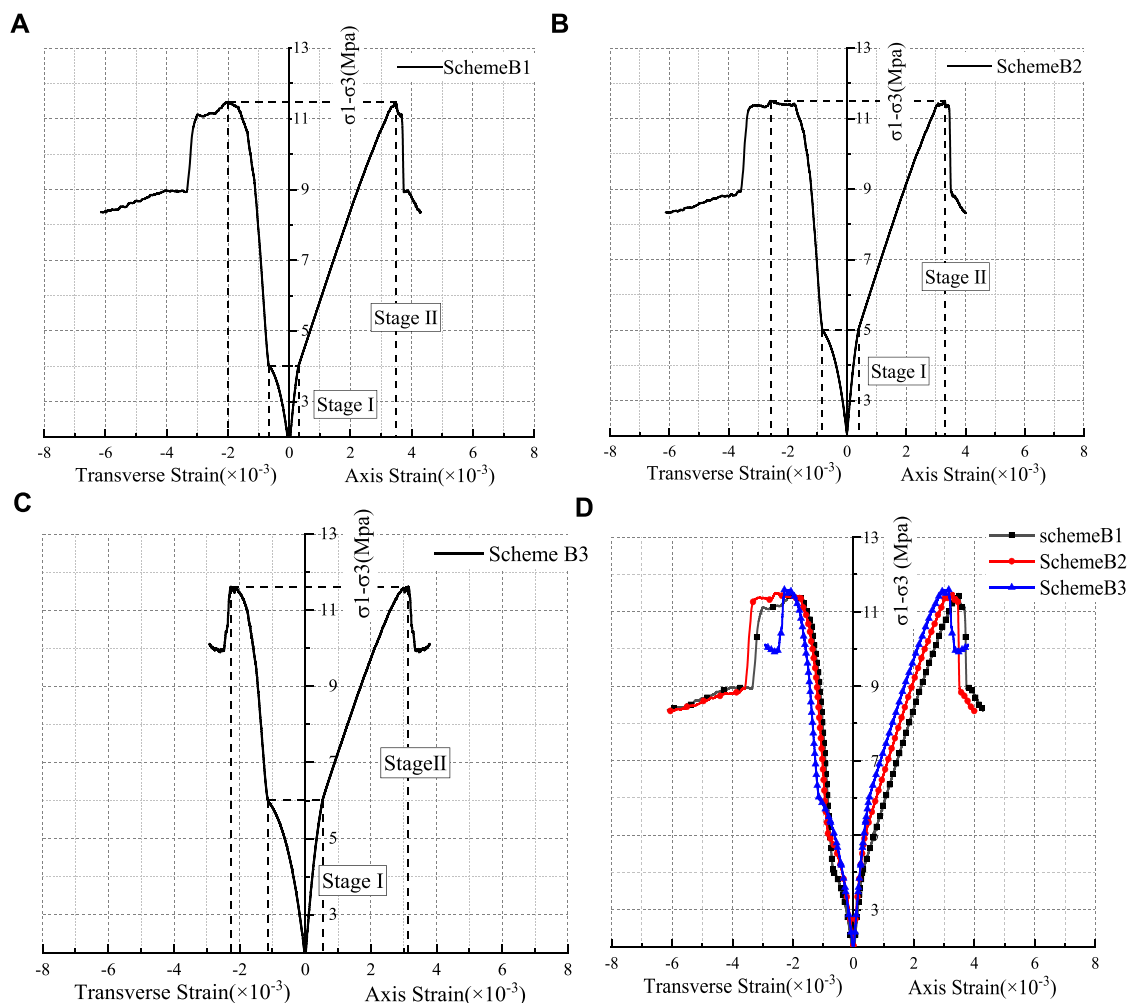


FIGURE 6 | Deformation characteristics of the rock mass with different depth and plan B. **(A)** Loading scheme B1; **(B)** loading scheme B2; **(C)** loading scheme B3; and **(D)** comparison curves.

unloading surface; however, the airfoil cracks at both ends extend to the upper left and the lower right corner of the specimen, and tensile (red fracture in the simulation result) failure and shear failure (green fracture in the simulation result) occur during the crack propagation. Moreover, bond-tensile failure occurs earlier than shear failure, and the total amount of tensile failure is greater than that of shear failure. The crack near the excavation unloading surface expands more, and the crack in the middle of the precast fracture continues to expand to the right and has a tendency to run through, and the damage of the adjacent excavation unloading surface is more obvious. The final specimen was cut through by 20 mm cracks and airfoil tensile cracks. The specimen was completely destroyed, reached the peak stress, and lost the load-bearing capacity.

5.2.2 Vertical Loading and Lateral Unloading Plan B

The simulation results of fracture propagation under plan B and the sketch drawings are shown in **Figures 8A,B**.

The fracture characteristics of specimens under plan A and plan B are compared. The fracture trend of specimens is similar; the

secondary airfoil-type tension cracks appear at the tip of the preformed cracks, and the small cracks appear in the middle of the preformed cracks. The cracks on both ends extend to the upper left corner and lower right corner of the specimen. But under the condition of plan B, the initial bonding fracture appears earlier, and the crack near the excavation unloading surface expands more. The crack is more concentrated, and the upper right part of the specimen has a bifurcated crack along the precast crack and has a tendency of penetrating with the upper right corner of the specimen. The failure of the unloading surface near excavation is more severe.

5.3 Deformation and Fracture Propagation Characteristics Under Different Water Content

5.3.1 Deformation Characteristics Under Different Water Content

Figures 9A–C show the stress–strain curve of cracked specimens in dry, natural, and saturated conditions under loading and

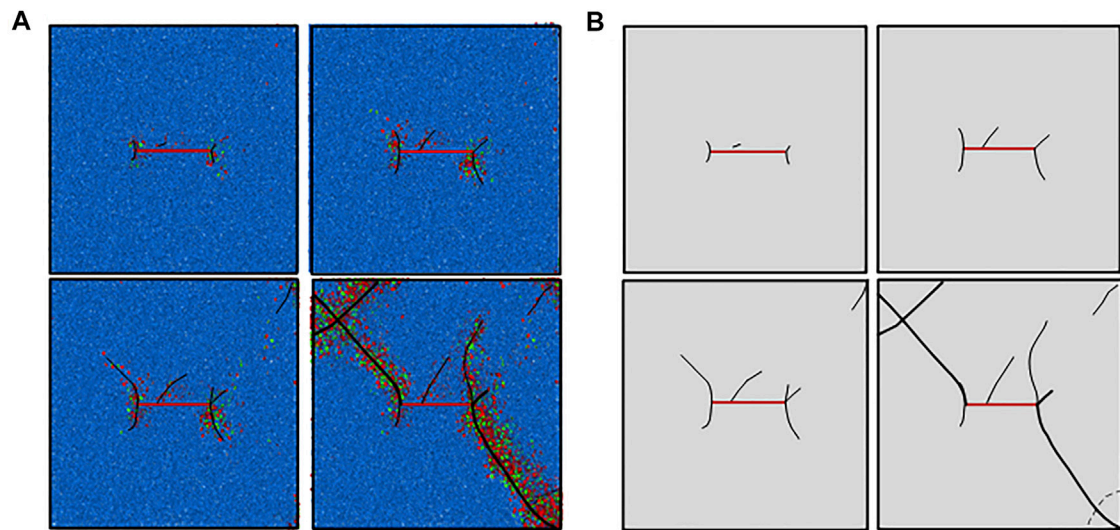


FIGURE 7 | Sample simulation and sketch under loading plan A. **(A)** Simulation diagram of loading plan A; **(B)** sketch of the fracture.

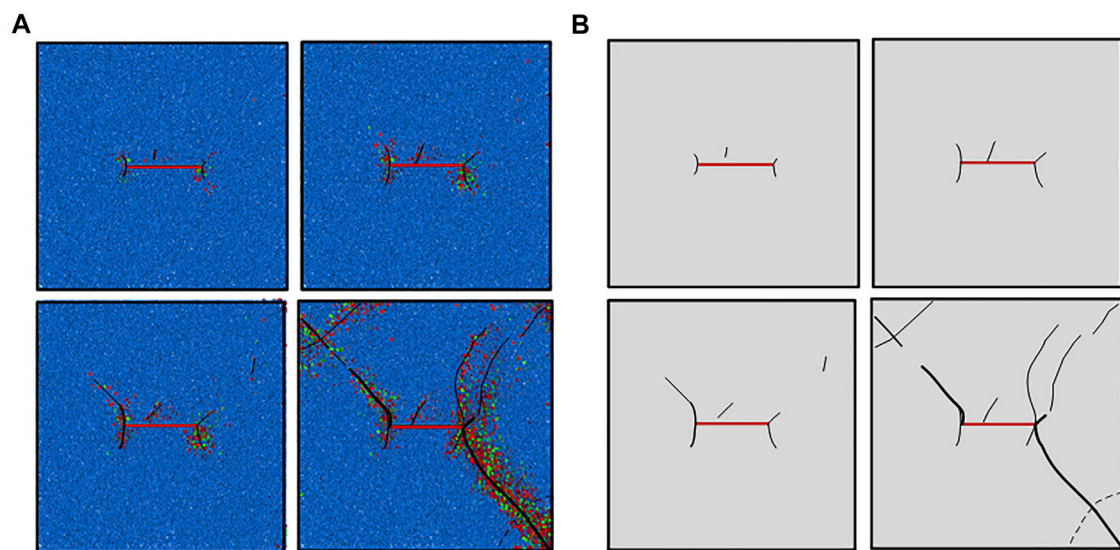


FIGURE 8 | Sample simulation and sketch under loading plan B. **(A)** Simulation diagram of loading plan B; **(B)** sketch of the fracture.

unloading plan A2, with stage I showing simultaneous loading and unloading and stage II is the unloading complete and the axial continuous loading stage. **Figure 9D** shows the stress–strain curves of three groups of specimens.

In **Figure 9**, the stress–strain curve shows that when the moisture content of the specimen increases, the compressive strength and the elastic modulus decrease and the transverse peak strain increases. For example, when the water content increased from 1.12 to 4.85%, the compressive strength decreased from 17.65 to 11.59 Mpa, the elastic modulus decreased from 3.39 to 2.46 Gpa, and the transverse peak

strain increased from 0.00188 to 0.00235. The decrease of compressive strength is about 56.33%, the decrease of elastic modulus is about 63.45%, and the increase of transverse peak strain is about 40.85%.

The mechanical properties and deformation characteristics of the specimen with different moisture content have the same tendency, and when the water content increases, the compressive strength and the elastic modulus of the specimen decrease. In this test, the dry specimen shows linear elastic change before reaching the peak strength, and the stress drop rate is faster after reaching the peak strength, and the brittleness of the

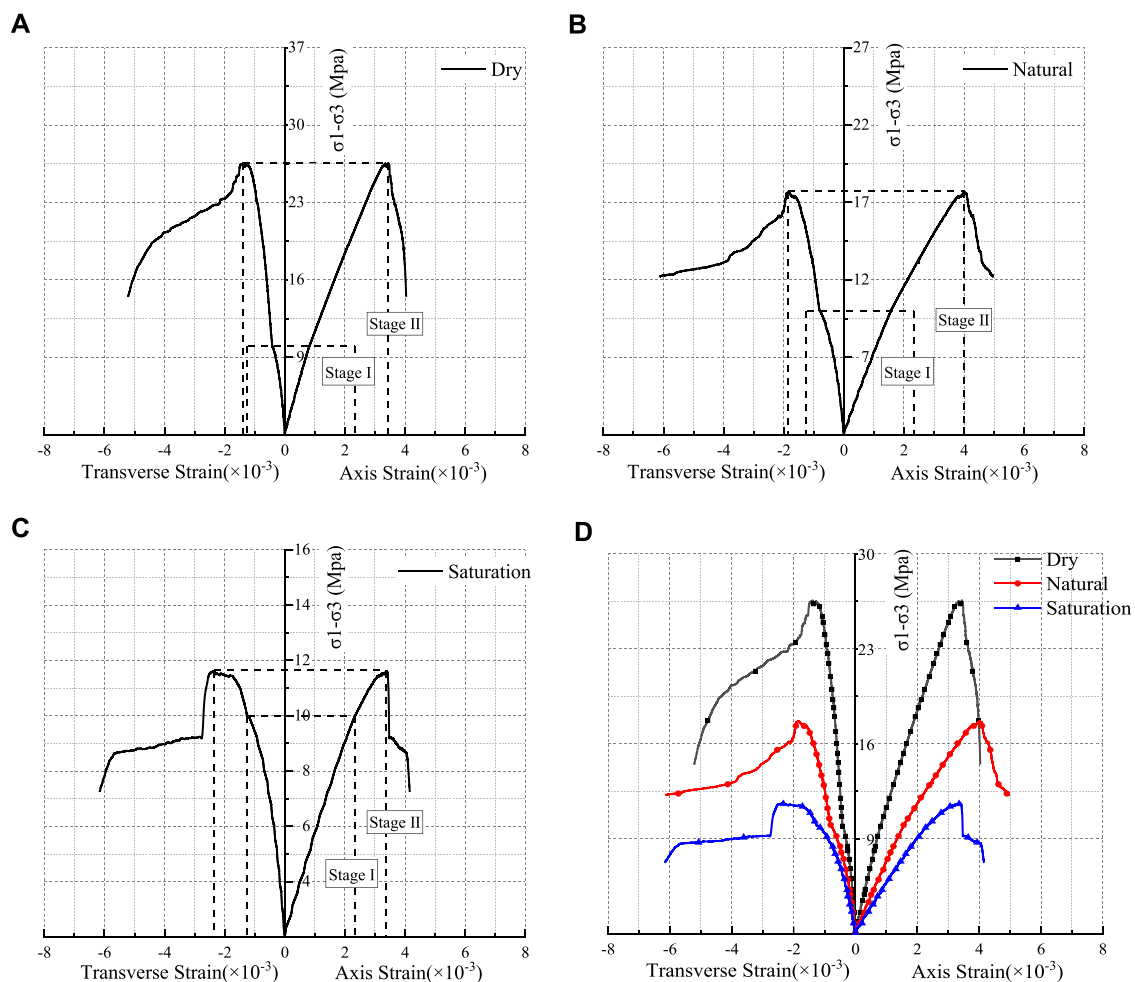


FIGURE 9 | Specimen stress-strain curve under different water content. (A) Dry curve; (B) natural curve; (C) saturation curve; and (D) comparative curves.

specimen is obvious. According to the stress-strain curve, the higher the water content is, the longer the compaction stage, the shorter the elastic stage, and the more obvious the yield of the specimen are.

5.3.2 Fracture Propagation Characteristics Under Different Water Content

As shown in **Figure 10** below, the results of the simulation and the sketch of the fracture propagation of the cracked specimen under plan A2 under dry, natural, and saturated conditions show that the generation and propagation of the cracks in the three specimens are similar. The secondary airfoil-shaped cracks appear at both ends of the precast cracks, and the small cracks appear in the middle of the precast cracks and extend toward the unloading surface. The airfoil cracks at both ends extend to the upper left and the lower right corner of the specimen. In the process of fracture propagation, both tensile failure and shear failure occur, and bond tensile failure occurs earlier than shear failure, and the total amount of tensile failure is greater than that of shear failure. The main failure mode of rock is tensile failure, while shear failure is subsidiary.

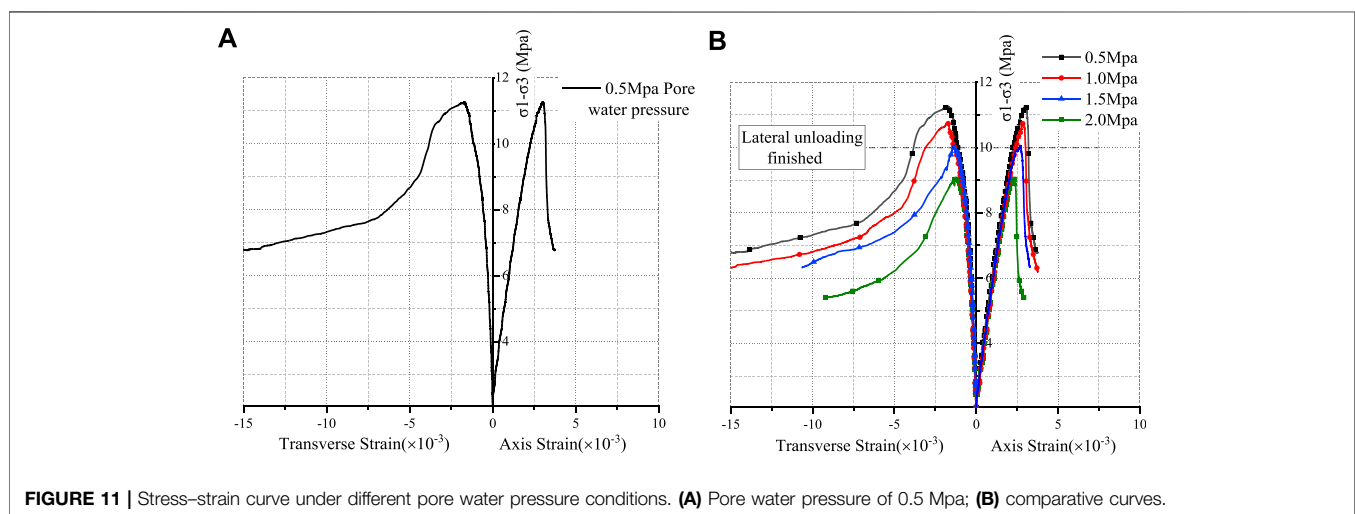
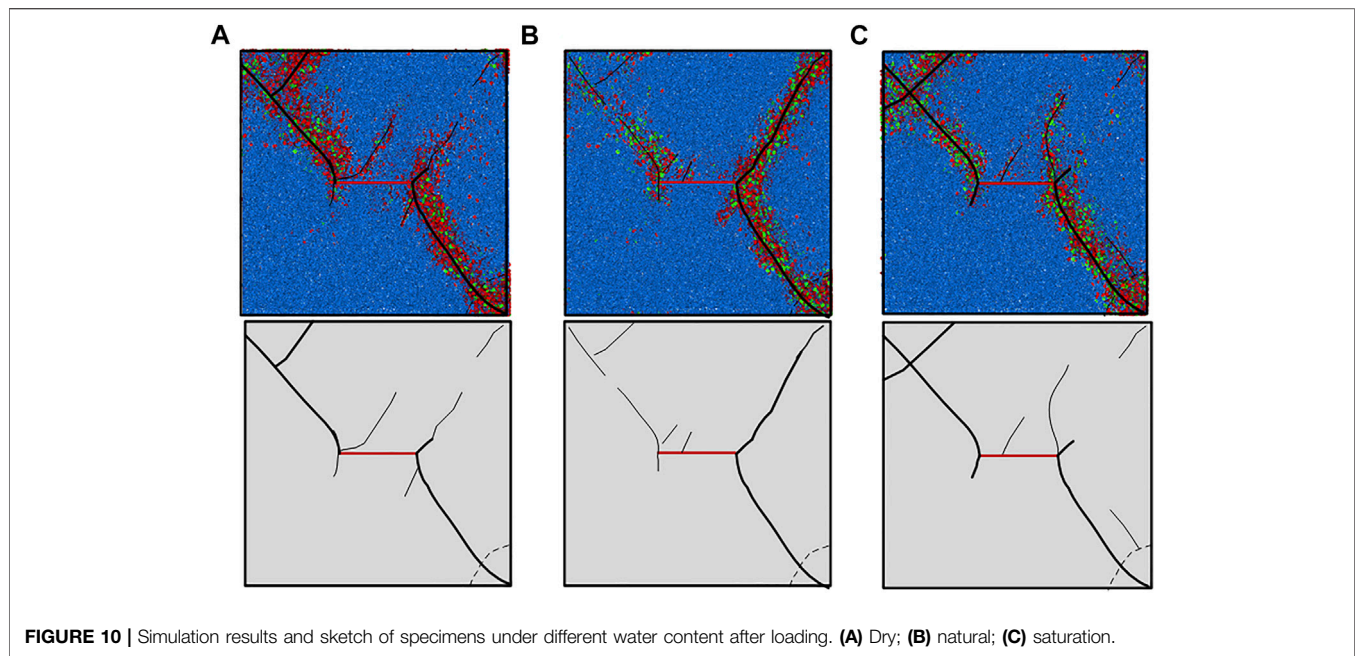
The brittle failure characteristics of dry specimen are more obvious than those of natural and saturated specimens, and the number of bond tensile failure is the most. In the natural state, the right part of the specimen is damaged more severely near the unloading surface, resulting in larger and deeper cracks, and generates more cracks and more complicated damage in the saturated state.

5.4 Deformation and Fracture Propagation Characteristics Under Different Pore Water Pressure

5.4.1 Deformation Characteristics Under Different Pore Water Pressure

Figure 11A shows the specimen stress-strain curve under pore water pressure of 0.5 Mpa, and **Figure 11B** shows the stress-strain curve of cracked specimens at 0.5, 1.0, 1.5, and 2.0 Mpa under loading and unloading scheme A2.

From **Figure 11**, the stress-strain curve shows that the compressive strength and peak strain of the specimen decrease when the pore water pressure increases. For example, when the



pore water pressure increased from 1.0 to 1.5 Mpa, the compressive strength decreased from 10.75 to 10.04 Mpa, and the peak strain decreased from 0.00289 to 0.00271. For the overall test of pore water pressure from 0.5 to 2.0 Mpa, the compressive strength and peak strain decreased by about 19.38 and 22.85%, respectively. When the pore water pressure is 0.5 Mpa, the elastic modulus of the sample is 2.82 Gpa, and when the pore water pressure is increased to 2.0 Mpa, the elastic modulus of the sample decreases to 2.40 Gpa, and the elastic modulus of the whole sample decreases to 14.89%.

Under different pore water pressure conditions, the mechanical properties and deformation characteristics of the stress-strain curve are similar—when the pore water pressure increases, the compressive strength decreases and

the peak strain decreases, but the elastic modulus does not change much.

5.4.2 Fracture Propagation Characteristics Under Different Pore Water Pressure

Figure 12 shows the simulation results and the sketch of the fracture propagation of the fractured specimen under pore water pressures of 0.5, 1.0, 1.5, and 2.0 mpa. It can be seen from the drawing, under the conditions of four kinds of pore pressure, the crack initiation and propagation of the specimen are similar. The secondary airfoil-type tensile cracks appear at both ends of the preformed crack, and the small cracks appear in the middle of the preformed crack and extend to the unloading surface. The airfoil cracks at both ends extend to the upper left and the lower right

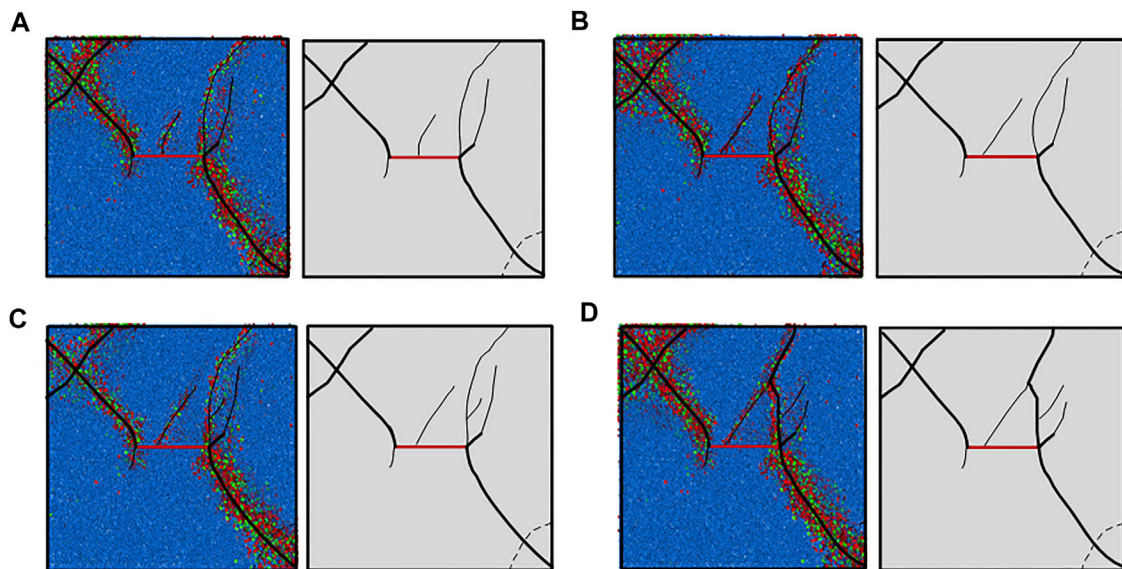


FIGURE 12 | Simulation results and sketch of specimens under different pore water pressures. **(A)** 0.5 Mpa pore water pressure; **(B)** 1.0 Mpa pore water pressure; **(C)** 1.5 Mpa water pressure; and **(D)** 2.0 Mpa water pressure.

corner of the specimen. In the process of fracture propagation, both tensile failure and shear failure occur, and bond tensile failure occurs earlier than shear failure, and the total amount of tensile failure is greater than that of shear failure. The main failure mode of rock is tensile failure, while shear failure is subsidiary.

With the increase of pore water pressure, the failure of the specimen becomes more severe, such as the crack in the middle of the preformed crack, which spreads to the right side and passes through the main crack in the right side of the preformed crack. There are more and more cracks in the right part near the unloading surface, and the distribution of the cracks is more complex. The pore water pressure softens the rock material and causes stress concentration. The increase of pore water pressure accelerates the failure of rock.

The influence of pore water pressure on the fractured rock mass is analyzed as follows: the stress concentration phenomenon is easily formed between the micro-cracks and the particles by water pressure, and there is the phenomenon of hydraulic fracturing, which promotes the development of the crack of the specimen, and finally makes the micro-cracks gradually run through to form macro-failure. Because of this effect of the pore water pressure on the rock, the macroscopic mechanical properties of rock in the coupling state weaken obviously.

6 CONCLUSION

In the present study, several kinds of specimens with different water content, different loading plan, and different pore water pressure were tested by true triaxial numerical simulation tests. The mechanical properties and fracture propagation characteristics of the fractured rock mass under coupling of heavy rainfall infiltration and mining unloading are analyzed. The specific conclusions are as follows:

- 1) The faster the unloading rate is, the greater the influence on the rock strain is. After unloading, the stress jump point appears and the strain increase rate becomes larger, the volume of the rock increased and occurs as large deform in the unloading direction, and finally it leads to severe brittle failure of the rock.
- 2) The larger the initial *in situ* stress is, the smaller the peak strain, the lower the ductility, the faster the drop rate after the peak, and the more obvious the brittleness are, and the surrounding rock is easier to be damaged.
- 3) With the increase of the water content, the rock compaction stage increases, the elastic stage shortens, and the yield stage becomes more obvious. The failure mode begins with shear failure, followed by a combination of tensile and shear failure.
- 4) When the pore water pressure increases, the compressive strength and the peak strain of the specimen decrease, the pore water pressure accelerates the failure of the rock, and stress concentration and hydraulic fracturing are easily formed between micro-cracks and particles, which promotes the development of the crack.

DATA AVAILABILITY STATEMENT

The original contributions presented in the study are included in the article/Supplementary Material; further inquiries can be directed to the corresponding author.

AUTHOR CONTRIBUTIONS

All authors listed have made a substantial, direct, and intellectual contribution to the work and approved it for publication.

FUNDING

The research work was funded by the National Natural Science Foundation of China (NSFC) (Grant No.

41867033), State Key Laboratory of Safety and Health of Metal Mines Open Fund (Grant No. zdsys 2019-005), and China Postdoctoral Science Foundation Program (Grant No. 2019M650144).

REFERENCES

- Bai, M., and Elsworth, D. (2020). *Coupled Processes in Subsurface Deformation, Flow, and transport*[M]. Reston, VA: American Society of Civil Engineers
- Chen, C., and Jing, B. X. (2016). Progress and Trend of the Theoretical Research and Practice of the Covering Layers of Open-Pit to Underground. *Mod. mining* 2, 5–10. doi:10.3969/j.issn.1674-6082.2016.02.002
- Cheng, H., and Zhou, X. (2015). A Multi-Dimensional Space Method for Dynamic Cracks Problems Using Implicit Time Scheme in the Framework of the Extended Finite Element Method. *Int. J. Damage Mech.* 24 (6), 859–890. doi:10.1177/1056789514555149
- Deng, W. X., Yang, T. H., Liu, F. Y., Li, H., Yang, Y. D., and Liu, Y. (2021). Study of Geometric Parameters Spatial Variability of Outcrops in Thin-Layered Rock Mass of Yanshan Iron Open-Pit Mine. *Metal mine*. 2, 139–145. doi:10.19614/j.cnki.jsks.202102021
- Du, J., Chen, J., Pu, Y., Jiang, D., Chen, L., and Zhang, Y. (2021). Risk Assessment of Dynamic Disasters in Deep Coal Mines Based on Multi-Source, Multi-Parameter Indexes, and Engineering Application. *Process Saf. Environ. Prot.* 155, 575–586. doi:10.1016/j.psep.2021.09.034
- Erdogan, F., and Sih, G. C. (1963). On the Crack Extension in Plates Under Plane Loading and Transverse Shear. *Transaction ASME, J. Basic Eng.* 85 (4), 519–525. doi:10.1115/1.3656899
- Griffith, A. A. (1921). VI. The Phenomena of Rupture and Flow in Solids. *Phil. Trans. R. Soc. Lond. A*. 221 (587), 163–198. doi:10.1098/rsta.1921.0006
- Griffith, A. A. (1924). *The Theory of rupture*[C]. Denver, Colo: First International Congress for Applied Mechanics, 55–63
- Guo, K. L., Yang, L., Sheng, X. C., Mei, J., Li, B. X., Zhang, B., et al. (2019). Fracture Mechanical Behavior and AE Characteristics of Rock-like Material Containing 3-D Crack under Hydro-Mechanical Coupling. *Rock Soil Mech.* 40 (11), 4380. doi:10.16285/j.rsm.2018.2052
- Huang, D., Hunag, R. Q., and Wang, J. X. (2007). Contrastive Analysis of Stability of Block in Large Underground Caverns under Conditions of Excavation and Unloading. *Chin. J. Rock Mech. Eng.* 26 (S2), 4115–4122. CNKI:SUN:YSLX.0.2007-S2-077
- Irwin, G. R. (1957). Analysis of Stresses and Strains Near the End of a Crack Traversing a Plate. *Transaction ASME, J. Appl. Mech.* 24, 361–364. doi:10.1115/1.4011547
- Jia-jun, Z., Zhi-Jun, Z., and Cheng-zhi, P. (2020). Development and Application of a Hydraulic Loading Test System that Provides Continuous and Stable Hydraulic Pressure. *Front. Earth Sci.* 8, 1–7. doi:10.3389/feart.2020.00077
- Jiang, P., Li, J., Zuo, S., Cui, X. Z., and Zhang, D. J. (2020). Ecological Retaining Wall for High-Steep Slopes: A Case Study in the Ji-Lai Expressway, Eastern China. *Adv. Civil Eng.* 2020 (2), 1–13. doi:10.3963/j.issn.1001-487X.2020.02.001
- Kou, M., Liu, X., Tang, S., and Wang, Y. (2019). 3-D X-ray Computed Tomography on Failure Characteristics of Rock-like Materials under Coupled Hydro-Mechanical Loading. *Theor. Appl. Fracture Mech.* 104, 102396. doi:10.1016/j.tafmec.2019.102396
- Lee, H. S., and Cho, T. F. (2002). Hydraulic Characteristics of Rough Fractures in Linear Flow Under Normal and Shear Load. *Rock Mech. Rock Eng.* 35 (4), 299–318. doi:10.1007/s00603-002-0028-y
- Li, J., Chen, S. X., Yu, F., Jiang, L. F., and Dai, Z. J. (2020). Discussion on Mechanism of Reinforcing High and Steep Slope with Prestressed Anchor Cable. *Rock Soil Mech.* 41 (2), 707–713. doi:10.16285/j.rsm.2019.0034
- Li, H. F., Feng, P., and Zhang, S. (2021). Comprehensive Control of High and Steep Slope in North Slope of Fushun West Open-Pit Mine. *OpenCast Mining Technology*. 36 (4), 83–86. doi:10.13235/j.cnki.ltcn.2021.04.022
- Li, L. K., Zhu, W. C., Dai, F., Liu, X. G., and Deng, W. X. (2021). Modelling of Dagushan Open-Pit Mine Slope with One Hundred Million Degrees of Freedom and Associated Numerical Simulation with RFPA3D. *Metal mine* 2, 179–185. doi:10.19614/j.cnki.jsks.202102027
- Li, X. S., Wang, Y. M., Yang, S., Xiong, J., and Zhao, K. (2021). Research Progress in the Mining Technology of the Slowly Inclined, Thin to Medium Thick Phosphate Rock Transition from Open-Pit to Underground Mine. *Appl. Mathematics Nonlinear Sci.* 6 (1), 319–334. doi:10.2478/amns.2021.2.00017
- Li, X., Liu, Z., and Yang, S. (2021a). Similar Physical Modeling of Roof Stress and Subsidence in Room and Pillar Mining of a Gently Inclined Medium-Thick Phosphate Rock. *Adv. civil Eng.* 2021, 1–17. doi:10.1155/2021/6686981
- Li, X., Peng, K., Peng, J., and Hou, D. (2021b). Experimental Investigation of Cyclic Wetting-Drying Effect on Mechanical Behavior of a Medium-Grained sandstone. *Eng. Geology*. 293, 106335. doi:10.1016/J.ENGEO.2021.106335
- Li, X., Peng, K., Peng, J., and Xu, H. (2021c). Effect of Cyclic Wetting-Drying Treatment on Strength and Failure Behavior of Two Quartz-Rich Sandstones under Direct Shear. *Rock Mech. Rock Eng.* 54, 5953–5960. doi:10.1007/s00603-021-02583-z
- Li, X., Yang, S., Wang, Y., Nie, W., and Liu, Z. (2021d). Macro-micro Response Characteristics of Surrounding Rock and Overlying Strata Towards the Transition from Open-Pit to Underground Mining. *Geofluids*. 2021, 1–18. doi:10.1155/2021/5582218
- Li, X. S., Wang, Y. M., Zhao, K., and Yang, S. (2019). Research Progress on the Key Problems in Transition from Open-Pit to Underground Mining for Metal Mines. *Metal mine*. 12, 12–20. doi:10.19614/j.cnki.jsks.201912002
- Lin, Q., Cao, P., Wang, H., Cao, R., and Chaliotis, C. (2018). An Experimental Study on Cracking Behavior of Pre-cracked Sandstone Specimens Under Seepage Pressure. *Adv. Civil Eng.* 2018, 1–10. doi:10.1155/2018/4068918
- Liu, S., Bai, J., Wang, X., Wang, G., Wu, B., Li, Y., et al. (2021). Study on the Stability of Coal Pillars Under the Disturbance of Repeated Mining in a Double-Roadway Layout System. *Front. Earth Sci.* 9, 1–19. doi:10.3389/feart.2021.754747
- Liu, W., Zhang, X., Fan, J., Zuo, J., Zhang, Z., and Chen, J. (2020a). Study on the Mechanical Properties of Man-Made Salt Rock Samples with Impurities. *J. Nat. Gas Sci. Eng.* 84, 103683. doi:10.1016/j.jngse.2020.103683
- Liu, W., Zhang, Z., Fan, J., Jiang, D., Li, Z., and Chen, J. (2020b). Research on Gas Leakage and Collapse in the Cavern Roof of Underground Natural Gas Storage in Thinly Bedded Salt Rocks. *J. Energ. Storage*. 31, 101669. doi:10.1016/j.est.2020.101669
- Liu, X., Zhu, Z., and Liu, A. (2019). Permeability Characteristic and Failure Behavior of Filled Cracked Rock in the Triaxial Seepage experiment. *Adv. Civil Eng.* 2019, 1–12. doi:10.1155/2019/3591629
- Liu, Z. F., and Li, X. S. (2020). Research Progress on Fracture Evolution of Fractured Rock Mass. *Nonferrous Met. Sci. Eng.* 11 (04), 77–81. doi:10.13264/j.cnki.jsks.2020.04.012
- Pu, Y., Apel, D. B., Liu, V., and Mitri, H. (2019). Machine Learning Methods for Rockburst Prediction-State-Of-The-Art Review. *Int. J. Mining Sci. Technology*. 29 (4), 565–570. doi:10.1016/j.ijmst.2019.06.009
- Rutqvist, J., and Stephansson, O. (2003). The Role of Hydromechanical Coupling in Fractured Rock Engineering. *Hydrogeology J.* 11 (1), 7–40. doi:10.1007/s10040-002-0241-5
- Sarfraz, V., Abharian, S., and Ghorbani, A. (2021). Physical Test and PFC Modelling of Rock Pillar Failure Containing Two Neighboring Joints and One Hole. *Smart Structures Systems*. 27, 123–137. doi:10.12989/sss.2021.27.1.123
- Shao, J. F., and Rudnicki, J. W. (2000). A Microcrack-Based Continuous Damage Model for Brittle Geomaterials. *Mech. Mater.* 32 (10), 607–619. doi:10.1016/S0167-6636(00)00024-7
- Shao, J. F., Zhou, H., and Chau, K. T. (2005). Coupling Between Anisotropic Damage and Permeability Variation in Brittle Rocks. *Int. J. Numer. Anal. Meth. Geomech.* 29, 1231–1247. doi:10.1002/nag.457
- Shi, C., Zhang, Q., and Wang, S. N. (2018). *Numerical Simulation Technology and Application with Particle Flow Code (PFC5.0) [M]*. Beijing: China Architecture & Building Press

- Shuai, B. (2021). Treatment Technology of Dangerous Rock Mass at High and Steep Slope. *Sichuan Water Powe.* 40 (1), 105–108. doi:10.3969/j.issn.1001-2184.2021.01.024
- Song, C. R., Li, Z. B., and Zhang, Y. (2020). Experimental Study on Group Anchor Effect in Strongly Unloading Rock Mass of a High and Steep Slope. *J. Yangtze River Scientific Res. Inst.* 37 (10), 117–124. doi:10.11988/ckyyb.20190772
- Song, Z. H., Li, X. F., Qi, F. F., and Liu, H. (2021). Analysis of the Triggering Factors for Dangerous rockfall Accident in Open Pit Mine. *J. Guangxi Univ. (Natural Sci. Edition).* 46 (1), 159–165. doi:10.13624/j.cnki.issn.1001-7445.2021.0159
- Souley, M., Homand, F., Pepa, S., and Hoxha, D. (2001). Damage-Induced Permeability Changes in Granite: A Case Example at the URL in Canada. *Int. J. Rock Mech. Mining Sci.* 38, 297–310. doi:10.1016/S1365-1609(01)00002-8
- Stacey, T. R. (1981). A Simple Extension Strain Criterion for Fracture of Brittle Rock. *Int. J. Rock Mech. Mining Sci. Geomechanics Abstr.* 18 (6), 469–474. doi:10.1016/0148-9062(81)90511-8
- Tang, S. B., Bao, C. Y., and Liu, H. Y. (2017). Brittle Fracture of Rock Under Combined Tensile and Compressive Loading Conditions. *Can. Geotech. J.* 54 (1), 88–101. doi:10.1139/cgj-2016-0214
- Tian, Y., Wu, Y., Li, H., Ren, B., and Wang, H. (2021). Earthquake Dynamic Failure Mechanism of Dangerous Rock Based on Dynamics and PFC3D. *Front. Earth Sci.* 9, 1–14. doi:10.3389/feart.2021.683193
- Valkó, P., and Economides, M. J. (1994). Propagation of Hydraulically Induced Fractures-A Continuum Damage Mechanics Approach. *Int. J. Rock Mech. Mining Sci. Geomechanics Abstr.* 31 (3), 221–229. doi:10.1016/0148-9062(94)90466-9
- Vandamme, L. M., and Roegiers, J.-C. (1990). Poroelasticity in Hydraulic Fracturing Simulators. *J. Pet. Technology.* 42, 1199–1203. doi:10.2118/16911-PA
- Wang, T., and Zhao, R. H. (2021). Deformation Characteristics of Open-Pit Slope Affected by Excavation Loading. *Saf. Coal Mines.* 52 (2), 231–234. doi:10.13347/j.cnki.mkaq.2021.02.042
- Wang, X., Xia, Z., Li, P., and Liu, H. (2021). Numerical Study on Strength and Failure Behavior of Rock with Composite Defects Under Uniaxial Compression. *Energies.* 14, 4418. doi:10.3390/en14154418
- Wei, M.-D., Dai, F., Xu, N.-W., Liu, Y., and Zhao, T. (2017). Fracture Prediction of Rocks under Mode I and Mode II Loading Using the Generalized Maximum Tangential Strain Criterion. *Eng. Fracture Mech.* 186, 21–38. doi:10.1016/j.engfracmech.2017.09.026
- Xu, Y.-r., and Xu, Y. (2021). Numerical Simulation of Direct Shear Test of Rockfill Based on Particle Breaking. *Acta Geotech.* 16, 3133–3144. doi:10.1007/s11440-021-01172-2
- Yang, S., Li, X. S., Liu, Z. F., Geng, J. B., and Rao, Y. B. (2021). Research on Overlying Strata Destruction and Instability of Underground Mining Stope in Different Inclined Ore Body. *Mining Res. Development.* 41 (04), 32–37. doi:10.13827/j.cnki.kyyk.2021.04.007
- Yao, Q., Zheng, C., Tang, C., Xu, Q., Chong, Z., and Li, X. (2020). Experimental Investigation of the Mechanical Failure Behavior of Coal Specimens with Water Intrusion. *Front. Earth Sci.* 7, 348. doi:10.3389/feart.2019.00348
- Yuan, S. C., and Harrison, J. P. (2006). A Review of the State of the Art in Modelling Progressive Mechanical Breakdown and Associated Fluid Flow in Intact Heterogeneous Rocks. *Int. J. Rock Mech. Mining Sci.* 43, 1001–1022. doi:10.1016/j.jrmms.2006.03.004
- Zhang, G., Chen, G., Xu, Z., Yang, Y., and Lin, Z. (2020). Crack Failure Characteristics of Different Rocks under the Action of Frost Heaving of Fissure Water. *Front. Earth Sci.* 8, 1–11. doi:10.3389/feart.2020.00013
- Zhang, Y., Shi, C., Zhang, Y., Yang, J., and Chen, X. (2021). Numerical Analysis of the Brittle-Ductile Transition of Deeply Buried Marble Using a Discrete Approach. *Comp. Part. Mech.* 8, 893–904. doi:10.1007/s40571-020-00375-w
- Zhao, C., Zhang, R., Zhang, Q., Shi, Z., and Yu, S. (2018). Shear-flow Coupled Behavior of Artificial Joints with Sawtooth Asperities. *Processes.* 6 (9), 152. doi:10.3390/pr6090152
- Zhao, Y.-L., Cao, P., Wang, W.-j., Wan, W., and Chen, R. (2012). Wing Crack Model Subjected to High Hydraulic Pressure and Far Field Stresses and its Numerical Simulation. *J. Cent. South. Univ. Technol.* 19 (2), 578–585. doi:10.1007/s11771-012-1042-1
- Zhong, X. Y., Liu, B. W., Chen, J. B., Wang, Z. W., and Wang, Y. C. (2021). Deformation Features of Slope Excavation and Parameter Optimization of Soft-Rock Bedding Slope in Open-Pit Mine. *Coal Eng.* 53 (3), 151–155. doi:10.11799/ce202103030
- Zuo, X. H., Yang, Y., Chen, F., Pan, Y. W., Ye, Z. C., and Li, Y. F. (2021). Study on the Slope Stability and Sensitive Factors of an Open-Pit Dump under Seepage. *Ind. Minerals Process.* 50 (2), 412–417. doi:10.16283/j.cnki.hgkwyjg.2021.02.002

Conflict of Interest: MW was employed by Yunnan Phosphating Group Co. LTD.

XL was employed by Sinosteel Maanshan General Institute of Mining Research Co. LTD.

The remaining authors declare that the research was conducted in the absence of any commercial or financial relationships that could be construed as a potential conflict of interest.

Publisher's Note: All claims expressed in this article are solely those of the authors and do not necessarily represent those of their affiliated organizations, or those of the publisher, the editors, and the reviewers. Any product that may be evaluated in this article, or claim that may be made by its manufacturer, is not guaranteed or endorsed by the publisher.

Copyright © 2022 Wang, Li, Yang, Teng, Chen and Jiang. This is an open-access article distributed under the terms of the Creative Commons Attribution License (CC BY). The use, distribution or reproduction in other forums is permitted, provided the original author(s) and the copyright owner(s) are credited and that the original publication in this journal is cited, in accordance with accepted academic practice. No use, distribution or reproduction is permitted which does not comply with these terms.



Characteristics of Stress Field and Damage Law of Coal Rock in Residual Pillar of Top Slice and Its Application

Fengfeng Wu^{1,2}, Xin Yu^{1,2*}, Gaoliang Zhao³, Beiju Du^{1,2}, Bo Lv^{1,2} and Jian Zhang^{1,2}

¹School of Mines, China University of Mining and Technology, Xuzhou, China, ²State Key Laboratory of Coal Resources and Safe Mining, China University of Mining and Technology, Xuzhou, China, ³Shanxi Yangcheng Shancheng Coal Industry Co., Ltd., Jincheng, China

OPEN ACCESS

Edited by:

Qingsheng Bai,
Freiburg University of Mining and
Technology, Germany

Reviewed by:

Zhenlei Li,
University of Science and Technology
Beijing, China
Baobao Chen,
Anhui University of Science and
Technology, China

*Correspondence:

Xin Yu
TS20020070A31LD@cumt.edu.cn

Specialty section:

This article was submitted to
Geohazards and Georisks,
a section of the journal
Frontiers in Earth Science

Received: 14 December 2021

Accepted: 19 January 2022

Published: 18 February 2022

Citation:

Wu F, Yu X, Zhao G, Du B, Lv B and
Zhang J (2022) Characteristics of
Stress Field and Damage Law of Coal
Rock in Residual Pillar of Top Slice and
Its Application.
Front. Earth Sci. 10:835531.
doi: 10.3389/feart.2022.835531

This article presents a theoretical analysis and numerical simulation studies to determine the suitable position for the lower slice roadway in a residual pillar area after top slicing a thick coal seam. We considered the load concentration on the coal pillar, the goaf floor, and the stress distribution characteristics of the coal pillar area before and after the top slice. With a mechanical model built of the residual pillar load propagation in the floor and the failure model of the floor surrounding rock, the analytical formula we deduced for the coal pillar floor stress and the expression of the floor failure depth of the roadway provides a basis for the reasonable determination of the position of the lower slicing roadway. Studies proved that after mining the top slice working face, the floor stress field of the residual pillar area presented characteristics of the non-uniform distribution. The stress concentration occurred below the coal pillar. The stress variation area appeared at the edge of the coal pillar, with a stable stress area appearing far away from the coal pillar area. Therefore, the roadway layout should avoid the areas below the coal pillar and the coal pillar edge with high stress levels and a large stress variation gradient. High stress concentration formed on the coal pillar transferred to the lower layered coal and floor strata, and decreased the stress concentrations layer by layer. However, mining of the top-layered working face affected the coal, and rock mass damaged the coal pillar floor area and weakened the mechanical properties, which was not conducive to the control of the roadway surrounding rock. The research results applied to No. 30117 working face of the lower slice of the Shancheng Coal Industry, and the proper position of the return airway of the working face was determined to be 8 m outside the east side of the residual pillar in the top slice, achieving a good surrounding rock control effect.

Keywords: slice mining, residual pillar, stress distribution, floor failure depth, numerical simulation

INTRODUCTION

In Chinese coal reserves, thick coal seams account for more than 40% of the total resources and account for more than 50% of the coal production (Wang, 2009; Dai et al., 2013). Thick coal seam mining technology has experienced three gradual optimization stages: layered mining, top coal caving mining, and large mining height mining (Zhang, 2001; Wang and Zhong, 2008). However, due to the problems of different sizes of coal enterprises, unbalanced development of mining technology, and complex coal seam occurrences (Xu, 2003; Bai et al., 2014, 2017), many thick coal

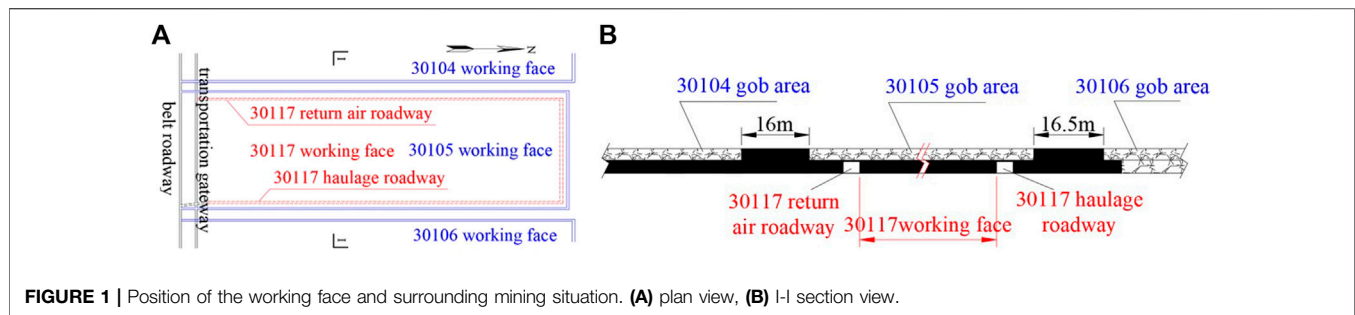


FIGURE 1 | Position of the working face and surrounding mining situation. (A) plan view, (B) I-I section view.

seam mines in Datong, Huainan, Chifeng, and other mining areas in China are still adopting layered mining technology, while in Jincheng and other mining areas, there is a situation of top-layered mining and bottom-layered re-mining. For the downward mining working face of a thick coal seam, the lower layered coal becomes affected by the top-layered mining, leaving a coal pillar; the stress environment is complex, seriously damaging the surrounding rock. Therefore, it was vital to clarify the stress distribution characteristics and damage law of the surrounding rock under the residual coal pillar to determine the lower layered roadway's reasonable spatial layout.

Many scholars have studied the stress field characteristics and coal rock damage law of the left coal pillar area. Mu et al. (2021) constructed a mechanical model of the left coal pillar in close coal seam mining and found that the left coal pillar was the main reason for the stress concentration of the lower coal seam roadway. Tian et al. (2019) studied the stress evolution law of the lower coal seam under the influence of coal pillar disturbance after upper coal seam mining using the combination of physical and numerical simulations. Liu et al. (2016) studied the stress distribution characteristics of the residual coal pillar floor. They proposed that the stress in the coal pillar area is proportional to the abutment pressure on the coal pillar, inversely proportional to the vertical distance and diffusion angle, and extends elliptically along the direction of gravity. Yue et al. (2021) constructed the structural mechanics model of "elliptical stress arch" in the overlying coal seam and calculated the additional mining stress of the floor roadway under the left coal pillar. Zhao et al. (2020, 2021a, 2021b) studied the damage and failure characteristics and the stress distribution characteristics of floor strata under isolated island coal pillars and analyzed the asymmetric deformation mechanism of the lower layered roadway. Huang et al. (2019, 2020, 2021) studied the three-field evolution characteristics of close coal seam mining using the numerical simulation, established a coupling control model of the stress field, displacement field, and fracture field and proposed a reasonable calculation method of the lower roadway position. Shen et al. (2018) put forward the "three index method" of the roadway layout under the left coal pillar. They pointed out that the lower layered roadway was preferentially arranged in the area of $0 \leq$ stress concentration coefficient (ratio of local stress to original material rock stress) ≤ 1 , $0.8 \leq$ coefficient of horizontal pressure (ratio of horizontal stress to vertical stress) ≤ 1.4 , and $0 \leq$ stress gradient ≤ 1 . Many scholars have studied the stress

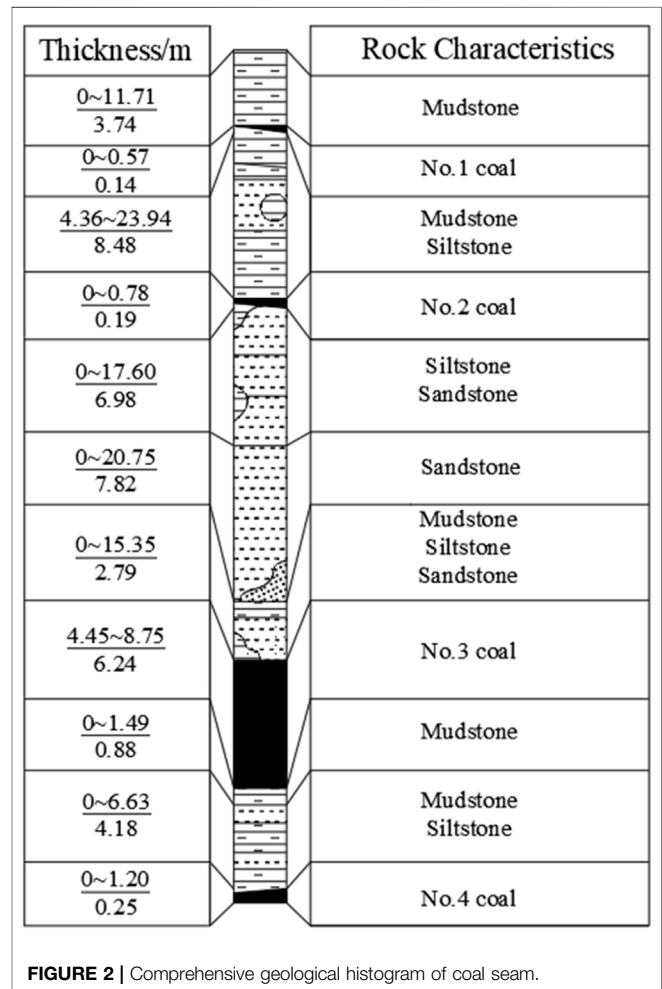


FIGURE 2 | Comprehensive geological histogram of coal seam.

distribution and the failure zone of the floor under the load effect of the coal pillar, but there is little research on the stress field characteristics of the floor rock and the damage law of the surrounding rock under the condition of the top slicing mining and the lower slicing mining, which did not lead to solve the problem of the roadway layout under this condition.

Based on the existing research, this study takes the 30117 lower layers working face of the Shancheng Coal Industry as the engineering background, and established the calculation model of the load concentration of the top-layered left coal pillar and the

TABLE 1 | Test results of physical and mechanical properties parameters of the No. 3 coal seam and roof-floor strata.

Rock specimen	Bulk density/kg·m ⁻³	Uniaxial compressive strength/MPa	Uniaxial tensile stress/MPa	Elastic modulus/GPa	Poisson ratio	Cohesion/MPa	Internal friction angle/°
No. 3 coal seam	1,435	13.72	1.58	0.85	0.32	2.09	40
Mudstone	2,583	38.61	1.67	2.02	0.27	2.41	30
Siltstone	2,480	32.13	3.14	1.85	0.27	7.31	17

TABLE 2 | Test results of hydraulic fracturing stress.

Measuring station	Buried depth/m	Vertical stress/MPa	Maximum horizontal stress/MPa	Minimum horizontal stress/MPa	Direction of maximum horizontal stress
1	460	12.42	6.24	3.53	N5.41°E
2	460	21.42	5.4	3.9	N10.83°E

goaf, used theoretical analysis and numerical simulation to derive the analytical formula of the stress of the coal pillar floor, and analyzed the distribution characteristics of the stress field. Finally, based on slip line theory, the coal and rock damage law under the coal pillar's influence was studied, providing a theoretical basis for the proper location selection of the lower layer roadway.

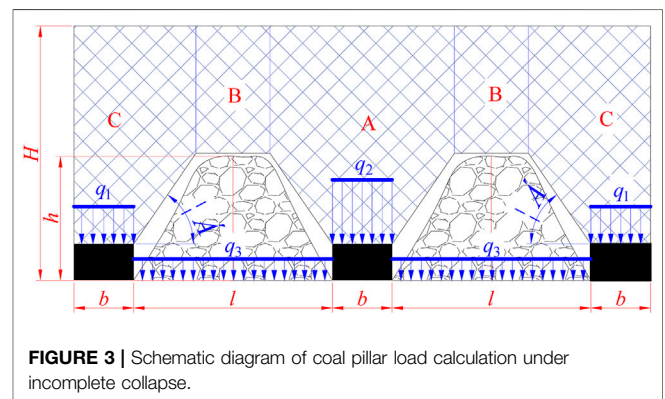
ENGINEERING BACKGROUND

Position of Working Face and Surrounding Mining Situation

The Shancheng Coal Industry is located in Beiliu town, Yangcheng County, Shanxi Province, with a production capacity of 0.6 Mt/a, belonging to medium-sized mines, mainly mining the No. 3 coal seam. The No. 3 coal seam thickness is 5.43 ~ 6.60 m, the average thickness is 6.24 m, and the dip angle is 1 ~ 4°. Historically, the No. 3 coal seam mining was only the top layer, and the mining height was 2.3 m. However, it has the lower layer working face mining of 30117 located in 301 mining areas. Therefore, the goaf of 30105 top layer working face is above the working face, the goaf of 30,106 top layer working face is on the right, and the goaf of 30104 top layer working face is on the left. **Figure 1** shows the underground relative position relationship of the 30117 working face.

Characteristics of Coal Seam and Roof-Floor Strata

Figure 2 gives the comprehensive geological column of the No. 3 coal seam. The direct roof of the No. 3 coal seam is mudstone, siltstone, coal grained, and fine-grained sandstone strip with an average thickness of 2.79 m; the direct floor is mudstone with an average thickness of 2.48 m. According to the data provided by the mine production geological report, the physical and mechanical parameters of the No. 3 coal seam and roof and floor strata are in **Table 1**.

**FIGURE 3** | Schematic diagram of coal pillar load calculation under incomplete collapse.

Test Results of Ground Stress

The ground stress test results of the No. 3 coal seam are in **Table 2**. The vertical stress in the area near the 30117 working face is much higher than the horizontal stress, which varied from 12.42 to 21.42 MPa.

LOAD CONCENTRATION CALCULATION OF RESIDUAL PILLAR AND LOWER LAYER

With mining the top layer working face, the roof strata were broken, moved, and deformed, and finally, the masonry beam structures were formed to bear the upper rock. **Figure 3** shows the load on the coal pillar from the weight of the overlying strata and the exposed strata on one or both sides of the coal pillar transferred to the coal pillar.

As seen in **Figure 3**, with mining of one side of the coal pillar, its weight bears mainly on the rock layer in the C area, and then load concentration q_1 on the coal pillar is as follows:

$$q_1 = \left[(b + h \cot \alpha)H - \frac{h^2 \cot \alpha}{2} \right] \frac{\gamma}{b} \quad (1)$$

The mining of the two side sections of the coal pillar mainly undertakes the weight of the rock layer in the area A. The load set q_2 on the coal pillar is as follows:

$$q_2 = [(b + 2h \cot \alpha)H - h^2 \cot \alpha] \frac{\gamma}{b} \quad (2)$$

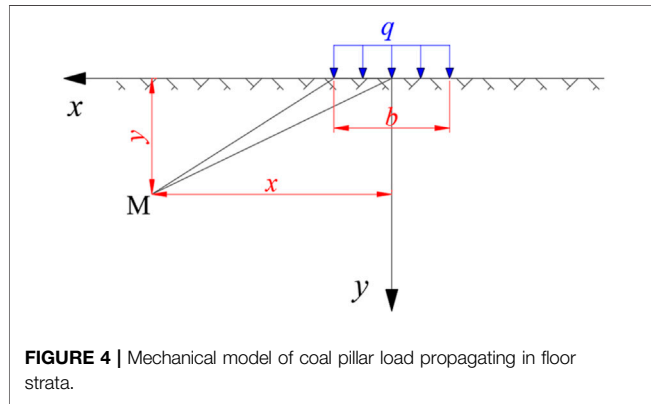


FIGURE 4 | Mechanical model of coal pillar load propagating in floor strata.

The load concentration q_3 of the goaf floor is as follows:

$$q_3 = \gamma h, \quad (3)$$

where b is the section width of the coal pillar, m; h is the rock roof caving height, m; and α is the caving angle of strata overlying goaf.

DISTRIBUTION CHARACTERISTICS OF THE STRESS FIELD IN THE RESIDUAL PILLAR AREA

Analysis Based on Elastoplastic Theory

Mining of the top slice working face caused the redistribution of the surrounding rock stress. Additionally, causing the stress concentration of the coal and rock mass around the mining space will also transfer the stress to the deep floor through the remaining coal pillars. Therefore, simplifying the coal rock assembly to a homogeneous elastic body makes the stress distribution of the coal seam floor to the case of uniform load q acting on the semi-infinite plane, and the mechanical model of

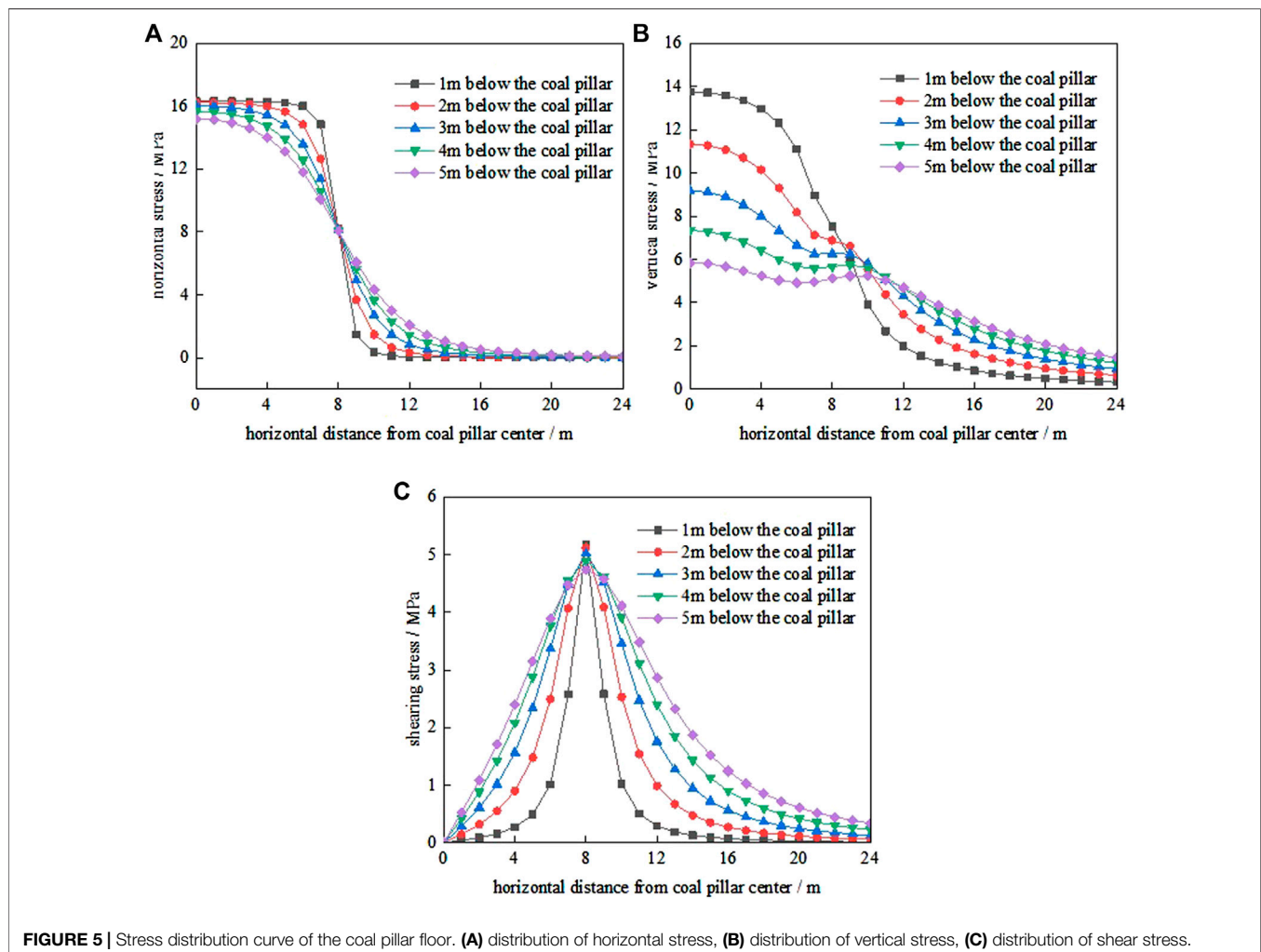


FIGURE 5 | Stress distribution curve of the coal pillar floor. (A) distribution of horizontal stress, (B) distribution of vertical stress, (C) distribution of shear stress.

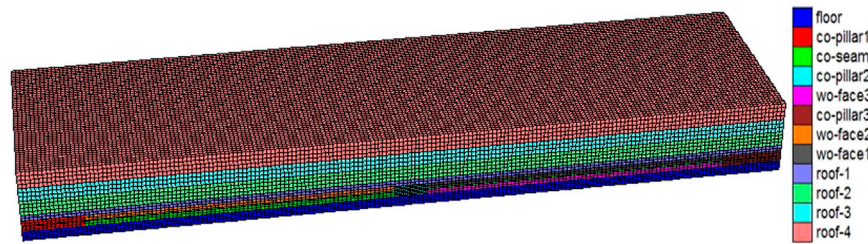


FIGURE 6 | Numerical calculation model diagram.

TABLE 3 | Physical and mechanical parameters of the coal seam in the model.

Rock name	Bulk modulus/GPa	Shear modulus/GPa	Tensile strength/MPa	Cohesion/MPa	Internal friction angle/°	Density/kg·m ⁻³
Roof mud sandstone	4.14	2.28	2.98	4.18	28.4	2,500
Roof mud sandstone	6.67	4.00	3.60	7.60	24.2	2,580
Roof mud sandstone	6.55	4.51	3.40	5.63	27.6	2,450
Roof mudstone	3.14	1.98	2.98	3.98	28.7	1,850
No. 3 coal seam	1.86	1.17	2.62	3.72	27.4	1,650
Floor sandstone	7.79	4.91	3.41	4.61	27.6	2,650

the residual coal pillar load propagating in the floor strata after stratified mining becomes as shown in **Figure 4**.

Using the elastic theory (Xu, 1979), the stress calculation at any point M in the bottom rock under uniform load on the free boundary was done by using the superposition principle:

$$\sigma_x = \frac{q}{\pi} \left[\arctan \frac{x+b2}{y} - \arctan \frac{x-b2}{y} + \frac{y(x+b2)}{y^2 + (x+b2)^2} - \frac{y(x-b2)}{y^2 + (x-b2)^2} \right], \quad (4)$$

$$\sigma_y = \frac{q}{\pi} \left[\arctan \frac{x+b2}{y} - \arctan \frac{x-b2}{y} - \frac{y(x+b2)}{y^2 + (x+b2)^2} + \frac{y(x-b2)}{y^2 + (x-b2)^2} \right], \quad (5)$$

$$\tau_{xy} = \frac{q}{\pi} \left[\frac{y^2}{y^2 + (x+b2)^2} - \frac{y^2}{y^2 + (x-b2)^2} \right], \quad (6)$$

where σ_x is the positive stress along the horizontal direction, MPa; σ_y is the normal stress along the vertical path, MPa; τ_{xy} is the shearing stress, MPa; q is the uniform load on the coal pillar, kN/m; x is the horizontal distance from point M to the coal pillar center, m; and y is the vertical distance from point M to the coal pillar center, m.

The earlier equations show that the stress at any point in the floor strata mainly depends on the load of the upper coal pillar, the width of the coal pillar, the vertical distance between the point and the coal pillar, and the horizontal distance between the point and the central line of the coal pillar.

Taking the condition of the 30117 working face as an example, the width of the remaining coal pillar is 16 m. After mining, the 30105 working face of the top layer, the overburden of the stope is prone to non-full collapse. Therefore, the load concentration of the coal pillar became as in **Eq. 2**:

$$q = [(b + 2h \cot \alpha)H - h^2 \cot \alpha] \frac{\gamma}{b} = 16.33 \text{ MPa}.$$

On substituting the coal pillar width and load concentration into **Eqs 4–6**, the horizontal stress distribution, vertical stress, and shear stress at different depths are as shown in **Figure 5**, respectively. The central point O in the figure is the central position of the coal pillar.

Figure 5A shows:

- ① The horizontal stress that transmits downward from the coal pillar toward left by the top layer is mainly the compressive stress under the coal pillar ($x = 0 \sim 8$ m), showing an apparent stress concentration.
- ② Near the edge of the coal pillar ($x = 8 \sim 12$ m), the horizontal stress decreases rapidly, and its change rate decreases with the increase in depth, which belongs to the transition zone affected by the coal pillar.
- ③ In the range of $x = 12 \sim 24$ m, the horizontal stress tends to be stable and is less affected by the coal pillar.

Similarly, **Figure 5B** shows:

- ① The distribution of vertical stress transmitted from the remaining coal pillars to the floor is relatively concentrated, and the constrained high-stress area under the coal pillar ($x = 0 \sim 8$ m) decreases with the increase in depth.
- ② Near the edge of the coal pillar ($x = 8 \sim 14$ m), the vertical stress in floor strata fell rapidly, which belonged to the transition zone of the coal pillar influence; ③ In the range of

$x = 14 \sim 24$ m, the relatively minor vertical stress in the floor strata tends to be stable and less affected by the coal pillar.

Figure 5C shows:

- ① When the horizontal distance from the center of the coal pillar increases, the shear stress below the coal pillar increases. The shear stress is zero at the center of the coal pillar and reaches the maximum at the edge of the coal pillar.

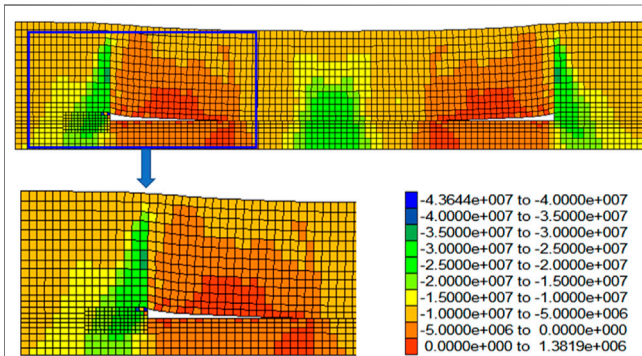


FIGURE 7 | 30105 working face after mining vertical stress distribution of surrounding rock.

- ② Near the edge of the coal pillar and in the range of $x = 8 \sim 16$ m, the shear stress decreased with the increase in horizontal distance from the center of the coal pillar was the transition zone affected by the coal pillar.
- ③ In the range of $x = 16 \sim 24$ m, the shear stress was relatively small and tended to be stable.

The previous analysis shows that the lower part of the residual coal pillar ($x = 0 \sim 8$ m) was the coal pillar's concentration area; the horizontal and vertical stresses were higher, and the shear stress gradient was large. The coal pillar edge ($x = 8 \sim 16$ m) was the transition zone affected by the coal pillar, and the various gradients of horizontal stress, vertical stress, and shear stress were significant; arranging roadways in these two areas is not conducive to the stability control of the roadway surrounding rock; in the range of $x = 16 \sim 24$ m, the horizontal stress, vertical stress, and shear stress were low, the stress gradient was slight and beneficial to the roadway control surrounding rock, and was a reasonable roadway layout range.

Analysis Based on Numerical Simulation Model Set-Up

Based on mining geological conditions around the 30,117 working face of the Shancheng Coal Industry, FLAC3D (version 6.0) (Itasca, 2019) numerical further understands the stress field characteristics of the residual coal pillar area. The model is shown in **Figure 6**.

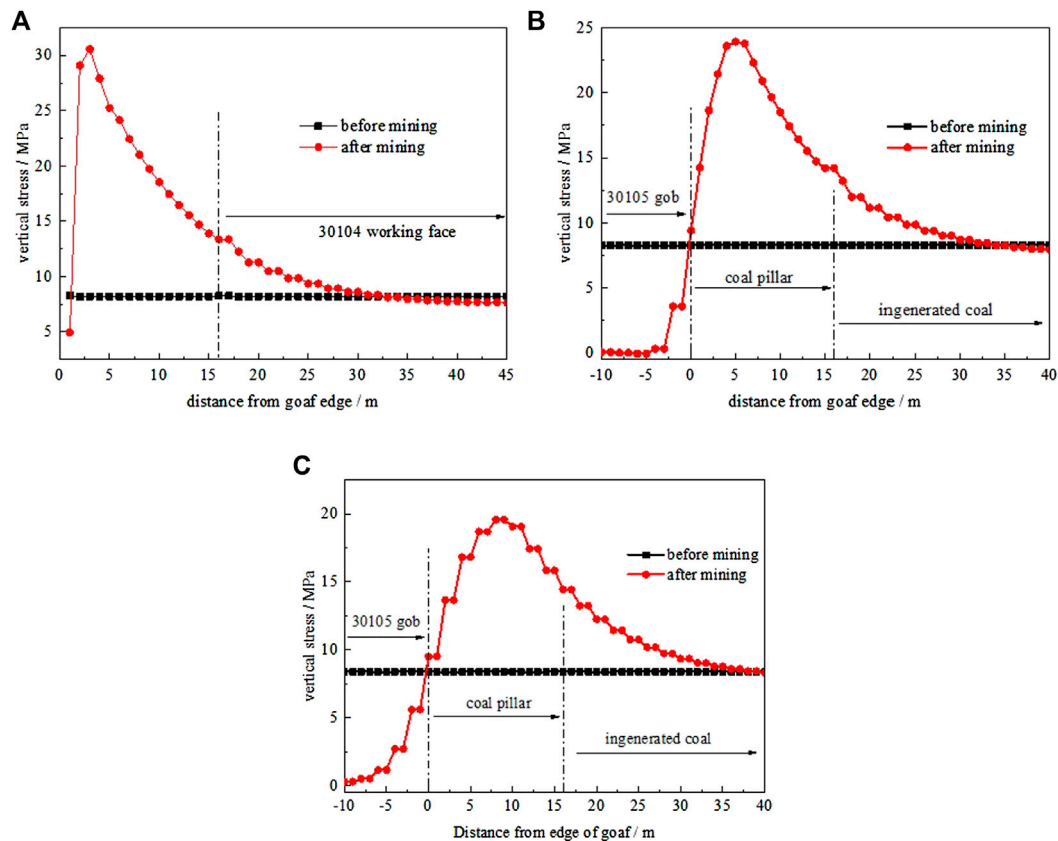


FIGURE 8 | Vertical stress distribution of the surrounding rock at different positions before and after mining in 30105 working face. **(A)** the vertical stress distribution of coal pillar, **(B)** the vertical stress distribution of lower layered coal, **(C)** the vertical stress distribution of pavement stratum.

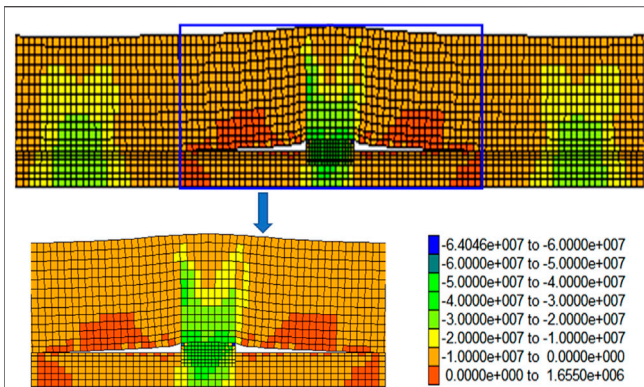


FIGURE 9 | Vertical stress distribution of the surrounding rock after mining of 30104 working face.

The size of the model was $376 \times 100 \times 38$ m (length \times width \times height). Horizontal constraints were applied around the model. Horizontal displacement and vertical displacement were constrained at the bottom of the model. We used the vertical load at the model's top according to the *in situ* stress of 550 m

depth. The failure criterion adopted was the elastoplastic constitutive model, and the failure criterion was the Mohr–Coulomb.

Based on the rock mechanics experiment, we determined a particular reduction coefficient according to different weights to obtain the rock mechanics parameters that were more consistent with the actual field. **Table 3** gives each rock stratum's physical and mechanical parameters in the model. The null element excavates the model, and the excavation sequence is the initial ground stress balance \rightarrow excavation of the 30105 working face \rightarrow excavation of the 30104 working face.

Simulation Result Analysis

1) The stress distribution characteristics of 30105 working face after mining

Figure 7 illustrates the vertical stress distribution of the surrounding rock after the end of mining in the 30105 working face. The diagram showed that after mining the 30105 working face, the failure movement of roof strata and the stress redistribution of the surrounding rock occur. As the activity of the mined-out rock tends to be stable, the falling gangue in the mined-out area is

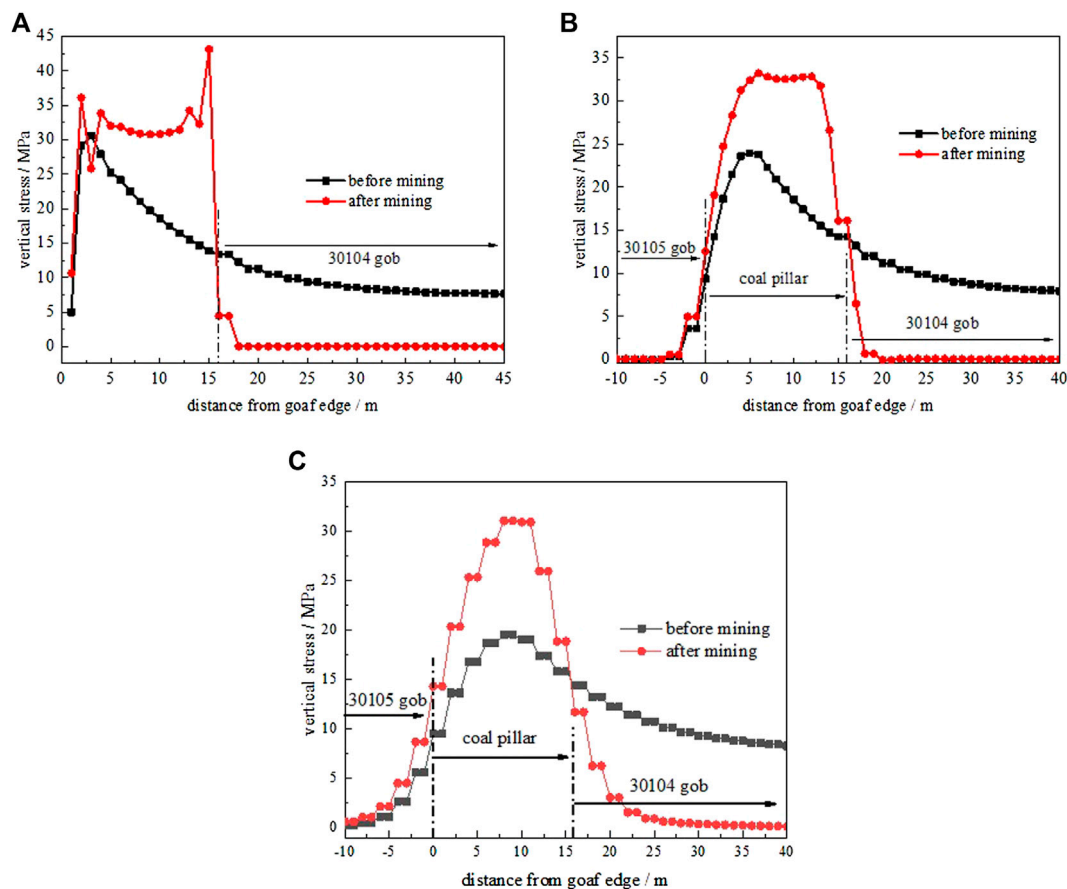
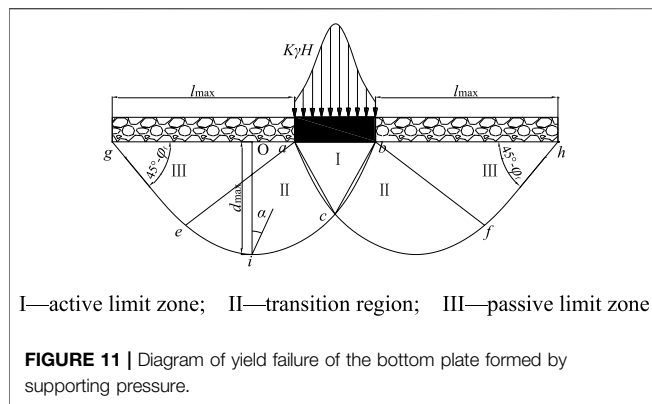


FIGURE 10 | Vertical stress distribution of the surrounding rock at different positions before and after mining in 30104 working face. **(A)** the vertical stress distribution of coal pillar, **(B)** the vertical stress distribution of lower layered coal, **(C)** the vertical stress distribution of pavement stratum.



gradually compacted and restored the surrounding rock stress in the middle of the working face to the original rock stress. The roof strata near the coal pillar have rotary deformation and tensile failure, and the stress of the surrounding rock transfers to the coal pillar. The stress concentration formed at the coal pillar's edge near the goaf was transferred to the coal and rock below.

Figure 8 shows the vertical stress distribution curves of the surrounding rock before and after stopping the 30105 working face. The diagram indicates that after mining 30105 working face, the stress of roof overburden transfers to the section coal pillar and passes down to the lower layered coal and the floor strata through the section coal pillar. Among them, stress concentration on the coal pillar was the highest, and a high-stress concentration area resulted in the range of 2 ~ 4 m deep into the coal pillar. The stress value exceeds 25 MPa, the maximum is 30.55 MPa, and the stress concentration coefficient is 3.73. The high-stress concentration degree of the lower layered coal was the second, and the high-stress concentration area formed in the range of 3 ~ 8 m from the edge of the goaf. The stress value exceeds 20 MPa, the maximum is 23.93 MPa, and the stress concentration coefficient is 2.89. The high-stress concentration degree of the floor strata was the lowest, close to 20 MPa in the range of 7 ~ 11 m from the edge of goaf, the maximum was 19.57 MPa, and the stress concentration factor is 2.36. Finally, we noted that in the stress transfer of the weathered rock, the stress concentration degree shows the characteristics of the upper section coal pillar > lower layer coal > floor rock.

Figures 8B,C show that after the end of the mining of the 30105 working face, the coal and rock under the goaf have a tensile failure, surrounding rock pressure relief, and stress reduction. From the distribution of the stress value, the

pressure relief degree of lower layered coal is greater than that of the floor rock. Consequently, the mining influence of lower layered coal is more significant than that of the floor rock.

- 2) The stress distribution characteristics of the 30104 working face after mining

Figure 9 shows the surrounding rock's vertical stress distribution after mining in the 30104 working face. The figure shows that the vertical stress distribution of the surrounding rock changes significantly with the mining of the upper layer 30104 working face. With the activity of the upper strata in the middle of the 30104 working face stabilized, the gangue in the goaf was compacted, and the stress of some surrounding rock returned to the original rock stress before mining, and some exceeded the initial rock stress to form stress concentration. The roof strata near the coal pillar edge caused tensile failure due to rotary deformation and reduced the unloading stress of the surrounding rock. However, the coal pillar section bore more rock stress due to the support and thus formed high-stress concentration.

Figure 10 illustrates the vertical stress distribution curve of the surrounding rock after mining in the 30104 working face. It is seen from **Figure 10A** that with the mining of the 30104 working face, the vertical stress on the section coal pillar changed significantly: the stress increase in the coal pillar near the edge of the 30104 goaf is the largest, from 13.89 to 43.11 MPa, the stress increase was as high as 29.22 MPa, and the stress concentration coefficient was 3.22. The vertical stress of the edge side of the 30105 goaf near the coal pillar also increased, but it was significantly smaller than that with the increase of the 30104 goaf side. The main reason was that the horizontal distance from the 30104 working face was far, and the influence of mining disturbance was small. We noted that due to the mining influence of the top layer 30104 working face, the stress increase amplitude of the coal pillar on the edge of the 30104 goaf was the largest. The stress increase amplitude of the coal pillar on the edge of the 30105 goaf was the smallest. With the increase in the distance from the mining face, the mining influence degree decreases, and the corresponding stress increase, amplitude decreases.

Figures 10B,C show that the vertical stress in the surrounding rock was significantly reduced due to the mining effect of top slicing the 30104 working face. At the same time, due to the increase in vertical stress on the section coal pillar caused by the mining of the 30104 working face, the vertical stress transmitted to the floor coal and rock mass was

TABLE 4 | Relevant calculation parameters of 30117 working face.

Parameter	Value	Parameter	Value
Mining high of top slice/m	2.3	Width of working face/m	148.5
Buried depth/m	320	Internal friction angle/°	40
Caving angle/°	65	Coal seam cohesion/MPa	2.09
Bulk density/kN·m ⁻³	25	Uniaxial compressive strength/MPa	13.72
Stress concentration factor	3.2	Joint influence coefficient	2.0
Friction coefficient	0.12	Mining high/m	3.9

also increased, and the stress growth change on the coal pillar section was also reflected in the floor coal and rock mass, that is, the stress increase in the floor coal and rock mass near the edge of the 30104 goaf is the largest, and it is attached to the edge of the 30105 goaf.

The complete simulation results show that after mining 30104 and 30105 working faces in the top layer, high-stress concentration is formed on the coal pillar and transferred to the lower layer of coal and floor strata. The stress decreases gradually with the distance from the center of the coal pillar, which is consistent with the law obtained by theoretical calculation. However, due to the mining pressure relief, the surrounding rock stress of the lower layer of coal and floor strata in the goaf decreases.

ANALYSIS OF COAL ROCK DAMAGE AND FAILURE LAW IN RESIDUAL PILLAR AREA

According to the slip line field theory (Li, 2004), the failure depth in the floor caused by abutment pressure is evident in **Figure 11**.

I—active limit zone; II—transition region; and III—passive limit zone.

The yield failure depth of floor under slip line field theory is expressed by **Eq. 7**:

$$d = r_0 \cdot e^{\alpha \tan \varphi_f} \cdot \cos\left(\alpha + \frac{\varphi}{2} - \frac{\pi}{4}\right) \quad (7)$$

$$r_0 = \frac{x_0}{2 \cos\left(\frac{\pi}{4} + \frac{\varphi_f}{2}\right)}, \quad (8)$$

where d is the floor yield failure depth, m; φ_f is the internal friction angle of floor rock, °; r_0 is the area II starting point c to pole distance; and α is the angle between any point axis and starting point axis.

By derivation, the maximum yield failure depth of the floor rock is as follows:

$$d_{\max} = \frac{x_0 \cos \varphi_f}{2 \cos\left(\frac{\pi}{4} + \frac{\varphi_f}{2}\right)} e^{\left(\frac{\varphi_f}{2} + \frac{\pi}{4}\right) \tan \varphi_f}, \quad (9)$$

where x_0 is the width of the plastic zone of the coal wall, calculated by limit equilibrium theory:

$$x_0 = \frac{M}{2\xi f} \ln \frac{k\gamma H + C \cot \varphi}{\xi(P_i + C \cot \varphi)} \quad (10)$$

$$\xi = \frac{1 + \sin \varphi_f}{1 - \sin \varphi_f}. \quad (11)$$

So the maximum failure depth of stope floor calculated by slip line field theory is follows:

$$d_{\max} = \frac{M \cos \varphi_f \ln \frac{k\gamma H + C \cot \varphi}{\xi(P_i + C \cot \varphi)}}{4\xi f \cos\left(\frac{\varphi_f}{2} + \frac{\pi}{4}\right)} e^{\left(\frac{\varphi_f}{2} + \frac{\pi}{4}\right) \tan \varphi_f}. \quad (12)$$

Similarly, the maximum horizontal range of floor yield failure under slip line field theory expressing **Eq. 13**:

$$l_{\max} = \frac{M \cos\left(\frac{\pi}{4} - \frac{\varphi_f}{2}\right) \ln \frac{k\gamma H + C \cot \varphi}{\xi(P_i + C \cot \varphi)}}{2\xi f \cos\left(\frac{\pi}{4} + \frac{\varphi_f}{2}\right)} e^{\frac{\pi}{4} \tan \varphi_f}, \quad (13)$$

where C is the coal cohesion, f is the friction coefficient of the contact surface between the coal seam and the roof and floor, ξ is the triaxial stress coefficient, P_i is the resistance of support to coal rib, and M is the coal seam thickness.

ENGINEERING PRACTICE

To ensure the regular mining replacement of the working face, the Shancheng Coal Industry needs to optimize the location of the return airway of the 30117 working face. The relevant calculation parameters of 30117 working face are in **Table 4**.

According to the theoretical analysis in *Analysis Based on Elastoplastic Theory* before, the stress concentration area is below the coal pillar of 16 m, and the stress level is high. The stress variation area is within the range of 0–8 m at the edge of the coal pillar, and the stress variation gradient is large. Therefore, the stable stress area is outside 8 m at the edge of the coal pillar. Outside the edge of the coal pillar, 8 m is the stable stress area, the stress level is low, and the stress gradient is slight. Therefore, the return airway of the 30117 working face should be outside 8 m on both sides of the left coal pillar.

From **Eqs 12, 13**, the plastic failure range of floor based on slip line field theory is:

$$\begin{aligned} d_{\max} &= \frac{M \cos \varphi_f \ln \frac{k\gamma H + C \cot \varphi}{\xi(P_i + C \cot \varphi)}}{4\xi f \cos\left(\frac{\varphi_f}{2} + \frac{\pi}{4}\right)} e^{\left(\frac{\varphi_f}{2} + \frac{\pi}{4}\right) \tan \varphi_f} \\ &= 4.45 \text{ m} \\ l_{\max} &= \frac{M \cos\left(\frac{\pi}{4} - \frac{\varphi_f}{2}\right) \ln \frac{k\gamma H + C \cot \varphi}{\xi(P_i + C \cot \varphi)}}{2\xi f \cos\left(\frac{\pi}{4} + \frac{\varphi_f}{2}\right)} e^{\frac{\pi}{4} \tan \varphi_f} \\ &= 7.95 \text{ m} \end{aligned}$$

According to the theoretical calculation results, the coal to be mined in the lower layer 30117 working face is affected by mining the top layer. Therefore, in the range of $l \times d = 7.95 \times 4.45$ m on both sides of the coal pillar floor, it will be damaged to varying degrees, and the mechanical properties of the surrounding rock will be weakened, which is not conducive to the control of the surrounding rock of the roadway. Therefore, the roadway layout was outside the above range.

In addition, **Figure 1** showed that when the roadway was on the east side of the left coal pillar, the left coal pillar was outside the end area of the working face, which is conducive to the rapid advancement of the working face and the high safety factor. In contrast, when the roadway was on the west side of the left coal pillar, because of the existence of the left coal pillar, the pressure at the end area of the working face was significant, and there was a security risk.

Based on the earlier analysis results, the layout position of the return airway in the 30117 working face is determined to be 8 m away from the east side of the left coal pillar. In addition, field

practice shows that the roadway surrounding rock control effect is favorable.

CONCLUSION

- 1) Based on the collapse of the mined-out area, we constructed the coal pillar and mined-out area's load calculation model and the load set calculation method was obtained.
- 2) The mechanical model of residual pillar load propagation in the floor is established, and the analytical formula of floor stress is derived. We concluded that the stress field in the residual coal pillar area presents the characteristics of the non-uniform distribution. The stress concentration area appears below the coal pillar, the stress variation area appears at the edge of the coal pillar, and the stress stability area appears in the distance. The stress level below the coal pillar is high, and the stress gradient at the edge of the coal pillar is large, which is not conducive to the layout of the roadway. On the other hand, the stress level away from the coal pillar area is low, and the stress change gradient is slight, which is a proper roadway layout position.
- 3) FLAC3D was used to simulate the stress distribution of the coal pillar area before and after mining the top-stratified working face. After mining the top-stratified working face, the results showed that a high-stress concentration was formed on the coal pillar and transmitted to the lower stratified abutment area and the floor rock layer. In contrast, the lower stratified abutment area and the floor rock layer in the goaf is due to mining pressure relief, the stress of the surrounding rock was reduced, and the degree of stress concentration was characterized by the section coal pillar > lower stratified abutment area > floor rock layer.
- 4) Based on the slip line field theory, the yield failure model of the floor is established. The expressions of yield failure depth of floor were obtained and the damage range of coal and rock mass, on both sides of coal pillar floor affected by the mining of top slice working face was defined.

REFERENCES

- Bai, Q.-S., Tu, S.-H., Wang, F.-T., Zhang, X.-G., Tu, H.-S., and Yuan, Y. (2014). Observation and Numerical Analysis of the Scope of Fractured Zones Around Gateroads under Longwall Influence. *Rock Mech. Rock Eng.* 47 (5), 1939–1950. doi:10.1007/s00603-013-0457-9
- Bai, Q., Tu, S., Wang, F., and Zhang, C. (2017). Field and Numerical Investigations of Gateroad System Failure Induced by Hard Roofs in a Longwall Top Coal Caving Face. *Int. J. Coal Geology*. 173, 176–199. doi:10.1016/j.coal.2017.02.015
- Dai, H., Guo, J., Yi, S., Wang, G., Liu, A., Kong, B., et al. (2013). The Mechanism of Strata and Surface Movements Induced by Extra-thick Steeply Inclined Coal Seam Applied Horizontal Slice Mining. *J. China Coal Soc.* 38 (07), 1109–1115. doi:10.13225/j.cnki.jccs.2013.07.017
- Huang, Q., Cao, J., and Du, J. (2019). Research on Three-Field Evolution and Rational Coal Pillar Staggered Distance in Shallow Buried Closely Spaced Multi-Seam Mining. *J. China Coal Soc.* 44 (03), 681–689. doi:10.13225/j.cnki.jccs.2018.6035
- Huang, Q., Cao, J., and Gao, B. (2020). Damage-Reducing Mining Based on Three Fields Evolution in Shallow Buried Closely Spaced Multi-Seam. *J. Mining Saf. Eng.* 37 (06), 1171–1179. doi:10.13545/j.cnki.jmse.2020.06.011

- 5) Based on the research results of the stress field distribution characteristics and the failure law of coal and rock in the residual coal pillar area, the excellent layout area of the roadway was determined to be 8 m away from the two sides of the coal pillar, avoiding the influence of stress concentration, facilitated the rapid advancement of the working face, and solved the problem that the residual coal pillar was located in the end area of the working face, which caused the hydraulic support to be stressed.

DATA AVAILABILITY STATEMENT

The raw data supporting the conclusion of this article will be made available by the authors, without undue reservation.

AUTHOR CONTRIBUTIONS

Conception and design of study: FW, XY, and GZ; Acquisition of data: BD, BL, JZ, and GZ; Analysis and/or interpretation of data: FW, XY, and BD; Drafting the manuscript: XY, BL, and JZ; Revising the manuscript critically for important intellectual content: FW, XY, and GZ; Article polishing: GZ and XY.

FUNDING

The work was supported by the National Natural Science Foundation of China (52174138).

ACKNOWLEDGMENTS

The authors gratefully acknowledge the financial support of the agencies aforementioned.

- Huang, Q., Du, J., Chen, J., and He, Y. (2021). Coupling Control on Pillar Stress Concentration and Surface Cracks in Shallow Multi-Seam Mining. *Int. J. Mining Sci. Tech.* 31 (01), 95–101. doi:10.1016/j.ijmst.2020.12.019
- Itasca (2019). *User's Manuals of FLAC3D: Fast Lagrangian Analysis of Continua in 3D*. version 4. Minneapolis, MN: Itasca Consulting Group Inc.
- Li, G. (2004). *Soil Mechanics*. Beijing: Higher Education Press.
- Liu, X., Li, X., and Pan, W. (2016). Analysis on the Floor Stress Distribution and Roadway Position in the Close Distance Coal Seams. *Arabian J. Geosciences* 9 (2), 83.
- Mu, H., Bao, Y., Song, D., and Su, D. (2021). Investigation of Strong Strata Behaviors in the Close-Distance Multiseam Coal Pillar Mining. *Shock and Vibration* 2021, 1–14. doi:10.1155/2021/1263275
- Shen, W., Bai, J., Zhao, Z., Shen, X., Wang, X., and Kang, J. (2018). Three Indexes Method for Roadway Layout below the Closed Residual Bearing Coal Pillar. *J. Mining Saf. Eng.* (03), 465–472.
- Tian, C., Yang, X., Sun, H., Liu, Y., and Hu, Q. (2019). Experimental Study on the Overburden Movement and Stress Evolution in Multi-Seam Mining with Residual Pillars. *Energ. Sci. Eng.* 7 (6), 3095–3110. doi:10.1002/ese3.482
- Wang, J. (2009). *Theory and Technology of Thick Coal Seam Mining*. Beijing: Metallurgical Industry Press. doi:10.3969/j.issn.2095-2783.2008.11.007

- Wang, J., and Zhong, S. (2008). The Present Status and the Key Issues to Be Resolved of Thick Seam Mining Technique in China. *Sci. paper Online* 3 (11), 829–834.
- Xu, Y. (2003). *Mining Science*. Xuzhou: China University of Mining and Technology Press.
- Xu, Z. (1979). *Elasticity*. Beijing: People's Education Press.
- Yue, X., Tu, M., and Li, Y. (2021). Calculation of Subsidiary Mining Stress in Floor Roadway under the Remaining Boundary Pillar of Close Coal Seam Mining. *J. Mining Saf. Eng.* 38 (02), 246–252+259. doi:10.13545/j.cnki.jmse.2019.0501
- Zhang, B. (2001). *High-Productive & High-Efficient Technologies of China's Coalmines*. Xuzhou: China University of Mining and Technology Press.
- Zhao, H., Cheng, H., and Ji, D. (2021b). Study of the Mechanism and Evolution Law of Unsymmetrical Failure of the Mining Roadway in Close Distance Coal Seam. *J. China Univ. Mining Tech.* 50 (06), 1029–1040+1050. doi:10.13247/j.cnki.jcumt.001342
- Zhao, H., Cheng, H., and Li, J. (2020). Study on Asymmetric Deformation Mechanism of Surrounding Rock of Roadway under the Effect of Isolated Coal Pillar. *Chin. J. Rock Mech. Eng.* 39 (S1), 2771–2784. doi:10.13722/j.cnki.jrme.2019.0934
- Zhao, H., Liu, Y., and Li, J. (2021a). Analysis of Damage Process and Zonal Failure Characteristics of Rock Mass under Floor of Isolated Coal Pillar. *J. China Univ. Mining Tech.* 50 (05), 963–974. doi:10.13247/j.cnki.jcumt.001329
- Conflict of Interest:** GZ was employed by the company Shanxi Yangcheng Shancheng Coal Industry Co., Ltd.
- The remaining authors declare that the research was conducted in the absence of any commercial or financial relationships that could be construed as a potential conflict of interest.
- Publisher's Note:** All claims expressed in this article are solely those of the authors and do not necessarily represent those of their affiliated organizations, or those of the publisher, the editors, and the reviewers. Any product that may be evaluated in this article, or claim that may be made by its manufacturer, is not guaranteed or endorsed by the publisher.
- Copyright © 2022 Wu, Yu, Zhao, Du, Lv and Zhang. This is an open-access article distributed under the terms of the Creative Commons Attribution License (CC BY). The use, distribution or reproduction in other forums is permitted, provided the original author(s) and the copyright owner(s) are credited and that the original publication in this journal is cited, in accordance with accepted academic practice. No use, distribution or reproduction is permitted which does not comply with these terms.



A New Repeated Mining Method With Preexisting Damage Zones Filled for Ultra-Thick Coal Seam Extraction – Case Study

Liang Chen^{1,2,3}, Dongsheng Zhang^{1,2}, Gangwei Fan^{1,2}, Shizhong Zhang^{1,2*}, Xufeng Wang^{1,2} and Wei Zhang^{1,2}

¹State Key Laboratory of Coal Resources and Safe Mining, China University of Mining and Technology, Xuzhou, China, ²School of Mines, China University of Mining and Technology, Xuzhou, China, ³Hubei Key Laboratory for Efficient Utilization and Agglomeration of Metallurgic Mineral Resources, Wuhan, China

OPEN ACCESS

Edited by:

Wei Liu,
Chongqing University, China

Reviewed by:

Huafu Qiu,
Xi'an University of Science and
Technology, China
Xuesheng Liu,
Shandong University of Science and
Technology, China

*Correspondence:

Shizhong Zhang
zhangshizhong@cumt.edu.cn

Specialty section:

This article was submitted to
Geohazards and Georisks,
a section of the journal
Frontiers in Earth Science

Received: 15 December 2021

Accepted: 04 February 2022

Published: 23 February 2022

Citation:

Chen L, Zhang D, Fan G, Zhang S,
Wang X and Zhang W (2022) A New
Repeated Mining Method With
Preexisting Damage Zones Filled for
Ultra-Thick Coal Seam Extraction –
Case Study.
Front. Earth Sci. 10:835867.
doi: 10.3389/feart.2022.835867

Arbitrary mining activities done by previous small-scale mines left many irregular damage zones in the ultra-thick coal seam, consequently leading to serious roof caving disasters and recovery ratio decline during repeated mining. Pre-filling the damage zones is an effective method to prevent mining-induced geological disasters. In this study, a novel method regarding damage zone filling-based repeated mining (FBRM) was proposed by combining the lower cutting layer (LCL) with the upper key bearing layer (UKBL) based on analyzing the disaster state when the workface passes through damage zones. To determine filling thickness, a method for calculating UKBL thickness was developed to preliminarily identify the filling thickness parameters of UKBL. On this basis, a numerical model incorporating damage zones and coal extractions was established to investigate the impact of UKBL thickness on fracture propagation and the maximum principal stress profiles around the damage zones. The proposed FBRM method was verified using the ground pressure data collected from Panel B909 of Pingshuo No.2 Colliery. The results show that 1) filling material with low strength and good cuttability is suitable for LCL, while material with high strength and robust bearing capacity is suitable for UKBL; 2) with increasing the UKBL filling thickness, the height of fracturing decreases, obeying a negative exponential function, suggesting a good effectiveness of the damage zone pre-filling technique; 3) as the UKBL filling thickness rises to 5 m, the maximum principal stress relocates from the area above both damage zones to the area closely in front of the workface, indicating a filling thickness threshold of 5 m that can ensure roof stability; 4) the maximum working resistance and bed separation were 11,800 kN and 26 mm, respectively, when the workface passed through damage zones B and E, favoring a good reliability of the FBRM method. The research can provide best-practice references for preventing roof caving disasters while exploiting the ultra-thick coal deposits affected by previous mining activities.

Keywords: ultra-thick coal seam, damage zones, filling-based repeated mining, lower cutting layer, key bearing layer

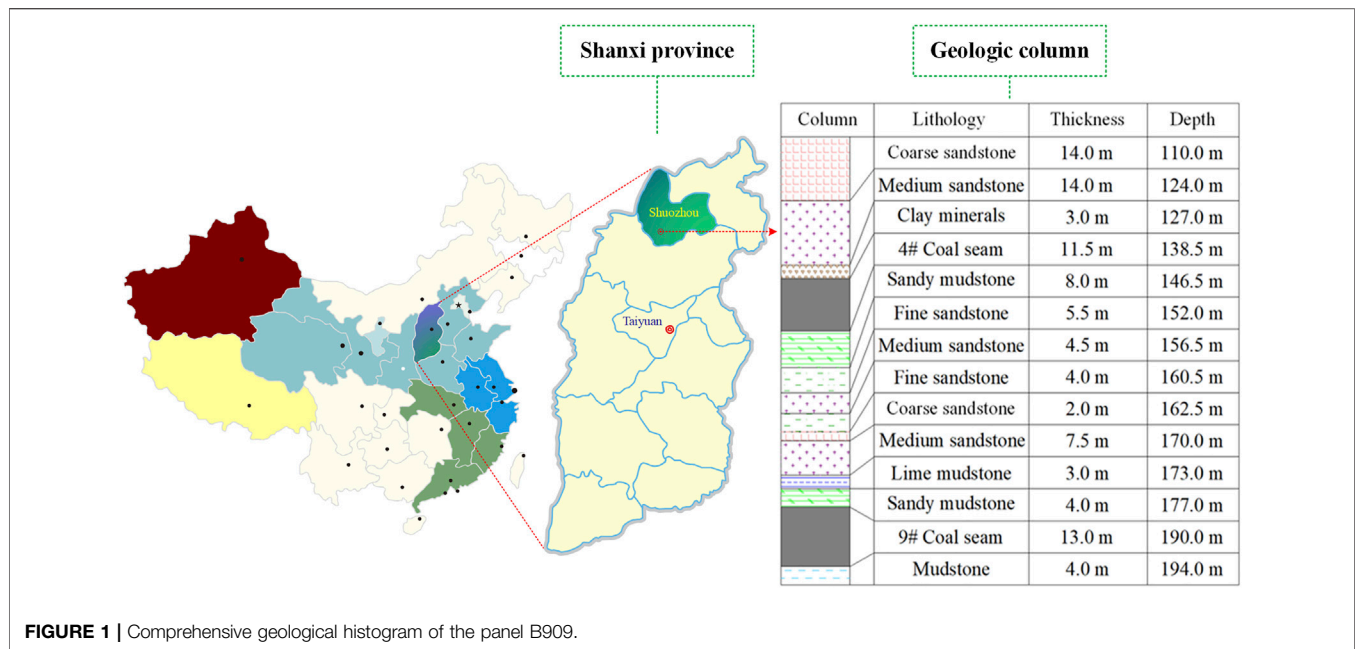
INTRODUCTION

Due to lacking advanced production facility and good management, in the 1980s, small-scale coal mines prevailed in several major coal mining areas of China, such as Shanxi and Inner Mongolia provinces. The methods employed for exploiting underground coal resources were backward and had many issues concerning arbitrary exploitation, disordered management, and low recovery ratios (Wu and Xu, 2012; Yujiang Zhang et al., 2016). In the last two decades, large-scale coal production enterprises started to incorporate small mines (Shi, 2013) to manage underground mining strategically. For example, more than 3,300 small-scale coal mines in Shanxi Province, China, were closed or merged in the 4 years from 2005 to 2009 (Wang and Weng, 2012). By deploying more advanced production equipment, the new mines operate fully mechanized longwall mining with working efficiency and recovery ratio higher than before. However, due to previous arbitrary mining activities and lacking engineering drawings for indicating the pre-existing mined-out areas, newly designed longwall panels sometimes enter irregular mining areas left by the former mines. The irregular mining areas, called damage zones, are generally some cavities with a certain aspect ratio, and there are some residual coals accumulated at the bottom of the damage zones. As the longwall face approaches damage zones, the localized ground stress changes dramatically due to coal body removal, leading to significant stress concentration in the panel roof and abutment. A series of issues such as roof caving and rib spalling arise and deteriorate mine production and safety conditions. The problem becomes more pronounced if there are extensive damage zones existing in ultra-thick coal deposits. Furthermore, when the damage zone is higher than the maximum working height of hydraulic chocks, the overlying fragmented rocks tend to collapse into the face, potentially threatening the safety of workers and facilities. In this circumstance, the hydraulic chock cannot closely touch the roof and provide sufficient supporting resistance, meaning that the chock itself and the armored face conveyor (AFC) pushed by chocks have to progress slowly. However, it is unreasonable to abandon the damage zones considering the high volume of residual coals thereof. On the other hand, discarding the damage zones means that the panel is shortened, and various equipment has to be moved to the next panel in a short duration, which is an unpractical operation potentially decreasing coal recovery ratios. In Pingshuo No. 2 Colliery, the damage zones existing in the Second District can cause more than 4.5 million tons of coals to be wasted if there is no appropriate treatment. Therefore, it is vital to develop a scientific and practical mining method for retrieving the coals. Existing mining experience shows that backfilling is an effective technique to improve the stress condition of damage zones, alleviate stress concentration in frontal and side abutments, and address the problem regarding hydraulic chocks not touching roof rocks. Therefore, investigating the mechanism and method of repeated mining with

preexisting damage zones filled is essential for ultra-thick coal seam extraction from safety and economy perspectives.

The backfilling technique has attracted extensive attention in the mining industry considering its advantages in controlling surface subsidence, decreasing rockburst risks, reducing gangue discharge, and protecting the localized hydrogeological environment (Chang et al., 2014; Edraki et al., 2014; Howladar and Karim, 2015; Jixiong Zhang et al., 2016; Hefni et al., 2021). The preliminary research mainly focused on developing backfilling materials and methods (Tapsiev et al., 2011; Seryakov, 2014; Deng et al., 2021). Mitchell et al. assessed the strength of filling materials regarding cemented classified tailings and sand using physical simulation (Mitchell et al., 2011). By numerical simulation and lab tests, respectively, Helinski and Zhang et al. studied the mechanical property of cemented tailing-based filling materials with variation in the cement-to-sand ratio, curing age, and consolidation (Helinski et al., 2010; Sasa et al., 2019). Benzaazoua and Nujaim et al. revealed that acid water and sulphate can degrade the cementing property of composite materials and decrease the strength and durability of the backfilling body (Benzaazoua et al., 2002; Nujaim et al., 2020). It was recognized that the size of gangue particles, mineral compositions, and cementing agents can affect the porosity, concreteness, and compressive strength of cemented paste backfills (Benzaazoua et al., 2004; Sivakugan et al., 2015; Walske et al., 2016; Xu et al., 2018; Li et al., 2020).

For the backfilling mining method, Ma et al. established a mechanical model incorporating the coal pillar in mined-out areas coupled with the roof backfilling. Based on this, the principles for calculating roof deflection and pillar compressibility were obtained to provide theoretical guidance for backfilling-based room-and-pillar mining (Ma et al., 2011). Kostecki and Spearing proposed the high-density backfilling method for room-and-pillar mining and analyzed how the shear strength, tensile strength, and stiffness of the filling body affect pillar strength and the bearing capacity of the lithologically soft floor (Kostecki and Spearing, 2015). By combining the advantages of backfilling-based longwall mining and room-and-pillar mining methods, Yu et al. put forward the concept of continuous mining and backfilling with a wall system (Yu et al., 2019). Zhou et al. analyzed the impact of solid backfill ratio on the movement and deformation behavior of overlying strata and the frontal abutment pressure through physical simulation (Zhou et al., 2017). Zhang et al. established a shortwall block mining method to collect coal residuals such as pillars and boundaries (Zhang et al., 2018). The previous research has performed extensive theoretical analysis and engineering practice in terms of the physical and mechanical properties of filling materials and backfilling mining technology, to some extent providing references for this study. One characteristic of these previous cases is that the backfilling operation was conducted following longwall face advancement. However, in the case of this study, the filling operation should be performed before longwall mining for addressing the damage zones left by the previous mining activities. In



addition, the uncertain position and unregular profile of damage zones enhance the difficulty and complexity of repeated mining whether or not to fill the damaged zones.

With Panel B909 of Pingshuo No.2 Colliery as the case, this study first analyzed the geological condition of damage zones existing in ultra-thick coal seams due to the previous arbitrary mining activities. Then a new damage zone filling-based repeated mining (FBRM) method was first proposed by combining the lower cutting layer (LCL) with the upper key bearing layer (UKBL) based on the disaster analysis of the working face approaching damage zones. Furthermore, a new calculation method of UKBL thickness was given and used to preliminarily determine the filling thickness parameters of UKBL. Moreover, the numerical calculation model of the over-irregular damage zone was established to investigate the influence of UKBL filling thickness on crack propagation and maximum principal stress distribution around irregular damage zones. Finally, the FBRM method was performed in Panel B909 of Pingshuo No. 2 Colliery, and ground pressure data were also monitored. The research studies can provide a new idea for preventing roof caving and retrieving the coals left by the previous mining activities.

GEOLOGICAL AND ENGINEERING CONDITIONS

As shown in **Figure 1**, Pingshuo No. 2 Colliery is located in the north of Shanxi province in China. The depth and dip angle of Panel B909 are 190.0 m on average and 2.5°, respectively. The coal seam thickness is about 13.0 m. The Panel operates the top coal caving mining method, with a width and length of 282.0 and 1,590.0 m, respectively. The height of cutting is 3.5 m, with the above 9.5-m-thick coals technically caved. The ratio of coal

recovery is about 85%. The longwall workface is shielded by hydraulic chocks (ZFY12000/23/40D) that are 1.8 m in width and 12,000 kN in the maximum working resistance. No. 4 Coalbed is above Panel B909, whose average thickness is 11.5 m. The comprehensive geological histogram of panel B909 is exhibited in **Figure 1**.

Pingshuo No. 2 Colliery incorporates several preexisting small mines, making it possible for the current longwall workface to be affected by the previous mining activities. These small-scale mines used tunneling to cave coals, leaving many damage zones in Panel B909 area. Also, due to lacking engineering drawings for explicitly indicating the location and geology of damage zones, it is challenging to conduct ultra-thick coal seam mining smoothly. Transient electromagnetic methods and advanced detection were employed to capture the spatial position and dimension of these damage zones. Field observation identified seven damage zones within the designated area of Panel B909, labeled A to G in **Figures 2A,B**. The seven damage zones cover 173.0 m along the longitudinal direction (longwall retreating direction) and 175.0 m along the transverse direction. The distance between these damage zones and the set-up position of Panel B909 is about 410.0 m.

Field detection details show that all the damage zones are of semi-ellipsoidal profiles but different in the maximum height, dimension, and volume of residual coals. According to the geological conditions, the seven damage zones can be divided into three categories, including ① the case without residual coals in damage zones, ② the case where residual coals are thinner than the cutting height, and ③ the case where residual coals are thicker than the cutting height.

Taking damage zones B and E as examples, *via* the peak of both damage zones, a longitudinal section is made and labeled I-I in **Figure 2A**. It can be seen from **Figure 2** that both damage

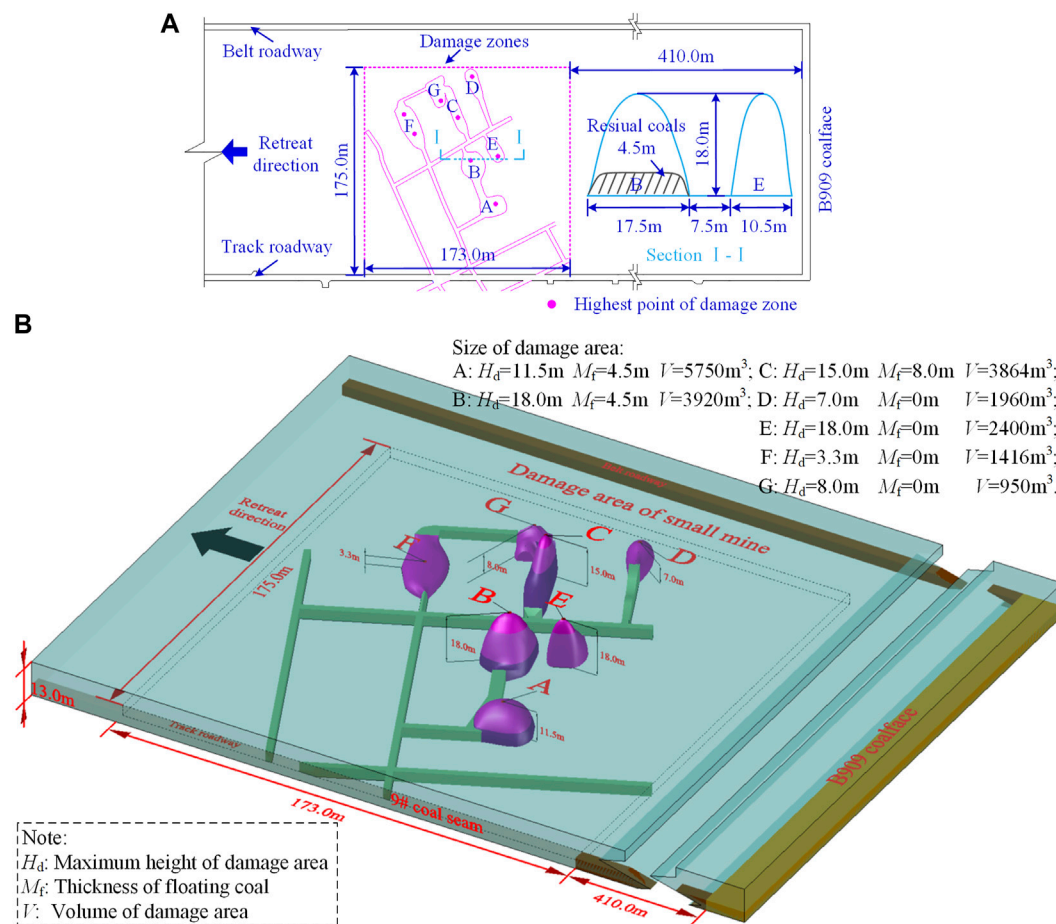


FIGURE 2 | Position of seven damage zones with respect to Panel B909: **(A)** planform; **(B)** three-dimensional stereogram.

zones are of a semi-ellipsoidal profile, and the maximum height of both reaches 18.0 m. There are 4.5-m-thick coals left in damage zone B but none in damage zone E. The characteristic parameters of the seven damage zones are shown in **Figure 2B**.

MECHANISM AND METHOD

FBRM Mechanism

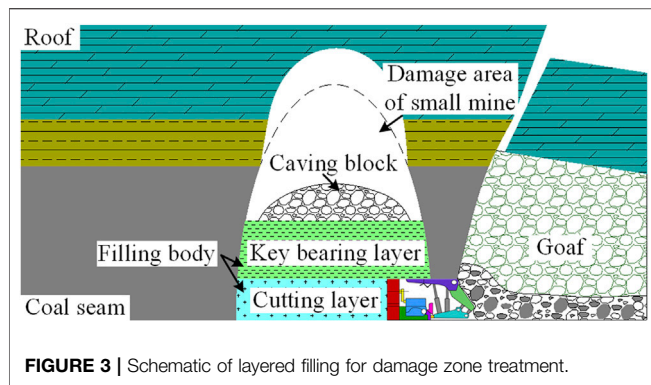
The damage zones left by the previous small-scale mining activities can delay the routine work of newly scheduled longwall panels. If there are no pre-mining treatments, the damage zones are likely to connect the longwall face and lead to a series of mine hazards, which mainly include the following two aspects.

- 1) Hydraulic chocks are directly exposed to a high volume of fragmented rocks and are thus less capable of ensuring the safety of workers passing through the face. Within the area that is 20–60 m ahead of the face, hydraulic chocks provide substandard resistance against roof loads, slowing the

advancement of the chock itself and the AFC pushed by chocks.

- 2) As they are filled with fragmented rocks, the damage zones are structurally unstable and prone to collapse due to the mining effect. The caved rocks shock mining equipment and impact their routine operation. Backfilling treatment is an effective tool in optimizing stress distribution and consolidating cracked rock masses in damage zones. Therefore, the damage zones can be filled in advance so that the intact coal body and the coals left by the previous mining activities can be extracted safely.

The coal mining in Panel B909 is expected to achieve the following targets. First, the filling thickness should be greater than the cutting height, and a particular part of the filling body should maintain above hydraulic chocks during cutting. The remaining layer allows hydraulic chocks to receive sufficient reactive force to push AFC forward and protect underlying facilities from caved materials. Second, the lower part of the filling body can be peeled off easily by the shearer so that the cutter teeth can be saved from wear and tear to a great extent.



According to the above analysis, this study proposes the FBRM method, whose essence is that the filling into preexisting damage zones should be performed before longwall panel extraction. The filling materials should not only satisfy the above targets but also consider filling expenditures. For acquiring a robust bearing capacity for the upper layer and satisfactory cuttability for the lower layer, different kinds of functional materials are expected to strengthen the two parts. Material with low strength and good cuttability applies to the lower part, namely, cutting layer filling. In contrast, high strength and strong bearing capacity material is used for the upper part to form a key bearing layer. The layered filling scenario is schematically exhibited in **Figure 3**.

Critical Procedures for FBRM Method

According to the FBRM mechanism, the procedure for the layered filling of damage zones is designed as follows:

- 1) Conduct precise detection towards the damage zone. The transient electromagnetic method, three-dimensional earthquake, and channel waves can capture key geological parameters, including spatial position, dimension, height, and thickness of residual coals.
- 2) Apply different filling materials to different layers. The material selection should be according to the designed function of the LCL and UKBL, as analyzed in **Section 3.1**.
- 3) Determine the filling thickness of the LCL. Specific filling parameters must be determined according to the relationship between maximum height of damage area (H_d) and cutting

height of shearer (H_s). The determination method of filling thickness of the LCL is shown in **Table 1**.

- 4) Determine the filling thickness of the UKBL. It should consider the filling material property and rock caving impact and ensure that the UKBL remains intact during mining. The theoretical determination method of the thickness of the UKBL is shown in **Table 1**.
- 5) Perform *in situ* industrial tests, through which the material and filling thickness of the LCL and UKBL can be evaluated by monitoring roadway deformation and hydraulic chock reaction.

The critical procedures of the FBRM method are shown in **Figure 4**.

THEORETICAL ANALYSIS OF THE UKBL FILLING THICKNESS

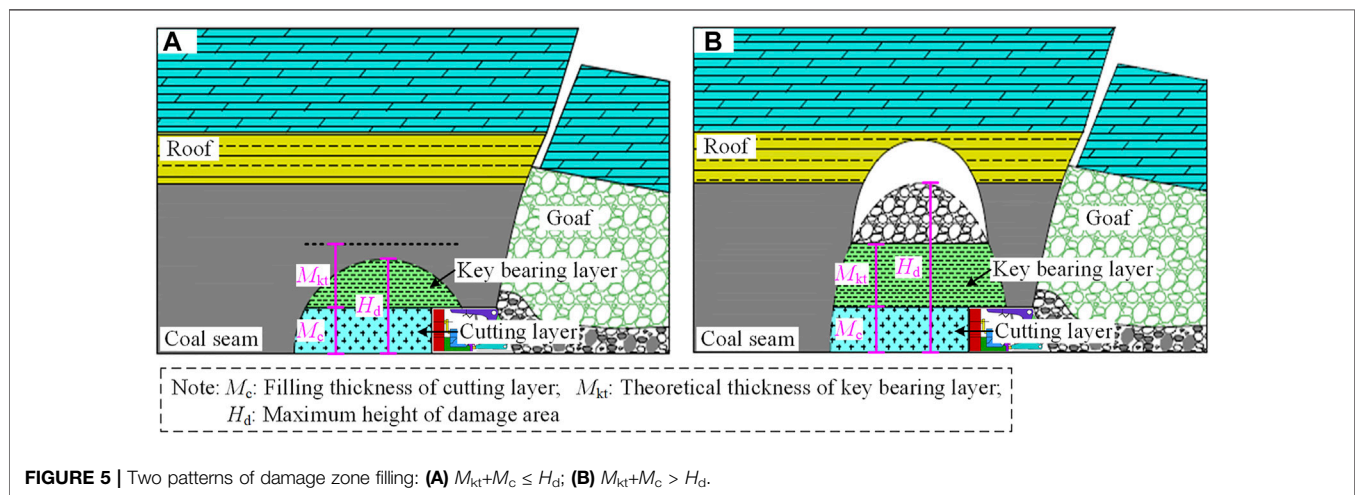
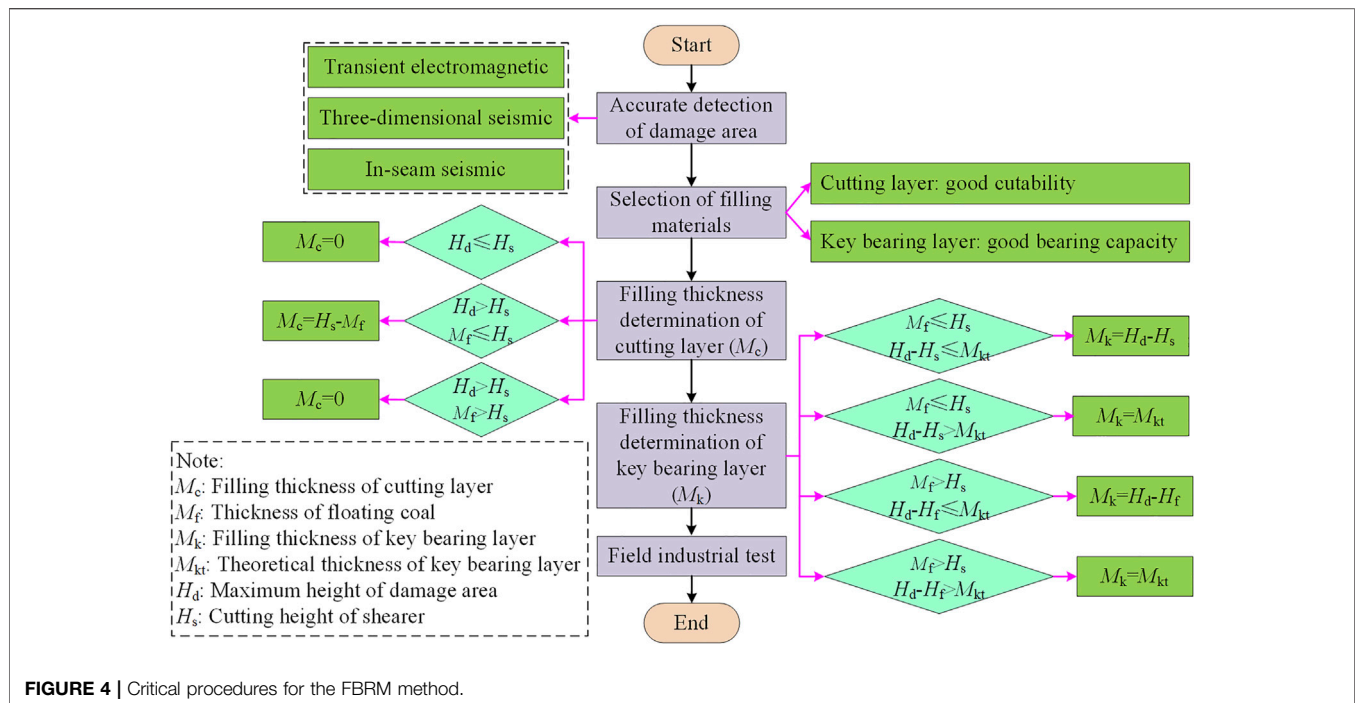
As described in **section 3.2**, the filling thickness determination of the UKBL was the most important step in the FBRM method. The theoretical solution of the filling thickness of the UKBL can be obtained *via* the mechanical balance principle. The theoretical solution can provide a preliminary reference for the final determination of the filling thickness of the UKBL. Based on this theoretical solution, a numerical model representing the FBRM mechanism is established to acquire the optimal solution of the filling thickness.

The above analysis indicates two circumstances regarding the pre-mining filling of the UKBL when the LCL thickness is fixed. The first circumstance refers to a situation where the distance from the maximum damage height to the filling thickness of the LCL is no greater than the theoretical filling thickness of the UKBL. The area to be cut or the damaged area above residual coals are filled to consolidate fragmented rocks and keep mining safe, as shown in **Figure 5A**. **Figure 5B** describes another circumstance where the aforementioned distance is greater than the theoretical filling thickness of the UKBL. In this case, there is an unfilled void existing above, and mining-induced coal/rock caving impacts the underlying rock units and deteriorates the stability of the UKBL. The scenario in **Figure 5B** is taken as an example to calculate the filling thickness of the UKBL.

TABLE 1 | Determination method of thickness of the cutting layer and key bearing layer.

Cutting layer	Determinant condition	Hd ≤ Hs		Hd > Hs	
				Mf ≤ Hs	Mf > Hs
	Filling thickness of the cutting layer (m)	0		Hs-Mf	0
Key bearing layer	Determinant condition	Mf ≤ Hs		Mf > Hs	
		Hd-Hs ≤ Mkt	Hd-Hs > Mkt	Hd-Hf ≤ Mkt	Hd-Hf > Mkt
	Filling thickness of the key bearing layer (m)	Hd-Hs	Mkt	Hs-Hf	Mkt

H_d , Maximum height of damage area; H_s , Cutting height of shearer; M_f , Thickness of floating coal; M_{kt} , Theoretical thickness of key bearing layer.



According to the designed longwall operation, two to three hydraulic chocks move together following the shearer, as shown in the close-up view of **Figure 6**. This operation inevitably causes a particular area of the roof to be suspended, that is, a rectangular support lagging area. As a result, the rocks caving from the top of the support lagging area can directly stress the UKBL and lead to cracking and failure.

It is assumed that the theoretical filling thickness of the UKBL is M_{kt} , the maximum height of a failure zone is H_d , and the filling thickness of the LCL is M_c . The maximum caving height H of failure zones can be expressed as follows:

$$H = H_d - (M_{kt} + M_c) \quad (1)$$

The total width of the hydraulic chocks that are delayed in moving is a , and the distance from the delayed chocks to the frontal rib is l . The maximum shock load of overlying rocks caving onto the UKBL is as follows:

$$F = K_d (a \times l \times H) \rho g \quad (2)$$

where K_d refers to the dynamic factor and equals $1 + \sqrt{1 + 2H/\Delta}$ in free fall condition, Δ is vertical deformation of the UKBL and ranges from 0.8 to 1.0, ρ is density of caving rocks, and g is gravitational acceleration.

Assuming that the UKBL within the support lagging area fails in shear effect, the shear stress of the UKBL is as follows:

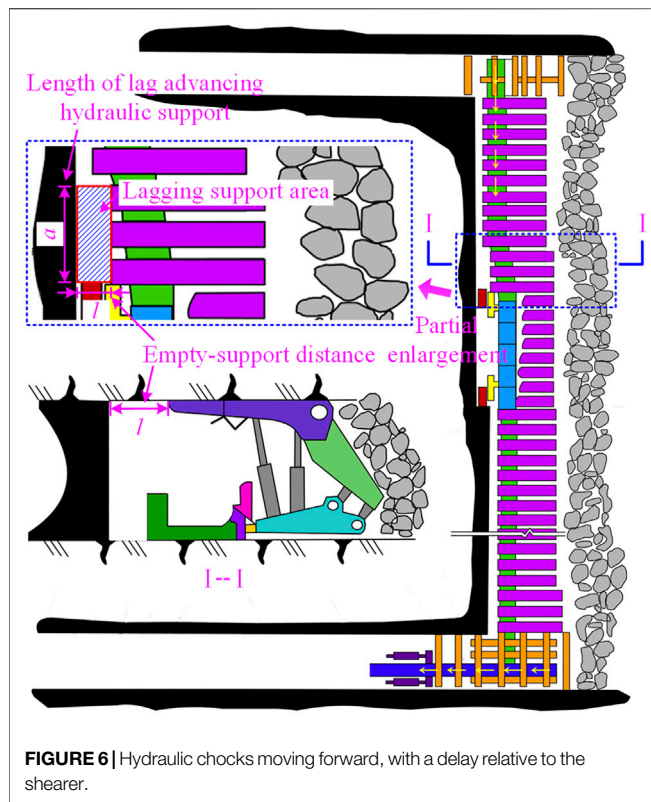


FIGURE 6 | Hydraulic chocks moving forward, with a delay relative to the shearer.

$$\tau = \frac{F}{2M_{kt}(l+a)} \quad (3)$$

In line with Tresca failure criterion (Inoue, 1996; Cai and Wang, 2018), we have the following:

$$2\tau = \sigma_s \quad (4)$$

where σ_s refers to the tensile strength of the filling material of the UKBL.

By incorporating Eqs 1–4, the filling thickness of the UKBL is as follows:

$$\begin{cases} M_{kt} = \frac{(1 + \sqrt{1 + 2H/\Delta})(a \times l \times H)\rho g}{\sigma_s(a+l)} \\ H = H_d - (M_{kt} + M_c) \end{cases} \quad (5)$$

For the UKBL, the filling body is anticipated to bear plastic deformation to alleviate the impact of rock caving on hydraulic chocks. The Remy filling materials from Minova International can meet the requirements mentioned above and generate microbubbles. Hence, two various Remy materials were used to fill the LCL (Label No. 2) and UKBL (Label No. 1). The two materials No. 1 and No. 2 are 1,250 kg/m³ and 600 kg/m³ in density, 1.6 and 1.9 GPa in elastic modulus, and 4.0 and 1.5 MPa in UCS, respectively.

By combining Panel B909 parameters and filling material properties to Eq. 5, the theoretical solution of the filling thickness of the UKBL is determined. Relevant numerical parameters are listed in Table 2, among which the maximum damage height is chosen from all damage zones.

TABLE 2 | Parameters for calculating the filling thickness of the key bearing layer.

Parameter	Value	Parameter	Value	Parameter	Value
H_d	18.0 m	L	1.2 m	g	9.8 N/kg
M_c	3.5 m	Δ	0.4–0.6	σ_s	0.38 MPa
a	5.4 m	ρ	2,500 kg/m ³	—	—

Applying the parameters in Table 2 to Eq. 5, it is found that the filling thickness of the UKBL (M_{kt}) equals 4.40–4.88 m.

NUMERICAL SIMULATION OF THE UKBL FILLING THICKNESS

A numerical model of the over-irregular damage zone was established to determine the optimal filling thickness of the UKBL by comparing mining-induced fracture propagation and maximum principal stress level. The software adopted is Universal Distinct Element Code (UDEC).

Model Construction and Calibration

Numerical modeling has been extensively applied to address geotechnical issues regarding underground mining, tunneling, and slope movement, requiring an indispensable procedure that parameters for mechanical computation should be calibrated using actual data (Zhang et al., 2021a; 2021b). Existing studies show that uniaxial compression and Brazilian splitting tests are two frequently used methods to verify the property of the rock matrix and joints (Bai et al., 2016; Zhu et al., 2020). The modeled samples subjected to uniaxial compression and Brazilian splitting are exhibited in Figure 7A. The uniaxial compression test uses samples 100 mm in length and 50 mm in diameter, while the Brazilian splitting test uses samples 50 mm in diameter. In constitutive settings, both loading ends are rigid, and the rock matrix and joints are assigned as the elastic and residual strength models, respectively. The loading process is controlled via the rate. More detailed procedures are described in the studies by Singh and Rao (2005) and Kazerani and Zhao (2010). Take the 7.5-m-thick medium sandstone unit (shown in Figure 1) as an example; the simulated compression and tension on samples cored from this layer are exhibited in Figures 7B,C, accompanied by laboratory test results for comparison. The sample failure pattern and stress-strain curve indicate that the calibrated model has a good agreement with laboratory tests, possessing an error of 1.82% in uniaxial compressive strength and 0.32% in tensile strength with respect to the actual experimental data. The results indicate that various physical and mechanical parameters for the 7.5-m-thick medium sandstone stratum have been reliably calibrated. Similarly, numerical models for other rock units are also verified, and the parameters after calibration are summarized in Table 3.

A large-scale model is then constructed with the geology of Panel B909 as the background, in which the calibrated physical and mechanical parameters are assigned to the corresponding rock units. Field measurement shows that the damage zone reaches its maximum height (18.0 m) in zones B and E. Damage zones B and E are close to each other and located almost along the longitudinal direction (longwall retreating direction), as shown in Figure 2. It

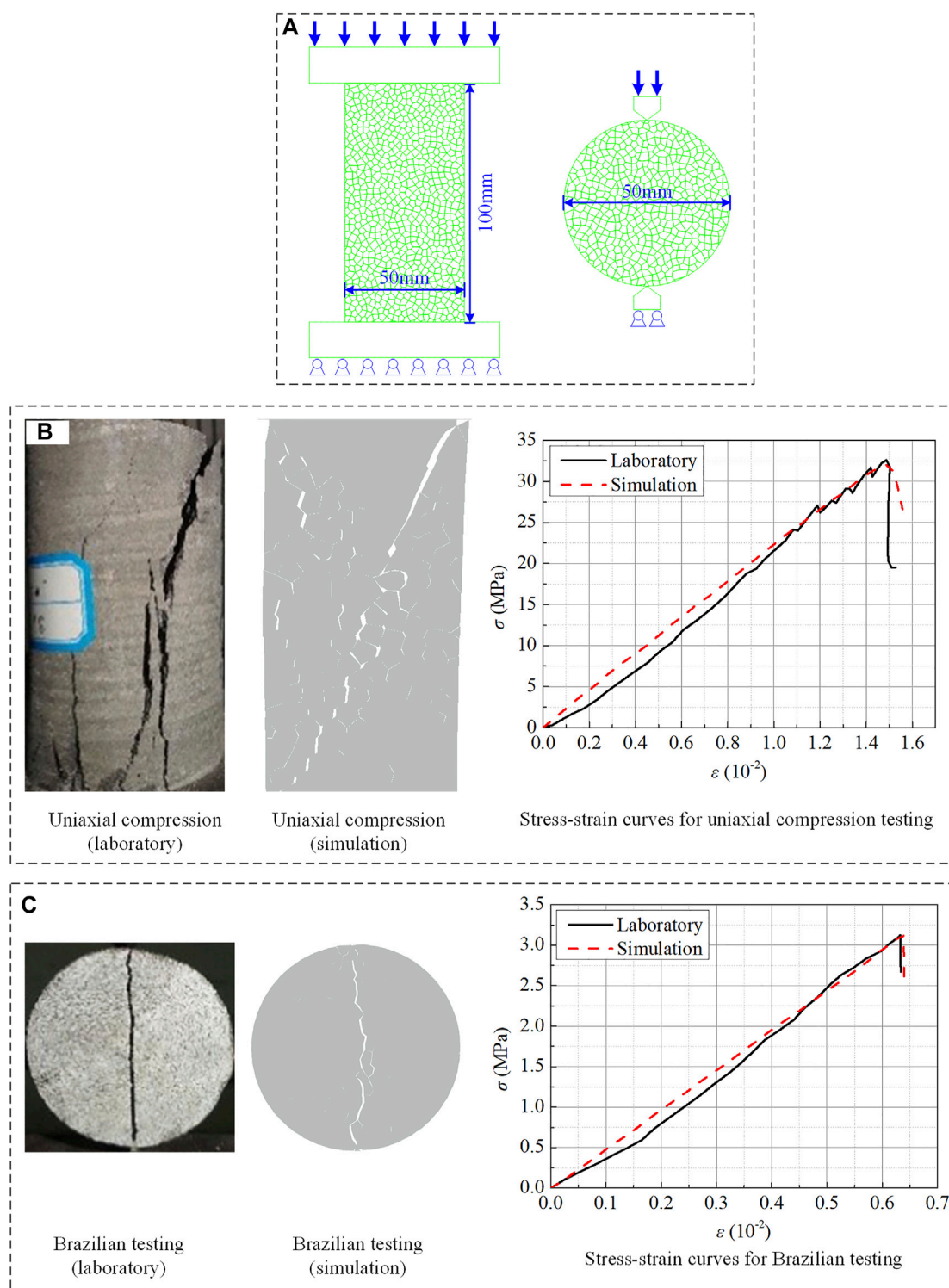


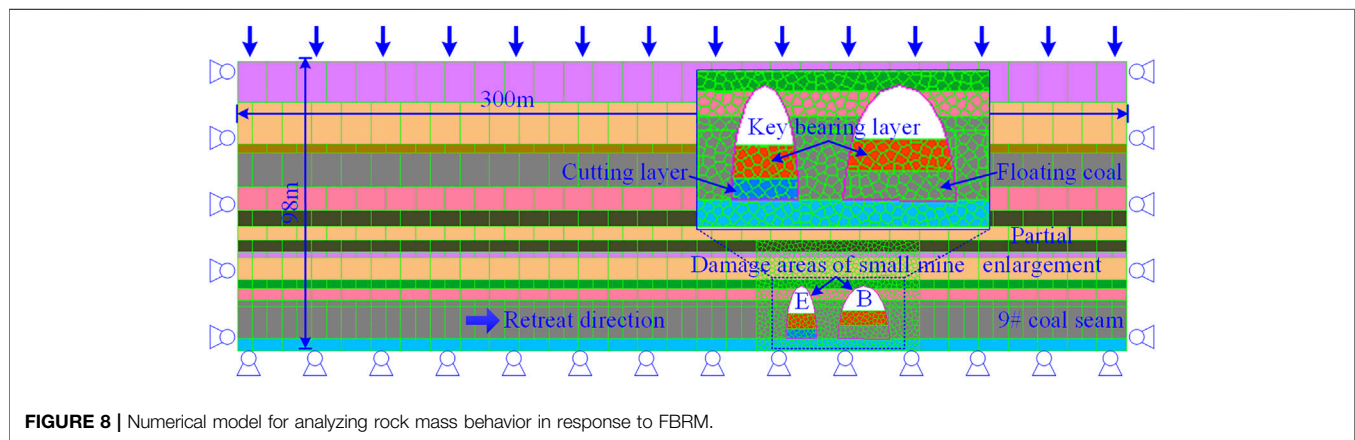
FIGURE 7 | Construction and calibration of numerical modeling: **(A)** model construction; **(B)** comparison of uniaxial compression; **(C)** comparison of Brazilian splitting.

can be extrapolated that, as the longwall face progresses, the strata above zones B and E experience more drastic impacts than other zones. Therefore, the large-scale model considers the case where

the longwall face successively passes through zones E and B. **Figure 8** shows the model incorporating a longwall panel, the overlying strata, and damage zones E and B.

TABLE 3 | Numerical simulation calculation parameters.

Lithology	Unit weight (kg/m ³)	Elastic modulus (MPa)	Poisson's ratio	Cohesion (MPa)	Friction angle (°)	Tensile strength (MPa)
Coarse sandstone	2,350	3,000	0.34	2.8	38	1.14
Medium sandstone	2,400	3,100	0.33	2.9	39	1.59
Clay minerals	2,355	2,015	0.23	0.5	40	0.65
No. 4 coal	1,440	1,300	0.38	1.6	36	0.30
Sandy mudstone	2,360	2,050	0.24	0.5	39	1.10
Fine sandstone	2,400	2,500	0.33	3.2	40	1.72
Medium sandstone	2,380	2,300	0.32	3.1	40	1.61
Fine sandstone	2,400	2,500	0.33	3.2	40	1.73
Coarse sandstone	2,350	3,000	0.34	2.8	38	1.28
Medium sandstone	2,600	2,800	0.32	5.0	38	1.65
Lime mudstone	2,300	2,000	0.25	0.4	38	0.48
Sandy mudstone	2,360	2,050	0.24	0.5	39	1.10
No. 9 coal	1,330	1,200	0.36	1.6	39	0.30
Mudstone	2,300	2,000	0.25	0.4	38	0.84
Key bearing layer	1,250	1,600	0.33	2.4	40	1.21
Cutting layer	600	1,900	0.29	2.2	38	0.94
Residual coals	980	860	0.44	0.1	36	0.02

**FIGURE 8** | Numerical model for analyzing rock mass behavior in response to FBRM.

The geo-mechanical model is 300 m in length and 98 m in height, with the 50-m-long coal body kept unmined for boundaries on both sides. The model is fixed along both sides and the bottom edge *via* zero velocity, and the top surface is treated as a stress boundary bearing vertical stress of 2.4 MPa. The ratio of horizontal stress to vertical stress is 1.2 throughout the whole profile. Phased excavation is used for simulating actual longwall work, for which the excavation command is executed per 5 m. According to the theoretical filling thickness calculated in **Section 4**, four scenarios are designed where the filling thickness of the key bearing ranges from 3 to 6 m. Besides, Voronoi meshing is adopted to densify the joints around the two damage zones for detailing rock mass deformation and caving behavior, as shown in **Figure 8**.

Result Analysis

Figure 9 shows four fracture propagation scenarios where the longwall工作面 is 5 m away from the damage zone E, with

filling thickness ranging from 3 to 6 m, as exhibited in **Figures 9A–D**, respectively. **Figure 10** suggests that peak positions of the maximum principal stress are varied under different filling thicknesses of the UKBL.

The comparison between **Figures 9A–D** indicates that fracture density gradually decreases with increasing filling thickness of the UKBL. When a 3-m-thick area is filled, as shown in **Figure 9A**, the fractures are extremely dense around the damage zone, and the UKBL in both damage zones lose bearing capacity due to extensive fracturing. Simultaneously, pronounced rock caving occurs along the roof of both damage zones, shocking the underlying key bearing stratum. As the thickness of filling enlarges to 4 m, fractures about damage zones become slightly sparse, especially within the UKBL of damage zone B. The roof of damage zone E cracks but keeps its position, and roof rock cracking and caving are also relieved to some extent, as shown in **Figure 9B**. With filling thickness further increased to 5 m, fractures become lesser in the UKBL of

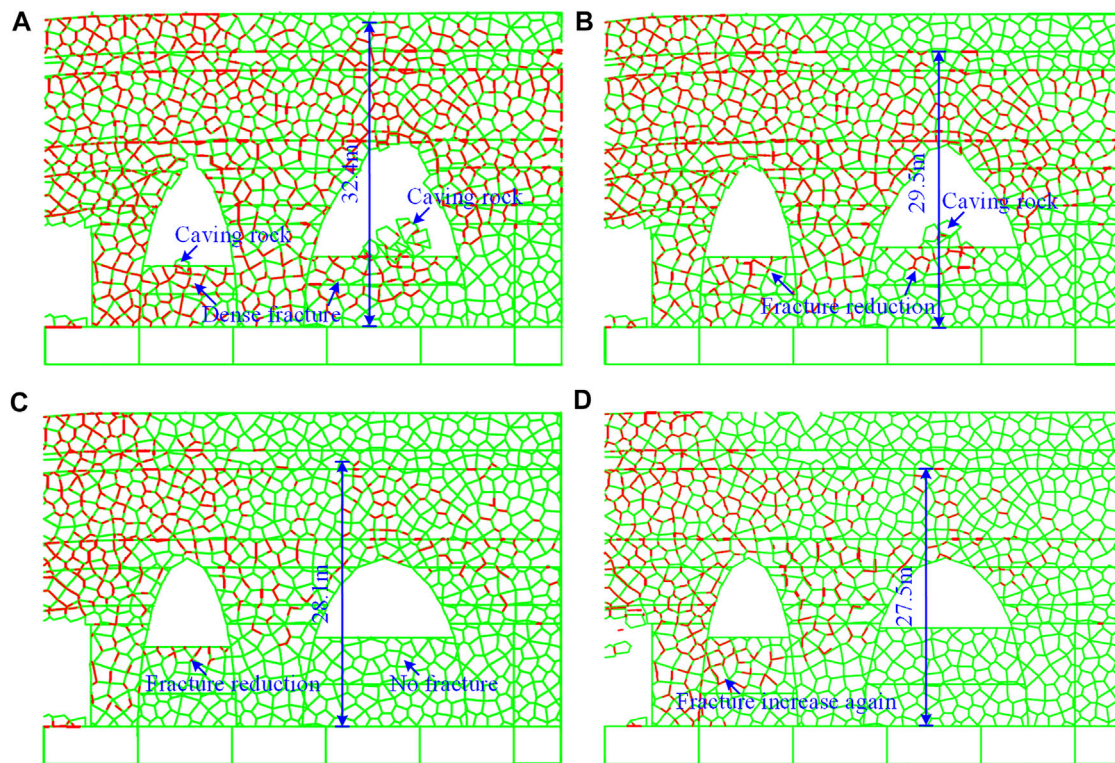


FIGURE 9 | Fracture propagation profile: (A) 3 m; (B) 4 m; (C) 5 m; (D) 6 m.

damage zone E and fade away in damage zone B, and roof rocks remain uncaved in both damage zones, as shown in **Figure 9C**. **Figure 9D** shows that when a 6-m-thick area is filled, there is an increase in fracture population, especially within the UKBL of damage zone E, characterizing an increasing trend contrary to previous scenarios. Quantitatively, the distance between the top of continuous fracturing and the coal seam floor exponentially decreases with filling thickness enlarged; the height of fracturing above damage zone B declines from 32.4 to 28.1 m with filling thickness increased from 3 to 5 m. However, the decrease becomes slight if the filling thickness is further enlarged. The relationship between the height of fracturing and filling thickness is depicted in **Figure 11**.

From **Figure 10**, when the filling thickness is no greater than 4 m, the maximum principal stress reaches its peak value in the area above the pillar between damage zones E and B and forms significant stress concentration, as shown in **Figures 10A,B**. It can be understood by combing **Figures 9A,B** that in both filling thicknesses, around damage zones E and B, the fractures drastically propagate, degrading the bearing capacity of surrounding rock masses and causing the peak stress to be transferred to a deep position. When a 5-m-thick area is filled, the maximum principal stress peaks in the frontal abutment, suggesting an adequate bearing capacity of the UKBL, as shown in **Figure 10C**. In the case of 6-m filling thickness, **Figure 10D** shows that stress

concentration occurs in front of the workface and along the roof of damage zone E. The maximum principal stress shows a decrease-increase trend with filling thickness enlarged, as depicted in **Figure 11**.

The above analysis indicates that when the filling thickness is 5 m, the UKBL slightly cracks, and rock masses surrounding damage zones E and B remain stable. The maximum principal stress reaches the lowest level by adopting this filling thickness, and the UKBL shows good bearing capacity. Therefore, the optimal filling thickness of the UKBL is 5 m.

IN SITU TESTING

To verify the proposed FBRM method and appropriateness of technical parameters, *in situ* industrial tests were performed in Panel B909. Before longwall mining, each damage zone was treated with layered filling *via* grouting holes from belt and track roadways. Four monitoring points were placed along both roadways and corresponding to the top caving position of damage zones B and E for recording bedding plane separation, as shown in **Figure 12A**. The deep and shallow ends of the monitoring instrument were fixed to the middle of the overlying medium sandstone unit (basic roof) and sandy mudstone unit (immediate roof). In addition, the working resistance of the No. 54 hydraulic chock was continuously recorded to reflect roof pressure

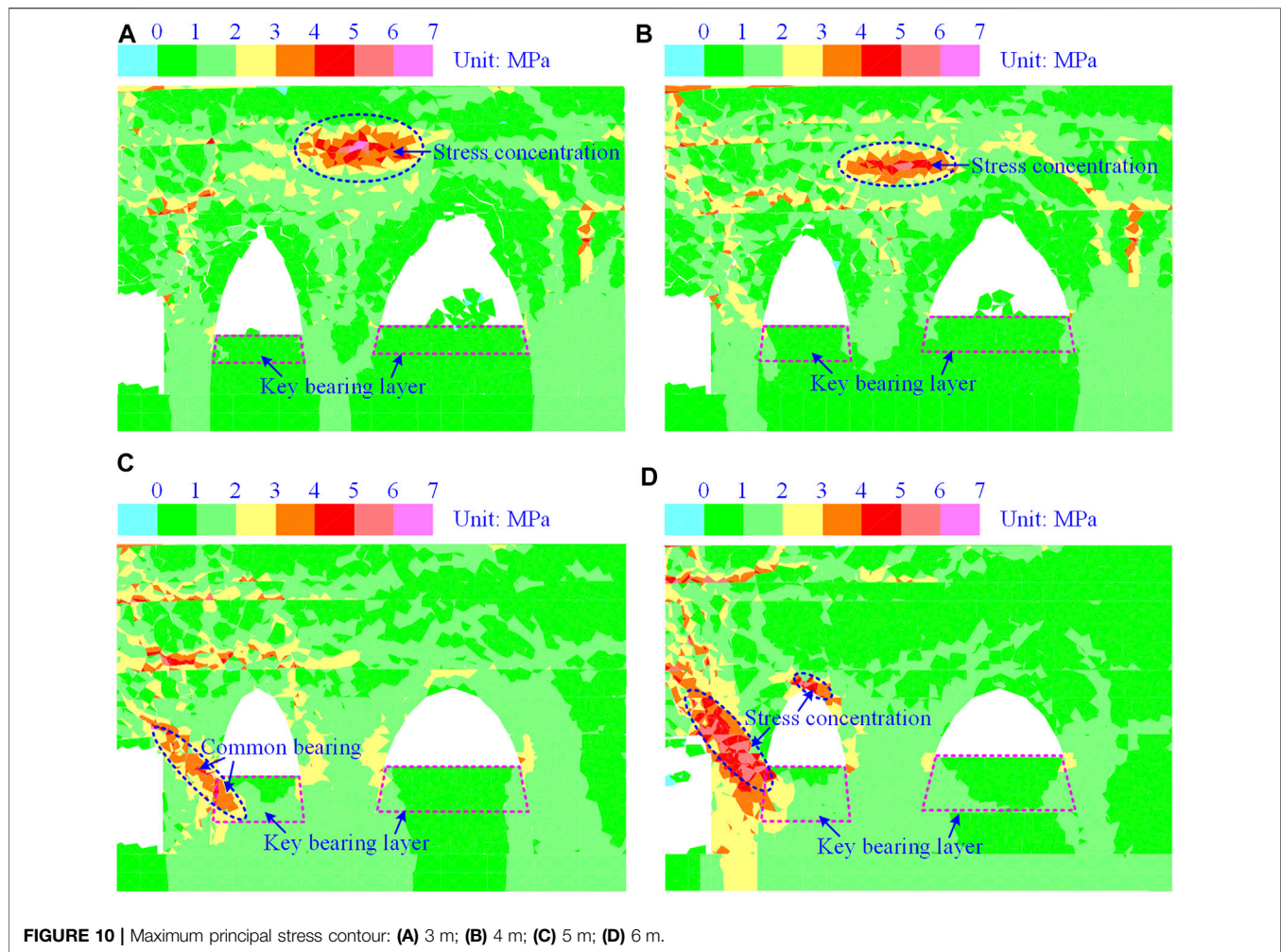


FIGURE 10 | Maximum principal stress contour: (A) 3 m; (B) 4 m; (C) 5 m; (D) 6 m.

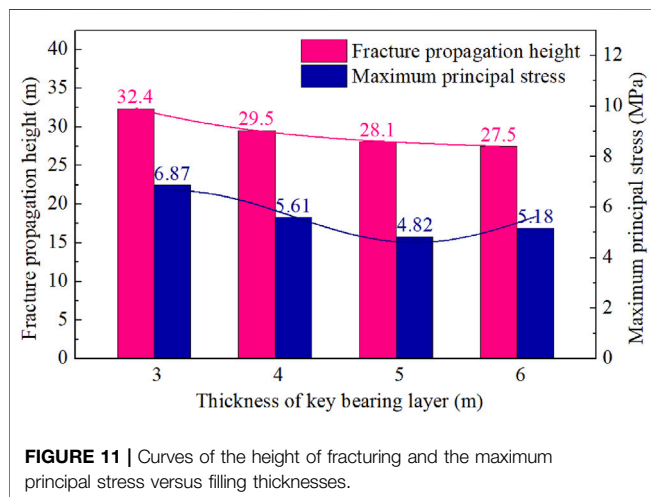


FIGURE 11 | Curves of the height of fracturing and the maximum principal stress versus filling thicknesses.

response to the filling-based longwall mining. **Figures 12B,C** show the records of bedding plane separation and resistance of hydraulic chocks.

Figure 12B shows that with the workplace approaching, bedding plane separation experienced a general increase-decrease trend. The separation phenomenon started to occur as the workplace was 40 m away from monitoring points. No. 4 point recorded the maximum separation level reaching 26 mm, reflecting the stability and slight deformation of the roadway. **Figure 12C** shows that when the working face passed through damage zones E and B, the maximum working resistance was 11,800 kN, still lower than the rated level (12,000 kN). The working resistance started to increase as the face was 25 m away from damage zone E, dramatically decreased to 9,100 kN as the coalface entered damage zone E, and then increased again beneath the pillar between damage zones E and B. Similar fluctuation of working resistance repeated when the workplace walked through damage zone B. The average working resistance of No. 52 hydraulic chock was 10,400 kN, reflecting a steady state throughout the repeated mining process. Also, roof caving and hydraulic chock failure did not occur. It means that the FBRM method developed in this study and the corresponding filling parameters are reasonable and reliable.

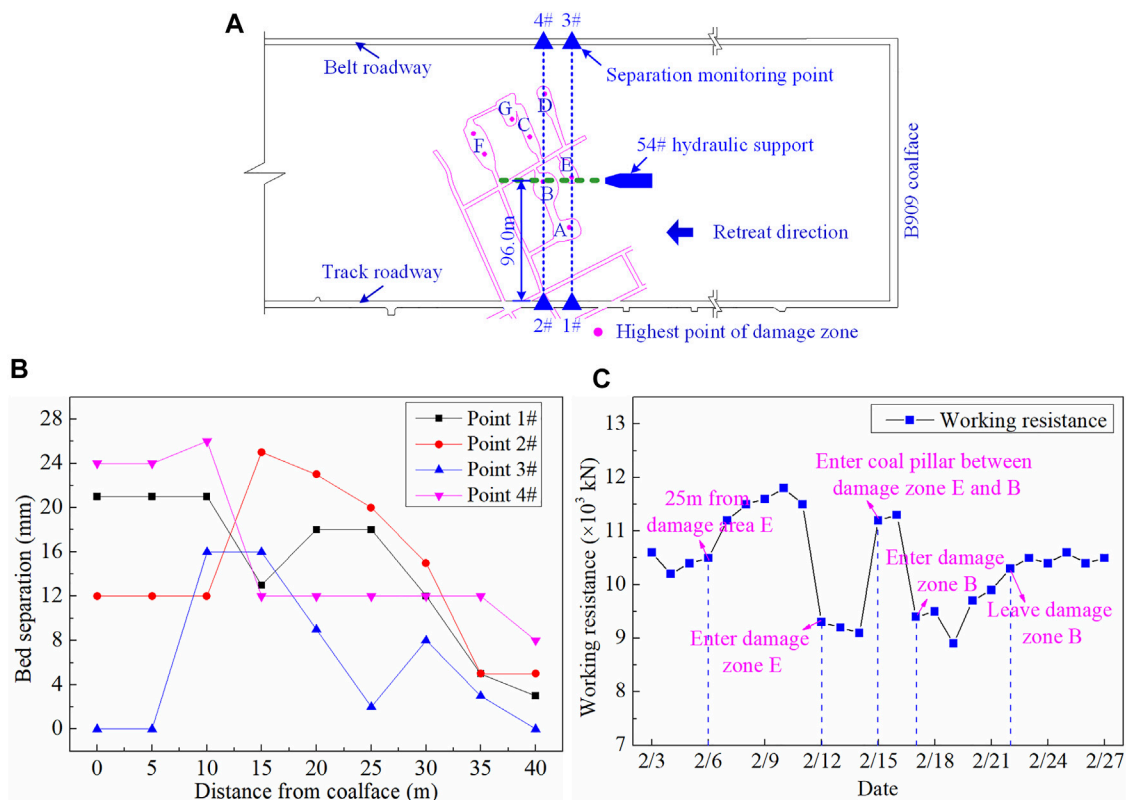


FIGURE 12 | Location of monitoring points and field measurement results: **(A)** location of monitoring points relative to Panel B909; **(B)** bedding plane separation; **(C)** working resistance of hydraulic chocks.

CONCLUSION

Pre-filling the irregular damage zone is an effective method for preventing roof caving disasters and improving the recovery ratio of ultra-thick coal deposits. Taking Panel B909 of Pingshuo No. 2 Colliery as the case, this study proposed a damage zone filling-based repeated mining method and detailed its procedures. A novel calculation method was developed to preliminarily determine the filling thickness of UKBL. By establishing a numerical model incorporating over-irregular damage zones and longwall mining, fracture propagation and the maximum principal stress profiles in the vicinity of damage zones were evaluated. *In situ* tests were performed to verify the reliability of the FBRM method. Conclusions are drawn as follows:

- 1) Pre-mining filling is an effective tool to strengthen the damage zone left by previous mining activities. The filling-based mining should guarantee that 1) the upper filling body has robust bearing capacity to provide sufficient reactive force for hydraulic chocks and to proof mining equipment from being impacted by caving rocks and 2) the lower filling body is of satisfactory cuttability so that cutter teeth can be saved to a great extent.
- 2) With enlarging the UKBL filling thickness, the fracture propagation height decreases, obeying a negative exponential function. The maximum principal stress shifts from the area above damage zones downward to the frontal abutment as the filling thickness is beyond

5 m, indicating a filling thickness threshold of 5 m where the roof can be stabilized in repeated mining.

- 3) The optimal filling thickness of the UKBL was determined to be 5 m by comprising the results of numerical simulation and theoretical calculation. *In situ* tests show that when the workface passed through damage zones B and E, the maximum working resistance of hydraulic chocks was 11,800 kN (12,000 kN in rated resistance), and the roof separation was 26 mm. The results suggest that the FBRM method is reliable and effective in addressing the pre-existing damage zones, thus providing best-practice references for retrieving the coals left by previous mining activities with roof caving hazards minimized.

DATA AVAILABILITY STATEMENT

The original contributions presented in the study are included in the article; further inquiries can be directed to the corresponding author.

AUTHOR CONTRIBUTIONS

LC: formal analysis; writing—original draft. DZ and GF: conceptualization; methodology. SZ: data curation; numerical calculation. XW and WZ: design of the experiment; editing. All authors contributed to manuscript revision and read and approved the submitted version.

FUNDING

This study is supported by the National Natural Science Foundation of China (Nos. 52104100 and 51874278), the China Postdoctoral Science Foundation (No. 2021M703503),

REFERENCES

- Bai, Q.-S., Tu, S.-H., Zhang, C., and Zhu, D. (2016). Discrete Element Modeling of Progressive Failure in a Wide Coal Roadway from Water-Rich Roofs. *Int. J. Coal Geology*. 167, 215–229. doi:10.1016/j.coal.2016.10.010
- Benzaazoua, M., Belem, T., and Bussière, B. (2002). Chemical Factors that Influence the Performance of Mine Sulphidic Paste Backfill. *Cement Concrete Res.* 32, 1133–1144. doi:10.1016/s0008-8846(02)00752-4
- Benzaazoua, M., Fall, M., and Belem, T. (2004). A Contribution to Understanding the Hardening Process of Cemented Pastefill. *Minerals Eng.* 17, 141–152. doi:10.1016/j.mineng.2003.10.022
- Cai, S.-P., and Wang, Z.-J. (2018). An Analytical Solution of Eccentric Transverse Deflection in Rigid-Plastic Solids. *Int. J. Mech. Sci.* 145, 188–199. doi:10.1016/j.ijsmecc.2018.06.013
- Chang, Q., Chen, J., Zhou, H., and Bai, J. (2014). Implementation of Paste Backfill Mining Technology in Chinese Coal Mines. *Scientific World J.* 2014, 1–8. doi:10.1155/2014/821025
- Deng, D. Q., Jiang, N., and Duan, Y. (2021). Sampling and Mechanical Testing of Backfill in Large Mined-Out Area. *Geofluids* 2021, 1–8. doi:10.1155/2021/6686385
- Edraki, M., Baumgartl, T., Manlapig, E., Bradshaw, D., Franks, D. M., and Moran, C. J. (2014). Designing Mine Tailings for Better Environmental, Social and Economic Outcomes: A Review of Alternative Approaches. *J. Clean. Prod.* 84, 411–420. doi:10.1016/j.jclepro.2014.04.079
- Farhad Howladar, M., and Mostafijul Karim, M. (2015). The Selection of Backfill Materials for Barapukuria Underground Coal Mine, Dinajpur, Bangladesh: Insight from the Assessments of Engineering Properties of Some Selective Materials. *Environ. Earth Sci.* 73, 6153–6165. doi:10.1007/s12665-014-3841-1
- Hefni, M., Ahmed, H. A. M., Omar, E. S., and Ali, M. A. (2021). The Potential Re-use of Saudi Mine Tailings in Mine Backfill: A Path towards Sustainable Mining in Saudi Arabia. *Sustainability* 13, 6204. doi:10.3390/su13116204
- Helinski, M., Fahey, M., and Fourie, A. (2010). Coupled Two-Dimensional Finite Element Modelling of Mine Backfilling with Cemented Tailings. *Can. Geotech. J.* 47, 1187–1200. doi:10.1139/T10-020
- Inoue, T. (1996). Analysis of Plastic Buckling of Steel Plates in Shear Based on the Tresca Yield Criterion. *Int. J. Sol. Structures* 33, 3903–3923. doi:10.1016/0020-7683(95)00222-7
- Jixiong Zhang, J., Sun, Q., Zhou, N., Haiqiang, J., Germain, D., and Abro, S. (2016). Research and Application of Roadway Backfill Coal Mining Technology in Western Coal Mining Area. *Arab. J. Geosci.* 9, 1–10. doi:10.1007/s12517-016-2585-5
- Kazerani, T., and Zhao, J. (2010). Micromechanical Parameters in Bonded Particle Method for Modelling of Brittle Material Failure. *Int. J. Numer. Anal. Meth. Geomech.* 34, 1877–1895. doi:10.1002/nag.884
- Kostecki, T., and Spearing, A. J. S. (2015). Influence of Backfill on Coal Pillar Strength and Floor Bearing Capacity in Weak Floor Conditions in the Illinois Basin. *Int. J. Rock Mech. Mining Sci.* 76, 55–67. doi:10.1016/j.ijrmms.2014.11.011
- Li, M., Li, A., Zhang, J., Huang, Y., and Li, J. (2020). Effects of Particle Sizes on Compressive Deformation and Particle Breakage of Gangue Used for Coal Mine Goaf Backfill. *Powder Tech.* 360, 493–502. doi:10.1016/j.powtec.2019.10.075
- Ma, Z., Fan, J., Sun, K., Zhao, G., and Pan, Y. (2011). Study on Stope Stability during Repeated Mining with Fully-Mechanized Solid Filling Technology in Residual Coal Pillar Area. *J. Min. Saf. Eng.* 28, 499–504. doi:10.3969/j.issn.1673-3363.2011.04.001
- Mitchell, R. J., Olsen, R. S., and Smith, J. D. (1982). Model Studies on Cemented Tailings Used in Mine Backfill. *Can. Geotech. J.* 19, 14–28. doi:10.1139/t82-002
- Nujaim, M., Belem, T., and Giraud, A. (2020). Experimental Tests on a Small-Scale Model of a Mine Stope to Study the Behavior of Waste Rock Barricades during Backfilling. *Minerals* 10, 941. doi:10.3390/min10110941
- Sasa, Z., Gaofeng, R., Xinping, L., Yujie, W., and Ashraf, M. A. (2019). Proportion Optimization of Cemented Tailing Backfill and its Interaction Mechanism with Rocks in Room-And-Pillar Stope: A Case Study. *Int. J. Electr. Eng. Edu.* 1, 002072091984420. doi:10.1177/0020720919844208
- Seryakov, V. M. (2014). Mathematical Modeling of Stress-Strain State in Rock Mass during Mining with Backfill. *J. Min. Sci.* 50, 847–854. doi:10.1134/S1062739114050044
- Shi, X. (2013). China's Small Coal Mine Policy in the 2000s: A Case Study of Trusteeship and Consolidation. *Resour. Pol.* 38, 598–604. doi:10.1016/j.resourpol.2013.09.009
- Singh, M., and Seshagiri Rao, K. (2005). Empirical Methods to Estimate the Strength of Jointed Rock Masses. *Eng. Geology*. 77, 127–137. doi:10.1016/j.enggeo.2004.09.001
- Sivakugan, N., Veenstra, R., and Naguleswaran, N. (2015). Underground Mine Backfilling in Australia Using Paste Fills and Hydraulic Fills. *Int. J. Geosynth. Ground Eng.* 1, 18. doi:10.1007/s40891-015-0020-8
- Tapsiev, A. P., Freidin, A. M., Filippov, P. A., Neverov, A. A., Neverov, S. A., Artemenko, Y. V., et al. (2011). Extraction of Gold-Bearing Ore from under the Open Pit Bottom at the Makmal deposit by Room-And-Pillar Mining with Backfill Made of Production Waste. *J. Min. Sci.* 47, 324–329. doi:10.1134/s1062739147030099
- Walske, M. L., McWilliam, H., Doherty, J., and Fourie, A. (2016). Influence of Curing Temperature and Stress Conditions on Mechanical Properties of Cementing Paste Backfill: Influence of Curing Temperature and Stress Conditions on Mechanical Properties of Cementing Paste Backfill. *Can. Geotech. J.* 53, 148–161. doi:10.1139/cgj-2014-0502
- Wang, X., and Weng, M. (2012). Prediction and Backfill Mining Technology of Ultra Thick Seam in Goaf of Small Mine. *Coal Sci. Technol.* 40, 41–44. doi:10.13199/j.cst.2012.10.47.wangx.019
- Wu, J., and Xu, J. (2012). Key Technology for Fully Mechanized Top Coal Caving Mining in Thick Seam Passing through Small Mine Goaf with Backfill. *Coal Sci. Technol.* 40, 30–33. doi:10.13199/j.cst.2012.04.35.wujn.013
- Xu, W., Cao, P., and Tian, M. (2018). Strength Development and Microstructure Evolution of Cemented Tailings Backfill Containing Different Binder Types and Contents. *Minerals* 8, 167. doi:10.3390/min8040167
- Yu, Y., Ma, L., and Zhang, D. (2019). Characteristics of Roof Ground Subsidence while Applying a Continuous Excavation Continuous Backfill Method in Longwall Mining. *Energies* 13, 95. doi:10.3390/en13010095
- Yujiang Zhang, Y., Feng, G., Zhang, M., Ren, H., Bai, J., Guo, Y., et al. (2016). Residual Coal Exploitation and its Impact on Sustainable Development of the Coal Industry in China. *Energy Policy* 96, 534–541. doi:10.1016/j.enpol.2016.06.033
- Zhang, Y., Cao, S., Guo, S., Wan, T., and Wang, J. (2018). Mechanisms of the Development of Water-Conducting Fracture Zone in Overlying Strata during Shortwall Block Backfill Mining: A Case Study in Northwestern China. *Environ. Earth Sci.* 77, 1–17. doi:10.1007/s12665-018-7726-6
- Zhang, S., Fan, G., Jiang, S., Fan, Z., Li, S., and Ni, H. (2021a). Dual-hazard Control Mechanism of Burst-Prone and Spontaneous Combustion Coalface Considering Effect of Retreat Speed. *Energ. Rep.* 7, 278–288. doi:10.1016/j.egyr.2020.12.033
- Zhang, S., Fan, G., Zhang, D., Li, S., Chen, M., Fan, Y., et al. (2021b). Impacts of Longwall Mining Speeds on Permeability of Weakly Cemented Strata and Subsurface Watertable: a Case Study. *Geomatics, Nat. Hazards Risk* 12, 3063–3088. doi:10.1080/19475705.2021.1993354
- Zhou, N., Zhang, J., Yan, H., and Li, M. (2017). Deformation Behavior of Hard Roofs in Solid Backfill Coal Mining Using Physical Models. *Energies* 10, 557. doi:10.3390/en10040557

Zhu, D., Wu, Y., Liu, Z., Dong, X., and Yu, J. (2020). Failure Mechanism and Safety Control Strategy for Laminated Roof of Wide-Span Roadway. *Eng. Fail. Anal.* 111, 104489. doi:10.1016/j.engfailanal.2020.104489

Conflict of Interest: The authors declare that the research was conducted in the absence of any commercial or financial relationships that could be construed as a potential conflict of interest.

Publisher's Note: All claims expressed in this article are solely those of the authors and do not necessarily represent those of their affiliated organizations, or those of

the publisher, the editors, and the reviewers. Any product that may be evaluated in this article, or claim that may be made by its manufacturer, is not guaranteed or endorsed by the publisher.

Copyright © 2022 Chen, Zhang, Fan, Zhang, Wang and Zhang. This is an open-access article distributed under the terms of the Creative Commons Attribution License (CC BY). The use, distribution or reproduction in other forums is permitted, provided the original author(s) and the copyright owner(s) are credited and that the original publication in this journal is cited, in accordance with accepted academic practice. No use, distribution or reproduction is permitted which does not comply with these terms.



Early Warning Method for Coal and Gas Outburst Prediction Based on Indexes of Deep Learning Model and Statistical Model

Chong Wang^{1,2,3}, Like Wei^{3,4*}, Haiyong Hu³, Jiren Wang^{1,2} and Mengfeng Jiang³

¹College of Safety Science and Engineering, Liaoning Technical University, Liaoning Technical University, Fuxin, China, ²Key Laboratory of Mine Thermodynamic Disasters and Control of Ministry of Education, Huludao, China, ³Information Research Institute, Ministry of Emergency Management, Beijing, China, ⁴College of Resource and Safety, Chongqing University, Chongqing, China

OPEN ACCESS

Edited by:

Jie Chen,
Chongqing University, China

Reviewed by:

Alexey Lyubushin,
Institute of Physics of the Earth (RAS),
Russia
Gaofeng Song,
North China University of Technology,
China

*Correspondence:

Like Wei
wlkyo@qq.com

Specialty section:

This article was submitted to
Geohazards and Georisks,
a section of the journal
Frontiers in Earth Science

Received: 09 November 2021

Accepted: 24 January 2022

Published: 02 March 2022

Citation:

Wang C, Wei L, Hu H, Wang J and
Jiang M (2022) Early Warning Method
for Coal and Gas Outburst Prediction
Based on Indexes of Deep Learning
Model and Statistical Model.
Front. Earth Sci. 10:811978.
doi: 10.3389/feart.2022.811978

The early warning models for coal and gas outburst have become increasingly more important and have gained more attention in the mining industry in an effort to further improve mine safety. In the warning process, however, the theoretical models do not always work in a timely manner largely due to the delayed capture of the real time parameters. Based on the evolving mechanism of gas outburst, the gas emission is considered a dominant factor in this work because its data is attainable in real time and clearly characterizes the entire outburst process. In order to characterize and distinguish the variation of the gas emission during an outburst and normal mining activity, a total of four statistical methods were employed to quantify the variation of gas emission: the moving average, the deviation ratio, the dispersion ratio, and the fluctuation ratio. Also, the Root Mean Square Error (RMSE) and Mean Absolute Percentage Error (MAPE) are also included to demonstrate the accuracy of the deep learning model for predicting the variation of gas emission. Developed from these six indicators, the multi-factor fuzzy comprehensive evaluation model forms the outburst early warning system by calculating the combined index of the difference among the indicators. The accuracy of the early warning system is examined in the case study of the “3.25” gas outburst hazard in Shigang Coal Mine. The results show advantages of the comprehensive evaluation model established from the six characteristic indicators when predicting an outburst.

Keywords: gas emission quantity, coal and gas outburst, deep learning, Bi-LSTM, coal

INTRODUCTION

In 2020, China’s coal consumption accounted for 56.8% of the domestic primary energy consumption (National Bureau of Statistics China, 2021). Before the carbon peak expected in 2030, coal energy will remain an important part of China’s energy consumption. There are many disaster factors in the process of coal mining. Among those, gas disasters are the “first killer” (Wang, 2018). After decades of research and hazard control in this field, for the first time, no major coalmine gas accident occurred in 2020 (a major gas accident refers more than 10 dead in an accident) (Wu et al., 2021). However, recent gas outburst accidents have been on the rise and have occurred more frequently in China. They include the gas outburst at Shanxi Shigang Coal Industry Company on March 25, 2021, the gas outburst in

Dongfeng Coal Mine, Guizhou, April 9, 2021, the gas outburst at Sanbao Coal Mine, Guizhou, April 26, 2021, the gas outburst in the Sixth Mine of Henan Hebi Coal and Electricity Co., Ltd. on June 4, 2021, and the gas outburst in the shaft at Didaoshenghe Coal Mine, Heilongjiang, June 5, 2021.

Due to the continuous occurrence of these gas outburst accidents, scholars have paid more attention to the characteristics of gas accidents to find a method to predict them. The spatial-temporal distribution of the outburst accidents in China was further analyzed by using the statistical method (Wang E. Y. et al., 2020; Zhang et al., 2021). Some experts and scholars introduced the various disaster factors of gas outbursts into algorithms and models including the extreme learning machines (Han et al., 2019), the random forests (Long et al., 2021), the machine learning (Pu et al., 2019), the Neural Network (Xu and Cheng, 2021), the Grey Correlation Analysis (Yang and Zhou, 2021), etc. The correlation between the various factors to the gas disasters were analyzed to realize the disaster prediction. Some scholars used the engineering technology and geophysical methods to predict the dynamic disaster hazard, including the drill cuttings index method (Qi et al., 2021), the initial velocity of gas emission from drilling holes, the R index method (Wu, 2021), the acoustic emission method (Wang et al., 2018), the micro-seismic method (Song et al., 2021; Chen et al., 2022), the electromagnetic radiation method (Wang H. et al., 2020), etc. Based on the gas monitoring data, some other scholars utilized the data driven prediction algorithms, such as data mining (Long et al., 2020), the Gaussian process model (Li et al., 2021), the deep learning (Wang E. Y. et al., 2020) and the multi-parameter fusion (Du et al., 2021) for predicting the coal mine gas concentration. However, some influencing factors, including the real time seam gas content and gas pressure, cannot be obtained. The use of the drill cuttings method and the electromagnetic radiation method are easily affected by human activities and the underground geological environment. Therefore, the prediction results may show a certain degree of delay and also relatively large errors.

In order to improve the accuracy of the gas outburst early warning model and to facilitate the real time on-site decision-making, the influencing factors in the model must be obtained in real time in the first place. Based on the evolving mechanism of gas outburst, the gas emission can be obtained in real time and also clearly characterizes the entire outburst process, which should be considered as a main factor. This paper employed four statistical methods including the moving average, the deviation ratio, the dispersion ratio, and the fluctuation ratio to quantify the variation of the gas emission. The Root Mean Square Error (RMSE) and the Mean Absolute Percentage Error (MAPE) were included in the model to demonstrate the accuracy of the deep learning model for predicting the variation of the gas emission. The outburst early warning system was then formed by calculating the combined index of the difference among the indicators. Based on the data of the real outburst accidents, the early warning results of this model were compared with the results of previous models. The research results showed important practical significance in improving the outburst early warning accuracy and ensuring the safety of production during the tunneling process.

CHARACTERISTIC ANALYSIS OF MAIN FACTORS IN THE PROCESS OF COAL AND GAS OUTBURST

Main Controlling Factors

Coal and gas outburst is an extremely complex coal-rock dynamic disaster that often occurs during the mining process in coalmines. It is a strong and complex dynamic process of gas-containing coal and rock fluids that instantly evolve in time and space. The outburst generates dynamic effects, which include releasing powerful energy, damaging mining equipment, and causing casualties. Secondary disasters such as gas explosions are not unusual, which seriously threatens the safety in the mine production (Wang W. et al., 2020). At present, experts and scholars generally believe that the coal and gas outburst is the result of the combined effects of stress, gas, and the physical and mechanical properties of the coal seam (Zhu et al., 2018). Coal and gas outburst is the dynamic evolving process of the coal seam including the energy accumulation, development, destruction and release. It can be divided into four phases including the evolution, formation, development and the termination (Luo et al., 2018). The evolution model of the coal and gas outburst is shown in **Figure 1**.

Evolution Phase

In-situ stress is the dominant cause of an outburst. After the start of the mining operations, the load in the mining field is transferred to the coal wall, and the *in-situ* stress gradient of the coal wall increases and concentrates, raising the gas pressure. In addition, changes in the ground stress affect the internal structure of the coal seam, alter the preservation and movement of gas (Qin et al., 2021), and provide energy to the occurrence of the coal and rock dynamic disasters. At this stage, various outburst signs including the muffled thunder, the fluctuation of the gas concentration and the abnormal gas emission would appear in coal and rock masses.

Formation Phase

The combined action of the *in-situ* stress and gas leads to the fracture and instability of the coal mass, promoting the development of an outburst. The pressure of the gas increases by several to over ten times. The coal mass expands and deforms when adsorbing the gas. A large amount of the adsorbed gas enters the desorption process and participates in the outburst. Gas expansion energy is the main energy source for a gas outburst (Lichtenberger, 2006). The elastic potential energy, the gas internal energy, and the gravitational potential energy of the unstable coal and rock masses break the unstable coal mass and throw it out in the space, forming small outburst holes (Hu et al., 2008).

Development Phase

When the external pressure drops suddenly, the higher pressure in the coal mass causes rapid gas release and resultant failure of coal mass. The gas storm with high gas pressure gradient moves the fractured coal mass (Wang, 2020). The development of the outburst depends on the physical and mechanical properties of the coal. A smooth outburst hole promotes the development of

the outburst, while resistance in the hole prevents the outburst from developing.

Termination Phase

The pressure gradient of the ground stress and gas would sharply drop when the outburst energy gradually decays to a degree that hardly damages the coal mass or the outburst holes are blocked. Furthermore, the gas outburst would stop when the conditions for continuous damage and instability are not met.

In the evolution process of coal and gas outbursts, underground mining activities can destroy the original equilibrium of stress in the coal seam. *In-situ* stress affects the gas movement in the deep coal mass by controlling the porosity and permeability in the coal mass. The seam gas content surrounding the excavation face affects the distribution and gradient of the gas pressure. It also determines the gas emission quantity. The dynamic changing characteristics of the gas emission are affected and controlled by various factors such as the coal and rock mass stress, the gas pressure, the coal and rock permeability. All these factors contribute to the deformation and fracture of the coal mass. The pattern change is basically consistent with the hazard of the gas outburst.

In summary, the gas emission participates in the entire process of the coal and gas outburst. The parameter values can be calculated by the gas concentration, the wind speed, and the cross-sectional area of the tunnel. More importantly, the values can be obtained in a real time manner, as described in Eq. 1. Therefore, this parameter was selected as the main factor for in-depth analysis.

$$Q_s = 60Cv_sS \quad (1)$$

Where Q_s is the value of gas emission quantity in the tunnel, in m^3/min ; C denotes the gas concentration, in percentage; v_s denotes the wind speed, in m/s ; S is the cross-sectional area at the testing location in the tailgate, in m^2 .

According to Eq. 1, the gas emission is a function of the gas concentration, the wind speed, and the roadway cross-sectional area. By selecting the gas sensor data, the wind speed and the cross-sectional area of the tailgate, the analysis of the precursory characteristic law of gas outburst was carried out.

Choosing the Indicators for Coal and Gas Outburst Based on Statistics

In order to accurately analyze the variation characteristics of gas emission, this paper employed the moving average, the deviation ratio, the dispersion ratio, and the fluctuation ratio as the characteristic indicators for the dynamic change of the gas emission quantity.

Moving Average

The moving average is a series of averages on the gas emission quantity of different subsets in the full observing time period. It reflects the change trend of the gas emission quantity over time, indicating the dynamic engineering disturbance in the mining activity process, and the change of the gas emission quantity in a

certain period of time (increasing, horizontal and declining). The trend is stable, which means it will continue for a period of time once established and will remain stable until external factors force it to change.

$$\bar{C}_n = \frac{1}{n-1} \sum_{i=1}^{n-1} C_i \quad (2)$$

Where \bar{C}_n is the n th average of gas emission quantity, n is the number of subset in the full period, C_i denotes the i th gas emission quantity recorded.

Deviation Ratio

Deviation ratio is the value by which the real-time gas emission quantity deviates from the moving average in a period of time. It reflects the change pattern of gas emission quantity affected by the seam gas content, the gas pressure, the coal seam permeability coefficient, and other factors during that time.

$$A(n) = \frac{C_t - \bar{C}_n}{\bar{C}_n} \quad (3)$$

Where C_t denotes gas emission quantity at time t , \bar{C}_n denotes n th average of gas emission quantity.

Dispersion Ratio

The dispersion rate reflects the dispersion degree of the gas emission data series, that is, the degree to which each value deviates from the mean value. Dispersion of the gas emission quantity in a certain subset of time period indicates the extent of the change of the gas emission.

$$D(m) = \left. \begin{aligned} \mu &= \frac{1}{m} \sum_{t=1}^m C_t \\ &\frac{1}{m-1} \sum_{t=1}^m (C_t - \mu)^2 \end{aligned} \right\} \quad (4)$$

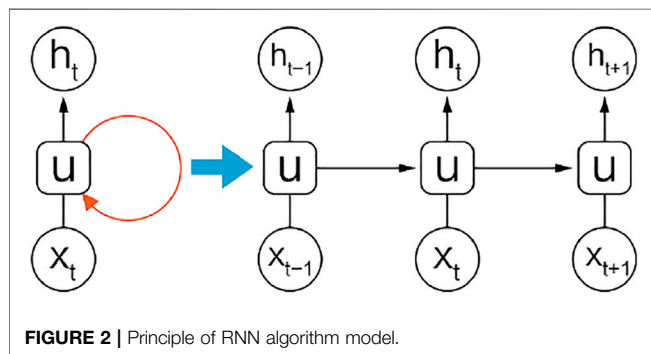
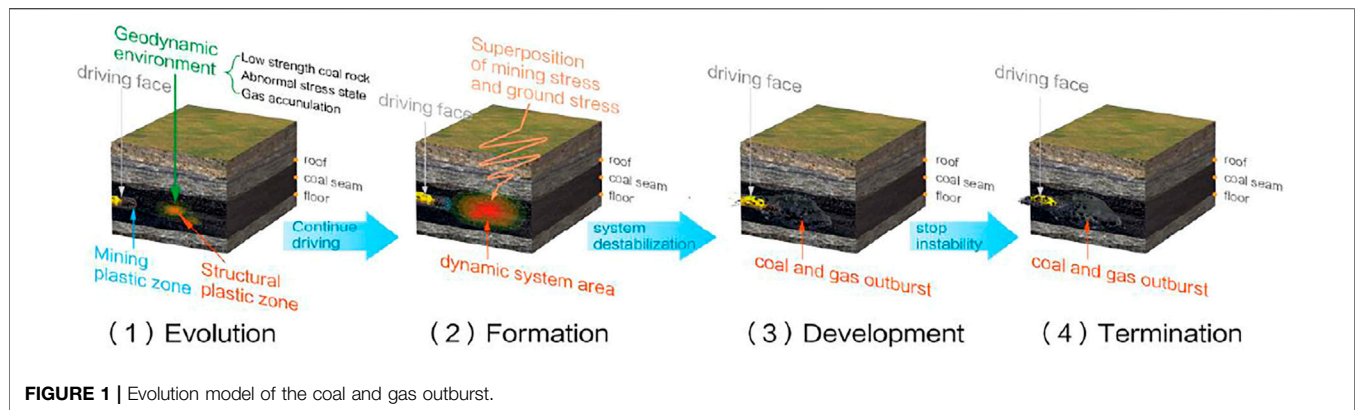
Where C_t denotes gas emission quantity at time t , m is the number of the subset of time period.

Fluctuation Ratio

The fluctuation ratio can describe the vibration amplitude of the sequence expressed by the amplitude variation ratio R_{OSC} . This ratio means the relative rate of change between the gas emission quantity at the initial moment and the gas emission quantity at the end moment of a certain time interval. Meanwhile, it reveals change times in the sequence as reflected by the frequency of change R_{OFC} , meaning change times in the gas emission quantity within a certain time interval. The combination of these two aspects describes the actual situation of the gas emission quantity changes.

$$R_{OSC}(n) = [(C_{Tmax} - C_{Tmin})/C_{Tmax}] \quad (5)$$

Where $R_{OSC}(n)$ denotes the ratio of the max concentration changes in time period n , C_{Tmax} , C_{Tmin} denote the maximum and minimum values of gas emission quantity during that time period individually.



$$R_{OFC} = f(C_{(t-n)-t}) \quad (6)$$

Where $C_{(t-n)-t}$ denotes gas emission quantity from time $t-n$ to time t , $f()$ denotes the change times.

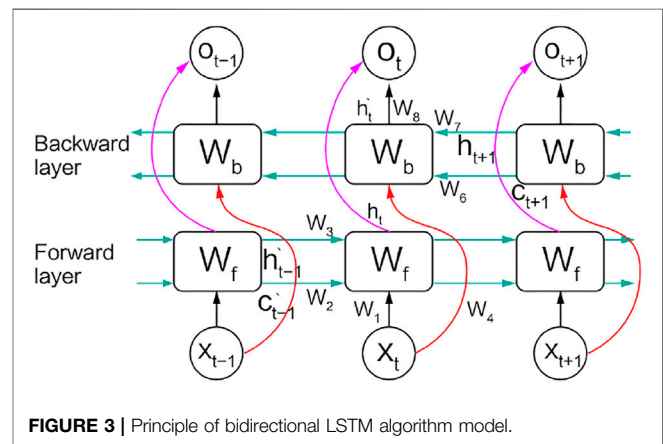
In a variety of coal mining and tunneling technology conditions, the gas emission from the normal coal mining face and tunneling face periodically fluctuates within a certain range. The moving average of the gas emission is a horizontal line that changes steadily. The curves of deviation ratio, the dispersion ratio, and the fluctuation ratio of gas emission quantity are relatively stable. When the gas emission quantity sharply increases or decreases, the moving average, deviation ratio, dispersion ratio, and fluctuation ratio of gas emission quantity exhibit abnormal changes.

Choosing the Indicators for Coal and Gas Outburst Based on Deep Learning

The Principle of Bidirectional LSTM Neural Network

Recurrent Neural Network (RNN) is a simple loop that repeats in the form of a chain. The schematic diagram of the structure is shown in **Figure 2**.

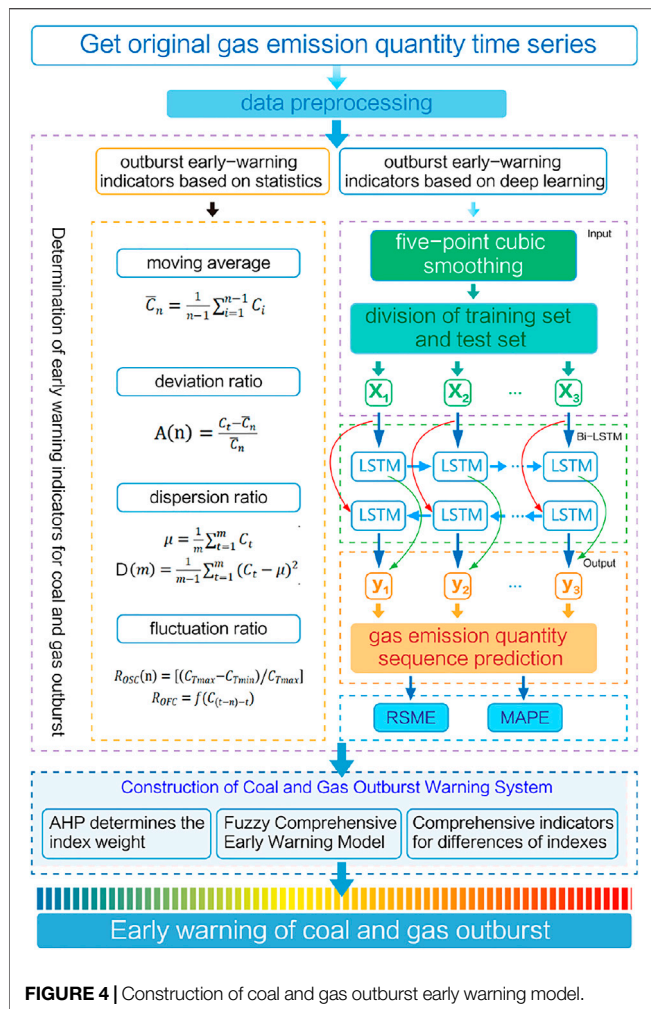
The RNN returns the output of the hidden layer to the input forming a cycle. When training RNN, as the input sequence samples increase, the partial derivative weight matrix of the loss function tends to zero or infinity, resulting in vanishing gradient problem or exploding gradient problem, which makes the RNN incapable of dealing with the long-term dependence problem



effectively. Long short-term memory (LSTM) is an optimized and improved recurrent neural network model that controls the proportion of information that needs to be retained or forgotten in the cell state C_t in the neural unit by adding three different “gate” structures (i.e., the input gate, the forget gate, and the output gate). The gate structure enables the LSTM with the long-term learning capabilities and solves the vanishing gradient problem and exploding gradient problem that RNN cannot solve.

Compared with RNN, LSTM shows certain advantages in dealing with the long-term dependence problems. However, it can only predict the state of the next moment based on the temporal information of the previous moment. In some problems, the output of the current moment is not only related to the state at the previous moment. It may also relate to the state in the future and as a result, there are still deficiencies in the actual application of the LSTM.

The bidirectional LSTM neural network (Bi-LSTM) can use past and future data information for learning. In other words, it can use the information from the upper memory as well as the lower memory to predict reservoir physical parameters, which remedies the LSTM’s shortcomings. **Figure 3** is the schematic diagram showing the input layer, the forward layer, the backward layer, and the output layer from bottom to top. Of the two LSTM network layers with opposite information transfer directions, the forward LSTM layer can obtain the timing information of the



previous moment, and the backward LSTM layer can obtain the timing information of the future moment. Consequently, the model can fully obtain the information of upper and lower memory from both the front and back directions to predict the current state and the model's performance is therefore improved.

The Bi-LSTM model has 8 weights used in cycles at each moment: the weights of the input layer to the forward and backward hidden layers (w_1, w_4); the weights of the forward hidden layers (w_2, w_3); the weights of the backward hidden layers (w_6, w_7); the weight of the forward and backward hidden layers to the output layer (w_5, w_8). The formulas for the forward hidden layer h_t^f , the backward hidden layer h_t^b and the output layer o_t are listed as follows:

$$h_t^f = f(w_1 x_t + w_2 C_{t-1} + w_3 h_{t-1}^f) \quad (7)$$

$$h_t^b = f(w_4 x_t + w_6 C_{t-1} + w_7 h_{t-1}^b) \quad (8)$$

$$o_t = g(w_5 h_t^f + w_8 h_t^b) \quad (9)$$

During the training of the network model, problems such as the insufficient training data sets, the sample uniformity, the excessive noise interference in the training data, or the model over

complexity may arise, resulting in over-fitting. Aiming at the over-fitting problem of the bidirectional LSTM model in predicting with waveform data, the dropout mechanism is introduced to restrict the sparsity in the random region of the model (Cai et al., 2021). The dropout mechanism randomly discards a certain fraction of neural units from the network temporarily. The entire model training process is equivalent to training many different networks. The update of weights will not rely heavily on some features, and the network can be forced to learn more robust features. It not only prevents over-fitting, but also makes the model more generalized, thus improving the efficiency and accuracy of model training.

Choosing the Outburst Indicators Based on Deep Learning

RMSE and MAPE are used as indicators to measure the prediction accuracy of the model. RMSE and MAPE reflect the deviation between the predicted gas emission quantity and the actual quantity. A smaller value indicates better prediction accuracy, and vice versa. MAPE is more robust to outliers of the two, reflecting the overall prediction effectiveness of the model. Conversely, RMSE, emphasizes the influence of outliers on the prediction effectiveness of the model. Employing both can better evaluate the accuracy of the model's prediction.

The calculation formulas are:

$$RMSE = \sqrt{\frac{1}{n} \sum_{i=1}^n (C_i - \hat{C}_i)^2} \quad (10)$$

$$MAPE = \frac{1}{n} \sum_{i=1}^n \left| \frac{C_i - \hat{C}_i}{C_i} \right| \quad (11)$$

Where C_i denotes actual gas emission quantity, \hat{C}_i denotes predicted gas emission quantity, and n denotes the size of the sample.

DEVELOPMENT OF EARLY WARNING SYSTEM FOR COAL AND GAS OUTBURST

The coal and gas outburst early warning index system is established from the dynamic characteristics of the gas emission quantity and the gas emission quantity prediction model based on the RNN. The criteria priority and member function are created with the fuzzy comprehensive early warning model and then the method for early warning of the coal and gas outbursts, based on the characteristics of the online monitoring gas emission quantity, is realized.

Determining the Severity of the Gas Emission Quantity Model Abnormality

This paper combines the analytic hierarchy process (AHP) with fuzzy theory to evaluate the probability of the coal and gas outburst.

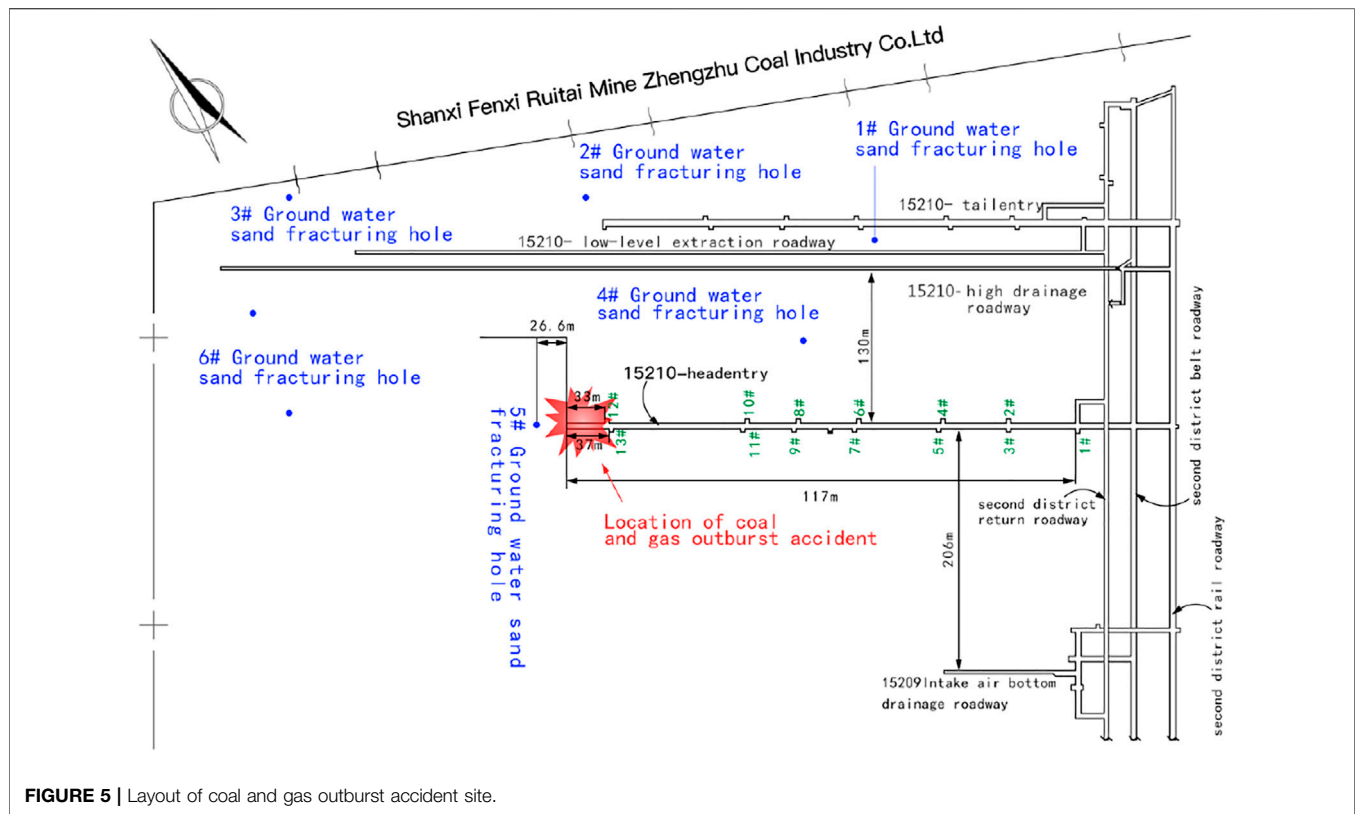


FIGURE 5 | Layout of coal and gas outburst accident site.

Determining the Indicator Weights With AHP

I. The 1–9 scale method is used to construct the judgment matrix A , the principle eigenvalue λ_{\max} and the criteria priority vector w are then calculated.

II. Check the consistency of the judgment matrix. In order to test if the judgement criteria priorities are reasonable, the formula of the consistency ratio for the judgment matrix is used.

$$C_1 = \frac{\lambda_{\max} - n}{R_1(n-1)} \quad (12)$$

Where C_1 is the consistency ratio, n is the number of criteria, R_1 is the random consistency indicator. When $C_1 < 0.1$, the constructed judgement matrix is acceptable.

Establishing the Fuzzy Comprehensive Early Warning Model

Fuzzy comprehensive evaluation contains three elements: the factor set, the evaluation set, and the single-factor evaluation. On the basis of single-factor evaluation, a multi-factor fuzzy comprehensive evaluation is carried out.

Building the Factor Set

The factor set U is a set of all the factors that affect the evaluation object, which can be expressed as $U = (u_1, u_2, \dots, u_n)$. Among them, the element u_i ($i = 1, 2, \dots, n$) represent influencing factors. In this paper, the evaluation factor index set consists of two evaluation factors, i.e., the gas emission quantity variation characteristics

and the gas prediction model output, which can be expressed as $U = (u_1, u_2)$.

Creating the Evaluation Set

The evaluation set is a set of possible evaluation results to the evaluation objects, which can be expressed as $V = (v_1, v_2, \dots, v_m)$, where the element v_j ($j = 1, 2, \dots, m$) indicates the result of the evaluation. The evaluation result set in this paper includes two kinds of results: outburst and no outburst, namely $V = (\text{outburst}, \text{no outburst})$.

Creating the Weight Set

The weight of each element in the factor set U is different to the evaluation, so each element u_i should have a different weight w_i according to its importance. W is a fuzzy set of the factor set U , which can be expressed as $W = (w_1, w_2, \dots, w_n)$. In this paper, since it has 2 factors in the factor set, the weight set is $W = (w_1, w_2)$, and $w_1 + w_2 = 1$.

Single Factor Fuzzy Evaluation

The evaluation begins from one factor alone to determine the degree of membership of the evaluated object to the elements of the evaluation set. Suppose the object evaluated according to the i th factor u_i in the factor set, and the degree of membership of the j th element v_j in the evaluation set is r_{ij} , then the evaluation result can be expressed as $R_i = (r_{i1}, r_{i2}, \dots, r_{im})$, where R_i representing the single factor judgment set.

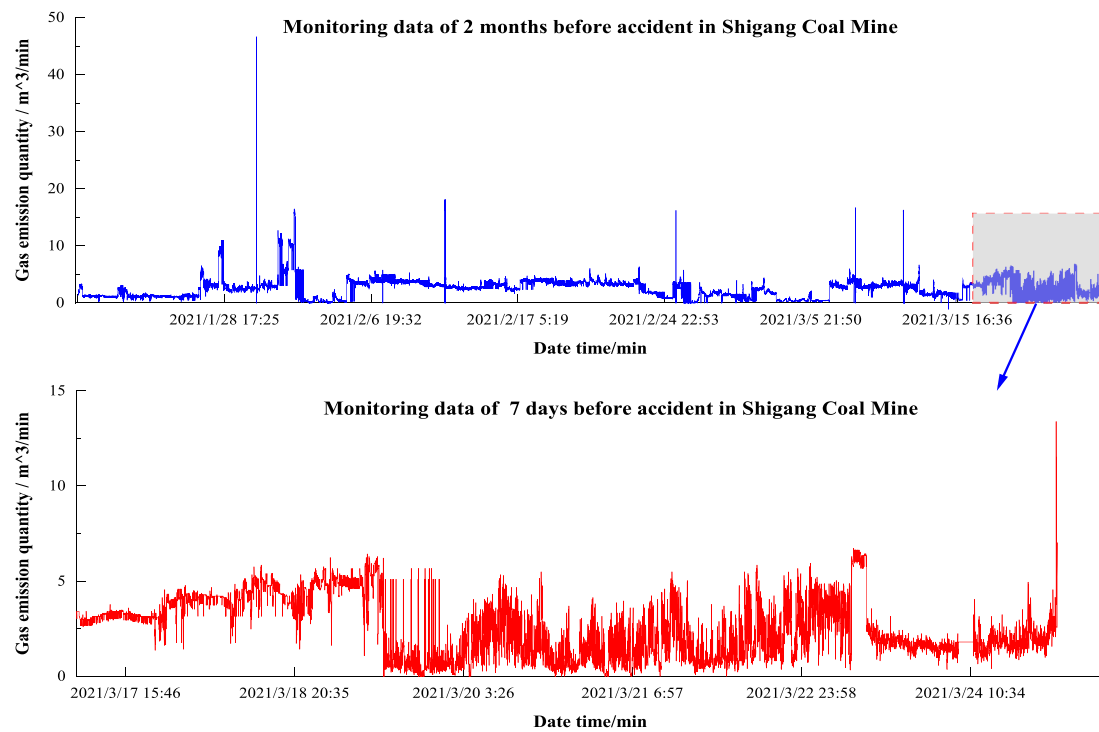


FIGURE 6 | Pre-accident monitoring data in Shigang Coal Mine.

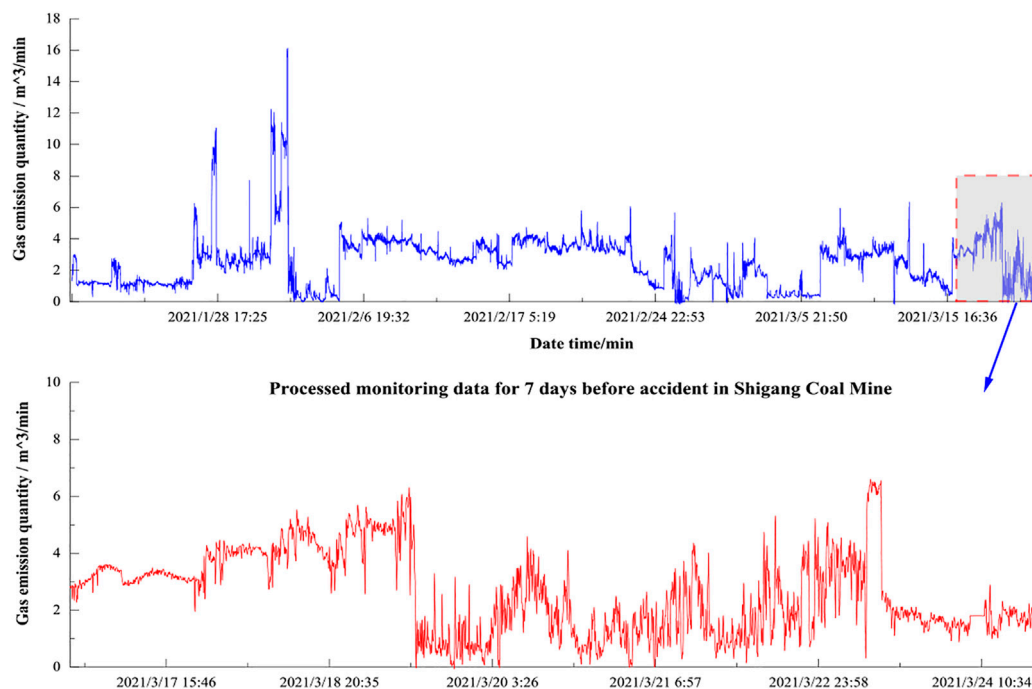


FIGURE 7 | Processed monitoring data in Shigang Coal Mine.

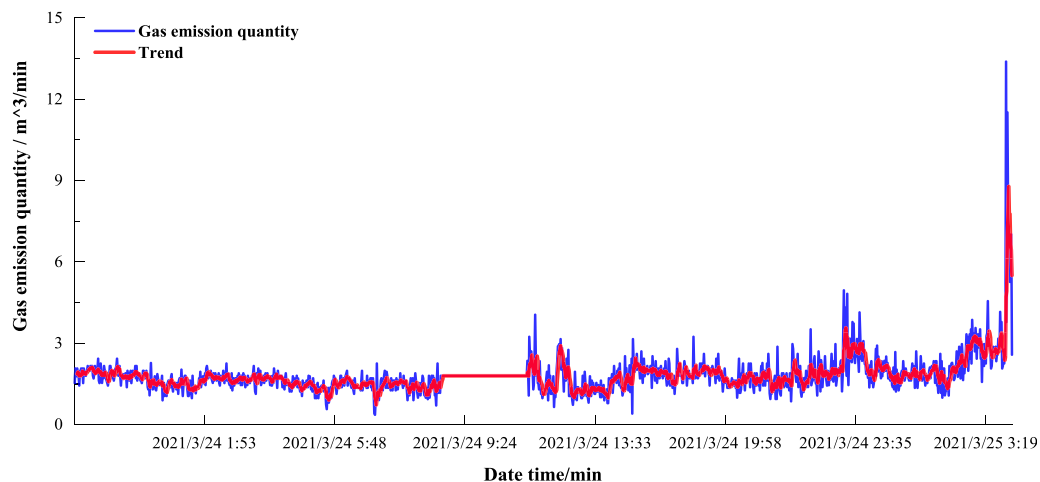


FIGURE 8 | Gas emission quantity moving average curve.

Fuzzy Comprehensive Evaluation

The multi-factor comprehensive evaluation (R evaluation matrix) is constructed from the single-factor evaluation sets, namely $R = (R_1, R_2)^T$. Using the weighted average model, according to the multiplication operation of the fuzzy matrix, we can obtain the fuzzy comprehensive evaluation set B given as

$$B = WR = \{b_1, b_2, \dots, b_m\} \quad (13)$$

Where $b_i (i = 1, 2, \dots, m)$ is the fuzzy comprehensive evaluation indicator, denoting the membership degree of the evaluated object relative to the i th element in the evaluation set V , while taking into account all the factors.

The value of the fuzzy comprehensive evaluation set B is used to represent the comprehensive indicator of the differential individual indicator, based on the evaluation indicators RMSE and MAPE of the prediction model. The gas emission quantity dynamic change characteristic indicators are used for the

evaluation and early warning for the coal and gas outburst. The data of gas emission during the normal production period of a coal mine are analyzed by using the difference comprehensive index. The maximum value of the calculation result is multiplied by the safety factor (1.2–1.5) to determine the early warning threshold. When the comprehensive indicator reaches the maximum value within the normal range, an orange alarm is given; when the comprehensive indicator approaches 1, it means that the probability of a coal and gas outburst is high and the red alarm is sent out.

Construction of Early Warning Model for Coal and Gas Outburst

This system continuously collects the gas concentration and the wind speed data from the sensors in the tailgate of the driving face. After removing the interference data, the value of gas

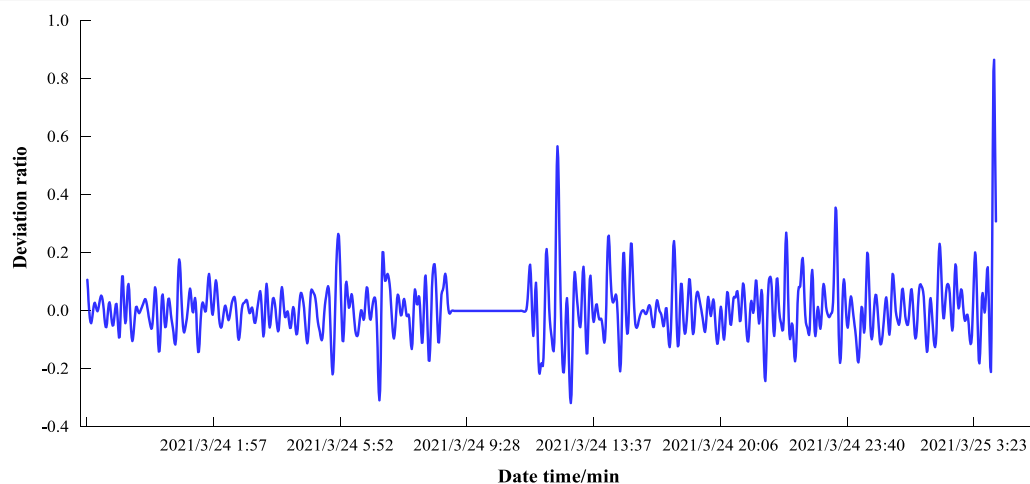


FIGURE 9 | Gas emission quantity deviation ratio curve.

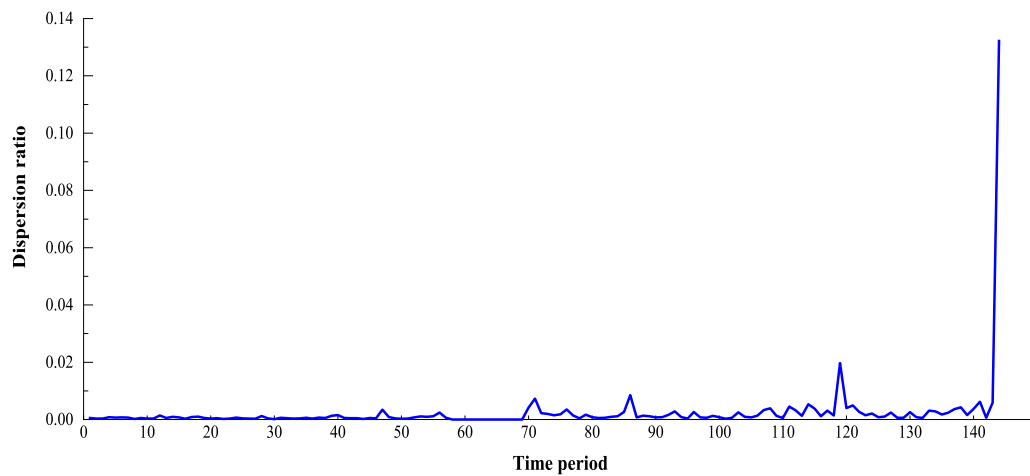


FIGURE 10 | Gas emission quantity dispersion ratio curve.

emission quantity is calculated, then the moving average, the deviation ratio, the dispersion ratio, and the fluctuation ratio of the gas emission quantity change values are extracted as characteristic indicators. At the same time, the data collected during the normal excavation process in the past period of time is input into the Bi-LSTM neural network model for training and tuning, so that the model training error meets the predetermined requirements and the data model under normal production conditions is established. The newly collected data is then input into the model as the test data set to calculate the predicted value of the gas emission quantity and the loss value. The predicted gas emission quantity is combined with the characteristic indicators of gas emission quantity variation to form the early warning indicators for the coal and gas outburst. Next, the early warning indicators are used for the fuzzy comprehensive early warning model. By calculating the differential individual index, the threshold is

determined and the evaluation and early warning of the risk level of coal and gas outburst is implemented. The construction of coal and gas outburst early warning model is shown in **Figure 4**.

APPLICATION RESULT ANALYSIS

Data Collection and Analysis

The national mine safety production risk monitoring and early warning system platform has collected the safety monitoring system data of all production and construction coal mines. The data includes information such as the sensor type, the sensor location, the real-time monitoring data value of the sensor and the collection time. The data is transmitted once a minute in a message queue. The platform data provides data support for the time series data analysis of this study.

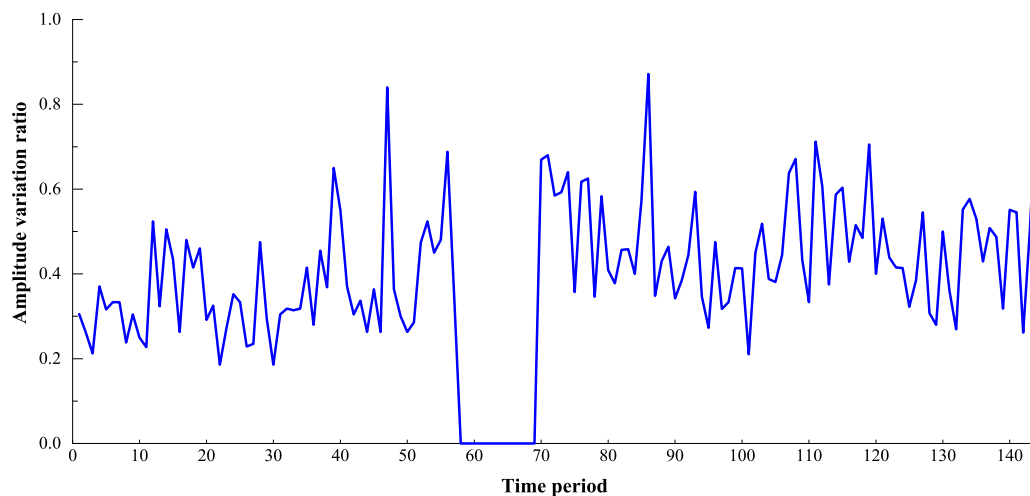


FIGURE 11 | Gas emission quantity amplitude variation ratio curve.

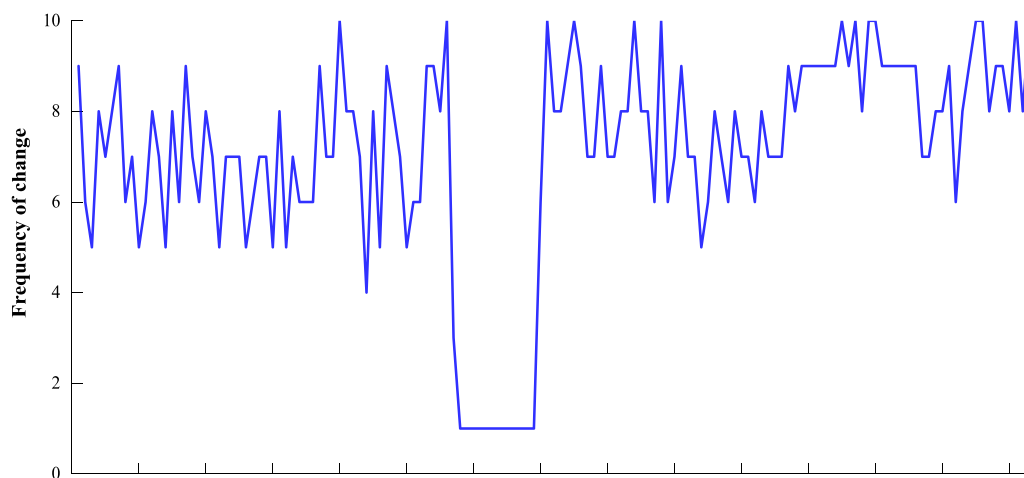


FIGURE 12 | Gas emission quantity frequency of change curve.

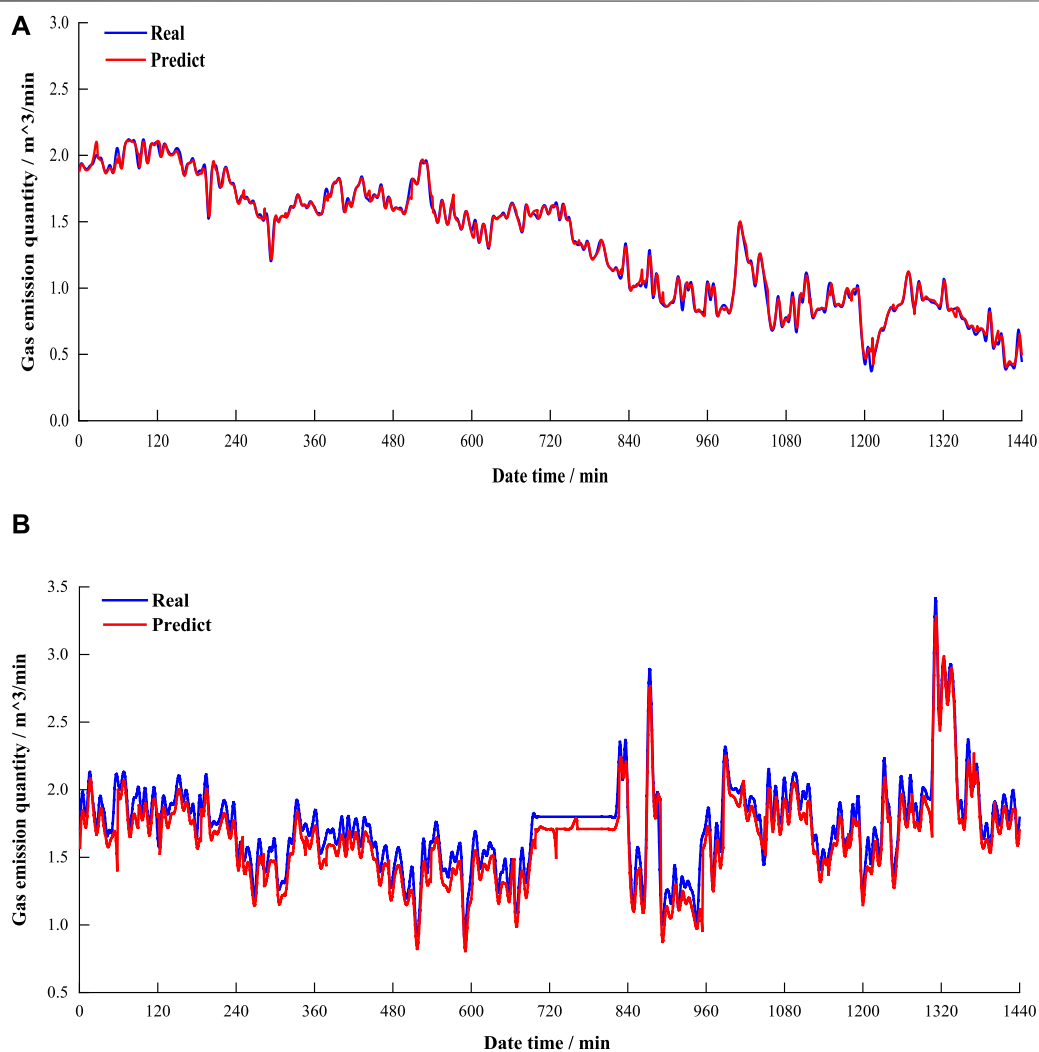
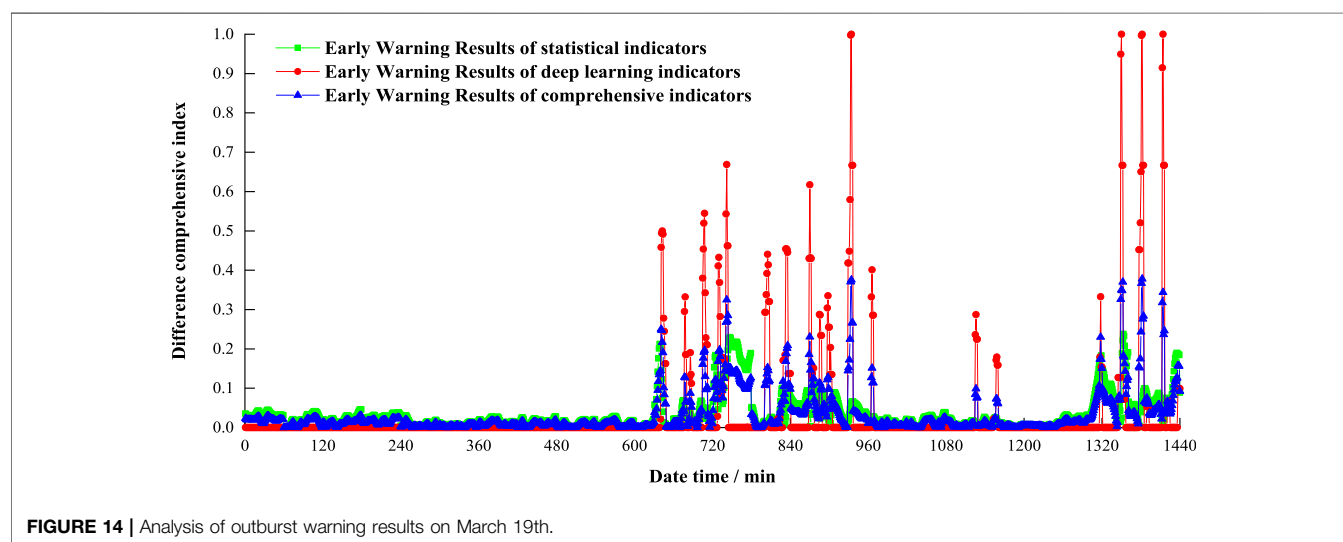


FIGURE 13 | Gas emission prediction based on Bi-LSTM. **(A)** Gas emission prediction in normal production **(B)** Gas emission prediction before the accident

TABLE 1 | Weights of all criteria and sub criteria.

Early warning criteria	Weights (%)	Early warning sub criteria	Weights (%)
Statistical indicators	66.67	Moving average	54.07
		Dispersion ratio	9.65
		Diversification ratio	30.07
		Fluctuation ratio	6.21
Prediction model indicators	33.33	RSME	66.67
		MAPE	33.33

**FIGURE 14** | Analysis of outburst warning results on March 19th.

In the first half of 2021, coal and gas outburst accidents occurred frequently. They provide copious data source for analysis in this work. There were three coal and gas outburst accidents occurred in this period, cost 20 lives.

I. At 3:51 a.m. 25 March 2021, outburst accident happened at the 15210 headentry in Huayang New Material Technology Group Co., Ltd., Shanxi Shigang Coal Industry Co., Ltd., causing four people died.

II. At 11:33 a.m. April 9, 2021, outburst accident happened at the open-off cut of 10901 headentry in Dongfeng Coal Mine, Guizhou, causing eight people died.

III. At 17:50 4 June 2021, outburst accident happened at the tailentry of the 3,002 excavation face in the No. 6 mine of Henan Hebi Coal and Electricity Co., Ltd. The accident caused eight deaths.

Based on gas emission quantity statistical indicators and the deep learning indicators, the early warning model in this work is used to analyze the data of Shigang coal mine for the research on early warning of coal and gas outburst. The accident occurred at the excavation face of 15210 headentry. The gate is a rectangular section with 3 m height and 5 m wide. The mining layout is shown in **Figure 5**. This work selects the gas concentration data and the wind speed data of 15210 headentry from the 2 months before the outburst for analysis. A total of 86,400 pieces of monitoring data were collected. On the whole, the gas emission quantity fluctuates with the progress of mining

activities. About 4 days before the accident, the frequency of gas emission quantity fluctuations increased significantly, and the variation of gas emission quantity was abnormal. This is a sign of coal and gas outbursts. Through the early warning model, the prediction of coal and gas outburst is realized.

The commonly used training strategies are adopted in deep learning to select the hyperparameters for the Bi-LSTM model. The initial value of the learning rate is set as $1e^{-4}$; the dropout set as 0.2 to suppress overfitting; the lag set at 16; the batch size set at 32; the frequency set at 8 the epoch set at 20; the number of nodes in the hidden layer set at 64; the optimization method selected is Adam.

On the 15210 headentry excavation face, the original monitoring data curve is shown in **Figure 6**. The involved manual calibrations were found in monitoring data collected by the gas sensors. The calibration would cause interruption to the continuity of the data, and the data manifests the abnormal increase. Therefore, this part of the data needs to be removed, which interpolated with the cubic spline curve. The overall gas emission quantity sequence is reduced noise with five-point cubic smoothing. The processed curve is shown in **Figure 7**:

This work selects the gas emission quantity data from 19 February to 20 March 2021 for the model training. Totally 43,200 pieces of data are divided into the training set and the test set at a ratio of 0.8. After the model was trained, the gas emission quantity data from 21 March to the moment before the accident was input into the model as a test set. The obtained

loss values RSME and MAPE, combined with the moving average, the deviation, the dispersion and the volatility of gas emission time series can comprehensively reflect the abnormal changes of gas emission before the outburst accident.

Determination of Indicators Weights and Membership Functions

Based on the indicators change before the coal and gas outburst, the judgment matrix is constructed by the AHP to calculate indicators weights. Since the calculated $C_1 = 0.0123 < 0.1$, the judgment matrix confirms that the result is acceptable. The weights of the indicators are shown in **Table 1**:

According to the principle of determining the membership function, a large amount of the experimental data is used to determine the membership function of various indicators.

I. Moving average: it is defined as the ratio of the real-time gas emission moving average to the previous period (1 h) gas emission average \bar{C}_{ave} .

II. Deviation ratio, dispersion ratio: the value interval is divided by the ratio of the real-time deviation, dispersion and the average value of their respective calculation periods.

III. Fluctuation ratio: the value interval for volatility is divided by the real-time volatility with its average in the calculation period. Then the larger value of the amplitude change rate and the frequency change rate was taken as the final value.

IV. RSME, MAPE: the value interval is divided by the ratio of the loss value of the predicted gas emission quantity before the real-time accident to the average value of the predicted loss of the gas emission quantity in the normal production.

$$U_1(\bar{C}_i) = \begin{cases} 1 \left(\frac{\bar{C}_i}{\bar{C}_{ave}} \geq 2 \cup \frac{\bar{C}_i}{\bar{C}_{ave}} \leq 0.5 \right) \\ \left| \frac{\bar{C}_i}{\bar{C}_{ave}} - 1 \right| \left(1 < \frac{\bar{C}_i}{\bar{C}_{ave}} < 2 \cup 0.5 < \frac{\bar{C}_i}{\bar{C}_{ave}} < 1 \right) \\ 0 \left(\frac{\bar{C}_i}{\bar{C}_{ave}} = 1 \right) \end{cases} \quad (14)$$

$$U_2(A_i) = \begin{cases} 1 \left(\left| \frac{A_i}{A_{ave}} \right| \geq 4 \right) \\ \frac{1}{2} \left| \frac{A_i}{A_{ave}} \right| - 1 \left(2 < \left| \frac{A_i}{A_{ave}} \right| < 4 \right) \\ 0 \left(\left| \frac{A_i}{A_{ave}} \right| \leq 2 \right) \end{cases} \quad (15)$$

$$U_3(D_i) = \begin{cases} 1 \left(\frac{D_i}{D_{ave}} \geq 4 \right) \\ \frac{1}{2} \frac{D_i}{D_{ave}} - 1 \left(2 < \frac{D_i}{D_{ave}} < 4 \right) \\ 0 \left(\frac{D_i}{D_{ave}} \leq 2 \right) \end{cases} \quad (16)$$

$$U_4(R_i) = \begin{cases} 1 \left(\frac{R_i}{R_{ave}} \geq 2 \right) \\ \frac{R_i}{R_{ave}} - 1 \left(1 < \frac{R_i}{R_{ave}} < 2 \right) \\ 0 \left(\frac{R_i}{R_{ave}} \leq 1 \right) \end{cases} \quad (17)$$

$$U_5(RS_i) = \begin{cases} 1 \left(\frac{RS_i}{RS_{tave}} \geq 5 \right) \\ \frac{1}{3} \left(\frac{RS_i}{RS_{tave}} - 2 \right) \left(2 < \frac{RS_i}{RS_{tave}} < 5 \right) \\ 0 \left(\frac{RS_i}{RS_{tave}} \leq 2 \right) \end{cases} \quad (18)$$

$$U_6(M_i) = \begin{cases} 1 \left(\frac{M_i}{M_{tave}} \geq 5 \right) \\ \frac{1}{3} \left(\frac{M_i}{M_{tave}} - 2 \right) \left(2 < \frac{M_i}{M_{tave}} < 5 \right) \\ 0 \left(\frac{M_i}{M_{tave}} \leq 2 \right) \end{cases} \quad (19)$$

Analysis of Changes in Indicators Before the Outburst Accident

For the “3.25” coal and gas outburst accident in Shigang Coal Mine, the gas emission monitoring data from 4 a.m. on 24 March to 4 a.m. on 25 March is collected to calculate the moving average, the deviation, the dispersion, the amplitude change and the variation frequency. The change law of the gas emission quantity change on the eve of the outburst accident is analyzed.

I. Moving average

The moving average is calculated using **Eq. 2** during the 5-min periods. The gas emission quantity moving average curve is shown in **Figure 8**. According to the calculation results, it can be found that the gas emission variation is relatively stable from 24 to 12 h before the outburst accident. At 12 h before the outburst, the gas emission drastically changes with a pattern of “suddenly large and suddenly small”. The moving average reaches the highest value of 4.95 m³/min at 4 h before the outburst, and then drops sharply. The gas emission begins to increase at 2 h before the outburst and reaches the peak value of 4.56 m³/min. Just before the outburst, the gas emission reaches the maximum value of 13.4 m³/min. Overall, the gas emission quantity presents a dynamic trend of “stable-rising-falling-rising”, which is similar to a “W” shape, with multiple peaks.

Deviation Ratio

The deviation of the gas emission quantity sequence is calculated from **Eq. 3** and the result of the moving average. The gas emission quantity deviation ratio curve is shown in **Figure 9**. According to the calculation results, it can be found

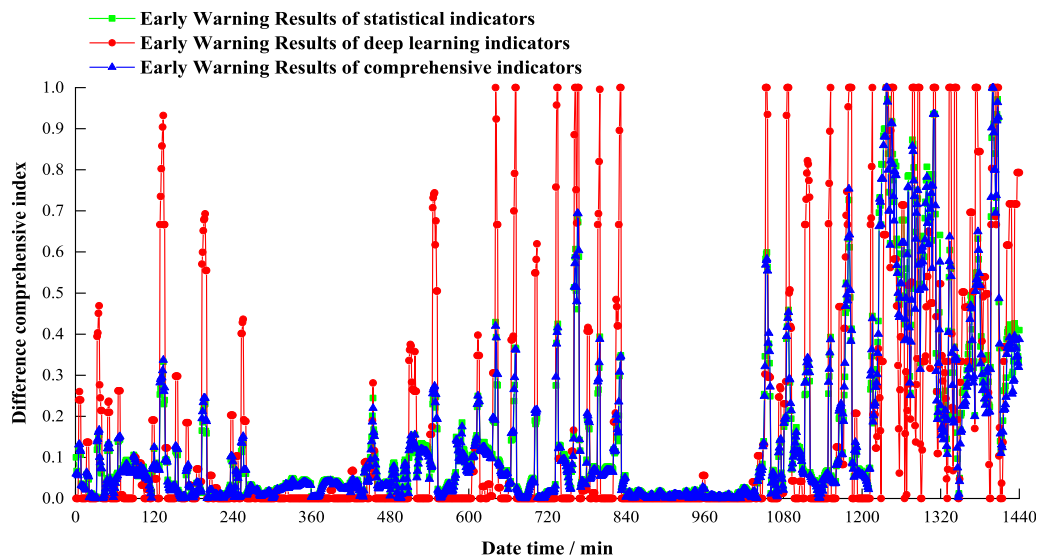


FIGURE 15 | Analysis of outburst warning results on March 20.

that the deviation from 24 to 14 h before the outburst changes within the range of ± 0.2 . There is an abnormal value of 0.567 at 12 h before the outburst. The peak value of the gas emission quantity deviation is 0.866 just before the outburst. The “suddenly large and suddenly small” pattern of changes in gas emission quantity leads to an overall increase of 2–3 times higher than the deviation rate at 24–14 h before the outburst.

Dispersion ratio

The dispersion of the gas emission quantity sequence is calculated with Eq. 4. The time period is 10 min. The gas emission quantity dispersion ratio curve is shown in Figure 10. According to the calculation results, it can be found that the dispersion is at around 0.0007 from 24 to 14 h before the outburst. From 12 h before the outburst to the outburst time, the average value of the dispersion rate is 0.0023, an increase of 3 times. The peak value of the gas emission quantity dispersion is 0.132 just before the outburst. Abnormal changes in gas emission quantity leads to the increased dispersion.

Amplitude variation ratio

The amplitude variation ratio of the gas emission quantity sequence is calculated with Eq. 5. The time period is 10 min. The gas emission quantity amplitude variation ratio curve is shown in Figure 11. According to the calculation results, it can be found that the fluctuation range of the amplitude variation ratio from 24 to 14 h before the outburst accident is large, with an average value of 0.362. The peak value of the gas emission quantity amplitude variation ratio is 0.87 at 12 h before the outburst. It tends to be stable from 12 h before the outburst to the outburst time, with an average value of 0.474. From the data, the overall amplitude variation ratio before the outburst tends to be relatively frequent.

Frequency of Change

The frequency of change of the gas emission quantity is calculated with Eq. 6. The time period is 10 min. The gas emission quantity frequency of change curve is shown in Figure 12. According to the calculation results, it can be found that the frequency of change from 24 h to 14 h before the outburst fluctuates around 7 times. The average of the frequency of change is about 8 times from 12 h before the outburst to the outburst time. Over time, the closer it is to the outburst time, the more frequent the changes. The frequency of change approaches 10 times.

The Bi-LSTM prediction model is used to simulate the normal production gas emission quantity sequence and the gas emission quantity sequence including the eve of the accident. The average RSME of normal production gas emission quantity sequence is 0.006, and the average MAPE is 2.274%. The prediction results are in good agreement with the actual value, indicating that the Bi-LSTM prediction model has high accuracy for the gas emission quantity sequence. The gas emission prediction curve in normal production is shown in Figure 13A. The average RSME of gas emission quantity sequence at the moment before the outburst is 0.023, and the average MAPE is 10.14%, which are 3.8 times and 4.5 times of the normal, respectively. The gas emission prediction curve before the accident is shown in Figure 13B. This indicates that abnormal changes in gas emission quantity before the outburst has led to a decrease in the accuracy of the model. The loss functions of the model could be used as the early warning indicators for the outburst.

Analysis of Early Warning Results of Each Indicator System

The gas emission quantity data of Shigang Coal Mine during the normal production from 19 March to 20 March is used to calculate the statistical indicators, the deep learning indicators and the comprehensive indicators to conduct the early warning

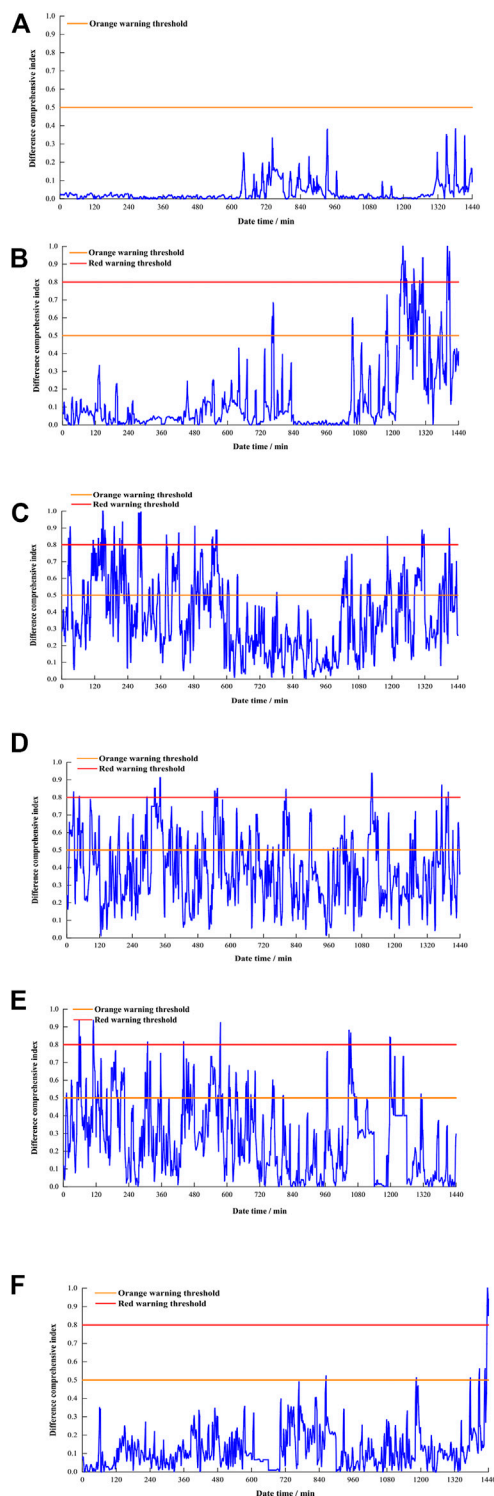


FIGURE 16 | Analysis of outburst warning results on March 19–24. **(A)** Analysis of outburst warning results on March 19 **(B)** Analysis of outburst warning results on March 20 **(C)** Analysis of outburst warning results on March 21 **(D)** Analysis of outburst warning results on March 22 **(E)** Analysis of outburst warning results on March 23 **(F)** Analysis of outburst warning results on March 24.

research and the judgment on the gas emission quantity. The results of the research are shown in **Figures 14, 15**:

As reflected by early warning results of gas emission quantity on March 19th and 20th, the deep learning indicators are used to analyze the gas emission quantity. Orange warnings with more than 0.5 appear many times, indicating that the deep learning indicators are overly sensitive to outburst early warnings; Statistical-based indicators can describe the characteristics of the abnormal changes in gas emission quantity to a certain extent, but the sensitivity is lower. The comprehensive indicators combine the sensitivity of deep learning indicators and the statistical indicators to abnormal changes in gas emission quantity, which have significant advantages in the accuracy of the gas outburst early warning.

Analysis of the Outburst Early Warning Results

According to the gas emission data of Shigang Coal Mine from March 19th to 24th, the comprehensive index model is used to carry out the early warning of the coal and gas outburst. The results are shown in **Figure 16**:

Through the analysis of the early warning of coal and gas outburst in Shigang Coal Mine from March 19th to 24th, the results show that the comprehensive index of gas outburst early warning fluctuates below 0.5 during the normal production period. At around 20:00 on March 20th, the early warning index rose sharply with many red warnings (comprehensive index exceeding 0.8) and continuous orange warnings (comprehensive index exceeding 0.5). From the 21st to 23rd, as the driving activity continued, the comprehensive index fluctuated rapidly and longer-time red warnings (exceeding 0.8) appeared every day, which reveals that the coal and gas outbursts was in the formation phase, and the gas was gushing out rapidly. From 22:00 on the 23rd to 12:00 on the 24th, the comprehensive index fluctuated below 0.5. It might be caused by the fact that the formed small protruding holes were blocked at the development phase, which stopped the gas from gushing out. After 12:00 on the 24th, the gas emission quantity changed drastically until the outburst occurred, and red warnings appeared many times at this stage.

The coal and gas outburst early warning model is used to verify and analyze the data of outburst accidents in Dongfeng Coal Mine and Hebi No. 6 mine. By collecting 24-h period of data at Dongfeng Coal Mine from 8:00 on April 8th to 8:00 on April 9th for early warning analysis, there were many orange warnings and red warnings. The outburst warning results of on Dongfeng coal mine are shown in **Figure 17A**. By collecting the data of Hebi No. 6 mine from 17:00 on June 3rd to 17:00 on June 4th for early warning analysis, it showed many orange warnings and red warnings. The outburst warning results of on Hebi Six Mineral are shown in **Figure 17B**. By comparing and analyzing the time series of the gas emission quantity, it is found that the gas emission quantity changes abnormally on the eve of coal and gas outburst, which is consistent with the occurrence law of coal and gas outburst.

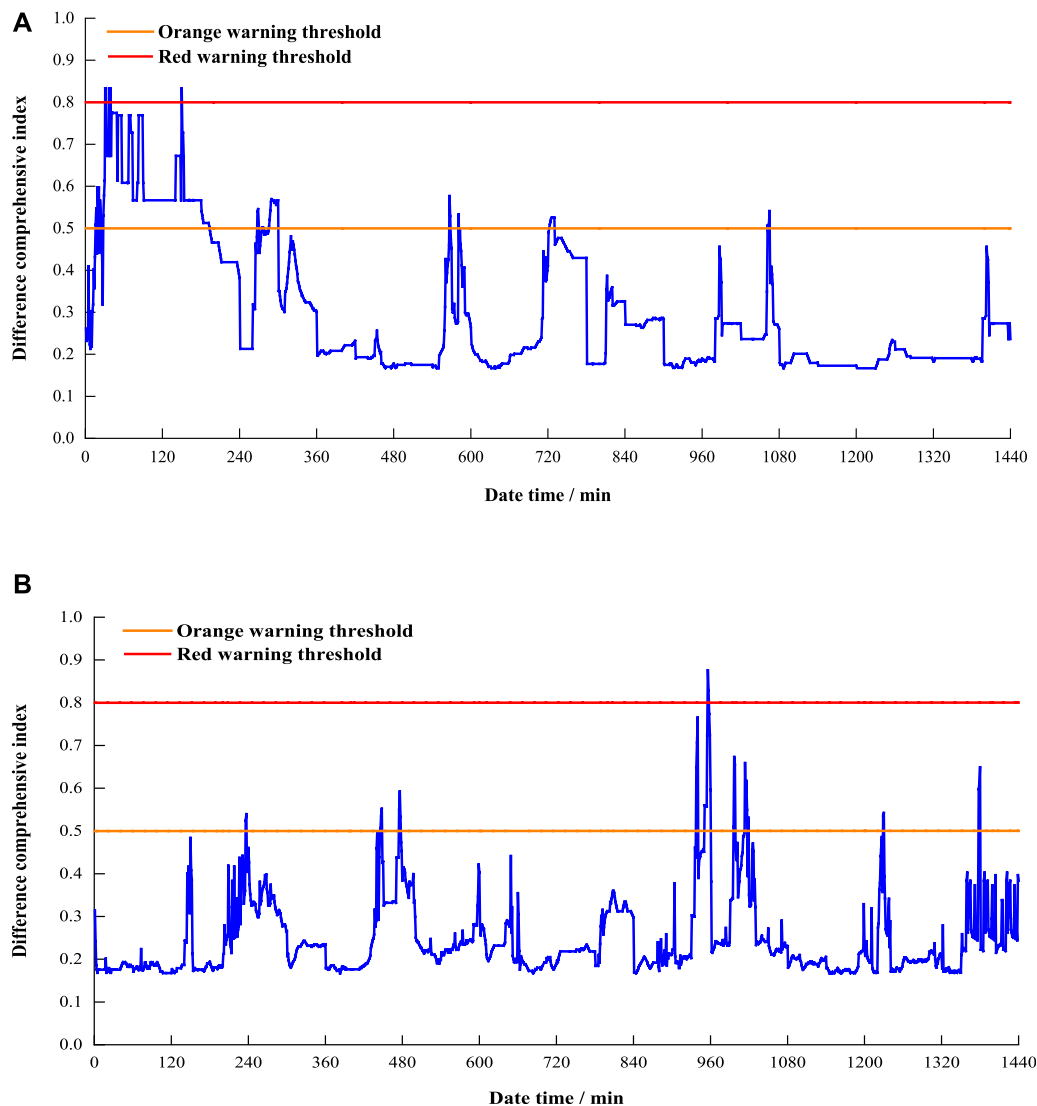


FIGURE 17 | Prominent warning results validation analysis. **(A)** Outburst warning results of on Dongfeng coal mine **(B)** Outburst warning results of on Hebi Six Mineral.

CONCLUSION

I. According to the analysis of the coal and gas outburst evolution process, a coal and gas outburst early warning index based on the combination of statistical indicators of the gas emission and deep learning indicators is proposed, which includes the moving average, the deviation ratio, the dispersion ratio, the fluctuation ratio, RMSE and MAPE.

II. The early warning indicators are examined in the “3.25” coal and gas outburst accident in Shigang Coal Mine. The statistical indicators, deep learning indicators and the comprehensive indicators are used for the early warning analysis on the gas emission quantity during the normal production period. By using the deep learning indicators to analyze the gas emission quantity, orange warnings (exceeding

0.5) appear many times, indicating that the deep learning indicators are overly sensitive to outburst early warnings. Statistical-based indicators can describe the characteristics of abnormal changes in gas emission quantity to a certain extent, but the sensitivity is lower. The comprehensive indicators combined with the deep learning indicators and statistical indicators successfully captures the abnormal changes in the gas emission quantity, which has significant advantages in the accuracy of gas outburst early warning and interprets the change rule of the gas emission quantity before the gas outburst.

III. Comprehensive indicators are used to mine and analyze the gas emission quantity data of Shigang Coal Mine. The model proposed in this work captured signals of abnormal changes in the gas emission on March 20th

(4 days before the accident), and orange warnings and red warnings were given continuously for many times. The accuracy and practicality of the model is also verified by the gas emission quantity data of Dongfeng Coal Mine and Hebi No. 6 mine.

DATA AVAILABILITY STATEMENT

The original contributions presented in the study are included in the article/Supplementary Material, further inquiries can be directed to the corresponding author.

REFERENCES

- Cai, C. C., Tao, Y., Zhu, T. Q., and Deng, Z. X. (2021). Short-Term Load Forecasting Based on Deep Learning Bidirectional LSTM Neural Network. *Appl. Sci.* 11 (17), 9383. doi:10.3390/app1120938310.3390/app11178129
- Chen, J., Zhu, C., Du, J., Pu, Y., Pan, P., Bai, J., and Qi, Q. (2022). A quantitative pre-warning for coal burst hazard in a deep coal mine based on the spatio-temporal forecast of microseismic events. *Process Saf. Environ. Protect.* doi:10.1016/j.psep.2022.01.082
- Du, J., Chen, J., Pu, Y., Jiang, D., Chen, L., and Zhang, Y. (2021). Risk Assessment of Dynamic Disasters in Deep Coal Mines Based on Multi-Source, Multi-Parameter Indexes, and Engineering Application. *Process Saf. Environ. Prot.* 155, 575–586. doi:10.1016/j.psep.2021.09.034
- Han, Y. L., Li, S., Hu, H. Y., and Luo, M. K. (2019). Prediction Model of Coal and Gas Outburst Based on Optimized GA-ELM. *Chin. J. Underground Space Eng.* 15 (6), 1895–1902. doi:10.1016/j.psep.2019.10.002
- Hu, Q. T., Zhou, S. N., and Zhou, X. Q. (2008). Mechanical Mechanism of Coal and Gas Outburst Process. *J. China Coal Soc.* 33 (12), 1367–1372. doi:10.13225/j.cnki.jccs.2008.12.018
- Li, X. Y., Li, T., and Ma, J. W. (2021). Soft Prediction of Coal-Mine Gas Concentration through the Mixture of Gaussian Processes under the Noisy Input Prediction Strategy. *J. Signal Process.* 37 (11), 2031–2040. doi:10.16798/j.issn.1003-0530.2021.11.003
- Lichtenberger, M. (2006). Underground Measurements of Electromagnetic Radiation Related to Stress-Induced Fractures in the Odenwald Mountains (Germany). *Pure Appl. Geophys.* 163 (8), 1661–1677. doi:10.1007/s00024-006-0083-5
- Long, N. Z., Yuan, M., Wang, G. L., Wang, Q. H., Xu, S. Q., and Li, X. L. (2020). Real-time Warning of Coal and Gas Outburst Based on Data Mining. *China Mining Mag.* 29 (11), 88–93+99. doi:10.12075/j.issn.1004-4051.2020.11.02
- Long, N. Z., Yuan, M., Wang, G. L., Xu, S. Q., and Li, X. L. (2021). Research on Early Warning of Coal and Gas Outburst Microseismic-Gas Interactive Response. *China Saf. Sci. J.* 31 (4), 125–132. doi:10.16265/j.cnki.issn1003-3033.2021.04.017
- Luo, M. K., Fan, C. J., LiYangZhang, S. Z. H. H. H., Yang, H. Z., and Lan, T. W. (2018). Failure Criteria of the Geological Dynamic System of Coal and Gas Outburst. *J. China Univ. Mining & Technology* 47 (1), 137–144. doi:10.13247/j.cnki.jcumt.000820
- National Bureau of Statistics China (2021). Statistical Bulletin of National Economic and Social Development of the People's republic of China in 2020. Available at: http://www.stats.gov.cn/tjsj/zxfb/202102/t20210227_1814154.html.
- Pu, Y., Apel, D. B., Liu, V., and Mitri, H. (2019). Machine Learning Methods for Rockburst Prediction-State-Of-The-Art Review. *Int. J. Mining Sci. Tech.* 29 (4), 565–570. doi:10.1016/j.ijmst.2019.06.009
- Qi, L. M., Lu, Y. T., Guan, L. H., and Qi, M. (2021). Exploration and Application of Determination Method of Sensitive index for Prediction of Coal and Gas Outburst. *Mining Saf. Environ. Prot.* 48 (3), 85–89. doi:10.19835/j.issn.1008-4495.2021.03.016
- Qin, H. J., Wei, J. P., Li, D. H., and Wu, Z. Q. (2021). Research on the Mechanism of In-Situ Stress in the Process of Coal and Gas Outburst. *J. China Univ. Mining & Technology* 50 (05), 933–942. doi:10.13247/j.cnki.jcumt.001327
- Song, D. Z., He, X. Q., Dou, L. M., Zu, Z. Y., Wang, A. H., and Li, Z. L. (2021). Research on MS Regional Detection Technology for Coal and Gas Outburst hazard. *China Saf. Sci. J.* 31 (1), 89–94. doi:10.16265/j.cnki.issn1003-3033.2021.01.013
- Wang, E. Y., Li, Z. H., Li, D. X., Liu, X. F., and Li, J. Z. (2020a). Application of Electromagnetic Radiation Monitoring Equipment in Monitoring and Warning of Coal and Gas Outburst. *Saf. Coal Mines* 51 (10), 46–51. doi:10.13347/j.cnki.mkaq.2020.10.008
- Wang, H., Wang, H., Xu, K., and Xu, Y. S. (2020b). Evolutionary Recurrent Neural Network for Image Captioning. *Neurocomputing* 401 (2), 249–256. doi:10.13976/j.cnki.xk.2020.920410.1016/j.neucom.2020.03.087
- Wang, S. Q. (2018). *Gas Time Series Prediction and Anomaly Detection Based on Deep Learning*. China: University of Mining and Technology. Doctoral dissertation. Available At: <https://kns.cnki.net/KCMS/detail/detail.aspx?db-name=CDFDLAST2019&filename=1019812115>.
- Wang, W., Li, Y., and Li, X. G. (2020c). Spatial -temporal Coupling Association Analysis of Coal Mine Gas Accidents from 2010 to 2018. *Saf. Coal Mines* 51 (5), 177–182. doi:10.13347/j.cnki.mkaq.2020.05.038
- Wang, Y. H., Liu, L. L., Fu, H., and Xu, Y. S. (2018). Esearch on Acoustic Emission Multi-Parameter Time Series Based Prediction of Gas Outburst. *China Saf. Sci. J.* 28 (5), 129–134. doi:10.16265/j.cnki.issn1003-3033.2018.05.022
- Wang, Y. H. (2020). Research on the Method of Coal and Gas Outburst Situation Awareness. Liaoning: Liaoning Technical University. Doctoral dissertation. Available at: <https://kns.cnki.net/KCMS/detail/detail.aspx?dbname=CDFDLAST-2021&filename=1020422328>.
- Wu, X. S., Tian, S. X., Ma, R. S., Xu, S. Q., Lin, H. Y., Yu, J., et al. (2021). Study on Prediction of Outburst Risk of Coal Roadway by Initial Gas Emission Law of Coal Body. *J. Saf. Sci. Tech.* 17 (4), 116–121. doi:10.1016/j.ijrmms.2015.07.006
- Wu, Y. (2021). *A Brilliant Answer Sheet of Coal Mine Gas Prevention and Control*. Beijing: China Energy News. Available at: http://www.cnenergynews.cn/meitan/2021/03/17/detail_2021031793399.html
- Xu, Y. S., and Cheng, Y. W. (2021). Prediction and Forecast of the SKPCA with NEAT Coal and Gas Outburst Risks. *J. Saf. Environ.* 21 (4), 1427–1433. doi:10.13637/j.issn.1009-6094.2020.0421
- Yang, Y., and Zhou, T. (2021). Comprehensive Analysis on Sensitive index of Coal and Gas Outburst Prediction in Working Face. *China Mining Mag.* 30 (z1), 325–331. doi:10.12075/j.issn.1004-4051.2021.S1.020
- Zhang, C. L., Wang, E. Y., Wang, Y. B., and Zhou, X. F. (2021). Spatial-temporal Distribution of Outburst Accidents from 2001 to 2020 in China and Suggestions for Prevention and Control. *Coal Geology. Exploration* 49 (04), 134–141. doi:10.3969/j.issn.1001-1986.2021.04.016
- Zhu, L. K., Yang, T. H., Xu, T., Zhao, G. H., and Xie, Z. H. (2018). Explore the Mechanism of Ground Stress and Gas Pressure in Coal-Gas

AUTHOR CONTRIBUTIONS

CW, LW and HH contributed to conception and design of the study. MJ organized the database. HH performed the statistical analysis. CW wrote the first draft of the manuscript. JW revised sections of the manuscript.

FUNDING

This paper was funded by the National Nature Science Foundation of China (Grant No. 52004243).

Outburst. *J. Mining Saf. Eng.* 35 (5), 1038–1044. doi:10.13545/j.cnki.jmse.2018.05.022

Conflict of Interest: The authors declare that the research was conducted in the absence of any commercial or financial relationships that could be construed as a potential conflict of interest.

Publisher's Note: All claims expressed in this article are solely those of the authors and do not necessarily represent those of their affiliated organizations, or those of the publisher, the editors and the reviewers. Any product that may be evaluated in

this article, or claim that may be made by its manufacturer, is not guaranteed or endorsed by the publisher.

Copyright © 2022 Wang, Wei, Hu, Wang and Jiang. This is an open-access article distributed under the terms of the Creative Commons Attribution License (CC BY). The use, distribution or reproduction in other forums is permitted, provided the original author(s) and the copyright owner(s) are credited and that the original publication in this journal is cited, in accordance with accepted academic practice. No use, distribution or reproduction is permitted which does not comply with these terms.



Study on the Overburden Failure Law of High-Intensity Mining in Gully Areas With Exposed Bedrock

Tan Yi^{1,2}, Xu Han¹, Yan Weitao^{2*}, Guo Wenbing^{1,2}, Bai Erhu^{1,2}, Qi Tingye³, Yin Dawei⁴, Hao Bingyuan³, Cheng Hao¹ and Shao Minghao¹

¹School of Energy Science and Engineering, Henan Polytechnic University, Jiaozuo, China, ²State Collaborative Innovation Center of Coal Work Safety and Clean-efficiency Utilization, Henan Polytechnic University, Jiaozuo, China, ³College of Mining Engineering, Taiyuan University of Technology, Taiyuan, China, ⁴College of Energy and Mining Engineering, Shandong University of Science and Technology, Qingdao, China

OPEN ACCESS

Edited by:

Wei Liu,
Chongqing University, China

Reviewed by:

Guangming Zhao,
Anhui University of Science and
Technology, China
Wen Nie,
Jiangxi University of Science and
Technology, China

*Correspondence:

Yan Weitao
yanweitao@hpu.edu.cn

Specialty section:

This article was submitted to
Geohazards and Georisks,
a section of the journal
Frontiers in Earth Science

Received: 11 December 2021

Accepted: 14 February 2022

Published: 03 March 2022

Citation:

Yi T, Han X, Weitao Y, Wenbing G,
Erhu B, Tingye Q, Dawei Y,
Bingyuan H, Hao C and Minghao S
(2022) Study on the Overburden
Failure Law of High-Intensity Mining in
Gully Areas With Exposed Bedrock.
Front. Earth Sci. 10:833384.
doi: 10.3389/feart.2022.833384

Most hilly areas are dotted with gullies, some of which contain plenty of water, especially in rainy seasons. Once surface water penetrates the underground working face, it will lead to an increased water inflow of the working face. Even worse, it may induce water and sand burst accidents. To prevent geological disasters such as water and sand burst and ensure the safe production in coal mines, it is necessary to reveal the development law of “two zones” in the overburden caused by shallow-seam fully mechanized top coal caving high-intensity mining in hilly areas with exposed bedrock and timely grasp the communication between the water-flowing fractured zone (WFFZ) and the water in surface gullies. In this study, the working face P2 of the exposed bedrock surface in the Coal Mine DN is taken as the research object. First, the characteristics of overburden movement and the law of exposed bedrock surface movement in areas with exposed bedrock were investigated through similar simulation. Meanwhile, the temporal-spatial evolution of overburden movement caused by shallow-seam fully mechanized top coal caving high-intensity mining was clarified, and the mode of overburden movement was revealed. Moreover, the reason why the water inflow of the underground working face increases suddenly was theoretically explained. The following conclusions were drawn: Under shallow-seam fully mechanized top coal caving high-intensity mining, the WFFZ of the working face P2 is directly connected to the exposed bedrock surface, and the movement of the overburden is subject to the typical “two-zone” mode. The development height of the WFFZ is greater than the value in the traditional “three-zone” mode calculated according to the empirical formulas. The ratio of the WFFZ height to the mining thickness is 43.75. Under the “two-zone” mode, a water-flowing channel exists in the overburden near the open-off cut and the stopping line. When the surface water source is in the right position, the water inflow of the underground working face will increase suddenly.

Keywords: water-containing gullies, exposed bedrock, shallow thick coal seam, fully mechanized top coal caving mining, water-flowing fractured zone

INTRODUCTION

Underground coal mining often induces large-scale damage to overburden and surface movement, further accelerating the occurrence of mine geological disasters such as water and sand burst under the condition of shallow-seam mining (Kratzsch, 1983; Gray, 1990). The key to preventing water and sand burst is to reveal the height of “two zones” (i.e., the caved zone and the fractured zone) in the overburden (Sun et al., 2011; Author Anonymous, 2014). At present, the prediction of the height of the “two zones” in China is mainly based on the calculation formulas concluded with reference to the conventional mining and fully mechanized mining faces in the 1950s and 1990s. The formulas are presented in the *Code for coal pillar preservation and pressed coal mining of buildings, water bodies, railways, and main tunnels* (hereinafter referred to as the *Code*) (State Administration of s, 2017). With the popularization of fully mechanized top coal caving mining and one-time full thickness mining under a large mining height, the mining height and advancing speed of the working face, together with the height of “two zones,” have increased significantly (Yonghua and Renchang, 2003; Yanchun et al., 2011). Relevant scholars have found the limitations of the calculation formulas for the height of “two zones” in the *Code* and conducted studies on the height of “two zones” under large mining height, thin bedrock, small buried depth, and fully mechanized top coal caving mining (Minggao and Xiexing, 1995; Baobin and Xiaolei, 2013; Jianjun et al., 2008; Xiaoqian and Zhenquan, 2015; Duan et al., 2011; Qingxian et al., 2013; Yiqiong, 2008), following which some conclusions have been put forward.

However, studies on the height of “two zones” in the overburden of fully mechanized top coal caving high-intensity mining working faces in the shallow-seam gully areas remain insufficient. Such studies are of prime importance for ensuring the production safety of the mines, especially for those water-containing gully areas in the overburden. Therefore, research on the structural characteristics of overburden under fully mechanized top coal caving mining in the shallow-seam gully areas with exposed bedrock, as well as the development height of “two zones” in the flowing fractured zone, is of great significance for improving the basic theory and guiding the field production.

The key to studying the height of “two zones” is to reveal the mechanism of overburden migration. Currently, studies on the mechanism of overburden migration in shallow-seam high-intensity mining working faces mainly focus on the displacement migration mode of the overburden (Weitao et al., 2021; Yunjiang et al., 2021), the distribution law of overburden failure (Rezaei et al., 2015; Sasaoka et al., 2015; Thongrapha et al., 2015; Vervoort, 2016; Enke et al., 2020), and the conduction relationship concerning overburden failure (Zhiguo et al., 2019; Xiaoshuai et al., 2021; Zhenkang et al., 2021).

In this study, the working face P2 in the Coal Mine DN, which is located in hilly areas with an exposed bedrock surface and is mined by the method of shallow-seam fully mechanized top coal caving, is taken as the research object. First, the geological conditions of fully mechanized top coal caving in hilly areas with exposed bedrock were analyzed, and the structural

TABLE 1 | Gully distribution.

Gully No.	Strike (angle with the direction of working face advancement, °)	Location (distance from the open-off cut of the working face, m)
1	30	–290~–570
2	70	850~970
3	90	1,100

characteristics of the roof overburden in the working face were experimentally determined. Besides, the overburden fractures and the height of “two zones” in the working face were investigated by means of experiments and theoretical analysis. Furthermore, the height of “two zones” in the overburden was explored based on the changes of mine water inflow. Finally, the on-site measured height and the results obtained from the empirical formulas were compared. The research results obtained are crucial.

PROJECT BACKGROUND

Surface Profile

The Coal Mine DN has a designed production scale of 4.0 Mt/a. The working face P2, which is 220 m in width and 1,138 m in the designed mining length, is the second working face in the first panel. The coal seam 3#, whose ground elevation ranges from +658 m to +780 m and floor height ranges from +509 m to +472 m, is the mining coal seam. The working face P1 (450 m in the north) and the unexploited region lie on the west of the working face P2, while the working face P3 (unexploited) lies on the east of it.

In terms of its surface landform, the working face features unique loess-covered low mountains and an exposed bedrock surface. Three gullies (numbered 1, 2, and 3 from south to north) where water flows all year round with a total volume of 15–20 tons/h (larger in the rainy season) exist in the working face (Table 1). The water mainly comes from descending springs in the weathered crust (Figure 1).

Mining Technical Parameters

The working face adopts longwall fully mechanized top coal caving, and the roof is managed by the all caving method. The relevant mining technical parameters are listed in Table 2.

MEASURED HEIGHT OF “TWO ZONES” IN THE OVERBURDEN

Calculation Based on Empirical and Literature Formulas

According to the relevant data of the mines, the coal seam 3# of the working face P2 belongs to the Taiyuan Formation of the upper carboniferous system and has a thickness of 4.8 m, a stable morphology, and a complex structure. In addition, the drilling

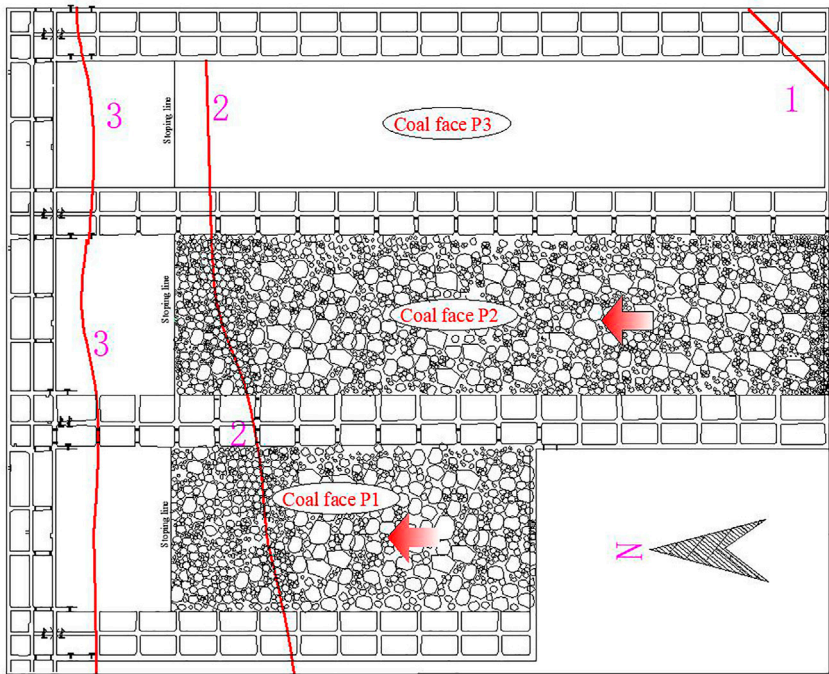


FIGURE 1 | Gullies of working faces P2 and P3.

TABLE 2 | Mining technical parameters of the fully mechanized caving faces P2 and P1.

Name		Mining technical parameters of P2	Mining technical parameters of P1
Working face parameter	Strike length D ₃	1,138 m	550 m
	Dip length D ₁	220 m	230 m
	Boundary mining depth	210 m	240 m
	Average on the rise H ₂	190 m	220 m
	Average at the open-off cut H ₃	180 m	190 m
	Average at the stopping line H ₄	240 m	240 m
Mining coal seam	Average mining depth	200 m	229 m
		3# coal seam	3# coal seam
	Average mining thickness	4.8 m	4.8 m
	Average inclination angle	5.0°	5.0°
	Advancement speed	4 m/d	4 m/d
	Working face strike	0°	0°
Mining method	Working face dip	90°	90°
		Longwall fully mechanized mining on the strike (large mining height)	Longwall fully mechanized mining on the strike (large mining height)
Roof management method		All caving method	All caving method

histogram near the working face reveals that the lithology of the overburden of the working face P2 is comprehensively evaluated as medium-hard (Figure 2).

Based on a large number of measured data of the water-flowing fractured zone (WFFZ) under the condition of top coal caving mining, Chinese scholars, after regression, have obtained empirical formulas for the height of the WFFZ applicable to top coal caving mining. Among them, the empirical and literature formulas of the height of the WFFZ under top coal caving mining

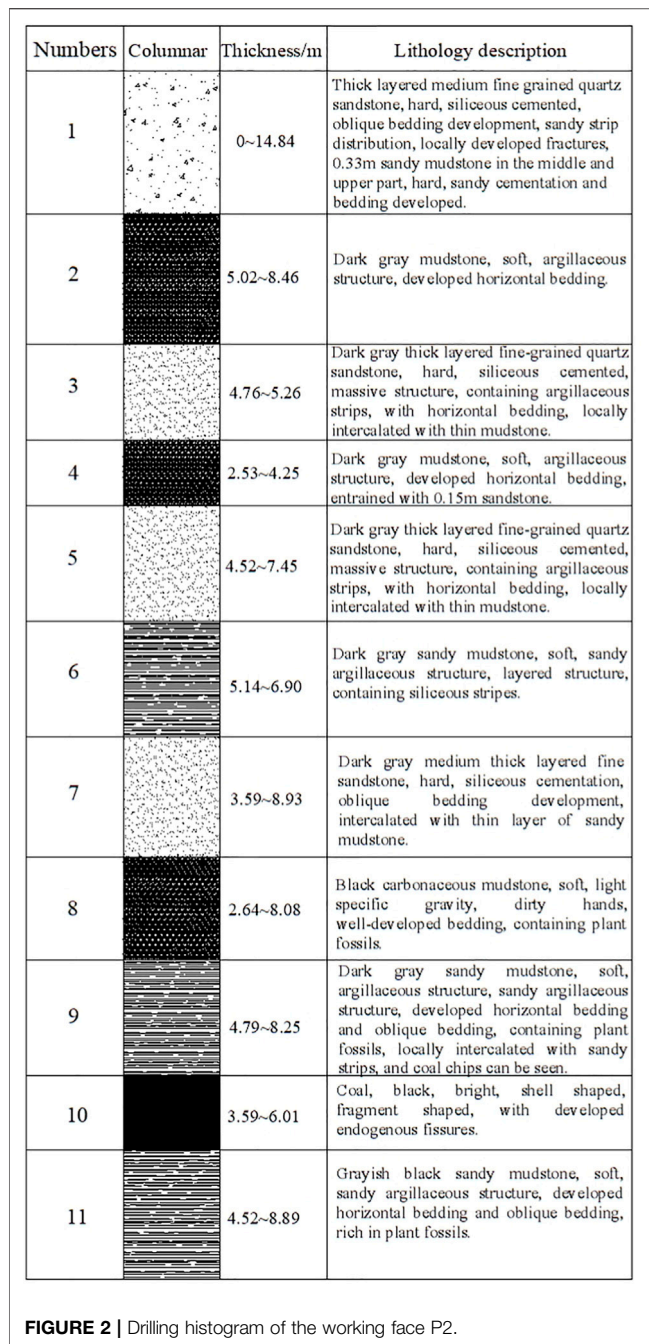
of gently sloped medium-hard overburden thick coal seam are as follows.

The formula proposed by Liu is

$$H_{li} = \frac{100M}{0.23M + 6.1} \pm 10.42 = 56.21\text{m} \sim 77.05\text{m}, \tag{1}$$

The formula proposed by Teng is

$$H_{li} = 20M + 10 = 106\text{m}, \tag{2}$$



The formula proposed by Xu is

$$H_{li} = \frac{100M}{0.26M + 6.88} \pm 11.49 = 47.57\text{m} \sim 70.55\text{m} \quad (3)$$

The formula proposed by Ding is

$$H_{li} = \frac{100M}{0.19M + 7.74} \pm 13.26 = 42.22\text{m} \sim 68.74\text{m}, \quad (4)$$

According to the above formulas, the selected points for calculating the height of the WFFZ in the working face P2 are

56.21–77.05 m, 106 m, 47.57–70.55 m, and 42.22–68.74 m, respectively. The height of the WFFZ in the working face P2 under thick-seam top coal caving mining ranges from 42.22 to 106 m, and the ratio of the WFFZ height to the mining thickness is 8.80–22.08.

Measurement and Analysis of WFFZ

In the light of the theory of mining subsidence, the judgment formula for sufficient mining of the working face is

$$c = D/H,$$

When c is greater than or equal to 1.2–1.4, the working face is mined sufficiently, and the vertical and horizontal ranges of overburden failure reach the maximum. When c is smaller than 1.2–1.4, the working face is mined insufficiently, and the damage range of overburden is not fully developed. The mining of the P1 working face was completed in early February 2006, with a dip of 230 m, a strike of 550 m, and a mining depth of 229 m:

$$c_1 = D_1/H = 230/229 \approx 1.0, \\ c_3 = D_3/H = 550/229 \approx 2.4,$$

It can be seen from the above formula that the strike of the P1 working face is mined sufficiently, while the dip is mined insufficiently. That is, the overburden failure of the working face is not fully developed.

According to the hydrological observation data, there are three sources of water in the overburden, that is, the earth surface, the loose layer, and the bedrock. Relatively less water comes from the loose layer and the bedrock. The bedrock in the overburden and the aquifer of loose layer have been connected to the working face after the recovery of the working face P1, but the water inflow is merely 6 m³/h during the recovery.

The working face P2 is close to the working face P1, and they share similar hydrogeological and mining conditions. After the working face P2 starts to be recovered following the working face P1, the dip of the working face P2 can be sufficiently mined, and the longitudinal failure of the overburden can reach the maximum range. At this time, if the longitudinal failure of the overburden reaches the surface, the surface water will flow into the working face, increasing the water inflow of the working face. Therefore, the surface cracks and changes of water inflow of the working face P2 can tell whether the WFFZ in the overburden has reached the surface.

In view of the above situation, observation stations shall be established on the surface for crack observation, and monitoring points shall be established underground for water inflow monitoring. The specific layout scheme is as follows:

① The three gullies above the working face are mainly composed of descending springs in the weathered crust. The location of the gullies and observation line is shown in **Figure 3**. An observation line A with 46 observation stations (spacing 20 m) is arranged along the strike of the working face. Among the observation stations, A1–A6, A17–A19, and A28–A32 are on the exposed bedrock surface and the others are on the loess-covered surface. Besides, an observation line B with 18

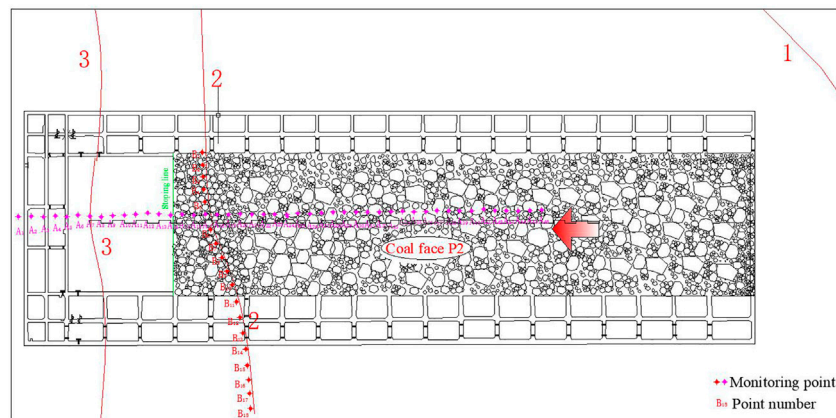


FIGURE 3 | Location of gully and observation lines.

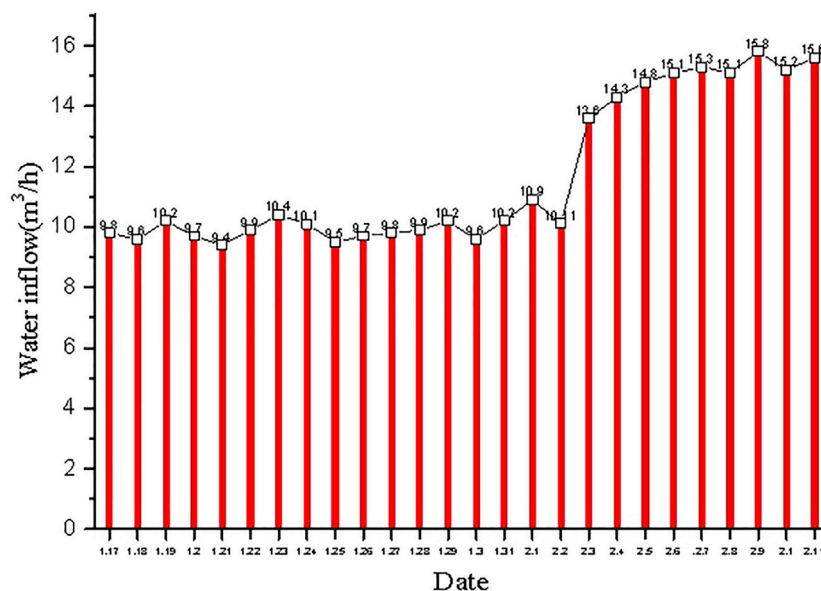


FIGURE 4 | Change of water inflow in the working face P2.

observation stations (spacing 20 m) is arranged along the No. 2 gully, and the whole line is on the exposed bedrock surface.

② During the recovery of the working face P2, the water inflow of the working face is monitored underground six times a day. The relevant data on the hourly water inflow are listed in Table 3.

As illustrated in Figure 4, during the recovery, the water inflow of the working face P2 was around 10 m³/h. On 3 February 2007, the water inflow increased abruptly to 13.6 m³/h and then was maintained at about 15 m³/h. Taking the mining surface overburden during the recovery (Figure 5) into consideration, at this time, penetrating cracks had been found at the A17 observation station of the No. 2 gully. Therefore, it is determined that the WFFZ in the overburden had developed to the exposed bedrock surface,

with the maximum WFFZ height and the ratio of the WFFZ height to the mining thickness being 226 m and 47.08, respectively. The ratio calculated by the empirical formulas mentioned above is only 8.80–22.08, which is far smaller than the measured value.

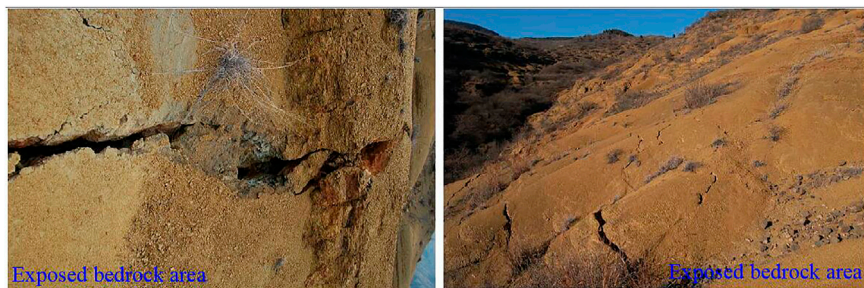
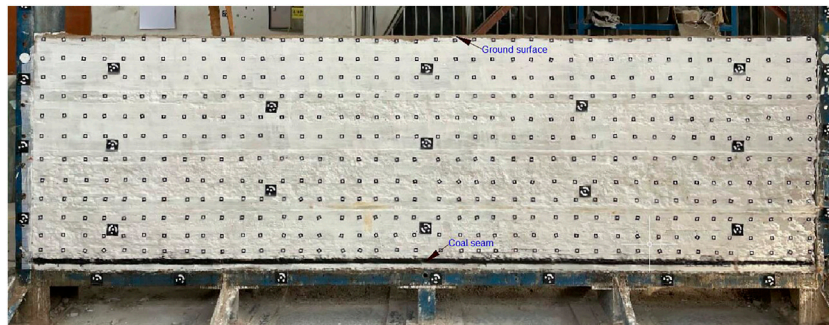
EXPERIMENTS AND RESULTS

Experimental Design

To simulate WFFZ development under high-intensity mining, a physical simulation experiment was performed according to the mine geological and mining data. To simplify the experimental conditions, the surface is simplified to horizontal terrain in this paper. According to the characteristics of overburden and simulated

TABLE 3 | Water inflow of the fully mechanized caving face P2.

Time	Water inflow (m ³ /d)	Water inflow (m ³ /d)	Date	Water inflow (m ³ /d)	Water inflow (m ³ /d)
1.17	235.2	9.8	1.30	230.4	9.6
1.18	230.4	9.6	1.31	244.8	10.2
1.19	244.8	10.2	2.1	261.6	10.9
1.20	232.8	9.7	2.2	242.64	10.11
1.21	225.6	9.4	2.3	326.4	13.6
1.22	237.6	9.9	2.4	343.2	14.3
1.23	249.6	10.4	2.5	355.2	14.8
1.24	242.4	10.1	2.6	362.4	15.1
1.25	228	9.5	2.7	367.2	15.3
1.26	232.8	9.7	2.8	362.4	15.1
1.27	235.2	9.8	2.9	379.2	15.8
1.28	237.6	9.9	2.10	364.8	15.2
1.29	244.8	10.2	2.11	374.4	15.6

**FIGURE 5** | Surface rock cracks above the working face.**FIGURE 6** | Physical model experiment.

materials, the simulated geometric similarity ratio is 1:200, the unit weight ratio is 0.6, the stress ratio is 0.004, and the time ratio is 0.082. Gypsum, calcium carbonate, and fine sand are used as raw materials for the production of simulation materials. After each layer is laid, the mica powder is evenly spread as the joint surface between rock layers. The finished model is shown in **Figure 6**.

Overburden Failure Law

After the model was made and dried for 1 week, the simulated excavation was carried out by means of one-time full thickness

mining in sections. The rock stratum failure in each excavation stage is shown in **Figure 7**.

When the working face is excavated for 15 cm, the roof of the coal seam falls and accumulates in blocks in the goaf (**Figure 7A**). When the working face is excavated for 60–100 cm, the immediate roof falls. As the excavation proceeds, the roof continues to collapse, forming a trapezoidal collapse space above the goaf (**Figures 7B,C**). When the working face is excavated for 110 cm, all overburden bedrock in the coal seam collapses, and surface cracks run through the working face (**Figure 7D**).

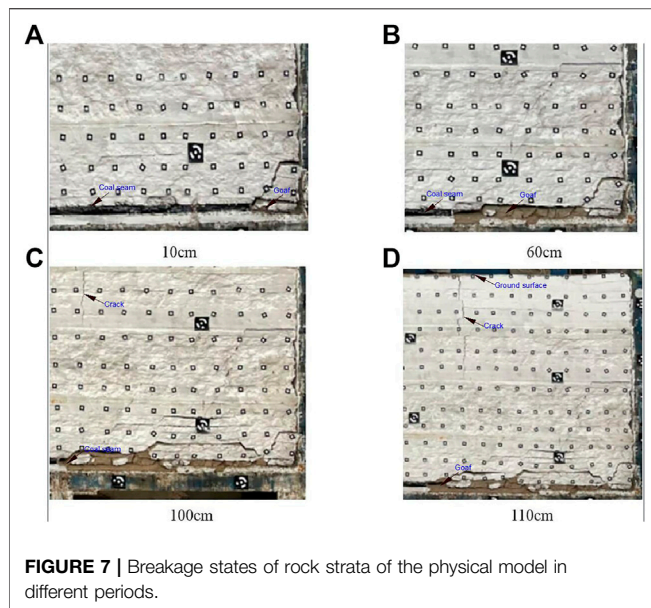


FIGURE 7 | Breakage states of rock strata of the physical model in different periods.

According to the pressure arch theory, a pressure arch exists on the periphery of the collapse space. In the initial stage of excavation, the height of the rock arch increases continuously, and the roof repeats the cyclic process of “arch formation and arch breakage.” In this process, the rock and soil mass above the rock arch only undergo bending compression, and the overburden balance structure belongs to a “rock arch.” When the excavation reaches 110 cm, the thickness of the overburden becomes smaller than the critical arch height of the rock arch. Consequently, the rock arch is broken, and the overburden movement directly enters the “no arch” stage. In addition, the cracks connect the surface and the working face, and the WFFZ directly reaches the surface. Under such conditions, the mining balance structure of rock and soil mass develops from “rock arch” to “no arch.”

DISCUSSION

High-intensity mining is characterized by shallow seam, large mining thickness, and high advancing speed. Under high-intensity mining, the overburden and the surface are seriously damaged, which mainly goes through the following three periods.

Period 1. When the failure height of the overburden is smaller than its thickness:

In this stage, as the working face continues to advance, the overburden first bends and then breaks when the maximum tensile intensity in the middle of the rock stratum is exceeded. The collapse degree of the roof mainly depends on the thickness and lithology of the overburden as well as the mining method. With the continuous expansion of the goaf area, the lower strata of the roof will fracture and collapse when their limit span is reached. When the collapsed gangue fails to completely fill the goaf, the overburden becomes suspended, adding its own weight to the surrounding rock of the goaf via beams and plates. As a result, a

pressure arch is formed in the surrounding rock. As the horizontal and vertical failures of the overburden expand, the span and height of the pressure arch are also increasing. In this stage, the failure height of the overburden is smaller than its thickness (**Figure 8A**).

Period 2. When the failure height of the overburden equals its thickness:

At this time, the overburden is in a critical state of failure. The height of the pressure arch in the overburden and the failure height of the overburden both reach the maximum. The overburden is damaged in its full thickness, and the WFFZ reaches the surface (**Figure 8B**).

Period 3. After the failure height of the overburden equals its thickness:

As the working face continues to advance, the overburden failure only develops horizontally. That is, the failure height of the overburden no longer changes, but the horizontal failure range of the overburden expands with the advancement of the working face (**Figure 8C**).

The above stages can be divided into two states, i.e., “rock arch” and “no arch,” according to the existence state of a pressure arch in the overburden.

State 1: “Rock Arch”

In this state, the rock strata in the pressure arch are broken seriously and are in the pressure release area. The weight of the rock strata outside the pressure arch is transmitted to the foot of the pressure arch. As the working face advances, the height and dimension of the pressure arch are increasing, and the arch foot on the advancing side of the working face is also moving forward. The height of the pressure arch reaches the limit if it equals the thickness of the overburden. This state corresponds to Periods 1 and 2 described above.

State 2: “No Arch”

In this state, as the working face continuously advances, the pressure arch breaks, and hence, no pressure arch exists in the overburden. At this time, a conduction channel, which directly connects to Positions A and B on the surface, occurs between the continuous moving rock stratum and the broken rock stratum above the open-off cut and the advancing position of the working face. The two positions can be determined through the following methods:

$$L = H \cot \varphi,$$

where L is the horizontal distance from Position A to the open-off cut or from Position B to the advancing position of the working face, m; H is the thickness of the overburden, m; and φ is the breaking angle of the bedrock, °. Similar material model tests show that the breaking angle of the bedrock is about 48°.

When there are water-containing gullies near Positions A and B, the water will flow into the working face, hence increasing its water inflow.

Actual measurement reveals that the No. 2 gully is 168–288 m away from the stopping line where the mining depth is about 240 m. The calculated distance between Position B and the stopping line is

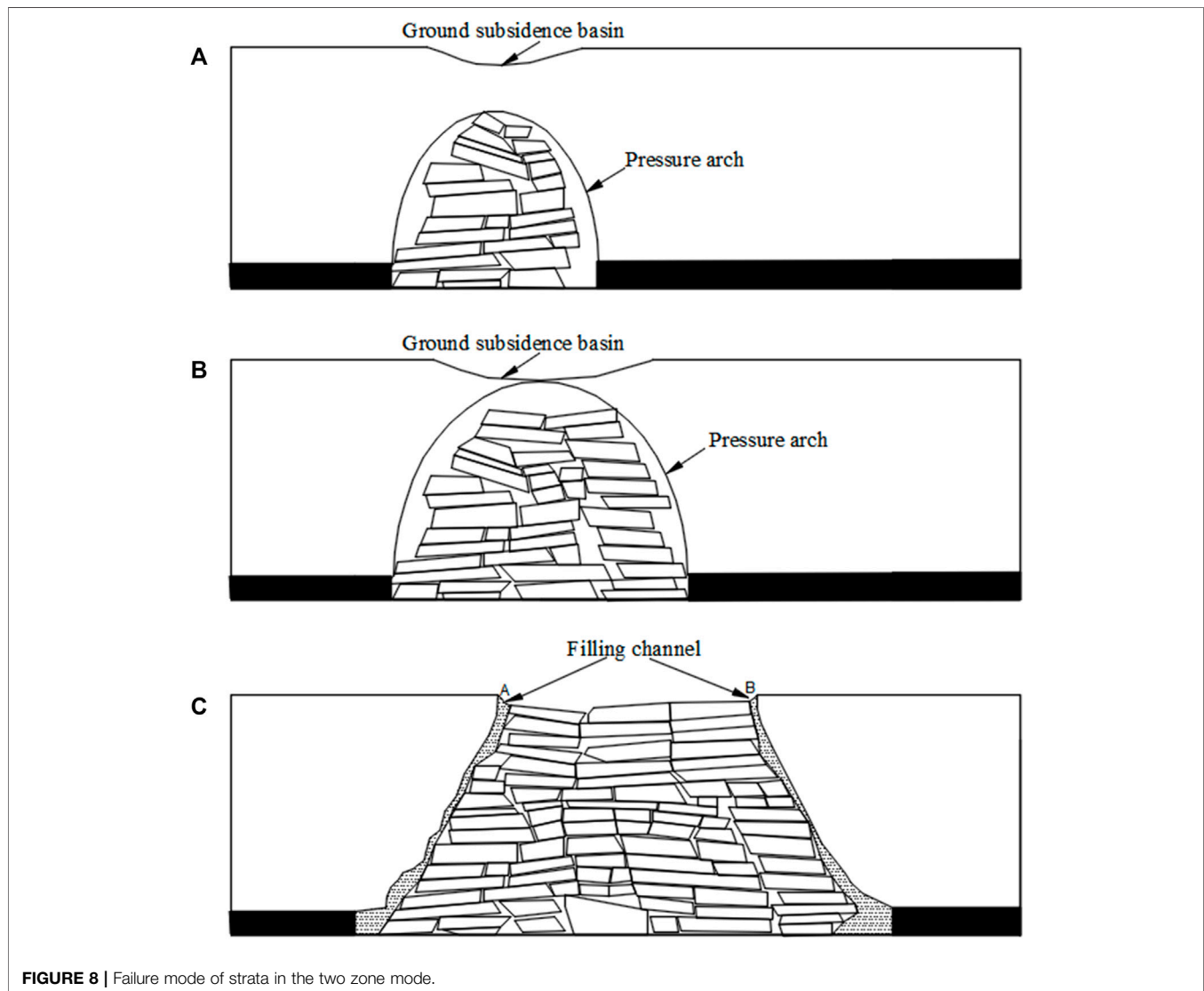


FIGURE 8 | Failure mode of strata in the two zone mode.

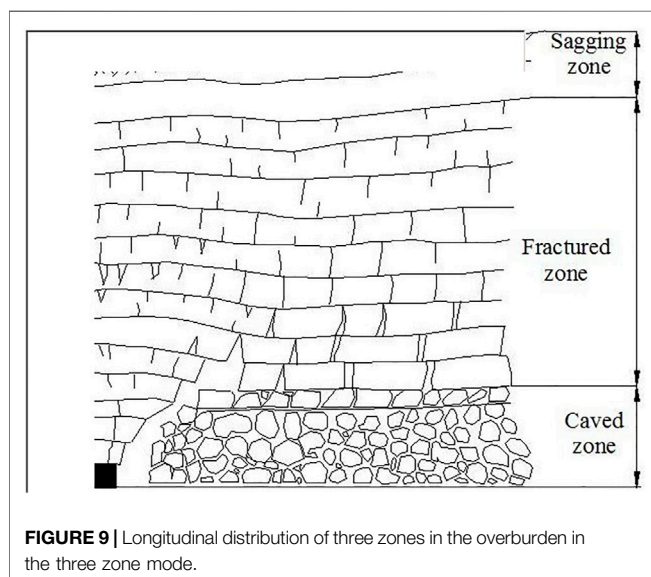


FIGURE 9 | Longitudinal distribution of three zones in the overburden in the three zone mode.

$$L_1 = H_t \cot 48^\circ = 240 \times 0.9 = 216\text{m}$$

It can be concluded that the No. 2 gully is located near Position B of the working face P2. After the working face P2 starts to be recovered following the working face P1, the dip can reach the state of sufficient mining, and the longitudinal failure of the overburden can reach the maximum range. The WFFZ reaches the surface, forming water-flowing channels on both sides of the stopping line and open-off cut. As a result, the water inflow in the underground working face increases.

Traditionally, “three zones” (i.e., caved zone, fractured zone, and sagging zone) exist in the overburden of the working face (Figure 9). The prediction formulas for the height of the WFFZ described in *Project Background* are based on the “three-zone” mode. After the recovery of the working face P2, only the caved zone and fractured zone remain in the overburden of the working face, which belongs to a typical “two-zone” mode. The prediction formula of the WFFZ based on the traditional “three-zone” mode is not suitable for the “two-zone” mode, which explains the large deviation of predicted values through the formulas.

CONCLUSION

- 1) The overburden of the working faces P2 and P1 moves under the “two-zone” mode. The height prediction formula of the WFFZ based on the traditional “three-zone” mode is inapplicable to the “two-zone” high-intensity mining mode, which results in the relatively small calculated result. After the working faces P2 and P1 were recovered, both the strike and the dip reach the state of sufficient mining, and the height of the WFFZ is the most fully developed.
- 2) Under the “two-zone” mode, a conduction channel that directly connects to the surface exists between the continuous moving rock stratum and the broken rock stratum above the open-off cut and the advancing position of the working face. If there is a water source near the surface of the channel, the water will flow into the working face, causing an increase in the water inflow of the underground working face.

DATA AVAILABILITY STATEMENT

The raw data supporting the conclusion of this article will be made available by the authors, without undue reservation.

REFERENCES

- Dingtao, C., and Wenping, L. (2014). Estimation Method for Height of Fratured Zone with in Coal Mining Area. *Chin. J. Geol. Hazard Control*. 1, 63–69.
- Baobin, G., and Xiaolei, Z. M. W. (2013). Dynamic Development Characteristics of Two Zones of Overburden Strata under Conditions of Compound Roof Highly Gassy and Thick Coal Seam in Full-Mechanized Top Coal Caving Faces. *Chin. J. Rock Mech. Eng.* 31, 3444–3451.
- Duan, H., Zhu, S., and Cao, S., Zhang, M. (2011). Study on Method to Set Safety Coal and Rock Pillar for Full Mechanized Top Coal Caving Mining under Water Body. *Coal Sci. Tech.* 11, 1–4.
- Enke, H., Qiang, W., Zhenni, Y., Wei, C., and Jiangbo, W. (2020). Height Prediction of Water-Flowing Fracture Zone with a Genetic-Algorithm Support-Vector-Machine Method. *Int. J. Coal Sci. Tech.* 7, 740–751.
- Gray, R. E. (1990). Mining Subsidence ? Past, Present, Future. *Int. J. Mining Geol. Eng.* 8, 400–408. doi:10.1007/bf00920651
- Jianjun, C., Qihua, M., and Yitai, W. (2008). Study of Wide Strip Mining Based on Spatial Structure Principle of Overlying Strata. *Coal Sci. Tech.* 1, 68–72.
- Kratzsch, H. (1983). *Mining Subsidence Engineering*. Springer, Berlin.
- Minggao, Q., and Xiexing, M. (1995). Theoretical Analysis of the Structural Form and Stability of Overlying Strata in Long Wang Mining. *Chin. J. Rock Mech. Eng.* 2, 97–106.
- Qingxian, S., Yi, M., and Xinliang, Y. (2013). Study on “Two Zones” Height of Overlying of Fully-Mechanized Technology with High Mining Height at Hongliu Coal Mine. *J. China Coal Soc.* 38, 283–286.
- Rezaei, M., Hossaini, M. F., and Majdi, A. (2015). A Time-independent Energy Model to Determine the Height of Distressed Zone above the Mined Panel in Longwall Coal Mining. *Tunnelling Underground Space Tech.* 47, 81–92. doi:10.1016/j.tust.2015.01.001
- Sasaoka, T., Takamoto, H., Shimada, H., Oya, J., Hamanaka, A., and Matsui, K. (2015). Surface Subsidence Due to Underground Mining Operation under Weak Geological Condition in Indonesia. *J. Rock Mech. Geotechnical Eng.* 7, 337–344. doi:10.1016/j.jrmge.2015.01.007
- State Administration of safety, State Administration of coal mine safety, state energy administration, state railway administration (2017). *Buildings Water, Railways and Main Well Lane of Coal Pillar and Mining Regulations*. Beijing: China Coal Industry Publishing Huose.
- Sun, Y., and Xu, Z., Dong, Q. (2011). Monitoring and Simulation Research on Development of Water Flowing Fractures for Coal Mining under Xiaolangdi Reservoir. *Chin. J. Rock Mech. Eng.* 31, 3444–3451.
- Thongprapha, T., Fuenkajorn, K., and Daemen, J. J. K. (2015). Study of Surface Subsidence above an Underground Opening Using a Trap Door Apparatus. *Tunnelling Underground Space Tech.* 46, 94–103. doi:10.1016/j.tust.2014.11.007
- Vervoot, A. (2016). Surface Movement above an Underground Coal Longwall Mine after Closure. *Nat. Hazards Earth Syst. Sci.* 16, 2107–2121. doi:10.5194/nhess-16-2107-2016
- Weitao, Y., Junjie, C., and Tan, y. (2021). Theoretical Analysis of Mining Induced Overburden Subsidence Boundary with the Horizontal Coal Seam Mining. *Adv. civil Eng.* 6657738.
- Xiaoqian, S., and Zhenquan, W. Z. J. (2015). Height Prediction of the “Two Zones” in Shallow Coal Seam by Slicing Ming. *Mining Res. Dev.* 2, 69–72.
- Xiaoshuai, L., Kun, P., Jun, P., and Di, H. (2021). Experimental Investigation of Cyclic Wetting-Drying Effect on Mechanical Behavior of a Medium-Grained sandstone. *Eng. Geology* 293, 106335.
- Yanchun, X., Juncheng, L., and Shiqi, L. (2011). Calculation Formula of “Two-zone” height Overlying Strata and its Adaptability Analysis. *Coal Mining Tech.* 2, 4–7.
- Yiqiong, X. (2008). Research on Movement and Evolution Law of Breaking of Overlying Strata in Shallow Coal Seam with a Thin Bedrock. *Rock Soil Mech.* 2, 512–516.
- Yonghua, K., and Renchang, J. (2003). Actuality and Developing Trend of Long wall Top Coal Caving Mining under Water. *Coal Mining Tech.* 1, 15–18.
- Yunjiang, Sun., Jianping, Zuo., and Karakus, Murat. (2021). A New Theoretical Method to Predict Strata Movement and Surface

AUTHOR CONTRIBUTIONS

TY conceptualized the research idea, wrote the original draft, and was involved in funding acquisition. YW performed the methodology, ran the software, supervised the project, and reviewed and edited the paper. XH and GW validated the data. BE was involved in formal analysis. YD and HB investigated the data. QT obtained the resources. TY and XH curated the data. GW was involved in data visualization. XH was responsible for project administration. All authors have read and agreed to the published version of the manuscript.

FUNDING

This work was financially supported by the National Natural Science Foundation of China (52174108, 51974105, and 52104127), Program for Outstanding Young Talent Projects of Henan Province (222300420045), Program for Science and Technology Innovation Talents in Universities of Henan Province (21HASTIT024), Open Fund of State Key Laboratory of Water Resource Protection and Utilization in Coal Mining (GJNY-18-73.16), State Key Laboratory of Coal Resources in Western China (SKLCRK1912), and Scientific and Technological Innovation Research Team of Henan Polytechnic University (T2021-5).

- Subsidence Due to Inclined Coal Seam Mining. *Rock Mech. Rock Eng.* 54, 2723–2740.
- Zhenkang, Wang., Wenping, Li., Qiqing, Wang., Yanbo, Hu., and Jiafa, Du. (2021). Monitoring the Dynamic Response of the Overlying Rock–Soil Composite Structure to Underground Mining Using BOTDR and FBG Sensing Technologies. *Rock Mech. Rock Eng.* 54, 5095–5116.
- Zhiguo, Cao., Jinfeng, Ju., and Jialin, Xu. (2019). Distribution Model of Water-Conducted Fracture Main Channel and its Flow Characteristics. *J. China Coal Soc.* 12, 3719–3728.

Conflict of Interest: The authors declare that the research was conducted in the absence of any commercial or financial relationships that could be construed as a potential conflict of interest.

Publisher's Note: All claims expressed in this article are solely those of the authors and do not necessarily represent those of their affiliated organizations, or those of the publisher, the editors, and the reviewers. Any product that may be evaluated in this article, or claim that may be made by its manufacturer, is not guaranteed or endorsed by the publisher.

Copyright © 2022 Yi, Han, Weitao, Wenbing, Erhu, Tingye, Dawei, Bingyuan, Hao and Minghao. This is an open-access article distributed under the terms of the Creative Commons Attribution License (CC BY). The use, distribution or reproduction in other forums is permitted, provided the original author(s) and the copyright owner(s) are credited and that the original publication in this journal is cited, in accordance with accepted academic practice. No use, distribution or reproduction is permitted which does not comply with these terms.



3D Visualization Monitoring and Early Warning System of a Tailings Dam—Gold Copper Mine Tailings Dam in Zijinshan, Fujian, China

Wen Nie^{1,2,3*}, Minghua Luo^{1,2}, Yunmin Wang^{2,3} and Ruixiang Li⁴

¹School of Geoscience and Technology, Southwest Petroleum University, Chengdu, China, ²State Key Laboratory of Safety and Health for Metal Mines, Maanshan, China, ³Sinosteel Maanshan General Institute of Mining Research Co., LTD, Maanshan, China, ⁴Zijin Mining Company Limited, Shanghang, China

OPEN ACCESS

Edited by:

Jie Chen,
Chongqing University, China

Reviewed by:

Chen Qiusong,
Central South University, China
Wei Shao,
Nanjing University of Information
Science and Technology, China
Yulong Chen,
China University of Mining and
Technology, China

*Correspondence:

Wen Nie
wen.nie@vip.tom.com

Specialty section:

This article was submitted to
Geohazards and Georisks,
a section of the journal
Frontiers in Earth Science

Received: 24 October 2021

Accepted: 17 January 2022

Published: 08 March 2022

Citation:

Nie W, Luo M, Wang Y and Li R (2022)
3D Visualization Monitoring and Early
Warning System of a Tailings
Dam—Gold Copper Mine Tailings Dam
in Zijinshan, Fujian, China.
Front. Earth Sci. 10:800924.
doi: 10.3389/feart.2022.800924

A 3D tailings dam visualization early warning system was developed based on GIS (geographic information system) combining ARIMA (autoregressive integrated moving average model) and 3S (RS, GIS, GPS) technology for prediction of phreatic line changes and tailing dam deformation. It was applied for monitoring and early warning for the gold–copper tailing dam in Zijinshan Dadongbei tailing pond. The system consists of equipment management, data management, prediction, monitoring and early warning, and 3D visualization modules. It is able to do data management, visualization and disaster prediction, and early warning based on 79 monitoring points of rainfall, infiltration line, and deformation of the tailing dam in the Zijinshan mine. The design and application of the system reflect its features of rich functionality, high practicality, intuitive effect, and high reference value. The system solves the problems of low visualization of monitoring data, poor management of multiple data, and feasible prediction and early warning of point–surface combination. It realizes high-precision prediction of key factors and real-time warning of disaster.

Keywords: tailings dam, 3D geographic information system, cloud-side collaborative technique, monitoring and early warning system, 3D visualization

1 INTRODUCTION

Tailings have a great impact on environmental pollution and the ecological landscape (Jiang et al., 2021; Luo et al., 2021; Zhang et al., 2021). There are many kinds and quantities of tailing ponds in China, and most of them are in mountainous and upstream water source areas. Tailings mainly stored in tailing ponds are the largest bulk industrial solid waste produced by industrial and mining enterprises. Thus, the tailing pond is a facility with high environmental risk. The factors affecting the stability problem of the dam are complex (Hu et al., 2016; Clarkson and Williams, 2021a). Besides, safety events, such as tailing dam break, cause huge economic and property losses. The leakage of highly toxic chemicals, such as heavy metals and beneficiation agents contained in tailings, also very easily pollutes the surrounding soil, surface water, and groundwater, causing sudden environmental disasters (Del Rio-Salas et al., 2019; Ouyang et al., 2019). According to incomplete statistics, more than 100 tailing pond accidents have occurred in China since 2001. At present, the situation of tailing environmental risk management in China is still very serious, and the high incidence of environmental emergencies in tailing ponds has not been alleviated (Peng et al., 2020).

The early safety assessment of tailing dams in China was mainly based on manual monitoring (Yang et al., 2019). With the development and promotion of monitoring equipment, many tailing dams have used automatic monitoring devices and established a variety of monitoring systems based on wireless sensor network, the Internet of things, CAN-bus, and ZigBee technology (Wenxue et al., 2011; Wang and Yong, 2014; Bo and Shan, 2018; Meng, 2019; Gamperl et al., 2021). The installation of various types of automatic monitoring equipment on a tailing dam improves the monitoring efficiency and degree of automation (Pirsiavash et al., 2017; Ayhan and Almuslmani, 2021; Sarantsev, 2021; Zheng et al., 2021). However, some problems, such as isolation of multiple monitoring systems, invalid management of various types of data, and low visualization of data system are inevitable (Padsala et al., 2021). Therefore, the main aim of this study is to carry out the design and research of tailing dam monitoring and early warning system based on computer, cloud computing (Kanakaraja et al., 2021), GIS (geographic information system) (Kong, 2017; Thatcher, 2018), and time series prediction technology (Wen et al., 2021). 3D geographic information system can manage multisource data effectively and realize two- and three-dimensional visual displays (Cahyono et al., 2021). The system is built by cloud-side collaborative technology (Erbao et al., 2019), which is a widely used technology at present. It can solve the problems of data management and transmission. The system adopts the data-driven method for monitoring and early warning. Furthermore, it helps to improve prediction and early warning and also the three-dimensional visual display of tailing dam key factors, and finally promotes the construction of smart mine (Xu et al., 2019).

2 DESIGN OF SYSTEM

2.1 Theoretical Basis

This study is based on geographic information system (GIS), cloud computing, computer technology, time series prediction, and so on. GIS is a computer system integrating data acquisition, transmission, management, storage, analysis, display, and output. Until now, the data processing and spatial analysis functions of GIS are continuously developed, and have been widely used in all walks of life (Al Faisal et al., 2018). In this project, the system framework was built based on the idea of GIS. GIS can manage multisource data effectively and realize two- and three-dimensional visual displays (Li N. et al., 2021). Cloud computing is a dynamically scalable service related to information technology, software, and the Internet. It has the characteristics of large scale, distributed, high availability and scalability, virtualization, security, on-demand service, economy, and reliability. In recent years, cloud computing and big data have developed rapidly. Compared with local servers, cloud computing has higher data-processing efficiency, larger data volume, and less demand for local resources. Cloud computing is based on cloud servers, and in this study, ECS (Elastic Compute Service) has been chosen. The rapid development of the mobile network is also an

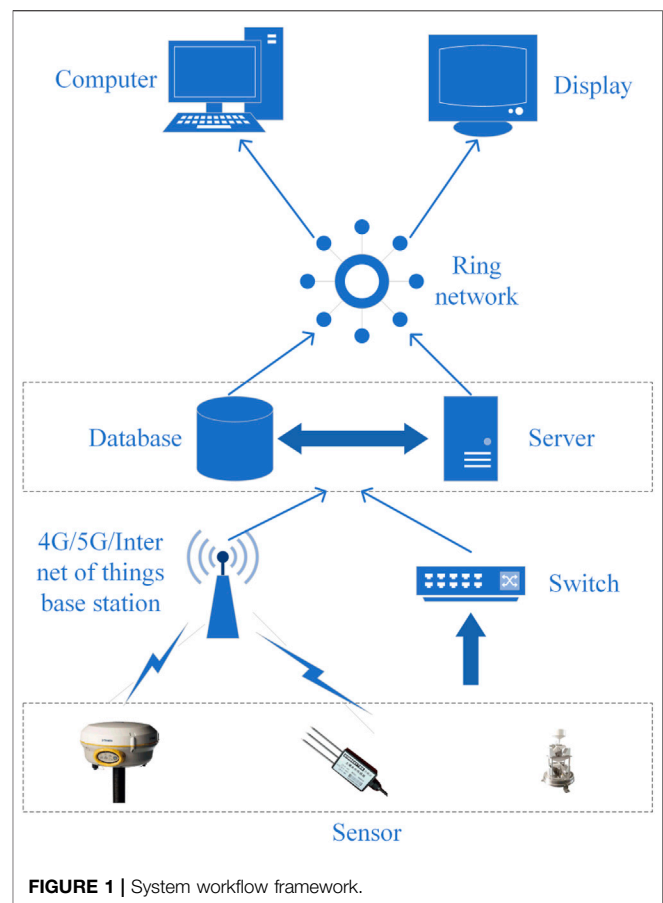
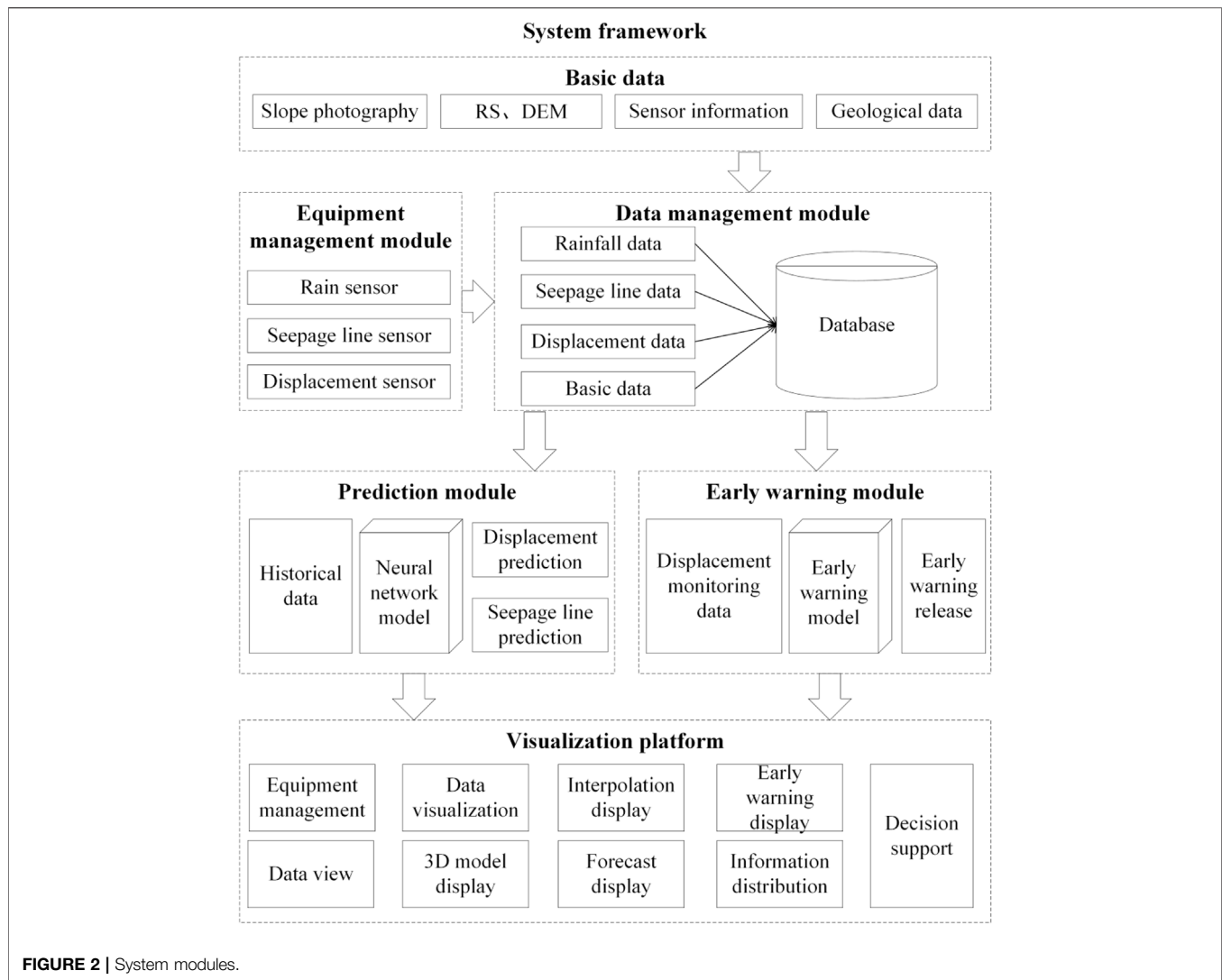


FIGURE 1 | System workflow framework.

important guarantee for the rapid development of cloud computing technology in recent years (Zhang, 2021). The system is built by cloud-side collaborative technology, and this technology is more conducive to system integration. Time series prediction analysis uses the time characteristics of an event in the past to predict the characteristics of the event in the future (Al-Zahrani and Abo-Monasar, 2015). The time series model is divided into stationary and nonstationary series, which depends on the sequence of events. Time series usually contains rich information. In many scenarios, this information can help people understand the phenomenon and predict the future. This technology has been widely used in many fields. In the proposed monitoring and early warning system, the time series method is used to predict the trend changed of phreatic line and dam deformation in the future.

2.2 Design Idea

The early warning system uses the remote sensing image (RS), DEM (digital elevation model) data, monitoring point distribution data, sensor information, and collected monitoring data to establish the data storage system, data processing model, and three-dimensional visualization model. The monitoring data can be collected, predicted, stored, managed, displayed, and output in real time. The stability state of tailing dam can be accurately analyzed in order to reduce the risk of tailing dam failure and environmental



pollution, and prevent potential economic and property losses (Zhou et al., 2015).

2.3 System Framework

The overall framework of the system is built by using cloud-side collaborative technology (Figure 1) (Erbao et al., 2019). The system server is deployed to the cloud server, and cloud computing is used to calculate data on the cloud server. Combined with edge computing and network transmission, the results are transmitted to the front end, and the front end is used for data rendering and display output.

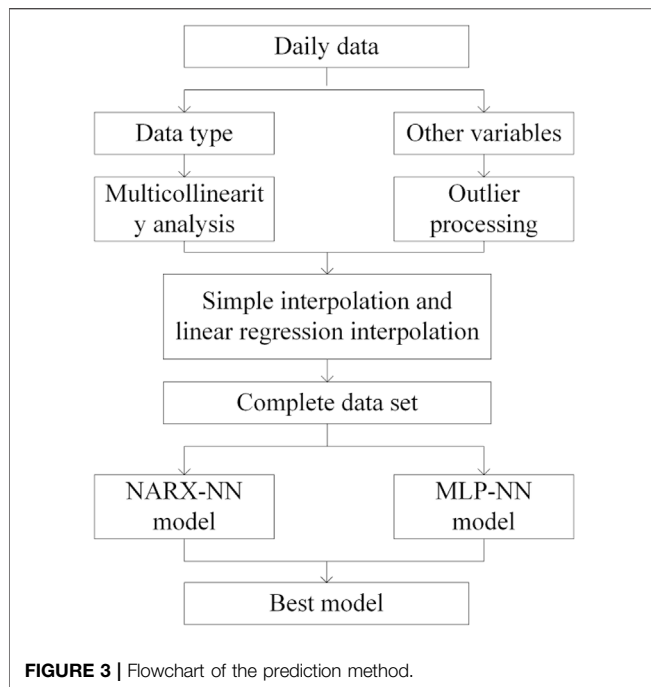
2.3.1 System Data Flow

The system data are mainly stored in the cloud database, including monitoring data, basic geological and geographic information data, model processing data, and manual monitoring data. The real-time monitoring data collected by the monitoring device are uploaded to the cloud database for storage through the transmission protocol, and the data

processing model of the cloud server is called for data analysis and processing. The analysis results are stored in the database. The basic geological and geographic information data are stored in the database when the database is established, which is mainly used for front-end call and display. The manual monitoring data are stored in the database through the manual input of the front end for calling and processing by the data processing model. The front end can store the above data manually or display its call, and output it for display.

2.3.2 Frame Module

The monitoring and early warning system of the tailing dam is composed of multiple modules, which cooperate with each other to achieve the purpose of comprehensive management of the dam. The system mainly includes equipment management, data management, prediction, early warning, and visualization modules (Figure 2). The main functions of each module are as follows:



- 1) The main function of the equipment management module is to manage the monitoring equipment. Various types of monitoring equipment shall be classified and managed. The equipment management module can add or delete stations.
- 2) The data management module mainly manages various data, including data collection, storage, display, and output. It can accurately add, delete, modify, and view single or multiple monitoring data.
- 3) The prediction module is to predict the change in phreatic line and dam deformation. The prediction module adopts the differential autoregressive integrated moving average model (ARIMA), which predicts future data changes through learning historical data (Yadav and Balakrishnan, 2014).
- 4) The early warning module can give the early warning signal for the monitoring area. The system uses the method of the cloud model (Peng et al., 2020). The early warning threshold of each level is determined with reference to the provisions of the engineering technical code for the online safety monitoring system of tailing ponds (GB51108-2015).
- 5) The visualization module is used for a visual display of monitoring and prediction data and areas. The visualization of sensor monitoring data is realized by ECharts. According to UAV images, DEM data, and monitoring point data, the three-dimensional model of the tailing dam is established, and the visualization of the model is realized by rendering at the front end with three.js.

2.4 Algorithm Models

2.4.1 Prediction Model

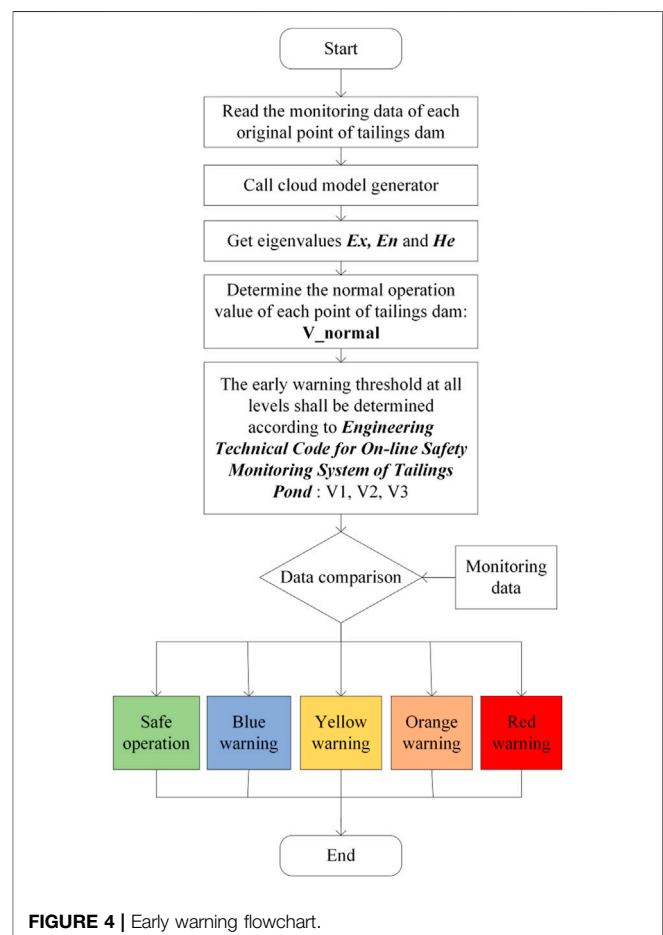
The prediction model is based on time series to do an analysis of previous monitoring data (Aggarwal et al., 2020). The time series model operation proposed in this study is divided into two stages (Figure 3): the first stage is mainly for interpolation

and preprocessing of data loss, and the second stage is mainly for 20% future prediction of the overall data by using the nonlinear autoregressive model (NARX) (Ma et al., 2020; Du et al., 2021) and multilayer perceptron (MLP-NN). The NARX model with a three-layer neural network and including nine climate variables and eight neurons is the best model (Pu et al., 2019).

2.4.2 Early Warning Model

For monitoring and early warning of tailing dam failures, it is necessary to study the early warning threshold. Four methods were considered: acceleration method, reciprocal velocity method, displacement rate ratio method, and cloud model, and finally, a suitable method to judge the early warning threshold was selected (Du et al., 2021).

1) The acceleration method divides the deformation into three stages: initial deformation, constant velocity deformation, and accelerated deformation. The acceleration method cannot provide a clear threshold (Xu and Zeng, 2009). 2) The reciprocal velocity method obtains the deformation rate according to the relationship between the monitored deformation and time. It also cannot provide a clear threshold (Wang et al., 2015). 3) The deformation rate ratio method judges the deformation of landslide mass through multipoint



deformation changes and determines a unified index for multiple points. This method is also uncertain about the selection of the threshold (Wang et al., 2014). 4) The cloud model method is an effective way to transform quantitative data into qualitative concepts, and this method can be used to establish the mapping between the monitoring data and the normal operation state of the tailing dam. By reading the monitoring data of the tailing dam in normal operation and converting the forward cloud and reverse cloud, the corresponding relationship between the monitoring data and the risk levels of the tailing dam is established. Finally, the functions of hierarchical early warning and prediction, decision making and hierarchical management, and control of the tailing dam based on massive data are realized (Peng et al., 2020) (**Figure 4**). The key calculation formula of the cloud model method is as follows:

1) Sample expectation of calculated data E_x is:

$$E_x = \frac{1}{n} \sum_{i=1}^n x_i \quad (1)$$

In **Equation 1**, x_i is the deformation rate of measuring point i , and n is the total number of measurements.

2) In data $\{x_1, x_2, x_3, \dots, x_n\}$, r data were randomly selected as one group, and a total of m groups were selected, getting data $\{x_{ij} | i = 1 \sim r; j = 1 \sim m\}$. The data expectations for each group $\bar{x}_j (j = 1, 2, \dots, m)$ are calculated, and new data are obtained from m groups of data $\{Y_j^2 | Y_1^2, Y_2^2, \dots, Y_m^2\}$:

$$\bar{x}_j = \frac{1}{r} \sum_{i=1}^r x_{ij} \quad (2)$$

$$Y_j^2 = \frac{1}{r-1} \sum_{i=1}^r (x_{ij} - \bar{x}_j)^2 \quad (3)$$

In **Equation 2**: x_{ij} is the i th data of the j th group randomly selected from the original data $\{x_1, x_2, x_3, \dots, x_n\}$.

The sample expectation ($E(Y^2)$) and variance ($D(Y^2)$) of the new data series $\{Y_j^2 | Y_1^2, Y_2^2, \dots, Y_m^2\}$ are calculated as:

$$E(Y^2) = \frac{1}{m} \sum_{i=1}^m Y_i^2 \quad (4)$$

$$D(Y^2) = \frac{1}{m-1} \sum_{i=1}^m (Y_i^2 - E(Y^2))^2 \quad (5)$$

3) The entropy (E_n) and super entropy (H_e) of the cloud model are calculated as follows:

$$E_n^2 = \frac{1}{2} \sqrt{4(E(Y^2))^2 - 2D(Y^2)} \quad (6)$$

$$H_e^2 = E(Y^2) - E_n^2 \quad (7)$$

4) According to the 3E rule of the cloud model, if the deformation rate of the tailing dam is within the interval $E_x - 3E_n$ to $E_x + 3E_n$, it is regarded as the normal operation of the tailing dam.

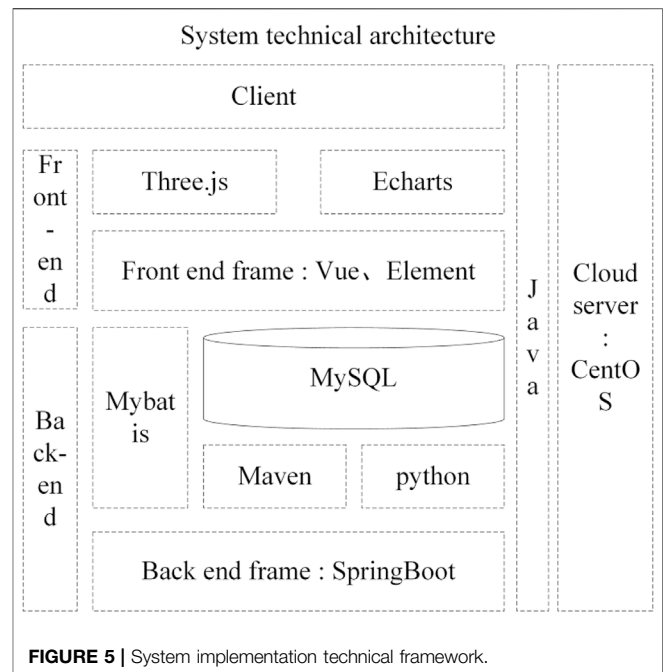


FIGURE 5 | System implementation technical framework.

Compared with the other three methods, the cloud model can calculate the specific early warning threshold more effectively. The cloud model method has been applied in the tailing dam (Peng et al., 2020), and the early warning threshold of each level of early warning can be calculated according to the historical monitoring data of the tailing dam stability. Therefore, in this study the cloud model method was employed to build the early warning model.

2.4.3 Interpolation Model

Through the interpolation method, the monitoring and early warning mode of point-to-area can be realized. This study mainly considers inverse distance weight interpolation as the interpolation model (Liu et al., 2021).

The implementation steps of inverse distance weight interpolation are as follows:

- (1) Sort out the coordinates and monitoring data of monitoring points;
- (2) Mesh the interpolation area, obtain the center coordinates of each grid, and take the coordinates of the grid as the coordinates interpolated;
- (3) Calculate the distance between the known discrete points, and then these points are interpolated. In two-dimensional plane space, the distance from discrete points (x_i, y_i) to grid points (A, B) is D_i :

$$D_i = \sqrt{(x_i - A)^2 + (y_i - B)^2} \quad (8)$$

- (4) Find out the distance of N discrete points nearest the grid point (A, B) , then the value estimated on the grid point (a, b) is:

$$Z_{(A,B)} = \sum_{i=1}^N \left(\frac{Z_i}{D_i} \right) / \sum_{i=1}^N \left(\frac{1}{D_i} \right) \quad (9)$$

Z_i is the monitor value on discrete point “I”, and $Z_{(A,B)}$ is the estimated value on the grid point (A, B);

- (5) By estimating each grid point according to the appeal step, the values estimated of all unknown points can be obtained. Furthermore, the interpolation of the whole monitoring area can be realized.

2.5 System Implementation

The system adopts B/S (browser/server) structure, which unifies the client. The core business processing is completed on the server, realizing the function that any client can request data interaction through the network using the browser (Figure 5). The system uses Alibaba cloud host CentOS, and the database uses Alibaba cloud MySQL server for data storage. The background data interaction is mainly realized by Java, and the front-end page display is mainly realized by HTML. The background framework is mainly built by Maven, Springboot, Mybatis, *Python*, and other tools in order to realize the management and control of the background. The front end mainly uses Vue, Element, three.js, ECharts, and other tools to realize the construction of front-end framework, data visualization, 3D rendering, etc.

3. APPLICATION AND ANALYSIS

3.1 Study Area

The Zijinshan gold–copper mine in Fujian Province is a proven super large metal mine. Its mining area is located in the southern

end of the Donglie mountain in the southern section of the Wuyi mountain range, which belongs to the middle and low mountain of structural erosion. This mine is a typical upper gold and lower copper mine. The mine has proven gold resource reserves of more than 300 tons and copper resource reserves of more than 5 million tons. It has a large open-pit mining site and underground mining site, as well as a large tailing pond. The Dadongbei tailing pond is in the northwest of the Zijinshan mining area. The gully trend is distributed in a nearly north–south direction. The cross section is in a “U” shape, and the slope gradient on the East and west sides is 25°–35°. The vegetation is developed, and the natural slope around is stable (Figure 6).

Currently, the tailing dam has a monitoring system in terms of manual monitoring, GNSS online monitoring, radar monitoring, phreatic line automatic monitoring, and rainfall automatic monitoring, including 1 rainfall monitoring point, 10 phreatic line monitoring points, and 68 deformation monitoring points. The existing monitoring system has some deficiencies: 1) There are many kinds of monitoring devices, but there is no comprehensive management of data. Therefore, it is not easy to conduct a comprehensive analysis. 2) There is no centralized management and postprocessing of the data collected, which is a waste of digital resources. “Data island” is outstanding, and the ability of prediction and early warning of the system is weak. 3) Most of the monitoring data are one- or two-dimensional plane data. The deficiencies in three-dimensional modeling and data analysis do not give a strong sense of intuition for decision makers.

3.2 Application

Based on the current information of the Zijinshan gold–copper mine tailing dam, a tailing dam monitoring and early warning

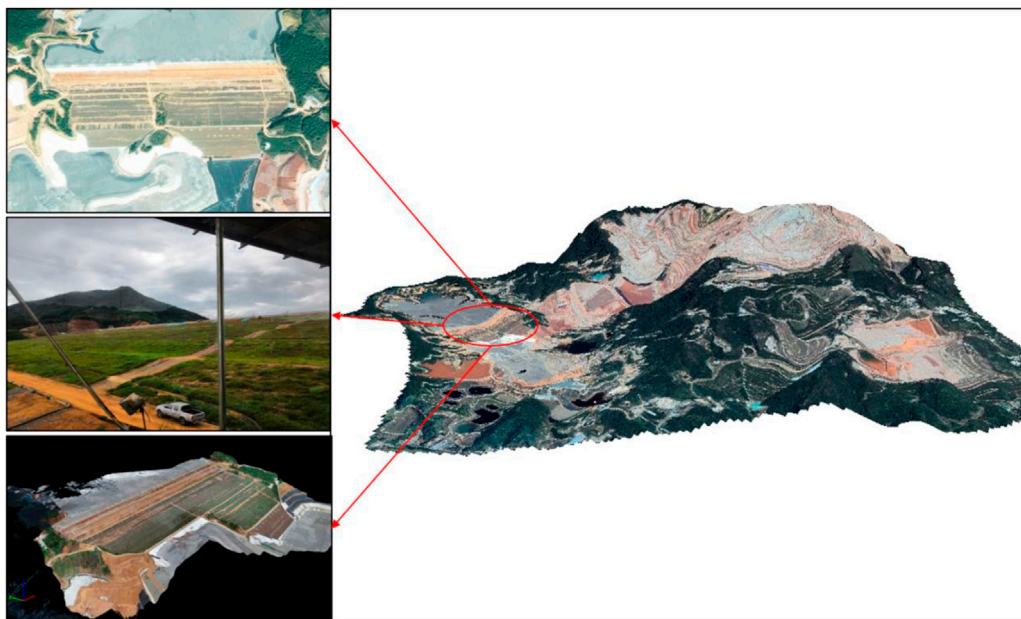


FIGURE 6 | Gold–copper mine tailing dam in Zijinshan.



FIGURE 7 | Interface of tailing dam monitoring and early warning system.

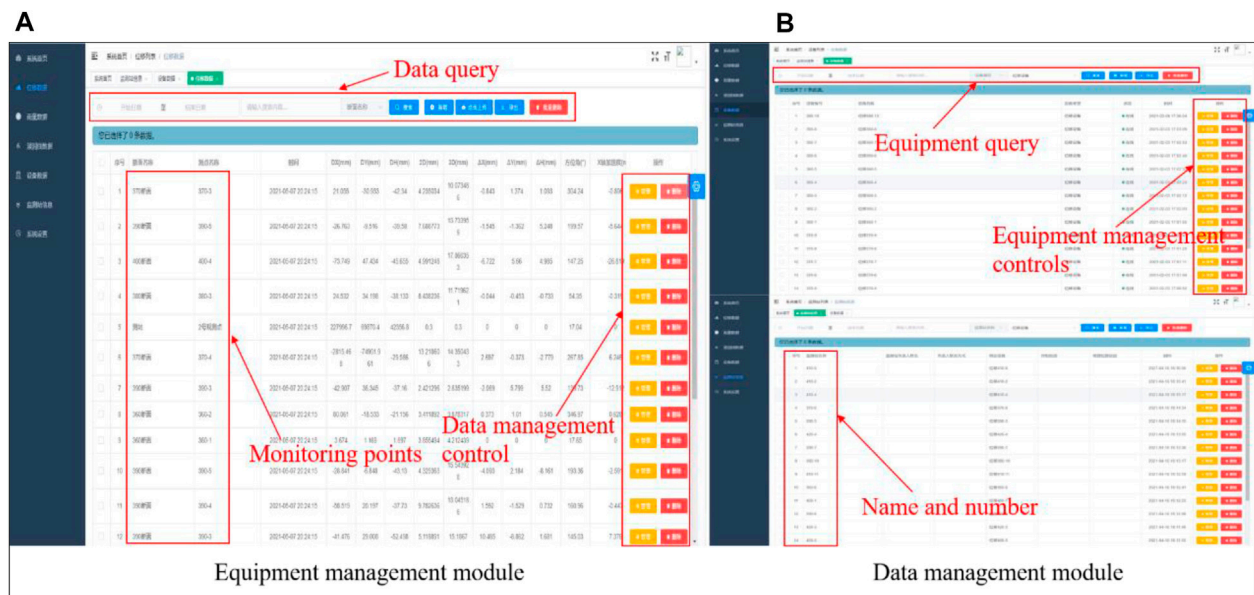


FIGURE 8 | Management module (A: Equipment management module; B: Data management module).

system was developed, which integrates data acquisition, transmission, management, storage, analysis, calculation, display, and output (Figure 7). The system is composed of equipment management, data management, prediction, early warning, and visualization modules. Through these modules, multisource data were more effectively applied, and the visualization ability was improved.

3.2.1 Equipment Management Module

In the monitoring and early warning system of the Zijinshan gold and copper mine tailing dam, the equipment management module mainly considers three kinds of equipment: phreatic line, rainfall, and deformation monitoring equipment. The equipment management module sets and manages grouping information. The system can automatically judge whether the

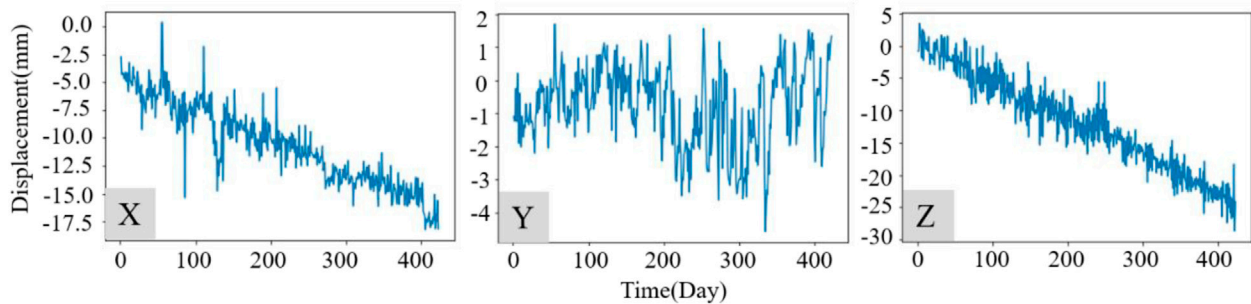


FIGURE 9 | Stationarity analysis of data in X, Y, and Z.

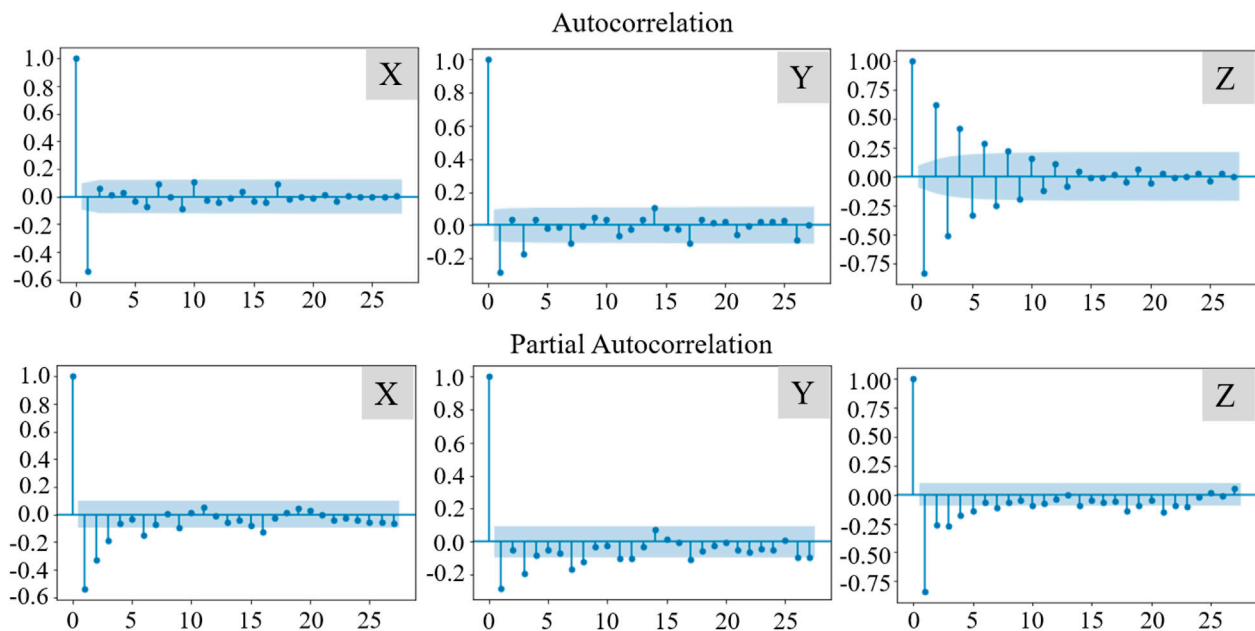


FIGURE 10 | Test of autocorrelation coefficient and partial autocorrelation coefficient in X, Y, and Z.

equipment works normally. The system sets up the personnel information in charge of the equipment for effective equipment management (**Figure 8A**).

3.2.2 Data Management Module

The management of various types of data is a necessary function of the system. In this system, the data management module realizes the management of phreatic line, rainfall, and deformation data. Through the data management module, the monitoring data can be queried, added, deleted, and modified, and also, a modification log can be set up to record the modification of each data (**Figure 8B**).

3.2.3 Prediction Module

The prediction module mainly includes phreatic line and deformation prediction. Through the historical monitoring data and real-time monitoring data, the change in data can be predicted. The accuracy of deformation prediction can reach

more than 90%, and the accuracy of phreatic line prediction can be over 95%. For the deformation change, the deformations in X, Y, and Z directions are considered, respectively. The stationarity of the data is first analyzed (**Figure 9**). The autocorrelation coefficient and partial autocorrelation coefficient are tested in the X, Y, and Z directions (**Figure 10**), and the prediction model in the X direction is determined as:

$$\nabla x = -0.0316 + \frac{\varepsilon_t}{1 - 0.7580B} \quad (10)$$

Prediction model in the Y direction:

$$\nabla y = -0.7467 + 0.8133x_{t-1} + \varepsilon_t - 0.2058\varepsilon_{t-1} \quad (11)$$

Prediction model in the Z direction:

$$\nabla z = -0.0603 + \frac{\varepsilon_t}{1 - 0.838B} \quad (12)$$

TABLE 1 | Display of deformation prediction data and real data.

	Real value of the next three periods (mm)	Forecast value of the next three phases (mm)	Accuracy (%)
X	-19.57	-17.25	96.72
	-17.9	-17.28	
	-19.33	-17.31	
Y	-28.93	-28.04	99.26
	-23.85	-24.91	
	-27.08	-27.65	
Z	0.87	0.82	99.7
	1.34	0.53	
	0.77	0.29	

For the evaluation of prediction accuracy, MSE (mean squared error) (Tsukuma, 2019) is used to evaluate the accuracy of regression results:

$$MSE = \frac{\sum_{i=1}^n (y_i - q_i)^2}{n} \quad (13)$$

In Equation 13, y_i represents the predicted value, q_i represents the actual value, and n is the number of test samples.

The monitoring data of deformation and phreatic line is from July 15, 2019 to March 29, 2020. There are 68 displacement

monitoring points, with 403 monitoring data at each monitoring point. Historical monitoring data (70%) of the tailing dam (deformation and phreatic line) is as the training set, and 30% data are as the test set. The accuracy of the above model has been tested many times. For example, prediction of the deformation data in the three directions of X, Y, and Z and real monitoring data are as shown in Table 1; the monitoring data and prediction data of displacement monitoring point 410-2 are from March 30 to April 1, 2020. For phreatic line data, there are 10 monitoring points in total, with 5,918 data at each monitoring point. The same method was used to analyze and predict the phreatic line prediction model, and the results also have a high accuracy (Table 2). In Table 2, the monitoring data and prediction data of the phreatic line on March 30, 2020 are given.

3.2.4 Early Warning Module

The tailing dam of the Zijin mine has been monitored for 2 years, with a large amount of deformation monitoring data ($n = 68,000$). The historical monitoring data are imported into the early warning model to calculate the early warning threshold at all levels. First, the model is adopted to calculate a normal operation value of 1.0709 cm/h. The early warning threshold of each level is determined through the standard: the threshold of yellow alert is 1.3922 cm/h, the threshold of orange alert is 2.1419 cm/h, and the threshold of red

TABLE 2 | Display of phreatic line prediction data and real data.

Phreatic line monitoring point	Real value of the next three periods (mm)	Forecast value of the next three phases (mm)	Accuracy (%)
370-2	19.80229513	19.8076	99.99
	19.80191219	19.8048	
	19.80199455	19.8012	
370-3	19.95976434	19.9605	99.99
	19.96022916	19.9582	
	19.96002616	19.9609	
390-2	34.70452539	34.7054	99.99
	34.70573858	34.706	
	34.70697669	34.7036	
390-3	24.98247116	24.9825	99.99
	24.982276	24.9849	
	24.98224142	24.9831	
390-7	26.99627284	26.9835	99.99
	26.99528222	26.9914	
	26.993942	26.9992	
390-8	29.47489298	29.4982	99.99
	29.47400438	29.4863	
	29.47311581	29.4758	
410-3	22.30746874	22.3174	99.99
	22.322533	22.2678	
	22.31492568	22.3421	
410-7	27.56821274	27.6095	99.99
	27.56782166	27.5779	
	27.56743059	27.5686	
410-8	29.71943339	29.7261	99.99
	29.72098269	29.7134	
	29.72030573	29.7235	

alert is 3.2128 cm/h. Through the comparison between the real-time monitoring data and the early warning threshold at all levels, the stability evaluation of each monitoring point is realized to achieve the purpose of monitoring and early warning. With the continuous increase in monitoring data, the more accurate thresholds can be adjusted automatically. In the case of early warning, the information is released in real time, and the corresponding early warning level is displayed at the early warning monitoring point for a more intuitive effect.

3.2.5 Visualization Module

The system visualization mainly includes the visualizations of monitoring data, three-dimensional model, phreatic line and deformation prediction, and early warning (Figure 11). These visualizations are mainly completed by the ECharts tool as shown in Figure 7. The monitoring data curve of monitoring points can be displayed and updated with the real data input.

3.2.5.1 Interpolation Visualization

There are 68 deformation monitoring points on the tailings dam with average equal intervals on the dam body. The area without monitoring points around is interpolated. First, the dam surface is meshed, and then the coordinate information of each grid is obtained. Using the known monitoring data of 68 points, the grid area is interpolated by the inverse distance weight interpolation method. The surface of the tailings dam is divided into more than 2000 grids, and more than 2000 interpolation data are obtained, realizing point-to-area coverage (Figure 12A).

3.2.5.2 Early Warning Visualization

Using the 2-year historical monitoring data of the tailing dam deformation, the normal operation value of the tailing dam can be calculated to obtain the threshold of each level of early warning. Once there is real-time monitoring data over the threshold, the early warning system begins to work (Figure 12B).

3.2.5.3 Phreatic Line Visualization

According to the data collected by the phreatic line sensor, the three.js tool is used and combined with the parabola principle to show the dynamic effect of water surface fluctuation at the front end (Figure 12C).

4 DISCUSSION

Compared with other existing systems, such as DAMSAT (Lumbroso et al., 2021), the proposed system has richer functions, stronger prediction and early warning ability, and more timely response. The establishment of the three-dimensional model and visual display can provide more intuitive and effective decision support for decision makers. Currently, some mainstream systems are shown in Table 3. In the table, the systems are evaluated by eight indicators. The performance levels of each indicator from low to high are average, good, and great, respectively. A monitoring system based on Micro-UAV (Torrero et al., 2015) only uses Micro-UAV monitoring, no other monitoring methods, and no prediction function. The Monitoring and early warning system based on aperture radar (Xu, 2021) can accurately analyze the surface change, but it does not have the ability of prediction and comprehensive analysis. The

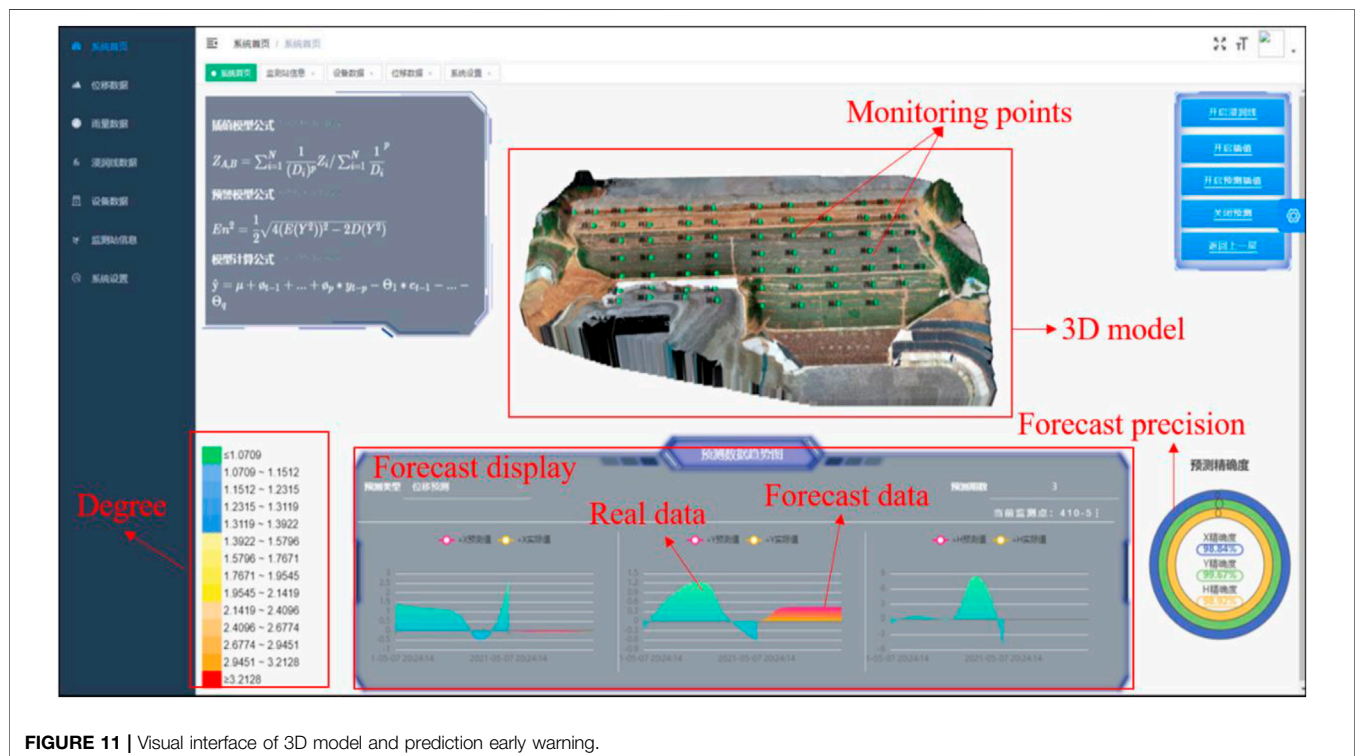


FIGURE 11 | Visual interface of 3D model and prediction early warning.

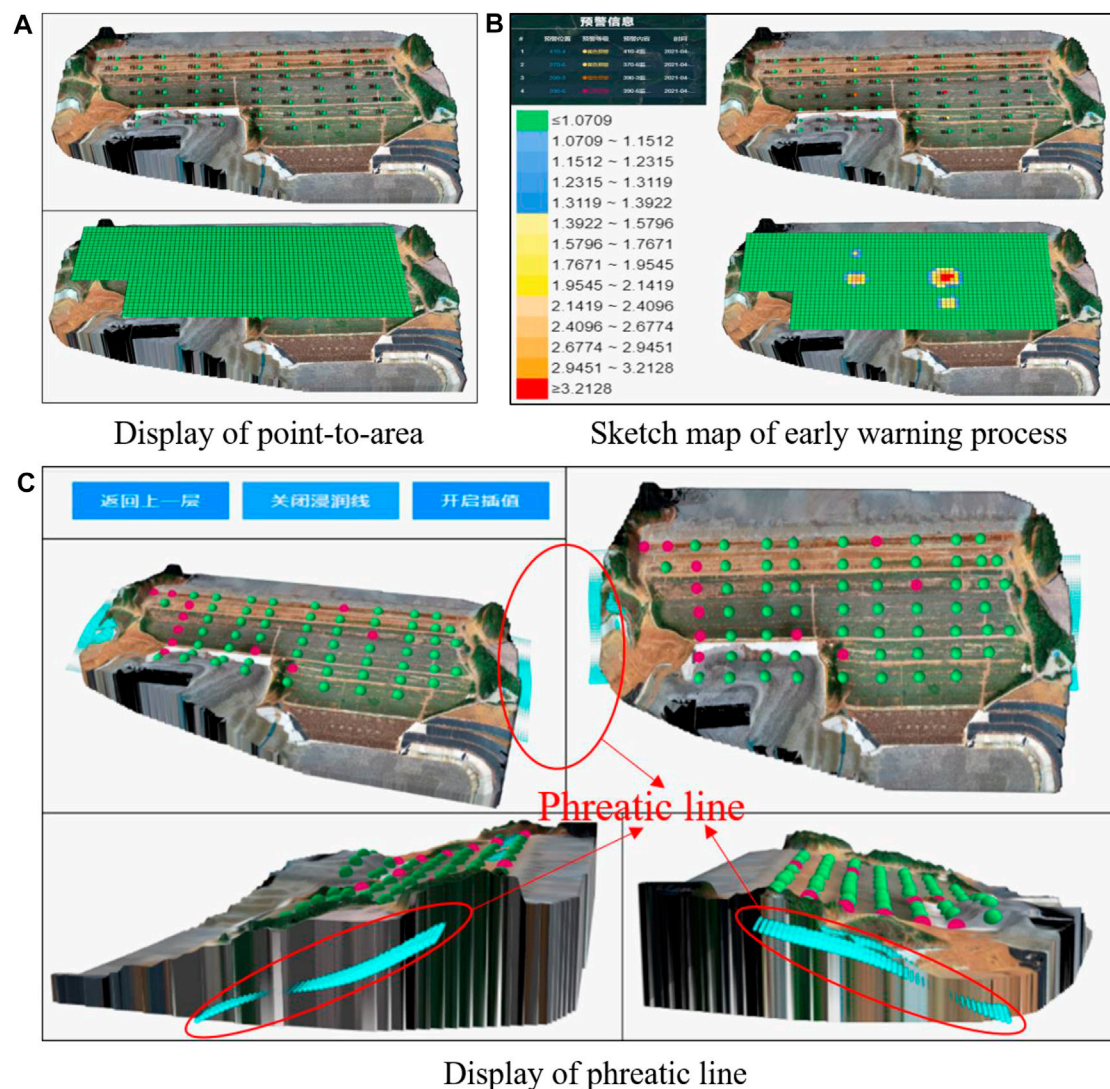


FIGURE 12 | 3D visualization module (A: Visual display of point-to-area; B: Visual display of early warning information; C: Visual display of phreatic line).

online safety monitoring system for tailing ponds (Bai, 2020) can manage and comprehensively analyze data, but it does not have the ability of prediction and 3D visualization, and the display effect is not good. The safety management system of tailing pond based on UAV intelligent cruise (Liao et al., 2021) also does not have the ability of comprehensive analysis and prediction of data. The mine geological disaster monitoring and early warning system based on Lora Technology (Zhu et al., 2021) reduces the time delay of the system, but the system function is relatively single, and the functions of 3D visualization and prediction are lacking. The currently proposed system is fully functional. The system designed in this research has the following advantages: 1) Comprehensive management capability. The system can comprehensively manage and analyze various types of monitoring data. 2) Strong forecasting and early warning function. The system is equipped with the prediction module and early warning module, which can monitor

and warn the monitoring area in real time. The combination of the prediction module and early warning module can provide a more accurate safety assessment. 3) Strong visualization ability. The system includes the visualization of monitoring data, three-dimensional model, monitoring station, and early warning information. It is not only a digital display but also is combined with a three-dimensional model, which is more visual and intuitive.

The system has some advantages. It also has room for progress. First, in the data acquisition and transmission mode of this system, the system uses the wireless transmission mode of sensor equipment by default. According to the current research, there are many data transmission methods, such as the wireless network and GPRS network (Li et al., 2021b). The development of this system is not compared with several other different transmission modes. Therefore, it is unknown which transmission method is more effective. Second, the design and

TABLE 3 | Function of some existing systems.

Name	Function							
	Equipment management	Data management	Prediction module	Early warning module	3D model	Regional early warning	Comprehensive analysis	Visualization platform
DAMSAT Lumbroso et al. (2021)	Average	Good	—	Good	—	Great	—	Great
Monitoring system based on Micro-UAV Torrero et al. (2015)	—	—	Average	Good	Great	Great	—	Good
Monitoring and early warning system based on aperture radar (Xu, 2021)	—	Average	—	Good	Great	Great	—	Good
On line safety monitoring system for tailings pond (Bai, 2020)	Average	Good	Average	Good	—	—	Average	Average
Safety management system of tailings pond based on UAV intelligent cruise (Liao et al., 2021)	—	Average	Average	Good	Great	Great	—	Good
Mine geological disaster monitoring and early warning system based on Lora Technology Zhu et al. (2021)	—	Good	—	Good	—	—	Average	Average
This system	Great	Great	Great	Great	Great	Good	Good	Great

development of this system are based on some existing data, such as data type, number, and location of sensors. These data cannot be changed, so the accuracy of different sensors and the economic efficiency of sensor placement are not considered (Clarkson and Williams, 2021b; Clarkson et al., 2021). Then in terms of data processing, this paper adopts the ARIMA and cloud model methods (Li H. et al., 2020). In the current research, there are a variety of data processing methods, such as normal distribution curve, random forest, and numerical simulation (Li S. et al., 2020, 2021c; Shi et al., 2020). Each method has its own advantages. For different actual situations, the application of each method is also different. Finally, in terms of visualization, the interpolation rendering and 3D rendering of the system adopt the three.js tool (Li, 2021), which has strong display ability and weak computing ability. When a large amount of data need to be calculated at the same time, there will be a loading delay in the front-end display. In this regard, a better tool needs to be discovered to realize 3D rendering display. At present, the interpolation interface is meshed and then interpolated. It does not fit the dam and is parallel to the dam. Cesium is also a tool to implement WebGL (Nishioka et al., 2015; Wang et al., 2021). Some scholars also used it for map visualization. In the later improvement, this tool can be tried.

5 CONCLUSION

This early warning system integrates data acquisition, transmission, storage, processing, analysis, output, and display. It is also a geographic information system containing various geographic elements and a visualization system including table curve display, and two- and three-dimensional model display. The following conclusions can be drawn:

- 1) The establishment of the three-dimensional visualization model solves the problem of low visualization. It can show the shape of the dam more intuitively than two dimensional. Combined with the abnormal information of monitoring points, it can quickly identify the location information of early warning monitoring points.
- 2) The system prediction and early warning module is a linkage mode. When the monitoring data is updated, it can respond in time, compared with the warning threshold, and release the early warning information in real time. Through the operation of the prediction model, it can accurately predict the deformation value of the dam in the future, offering a great reference.
- 3) The interpolation model is introduced into the system to combine point areas to achieve the purpose of regional risk assessment. It solves the problem of point and area early warning, visualizes the risk area, obtains a more intuitive effect, and gives a better decision support.
- 4) The system integrates data management, equipment management, interpolation, prediction, early warning, two- and three-dimensional visualization modules, and adopts the technical framework of cloud edge end cooperation to solve the problems of isolation of multiple monitoring systems and the “data island” phenomenon. The novel system can work reliably for a long time without cumulative errors.

DATA AVAILABILITY STATEMENT

The data analyzed in this study is subject to the following licenses/restrictions: Only by obtaining the permission of Zijin Mining Company Limited. Requests to access these datasets should be directed to RL, 826717644@qq.com.

AUTHOR CONTRIBUTIONS

WN directed and revised the writing content of the paper. ML completed the writing of the paper, the design and construction of the system, and the data processing model. YW directed the writing of the paper. RL provided the data for the whole system. All authors contributed to the article and approved the submitted version.

FUNDING

This research was supported by the Major Science and Technology Projects of Anhui Province (Nos.

201903a07020008 and 202003a0702002) and the Technology Development Project of Zijin Mining Company Limited (No. FW-2020-00091).

ACKNOWLEDGMENTS

We gratefully acknowledge the funding provided by the Major Science and Technology Projects of Anhui Province and the Technology Development Project of Zijin Mining Company Limited. We would also like to thank the handling editor and reviewers whose valuable and constructive comments greatly improved this article.

REFERENCES

- Aggarwal, A., Alshehri, M., Kumar, M., Alfarraj, O., Sharma, P., and Pardasani, K. R. (2020). Landslide Data Analysis Using Various Time-Series Forecasting Models. *Comput. Electr. Eng.* 88, 106858. doi:10.1016/j.compeleceng.2020.106858
- Al Faisal, A., Al Kafy, A., and Roy, S. (2018). Integration of Remote Sensing and GIS Techniques for Flood Monitoring and Damage Assessment: A Case Study of Naogaon District, Bangladesh. *J. Remote Sensing GIS* 07. doi:10.4172/2469-4134.1000236
- Al-Zahrani, M. A., and Abo-Monassar, A. (2015). Urban Residential Water Demand Prediction Based on Artificial Neural Networks and Time Series Models. *Water Resour. Manage.* 29, 3651–3662. doi:10.1007/s11269-015-1021-z
- Ayhan, M. E., and Almuslmani, B. (2021). Positional Accuracy and Convergence Time Assessment of GPS Precise point Positioning in Static Mode. *Arab. J. Geosci.* 14, 1263. doi:10.1007/s12517-021-07428-1
- Bai, Y. (2020). *Application of On-Line Safety Monitoring System in Tailings Pond (In Chinese)*. China Metal Bulletin, 65
- Bo, G., and Shan, J. (2018). Design of Early Warning System Based on Wireless Sensor Network. *Int. J. Onl. Eng.* 14, 66. doi:10.3991/ijoe.v14i01.8060
- Cahyono, A. B., Budisusanto, Y., and Hidayat, H. (2021). Geovisualization of 3D Modeling Representation of Topographic Relief Based on Open Source GIS. *IOP Conf. Ser. Earth Environ. Sci.* 731, 012023. doi:10.1088/1755-1315/731/1/012023
- Clarkson, L., and Williams, D. (2021a). An Overview of Conventional Tailings Dam Geotechnical Failure Mechanisms. *Mining, Metall. Exploration* 38, 1305–1328. doi:10.1007/s42461-021-00381-3
- Clarkson, L., and Williams, D. (2021b). Catalogue of Example Instrumentation and Monitoring Systems for Tailings Dams in Australia. *Mining Techn.* 130, 1–11. doi:10.1080/25726668.2021.1901026
- Clarkson, L., Williams, D., and Seppälä, J. (2021). Real-time Monitoring of Tailings Dams. *Georisk: Assess. Manag. Risk Engineered Syst. Geohazards* 15, 113–127. doi:10.1080/17499518.2020.1740280
- Del Rio-Salas, R., Ayala-Ramírez, Y., Loredó-Portales, R., Romero, F., Molina-Freaner, F., Minjarez-Osorio, C., et al. (2019). Mineralogy and Geochemistry of Rural Road Dust and Nearby Mine Tailings: A Case of Ignored Pollution Hazard from an Abandoned Mining Site in Semi-arid Zone. *Nat. Resour. Res.* 28, 1485–1503. doi:10.1007/s11053-019-09472-x
- Du, J., Chen, J., Pu, Y., Jiang, D., Chen, L., and Zhang, Y. (2021). Risk Assessment of Dynamic Disasters in Deep Coal Mines Based on Multi-Source, Multi-Parameter Indexes, and Engineering Application. *Process Saf. Environ. Prot.* 155, 575–586. doi:10.1016/j.psep.2021.09.034
- Erbao, X., Yan, L., Mingshun, Y., and Xi, C. (2019). “Design of Intelligent Monitoring System for Power Distribution Equipment Based on Cloud Edge Collaborative Computing,” in *Proceedings of the 2019 International Conference on Precision Machining, Non-traditional Machining and Intelligent Manufacturing (PNTIM 2019)* (Xi'an, China: Atlantis Press). doi:10.2991/pntim-19.2019.3
- Gamperl, M., Singer, J., and Thuro, K. (2021). Internet of Things Geosensor Network for Cost-Effective Landslide Early Warning Systems. *Sensors* 21, 2609. doi:10.3390/s21082609
- Hu, Z.-N., Li, G.-Q., and Hu, N.-L. (2016). Research on Catastrophe Risk Financing Mode for Tailings Pond Dam Break. *dtem*. doi:10.12783/dtem/iceme-ebm2016/4161
- Jiang, L., Sun, H., Peng, T., Ding, W., Liu, B., and Liu, Q. (2021). Comprehensive Evaluation of Environmental Availability, Pollution Level and Leaching Heavy Metals Behavior in Non-ferrous Metal Tailings. *J. Environ. Manage.* 290, 112639. doi:10.1016/j.jenvman.2021.112639
- Kanakaraja, P., Aswin Kumer, S. V., Kotamraju, S. K., Jhansi Lakshmi, M., Irfan, S., and Chandra Lekha, U. (2021). Environment Quality Monitoring System Based on Cloud Computing Analysis. *Mater. Today Proc.* 46, 3864–3870. doi:10.1016/j.matpr.2021.02.332
- Kong, N. (2017). Getting to Know Web GIS. *Cartographic J.* 54, 188–189. doi:10.1080/00087041.2017.1307041
- Li, D. (2021). Application of WebGL Technology in Web Graphics Based on Three.js (In Chinese). *J. Inner Mongolia Agric. Univ. (Natural Sci. Edition)* 42, 99–103. doi:10.16853/j.cnki.1009-3575.2021.02.019
- Li, H., Li, Z., Ma, F., and Liu, C. (2020a). Similarity Analysis of Dam Behavior Characterized by Multi-Monitoring Points Based on Cloud Model. *Int. J. Distributed Sensor Networks* 16, 155014772092022. doi:10.1177/1550147720920226
- Li, N., Li, C., Chu, W., Xiao, K., Tao, W., Song, X., et al. (2021a). Uncertainty Visualisation of a 3D Geological Geometry Model and its Application in GIS-Based Mineral Resource Assessment: A Case Study in Huayuan District, Northwestern Hunan Province, China. *J. Earth Sci.* 32, 358–369. doi:10.1007/s12583-021-1434-y
- Li, S., Yuan, L., Yang, H., An, H., and Wang, G. (2020b). Tailings Dam Safety Monitoring and Early Warning Based on Spatial Evolution Process of Mud-Sand Flow. *Saf. Sci.* 124, 104579. doi:10.1016/j.ssci.2019.104579
- Li, X., Li, J., Liu, C., and Chen, C. (2021b). Safety Monitoring System Based on Internet of Things Tailings Dam. *Ijs* 40, 3005–3014. doi:10.3233/JIFS-189339
- Li, X., Wen, Z., and Su, H. (2021c). An Approach Using Random forest Intelligent Algorithm to Construct a Monitoring Model for Dam Safety. *Eng. Comput.* 37, 39–56. doi:10.1007/s00366-019-00806-0
- Liao, W., Zhu, Y., and Wang, Q. (2021). Research on Safety Management System of Tailings Pond Based on UAV Intelligent Cruise (In Chinese). *Mining Res. Develop.* 41, 165–170. doi:10.13827/j.cnki.kyyk.2021.09.031
- Liu, Z.-N., Yu, X.-Y., Jia, L.-F., Wang, Y.-S., Song, Y.-C., and Meng, H.-D. (2021). The Influence of Distance Weight on the Inverse Distance Weighted Method for Ore-Grade Estimation. *Sci. Rep.* 11, 2689. doi:10.1038/s41598-021-82227-y
- Lumbroso, D., Collell, M. R., Petkovsek, G., Davison, M., Liu, Y., Goff, C., et al. (2021). DAMSAT: An Eye in the Sky for Monitoring Tailings Dams. *Mine Water Environ.* 40, 113–127. doi:10.1007/s10230-020-00727-1
- Luo, G., Han, Z., Xiong, J., He, Y., Liao, J., and Wu, P. (2021). Heavy Metal Pollution and Ecological Risk Assessment of Tailings in the Qinglong Dachang Antimony Mine, China. *Environ. Sci. Pollut. Res.* 28, 33491–33504. doi:10.1007/s11356-021-12987-7
- Ma, Q., Liu, S., Fan, X., Chai, C., Wang, Y., and Yang, K. (2020). A Time Series Prediction Model of Foundation Pit Deformation Based on Empirical Wavelet Transform and NARX Network. *Mathematics* 8, 1535. doi:10.3390/math8091535

- Meng, X. (2019). *Research on Monitoring and Early Warning System of Tailings Dam Deformation Based on Wireless Sensor Network*. Beijing, China: China Metal Bulletin, 6.
- Nishioka, Y., Shiroki, M., and Takizawa, T. (2015). Publishing of New Seamless Geological Map 3D in Japan Using WebGL. *Annu. Meet. Geol. Soc. Jpn.* 061. doi:10.14863/geosocabst.2015.0_061
- Ouyang, J., Liu, Z., Ye, T., and Zhang, L. (2019). Uranium Pollution Status and Speciation Analysis in the farmland-rice System Around a Uranium Tailings Mine in southeastern China. *J. Radioanal. Nucl. Chem.* 322, 1011–1022. doi:10.1007/s10967-019-06783-4
- Padsala, R., Gebetsroither-Geringer, E., Peters-Anders, J., and Coors, V. (2021). Inception of Harmonising Data Silos and Urban Simulation Tools Using 3d City Models for Sustainable Management of the Urban Food Water and Energy Resources. *ISPRS Ann. Photogramm. Remote Sens. Spat. Inf. Sci.* VIII-4/W1-2021, 81–88. doi:10.5194/isprs-annals-VIII-4-W1-2021-81-2021
- Pirsiavash, A., Broumandan, A., and Lachapelle, G. (2017). Characterization of Signal Quality Monitoring Techniques for Multipath Detection in GNSS Applications. *Sensors* 17, 1579. doi:10.3390/s17071579
- Pu, Y., Apel, D. B., Liu, V., and Mitri, H. (2019). Machine Learning Methods for Rockburst Prediction-State-Of-The-Art Review. *Int. J. Mining Sci. Techn.* 29, 565–570. doi:10.1016/j.ijmst.2019.06.009
- Sarantsev, M. I. (2021). From an Observation System to an Automatic Monitoring System: Engineering-Seismometric and Engineering-Seismological Observations at the Sayano-Shushenskaya HPP. *Power Technol. Eng.* 54, 771–781. doi:10.1007/s10749-021-01286-3
- Shi, Z., Gu, C., Zhao, E., and Xu, B. (2020). A Novel Seepage Safety Monitoring Model of CFRD with Slab Cracks Using Monitoring Data. *Math. Probl. Eng.* 2020, 1–13. doi:10.1155/2020/1641747
- Thatcher, J. (2018). Yes, We Can (Do GIS): a Review of New Lines: Critical GIS and the Trouble of the Map. *Int. J. Geographical Inf. Sci.* 32, 1272–1274. doi:10.1080/13658816.2018.1440398
- Torrero, L., Seoli, L., Molino, A., Giordan, D., Manconi, A., Allasia, P., et al. (2015). “The Use of Micro-UAV to Monitor Active Landslide Scenarios,” in *Engineering Geology For Society And Territory - Volume 5*. Editors G. Lollino, A. Manconi, F. Guzzetti, M. Culshaw, P. Bobrowsky, and F. Luino (Cham: Springer International Publishing, 701–704. doi:10.1007/978-3-319-09048-1_136
- Tsukuma, H. (2019). Exact Finite-Sample Bias and MSE Reduction in a Simple Linear Regression Model with Measurement Error. *Jpn. J. Stat. Data Sci.* 2, 1–29. doi:10.1007/s42081-018-0025-3
- Wang, H. J., and Yong, Z. Q. (2014). A Design of Coal Mine Security Monitoring Substation Based on ZIGBEE and CAN Bus. *Amr* 971-973, 1033–1036. doi:10.4028/www.scientific.net/AMR.971-973.1033
- Wang, L., Xie, M., and Cai, X. (2014). Research on Method of Displacement Speed Ratio for Spatial Evaluation of Landslide Deformation (In Chinese). *Rock Soil Mech.* 35, 519–528. doi:10.16285/j.rsm.2014.02.019
- Wang, M., Dong, Z., Shi, K., and Su, Z. (2021). Exploration of WebGL Technology and Comparison of Several WebGL Based Engines (In Chinese). *China Sci. Techn. Inf.*, 89–90. doi:10.3969/j.issn.1001-8972.2021.05.030
- Wang, Y., Xu, Q., Zheng, G., and Zheng, H. (2015). A Rheology Experimental Investigation on Early Warning Model for Landslide Based on Inverse-Velocity Method (In Chinese). *Rock Soil Mech.* 36, 1606–1614. doi:10.16285/j.rsm.2015.06.011
- Wen, J., Yang, J., Jiang, B., Song, H., and Wang, H. (2021). Big Data Driven Marine Environment Information Forecasting: A Time Series Prediction Network. *IEEE Trans. Fuzzy Syst.* 29, 4–18. doi:10.1109/TFUZZ.2020.3012393
- Wenxue, C., Longkang, W., Hui, W., and Zhuwu, Z. (2011). Zigbee-Based Prediction System for Coal Rock Dynamic Disasters. *Proced. Eng.* 26, 2253–2260. doi:10.1016/j.proeng.2011.11.2432
- Xu, Q., and Zeng, Y. (2009). Research on Acceleration Variation Characteristics of Creep Landslide and Early-Warning Prediction Indicator of Critical Sliding (In Chinese). *Chin. J. Rock Mech. Eng.* 28, 109
- Xu, Y. (2021). Application of Slope Stability Radar Monitoring and Early Warning System in a Mine (In Chinese). *Mod. Mining* 37, 159
- Xu, Y., Wei, J., Zhou, X., and Sun, F. (2019). Application and Development of Smart Mine in China. *MATEC Web Conf.* 295, 02005. doi:10.1051/mateconf/201929502005
- Yadav, R. K., and Balakrishnan, M. (2014). Comparative Evaluation of ARIMA and ANFIS for Modeling of Wireless Network Traffic Time Series. *J. Wireless Com Netw.* 2014, 15. doi:10.1186/1687-1499-2014-15
- Yang, P., Wang, N., Jiang, Z., Yang, Y., and Yan, H. (2019). Overview of Slope Monitoring Technology. *IOP Conf. Ser. Mater. Sci. Eng.* 472, 012009. doi:10.1088/1757-899X/472/1/012009
- Zhang, C., Wang, X., Jiang, S., Zhou, M., Li, F., Bi, X., et al. (2021). Heavy Metal Pollution Caused by Cyanide Gold Leaching: a Case Study of Gold Tailings in central China. *Environ. Sci. Pollut. Res.* 28, 29231–29240. doi:10.1007/s11356-021-12728-w
- Zhang, X. (2021). Prediction of Fire Risk Based on Cloud Computing. *Alexandria Eng. J.* 60, 1537–1544. doi:10.1016/j.aej.2020.11.008
- Zheng, N., Chen, P., and Li, Z. (2021). Accuracy Analysis of Ground-Based GNSS-R Sea Level Monitoring Based on Multi GNSS and Multi SNR. *Adv. Space Res.* 68, 1789–1801. doi:10.1016/j.asr.2021.04.024
- Zhou, H., Yuan, Z., Su, J., Yang, X., and Zhang, D. (2015). *The Present Situation and Prospects for Safety Online-Monitoring System of Tailings Pond*. Shenzhen, China: Shenzhen. doi:10.2991/icmra-15.2015.94
- Zhu, Y., Cao, W., An, P., and Liu, H. (2021). *Design of Mine Geological Disaster Monitoring and Early Warning System Based on Lora Technology (In Chinese)*. Beijing, China: World Nonferrous Metals, 207–208.

Conflict of Interest: Authors WN and YW were employed by Sinosteel Maanshan General Institute of Mining Research Company Limited, and RL was employed by the company Zijin Mining Company Limited.

The remaining authors declare that the research was conducted in the absence of any commercial or financial relationships that could be construed as a potential conflict of interest.

Publisher’s Note: All claims expressed in this article are solely those of the authors and do not necessarily represent those of their affiliated organizations, or those of the publisher, the editors, and the reviewers. Any product that may be evaluated in this article, or claim that may be made by its manufacturer, is not guaranteed nor endorsed by the publisher.

Copyright © 2022 Nie, Luo, Wang and Li. This is an open-access article distributed under the terms of the Creative Commons Attribution License (CC BY). The use, distribution or reproduction in other forums is permitted, provided the original author(s) and the copyright owner(s) are credited and that the original publication in this journal is cited, in accordance with accepted academic practice. No use, distribution or reproduction is permitted which does not comply with these terms.



Research on Roof Cutting Pressure Relief of the Gob-Side Entry Retaining With Roadside Backfilling

Kun Zhang, Changyou Liu*, Hanrui Zhang, Xin Yue and Huaidong Liu

School of Mines, China University of Mining and Technology, Xuzhou, China

OPEN ACCESS

Edited by:

Qingsheng Bai,
Freiburg University of Mining and
Technology, Germany

Reviewed by:

Defu Zhu,
Taiyuan University of Technology,
China

Baobao Chen,
Anhui University of Science and
Technology, China

*Correspondence:

Changyou Liu
cylucumt@163.com

Specialty section:

This article was submitted to
Geohazards and Georisks,
a section of the journal
Frontiers in Earth Science

Received: 14 December 2021

Accepted: 19 January 2022

Published: 09 March 2022

Citation:

Zhang K, Liu C, Zhang H, Yue X and
Liu H (2022) Research on Roof Cutting
Pressure Relief of the Gob-Side Entry
Retaining With Roadside Backfilling.
Front. Earth Sci. 10:835497.
doi: 10.3389/feart.2022.835497

Based on the application of the retained gob-side entry in a fully mechanized face E2307 headgate, the stress distribution and deformation characteristics of the roadside backfill body for different types of roof cutting were investigated in this study by employing a combination method of theoretical analysis, numerical simulation, and field measurement. The study uses RocLab software to accurately modify the lithology of the simulation area, discuss the position of roof cutting and the pressure relief parameters of roof cutting, and select the optimal solution of the roof-cutting plan. The results show that the advanced pre-cracking effectively blocks the stress transmission in the high-level roof strata; the roadway is in the stress unloading zone, the stress environment of the surrounding rock in the roadway is significantly optimized, and the deformation of the surrounding rock in the roadway is significantly reduced. In the roof-cutting scheme, the deformation of the surrounding rock in the 90° main roof-cutting scheme is reduced by 78% compared with the uncut roof and by 39% compared with the 90° immediate roof cutting. The research results were successfully applied at the E2307 headgate of the Gaohe coal mine; the maximum roof subsidence and the maximum rib convergence were 121 and 74 mm, respectively. Field monitoring indicates that the deformation of the retained entry was controllable, and the final retaining effects were good.

Keywords: pressure relief, fracturing roof, height, angle, roof cutting

1 INTRODUCTION

The longwall mining method is the most mainstream application of coal mining methods in China. Chain pillars can effectively provide stress buffers for adjacent longwall face, mining replacement, and gas isolation. However, coal pillars also caused problems such as waste of resource and hidden dangers of spontaneous combustion of coal pillars (Hou et al., 2019; He et al., 2017). The gob-side entry retaining solves this problem to a large extent. On the one hand, it reduces the waste of resource; on the other hand, it reduces the amount of roadway excavation and optimizes the ventilation method. But roadside backfilling leads to increased stress on the surrounding rock of the roadway and damage to the roof structure. Excessive confining pressure of the roadway is not conducive to support. The study adopts the roof-cutting pressure relief technology, which changes the stress environment of the roadway by adjusting the occurrence state of the roof. It can cut the roof according to the design position, block the stress transmission of the roof, and place it in the pressure relief zone, eliminating the threat of the high stress environment. So that the roadway is in the stress unloading zone, which is conducive to roadway maintenance, reduces the difficulty of support, and greatly reduces the construction cost and time (Chen et al., 2012; Liu et al., 2019, 2020; Ma et al., 2021).

In the study of the surrounding rock stress of gob-side entry, the most important thing to be studied is the roof pressure above the roadway. Zhang et al. conducted in-depth studies from the composite characteristics of the roof structure, deformation, and migration law of the roadway surrounding the rock, stability of the roadway surrounding the rock, and stability of the load-bearing structure, through theoretical analysis, numerical simulation, and field investigation; it is proposed that the stability of the surrounding rock of a roadway in gob-side entry retaining is improved by roof cutting and pressure relief, and it is concluded that the large amount of elastic energy stored in the hard roof in the gob-side entry retaining is the main reason for roadway instability (Li et al., 2012; Han et al., 2013a; Zhang et al., 2014; Ning et al., 2018). Han et al. proposed that the “three-high strength” bolt and cable support technology should be adopted in the gob-side entry retaining, and the segmented and zoned control of the surrounding rock in space and time should be carried out in combination with the single pillar (Zhang et al., 2012; Han et al., 2013b). Yu et al. established the mechanical model of a cantilever beam of roof cutting and studied the roof deformation law and the key factors; it is concluded that the turning angle of the roof and the width of the narrow coal pillar have an important influence on roof deformation, while the cable cannot prevent roof deformation, and give the reasonable cutting top height, and through the field test, results of theoretical calculation are verified (Han et al., 2017; He et al., 2021). He et al. optimized the principle of the roof cutting short-boom beam mining method (110 method) on the premise, systematically expounded the technical parameters of the top-cutting pressure relief, summarized the rule of mining stress distribution in the process of roof-cutting pressure relief, studied the change of stress distribution in the roof during roof-cutting pressure relief through theoretical analysis, and achieved fine effects in the field (Tai et al., 2020; Yu et al., 2020; Liu et al., 2021).

Different materials of roadside packing lead to different mechanical properties of different types, which lead to great differences in the mechanical response. The roadside packing plays an important role in air leakage and prevention of spontaneous combustion in goaf; generally speaking, roadside packing has five materials: wood, waste rock, concrete block, paste filler, and high-water material. At present, paste fillers and high-water materials are gradually replacing the previous traditional materials because of their advantages such as good ventilation and tightness, convenient transport, and good mechanical properties. In addition, Chinese researchers have conducted some experimental studies on the physical and mechanical properties of glass fiber-reinforced plastics prepared with paste filler materials or high-water materials. All of these suggest that the strength and deformability of the roadside packing depends on the proportion of its constituent materials mixed so that for roadside packing with a specific proportion, relevant laboratory tests are essential to ensure a reasonable and scientific mechanical description of its behavior.

Roof cutting has great significance for improving the coal recovery rate, reducing the amount of roadway driving, alleviating the tight connection between mining and excavation, controlling gas at the corners of the longwall face, and extending the service life of the mine. The technology of roof cutting and remained tunnel greatly improves the stress environment of the

surrounding rock of the roadway and eliminates the stress concentration above the coal of the adjacent longwall face.

The supporting strength of the roadside backfilling body changes the distribution of the bending moment above the roadway. The supporting strength of the roadside backfilling body not only can cut down the soft coal and immediate roof but also can control roof convergence. However, for a harder and thicker roof, the required supporting strength of the roadside backfilling body is also greater; sometimes the roadside backfilling body with the uncut roof may develop more fissures, which causes the roadway pressure to appear severe (Ma et al., 2018). Aimed at this phenomenon, the study compared and analyzed the plastic zone and stress changes of the surrounding rock of the roadway in different roof-cutting schemes while considering both the strain softening model of coal and the double-yield model of the goaf.

2 BACKGROUND

2.1 Engineering Background

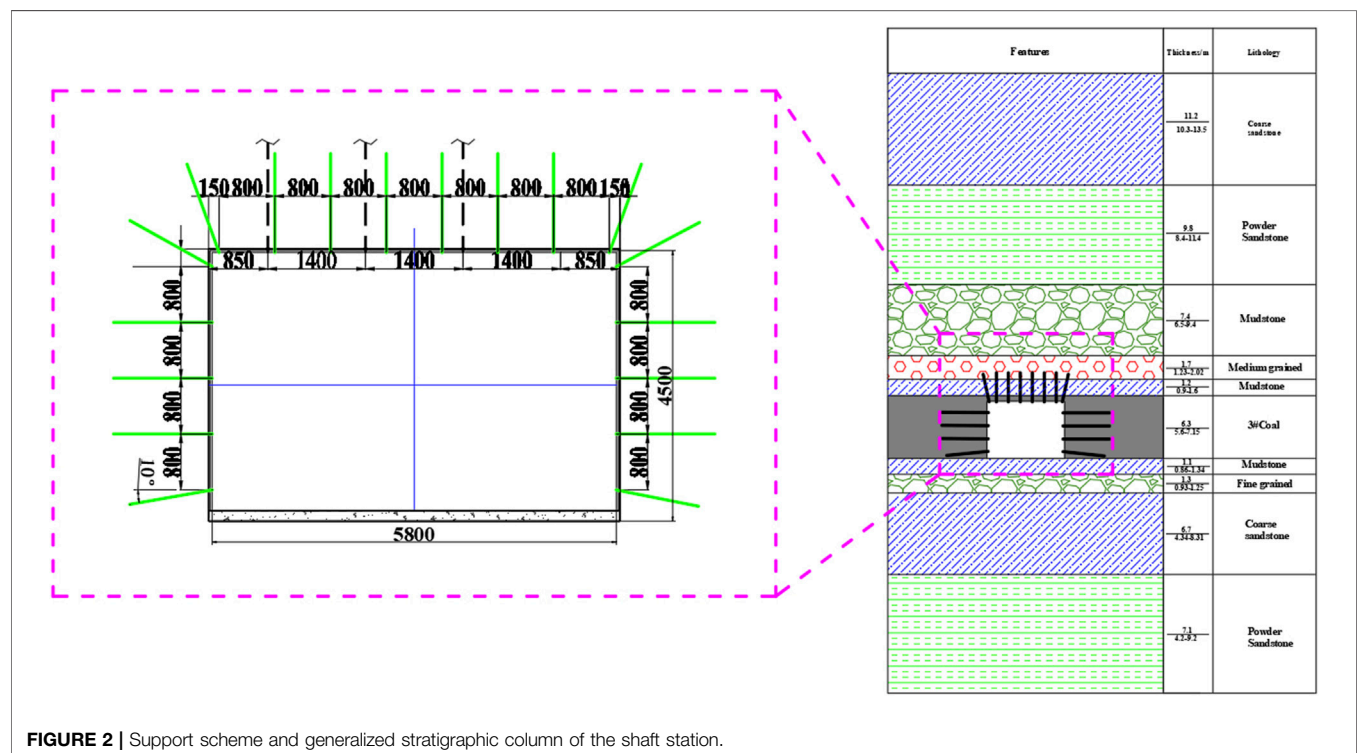
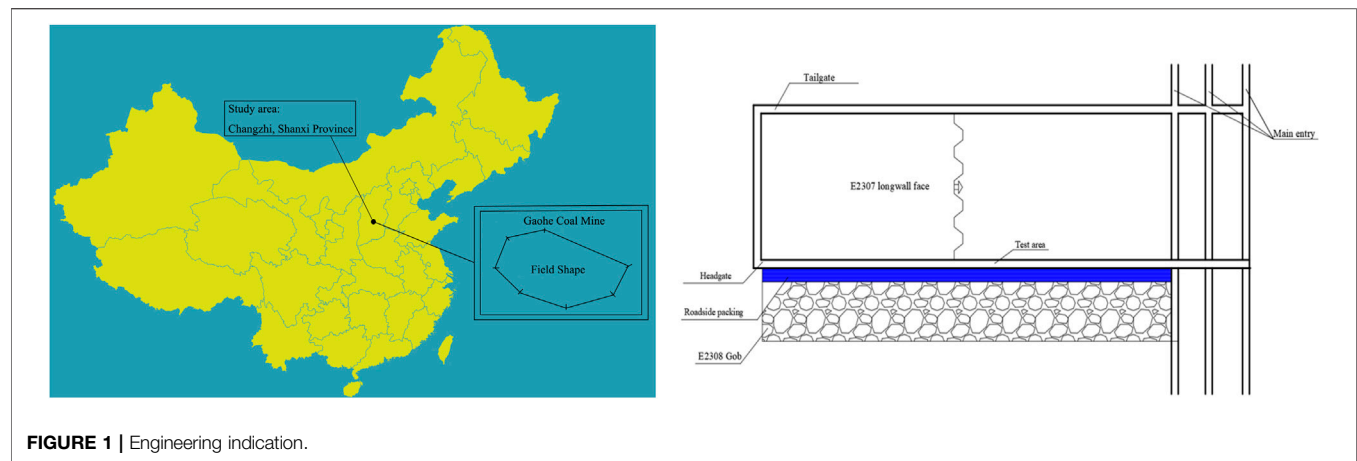
The Gaohe coal mine is located in Changzhi City, Shanxi Province, China (Figure 1). The coal seam is No.3, which lies at an average depth of 638.3 m, with an average thickness and average dip of 3.5 m and 5°, respectively. The roof rock strata are, in ascending order, marlstone (2.4 m), siltstone (4.2 m), medium sandstone (4.7 m), and limestone (6.4 m), while those below are, in descending order, mudstone (2.2 m), medium sandstone (2.9 m), and siltstone (4.2 m).

The bolts with 22 mm in diameter and 2,500 mm in length were used for roof and rib supporting. Roof and ribs bolts were installed with a spacing of 700 mm × 700 mm. In some local areas, anchor cables with 21.8 mm in diameter and 8,800 mm in length were used for reinforced support. The cables were installed with a spacing of 1,400 mm × 1,400 mm. A steel bar ladder beam (14 mm in diameter) and a metal mesh (6 mm in diameter) were used for surrounding rock control (Figure 2).

The surrounding rock above the E2307 headgate is a hard roof with an average thickness of 25.9 m (Figure 3).

Starting from the immediate roof of mudstone (4.9 m), the huge and hard roof with a thickness of 25.9 m has good integrity, and it is difficult for the roof to collapse after mining.

Field observations found that severe entry deformation and supporting system failure occurred about 1 month after the entry excavation (Figure 4). Roof sag was very common in the field; the measured convergence of the roof sag reached up to 1,200 mm, which significantly increased the risk of roof collapse and endangered the safety of workers and equipment. In some areas, there were large-scale roof collapse accidents. Fortunately, there were no casualties. The coal mass of two ribs was fractured into massive loose fragments, resulting in severe extrusion deformation with a maximum convergence of 892 mm in the middle-upper part of the ribs. This large deformation resulted in the conspicuous protuberances on the surface of the sidewalls and the failure of the steel mesh and beams. In addition, floor heave was also quite common, and the displacement induced by the floor heave reached up to 256 mm, causing the floor concrete to crack and further compromising the efficiency of underground transportation. As such, the entry



exhibited a drastic reduction in the cross section due to severe roof sag, rib convexity, and floor heave; the effective space used for ventilation and coal-mine transportation was less than 7.8 m^2 , resulting in excessive labor and costs for entry rehabilitation.

2.2 Rock Mechanics Parameters

In order to have a detailed understanding of the surrounding rock properties of the E2307 headgate, the suitable position of the E2307 headgate was selected to collect coal and rock samples. After being transported to the laboratory for standardized processing (Figure 5), the rock mechanics parameters are measured on the SANS (TAW-2000) machine.

After sampling in the E2307 headgate, standard specimens were made, and the rock parameters were measured, as shown in Table 1.

2.3 Summary of the Case Study

Using the rock properties' experiments and field observation, the ground conditions of the E2307 headgate have been comprehensively investigated. However, excessive deformation and poor stability have become the primary issues, and severe fractures and large deformations can significantly destabilize the surrounding rock, which leads to potential safety issues and economic losses due to E2307 headgate repair and secondary supporting installation. In the following sections, a numerical analysis of the case study is conducted

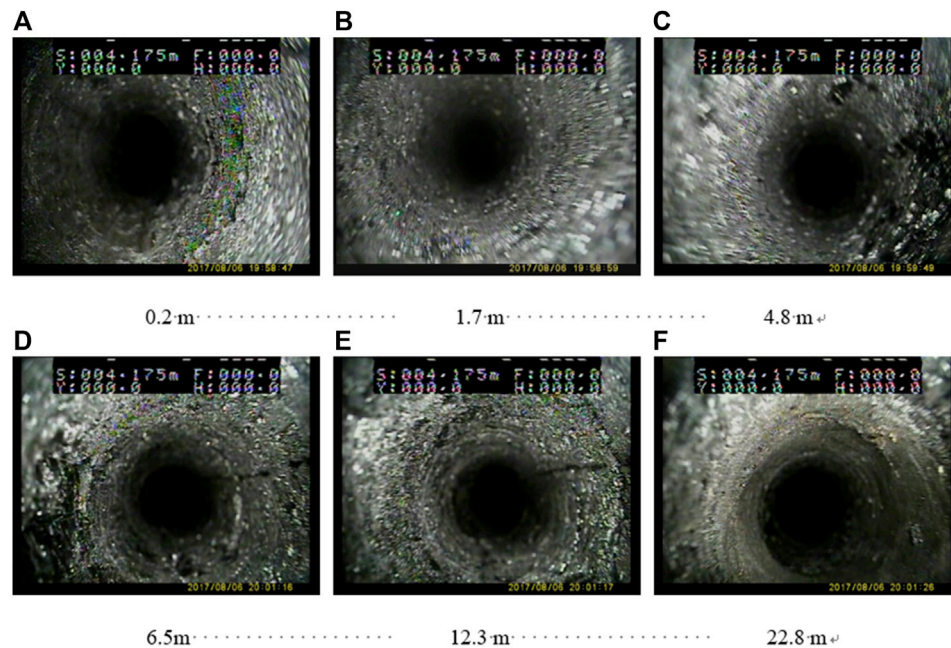


FIGURE 3 | E2307 headgate roof occurrence situation. (A) 0.2 m (B) 1.7 m (C) 4.8 m (D) 6.5 m (E) 12.3 m (F) 22.8 m.

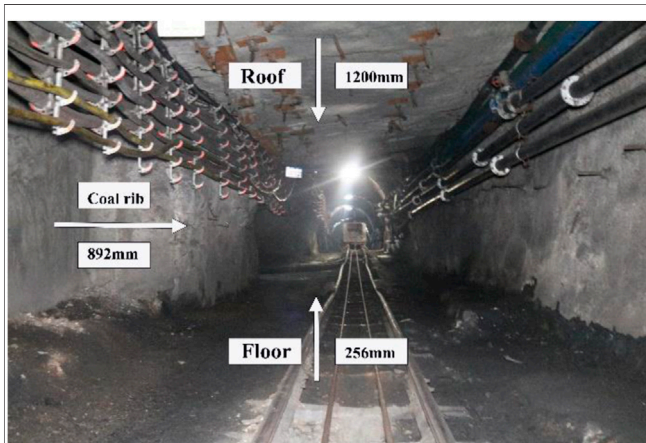


FIGURE 4 | Field monitoring and observation of ground stability.

using the three-dimensional finite-difference software FLAC^{3D}. At the same time, calculation and field test are discussed in the following section.

3 ANALYSIS OF PRESSURE RELIEF CAUSED BY ROOF CUTTING

Based on the geological and geotechnical conditions of the E2307 headgate, which is decided by field observation, the main roof is broken in the form of “masonry beam,” and the breaking line is

located above the E2307 headgate, which causes most of the weight of the rock block B to be applied to the roof of the E2307 headgate. The breaking structure of the overlying strata shows that the surrounding rock of the roadway bears greater vertical stress, which makes roadway supporting more difficult. The present study provides an efficient and simple tool to predict the breaking mode of the main roof and will be helpful to analyze the problems of roof cutting. As the coal seam is mined, the immediate roof will subsequently collapse and sink irregularly, slip, and separate from the main roof above it. After the overburden rock migration is stable, the main roof forms a hinged structure composed of the rock mass A and blocks B and C (Figure 6).

The roadside backfill body of the E2307 headgate is under the cantilever beam, and the longer thick cantilever causes the roadside backfill body to bear excessive additional load and damage, which leads to the deformation and instability of the surrounding rock structure of the roadway. So the structure B is very important for the stability of the surrounding rock structure of the gob-side entry, and the structure B mainly includes three basic dimensions: the lateral rift size of the main roof (D), the main roof periodic weighting L , and the thickness of the Block B (h). Among them, L is the step length of the main roof cycle compression, which can be obtained by field observation or theoretical calculation; h is the thickness of the basic top rock layer; D is related to the longwall face width S and the main roof periodic weighting L , which can be calculated with the following Eq. 1,

$$D = \frac{2L}{17} \left[\sqrt{\left(10 \frac{L}{S}\right)^2 + 102} - 10 \frac{L}{S} \right], \quad (1)$$



FIGURE 5 | Rock mechanics test equipment and samples.

TABLE 1 | Measurement results of rock mechanical parameters.

Lithology	Compressive strength/MPa	Shear strength/MPa	Tensile strength/MPa	Poisson ratio	Cohesion/MPa	Friction/°
Silty mudstone	12.2	3.5	1.6	0.27	6.4	28.1
Fine sandstone	38.9	13.7	2.9	0.26	11.2	36.8
Pelitic siltstone	28.4	14.4	2.4	0.24	12.1	34.1
Coal	9.8	5.1	1.7	0.31	4.4	28.5
Mudstone	7.8	20.3	1.8	0.32	5.7	32.5
Medium fine sandstone	43.4	32.3	2.3	0.24	10.7	36.2

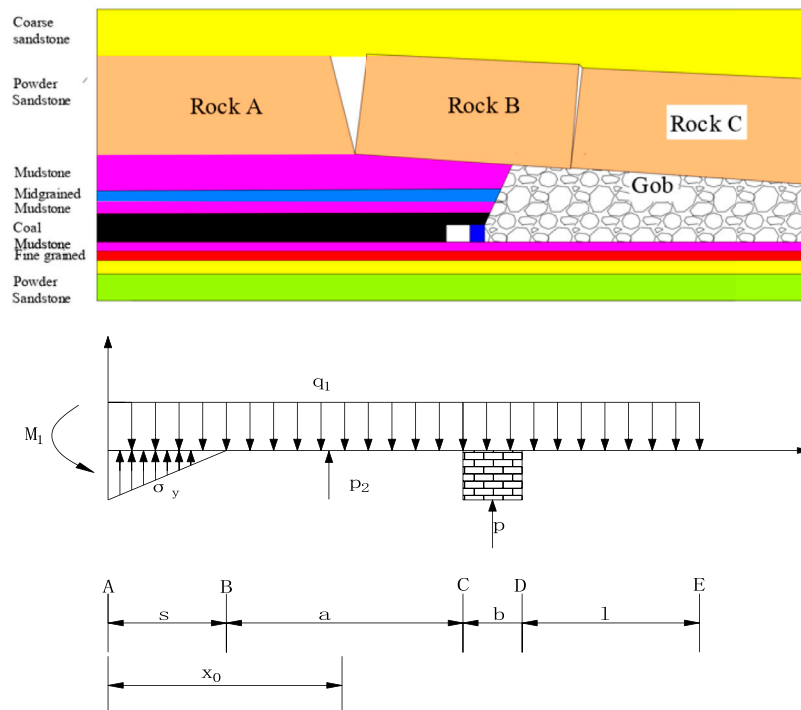


FIGURE 6 | Simplified physical model of a lateral cantilever beam.

For the force analysis of Block B, the mechanical model of the lateral cantilever beam (**Figure 5**), which assuming that the uniform roof load is $q_1 = gH$, the integrated coal

distributed load σ_z acts on the line AB, and the supporting resistance p_2 in the roadway acts at x_0 ($s < x_0 < s+a$).

The width of the stress limit equilibrium zone of the coal rib(s) and the distributed load of the integrated coal (σ_z) are, respectively,

$$s = \frac{mA_1}{2 \tan \varphi_0} \ln \frac{k\gamma H + c_0/\tan \varphi_0}{c_0/\tan \varphi_0 + P_0/A_1}, \quad (2)$$

$$\sigma_z = \left(\frac{c_0}{\tan \varphi_0} + \frac{P_0}{A_1} \right) \exp \left[\frac{2 \tan \varphi_0}{mA_1} (s - x_0) \right] - \frac{c_0}{\tan \varphi_0}, \quad (3)$$

where

P_0 —supporting strength of the coal rib, MPa;
 φ_0 —the internal friction angle of the interface between the coal seam and the roof and floor rocks, °;
 A_1 —the coefficient of lateral pressure;
 γ —the bulk density of the overlying strata, N/m³;
 k —the stress concentration factor;
 H —the mining depth, m;
 m —the mining height, m;
 c_0 —the cohesive force of the interface between the coal seam and the roof and floor rocks, MPa; the point A is balanced.

$$\begin{aligned} \sum M &= 0 \\ \frac{1}{2} q_1 (s + a + b + l)^2 - P_1 \left(s + a + \frac{1}{2} b \right) - P_2 x_0 - \int_0^s \sigma_z x dx - M_1 \\ &= 0, \end{aligned} \quad (4)$$

$$M_1 = \frac{1}{2} q_1 (s + a + b + l)^2 - P_1 \left(s + a + \frac{1}{2} b \right) - P_2 x_0 - M', \quad (5)$$

where

$$M' = \int_0^s \sigma_z x dx, \quad (6)$$

$$\begin{aligned} M' &= \frac{m^2 A_1^2 c_0 + m^2 A_1 P_0 \tan \varphi_0}{4 \tan^3 \varphi_0} (e^{2 \tan \varphi_0 / M A_1} - 1) \\ &\quad - \frac{m A_1 c_0 + m P_0 \tan \varphi_0}{2 \tan^2 \varphi_0} s - \frac{c_0}{2 \tan \varphi_0} s^2, \end{aligned} \quad (7)$$

For unit-width rectangular cells,

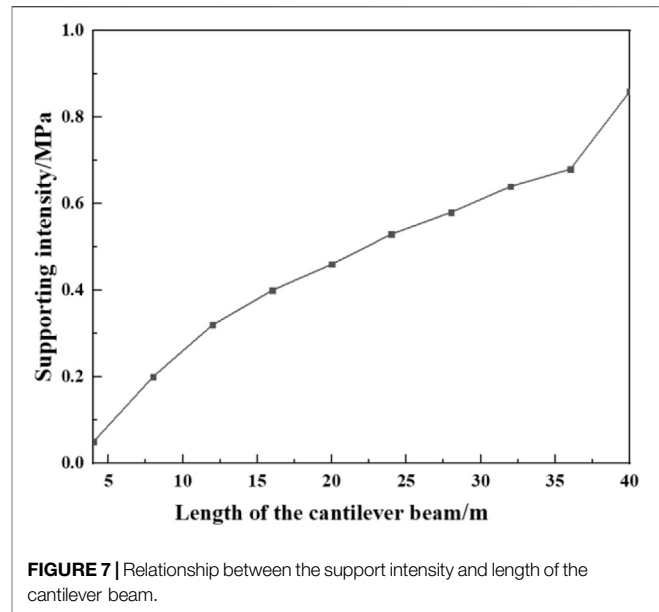
$$M = \frac{h^2}{6} R_t, \quad (8)$$

where

R_t —tensile strength of the roof rock, MPa;
 H —thickness of the hard immediate roof, m. The ultimate bending moment of the main roof lateral suspension cantilever is M_{\max} ; then, the relationship between the roadside backfilling body supporting strength P_1 and the suspension length l is from $M_1 < M_{\max}$.

$$P_1 = \frac{q_1 (s + a + b + l^2) - 2M_{\max} - 2P_2 x_0 - 2M'}{2s + 2a + b}. \quad (9)$$

It can be seen from Eq. 9 that the greater the length of the lateral cantilever beam (l) of the collapsed roof, the greater is the roadside backfilling body supporting strength when the roof is required to be cut. The relationship between the support intensity



and length of the cantilever beam can be seen in Figure 7. By controlling the length of the suspended ceiling, the pressure on the filling wall can be reduced, which plays a positive role in supporting the E2307 headgate.

When the main roof breaks at a certain position outside the roadside backfilling body, because the cantilever position of rock block A is longer, it will still cause a series of pressure problems on the roadside backfilling body and the roadway. A certain position above the roadside backfilling body breaks, and even rock block B will not be completely fractured; at this time, the roadside backfilling body bears less pressure from the roof, and the stability of the roadway is the best. The study uses the roof-cutting technology to release pressure (Figure 8).

After panel retreat, the caved zone and fracture zone are formed above the gob-side entry during overlying strata breaking and caving, and there will be a cantilever beam above the retained gob-side entry (Figure 7A). Because there is no supporting structure below the cantilever beam, the own weight of the rock and overburden loading of the cantilever area makes it bend, and the loading transforms to the gob gangue and virgin coal rib. Therefore, the existence of a cantilever beam makes it difficult to maintain the stability of the surrounding rock, which has a huge impact on roadway safety. The dam boards were installed at a height of 3.5 m along the gob-side and at a height of 3.4 m in the inner roadway side. A plastic membrane was laid inside of the dam-boards tightly. The width between outside and inside was maintained at 5.0 m. In this study, the roof cutting was performed by deep hole blasting to form a fracturing line above the goaf along the roadway (Figure 7B), and the cantilever beam weight and the overburden load caused it to break along the fracturing line to reduce the overhanging length. It can reduce the influence of its own weight and the load of the overlying rock, improve the stress environment, and ensure the stability of the roadway.

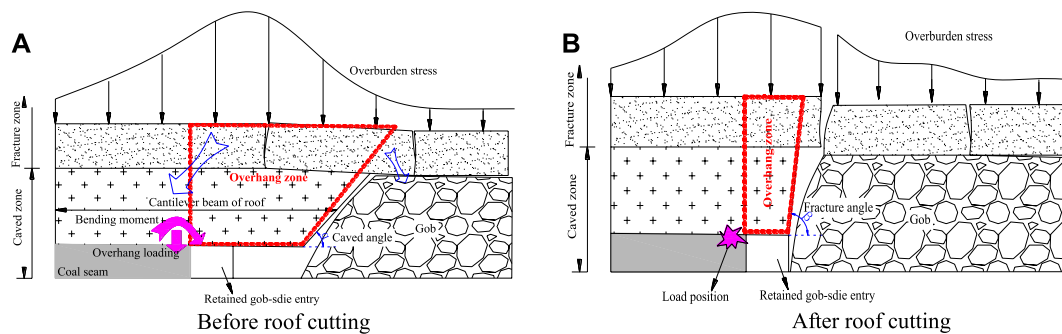


FIGURE 8 | Mechanism of roof cutting. (A) Before roof cutting. (B) After roof cutting.

FLAC3D 5.01
©2014 Itasca Consulting Group, Inc.

Zone
Colorby: Group Any
 coal
 floor-medium-fine-sandstone
 floor-mudstone
 obturator
 overlying-strata1
 overlying-strata2
 overlying-strata3
 roof-fine-mudstone-1
 roof-fine-mudstone-2
 roof-fine-sandstone

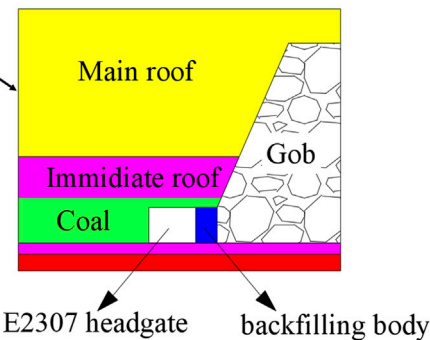
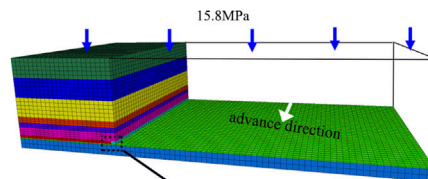


FIGURE 9 | Simulation model.

4 KEY PARAMETERS OF ADVANCED CUTTING AND PRESSURE RELIEF

According to the above analysis, this study analyzes and compares the two key parameters of the pre-crack cutting roof angle and the pre-crack cutting roof height through accurate numerical simulation calculations and optimizes the plan on this basis to obtain the optimal key parameters of the roof-cutting plan.

4.1 Establishment of the Numerical Model

According to the engineering geological conditions of the E2307 headgate, combined with the measured ground stress and stress data monitoring results, the study uses FLAC^{3D} to establish the model of the E2307 headgate, adjacent goaf, and surrounding rock formations, to compare and analyze the plastic zone distribution, surrounding rock displacement, and stress distribution under

different schemes so as to obtain an optimized plan. The average buried depth of the E2307 headgate is 630 m, so the upper load is 15.8 MPa; combined with the ground stress test results, a horizontal stress of 18.9 MPa with a direction angle of 31.55° and an inclination angle of 8.9° is applied (**Figure 9**).

For E2307 headgate roof cutting, two advanced pre-splitting schemes are proposed:

- 1) Punch the edge of the flexible mold to a vertical depth of 13 m, reaching the main roof;
- 2) The edge of the flexible mold is punched to a vertical depth of 6 m, reaching the immediate roof. The scheme is shown in **Figure 10**.

For the two schemes, pre-splitting schemes with different angles and different depths of pre-splitting holes are proposed, and the summary is shown in **Table 2**.

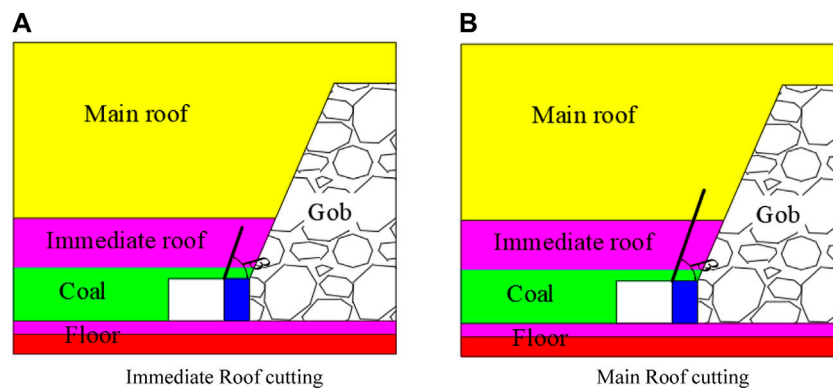


FIGURE 10 | Simulation schemes. **(A)** Immediate roof cutting **(B)** Main roof cutting.

TABLE 2 | Simulation scheme parameters.

Simulation schemes	Case 1	Case 2	Case 3	Case 4
Angle of the fracture line (deg.)	30°	45°	60°	90°
Height of the fracture line (m)	6 m	6 m	6 m	6 m
Simulation schemes	Case 5	Case 6	Case 7	Case 8
Angle of the fracture line (deg.)	30°	45°	60°	90°
Height of the fracture line (m)	13 m	13 m	13 m	13 m

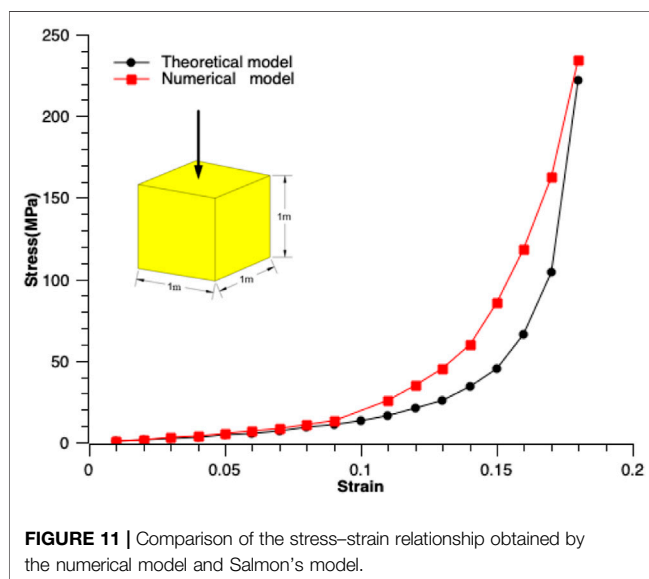


FIGURE 11 | Comparison of the stress-strain relationship obtained by the numerical model and Salmon's model.

4.2 Parameter Determination

4.2.1 Demonstration of Numerical Accuracy of Top-Cutting Pressure Relief

The numerical simulation is to study the improvement of the stress environment of the surrounding rock of the roadway by different roof-cutting parameters. The double-yield model is used to study the real behavior of the surrounding rock after roof cutting. The volume of the fall and the mined-out area is

compressed, and the original surrounding rock support capacity is also increased. According to the previous research study, the input parameters required for the double-yield model are cap pressure and materials' proper-ties (Bai et al., 2014; Zhang et al., 2015; Bai et al., 2017). The former can be calculated by empirical formulas, and the latter can be obtained by the trial and error method through single-element sub-models:

$$\sigma = \frac{E_0 \varepsilon}{1 - (\varepsilon/\varepsilon_{\max})}, \quad (10)$$

where σ is the stress of the rock mass, E_0 is the strength of the rock mass, and ε is the maximum volumetric strain of the rock mass. Combined previous studies, E_0 and ε can be estimated as follows (Wang et al., 2018; Yang et al., 2020):

$$\varepsilon_{\max} = \frac{b-1}{b}, \quad (11)$$

$$E_0 = \frac{1.039\sigma_c^{1.042}}{b^{7.7}}, \quad (12)$$

Here, σ_c is the strength of the collapsed rock, and b is the expansion coefficient; for the E2307 headgate, σ_c and b are set to 27 MPa and 1.23, respectively, and ε_{\max} and E_0 are 0.19 and 65.44 MPa, respectively.

In order to determine the rock parameters of the gob, a unit sub-model of $1\text{ m} \times 1\text{ m} \times 1\text{ m}$ was established. The load is simulated by applying different constant strain rates on the top surface of the model (**Figure 11**).

The stress-strain curve of the given variable obtained by the formula is fitted by the iterative changes of the volume and modulus, expansion angle, and friction angle of the rock in the mined-out area (**Figure 9**). The results show that the peak pressure predicted by the model is 223.77 MPa, and the strain is 18.2%. This value is consistent with the calculation result of the formula. The peak pressure predicted by the formula is 220.03 MPa, and the strain is 17.3%. Although the vertical pressure growth rate predicted by the sub-model is faster than that predicted by the formula, in general, the numerical model better predicts the correct rock loading characteristics and shows the calibration characteristics of the

TABLE 3 | Rock mass mechanical properties used in numerical simulation.

Lithology	GSI	<i>m</i>	<i>D</i>	<i>E</i>	<i>K</i>	<i>G</i>	$\Phi/^\circ$	<i>C</i> /MPa	ν
Silty mudstone	60	15	0.7	6.22	4.94	2.41	34	1.1	0.29
Fine sandstone	70	17	0.7	19.1	12.2	7.70	47	2.4	0.24
Pelitic siltstone	60	10	0.7	8.21	6.22	3.21	35	1.23	0.28
Coal	40	8	0.7	1.1	1.02	0.42	14	0.33	0.32
Mudstone	45	10	0.7	2.24	1.87	0.86	22.1	0.589	0.3
Medium fine sandstone	56	15	0.7	5.77	4.01	2.29	34.6	1.31	0.26

TABLE 4 | Coal strain-softening parameter.

Strain	0	1e-4	5e-3	2e-3
Cohesive force/MPa	2e6	2	1.6	1
Friction angle/°	26	24	23	22

materials in the goaf; the double-yield model is relatively accurate.

4.2.2 Parameter Determination

The effect caused by the size gap between the rock sample and the underground rock mass is different; the mechanical parameters of the rock sample measured in the laboratory do not consider the fractures and joints of the rock mass in the formation, and their values cannot truly reflect the mechanical properties of the rock mass (Yang et al., 2019; Zhang et al., 2020). Therefore, the mechanical parameters of rock blocks obtained in the laboratory should be calculated and corrected in the numerical analysis. The study uses RocLab software to modify the rock mechanics parameters.

$$\sigma_1 = \sigma_3 + \sigma_{ci} \left(m_b \frac{\sigma_3}{\sigma_{ci}} + s \right)^a, \quad (13)$$

where

σ_{ci} is the uniaxial compressive strength, σ_1 and σ_3 are the maximum and minimum principal stresses, respectively, m_b , and s and a are the rock mass constants, which can be obtained by the following formula:

$$m_b = m_{ci} \exp\left(\frac{GSI - 100}{28 - 14D}\right), \quad (14)$$

$$s = \exp\left(\frac{GSI - 100}{9 - 3D}\right), \quad (15)$$

$$a = 0.5 + \frac{1}{6} (e^{-GSI/15} - e^{-20/3}), \quad (16)$$

where

m_{ci} is the complete rock mass constant, D is the disturbance coefficient, and GSI is the fractured rock mass evaluation parameter.

$$K = \frac{E}{3(1 - 2\nu)}, \quad (17)$$

$$G = \frac{E}{2(1 + \nu)}, \quad (18)$$

where

K is the bulk modulus, G is the shear modulus, and ν is the Poisson ratio. RocLab software was used to obtain rock mass parameters (Table 3).

The failure process of coal can be divided into the elastic phase, plastic phase, and residual phase. It is pointed out that the strain-softening model can more realistically simulate the failure process of coal (Jiang et al., 2017; Zhang et al., 2017). Therefore, this study gives the coal a strain-softening constitutive model, which realizes the mechanical properties of the coal after its destruction by changing the cohesive force and residual angle of the coal (Zhang et al., 2011; Shi et al., 2013; Zhao et al., 2017; Smart and Haley, 2019). The relevant parameters in strain softening are obtained through mechanical tests (Table 4).

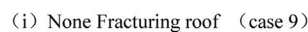
4.3 Analysis of the Position Effect of Roof Cutting

4.3.1 Distribution of the Elastic Zone and Plastic Zone

Accordingly, in order to study the position effect of roof cutting for pressure relief, the different cutting angles and lengths were chosen, and the structure variations with different cutting positions (Figure 12) are analyzed.

The plastic zone distribution of the surrounding rock of the roadway in different schemes is shown in Figure 12. The widths of the plastic zone on the side of the coal rib in the immediate roof-cutting scheme are 7.2 m, 6.8 m, 6.6 m, and 6.2 m, respectively; the plastic zone in the main roof-cutting plan range is 6.4 m, 6.1 m, 5.8 m, and 5.2 m, respectively, and the plastic zone depth in the floor is 1.8 m. The above data show that the plastic zone of the coal rib in Figure 12I is the largest (10.6 m). When the main roof is cut (a, b, c, and d), the plastic zone area is significantly reduced, and the maximum reduction is about 4.4 m. Compared with the uncut top (i), the maximum reduction of the plastic zone range is 5.4 m when the immediate roof is cut (e, f, g, and h). Under the same roof-cutting angle, the plastic zone range of the coal rib in the main roof cutting is smaller than the schemes of immediate roof cutting; at the same top-cutting height, the plastic zone range of the coal rib decreases with the increase of the roof-cutting angle.

It shows that the position and area of the elastic area in the different roof-cutting schemes will vary with different roof-cutting parameters (Figure 13). The undamaged elastic area in the roof of the gob-side entry gradually moves to the top of the roadway with the increase of the roof-cutting angle; under the same roof-cutting angle, the area of the elastic area is larger in the main roof-cutting schemes. When the main roof-cutting angle is 90°, the maximum area of the elastic area in the roof is 15.02 m², while the minimum area of the elastic area is 8.75 m² without roof



(Continued)

FIGURE 12 | (A) 30° (case 1) (B) Fracturing the immediate roof with 45° (case 2) (C) Fracturing the immediate roof with 60° (case 3) (D) Fracturing the immediate roof with 90° (case 4) (E) Fracturing the main roof with 30° (case 5) (F) Fracturing the main roof with 45° (case 6) (G) Fracturing the main roof with 60° (case 7) (H) Fracturing the main roof with 90° (case 8) (I) No fracturing of the roof (case 9).

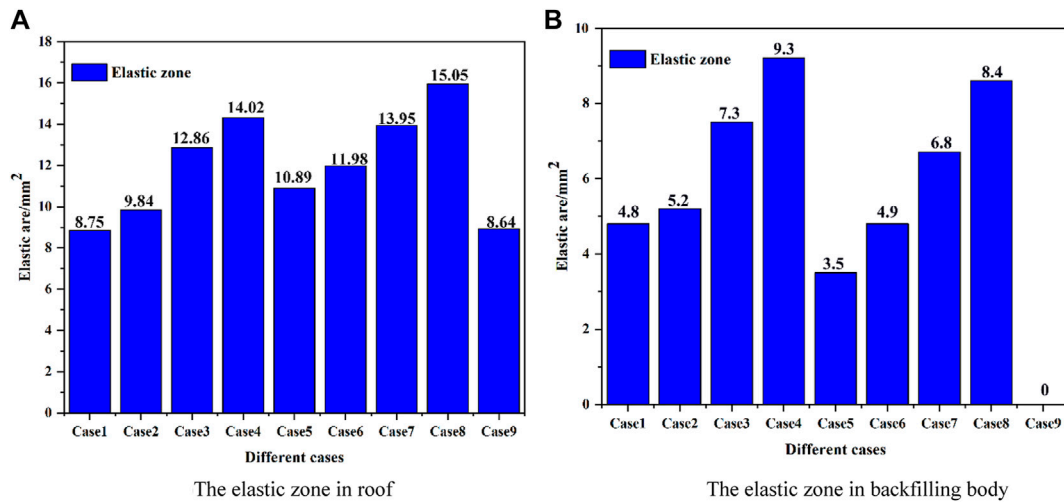


FIGURE 13 | Elastic zone area in the roadway. (A) The elastic zone in the roof (B) The elastic zone in the backfilling body.

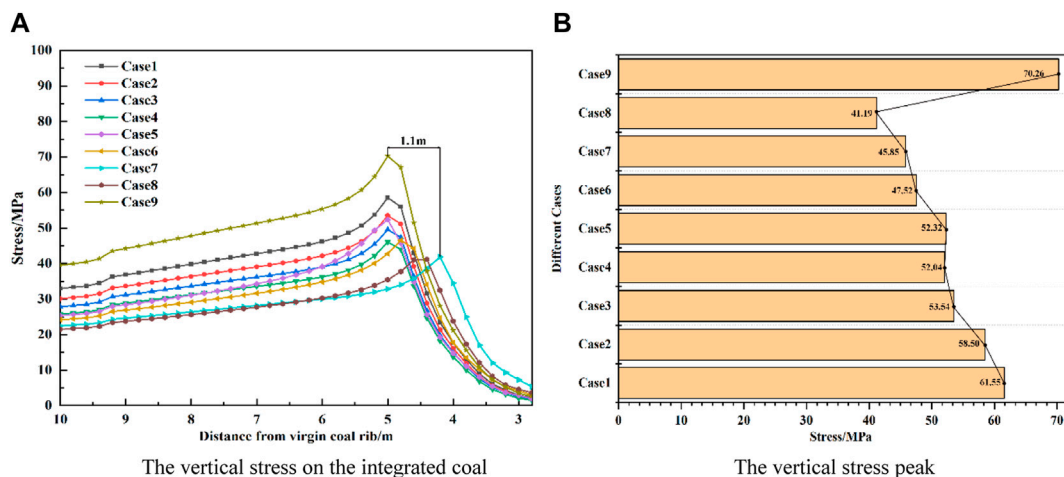


FIGURE 14 | Vertical stress distribution on the integrated coal side. (A) Vertical stress on the integrated coal (B) Vertical stress peak.

cutting, and the area of the elastic area has increased by more than 72%. Based on the above analysis, the roof-cutting plan should choose a large angle to cut the main roof. It shows that the elastic zone in the backfilling body is also different in every roof-cutting schemes

4.3.2 The Abutment Pressure Distribution

The abutment pressure distribution on the integrated coal side is shown in Figure 14; the peak abutment pressures of the nine groups

of plans are 70.26, 41.19, 45.55, 47.32, 52.32, 52.64, 53.54, 58.50, and 61.55 MPa, respectively. Comparing the abutment pressure of the nine groups shows that during the 90° pre-splitting main roof cutting, the minimum peak value of the supporting pressure on the side of the integrated coal is 41.19 MPa, and the influence range of the abutment pressure is smaller. But in the roof uncut scheme, the peak abutment pressure is 72.3 MPa, and the farthest distance from the peak to the coal rib is about 5.2 m; the abutment pressure has the largest influence range, and the influence range is reduced by 1.1 m.

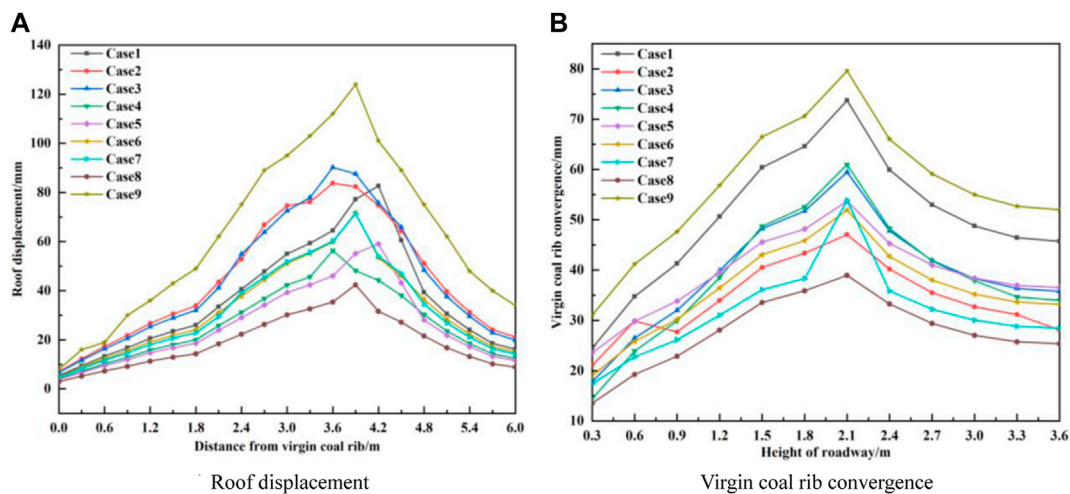


FIGURE 15 | Deformation of the surrounding rock of the roadway at different angles and height of roof cutting. **(A)** Roof displacement **(B)** Virgin coal rib convergence.

At the same top-cutting height, the peak abutment pressure of the main roof cutting is reduced by 11.13 MPa compared with the peak pressure of the immediate roof cutting, which effectively reduces the peak stress and improves the deformation of the surrounding rock of the roadway.

4.3.3 Deformation of the Surrounding Rock of the Roadway

The deformation of the roof and the coal rib under different roof-cutting schemes is quite different, while floor heaves are very small in the different schemes (Figure 15); the deformation of the roof and the coal rib under the main roof-cutting scheme is significantly less than that of the immediate roof cutting; under the same cutting height, the deformation of the roof and integrated coal decreases with the increase of the roof-cutting angle; the maximum deformation of the roof and coal pillar side in the 90° immediate roof cutting is 48.8 and 55.4 mm, respectively, while the maximum deformation of the roof and coal pillar in the main roof cutting is 38.8 and 32.4 mm, respectively. The reason for the above phenomenon is that after only cutting the direct roof, the basic roof remains overhanging and loses the original cantilever direct roof support underneath. Therefore, the basic roof itself and the overlying strata load toward the roadway surroundings. The rock transfer produces huge pressure and bending moment force on the roadway roof, so the deformation of the roadway roof is greater than the basic roof-cutting measures.

Based on the above analysis, comparing the nine groups of research programs, it is found that using Option 8 to cut the top of the overlying roof rock strata along the goaf roadway has the best effect in controlling the stability of the surrounding rock, which can effectively improve the surrounding rock stress environment and reduce the plastic zone range of the surrounding rock, reducing the deformation and destruction of the surrounding rock.

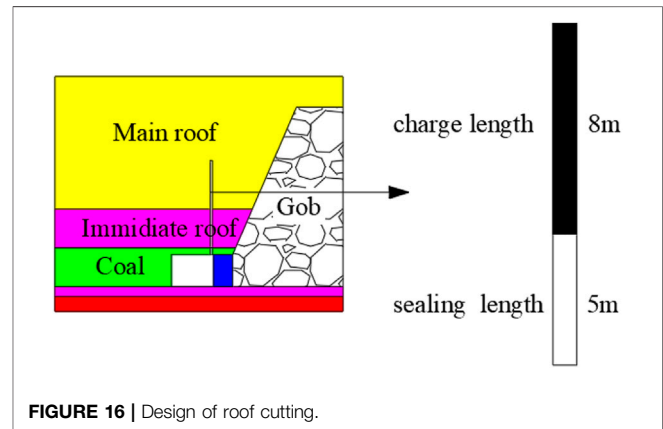


FIGURE 16 | Design of roof cutting.

5 FIELD OBSERVATIONS AND NUMERICAL VERIFICATION

Based on the results of numerical research, in the E2307 headgate, the field test of the roof-cutting technology was carried out to analyze the application effect of the technology and verify the numerical analysis results. The vertical height of the roof-cutting length is 13 m, and the roof-cutting angle is 90°; the borehole diameter is 50 mm, and the explosive charge volume parameters are the following: diameter $\Phi = 35$ mm, $l = 400$ mm, and weight $m = 2.56$ kg. The designed blast hole spacing is 0.8 m, the charge length is 8 m, and the sealing depth is 5 m, and implement pre-splitting is 50–60 m ahead of the longwall face (Figure 16).

5.1 On-Site Measurement of Abutment Pressure and Verification of Numerical Results

To evaluate the performance of the surrounding rock mass and the newly designed roof-cutting scheme, a series of field observations,

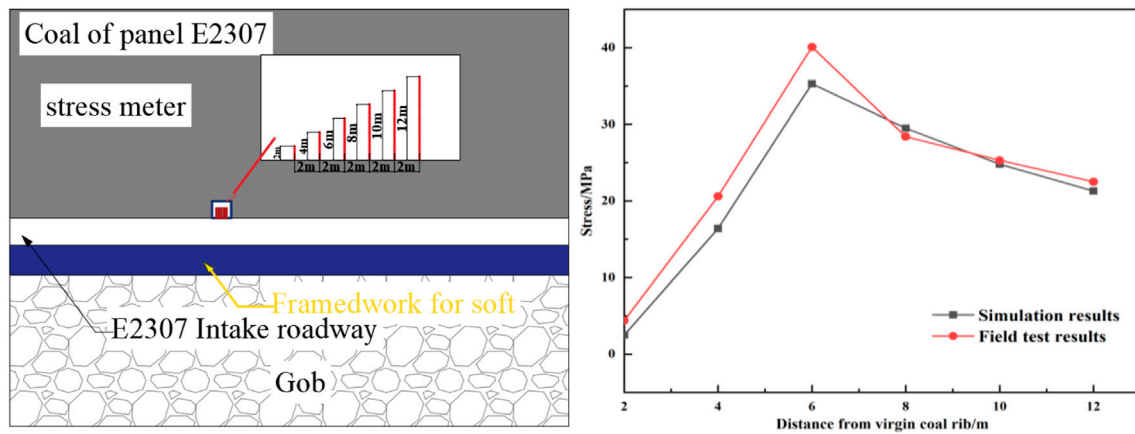


FIGURE 17 | On-site measurement and numerical verification of bearing stress.

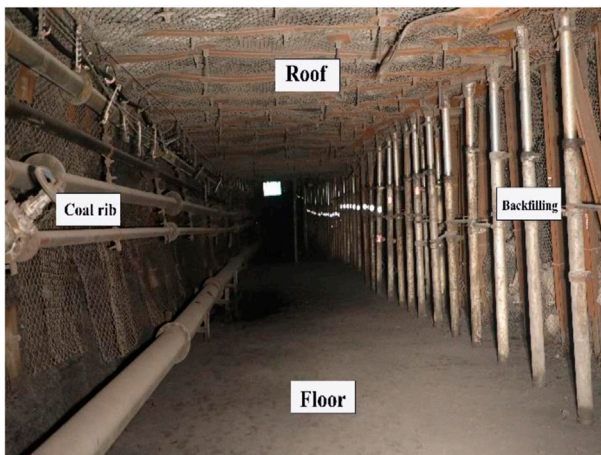
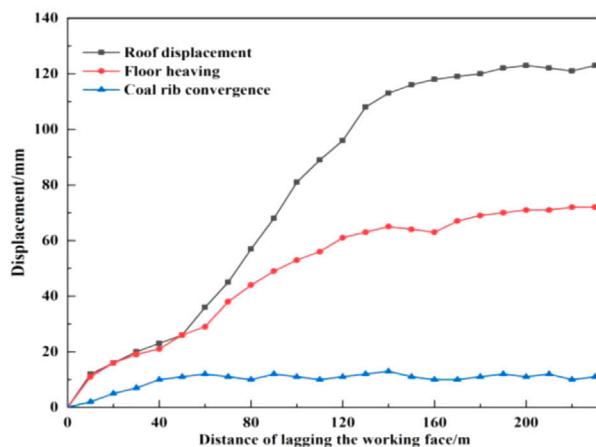


FIGURE 18 | Deformation of the surrounding rock of the roadway.

including entry convergence and stress measurement, was conducted in the E2307 headgate. The borehole stress gauge was used to measure the abutment pressure distribution in the coal pillar during the E2307 longwall face mining in order to analyze the abutment pressure distribution of the coal pillar. The strain gauges are located at 2 m, 4 m, 6 m, 8 m, 10 m, and 12 m, within the pillar with a distance of about 2 m (Figure 17). The on-site measurement result of the peak abutment pressure is 36.7 MPa, while the numerical analysis result is 39.8 MPa, with an error of 8.4%. At the same time, the on-site measurement curve of abutment pressure is consistent with the numerical analysis, so the numerical model and results are accurate and reliable, which can provide a reliable reference for the application research of this technology in similar engineering geological mines.

5.2 Monitoring of Convergence and Deformation of the Roadway

The convergent deformation of the surrounding rock of the E2307 headgate is monitored (Figure 18). It is observed that 50 m~140 m of

mining is the deformation acceleration period with an accumulated displacement accounting for 70% of the total. The deformation process began to slow down between the period 140 m~200 m; the entry was basically stable after the period 140 m~200 m. During the whole process, the maximum roof subsidence is 120 mm and the floor heave and rib-to-rib convergence are 17 and 74 mm, respectively. Observations were conducted for 2 months, and the variations of deformation of the backfilling body were monitored. The backfilling body is of large compressibility and high supporting capacity, enabling stability of the gob-side gateway (Figure 18). The above data show that the stability of the surrounding rock of the roadway is controlled after the roof-cutting technology is adopted, and the final on-site support effect is shown in Figure 18.

6 CONCLUSION

The objective of this study was to ensure stability of the gob-side entry when experiencing quick subsidence of the hard roof, by

establishing a roof-cutting mechanical model and using a numerical simulation. This study contains at least three original aspects.

- 1) Based on the analysis of roof cutting, a mechanical model of the roof cutting is established. The main roof-cutting technology reduces the overburden load and rotation deformation of the cantilever beam, thereby greatly reducing the load transmitted from the rock beam to the roadside backfilling body and the supporting structure in the roadway, and improves the stress environment of the roadway.
- 2) Taking the E2307 headgate of the Gaohe coal mine as the engineering background, the study established a numerical simulation considering strain softening and double-yield constitutive, compared and studied nine groups of roof-cutting schemes, and eventually determined that the 90° main roof cutting was adopted.
- 3) A new roof-cutting strategy was proposed for the E2307 headgate. Field monitoring demonstrated that this roof-cutting strategy has provided ideal stability for the E2307 headgate with a 650 m burial depth. In addition, this roof-cutting strategy provides sufficient details to allow its application in other coal mines.

DATA AVAILABILITY STATEMENT

The original contributions presented in the study are included in the article/Supplementary Material, further inquiries can be directed to the corresponding author.

REFERENCES

- Bai, Q.-S., Tu, S.-H., Wang, F.-T., Zhang, X.-G., Tu, H.-S., and Yuan, Y. (2014). Observation and Numerical Analysis of the Scope of Fractured Zones Around Gateroads under Longwall Influence. *Rock Mech. Rock Eng.* 47 (5), 1939–1950. doi:10.1007/s00603-013-0457-9
- Bai, Q., Tu, S., Wang, F., and Zhang, C. (2017). Field and Numerical Investigations of Gateroad System Failure Induced by Hard Roofs in a Longwall Top Coal Caving Face. *Int. J. Coal Geology*. 173, 176–199. doi:10.1016/j.coal.2017.02.015
- Chen, Y., Bai, J. B., and Wang, X. Y. (2012). Support Technology Research and Application inside Roadway of Gob Side Entry Retaining. *J. China Coal Soc.* 37 (6), 903–910. doi:10.13225/j.cnki.jccs.2012.06.015
- Han, C. L., Zhang, N., Kan, J. G., and Yuan, L. (2017). Mechanism and Application of Double Active Control with Pressure-Relieving and An-Choring for Gob-Side Entry Retaining. *J. China Coal Soc.* 42 (S2), 323330. doi:10.13225/j.cnki.jccs.2017.0132
- Han, C. L., Zhang, N., Li, G. C., Li, B. Y., and Ha, W. (2013). Stability Analysis for Compound Bearing Structure of Gob-Side Entry Retaining in Large Mining Height Condition. *Chin. J. Geotechnical Eng.* 35 (3), 969–976. doi:10.11779/CJGE201405023
- Han, C. L., Zhang, N., Yao, Y. H., Zhang, N. L., and Ji, M. (2013). Transfer Bearing Mechanism of Thick Composite Roof in Gob-Side Entry Retaining. *Rock Soil Mech.* 34 (S1), 318–323. doi:10.16285/j.rsm.2013.s1.040
- He, M., Gao, Y., Yang, J., and Gong, W. (2017). An Innovative Approach for Gob-Side Entry Retaining in Thick Coal Seam Longwall Mining. *Energies* 1785, 1–22. doi:10.1002/ese3.431
- He, M., Wang, Q., and Wu, Q. (2021). Innovation and Future of Mining Rock Mechanics. *J. rock Mech. geotechnical Eng.* 13 (1), 1–21. doi:10.1016/j.jrmge.2020.11.005
- Hou, G. Y., Hu, T., Li, Z. X., Li, Z. H., Chen, J. P., and Cui, Y. K. (2019). Effect of Cutting Roof Height on the Stability of Gob-Side Retaining Roadway with Roadside Support. *J. Mining Saf. Eng.* 36 (5), 925–931. doi:10.13545/j.cnki.jmse.2019.05.009
- Jiang, L., Zhang, P., Chen, L., Hao, Z., Sainoki, A., Mitri, H. S., et al. (2017). Numerical Approach for Goaf-Side Entry Layout and Yield Pillar Design in

AUTHOR CONTRIBUTIONS

All persons who meet authorship criteria are listed as authors, and all authors certify that they have participated sufficiently in the work to take public responsibility for the content, including participation in the concept, design, analysis, writing, or revision of the manuscript. Furthermore, each author certifies that this material or similar material has not been and will not be submitted to or published in any other publication before its appearance in the *Frontiers in Earth Science*. Authorship contributions Category 1: Conception and design of study: KZ; acquisition of data: KZ; and analysis and/or interpretation of data: XY, HZ, and HL. Category 2: Drafting the manuscript: KZ, CL, and HL; revising the manuscript critically for important intellectual content: CL. Category 3: Approval of the version of the manuscript to be published (the names of all authors must be listed): KZ, CL, XY, HZ, and HL.

FUNDING

This work was financially supported by the National Natural Science Foundation of China (No. 52074267), and the Graduate Innovation Project of Jiangsu Province (KYCX21_2366).

- Fractured Ground Conditions. *Rock Mech. Rock Eng.* 50 (11), 3049–3071. doi:10.1007/s00603-017-1277-0
- Li, Y. F., Hua, X. Z., and Cai, R. C. (2012). Mechanics Analysis on the Stability of Key Block in the Gob-Side Entry Retaining and Engineering Application. *J. Mining Saf. Eng.* 37 (6), 357–364. doi:10.13225/j.cnki.jccs.2012.06.015
- Liu, H., Dai, J., Jiang, J., Wang, P., and Yang, J. (20192019). Analysis of Overburden Structure and Pressure-Relief Effect of Hard Roof Blasting and Cutting. *Adv. Civil Eng.* 2019, 1–14. Article ID 1354652. doi:10.1155/2019/1354652
- Liu, J. N., He, M. C., Hou, S. L., Zhu, Z., Wang, Y. J., and Yang, J. (2021). Force Change of the Gravel Side Support during Gangue Heaping under a New Non-pillar-mining Approach. *Geomechanics Eng.* 27 (1), 31–43. doi:10.12989/gae.2021.27.1.031
- Ma, D., Kong, S., Li, Z., Zhang, Q., Wang, Z., and Zhou, Z. (2021). Effect of Wetting-Drying Cycle on Hydraulic and Mechanical Properties of Cemented Paste Backfill of the Recycled Solid Wastes. *Chemosphere* 282 (10), 131163. doi:10.1016/j.chemosphere.2021.131163
- Ma, X., He, M., Liu, D., He, L., and Jiang, Q. (2018). Study on Mechanical Properties of Roof Rocks with Different Cutting Inclinations. *Geotech. Geol. Eng.* 37 (4), 2397–2407. doi:10.1007/s10706-018-00764-2
- Ning, J. G., Liu, X. S., Tan, J., Gu, Q. H., Tan, Y. L., and Wang, J. (2018). Control Mechanisms and Design for a 'coal-Backfill-Gangue' Support System for Coal Mine Gob-Side Entry Retaining. *Ijogct* 18 (3-4), 444–466. doi:10.1504/IJOGCT.2018.093132
- Shi, J. J., Ma, N. J., and Bai, Z. S. (2013). Analysis on Roof Broken Location of Gateway Retained along Goaf and Technology of Roof Support. *Coal Sci. Technol.* 41 (7), 35–38. doi:10.13199/j.cst.2013.07.41.shijj.011
- Smart, B. G. D., and Haley, S. M. (2019). Further Development of the Roof Strata Tilt Concept for Pack Design and the Estimation of Stress Development in a Caved Waste. *Int. J. Rock Mech. Mining Sci. Technol.* 5, 121–130. doi:10.1016/0148-9062(87)92669-6
- Tai, Y., Yu, B., Xia, B., Li, Z., and Xia, H. (2020). Research on Stress Release for the Gob-Side Roadway Using the Roof-Cutting Technology with a Chainsaw Arm. *R. Soc. Open Sci.* 7 (3), 191663–191680. doi:10.1098/rsos.191663
- Wang, Y., Gao, Y., Wang, E., He, M., and Yang, J. (2018). Roof Deformation Characteristics and Preventive Techniques Using a Novel Non-pillar Mining

- Method of Gob-Side Entry Retaining by Roof Cutting. *Energies* 11 (3), 627–644. doi:10.3390/en11030627
- Yang, H. Y., Liu, Y. B., Cao, S. G., Pan, R. K., Wang, H., Li, Y., et al. (2020). A Caving Self-Stabilization Bearing Structure of Advancing Cutting Roof for Gob-Side Entry Retaining with Hard Roof Stratum. *Geomechanics Eng.* 21 (1), 23–33. doi:10.12989/gae.2020.21.1.023
- Yang, J., Wang, H. Y., Wang, Y. J., Gao, Y. B., Wang, J. W., and Liu, H. (2019). Fracture Characteristics of the Roof in Gob-Side Entry Retaining with Roof Cutting and Pressure Release. *J. Mining Saf.* 36 (6), 1138–1144. doi:10.13545/j.cnki.jmse.2019.06.009
- Yu, B., Tai, Y., Gao, R., Yao, Q., Li, Z., and Xia, H. (2020). The Sustainable Development of Coal Mines by New Cutting Roof Technology. *R. Soc. Open Sci.* 7 (6), 191913–191919. doi:10.1098/rsos.191913
- Zhang, B., Li, S. C., Yang, X. Y., and Zhang, D. F. (2011). Uniaxial Compression Tests on Mechanical Properties of Rock Mass Similar Material with Cross-Cracks. *Rock Soil Mech.* 33 (12), 3674–3679. doi:10.1007/s11783-011-0280-z
- Zhang, G.-c., He, F.-l., Jia, H.-g., and Lai, Y.-h. (2017). Analysis of Gateroad Stability in Relation to Yield Pillar Size: A Case Study. *Rock Mech. Rock Eng.* 50 (5), 1263–1278. doi:10.1007/s00603-016-1155-1
- Zhang, L., Zhao, J., Zang, C., and Wang, S. (2020). An Innovative Approach for Gob-Side Entry Retaining by Roof Cutting in Steeply Pitching Seam Longwall Mining with Hard Roof: a Case Study. *Mining, Metall. Exploration* 37 (8), 1079–1091. doi:10.1007/s42461-020-00219-4
- Zhang, N., Han, C. L., Kan, J. G., and Z, X. G. (2014). Theory and Practice of Surrounding Rock Control for Pillarless Gob-Side Entry Retaining. *J. China Coal Soc.* 39 (8), 1635–1641. doi:10.13225/j.cnki.jccs.2014.9026
- Zhang, N., Yuan, L., Han, C., Xue, J., and Kan, J. (2012). Stability and Deformation of Surrounding Rock in Pillarless Gob-Side Entry Retaining. *Saf. Sci.* 50 (4), 593–599. doi:10.1016/j.ssci.2011.09.010
- Zhang, Z., Bai, J., Chen, Y., and Yan, S. (2015). An Innovative Approach for Gob-Side Entry Retaining in Highly Gassy Fully-Mechanized Longwall Top-Coal Caving. *Int. J. Rock Mech. Mining Sci.* 80, 1–11. doi:10.1016/j.ijrmms.2015.09.001
- Zhao, T.-b., Guo, W.-y., Tan, Y.-l., Lu, C.-p., and Wang, C.-w. (2017). Case Histories of Rock Bursts under Complicated Geological Conditions. *Bull. Eng. Geol. Environ.* 77 (4), 1529–1545. doi:10.1007/s10064-017-1014-7
- Conflict of Interest:** The authors declare that the research was conducted in the absence of any commercial or financial relationships that could be construed as a potential conflict of interest.
- Publisher's Note:** All claims expressed in this article are solely those of the authors and do not necessarily represent those of their affiliated organizations, or those of the publisher, the editors, and the reviewers. Any product that may be evaluated in this article, or claim that may be made by its manufacturer, is not guaranteed or endorsed by the publisher.

Copyright © 2022 Zhang, Liu, Zhang, Yue and Liu. This is an open-access article distributed under the terms of the Creative Commons Attribution License (CC BY). The use, distribution or reproduction in other forums is permitted, provided the original author(s) and the copyright owner(s) are credited and that the original publication in this journal is cited, in accordance with accepted academic practice. No use, distribution or reproduction is permitted which does not comply with these terms.



Experimental Study on Coal and Gas Outburst Risk in Strong Outburst Coal Under Different Moisture Content

Zhuang Lu^{1,2}, Liang Wang^{1,2*}, Mingzhe Lv², Yang Lei^{1,2}, Hao Wang^{1,2} and Qingquan Liu^{1,2*}

¹Key Laboratory of Gas and Fire Control for Coal Mines, China University of Mining and Technology, Ministry of Education, Xuzhou, China, ²School of Safety Engineering, China University of Mining and Technology, Xuzhou, China

OPEN ACCESS

Edited by:

Jie Chen,
Chongqing University, China

Reviewed by:

Huafu Qiu,
Xi'an University of Science and
Technology, China
Chaojun Fan,
Liaoning Technical University, China
Zou Quanle,
Chongqing University, China
Haifei Lin,
Xi'an University of Science and
Technology, China

*Correspondence:

Liang Wang
wangliang@cumt.edu.cn
Qingquan Liu
cumtsafe@cumt.edu.cn

Specialty section:

This article was submitted to
Geohazards and Georisks,
a section of the journal
Frontiers in Earth Science

Received: 24 September 2021

Accepted: 15 February 2022

Published: 22 March 2022

Citation:

Lu Z, Wang L, Lv M, Lei Y, Wang H and
Liu Q (2022) Experimental Study on
Coal and Gas Outburst Risk in Strong
Outburst Coal Under Different
Moisture Content.
Front. Earth Sci. 10:782372.
doi: 10.3389/feart.2022.782372

Coal and gas outburst is an extremely serious dynamic phenomenon involving the comprehensive action of many factors, and remains a major disaster that needs to be solved in coal mine production. Considering the significant influence of moisture content on coal and gas outburst, it is necessary to carry out experimental research on coal and gas outburst under different moisture content conditions. The coal of the serious outburst coal seam in the Luling coal mine, which has had several coal and gas outburst accidents, was selected as the experimental sample. Firstly, the gas desorption law and outburst index characteristics of coal under different moisture content were studied, and the influence of moisture content on gas outburst parameters of coal was obtained. Then, the simulation tests of coal and gas outburst under different moisture content were carried out by using a triaxial coal and gas outburst simulation test system. Based on the above experimental research, the influence of moisture on coal and gas outburst was summarized, and the energy calculation and prevention countermeasures of coal and gas outburst under different moisture content conditions were carried out. With the increase of moisture content, the adsorption constant a , the initial velocity of gas diffusion Δp , and the gas desorption index of drill cuttings $K_1/\Delta h_2$ decrease, but the Protodyakonov coefficient f increases, all of which have an exponential relation to moisture content. Meanwhile, with the increase of moisture content, the threshold of coal and gas outburst pressure increases, and the intensity and energy of outburst decrease. At 0.45 MPa pressure, the outburst of 1.47% moisture content is the most serious, the outburst of 5% moisture content is weakened, while the outburst of 10% moisture content is not triggered. Five percent moisture content can be used as a critical index of hydraulic measures to prevent coal and gas outburst in No. 8 coal seam of the Luling coal mine. This research can provide new insights into the theoretical study of coal and gas outburst in serious outburst coal seams and the control of coal and gas outburst by hydraulic measures.

Keywords: coal and gas outburst, moisture content, gas desorption, hydraulic measures, simulation test

1 INTRODUCTION

With the growth of coal mining in China, factors such as geostress, gas pressure, geological structure, and mining activities are changing constantly. Coal seam gas has become the key factor that constrains safe and efficient production of Chinese deep coal mines (Cheng et al., 2011; Wang et al., 2012; Chen et al., 2022). The damage caused by coal and gas outburst dynamic disasters is increasing

day by day. At present, coal and gas outburst accidents have become the focus of attention (Cheng and Pan, 2020; Wang L. et al., 2020). Coal and gas outburst involves injecting a large amount of coal/rock and gas into the mining working face over a short time. The coal rock is injected from several tons to tens of thousands of tons, and the gas is emitted from hundreds to millions of cubic meters, which may lead to a series of disasters such as gas explosion (Beamish and Crosdale, 1998; Zhao et al., 2016; Zhi and Elsworth, 2016). Since the first outburst accident was recorded in the Isaac Coal Mine, France, in 1834, tens of thousands of outburst accidents have happened all over the world (Shepherd et al., 1981; Wang et al., 2013; Tu et al., 2021). In the past decades, coal and gas outburst, as one of the most destructive disasters in China's coal production, has caused serious economic losses and casualties (Cheng et al., 2011; Wang et al., 2017b; Cheng and Pan, 2020). According to incomplete statistics, there are more than 1,000 mines with strong coal and gas outburst danger in China. In the recent 20 years, there have been nearly 500 outburst accidents and more than 3,000 deaths (Sun, 2014; Zhang et al., 2021). Although coal and gas outburst accidents have been effectively controlled in recent years, they are still at a relatively high level and have become more and more prominent in coal mine accidents. From April to June 2021, four coal and gas outburst accidents happened in succession in China, causing 18 deaths. This shows that coal and gas outburst remains a major disaster that needs to be solved in China's coal mine production.

Coal and gas outburst is a very destructive and complex coal/rock dynamic process (Black, 2019). It is generally believed that the trigger of outburst is related to geological structure, coal properties, gas pressure, stress state, and other factors (Díaz Aguado and González Nicieza, 2007; Jin et al., 2018; Tu et al., 2021). Moisture is one of the most important factors that influence gas seepage and coalbed methane extraction (Ding and Yue, 2018). Generally, moisture in the coal seam will inhibit gas desorption, diffusion, and seepage, and greater moisture content generates lower outburst risk (Fan et al., 2017). Hydraulic measures are important technical measures that deal with gas hazards, such as coal seam water injection, hydraulic flushing, hydraulic slotting, and hydraulic fracturing (Lu et al., 2017; Zhang et al., 2017; Yan et al., 2019; Zhao et al., 2020). The implementation of hydraulic measures will increase the moisture content of coal seam while relieving *in situ* stress and improving gas drainage efficiency (Yang et al., 2019; Yi et al., 2021). The difference in moisture content affects the adsorption and desorption capacity of coal and then affects the outburst parameters and gas outburst capacity of coal (Pan et al., 2010; Wang K et al., 2021). Coal has a stronger adsorption capacity for water molecules than methane molecules (Zhang and Sang, 2009; Wang H et al., 2021). The affinity between methane molecules and the coal molecule is reduced, and methane molecules are less aggregated around the coal molecule because of the presence of water molecules (Meng et al., 2020). Matrix pores are the main storage space for methane (Fan et al., 2021; Zhang et al., 2022) and water molecules enter matrix pores of coal body by capillary suction and mainly act on micropore fractures. If the pressure difference between the inside and outside of pores cannot overcome the capillary force, water will block the gas

desorption path and reduce the gas desorption capacity of coal, resulting in the water lock effect (Hao et al., 2018; Liu et al., 2019; Qin et al., 2020). After the implementation of hydraulic measures, the moisture content of coal seam increases and the permeability decreases, which has a restraining effect on gas emission and will result in the change of desorption-induced strains (Chen et al., 2012).

However, most of the studies focus on the influence of different moisture content on gas adsorption/desorption in coal (Zhang et al., 2011; Chen and Cheng, 2014; Wang et al., 2017a; Hao et al., 2018; Zhao et al., 2018; Liu et al., 2019; Qin et al., 2019; Yao et al., 2020). There are still different views on the influence of moisture on the characteristics of gas adsorption and desorption in the coal industry, which is highly controversial. At present, most studies conducted are single studies, and water studies and coal and gas outburst experiments are separate. There are relatively few studies that examine the law of coal and gas outburst intensity under different moisture content conditions and the key control indexes of coal and gas outburst prevention under hydraulic measures combined with coal and gas outburst simulating tests. Most coal and gas outburst simulating tests are used to focus on the mechanism and characteristics of gas outburst, while moisture content experiments are used to study the characteristics and microscopic characteristics of coal body. In addition, the process of hydraulic measures implemented on site shows that too little water is not conducive to gas control, and too much water can lead to difficult gas extraction and environmental pollution. In addition, the process of hydraulic measures implemented on site shows that too little water is not conducive to controlling gas, while too much water will lead to gas extraction difficulty and environmental pollution. It is particularly important to select a suitable water content index for specific coal seam in hydraulic measures, but there is no unified method at present. Therefore, it is necessary to study the influence of moisture on the gas outburst parameters, the energy of coal and gas outburst, and the selection of key moisture content index in hydraulic measures, which is of great significance for preventing gas disasters and guiding the field production in coal mines.

A total of 26 coal and gas outburst accidents happened in the Luling coal mine in Anhui Province, China, with a high frequency and a high intensity of gas outburst. Among them, the one with the largest outburst intensity happened in No. 8 coal seam on April 7, 2002. A total of 10,500 t of coal/rock were injected, and 1.23 million m³ of gas was emitted, resulting in 13 deaths (Wang L. et al., 2020). Therefore, the test coal sample was taken from No. 8 coal seam in the Luling coal mine in view of its strong outburst risk. In this paper, based on the study of the outburst physical parameters of coal sample under different moisture content, the influence of different moisture content on gas desorption of coal was explored. The influence of moisture content on the gas outburst parameters of coal and the intensity of coal and gas outburst were studied by combining various experimental devices. Then, the simulation tests under different moisture content were carried out using the simulation test system to explore the influence of moisture on the laws and characteristics of coal and gas outburst. The characteristics of coal and gas outburst under different moisture content conditions and the key moisture content index of coal and gas outburst prevention under

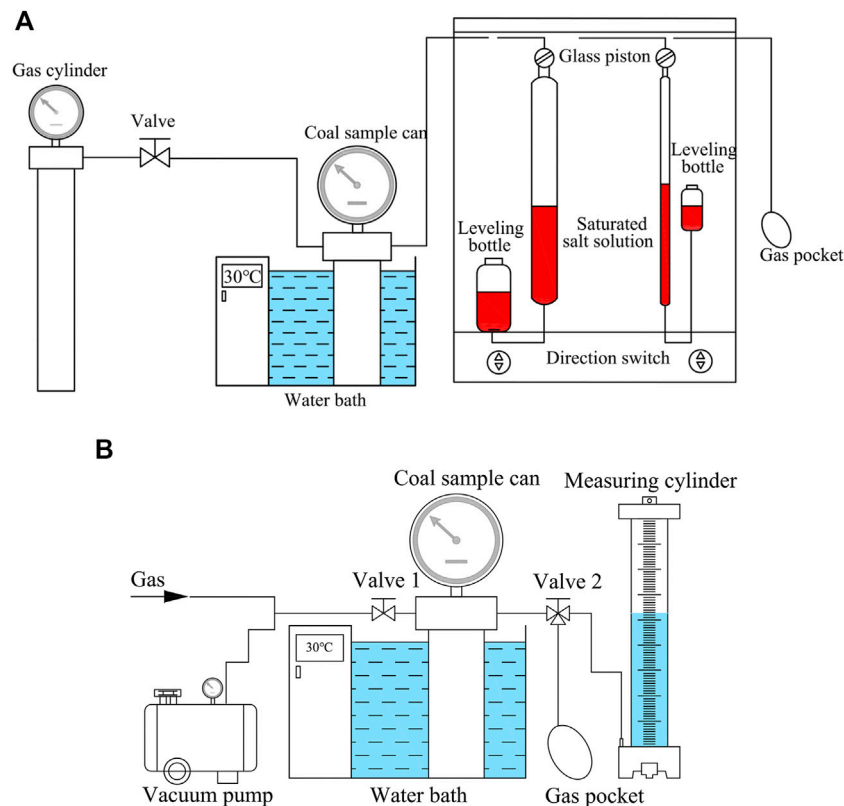


FIGURE 1 | Schematic of the gas adsorption/desorption experimental devices. **(A)** HCA gas adsorption experimental device. **(B)** FM-1 gas isothermal desorption device.

hydraulic measures were analyzed in the end. With this study, the relevant laws of coal and gas outburst dynamic disasters of strong outburst coal with different moisture content can be further understood. It is hoped that this study can provide technical guidance for hydraulic measures to prevent and control coal and gas outburst dynamic disasters.

2 MATERIALS AND METHODS

2.1 Coal Samples Preparation

The Luling coal mine is located in Huaibei Coalfield, Anhui Province, China. It has been affected by many geological tectonic movements, resulting in extremely complex geological environment and tectonic features. The *in situ* stress in the Luling coal mine is concentrated because it is located near the top of the lateral arc. No. 8 coal seam is the main mining seam, the roof of which is fine sandstone/mudstone and the floor is mudstone (Wang L. et al., 2020). The complex environment seals the gas in the coal seam, resulting in high gas content and pressure. In addition, because of the large number of folds and faults, the local thickness of No. 8 coal seam varies greatly, which increases the risk of coal and gas outburst. There have been many outburst accidents in No. 8 coal seam, which has strong

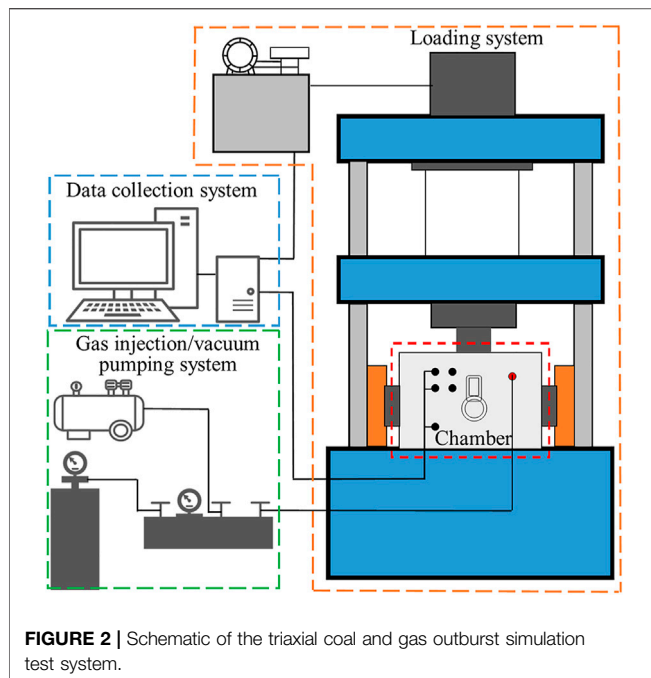
outburst risk. Therefore, coal samples were extracted from a working face of No. 8 coal seam in the Luling coal mine in this study.

The independent variable of this study is moisture content, so coal samples with different characteristic parameters need to be prepared. According to different experimental requirements, coal samples with corresponding particle size were crushed and screened. The drying oven was used to fully dry the coal samples. Then, the dry coal samples were saturated with distilled water for 3 days by the vacuum water saturation instrument for them to fully absorb water. After that, the wet coal samples were taken out and water drops on the surface of the coal particles were adsorbed using filter paper. Then, the vacuum drying oven was used to dry the sample sieves containing the coal samples to obtain different moisture content by controlling the drying time. Finally, the sieves were taken out and the coal samples therein were stored in the sealing bag, successively.

2.2 Gas Outburst Parameter Determination of Coal With Different Moisture Content

2.2.1 Adsorption Constant a

Coal is a porous medium with a large number of fractures and pores in its interior, which provide sufficient space for gas



adsorption. The relationship between gas adsorption and gas pressure can be represented as Eq. 1:

$$Q = \frac{abp}{1 + bp} \quad (1)$$

Where p is the equilibrium pressure of adsorption, MPa; Q is the gas adsorption capacity of coal sample per unit mass when the adsorption equilibrium pressure is p , m^3/t ; a is the limit adsorption capacity of coal sample per unit mass, m^3/t ; and b is the reciprocal of equilibrium pressure corresponding to the adsorption capacity reaching half of Langmuir volume, MPa^{-1} .

Adsorption constant a of coal samples was measured according to the China National standard MT-T 752-1997 via an HCA gas adsorption experimental device, as shown in Figure 1A. The particle size of coal samples with different moisture content used in the experiment is 0.2–0.25 mm and the mass is 50 g.

2.2.2 Protodyakonov Coefficient f

The Protodyakonov coefficient, f value, of coal samples (hereafter referred to as f) was determined according to the China National standard GB/T 23561.12-2010. The particle size of coal samples with different moisture content is 1–3 mm and the mass is 50 g. It is generally believed that the f of intact coal is in the range of 0.75–1.5. When f is less than 0.5, the coal properties indicate a risk of a coal and gas outburst. When f is less than 0.3, this coal is considered to be strong outburst risk (Wang C et al., 2020).

2.2.3 Initial Velocity of Gas Diffusion

The initial velocity of gas diffusion (hereafter referred to as Δp) was determined according to the China National standard AQ1080-2009 via a WT-1 gas diffusion velocity analyzer. The

particle size of coal samples with different moisture content is 0.2–0.25 mm.

2.3 Gas Desorption Experiment of Coal With Different Moisture Content

Gas desorption capacity of coal has an important influence on the generation and development of coal and gas outburst. The moisture content greatly affects the gas desorption capacity of coal. Therefore, it is of fundamental and important significance to study the gas desorption characteristics of strong outburst coal under different moisture content conditions. Gas desorption experiments were carried out under the adsorption equilibrium pressure of 0.74, 1, 2, 3, and 4 MPa via a FM-1 gas isothermal desorption device, as shown in Figure 1B (Zhao et al., 2016). The particle size of coal samples is 1–3 mm and the moisture content of coal used in the experiment are 1.68%, 3.42%, 5.19%, and 6.81%, respectively. After converting the measured data into standard data, the desorption curve was drawn.

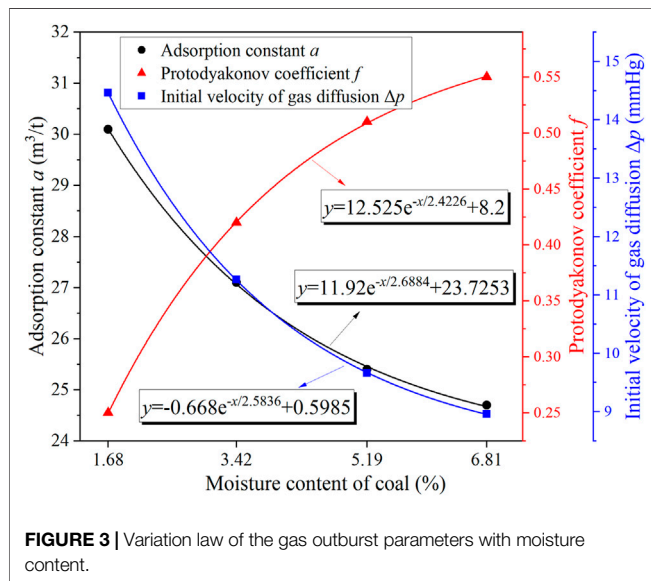
2.4 Coal and Gas Outburst Analogical Simulating Test Under Different Moisture Content

The triaxial coal and gas outburst simulation test system was designed and completed by the research team according to the similarity theory, which satisfies the geometric similarity, motion similarity, and dynamic similarity (Tu et al., 2016; Lei et al., 2020). It is mainly composed of four systems: outburst chamber, loading system, data collection system, and gas injection/vacuum pumping system, as shown in Figure 2. The interior space size of the outburst chamber is designed to be $250 \times 250 \times 310$ mm, and the wall thickness is about 80 mm. An outburst port of approximately 50 mm diameter is set in the front of the chamber, and a gas injection/exhaust port is set in the front right of the chamber. For safety reasons, CO_2 was used in place of explosive CH_4 . The ambient temperature was 25°C ; the triaxial loading pressures for σ_x , σ_y and σ_z were all 5 MPa; and the outburst pressure was set to 0.25–0.45 MPa. The test scheme is shown in Table 1. Each outburst simulation test was performed according to the following steps:

- 1) Coal sample preparation—the coal sample with the corresponding moisture content was prepared, and the particle size of coal was 0.25–0.5 mm.
- 2) Coal briquette pressing—the outburst chamber was filled with coal sample after the coal sample preparation was completed. Then, the coal sample in the chamber was preliminarily compacted horizontally using the loading system. After adding the appropriate amount of coal samples to the chamber, the press was increased to 48 MPa for secondary pressing and the loading time was kept for 40 min. In this way, the coal briquette will be pressed successfully according to previous studies.
- 3) Vacuum pumping/gas charging—after confirming that the chamber was sealed, it was vacuumed for 12 h. Then, CO_2 was

TABLE 1 | Scheme for coal and gas outburst simulation test.

Test number	Gas type	Moisture content (%)	Gas pressure (MPa)	Ambient temperature (°C)	Triaxial stress		
					σ_z (MPa)	σ_x (MPa)	σ_y (MPa)
1	CO ₂	1.47	0.25	25	5	5	5
2	CO ₂	1.47	0.35	25	5	5	5
3	CO ₂	1.47	0.45	25	5	5	5
4	CO ₂	5	0.35	25	5	5	5
5	CO ₂	5	0.45	25	5	5	5
6	CO ₂	10	0.45	25	5	5	5

**FIGURE 3** | Variation law of the gas outburst parameters with moisture content.

injected into the chamber for at least 48 h to make it fully adsorbed and balanced to the target pressure.

- 4) Outburst preparation—a loading stress of $\sigma_x = \sigma_y = \sigma_z = 5$ MPa was applied to the chamber, and the gas pressure in the chamber was confirmed with minimal changes by the pressure transmitters.
- 5) Outburst induced—the plug of the outburst port was removed, causing the outburst.
- 6) Data acquisition—the key parameters were obtained from the test site.

3 RESULTS AND ANALYSIS

3.1 Gas Outburst Parameter Characteristics

The adsorption constant a , f , and Δp of coal samples with a moisture content of 1.68%, 3.42%, 5.19%, and 6.81% were determined, as shown in **Figure 3**. The curves in **Figure 3** were obtained by fitting data points, and their goodness of fit were all above 0.99.

3.1.1 Results of Adsorption Constant a

Figure 3 illustrates that the adsorption constant a of coal decreases with the increase of moisture content. This indicates

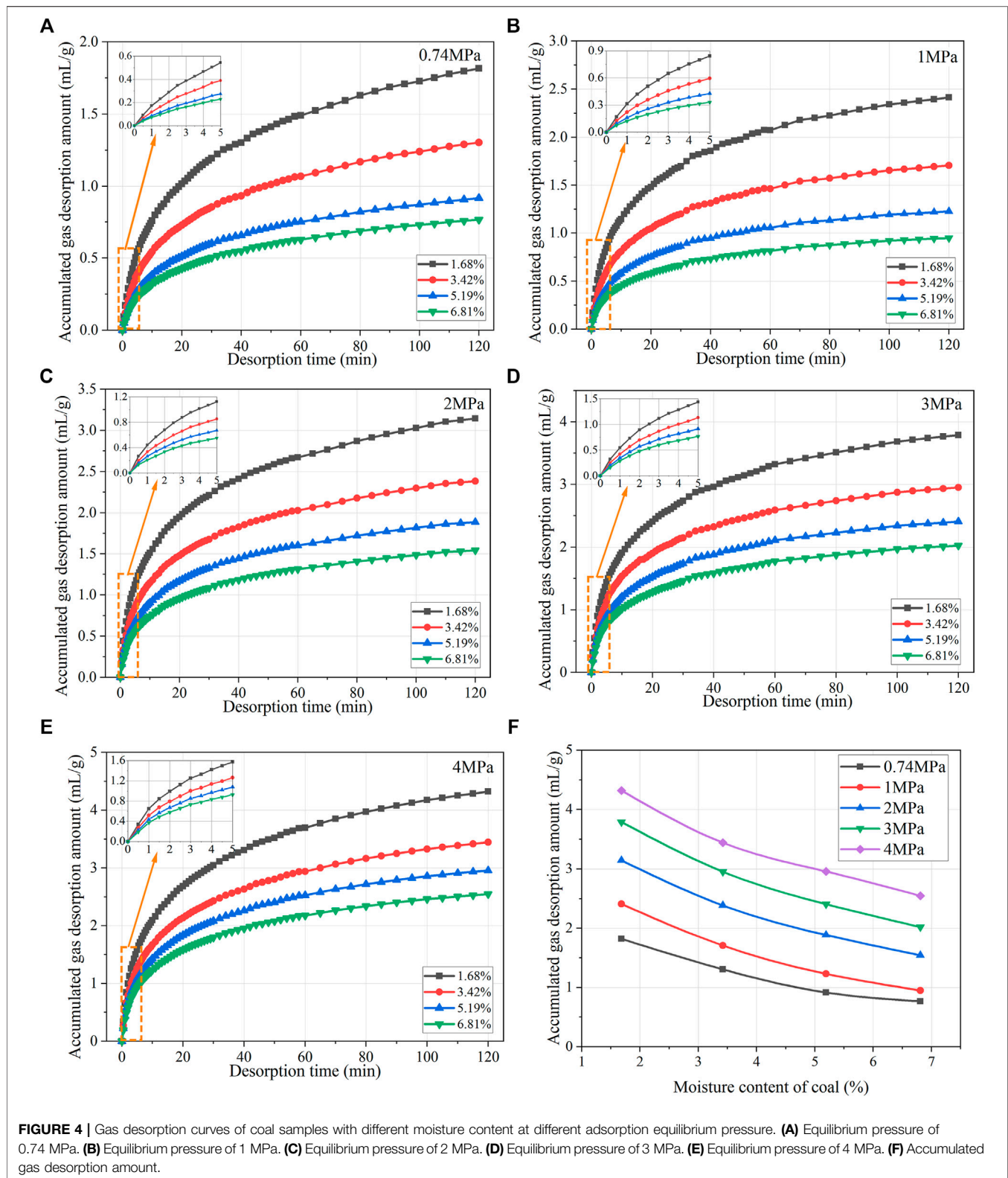
that the limit adsorption capacity of gas decreases due to the moisture of coal. In addition, with the increase of moisture content, the decline curve tends to flatten and the rate decreases. It is highly probable that the adsorption constant a will not change with the further increase of moisture content. The main reason for the above results is that the fractures and pores of coal are filled with water, which affects the adsorption of gas in three aspects: 1) A part of the decomposed water and free water in the coal body combine with the coal structure surface through acting force, occupying a certain amount of adsorption space on the coal structure surface. This reduces the effective space for gas adsorption to a certain extent, leading to the decrease in the amount of adsorbed gas. 2) Some fractures and pores in the coal body are very narrow, and free water cannot reach its interior. However, some water will enter into these narrow fractures and pores in the form of water vapor, which will form a competitive relationship with CH₄, resulting in a decrease in the amount of adsorbed gas. 3) The influence of moisture on the adsorption characteristics of coal will be greatly weakened after the coal is saturated with water (Yang et al., 2017).

3.1.2 Results of Protodyakonov Coefficient f

f can represent the ability of coal to resist outburst (Xue et al., 2014). The smaller the value of f , the lower the strength of coal and the higher the deformability. This means that coal and gas outburst is more dangerous (Fan et al., 2020). It can be seen from **Figure 3** that the f increases with the increase of moisture content, and the increase rate gradually decreases and tends to be gentle. The internal friction angle decreases linearly with the increase of moisture content while the cohesion increases parabolically with the increase of moisture content, which is beneficial to the consolidation of the coal body (Wang H et al., 2021). The more moisture content in the coal, the harder it is to be crushed, and the lower the risk of coal and gas outburst.

3.1.3 Results of Initial Velocity of Gas Diffusion

Δp is one of the important indicators for discriminating coal and gas outburst risk. It characterizes the microstructure of coal and indicates the gas emission capacity of coal, which greatly affects the intensity of coal and gas outburst. It can be used individually or combined with other parameters to predict the outburst risk tendency of coal seams (Zhou et al., 2019). As can be seen from **Figure 3**, Δp decreases with the increase of moisture content, and shows a gradual decrease and flattening trend, which is similar to



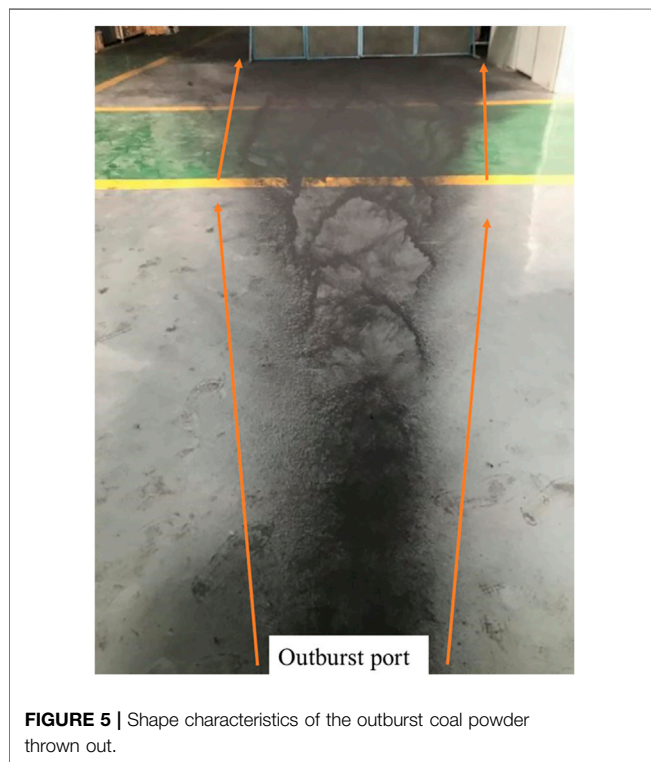
the change law of the adsorption constant a of coal. This shows that water has a significant inhibitory effect on gas emission. After water molecules enter the fractures and pores of coal body, the

water lock effect is generated, which hinders the movement of methane molecules, resulting in the decrease of gas desorption amount per unit time and the decrease of desorption rate. This is

TABLE 2 | Simulation test results of coal and gas outburst.

Test number	Moisture content (%)	Gas pressure (MPa)	Trigger of outburst (Y/N)	Coal briquette mass (kg)	Outburst coal powder mass (kg)	Maximum outburst distance (m)	Relative outburst intensity (%)
1	1.47	0.25	N	20.135	0	0	0
2	1.47	0.35	Y	20.367	3.785	11.54	18.21
3	1.47	0.45	Y	20.127	5.714	15.83	26.47
4	5	0.35	N	20.974	0	0	0
5	5	0.45	Y	20.726	3.538	11.13	17.07
6	10	0.45	N	21.869	0	0	0

The bold values indicate that the coal and gas outburst was triggered in this group test.

**FIGURE 5** | Shape characteristics of the outburst coal powder thrown out.

consistent with the findings of others (Wang et al., 2017a; Wang et al., 2018).

3.2 Gas Desorption Characteristics

The desorption curves of coal with different moisture content at the equilibrium pressure of 0.74, 1, 2, 3, and 4 MPa are shown in **Figure 4**.

The relationship between the accumulated gas desorption amount and desorption time is a monotonically increasing parabola (**Figure 4**). In the initial period of gas desorption, the gas desorption amount is large and the desorption rate is fast. With the passage of time, the desorption rate decreases and the desorption amount gradually flattens out. With the increase of adsorption equilibrium pressure, the accumulated gas desorption amount of coal samples with different moisture content increases. Under the same adsorption equilibrium pressure, the desorption curve of coal samples with higher moisture content is always

below that of coal samples with lower moisture content, indicating that the desorption amount decreases with the increase of moisture content in the coal.

Figure 4F shows the relationship between the gas desorption amount and moisture content in 120 min under different pressures. With the increase of moisture content, the gas desorption amount in 120 min decreased gradually. In general, the desorption quantity decreases greatly in the initial increasing stage of moisture content. With the increase of moisture content, the decrease of desorption capacity decreases gradually. This law is more obvious at lower adsorption equilibrium pressure because the influence factors of pressure on gas desorption is weakened.

3.3 Coal and Gas Outburst Characteristics

3.3.1 Test Results of Coal and Gas Outburst Simulation

The tests in **Table 1** were carried out under the same environmental conditions, and the results are shown in **Table 2**. The test results are divided into two cases: outburst and no outburst. For the outburst case, the coal powder thrown out has the same shape (spindle distribution), showing a wide shape in the middle of the two ends of the tip (**Figure 5**).

The test results show that the change of gas pressure and moisture content greatly affects the trigger and intensity of coal and gas outburst. It can be found that gas pressure threshold exists in the trigger of coal and gas outburst, and moisture content will greatly affect the pressure threshold (Ding and Yue, 2018; Lei et al., 2020). With the increase of moisture content, the threshold of gas pressure increases and the intensity of outburst decreases. Outburst was triggered at a gas adsorption equilibrium pressure of 0.35 and 0.45 MPa when the moisture content was 1.47%, while the coal with a moisture content of 5% was only triggered at a pressure of 0.45 MPa, and the amount of coal powder thrown out was relatively less. The coal with a moisture content of 10% did not even trigger outburst at a pressure of 0.45 MPa.

The characteristics of residual briquette after outburst are also significantly different, as shown in **Figure 6**. The outburst hole of the coal with 5% moisture content was complete and round. The residual coal in the chamber was relatively complete and less broken. When the moisture content was 1.47% and the gas pressure was 0.35 MPa, the outburst hole was larger and more fractures appeared on the surface and inside of the residual briquette. When the moisture content was 1.47% and the gas

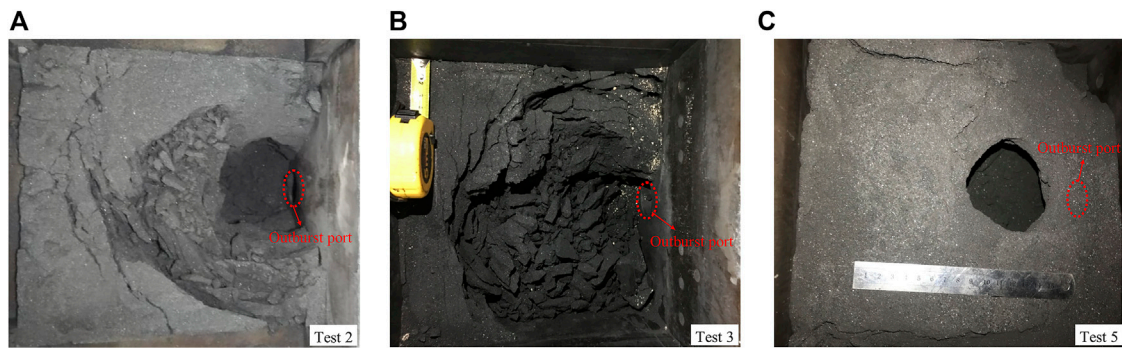


FIGURE 6 | Outburst hole characteristics of different simulation tests. **(A)** Test 2: 1.47% moisture content and 0.35 MPa pressure. **(B)** Test 3: 1.47% moisture content and 0.45 MPa pressure. **(C)** Test 5: 5% moisture content and 0.45 MPa pressure.

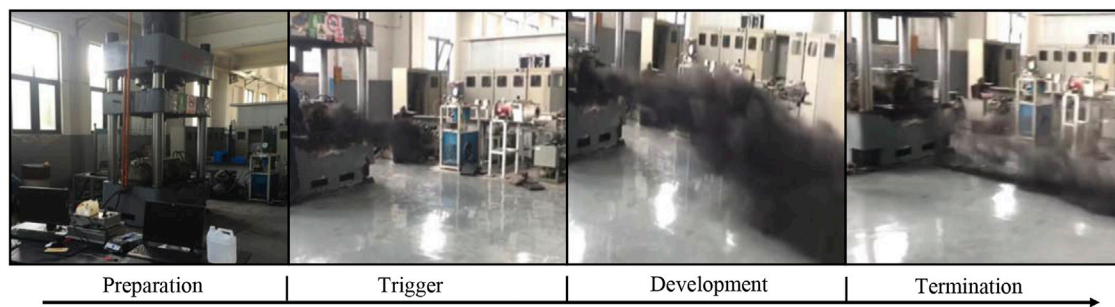


FIGURE 7 | The process of coal and gas outburst in simulation tests.

pressure was 0.45 MPa, the damage to the residual briquette was the most serious, and most of the coal in the chamber was broken.

3.3.2 Characteristics of Coal and Gas Outburst Process

When the outburst was triggered, the high-pressure gas carrying coal in the chamber was jetted out rapidly, and the duration was very short, only about 1 s. The two-phase gas–solid mixtures caused by the outburst propagated as shock waves and flows from the sources (Zhou et al., 2020). The entire outburst process was divided into four stages: preparation, trigger, development, and termination (Zhao et al., 2016). **Figure 7** shows the typical motion state in the outburst process of test 3. In the outburst trigger stage, the coal was broken and thrown out under the action of high-pressure gas and stress. At this time, the mass and velocity of the thrown coal were increasing. The free gas in the chamber had enough energy to break, transport, and throw away the coal. During the outburst development stage, the mass and velocity of the thrown coal were relatively stable because the desorption gas was converted into free gas to supplement energy. At the outburst termination stage, the effect of gas and stress was not able to further break down and throw out the coal, so the mass and velocity of the thrown coal

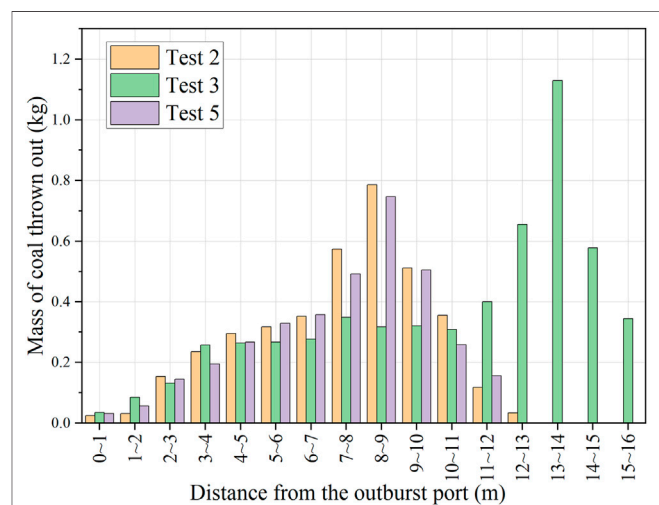


FIGURE 8 | Mass distribution of coal powder at different distances.

decreased, and finally the outburst came to an end. The whole outburst process experienced three periods: acceleration period, stabilization period, and attenuation period. The three stages are closely related to the energy of coal destruction and migration.

TABLE 3 | Distribution of outburst coal powder in different zones.

Test number	Moisture content (%)	Proportion of coal powder mass (%)				
		Zone I	Zone II	Zone III	Zone IV	Zone V
2	1.47	1.69	10.46	21.96	35.94	29.95
3	1.47	1.51	12.23	19.45	29.94	36.87
5	5	1.41	9.89	23.91	36.23	28.56

3.3.3 Distribution Characteristics of Coal Powder

After each outburst, the coal powder scattered on the ground was weighed to obtain the distance distribution, as shown in **Figure 8**. The distance between the thrown coal powder and the outburst port in a test was divided into five zones equally: zones I, II, III, IV, and V. The mass and proportion of the outburst coal powder in each zone are shown in **Table 3**.

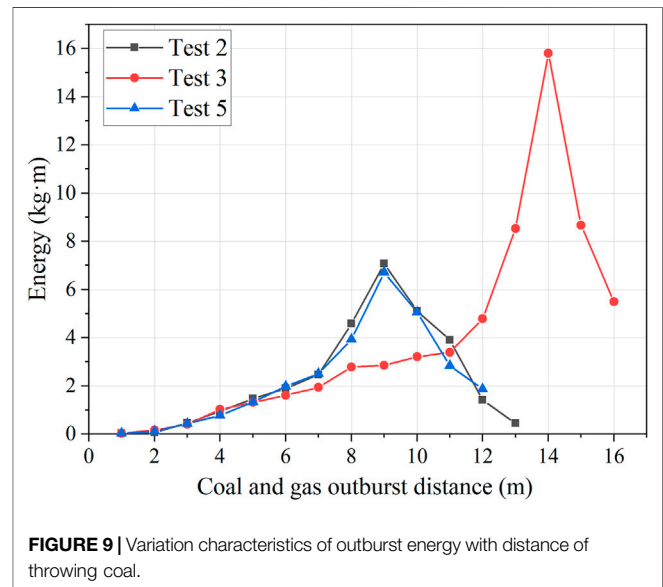
Most of the coal powder was concentrated in zones III, IV, and V, while the distribution in zones I and II was rare, the sum of which was less than 15%. This phenomenon indicates that there is enough energy in the chamber to break a large amount of coal and throw it out for a long distance in the early and middle stage of the outburst. With the continuous development of the outburst process, the energy is consumed greatly, and only a small part of the coal is broken and thrown out for a short distance. Finally, the outburst process terminates, which is also consistent with the outburst process analysis.

Compared with tests 3 and 5, when the moisture content of coal increased from 1.47 to 5%, the mass proportion of coal powder in zones III and IV increased significantly, while that in zones V decreased by 8.31%. In addition, the maximum distance of coal ejection was shortened by 4.67 m. The moisture content of coal has a great influence on the distance and distribution of the outburst coal powder. With the increase of moisture content, the bonding between coal particles increases (Wang H et al., 2021). Since coal rock mass is a porous medium, its internal pores and fractures are filled by water molecules, which increases the density of a single coal particle, so the thrown coal powder becomes more concentrated.

4 DISCUSSION

4.1 Energy Analysis of Coal and Gas Outburst

The complete coal and gas outburst process goes through four stages: the preparation stage, the trigger stage, the development stage, and the termination stage. The energy required for outburst changes constantly at each stage. In the preparation stage, gas pressure and stress fully compress the skeleton of coal, resulting in a large amount of elastic potential of coal (Tu et al., 2021). In addition, 90% of the gas in coal is in the adsorption state and has great expansion potential. In the trigger stage, the equilibrium state of the coal body is broken, the free gas and stress release energy quickly to do work on the coal body, and the outburst accident is triggered (Hou et al., 2021). In the development stage, adsorbed gas with high pressure gradient can be desorbed quickly

**FIGURE 9** | Variation characteristics of outburst energy with distance of throwing coal.

to supplement energy, and the coal body is continuously stripped, broken and thrown out by free gas. For the simulation test of coal and gas outburst in this study, the algorithm for defining energy is shown in **Eq. 2** (Guo, 2014). In the outburst simulation test, coal and gas are thrown into free open space, which is different from the coal and gas thrown into the roadway in the actual coal and gas outburst. The energy calculated by this method is also different from the actual outburst energy, but the energy variation trend is consistent.

$$E = \sum_{i=1}^n E_i \quad (2)$$

Where E is the total outburst energy of coal and gas outburst simulation test, kg·m; E_i is the energy of pulverized coal thrown out within the range of i , $E_i = im_i$; i is the per-unit distance between the thrown coal powder and the outburst port, which is an integer, m; and m_i is the mass of thrown coal powder within the range of i .

Figure 9 shows the variation characteristics of outburst energy per unit distance in different tests. The outburst energy of the three tests increased first and then decreased with the distance of coal powder thrown out. The calculated outburst energy was mainly concentrated in the rear, indicating that the outburst energy is large in the early and middle period of outburst, which can break the coal body and throw it to a long distance. The total energy of outburst in tests 2, 3, and 5 was 29.8554, 62.0029 and

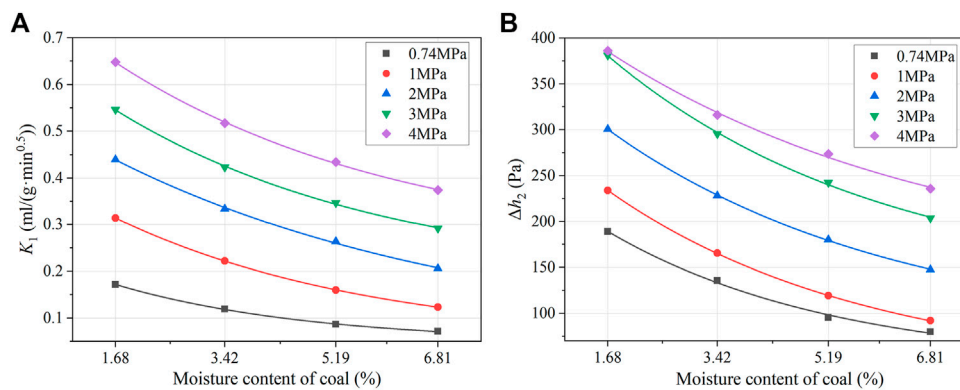


FIGURE 10 | Effect of different moisture content of coal on K_1 and Δh_2 . (A) Effect on K_1 . (B) Effect on Δh_2 .

27.5826 kg·m, respectively. The total outburst energy in test 3 was the largest. With the decrease of moisture content and gas pressure, the total outburst energy and outburst intensity decreased. Compared with tests 3, the total energy in test 5 was reduced by 34.4203 kg·m.

4.2 Effect of Moisture on Coal and Gas Outburst

The gas desorption index of drill cuttings K_1 and Δh_2 are indicators to predict and judge the risk of coal and gas outburst through the correlation law of gas adsorption and desorption of coal, which are widely used in gas prevention and control technology in China. K_1 reflects the gas desorption amount of coal in the first 1 min, and Δh_2 reflects the gas desorption amount within 4–5 min (State Administration of Work Safety, 2019; Wang F et al., 2020). K_1 and Δh_2 can be obtained by intercepting the corresponding data of gas desorption experiment in Section 3.2, which can further analyze the risk of coal and gas outburst, as shown in Figure 10. When the gas adsorption equilibrium pressure is 4 MPa and the moisture content is 1.68%, K_1 and Δh_2 are the largest. When the gas pressure is the same, K_1 and Δh_2 decrease and tend to be gentle with the increase of moisture content of coal, showing an exponential law. The gas outburst parameter experimental results show that with the increase of moisture content, the adsorption constant a of coal decreases and the limit adsorption amount of gas decreases. The f of coal increases, and the coal body strength increases, thus increasing the energy threshold required by coal and gas outburst. The desorption capacity of gas decreases as the Δp decreases. All of them have an exponential relation to moisture content. The results of gas desorption experiments show that with the increase of moisture content, the accumulated gas desorption amount and the initial desorption rate decrease obviously. All the above laws indicate that the increase of moisture content weakens the risk of coal and gas outburst. According to the variation law of each parameter with moisture content, it can be predicted that there is a certain limit of moisture content. When the moisture content exceeds its value, the increase of coal seam solidity coefficient and

the decrease of gas desorption velocity will no longer be obvious. Meanwhile, the adsorption constant a , f , Δp , K_1 , and Δh_2 of coal will not change significantly, but remain roughly stable at a certain value.

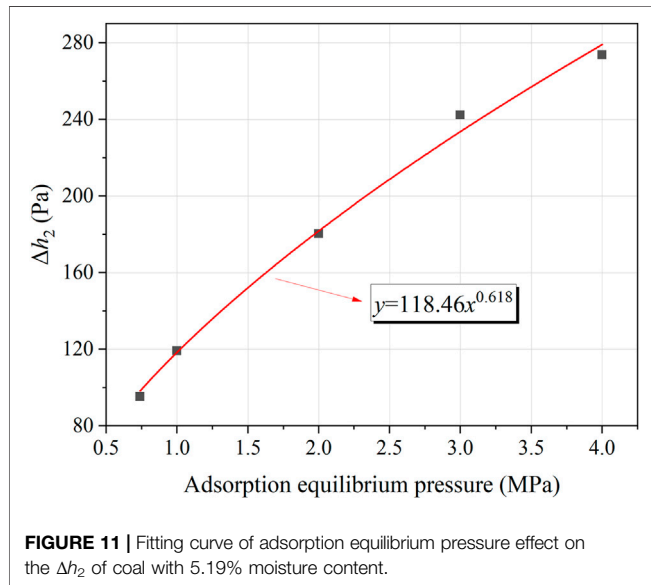
When the moisture content of coal is low, a large amount of adsorbed gas is desorbed into free gas, and the intensity of coal and gas outburst is large. On the contrary, when the moisture content increases, the water lock effect makes the desorption amount of coal decrease greatly. Moreover, the coal body plasticity increases, elasticity decreases, and the ability to resist damage also increases, which weakens the possibility of outburst. In the coal mine site, the stress concentration zone of the working face is transferred to the depth of the coal seam, so as to reduce the stress in front of the working face. At the same time, water will have an obvious blocking effect on gas migration, which can reduce the risk of outburst. Therefore, the risk of coal and gas outburst decreases with the increase of moisture content, and the outburst may not be triggered when the moisture content increases to a critical value.

4.3 Key Indexes of Coal and Gas Outburst Prevention Under Hydraulic Measures

Hydraulic measures can reduce the outburst risk of coal seam to a large extent and escort the smooth development of mining face. In the process of gas control in coal mine site, too little water is not conducive to control the risk of coal and gas outburst. However, too much water will lead to the water lock effect (Hao et al., 2018; Liu et al., 2019; Qin et al., 2020), making it difficult for gas to be pre-extracted, which is also not conducive to the prevention and control of coal and gas outburst. Table 4 shows the critical value of outburst risk index commonly used in China (State Administration of Work Safety, 2019). In this study, the gas outburst parameters of No. 8 coal seam in the Luling coal mine under different moisture content were obtained. According to the fitting formula in Figure 3, when the moisture content is greater than 5%, the Δp is <10 and the f is >0.5 . Figure 11 shows the Δh_2 fitting curve of coal with a moisture content of 5.19% under different gas pressures. When the gas pressure is 0.74 MPa, Δh_2 is 98.34 Pa, far less than the critical value of 160 Pa. The

TABLE 4 | Critical value of coal seam outburst risk index.

Index	Original coal seam gas pressure (MPa)	f	Δp (mmHg)	Δh_2 (Pa)
Risk of coal and gas outburst	≥ 0.74	≤ 0.5	≥ 10	≥ 160



simulation test of coal and gas outburst also shows that it is more difficult to outburst when the moisture content of coal is greater than 5%. Therefore, it can be inferred that in No. 8 coal seam of the Luling coal mine, the coal body moisture content interval of hydraulic measures for coal and gas outburst should be greater than 5%. Therefore, 5% moisture content of coal body can be used as a critical index of hydraulic measures to prevent coal and gas outburst in No. 8 coal seam of the Luling coal mine.

5 CONCLUSION

In this study, we systematically studied the gas outburst parameters and gas desorption characteristics of the strong outburst coal under different moisture content in No. 8 coal seam of the Luling coal mine. Additionally, the coal and gas simulation tests under different moisture content were carried out using the simulation test system to explore the influence of moisture on the law and characteristics of coal and gas outburst. The main conclusions are as follows:

- 1) With the increase of moisture content, the adsorption constant a , the initial velocity of gas diffusion Δp , and the gas desorption index of drill cuttings K_1 and Δh_2 of coal decrease, but the Protodyakonov coefficient f of coal increases. Meanwhile, the accumulated gas desorption amount and the

initial desorption rate decrease obviously. All of them have an exponential relation to moisture content. Increasing the moisture content of strong outburst coal is beneficial to reduce the outburst risk.

- 2) The entire outburst process is divided into four stages: preparation, trigger, development, and termination. The change of moisture content greatly affects the characteristics and energy of coal and gas outburst. With the increase of moisture content from 1.47% to 5%, the threshold of gas pressure increases and the intensity of outburst decreases, the amount of coal powder thrown out is relatively less, and the maximum distance of coal ejection is shortened by 4.67 m. Furthermore, the total outburst energy decreases by 34.4203 kg·m.
- 3) The coal and gas outburst may not be triggered when the moisture content increases to a critical value. When the moisture content of the strong outburst coal is greater than 5%, Δp is < 10 , f is > 0.5 , and Δh_2 is < 160 Pa, which indicate that the risk of outburst is greatly reduced. Therefore, 5% moisture content of coal body can be used as a critical index of hydraulic measures to prevent coal and gas outburst in No. 8 coal seam of the Luling coal mine.

DATA AVAILABILITY STATEMENT

The raw data supporting the conclusion of this article will be made available by the authors, without undue reservation.

AUTHOR CONTRIBUTIONS

ZL: Writing, Conceptualization, Methodology and Analysis. LW: Validation, Resources and Funding acquisition. ML: Investigation and Data curation. YL: Investigation. HW: Supervision and Review. QL: Review and Resources.

FUNDING

This research was supported by the National Natural Science Foundation of China (Nos 51974300 and 52174216), the Fundamental Research Funds for the Central Universities (Nos 2021YCPY0206 and 2020ZDPY0224), the Postgraduate Research and Practice Innovation Program of Jiangsu Province (KYCX21_2476), and a project funded by the Priority Academic Program Development of Jiangsu Higher Education Institutions.

REFERENCES

- Beamish, B. B., and Crosdale, P. J. (1998). Instantaneous Outbursts in Underground Coal Mines: An Overview and Association with Coal Type. *Int. J. Coal Geology*. 35 (1), 27–55. doi:10.1016/S0166-5162(97)00036-0
- Black, D. J. (2019). Review of Coal and Gas Outburst in Australian Underground Coal Mines. *Int. J. Mining Sci. Tech.* 29 (6), 815–824. doi:10.1016/j.ijmst.2019.01.007
- Chen, D., Pan, Z., Liu, J., and Connell, L. D. (2012). Modeling and Simulation of Moisture Effect on Gas Storage and Transport in Coal Seams. *Energy Fuels* 26 (3), 1695–1706. doi:10.1021/ef2014327
- Chen, X., and Cheng, Y. (2014). Influence of the Injected Water on Gas Outburst Disasters in Coal Mine. *Nat. Hazards* 76 (2), 1093–1109. doi:10.1007/s11069-014-1535-3
- Chen, J., Zhu, C., Du, J., Pu, Y., Pan, P., Bai, J., et al. (2022). A Quantitative Pre-warning for Coal Burst Hazardous Zones in a Deep Coal Mine Based on the Spatio-Temporal Forecast of Microseismic Events. *Process Safety and Environmental Protection* 159, 1105–1112. doi:10.1016/j.psep.2022.01.082
- Cheng, Y.-P., Wang, L., and Zhang, X.-L. (2011). Environmental Impact of Coal Mine Methane Emissions and Responding Strategies in China. *Int. J. Greenhouse Gas Control*. 5 (1), 157–166. doi:10.1016/j.ijggc.2010.07.007
- Cheng, Y., and Pan, Z. (2020). Reservoir Properties of Chinese Tectonic Coal: A Review. *Fuel* 260, 116350. doi:10.1016/j.fuel.2019.116350
- Díaz Aguado, M. B., and González Nicieza, C. (2007). Control and Prevention of Gas Outbursts in Coal Mines, Riosa-Olloniego coalfield, Spain. *Int. J. Coal Geology*. 69 (4), 253–266. doi:10.1016/j.coal.2006.05.004
- Ding, Y., and Yue, Z. Q. (2018). An Experimental Investigation of the Roles of Water Content and Gas Decompression Rate for Outburst in Coal Briquettes. *Fuel* 234, 1221–1228. doi:10.1016/j.fuel.2018.07.143
- Fan, C., Li, S., Elsworth, D., Han, J., and Yang, Z. (2020). Experimental Investigation on Dynamic Strength and Energy Dissipation Characteristics of Gas Outburst-prone Coal. *Energy Sci Eng* 8 (4), 1015–1028. doi:10.1002/ese3.565
- Fan, C., Li, S., Luo, M., Du, W., and Yang, Z. (2017). Coal and Gas Outburst Dynamic System. *Int. J. Mining Sci. Tech.* 27 (1), 49–55. doi:10.1016/j.ijmst.2016.11.003
- Fan, C., Yang, L., Wang, G., Huang, Q., Fu, X., and Wen, H. (2021). Investigation on Coal Skeleton Deformation in CO₂ Injection Enhanced CH₄ Drainage from Underground Coal Seam. *Front. Earth Sci.* 9. doi:10.3389/feart.2021.766011
- Guo, P. (2014). *Research on Laminar Spallation Mechanism of Coal and Gas Outburst Propagation [D]*. Xuzhou, Jiang su: China University of mining and technology.
- Hao, D., Zhang, L., Ye, Z., Tu, S., and Zhang, C. (2018). Experimental Study on the Effects of the Moisture Content of Bituminous Coal on its Gas Seepage Characteristics. *Arabian J. Geosciences* 11 (15). doi:10.1007/s12517-018-3758-1
- Hou, W., Wang, H., Yuan, L., Wang, W., Xue, Y., and Ma, Z. (2021). Experimental Research into the Effect of Gas Pressure, Particle Size and Nozzle Area on Initial Gas-Release Energy during Gas Desorption. *Int. J. Mining Sci. Tech.* 31 (2), 253–263. doi:10.1016/j.ijmst.2021.01.002
- Jin, K., Cheng, Y., Ren, T., Zhao, W., Tu, Q., Dong, J., et al. (2018). Experimental Investigation on the Formation and Transport Mechanism of Outburst Coal-Gas Flow: Implications for the Role of Gas Desorption in the Development Stage of Outburst. *Int. J. Coal Geology*. 194, 45–58. doi:10.1016/j.coal.2018.05.012
- Lei, Y., Cheng, Y., Ren, T., Tu, Q., Shu, L., and Li, Y. (2020). The Energy Principle of Coal and Gas Outbursts: Experimentally Evaluating the Role of Gas Desorption. *Rock Mech. Rock Eng.* 54 (1), 11–30. doi:10.1007/s00603-020-02246-5
- Liu, Y., Feng, G., Zuo, W., Liu, M., and Mitri, H. S. (2019). The Law and Mechanism of Dynamic Methane Diffusion from Coal Particles under Different Moisture Content. *Arabian J. Geosciences* 12 (24). doi:10.1007/s12517-019-4919-6
- Lu, Y., Ge, Z., Yang, F., Xia, B., and Tang, J. (2017). Progress on the Hydraulic Measures for Grid Slotting and Fracking to Enhance Coal Seam Permeability. *Int. J. Mining Sci. Tech.* 27 (5), 867–871. doi:10.1016/j.ijmst.2017.07.011
- Meng, J., Li, S., Niu, J., Meng, H., Zhong, R., Zhang, L., et al. (2020). Effects of Moisture on Methane Desorption Characteristics of the Zhaozhuang Coal: experiment and Molecular Simulation. *Environ. Earth Sci.* 79 (1). doi:10.1007/s12665-019-8788-9
- Pan, Z., Connell, L. D., Camilleri, M., and Connelly, L. (2010). Effects of Matrix Moisture on Gas Diffusion and Flow in Coal. *Fuel* 89 (11), 3207–3217. doi:10.1016/j.fuel.2010.05.038
- Qin, H., Wei, J., Li, D., and Li, S. (2019). Experimental Investigation on the Release Rule of the Gas Expansion Potential of Loaded Water-Filled Soft Coal. *Math. Probl. Eng.* 2019, 1–9. doi:10.1155/2019/1085296
- Qin, Y., Su, W., Tian, F., and Chen, Y. (2020). Research Status and Development Direction of Microcosmic Effect under Coal Seam Water Injection. *J. China Univ. Mining Tech.* 49 (03), 428–444. doi:10.13247/j.cnki.jcmt.001148
- Shepherd, J., Rixon, L. K., and Griffiths, L. (1981). Outbursts and Geological Structures in Coal Mines: A Review. *Int. J. Rock Mech. Mining Sci. Geomechanics Abstr.* 18 (4), 267–283. doi:10.1016/0148-9062(81)91192-x
- State Administration of Work Safety (2019). *Detailed Rules for Prevention and Control of Coal and Gas Outburst*. Beijing: China Coal Industry Publishing House.
- Sun, Q. (2014). Research on Status Quo and Prevention Countermeasures of Coal Mine Gas Disaster in China. *China Coal* 40 (03), 116–119. doi:10.19880/j.cnki.ccm.2014.03.027
- Tu, Q., Cheng, Y., Guo, P., Jiang, J., Wang, L., and Zhang, R. (2016). Experimental Study of Coal and Gas Outbursts Related to Gas-Enriched Areas. *Rock Mech. Rock Eng.* 49 (9), 3769–3781. doi:10.1007/s00603-016-0980-6
- Tu, Q., Cheng, Y., Xue, S., Ren, T., and Cheng, X. (2021). Energy-limiting Factor for Coal and Gas Outburst Occurrence in Intact Coal Seam. *Int. J. Mining Sci. Tech.* 31 (4), 729–742. doi:10.1016/j.ijmst.2021.05.009
- Wang, C., Cheng, Y., Yi, M., Lei, Y., and He, X. (2020). Powder Mass of Coal after Impact Crushing: A New Fractal-Theory-Based Index to Evaluate Rock Firmness. *Rock Mech. Rock Eng.* 53 (9), 4251–4270. doi:10.1007/s00603-020-02174-4
- Wang, C., Yang, S., Li, J., Li, X., and Jiang, C. (2018). Influence of Coal Moisture on Initial Gas Desorption and Gas-Release Energy Characteristics. *Fuel* 232, 351–361. doi:10.1016/j.fuel.2018.06.006
- Wang, F., Liang, Y., Sun, Z., Li, L., and Li, X. (2020). Determination of the Sensitivity index and its Critical Value for Outburst Risk Prediction: A Case Study in Fuxiang Mine, China. *Adsorption Sci. Tech.* 38 (9-10), 502–527. doi:10.1177/02636174200963735
- Wang, H., Cheng, Y., and Yuan, L. (2013). Gas Outburst Disasters and the Mining Technology of Key Protective Seam in Coal Seam Group in the Huainan coalfield. *Nat. Hazards* 67 (2), 763–782. doi:10.1007/s11069-013-0602-5
- Wang, H., Tao, Y., Wang, D., Sun, X., Gao, J., and Loupasakis, C. (2021). Experimental Study on Mechanical Properties of Briquette Coal Samples with Different Moisture Content. *Geofluids* 2021, 1–11. doi:10.1155/2021/6634378
- Wang, K., Dong, H., Guo, Y., Zhao, W., Shao, B., Yan, Z., et al. (2021). Gas Drainage Performance Evaluation in Coal under Non-uniform Stress with Different Moisture Content: Analysis, Simulation and Field Verification. *Fuel* 305, 121489. doi:10.1016/j.fuel.2021.121489
- Wang, L., Chen, E.-t., Liu, S., Cheng, Y.-p., Cheng, L.-b., Chen, M.-y., et al. (2017a). Experimental Study on the Effect of Inherent Moisture on Hard Coal Adsorption-Desorption Characteristics. *Adsorption* 23 (5), 723–742. doi:10.1007/s10450-017-9889-y
- Wang, L., Liu, S., Cheng, Y., Yin, G., Zhang, D., and Guo, P. (2017b). Reservoir Reconstruction Technologies for Coalbed Methane Recovery in Deep and Multiple Seams. *Int. J. Mining Sci. Tech.* 27 (2), 277–284. doi:10.1016/j.ijmst.2017.01.026
- Wang, L., Lu, Z., Chen, D.-p., Liu, Q.-q., Chu, P., Shu, L.-y., et al. (2020c). Safe Strategy for Coal and Gas Outburst Prevention in Deep-And-Thick Coal Seams Using a Soft Rock Protective Layer Mining. *Saf. Sci.* 129, 104800. doi:10.1016/j.ssci.2020.104800
- Wang, L., Xi, G., Keep, R. F., and Hua, Y. (2012). Iron Enhances the Neurotoxicity of Amyloid β . *Transl. Stroke Res.* 3 (1), 107–113. doi:10.1007/s12975-011-0099-8
- Xue, S., Yuan, L., Wang, Y., and Xie, J. (2014). Numerical Analyses of the Major Parameters Affecting the Initiation of Outbursts of Coal and Gas. *Rock Mech. Rock Eng.* 47 (4), 1505–1510. doi:10.1007/s00603-013-0425-4
- Yan, F., Xu, J., Lin, B., Peng, S., Zou, Q., and Zhang, X. (2019). Effect of Moisture Content on Structural Evolution Characteristics of Bituminous Coal Subjected

- to High-Voltage Electrical Pulses. *Fuel* 241, 571–578. doi:10.1016/j.fuel.2018.12.078
- Yang, M., Yuan, M., Xu, L., Xu, S., Li, C., and Wang, Y. (2017). Research of the Influence of Moisture on Initial Speed of Methane Diffusion. *Ind. Saf. Environ. Prot.* 43 (04), 11–13. doi:10.3969/j.issn.1001-425X.2017.04.004
- Yang, W., Wang, H., Zhuo, Q., Lin, B., Zhang, J., Lu, C., et al. (2019). Mechanism of Water Inhibiting Gas Outburst and the Field experiment of Coal Seam Infusion Promoted by Blasting. *Fuel* 251, 383–393. doi:10.1016/j.fuel.2019.04.064
- Yao, Q., Zheng, C., Tang, C., Xu, Q., Chong, Z., and Li, X. (2020). Experimental Investigation of the Mechanical Failure Behavior of Coal Specimens with Water Intrusion. *Front. Earth Sci.* 7. doi:10.3389/feart.2019.00348
- Yi, M., Wang, L., Liu, Q., Hao, C., Wang, Z., and Chu, P. (2021). Characteristics of Seepage and Diffusion in Gas Drainage and its Application for Enhancing the Gas Utilization Rate. *Transp Porous Med.* 137 (2), 417–431. doi:10.1007/s11242-021-01573-7
- Zhang, C., Wang, E., Wang, Y., and Zhou, X. (2021). Spatial-temporal Distribution of Outburst Accidents from 2001 to 2020 in China and Suggestions for Prevention and Control. *Coal Geology. Exploration* 49 (4), 134–141. doi:10.3969/j.issn.1001-1986.2021.04.016
- Zhang, G., Liu, X., Bi, Y., and Pu, W. (2011). Experimental Study of Penetrant Solution Impact on Gas Desorption. *Proced. Eng.* 26, 113–119. doi:10.1016/j.proeng.2011.11.2147
- Zhang, H., Cheng, Y., Liu, Q., Yuan, L., Dong, J., Wang, L., et al. (2017). A Novel In-Seam Borehole Hydraulic flushing Gas Extraction Technology in the Heading Face: Enhanced Permeability Mechanism, Gas Flow Characteristics, and Application. *J. Nat. Gas Sci. Eng.* 46, 498–514. doi:10.1016/j.jngse.2017.08.022
- Zhang, K. Z., Wang, S. L., Wang, L., Cheng, Y. P., Li, W., Han, X. W., et al. (2022). 3D Visualization of Tectonic Coal Microstructure and Quantitative Characterization on Topological Connectivity of Pore-Fracture Networks by Micro-CT. *J. Pet. Sci. Eng.* 208, 109675. doi:10.1016/j.petrol.2021.109675
- Zhang, S., and Sang, H. (2009). Physical Chemistry Mechanism of Influence of Liquid Water on Coalbed Methane Adsorption. *Proced. Earth Planet. Sci.* 1 (1), 263–268. doi:10.1016/j.proeps.2009.09.042
- Zhao, W., Cheng, Y., Jiang, H., Jin, K., Wang, H., and Wang, L. (2016). Role of the Rapid Gas Desorption of Coal Powders in the Development Stage of Outbursts. *J. Nat. Gas Sci. Eng.* 28, 491–501. doi:10.1016/j.jngse.2015.12.025
- Zhao, W., Wang, K., Zhang, R., Dong, H., Lou, Z., and An, F. (2020). Influence of Combination Forms of Intact Sub-layer and Tectonically Deformed Sub-layer of Coal on the Gas Drainage Performance of Boreholes: a Numerical Study. *Int. J. Coal Sci. Technol.* 7 (3), 571–580. doi:10.1007/s40789-020-00317-0
- Zhao, Y., Cao, S., Li, Y., Zhang, Z., Guo, P., Yang, H., et al. (2018). The Occurrence State of Moisture in Coal and its Influence Model on Pore Seepage. *RSC Adv.* 8 (10), 5420–5432. doi:10.1039/c7ra09346b
- Zhi, S., and Elsworth, D. (2016). The Role of Gas Desorption on Gas Outbursts in Underground Mining of Coal. *Geomech. Geophys. Geo-energy. Geo-resour.* 2 (3), 151–171. doi:10.1007/s40948-016-0026-2
- Zhou, A., Zhang, M., Wang, K., and Elsworth, D. (2020). Near-source Characteristics of Two-phase Gas-Solid Outbursts in Roadways. *Int. J. Coal Sci. Technol.* 8 (4), 685–696. doi:10.1007/s40789-020-00362-9
- Zhou, B., Yang, S., Wang, C., Cai, J., Xu, Q., and Sang, N. (2019). Experimental Study on the Influence of Coal Oxidation on Coal and Gas Outburst during Invasion of Magmatic Rocks into Coal Seams. *Process Saf. Environ. Prot.* 124, 213–222. doi:10.1016/j.psep.2019.02.017

Conflict of Interest: The authors declare that the research was conducted in the absence of any commercial or financial relationships that could be construed as a potential conflict of interest.

Publisher's Note: All claims expressed in this article are solely those of the authors and do not necessarily represent those of their affiliated organizations, or those of the publisher, the editors, and the reviewers. Any product that may be evaluated in this article, or claim that may be made by its manufacturer, is not guaranteed or endorsed by the publisher.

Copyright © 2022 Lu, Wang, Lv, Lei, Wang and Liu. This is an open-access article distributed under the terms of the Creative Commons Attribution License (CC BY). The use, distribution or reproduction in other forums is permitted, provided the original author(s) and the copyright owner(s) are credited and that the original publication in this journal is cited, in accordance with accepted academic practice. No use, distribution or reproduction is permitted which does not comply with these terms.



Analysis of Failure Mechanics and Energy Evolution of Sandstone Under Uniaxial Loading Based on DIC Technology

Like Wei^{1,2}, Qiang Yuan^{1*}, Yiwei Ren¹, Deyi Jiang^{1*}, Dingding Zhang³, Yongliang Liu³, Yunlong Zou⁴ and Shicong Ren⁵

¹State Key Laboratory of Coal Mine Disaster Dynamics and Control, Chongqing University, Chongqing, China, ²Information Research Institute, Ministry of Emergency Management, Beijing, China, ³College of Energy Engineering, Xi'an University of Science and Technology, Xi'an, China, ⁴China Coal Technology and Engineering Group Chongqing Research Institute, Chongqing, China, ⁵Chongqing Engineering Research Center of Automatic Monitoring for Geological Hazards, Ministry of Natural Resources, Chongqing, China

OPEN ACCESS

Edited by:

Xuanmei Fan,
Chengdu University of Technology,
China

Reviewed by:

Peng Feng,
Chengdu University, China
Jinwang Zhang,
China University of Mining and
Technology, China
Jing Xie,
Sichuan University, China

*Correspondence:

Qiang Yuan
qiangyuan@cqu.edu.cn
Deyi Jiang
deyij@cqu.edu.cn

Specialty section:

This article was submitted to
Geohazards and Georisks,
a section of the journal
Frontiers in Earth Science

Received: 13 November 2021

Accepted: 28 February 2022

Published: 08 April 2022

Citation:

Wei L, Yuan Q, Ren Y, Jiang D,
Zhang D, Liu Y, Zou Y and Ren S
(2022) Analysis of Failure Mechanics
and Energy Evolution of Sandstone
Under Uniaxial Loading Based on
DIC Technology.
Front. Earth Sci. 10:814292.
doi: 10.3389/feart.2022.814292

Energy evolution process of rock deformation is conducive to essentially reveal the rock failure mechanism and is of great significance to uncover the breeding of dynamic disasters in rock engineering. To characterize the damage evolution of energy dissipation during rock failure, the digital image correlation (DIC) technique is proposed to describe the rock failure mechanics and its energy evolution process. The uniaxial compression experiment of sandstone specimen was carried out, and the whole field deformation and failure characteristics of the rock had been captured by the DIC system. Measurement accuracy was verified by the fiber Bragg grating (FBG) sensor, the elastic region of the specimen was divided according to the location of strain localization band (SLB), and the evolution process of elastic strain energy of the rock was analyzed. The results show that the time history development of rock strain obtained by the FBG and DIC system matches identically, and the deviation of peak axial strain of both means is less than 5%, which verifies the applicability of DIC system. The uncoordinated evolution of rock deformation displacement field is discussed to reveal the crack development and failure form of the sandstone specimen under uniaxial compression. The energy evolution of the elastic region of the specimen is revealed, and the development of releasable elastic strain energy would be divided into three stages, which correspond to the stress-strain characteristics of rock failure mechanics. This study could provide an alternative analytical method for the experimental rock mechanics research studies.

Keywords: rock material, failure mechanics, DIC, strain, energy evolution

INTRODUCTION

The deformation and failure of rocks is an energy dissipation and irreversible process. The rock mass subjected to external force not only causes the change in rock stress and strain state but also leads to the change in rock damage state. Correctly understanding and describing the energy evolution in the process of rock deformation and failure has important scientific and practical significance for in-depth understanding of the damage, fracture, instability, and failure of rock materials, and the occurrence mechanism of rock engineering disasters (Mikhalyuk and Zakharov, 1997; Steffler et al., 2003; Sujatha and Kishen, 2003; Song et al., 2012).

In recent years, the energy analysis method has been used to describe the rock mechanics behaviors including deformation, broken, creeping, and permeation. Xie et al. (2005), Xie et al. (2009), and Feng et al. (2021) studied the internal relationship between energy dissipation, release and rock failure in the process of rock deformation and failure, and proposed rock strength and overall failure criteria based on the energy theory. On this basis, Zhang and Gao (2012) and Zhang and Gao (2012) analyzed different energy conversion mechanisms in the process of rock uniaxial compression, and established a self-inhibitory evolution model of energy conversion of loaded rock. Afterward, the evolution characteristics of energy dissipation, friction energy dissipation, and breakage energy dissipation were studied to show that the energy dissipation ratio shows a spoon shape characteristic (Miao et al., 2021). The jointed sandstone with different dip angles under uniaxial compression finds out that the energy evolution process is divided into five stages, and total elastic strain energy at the peak point of jointed sandstone exhibit asymmetrical “U” type evolution characteristics with the increase of dip angles of joint (Wang et al., 2020). The sandstone energy evolution behavior under the unconfined compressive condition revealed that the interface friction between fatigue damage and cracks will produce plastic deformation (Liu et al., 2020). The internal energy parameters of rock specimens during tensile failure were obtained to analyze the law of energy storage and consumption (Gong et al., 2018). Jiang et al. collected acoustic emission parameters during uniaxial compression of shale and analyzed the criticality of energy release during load fracture of brittle rock (Jiang et al., 2016). Zhao studied the energy variation law of rocks under different confining pressures and different unloading paths (Zhao et al., 2015). Song discussed the energy dissipation characteristics of the coal and rock in the process of uniaxial compression from the perspective of energy by using geophysical methods (Song et al., 2015).

Due to the complexity of rock deformation, different technical means were used to explore the principle of energy dissipation law during the rock deformation. Some emerging optical testing technologies, such as fiber Bragg grating (FBG) sensing technology and digital image correlation (DIC) technology, have also been applied to explore the precursor information of deformation and instability of rock mass materials (Chai et al., 2015; Chai et al., 2016; Wang et al., 2018). Simultaneously, tests in uniaxial compression of rocks with FBG sensor, MTS system, and laser strain gauge have shown that the sensor has high accuracy in rock strain measurement (Hatenberger et al., 2003). The stability and accuracy of resistance strain gauge and FBG sensor in rock uniaxial cyclic loading and unloading test were compared (Yang et al., 2007), and the damage evolution process of rocks during uniaxial compression by prefabricating speckles on the surface of the standard specimen was described (Ma et al., 2006).

The evolution of deformation field on the specimen surface during rock loading is measured by DIC technology, the non-uniform deformation process of rock materials is analyzed, and the parameters such as the width of localized zone are described quantitatively (Huang et al., 1990; Berthaud et al., 1997; Feng et al., 2021). Nowadays, the DIC method is widely being used in this type of research studies: insights by using DIC analysis into surface deformation of free-standing granite prisms with water

continuously infiltrating from the upper surface for over 24 h under ambient laboratory environmental conditions were presented (Li et al., 2021). Pre-cracked specimen compression test was carried out by using DIC system, and the crack initiation and propagation of rocks with pre-existing cracks were discussed (Xi et al., 2020). The failure mechanism of the tunnel in soft rock subjected to surcharge loading with the DIC measurement, which revealed that the stress loosening zone in the tunnel roof is larger than that in the tunnel sidewall, was investigated (Huang et al., 2020). Evolutions of displacement strain fields and non-linear and localized deformation of the specimen are obtained by the 3D-DIC system (Seisuke et al., 2019). The measurement accuracy of 3D DIC by comparing with the traditional extensometer measurement results and the finite element simulation results was verified (Chen et al., 2017).

As an advanced non-destructive monitoring method, the DIC method is widely used in the field of rock mechanics because of its advantages of non-contact testing, low cost, high precision, and full field observation. So far, focusing on how to use that mean to characterize the failure process and energy evolution could be a vital link to evaluate the geohazard development, and it would create a bridge between energy dissipation and the broken law of rock mass. In this study, the DIC technology is utilized to capture the full field strain distribution so as to explore the rock failure from the perspective of energy evolution.

METHODS AND MATERIALS

Experiment Setup

The uniaxial compression test is implemented, which includes the MTS electronic servo universal testing machine, GOM ARMIS three-dimensional digital speckle full field strain measurement system, and FBG strain acquisition system. MTS electronic servo universal test machine can carry out single-axis compression, stretching, shearing, splitting, and other tests of materials. The largest range is 50 KN, and the loading methods are displacement, strain, and force control. The FBG strain acquisition system consists of FBG sensor and optical demodulator. The GOM ARMIS 3D digital speckle full field strain measurement system is composed of two stable blue light sources, two 5-million-pixel CCD industrial cameras, a calibration system and a core software system (Figure 1).

Measurement Principle of Digital Image Correlation Technology

The DIC technology has been widely used because of its advantages of non-contact acquisition of full field strain and displacement data. It solves the displacement field and strain field data of the measured object by comparing the reference image and the deformed image, calculating the matching degree between the deformed point $P(X_0, Y_0)$ in the reference image and the square near the deformed image $P'(X_0', Y_0')$, determining the displacement components u_x and u_y of the point $P(X_0, Y_0)$ in the X and Y directions, and substituting in Eq. 2 to calculate the displacement of the deformed point $P(X_0, Y_0)$ (Pan et al., 2006; Satoru et al., 2016). The basic principle can be illustrated in Figure 2, where $P(X, Y)$ is the gray intensity of the reference

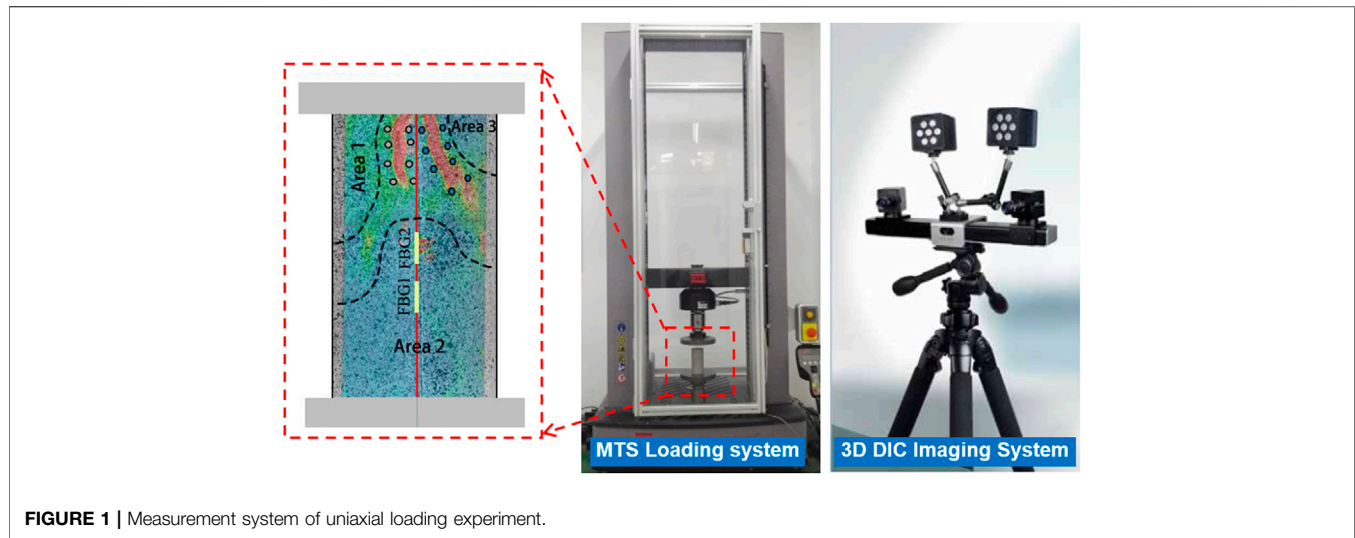


FIGURE 1 | Measurement system of uniaxial loading experiment.

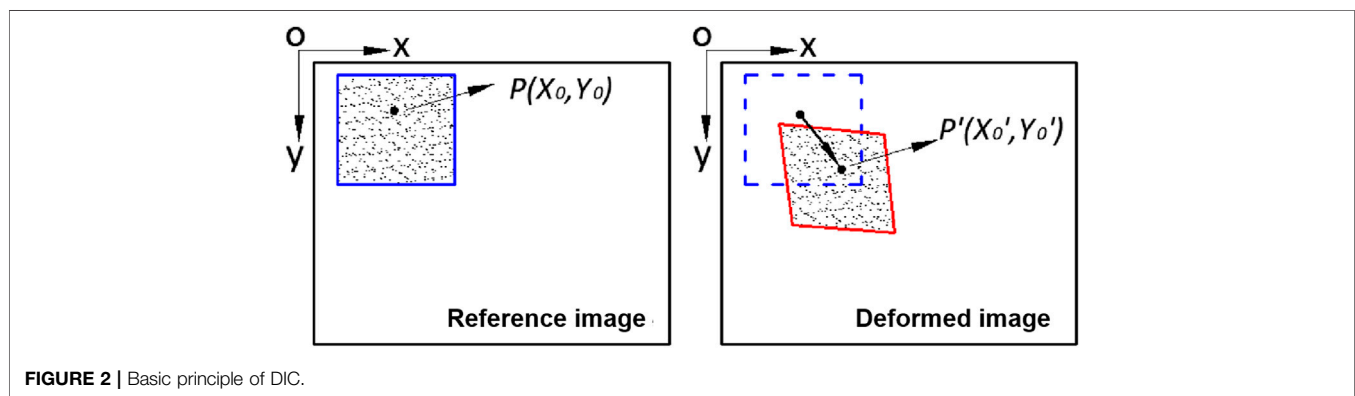


FIGURE 2 | Basic principle of DIC.

image target subset, and $P'(X', Y')$ is the gray intensity of the deformed image target subset.

$$C(x, y, x', y') = \frac{\sum F(x, y)G(x', y')}{\sqrt{\sum F(x, y)^2 \sum G(x', y')^2}} \quad (1)$$

$$\begin{aligned} x' &= x + u_x \\ y' &= y + u_y \end{aligned} \quad (2)$$

According to Eq.3, the sub-pixel gray value of any position in any subset of the deformed image can be calculated, and the gray value of any point in the deformed image can be obtained (Pan et al., 2006).

$$\begin{aligned} G(x', y') &= b_{33}x'^3y'^3 + b_{32}x'^3y'^2 + b_{31}x'^3y' \\ &+ b_{30}x'^3 + b_{23}x'^2y'^3 + b_{22}x'^2y'^2 \\ &+ b_{21}x'^2y' + b_{20}x'^2 + b_{13}x'y'^3 + b_{12}x'y'^2 \\ &+ b_{11}x'y' + b_{10}x' + b_{03}y'^3 + b_{02}y'^2 + b_{01}y' \\ &+ b_{00} = \sum_{i=0}^3 \sum_{j=0}^3 b_{ij}x'^i y'^j \end{aligned} \quad (3)$$

The displacement calculated by Eq. 2 is taken as the initial value and substituted in Eq. 4 for iterative calculation. When the $(u_{k+1}-u_k)$ is less than the threshold value, the displacement with an accuracy of 0.001 pixels and displacement gradient can be obtained.

$$\nabla \nabla C(u_k)(u_{k+1} - u_k) = -\nabla C(u_k) \quad (4)$$

where ∇ is the partial differential operator, u_i is the number i component of displacement vector of u , u_k is the number k iteration of displacement vector value of u , $(u_{k+1}-u_k)$ is a correction value, and $\nabla C(u_k)$ and $\nabla \nabla C(u_k)$ are the Jacobian matrix and Hessian matrix, respectively.

The determination of subset size is related to speckle size, and it is generally believed that each subset should contain at least 3–5 speckles to improve the matching degree. The subset spacing has a direct influence on the number of speckle field data points. The smaller the subset spacing, the longer the calculation time, and the higher the strain field resolution. In this study, each black speckle has 5 pixels, so that the subset size is determined as 19 pixels with a subset spacing of 16 pixels to meet the requirement of measuring accuracy.

Preparation of Rock Specimen and Experiment Procedure

In order to summarize the damage energy evolution law of sandstone-like materials during uniaxial compression, three kinds of sandstone specimens were prepared with quartz sand, iron powder, barite powder, gypsum, and alcohol resin



FIGURE 3 | Rock specimen preparation.

solution under different forming pressures. Quartz sand was used as the aggregate, iron powder and barite powder were used to improve the bulk density of materials, and resin and gypsum were used as the cementing agent and regulator, respectively. The material was weighed with a high-precision electronic balance, fully mixed, loaded into the mold, loaded to the design forming pressure at a speed of 50 N/s on the universal testing machine, and stabilized for 5 min. Finally, according to the standard for test methods of engineering rock mass (GBT 50266-2013), a cylindrical standard specimen with a height of 100 mm and a diameter of 50 mm is made (Figure 3). Table 1 shows the mechanical parameters of rock specimens and on-site sandstone.

In order to verify the accuracy of DIC system test results, S1 rock specimen was taken as an example, two groups of FBG sensors were pasted to the axial center line of the specimen, the position of the installation area was adjusted, and an appropriate amount of glue was applied along the axial direction of the FBG (Figure 4). In order to avoid large light loss of optical fiber at both ends of the specimen, about 1 cm should be reserved for the optical fiber at both ends of the specimen. After the FBG sensor was pasted, the surface of the specimen was sprayed with white primer. After the primer was dry, black speckles were made.

The size of speckles in this test is 0.24–0.4 mm, and the speckle density is 50%. Before the uniaxial compression test, the fabricated specimen should be placed in the center of the pressure plate of the testing machine, and the bending and breaking of the FBG should be avoided during the placement process. The height of the tripod was adjusted so that the height of the camera is consistent with that of the specimen. The included angle and aperture of the camera was adjusted to make the specimen clear in the picture, and the focal lengths of the two cameras were made as consistent as possible. After the adjustment was completed, the test

system was connected. At the beginning of the measurement, in order to ensure the synchronization of data acquisition of MTS, DIC, and FBG systems, the data acquisition frequency was set to 2 Hz.

The end face flatness of the specimen should be checked before the uniaxial compression test, which means the two end surfaces of the specimen should be polished with 0# sandpaper to ensure the flatness of the specimen conforms to the rock mechanics test specifications. Afterward, both the end surfaces are smeared with Vaseline to reduce the friction between the specimen and the loading head. Finally, the test chooses the displacement control principle with a loading speed of 1 mm/min.

FAILURE CHARACTERISTICS OF ROCK SPECIMEN

Comparative Analysis of Digital Image Correlation and Fiber Bragg Grating Measurement

The strain results of DIC 1 and DIC 2 in Figure 5 were extracted by DIC measurement data dealing with the least square regression method (LSR). The detailed operation is that the LSR method is used to obtain the strain distribution through the differential approximation function based on the local displacement region of the specimen. Assuming that the strain is uniform in the local area, the displacement can be expressed as a plane area, so that Eq. 1 can be obtained according to the LSR method.

$$\begin{aligned} u_x &= a_x x + b_x y + c_x \\ u_y &= a_y x + b_y y + c_y \end{aligned} \quad (5)$$

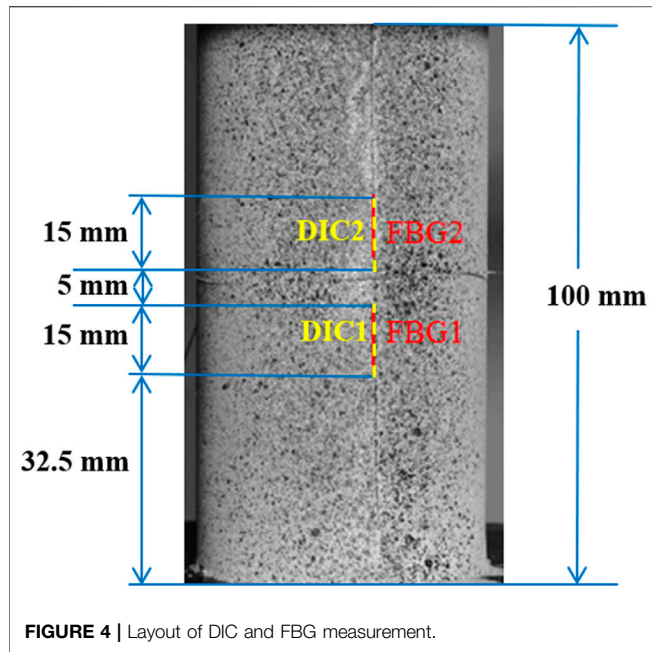
Furthermore, the local strain can be calculated by differentiating Eq. 1

$$\begin{aligned} \varepsilon_x &= \frac{\partial u_x}{\partial x} = a_x \\ \varepsilon_y &= \frac{\partial u_y}{\partial y} = b_y \\ \gamma_{xy} &= \frac{\partial u_y}{\partial x} + \frac{\partial u_x}{\partial y} = a_y + b_x \end{aligned} \quad (6)$$

where u is the displacement; ε and γ are the strains; x , y , and z are the positions; and a , b , and c are the coefficients of spline function. By repeating the aforementioned process for the displacement of the observed area, the strain distribution of the whole field can be

TABLE 1 | Proportion and mechanical parameters of the specimen.

Number	Iron powder/%	Resin/%	Gypsum/%	Pressure/MPa	Density/g × cm ³	σ_c /MPa	E/GPa	Poisson's ratio
S1	20	25	8	6.0	2.07	2.63	3.06	0.17
S2	35	25	6	4.0	2.18	2.31	2.87	0.15
S3	30	20	8	2.0	2.04	2.14	6.26	0.19
On-site sandstone					2.32	27.5	35.31	0.21

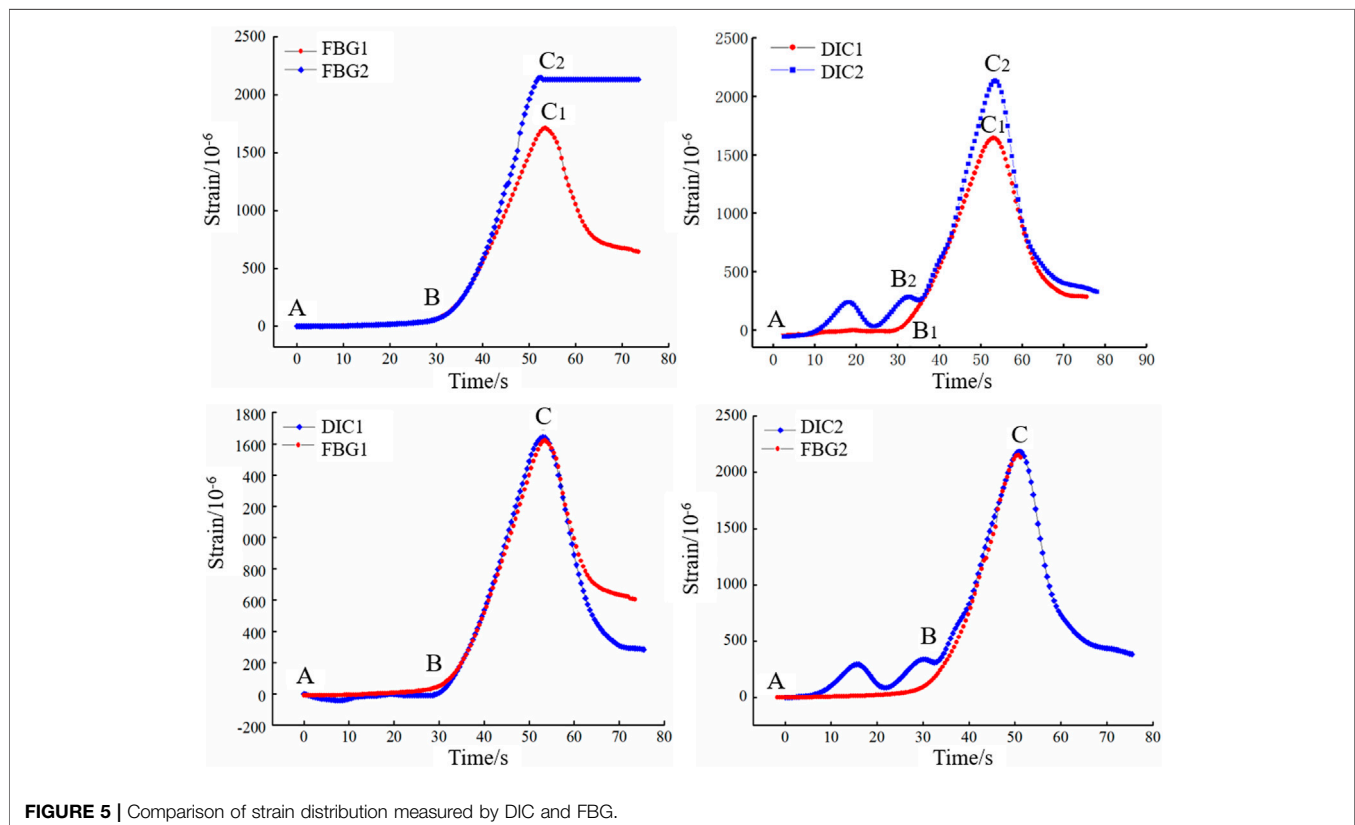


obtained. When the strain calculation window gets larger, the obtained strain data will be smoother.

Two measuring lines DIC1 and DIC2 were set exactly the same as the FBG sensor in the DIC system (Figure 5), and the axial

strain of the specimen measured by the FBG sensor and the DIC system was compared and analyzed.

As shown in Figure 4, in order to facilitate the analysis, the curve is divided into three sections: A, B, and C. In AB section, the strain data of FBG1 and FBG2 are smooth and consistent; the strain value of DIC1 fluctuates slightly, but the trend is consistent with that of FBG1. The large fluctuation of DIC2 data is mainly due to the small strain at the initial stage of specimen loading and the influence of noise on the DIC system. From point B, the strain of FBG1 and FBG2 increases rapidly with time and increases approximately linearly. It reaches the peak strain at point C. The strain measured by FBG2 is significantly greater than that of FBG1. This difference is mainly caused by the uncoordinated deformation of the specimen during uniaxial compression. At this stage, the strain curves of DIC1 and DIC2 are very close to those of FBG1 and FBG2, and the peak strains measured by DIC1 and FBG1 are 1712 $\mu\epsilon$ and 1644 $\mu\epsilon$, respectively. The relative deviation is 3.9%, and the peak strains measured by DIC2 and FBG2 are 2190 $\mu\epsilon$ and 2152 $\mu\epsilon$, respectively. The relative deviation was 1.7%. The trend of strain data measured by the DIC system is consistent with the FBG sensor, and the deviation of peak strain is less than 4%, which proves that DIC has high measurement accuracy and good stability. At the same time, compared with the FBG sensor, the DIC system has the advantages of non-contact and simple operation. Therefore, the DIC measurement results are verified and proved to be feasible to analyze the energy evolution of the rock specimen under the uniaxial compression test.



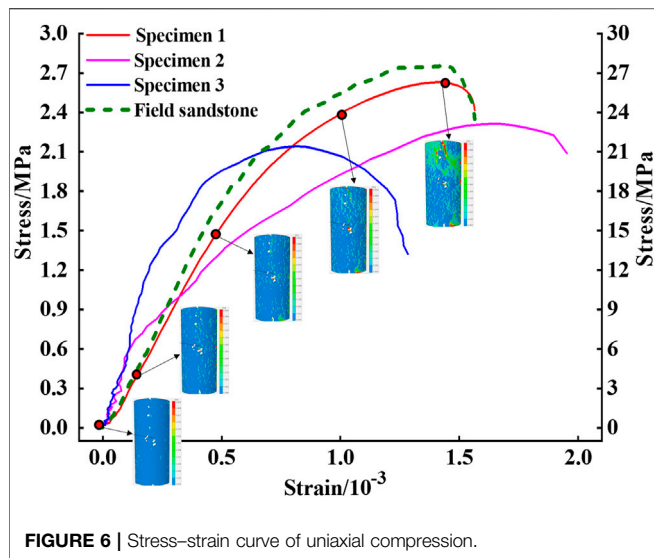


FIGURE 6 | Stress-strain curve of uniaxial compression.

Stress-Strain Analysis of Uniaxial Compression Test

The typical stress-strain curve of specimen S1–S3 and the actual state of specimen at points O, A, B, C, and D during deformation and failure are illustrated in **Figure 6**.

The original open cracks and micropores in the OA section specimen gradually close with the increase of stress, forming an early non-linear deformation stage, and the curve is concave as a whole. The specimen of the AC section changes from elastic deformation to elastic-plastic stage, where the specimen has an elastic deformation stage after compaction. After point B, the microcracks in the specimen begin to sprout and develop stably. The unstable microcracks in the specimen of the CD section develop rapidly after point C, and gradually form open cracks visible to the naked eye. After point D, the specimen is damaged and the stress decreases gradually.

The uniaxial compressive strength of specimens S1, S2, and S3 is about 2 MPa. The stress increases gradually with the increase of strain. After reaching the peak value, the stress decreases rapidly. It has obvious brittleness characteristics and is similar to field sandstone, indicating that the prepared rock material has good mechanic performance, which can be analyzed further.

Deformation Process Analysis

Five key points O, A, B, C, and D in the S1 stress-strain curve of the specimen are selected to analyze the displacement and strain evolution process of the specimen in the process of uniaxial compression. According to the radial displacement evolution process of specimen S1 in **Table 2**, in the compaction section OA, the radial displacement of the specimen as a whole is evenly distributed, and the specimen is uniformly deformed. With the increase of load, at point B, the upper end of the specimen moves left and right inconsistently, showing a trend of small left and large right. The specimen of the BC section enters the non-linear deformation stage. When it reaches point C, the upper end of the specimen moves left and right inconsistently, showing a trend of

accelerated development. With the further increase of load, the radial displacement of the specimen in the CD section continues to increase. At point D, there is a significant difference between the left and right displacement of the upper end face of the specimen. There is a large displacement difference between the blue-green junction and the red-green junction, and there are two obvious displacement mutation bands (DMB). Compared with the actual photos of the specimen, it can be found that the position of the displacement sudden change zone is the same as that of the macrocrack in the final failure of the specimen. Therefore, the evolution diagram of radial displacement can clearly reflect that the specimen begins to have non-uniform deformation in the radial direction from point B. Two obvious abrupt bands of radial displacement show that the upper end of the specimen is obviously subjected to tension, which leads to macrocracks and final failure.

According to the evolution process of S1 axial displacement in **Table 2**, the axial displacement field of the specimen in the OA section is evenly distributed, the specimen in the AB section gradually enters the linear elastic stage, and the axial displacement field increases uniformly. In the displacement field of point B, there is an uneven phenomenon that the axial displacement on the right side of the specimen is greater than that on the left side, entering the non-linear deformation stage. The axial displacement of the BC section specimen continues to increase, showing the phenomenon of small at the lower left and large at the upper right. The deformation of the specimen in the CD section accelerates, and the upper end of the specimen moves to D, showing a zoning phenomenon of small on the left and large on the right. The shear action of the specimen decreases gradually from top to bottom and from right to left.

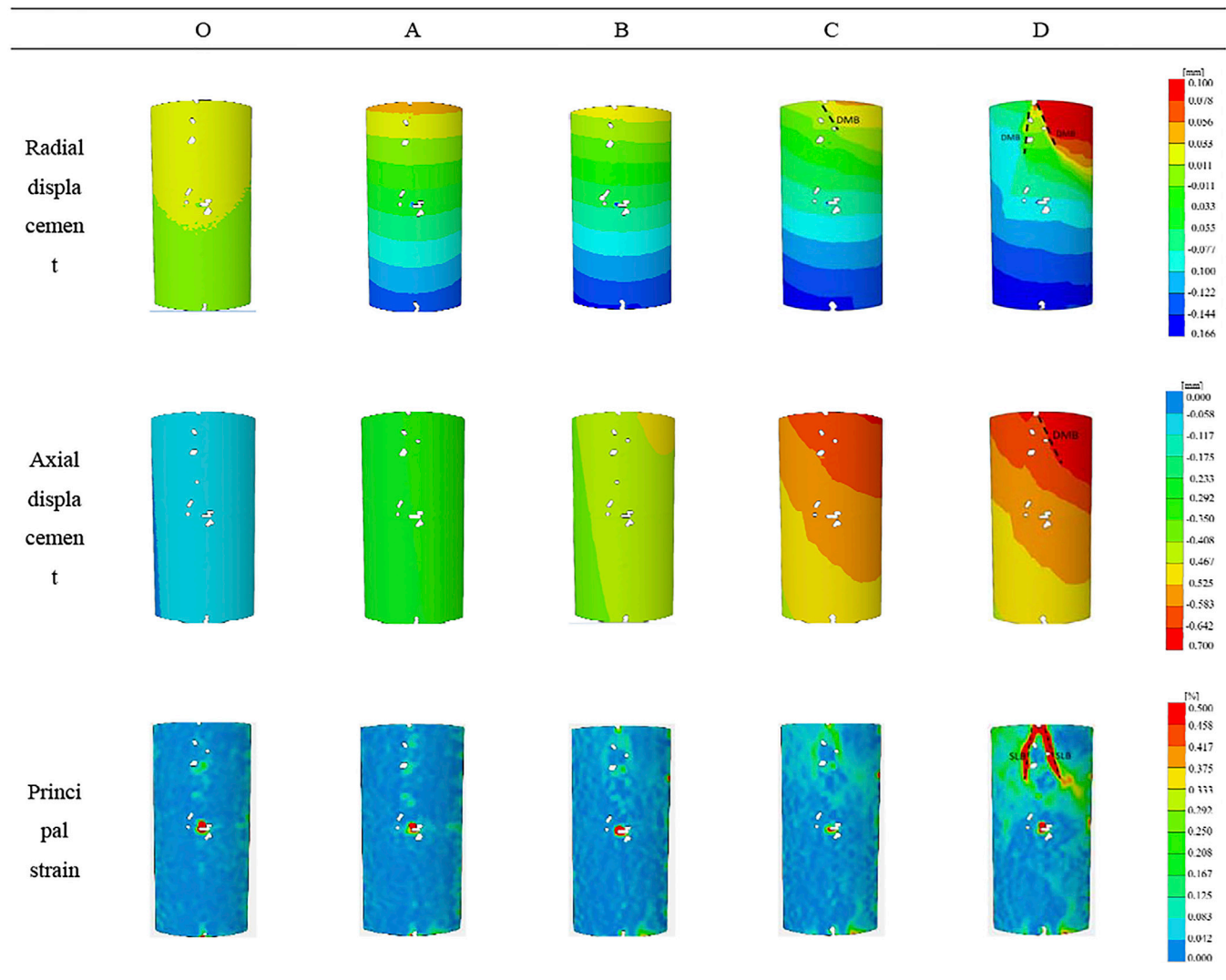
Therefore, the axial displacement evolution diagram can clearly reflect that the axial displacement at the right end of the specimen is large, and shear cracks are generated along the junction of the red and orange areas, which is consistent with the development of S1 crack of the specimen. The crack development of the specimen can be predicted by the evolution of the axial displacement field.

Based on the evolution process of S1 principal strain in **Table 2**, small strain localization band (SLB) appears on the surface of the specimen in OA and AB sections, and the SLB are relatively dispersed. In the BC section, each SLB is gradually connected to form a larger band. At point D, two obvious SLBs have been formed in the upper part of the specimen. The deformation of the CD section specimen and the SLB accelerates. Two SLBs are formed at the upper end of the specimen, which gradually become wider and longer, and the SLB at the other positions are gradually connected into a network and staggered distribution. At point D, two obvious SLBs have been formed, and the strain concentration of the right SLB at the upper end is greater than that of the left.

ANALYSIS OF ENERGY EVOLUTION CHARACTERISTICS

Analysis Method of Releasable Elastic Strain Energy

Uniaxial compression deformation of specimens is a process of strain accumulation and release failure accompanied by energy evolution. Based on the analysis of the energy evolution theory,

TABLE 2 | Displacement and strain development of rock specimen S1.

the full field strain and displacement data are obtained by DIC technology, and the failure of the specimen is explored from the perspective of energy. There is a clear SLB in the deformation process of the specimen.

According to the position of SLB, the study area of specimen S1–S3 is divided, and the medium in this area basically remains in an elastic state (Pan et al., 2002). The primary and secondary strain values of each area of the specimen are extracted, and the evolution process of the elastic strain energy that can be released from the surface area during the deformation of the specimen is calculated from Eq. 7 (Song et al., 2012).

$$U_e = \frac{E}{2} (\varepsilon_1^2 + \varepsilon_2^2 - 2\nu\varepsilon_1\varepsilon_2) \quad (7)$$

$$\varepsilon_{ij} = \varepsilon_{Eij} + \varepsilon_{Iij} = \varepsilon_{Eij} + \varepsilon_{edij} + \varepsilon_{idij} + \varepsilon_{pij}$$

where U_e is the releasable elastic strain energy; E and ν are the elasticity modulus and Poisson ratio, respectively; and ε_1 and ε_2 are the main strains of the rock specimen.

Analysis of Elastic Strain Energy Evolution

Elastic Strain Energy Evolution of S1 Specimen

The principle of elastic area dividing is based on the development of SLB during loading. The elastic area is determined by the SLB of the specimen. The strain in the SLB has the largest strain distribution, and will first enter into plastic deformation, that is, the deformation in this region is much larger than other positions of the specimen. Therefore, the elastic region can be divided by marking the place outside the strain localization zone.

As a result, the energy analysis area is divided according to the position of SLB during loading, and the specimen S1 is divided into three elastic areas (Figure 7). The average principal strain values in two directions of each area during loading are extracted, and the elastic strain energy of each area is calculated. Specimen S1 is taken as an example, and the same five key points O, A, B, C, and D on the stress–strain curve are selected for analysis (Figure 8) also

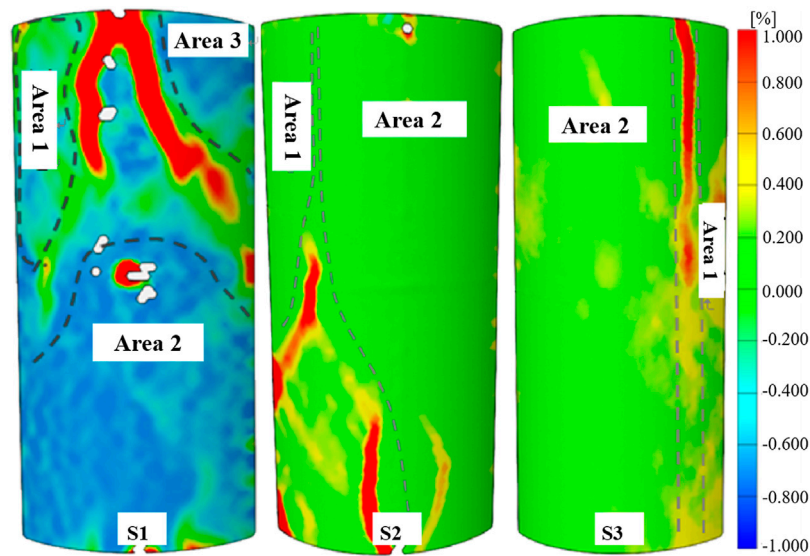


FIGURE 7 | Region division of rock specimen.

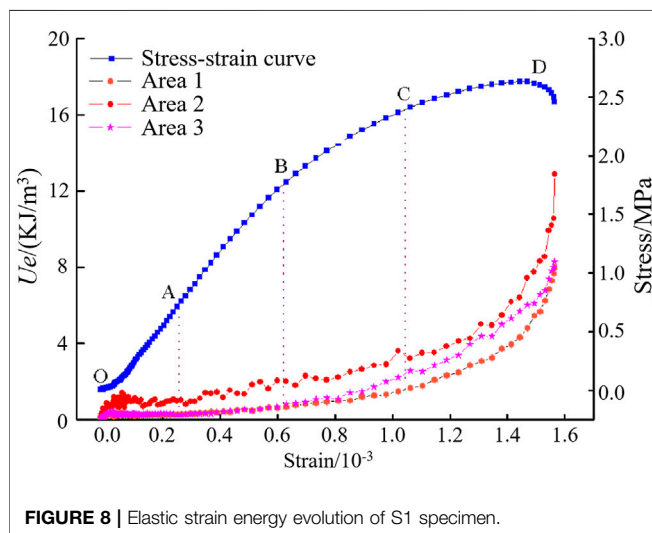


FIGURE 8 | Elastic strain energy evolution of S1 specimen.

the elastic strain energy density in different specimen region are shown in **Table 3**.

In the OA section, the micropore and crack gradually compacted section, with a maximum axial stress of $0.21\sigma_c$. The main strain in the three regions is small, most of the input energy is dissipated, and the elastic strain energy accumulation gets to be stable. The elastic strain energy densities in regions 1–3 are 0.278, 1.012, and 0.253 kJ/m^3 , respectively.

In the AB section, the linear elastic deformation section, the maximum axial stress is $0.65\sigma_c$. The main strain on the surface of the specimen is sporadically distributed, and most of the input energy is transformed into elastic strain energy. The elastic strain energy in three regions increases steadily, and the elastic strain energy densities in regions 1–3 are 0.670, 1.996, and 0.630 kJ/m^3 , respectively.

TABLE 3 | Elastic strain energy density in different specimen regions (kJ/m^3).

Specimen	Area	A	B	C	D
S1	1	0.278	0.670	1.655	7.982
	2	1.012	1.996	3.227	12.873
	3	0.253	0.813	2.559	8.284
S2	1	0.402	0.551	1.040	1.897
	2	0.846	1.227	2.214	5.205
S3	1	2.487	3.180	5.311	8.663
	2	1.298	1.660	3.199	5.436

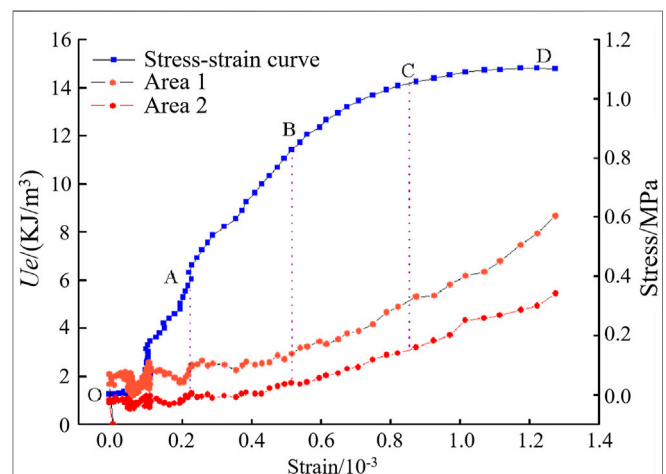


FIGURE 9 | Elastic strain energy evolution of S2 specimen.

In the BC section, the elastoplastic deformation section, the maximum axial stress is $0.93\sigma_c$. The main strain concentration areas on the specimen surface are connected with each other, the SLB becomes clear from fuzzy, the elastic strain energy continues

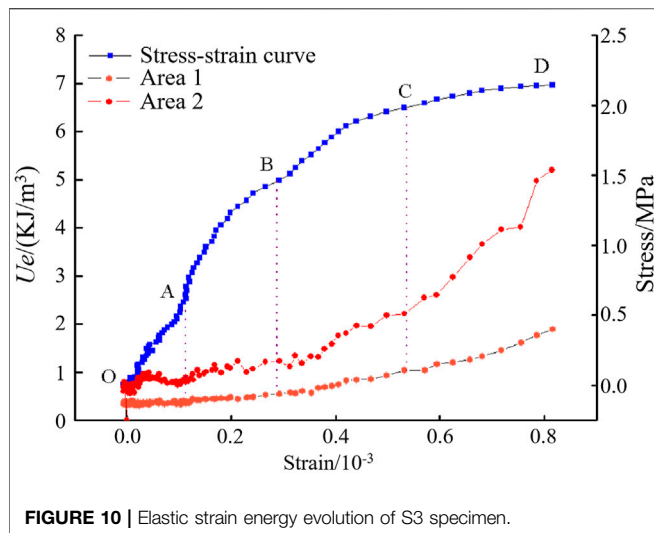


FIGURE 10 | Elastic strain energy evolution of S3 specimen.

to increase, the elastic strain energy at local positions reaches the surface energy, the elastic strain energy is released, and the strain concentration phenomenon occurs. The elastic strain energy densities in areas 1–3 are 1.655, 3.227, and 1.062 kJ/m³, respectively.

In the CD section, in the plastic deformation stage, the axial stress reaches the peak, the main strain concentration becomes higher and higher, and the SLB is staggered. With the continuous input of energy, the elastic strain energy in the three regions accelerates to accumulate, the number of unit rock mass at the localization band that reaches the surface energy is more and more, the damage evolution of the specimen is accelerated, and the damage is more and more serious. The elastic strain energy densities in areas 1–3 are 7.982, 12.873, and 8.284 kJ/m³, respectively. It is found that in the same stage, there is a certain difference in the strain concentration and elastic strain energy accumulation in regions 1–3, which is mainly caused by the uneven deformation in the process of uniaxial compression deformation.

Through the aforementioned analysis, the evolution process of strain energy in the elastic region before the load reaches the peak is divided into three stages:

- 1) OA section can release elastic strain energy in a stable stage. At this stage, most of the energy input by the specimen is dissipated, the releasable elastic strain energy absorbed in the unit rock mass is less, and the releasable strain energy is in a stable state.
- 2) AC section can release the linear growth stage of elastic strain energy. With the continuous increase of load, the elastic strain energy of unit rock mass is in the stable growth stage, and the releasable strain energy in the specimen continues to grow. The elastic strain energy of some unit rock mass reaches the surface energy, and the elastic strain energy is released, resulting in strain concentration, but the concentration degree is small, and the specimen is damaged.
- 3) CD section can release elastic strain energy and accelerate the growth stage. With the continuous input of energy, the

releasable strain energy of unit rock mass continues to accumulate, the number of unit rock mass reaching the surface energy is more and more, the damage evolution of the specimen is accelerated, and the damage is more and more serious. When the maximum load point D is reached, the number of releasable strain energy of single rock mass in the strain concentration area of unit rock mass in areas 1–3 increases sharply, and the elastic strain energy release shows an obvious SLB.

Elastic Strain Energy Evolution of S2 and S3 Specimen

The strain data extracted based on DIC technology and the theory of releasable strain energy can better describe the damage process of the specimen. Next, the evolution process of releasable strain energy during uniaxial compression of S2 and S3 is briefly analyzed by using the analysis method of S1. The division of the area outside the SLB of S2 and S3 at the peak stress is shown in Table 2.

Before reaching the peak load, the evolution trend of the releasable elastic strain energy in each region of S2 and S3 is similar to that of S1 (Figures 9, 10). The evolution process of the releasable elastic strain energy in each region of S2 and S3 can also be divided into three stages: stable stage OA, linear growth stage AC, and accelerated growth stage CD.

In the stable stage of releasable elastic strain energy OA, the S2 and S3 are in the compaction stage as a whole, the defects are gradually compacted, most of the input energy is dissipated, and only a small part is stored in a very small amount of unit rock mass as releasable strain energy. The overall stored energy of this stage is low, and the releasable elastic strain energy in each area is less than 2 kJ/m³.

In the AC section of the linear growth stage of the releasable strain energy, S2 and S3 gradually enter the elastic deformation stage. Most of the input energy is transformed into releasable elasticity energy that stored in the unit rock mass, and its energy value is less than which of the surface energy, which has little impact on the apparent strain, and the damage of the is small and occurs in the interior of the.

In the accelerated growth stage of releasable strain energy CD, S2 and S3 transition to elastic–plastic deformation, and the input energy continues to be transformed into releasable elastic strain energy. At this time, the releasable elastic strain energy in unit rock mass accumulates more, the releasable strain energy of some unit rock mass reaches surface energy, the damage evolves from interior to surface, and there is an obvious SLB on the surface.

Based on the global strain data obtained by DIC, the damage evolution process of specimens S1, S2, and S3 is analyzed to describe the damage process from the perspective of energy. Before reaching the peak load, the evolution process of releasable elastic strain energy can be divided into three stages: stable stage, linear growth stage, and accelerated growth stage.

CONCLUSION

- 1) The axial strain of the sandstone rock specimen measured by the FBG sensor and DIC system is compared. The strain–time

curves of specimens measured by DIC and FBG sensors are consistent, and the relative deviation of peak strain is less than 5%, which verifies the accuracy and applicability of the DIC system.

- 2) The non-conforming deformation evolution process of radial and axial displacement fields during uniaxial compression of S1 is analyzed. It shows that the evolution analysis of the displacement field can predict the development of crack and deformation failure form of S1.
- 3) The evolution of radial displacement shows that the specimen begins to have non-uniform deformation from point B. Two obvious abrupt bands of radial displacement show that the upper end of the specimen is obviously subjected to tension, which leads to macrocracks and final failure.
- 4) Based on DIC full field test and rock energy theory, the energy evolution process of the elastic region in the process of uniaxial compression is revealed. From the perspective of elastic strain energy density evolution, there are three stages: elastic strain energy stability stage, elastic strain energy linear growth stage, and elastic strain energy accelerated growth stage. It corresponds to the compaction stage, elastic-plastic deformation stage, and unstable fracture stage of the specimen.

REFERENCES

- Berthaud, Y., Torrenti, J. M., and Fond, C. (1997). Analysis of Localization in Brittle Materials through Optical Techniques. *Exp. Mech.* 37 (2), 216–220. doi:10.1007/bf02317862
- Chen, Y., Sun, S., and Ji, C. (2017). Development and Application of 3D Digital Image Correlation (3D DIC) in Deformation Measurement of Materials. *J. Aeronaut. Mater.* 37 (4), 90–100.
- Council, C. E. (2013). *Standard for Test Methods of Engineering Rock Mass*. GBT 50266-2013.
- Feng, P., Xu, Y., and Dai, F. (2021). Effects of Dynamic Strain Rate on the Energy Dissipation and Fragment Characteristics of Cross-Fissured Rocks. *Int. J. Rock Mech. Mining Sci.* 138, 104600. doi:10.1016/j.ijrmms.2020.104600
- Feng, P., Zhao, J., Dai, F., Wei, M., and Liu, B. (2021). Mechanical Behaviors of Conjugate-Flawed Rocks Subjected to Coupled Static-Dynamic Compression. *Acta Geotech.* doi:10.1007/s11440-021-01322-6
- Gong, F., Song, L., Li, X., and Yan, J. (2018). Linear Energy Storage and Dissipation Rule of Red sandstone Materials during the Tensile Failure Process. *Chin. J. Rock Mech. Eng.* 237 (02), 352–363.
- Huang, F., Wu, C., Jang, B., Hong, Y., Guo, N., and Guo, W. (2020). Instability Mechanism of Shallow Tunnel in Soft Rock Subjected to Surcharge Loads. *Tunnelling Underground Space Tech.* 99 (103350), 1–12. doi:10.1016/j.tust.2020.103350
- Huang, J., Chen, G., Zhao, Y., and Wang, R. (1990). An Experimental Study of the Strain Field Development Prior to Failure of a marble Plate under Compression. *Tectonophysics* 175 (1–3), 269–284.
- Jiang, D., Xie, K., Jiang, X., Chen, J., and Yuan, Xi. (2016). Statistical Analysis of Acoustic Emission Energy Distribution during Uniaxial Compression of Shale. *Chin. J. Rock Mech. Eng.* S2, 3822–3828.
- Jing, C., Yuan, Q., Wang, S., Yi, L., and Zhang, L. (2015). Detection and Representation of Mining-Induced Three Horizontal Zones Based on Fiber Bragg Grating Sensing Technology. *J. China Univ. Mining Tech.* 44 (6), 971–976.
- Jing, C., Yuan, Q., Yi, L., Zhang, D., and Qi, L. (2016). Experimental Study on Overlying Strata Deformation Based on Distributed Optical Fiber Sensing. *Chin. J. Rock Mech. Eng.* S2, 3589–3596.

DATA AVAILABILITY STATEMENT

The original contributions presented in the study are included in the article/Supplementary Material, further inquiries can be directed to the corresponding authors.

AUTHOR CONTRIBUTIONS

LW wrote the first draft of the manuscript. QY and YR wrote sections of the manuscript. QY and DJ contributed to conception and design of the study. YL and DZ organized the database. YZ and SR performed the statistical analysis. All authors contributed to manuscript revision, read, and approved the submitted version.

FUNDING

This work was funded by the National Natural Science Foundation of China, grant number 51804052, 51804244 and 51834003; the Natural Science Foundation of Chongqing, China, grant number CSTC2019JCYJ-BSH0088; and the Special Key Project of Chongqing Technology Innovation and Application Development, grant number cstc2019jscx-tjsbX0015.

- Li, Y., Leith, K., Perras, M. A., and Löw, S. (2021). Digital Image Correlation-Based Analysis of Hygroscopic Expansion in Hernholz Granite. *Int. J. Rock Mech. Mining Sci.* 146, 1–14. doi:10.1016/j.ijrmms.2021.104859
- Liu, Z., Wang, W., Luo, J., and Guanghong, M. (2020). Method of Energy Evolution of Rock under Uniaxial Compression Test. *J. China Coal Soc.* 45 (9), 3131–3139.
- Ma, S., Liu, S., and Zhao, Y. (2006). Gray Correlation of Digital Images from Loaded Rock Specimen Surface to Evaluate its Damage Evolution. *Chin. J. Rock Mech. Eng.* 3, 590–595.
- Miao, S., Liu, Z., Zhao, X., and Huang, Z. (2021). Energy Dissipation and Damage Characteristics of Beishan Granite under Cyclic Loading and Unloading. *Chin. J. Rock Mech. Eng.* 40 (5), 928–938.
- Mikhalyuk, A. V., and Zakharov, V. V. (1997). Dissipation of Dynamic-Loading Energy in Quasi-Elastic Deformation Processes in Rocks. *J. Appl. Mech. Tech. Phys.* 38 (2), 312–318. doi:10.1007/bf02467918
- Okubo, S., Tang, Y., Jiang, X., Peng, S., Chen, C., and Yan, Z. (2019). Application of 3D-DIC System in Rock Mechanic Test. *Rock Soil Mech.* 40 (8), 3263–3273.
- Pan, B., Xie, H., Xu, B., and Dai, F. (2006). Performance of Sub-pixel Registration Algorithms in Digital Image Correlation. *Meas. Sci. Tech.* 17 (6), 1615.
- Pan, Y., Yang, X., Ma, S., and Xu, B. (2002). Experimental Study on Deformation Localization of Geotechnical Materials. *J. China Coal Soc.* 3, 281–284.
- Ren, J., Ge, X., Pu, Y., Ma, W., and Zhu, Y. (2000). Preliminary CT Real-Time Analysis of Rock Unloading Damage Evolution Mechanism. *Chin. J. Rock Mech. Eng.* 6, 697–701.
- Ren, J., and Ge, X. (2001). Study on Meso Mechanism and Constitutive Model of Rock Damage Evolution under Uniaxial Compression. *Chin. J. Rock Mech. Eng.* 4, 425–431.
- Schmidt-Hattenberger, C., Naumann, M., and Borm, G. (2003). Fiber Bragg Grating Strain Measurements in Comparison with Additional Techniques for Rock Mechanical Testing. *IEEE Sensors J.* 3 (1), 50–55. doi:10.1109/jsen.2003.809025
- Song, D., Wang, E., Li, Z., Liu, J., and Xu, W. (2015). Energy Dissipation of Coal and Rock during Damage and Failure Process Based on EMR. *Int. J. Mining Sci. Tech.* 25 (5), 787–795. doi:10.1016/j.ijmst.2015.07.014
- Song, Y., Jiang, Y., Ma, S., Yang, X., and Zhao, T. (2012). Evolution of Deformation fields and Energy in Whole Process of Rock Failure. *Rock Soil Mech.* 33 (5), 1352–1365.

- Steffler, E. D., Epstein, J. S., and Conley, E. G. (2003). Energy Partitioning for a Crack under Remote Shear and Compression. *Int. J. fracture* 120 (4), 563–580. doi:10.1023/a:1025511703698
- Sujatha, V., and Kishen, J. M. C. (2003). Energy Release Rate Due to Friction at Bimaterial Interface in Dams. *J. Eng. Mech.* 129 (7), 793–800. doi:10.1061/(asce)0733-9399(2003)129:7(793)
- Wang, G., Wen, X., and Zhang, L. (2020). Dip Effect of Energy Evolution Mechanism of Jointed sandstone under Uniaxial Compression. *J. Cent. South Univ. (Science Technology)* 51 (7), 1913–1923.
- Wang, X., Hou, w., Pan, Y., and Dong, W. (2018). Experiments of Strain Localization Processes of Coal Specimens in Uniaxial Compression Based on the Digital Image Correlation Method. *J. China Coal Soc.* 43 (4), 984–992.
- Xi, X., Wu, X., Guo, Q., and Cai, M. (2020). Experimental Investigation and Numerical Simulation on the Crack Initiation and Propagation of Rock with Pre-existing Cracks. *IEEE Access* 8, 636–644. doi:10.1109/access.2020.3009230
- Xie, H., Peng, R., Yang, J., and Zhou, H. (2005). On Energy Analysis of Rock Failure. *Chin. J. Rock Mech. Eng.* 24 (15), 2603–2608.
- Xie, H., Li, L., Peng, R., and Ju, Y. (2009). Energy Analysis and Criteria for Structural Failure of Rocks. *J. Rock Mech. Geotechnical Eng.* 1 (1), 11–20. doi:10.3724/sp.j.1235.2009.00011
- Yang, Y. W., Bhalla, S., Wang, C., Soh, C. K., and Zhao, J. (2007). Monitoring of Rocks Using Smart Sensors. *Tunnelling Underground Space Tech.* 22 (2), 206–221. doi:10.1016/j.tust.2006.04.004
- Yoneyama, S. (2016). Basic Principle of Digital Image Correlation for In-Plane Displacement and Strain Measurement. *Adv. Compos. Mater.* 25 (2), 105–123. doi:10.1080/09243046.2015.1129681
- Zhang, Z., and Gao, F. (2012). Experimental Research on Energy Evolution of Red sandstone Samples under Uniaxial Compression. *Chin. J. Rock Mech. Eng.* 31 (5), 953–962.
- Zhang, Z., and Gao, F. (2012). Research on Nonlinear Characteristics of Rock Energy Evolution under Uniaxial Compression. *Chin. J. Rock Mech. Eng.* 31 (6), 1198–1207.
- Zhao, G.-y., Dai, B., Dong, L.-j., and Yang, C. (2015). Energy Conversion of Rocks in Process of Unloading Confining Pressure under Different Unloading Paths. *Trans. Nonferrous Met. Soc. China* 25 (5), 1626–1632. doi:10.1016/s1003-6326(15)63767-0

Conflict of Interest: The authors declare that the research was conducted in the absence of any commercial or financial relationships that could be construed as a potential conflict of interest.

Publisher's Note: All claims expressed in this article are solely those of the authors and do not necessarily represent those of their affiliated organizations, or those of the publisher, the editors, and the reviewers. Any product that may be evaluated in this article, or claim that may be made by its manufacturer, is not guaranteed or endorsed by the publisher.

Copyright © 2022 Wei, Yuan, Ren, Jiang, Zhang, Liu, Zou and Ren. This is an open-access article distributed under the terms of the Creative Commons Attribution License (CC BY). The use, distribution or reproduction in other forums is permitted, provided the original author(s) and the copyright owner(s) are credited and that the original publication in this journal is cited, in accordance with accepted academic practice. No use, distribution or reproduction is permitted which does not comply with these terms.



Coordinated slag Disposal From Horizontal Boreholes During Hydraulic Cutting Based on Two-Phase Flow Theory

Yongjiang Zhang^{1,2}, Fei Ji^{2*} and Quanle Zou^{3*}

¹State Key Laboratory of Mining-Induced Response and Disaster Prevention and Control in Deep Coal Mines, Anhui University of Science and Technology, Huainan, China, ²China Coal Technology and Engineering Group Chongqing Research Institute, Chongqing, China, ³State Key Laboratory of Coal Mine Disaster Dynamics and Control, School of Resources and Safety Engineering, Chongqing University, Chongqing, China

OPEN ACCESS

Edited by:

Qingsheng Bai,
Freiburg University of Mining and
Technology, Germany

Reviewed by:

Mingming He,
Xi'an University of Technology, China
Huafu Qiu,
Xi'an University of Science and
Technology, China
Huabin Zhang,
Liaoning Technical University, China

*Correspondence:

Fei Ji
872423807@qq.com
Quanle Zou
quanlezou2011@126.com

Specialty section:

This article was submitted to
Geohazards and Georisks,
a section of the journal
Frontiers in Earth Science

Received: 18 November 2021

Accepted: 21 March 2022

Published: 14 April 2022

Citation:

Zhang Y, Ji F and Zou Q (2022)
Coordinated slag Disposal From
Horizontal Boreholes During Hydraulic
Cutting Based on Two-Phase
Flow Theory.
Front. Earth Sci. 10:817531.
doi: 10.3389/feart.2022.817531

The purpose of the study is to explore the mechanism of coordinated slag disposal in the hydraulic cutting process, ensure the safety implementation of the hydraulic cutting operation and increase the success rate of hydraulic cutting. In the ultra-high pressure hydraulic cutting technique, the method for determining the cutting pressure is ambiguous, the coordination mechanism of various factors (including cutting pressure and coal-dropping speed) lingers unclarified; the slag disposal mechanism during hydraulic cutting is inexplicit. Aiming at these problems, a model for coordinated slag disposal during hydraulic cutting based on coal-water two-phase flow was established. The critical flow velocity in the moving laminar flow regime is taken as that during the coordinated slag disposal from boreholes. The relationship curve between the coal-dropping speed and cutting pressure under different Protodyakonov coefficients of coal seams was obtained. Hence, the model for coordinated slag disposal during hydraulic cutting was established; the selection interval of reasonable pressure for coordinated slag disposal during hydraulic cutting was determined. The reasonable cutting pressure for slag disposal in coal seams with a Protodyakonov coefficient of 0.48 was determined as about 80 MPa. During the cutting test, the average net gas extraction from the boreholes for hydraulic cutting was 4.5 times larger than that from the conventional boreholes. Furthermore, the gas permeability coefficient of the boreholes for hydraulic cutting increased by 25 times; the effective extraction radius was more than doubled. It indicated that the model for reasonably selecting the cutting pressure based on the coordinated slag disposal theory can effectively guide the selection of the cutting pressure on site. While solving various problems occurring in the hydraulic cutting process on site, the model can be used to improve the cutting effect, which provides a theoretical basis for reasonably selecting the pressure during ultra-high pressure hydraulic cutting.

Keywords: hydraulic cutting, cutting pressure, coordinated slag disposal, solid-liquid, two-phase flow

INTRODUCTION

Since 1950s, the average mining depth of coal mines in China has increased by years (Guo et al., 2020; Wang et al., 2021). Up to now, coal mines are still mined downwards at the rate of 8–12 m each year. Therefore, the safe and efficient mining of coal mines is particularly important (Zhang et al., 2019; Liang et al., 2022; Zhang et al., 2022). As deep coal seams in mines are extracted, the high gas and high geostress problems are gradually prominent (Zou et al., 2020; He et al., 2021a). Gas pre-drainage from horizontal boreholes in coal seams, as the most primary method for gas control at present, is widely applied (Hu et al., 2000; Cheng et al., 2009). However, the majority of coal seams in China belong to low-permeability ones, which leads to a poor effect of gas extraction and long time for reaching the extraction standard (Yi et al., 2021; Zhou et al., 2021). It greatly restricts the safe and efficient mining of mines (He et al., 2021b; Zou et al., 2022). Therefore, increasing the permeability of coal seams (Guo et al., 2021; Jia et al., 2021) becomes one of the most primary and effective means to improve the effect of gas extraction and shorten the time for reaching the extraction standard (Wang and Zhang, 2006; Zou et al., 2021).

In recent years, with the research and development of water jet technology, much more hydraulic measures have been applied in coal mines. The ultra-high pressure hydraulic cutting technique has been extensively used in various mine areas in China by virtue of its advantages such as high rated pressure, wide scope of application, simple operation, high safety and obvious local effect. Moreover, scholars all over the world have also explored the permeability-increase mechanism through pressure relief by hydraulic cutting. Yang et al. (2012) simulated the change laws of the stress field in coal seams, gas pressure field and gas extraction efficiency on hydraulic cutting conditions by utilizing Matlab software. The result showed that the stress on coal seams is effectively released after the hydraulic cutting, showing a significant pressure-relief effect; in addition, cracks in coal seams increase greatly in quantity to strengthen the permeability and the adsorbed gas can be effectively released. By simulating the stress release and stress damage in coal around the boreholes for hydraulic cutting, Zhao et al. (2020) analyzed the influences of the uniformity coefficient, Langmuir volume strain constant and overburden stress on damages in coal seams and gas drainage. By comparing the numerically simulated results with the field test data, it can be found that the damage zone in coal induced by the stress relief around the boreholes for hydraulic cutting gradually expands with the growth of the uniformity coefficient and overburden stress; the permeability of coal seams gradually grows with the increase of Langmuir volume strain constant and the reduction of the overburden stress. Shen et al. (2015) explored and analyzed the evolution equations for the effective stress and permeability coefficient as well as pressure-relief and permeability-increase mechanisms during water jet cutting. With the aid of FLAC three-dimensional (3D) percolation model, the evolutions of the effective stress on coal, growth rate of coal permeability and

pore pressure induced by fractures were calculated and analyzed. Additionally, the strengthening effect on permeability through hydraulic cutting and dynamic characteristics of gas drainage from boreholes were investigated through the field test. The results showed that the effective stress on coal obviously drops after the hydraulic cutting and the pressure-relief area around boreholes for hydraulic cutting is 4–7 times larger than that around conventional boreholes. Lin et al. (2015) proposed to prevent and control coal and gas outburst disasters during heading excavation by employing the hydraulic cutting technique. The application of the hydraulic cutting technique on coal can effectively enhance the permeability of coal seams, improve the effect of gas extraction and prevent and control coal and gas outburst disasters during the excavation. Through field tests, it can be found that after the hydraulic cutting, the average coal output from boreholes for hydraulic cutting is 8.2 t and the maximum coal output reaches 16 t. The diameter of boreholes subjected to hydraulic cutting is 12.87 times that of conventional boreholes, which effectively enlarges the impact area of boreholes. After the extraction for half a month, the average gas extraction concentrations from boreholes subjected to hydraulic cutting and conventional boreholes reach 26% and 7%, respectively; it implies that the average gas extraction concentration from boreholes subjected to hydraulic cutting is about 3.7 times larger than that of conventional boreholes.

Scholars in the world have also explored the slag disposal from boreholes. By establishing the models for slag disposal through normal drilling, open-type cave drilling and filled-type cave drilling, Wang et al. (2016) performed the gas-solid coupling dynamic analysis on migration of drilling cuttings in boreholes. The research result indicated that open-type cave drilling marginally affects the migration of drilling cuttings, which only causes a certain pressure loss; the filled-type cave drilling makes the mass fraction of drilling cuttings at the bottom of boreholes multiplies; the drilling cutting particles move along a zigzag path and therefore it takes a longer time to extract them. In the area experiencing the filled-type cave drilling, the instantaneous wave crest of dynamic pressure appears and the differential pressure loss is multiple times of that during the normal drilling and open-type cave drilling. On the basis of investigating the migration law of drilling cuttings during long helical drilling, Yang et al. (1994) proposed a new calculation method for the critical rotational speed and pointed out that the critical rotational speed varies along the radial direction of blades and changes with the feeding rate. Finally, the principle for determining the practical critical rotational speed and the actual rotational speed of drill pipes was discussed. Wei et al. (2017) analyzed the factors influencing the initiation of motion of drilling cuttings and migration law of drilling cuttings on normal drilling and termination of drilling conditions. They found that 1) the critical flow velocity for initiation of motion of drilling cuttings declines with the growth of the hydrate abundance and the value with consideration of hydrate cohesion is larger than that without considering hydrate

cohesion; moreover, the higher the hydrate abundance is, the more significant the influence of hydrate cohesion; 2) with the increase of the size of drilling cutting particles, the critical flow velocity for initiation of motion of drilling cuttings rises in the case that the hydrate abundance is lower than 85% while it drops after the hydrate abundance exceeds 85%; 3) the critical flow velocity for initiation of motion of drilling cuttings reduces with the elevation of the density and viscosity of drilling fluids; 4) the critical return-velocity required by saltation on same conditions is about 1.28 times that on rolling conditions.

In the hydraulic cutting process, coal is cut by high pressure water jets to form nonuniform coal particles, which are mixed with water to form solid-liquid two-phase mixed fluids under the thread effect of drill pipes and gravity effect of themselves. Therefore, it is feasible to analyze the slag disposal from boreholes for hydraulic cutting by utilizing the solid-liquid two-phase flow theory. Scholars all over the world have researched the solid-liquid two-phase flow theory. With the aid of fluent6.3 software, Liu and Zhu (2011) carried out the numerical simulation on the solid-liquid two-phase flow in the centrifugal sewage pump on different working conditions and particles sizes by using Eulerian hybrid model. Through simulation, the distribution law of solid particles in impeller flow passages was attained. The simulation result showed that the distribution law of solid particles in impeller flow passages is mainly related to the particle size. In addition, the particle volume fraction and operation conditions deliver influence on the distribution law of solid particles. The simulation result favorably explains the occurrence of wearing in pump flow passages when transmitting solid-liquid two-phase flow through pumps. Based on the standard model and SIMPLEC algorithm, Li *et al.* (Zhang et al., 2017) conducted the numerical simulation on the surface of micro-voids at different intake rates and further discussed the change laws of the turbulent kinetic energy, dynamic pressure and turbulence intensity in micro flow channels with the intake rate. Shogo Nagaoka *et al.* (Yamaguchi et al., 2011) proposed a method for measuring the solid-liquid two-phase flow based on measurement of electromagnetic signals. By comparing the visual results under three flow regimes (pseudo-homogeneous flow, inhomogeneous flow and inhomogeneous flow + sliding bed flow), the effectiveness of the method was validated. Pelin Ilker *et al.* (Ilker and Sorgun, 2020) conducted numerous computational fluid dynamics (CFD) simulations and test analysis on solid-liquid two-phase flows in wire-bore tubes, eccentric annulus and concentric annulus. The accuracy of the turbulence model is verified by test results and the data provided by Sorgun in 2010. The CFD simulation result well matches with the test results. The results showed that the RNG- ϵ model exhibits a favorable simulation result on the water flows in wide-bore tubes and eccentric annulus. For water flows in concentric annulus, the EARSM model is superior to the other turbulence models. Kramer et al. (2020) proposed a relation applicable for calculating the effective resistance to solid-liquid fluidization in actual devices based on the new insight into influences of the spatial and temporal heterogeneity on the effective fluid resistance of large-scale fluidized systems. Through CFD

simulation on the nonuniform distribution of solids, it is possible to increasingly accurately predict the inhomogeneous flow behaviors. However, it is not feasible to perform the computational-intensive simulation for the operation of many large-scale application programs. Therefore, the resistance relationship at full size is obviously needed to effectively consider the spatial distribution of heterogeneous and irregular particles. By measuring related friction coefficient, pressure loss and the transmission rate of particles, Han et al. (2020) suggested that the volume and concentration of particles are influenced by in-pipe flow. By exploring the conditions of homogeneous sand with 2 mm in concentric annulus with different inclinations with the ratio of the inner to outer pipe radius of 0.7, the test and numerical results of solid-liquid two-phase flow with fully developing non-Newtonian fluids in different carboxymethylcellulose (CMC) solutions were obtained. It was determined that both the transmission ratio and pressure loss are directly related to the drilling efficiency in the directional boreholes.

The slag disposal process is the most important during the hydraulic cutting in boreholes drilled along seams. However, researchers and scholars in the world have not clearly understood the selection of technological parameters for slag disposal through ultra-high pressure hydraulic cutting technique currently. Especially, selection of the cutting pressure in coal seams with different Protodyakonov coefficients and the coupling relationship between the cutting pressure and slag disposal with drill pipes during the hydraulic cutting have not been clearly understood. The cutting pressure is considered as one of the most important parameters of ultra-high pressure hydraulic cutting technique. Selecting an extremely low cutting pressure cannot break coal or reach the expected cutting depth; however, quite a high cutting pressure leads to too large instantaneous coal output and further triggers borehole outburst and borehole jamming to affect the normal construction, which induces gas exceeding the limit and even threatens workers' safety. The level of the cutting pressure not only influences the coal-dropping speed during the hydraulic cutting but also directly determines the water flow rate in boreholes, thus influencing the slag-disposal capacity from boreholes. Therefore, investigation on the selection of reasonable cutting pressure is significant for successful implementation of hydraulic cutting and improvement of the subsequent extraction effect.

MOTION CHARACTERISTICS OF COAL PARTICLES DURING HYDRAULIC CUTTING

Annular Solid-Liquid Two-Phase Flow Model

Whether coal cinders can be successfully discharged during the ultra-high pressure hydraulic cutting or not influences the cutting effect. The slag-disposal effect of hydraulic cutting is synergistically affected by various factors such as the hardness of coal seams, water jet pressure and flow rate. During the ultra-high pressure hydraulic cutting, coal is cut by high pressure water jets into nonuniform

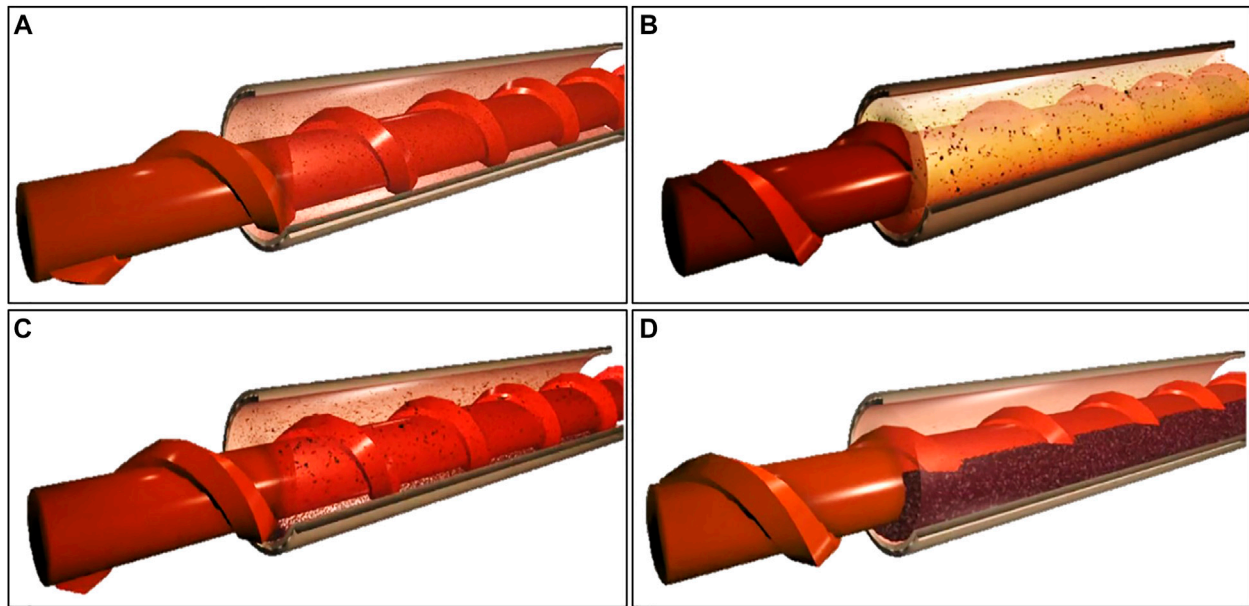


FIGURE 1 | The annular solid-liquid flow model. **(A)** Homogeneous suspended state; **(B)** Inhomogeneous suspended state; **(C)** Moving laminar flow regime; **(D)** Fixed laminar flow regime.

particles, which are mixed with water to form solid-liquid two-phase mixed fluids under the thread effect of drill pipes and gravity effect of themselves. Moreover, the annular space between the drill pipes and hole walls serves as the channel for mixed fluids and therefore it is feasible to theoretically analyze the slag disposal condition during hydraulic cutting by utilizing the theoretical model for annular solid-liquid two-phase flow.

When solid-liquid two-phase fluids flow through the annular channel of boreholes, four different flow regimes (homogeneous suspended state, inhomogeneous suspended state, moving laminar flow regime and fixed laminar flow regime) may occur according to the difference of the concentration of coal particles and the flow velocity, which is shown in **Figure 1**.

The homogeneous suspended state means that coal particles are completely uniformly diffused in liquids (**Figure 1A**). The flow model cannot be formed unless coal particles show a small size and small mass and are transported at a high speed in the completely turbulent state. In most cases, coal particles are in an inhomogeneous suspended state. On this condition, the concentration of coal particles in liquids presents a gradient along the cross section of the liquids, in which the **Figure 1B** concentration at the bottom is higher than that on the top (**Figure 1B**). With the reduction of the flow velocity and the growth of the particle density, the particles with a large size start to deposit at the bottom of liquids, thus forming a deposition layer. Within a certain transporting range, the deposition layer slides in liquids along the flow direction while coal particles above the layer flow at an inhomogeneous suspended state, which is called moving laminar flow regime (**Figure 1C**). As the flow velocity further drops, more coal particles deposit at the bottom of the boreholes and finally a fixed deposition layer is formed at the bottom, which is called the fixed laminar flow regime (**Figure 1D**).

Mechanical Analysis of Coal Particles in Various Motion Stages

According to the motion states of coal particles in coal-liquid two-phase flow from low to high flow velocities, coal particles experience four motion stages, including initiation, rolling, sliding and suspending stages.

Initiation Stage

The particles in the surface layer of coal particle groups generally roll in the initiation stage. Therefore, it is possible to explore the problem of coal particles in the initiation stage by performing the mechanical analysis on a single coal particle.

The force driving the sliding of the coal particle is calculated as follows:

$$F_d = F_D + F_g'' - F_f \quad (1)$$

The resistance to the coal particle is expressed as follows:

$$F_f = \mu(F_g' - F_L) \quad (2)$$

where, μ denotes the coefficient of sliding friction.

It can be obtained that coal particles are subjected to the effects of two force moments at the moment of rolling, which are separately expressed as follows:

The force moment driving the rolling of coal particles is calculated as follows:

$$M_d = F_D \cdot l_1 + F_L \cdot l_3 + (F_g'' - F_f) \cdot l_4 \quad (3)$$

The force moment resisting the rolling of coal particles is expressed as follows:

$$M_r = (F_g'' - F_L) \cdot l_3 \quad (4)$$

To make coal particles roll, it is necessary to satisfy $F_f > F_d$, $F_g' > F_L$ and $M_d > M_r$.

Rolling Stage

After coal particles roll, the drag force of water flow on coal particles constantly rises with the growing velocity of the water flow field, thus prompting more coal particles to roll. As a result, the motion of a single or multiple coal particles progressively transforms to rolling motion of coal particle groups.

Sliding Stage

As the velocity of the water flow field continues to grow, the force moment of rolling particles reverses, that is, $M_r > M_d$. This is because the growth of the flow velocity results in the constant reduction of the uplift force F_L and the growth of the fluctuating lift of water flows. However, coal particles cannot be in the suspended state owing to the effective gravity of the coal particles still dominates; nevertheless, the friction force between particles drastically reduces, thus leading to reversal of the force moment. The increase of the velocity of the water flow field also causes the drag force F_D of water flows parallel to the water flow direction to grow and gradually dominate, that is, $F_d > F_f$. Therefore, the motion state of coal particles is changed from the previously rolling state to sliding state when the velocity of the water flow field reaches a certain level. In this case, the relationship of forces on particles can be expressed as follows:

$$F_D > \mu \sum_{i=1}^n mg \cos \theta \quad (5)$$

Suspending Stage

After the velocity of the water flow field further increases on the basis of the sliding stage, the turbulence of the water flow field is further strengthened and the fluctuating lift of water flows constantly increases. Eventually, the fluctuating lift is larger than the effective gravity of coal particles and therefore coal particles are in the suspending state. In this context, the force condition of coal particles is calculated as follows:

$$F_g < F_t \quad (6)$$

where, F_t denotes the average fluctuating lift of coal-cinder particles within boreholes.

According to the research results obtained by scholars in China, the average fluctuating lift of water flows is expressed as follows:

$$F_t = -\frac{\xi \tau_f}{\tau_s} \frac{\partial}{\partial y} \left[nm \overline{v_d'^2} \right] \quad (7)$$

where, ξ and τ_f refer to the comprehensive coefficient of coal particles and the characteristic time of fluctuating water flows, respectively; $\tau_f = 0.4L^2 \text{Re}_w^{-7/8} \nu^{-1}$, in which L , Re_w and ν represent the flow scale, Reynolds number of water flows and the viscosity

coefficient during the motion, respectively; τ_s denotes the relaxation time of coal particles, satisfying $\tau_s = \rho_s d_s^2 (18\rho_w \nu)^{-1}$; $\overline{v_s'}$ stands for the average fluctuating component velocity of coal particles in the vertical direction and n and m separately refer to the number density and mass of a single coal particle, satisfying $nm = C_v \rho_s$.

It can be found that the solid-liquid two-phase flow in boreholes should be in a moving laminar flow regime in order to successfully discharge coal-cinder particles from the borehole orifice during the hydraulic cutting. In the case, the coal-cinder particles at the bottom of boreholes slide. If the concentration of coal particles or the flow velocity further declines, the motion state of coal particles in boreholes varies from the sliding state to rolling state. Furthermore, large-size coal particles start to deposit at the bottom of boreholes, thus further causing the borehole jamming. Therefore, the minimum flow velocity in boreholes should be the critical flow velocity at the moving laminar flow regime to ensure the successful drainage of coal cinders.

RELATIONSHIP BETWEEN CUTTING PRESSURE AND COAL BREAKING DURING HYDRAULIC CUTTING

Relationship Between Cutting Pressure and Flow Rate

The dynamic pressure of water jets at the nozzle outlet is calculated as follows:

$$P_0 = \frac{1}{2} \rho_0 v_0^2 \quad (8)$$

where, where P_0 , ρ_0 and v_0 separately represent the dynamic pressure at the nozzle outlet, the water density and the axial velocity at the nozzle outlet.

When water jets are just ejected out of the nozzle outlet, it is thought that the velocities at different positions of jets keep unchanged (being the axial velocity). Thus, the relationship between the jet flow rate and the velocity is expressed as follows:

$$Q = \frac{1}{4} \pi d^2 v_0 k_0 \quad (9)$$

By synchronously calculating Eqs. 11, 12, it can be attained that:

$$Q = \frac{1}{4} k_0 \pi d^2 \sqrt{\frac{2P_0}{\rho_0}} \quad (10)$$

where, k_0 and d denote the nozzle coefficient (0.95) and the nozzle diameter (2.5×10^{-3} m), respectively.

Relationship Between Cutting Pressure and Coal-Dropping Speed

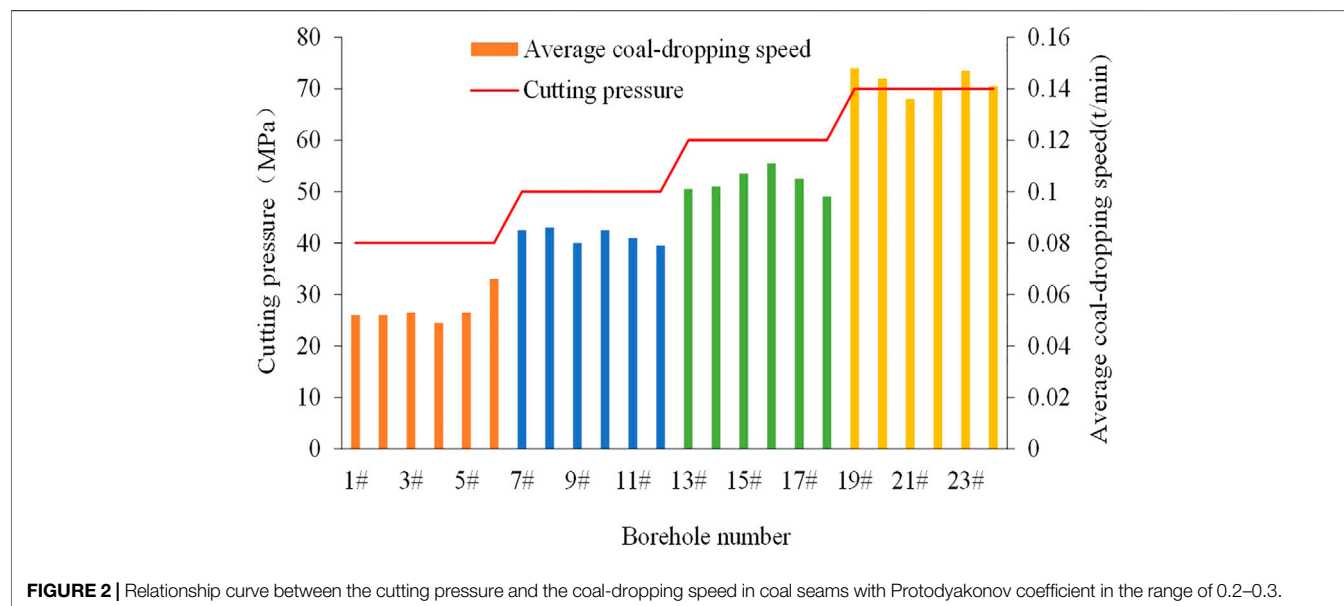
To analyze the relationship between different cutting pressure and coal-dropping speed during the cutting in coal seams with different Protodyakonov coefficients, the field test was carried out

TABLE 1 | Basic conditions of the test mines.

Name of coal mines	Main working coal seams	Protodyakonov coefficient of coal seams	Number of test boreholes
Xuehu coal mine	2-2 [#] coal seam	0.2–0.3	24
Zhaozhuang coal mine	3 [#] coal seam	0.3–0.5	16
Yuwu coal Mine	3 [#] coal seam	0.5–0.8	20
Zhaogu No. 2 mine	2-1 [#] coal seam	1.0–1.5	15

TABLE 2 | The coal-dropping speeds in coal seams with different Protodyakonov coefficients under different cutting pressures.

Pressure <i>f</i> values	40 MPa	50 MPa	60 MPa	70 MPa	80 MPa	90 MPa	100 MPa
0.2–0.3	0.054	0.083	0.104	0.143	—	—	—
0.3–0.5	—	0.035	0.056	0.092	0.119	—	—
0.5–0.8	—	—	0.019	0.030	0.051	0.068	—
1.0–1.5	—	—	—	—	0.021	0.031	0.042

**FIGURE 2** | Relationship curve between the cutting pressure and the coal-dropping speed in coal seams with Protodyakonov coefficient in the range of 0.2–0.3.

by selecting four mines with different Protodyakonov coefficients of coal seams. The basic conditions of the mines are displayed in **Table 1**.

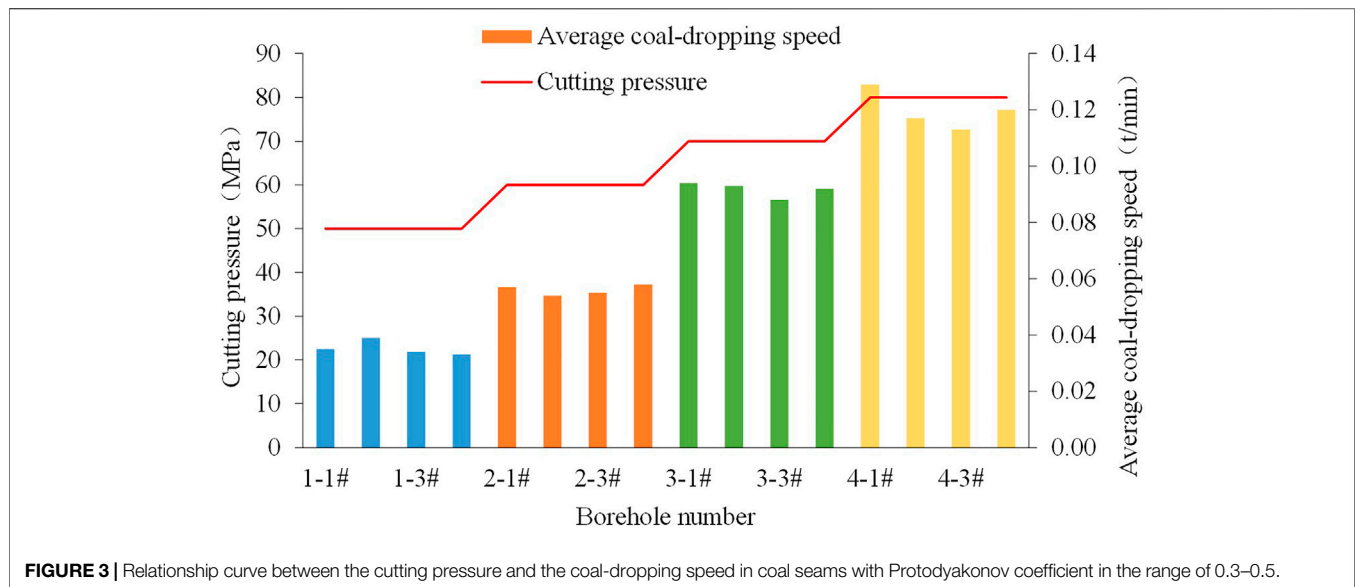
The ultra-high pressure hydraulic cutting test was conducted in the following four mines and the test results were described as follows:

The Ultra-High Pressure Hydraulic Cutting Test on Xuehu Coal Mine

Xuehu Coal Mine, located in the north of Yongcheng, Henan Province, China, is subordinated to Xuehu village in Yongcheng city. The 2-2[#] coal seam in Xuehu Coal Mine is taken as the main working coal seam. The coal seams in the coalfield occur steadily, with the thickness of 0–4.77 m, average thickness of 2.23 m, gas content within 4.6–16.2 m³/t and gas permeability coefficient of 0.0861 m³/(MPa²·d). The

Protodyakonov coefficient of the 2-2[#] coal seam is in the range of 0.25–0.7 and the attenuation coefficient of gas flows within the boreholes with one hundred meters is 1.38 days⁻¹. As for the test design, four groups of boreholes, each containing six boreholes, were distributed in the end-located drainage roadway of the No. 2306 airway in the mine, with 24 boreholes for hydraulic cutting in total. The hydraulic cutting was conducted in the four groups of boreholes for hydraulic cutting by separately using the cutting pressures of 40, 50, 60 and 70 MPa, during which coal outputs within the cutting time from borehole orifices were recorded. The test results are shown in **Figure 2**.

As shown in **Figure 2**, when the cutting pressures are 40, 50, 60 and 70 MPa, the average coal-dropping speeds of the coal seams with Protodyakonov coefficient of 0.2–0.3 are 0.052, 0.081, 0.10 and 0.143 t/min, respectively.



The Ultra-High Pressure Hydraulic Cutting Test in Zhaozhuang Coal Mine

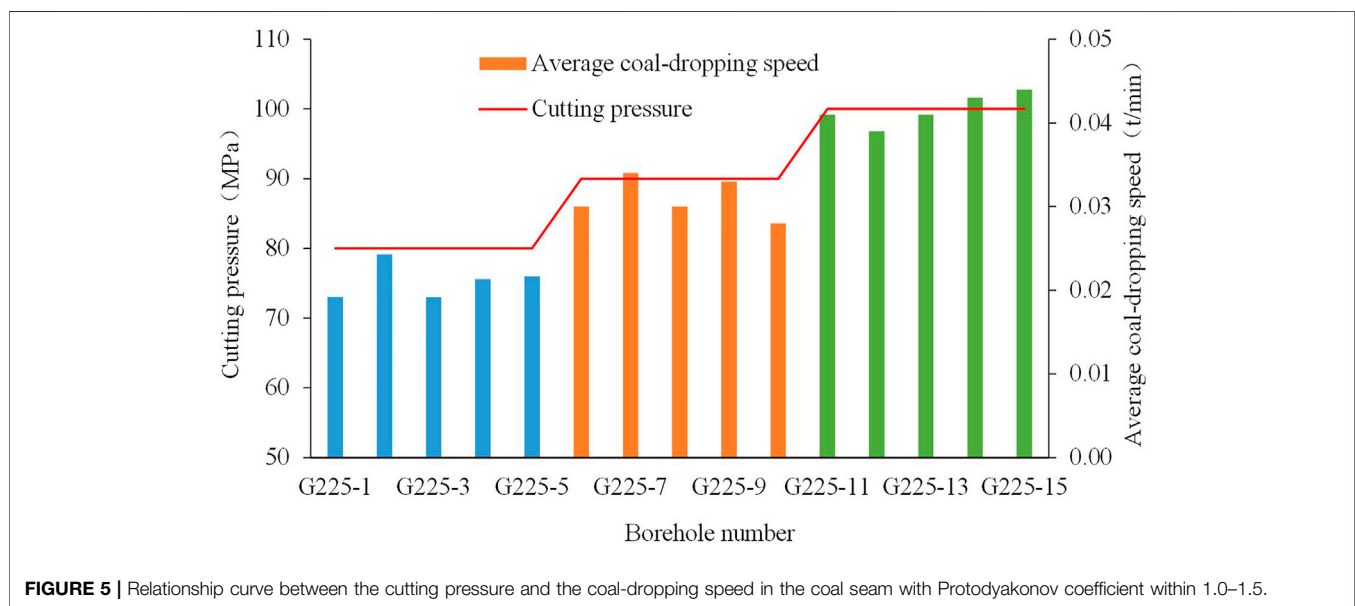
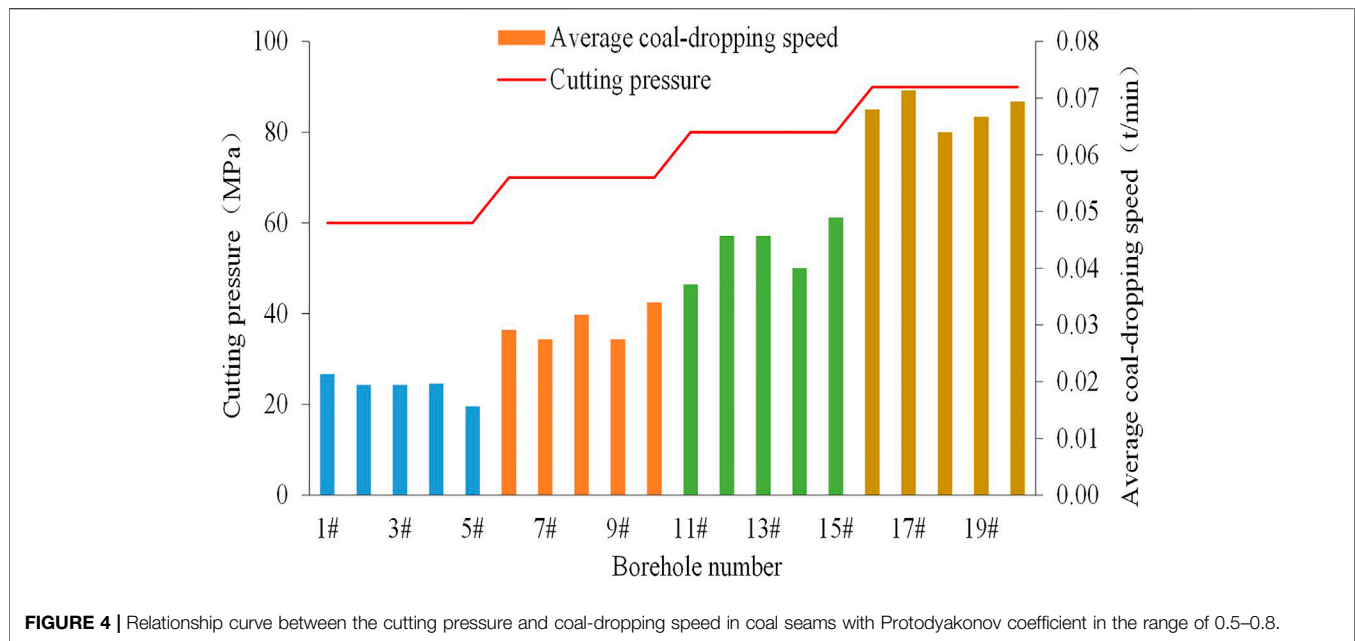
Zhaozhuang Coal Mine field is located in the southeast of Qinshui Coalfield, 53 km to the north of Jincheng City (Shanxi Province), 12 km to the north of Gaoping City, and 16 km to the south of Zhangzi County (Shanxi Province). The northern part of the coalfield is a sedimentary basin at Changzhi fault, and the middle and the southern parts correspond to the middle mountain areas eroded by Qinhe and Danhe river basins. In terms of the terrain of the areas, the altitude gradually reduces from the eastern and western parts to the middle part. To be specific, the highest point is situated in the northwest of Jubang Village at the western border, with the altitude of +1276.40 m; and the lowest point lies in the Dongdan River Valley in Guanzhai Village in the south, with the altitude of +880.70 m. It can be attained that the maximum relative altitude difference is 395.70 m. The bedrock in the southern and northern parts is mostly covered while that in middle and western parts are favorably outcropped. The coal-bearing strata in the coalfield are mainly subordinated to the Taiyuan Formation (C_3t) of the upper series of Carboniferous system and the Shanxi Formation (P_1s) of the lower series of Permian system, with shed coal scattered in the Lower Shihezi Formation and Benxi Formation. From top to bottom, Shanxi Formation contains 1[#], 2[#] and 3[#] coal seams and Taiyuan Formation contains 12 coal seams including 5[#], 6[#], 7[#], 8^{-1#}, 8^{-2#}, 9[#], 11[#], 12[#], 13[#], 14[#], 15[#] and 16[#]. The cumulative total thickness of Shanxi Formation and Taiyuan Formation is in the range of 118.19–206.86 m, generally showing the thickness of 153.57 m. The two formations involve 15 coal seams, with the total thickness of 3.38–18.21 m, the average thickness of 12.80 m and the coal-bearing coefficient of 8.33%.

The average thickness of the 3[#] coal seam in Zhaozhuang Coal Mine in the whole area is 4.69 m, with Protodyakonov coefficient in the range of 0.3–0.5. Four groups of boreholes were constructed in the airway in the north of Zhaozhuang Coal

Mine, each of which contained four boreholes, showing 16 boreholes in total. The cutting test was carried out on four groups of boreholes by separately applying the cutting pressure of 50, 60, 70 and 80 MPa. The test results are shown in **Figure 3**. Under the cutting pressures of 50, 60, 70 and 80 MPa, the average coal-dropping speeds of the coal seams with Protodyakonov coefficient within 0.3–0.5 were 0.040, 0.056, 0.092 and 0.119 t/min, respectively.

The Ultra-High Pressure Hydraulic Cutting Test in Yuwu Coal Mine

The 3[#] coal seam in Yuwu Coal Mine of Lu'an Chemical Group Co., Ltd. is located in the middle and lower part of Shanxi Formation of the lower series of Permian system. The coal seam with a large thickness is stable and recoverable in the whole area, which is 24.00–42.00 m (with an average of 33.00 m) away from K8 sandstone above and 50.48–73.12 m (with an average of 62.00 m) away from the 9[#] coal seam below. The coal seam shows the thickness in the range of 5–7.25 m, with the average thickness of 5.99 m and Protodyakonov coefficient of 0.5–0.8. The ultra-high pressure hydraulic cutting test was performed in the N1103 belt conveyor roadway (with the designed total length of about 2,068 m), with coal on the north, the N1103 working face (unmined) on the west, N1105 belt conveyor roadway (being excavated) on the east and connected to the 1[#] ventilation roadway (excavated) in the west wing of the northern air shaft on the south. The N1103 belt conveyor roadway was excavated along the roof of the 3[#] coal seam with the thickness of 6 m. In the excavation direction of the roadway, the dip angle of the 3[#] coal seam was in the range of +3° ~ -2°, showing the average dip angle of 1°. The N1103 belt conveyor roadway appeared as a rectangular cross section with the width of 5.4 m and height of 3.8 m, which was supported by using anchor nets and then strengthened with anchor cables. The N1103 belt



conveyor roadway was pre-drained by drilling long boreholes with the length of 135 m, dip angle of 1°, azimuth of 270° and spacing of 4.0 m along coal seams. In the N1103 belt conveyor roadway in Yuwu Coal Mine, four groups of boreholes were distributed along the seams, each of which five boreholes were drilled, with 20 test boreholes in total. The cutting test was conducted on the boreholes under the cutting pressures of 60, 70, 80 and 90 MPa, respectively. The test results are shown in **Figure 4**.

It can be seen from **Figure 4** that under the cutting pressures of 60, 70, 80 and 90 MPa, the average coal-dropping speeds in coal

seams with Protodyakonov coefficient of 0.5–0.8 were 0.019, 0.030, 0.044 and 0.068 t/min, respectively.

The Ultra-High Pressure Hydraulic Cutting Test in Zhaogu No. 2 mine

The main working coal seam 2-1[#] in Zhaogu No. 2 mine delivered the thickness of 4.73–6.77 m, with the average thickness of 6.16 m and Protodyakonov coefficient in the range of 1.0–1.5. Three groups of boreholes were designed in the belt roadway in the west of the mine, in which five boreholes were distributed in each group, amounting to 15 test boreholes. The cutting test was

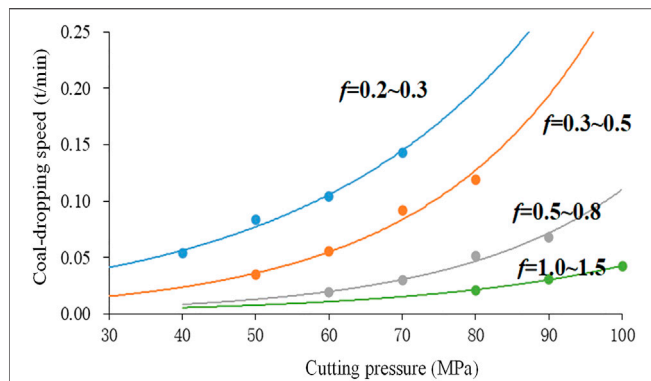


FIGURE 6 | The change curve between the jet pressure and the coal-dropping speed.

performed in the boreholes under the cutting pressures of 80, 90 and 100 MPa. **Figure 5** shows the test results.

As shown in **Figure 5**, the average coal-dropping speeds in the coal seam with Protodyakonov coefficient within 1.0–1.5 were 0.021, 0.031 and 0.042 t/min under the cutting pressures of 80, 90 and 100 MPa, respectively.

Through the above field tests, the changes of the coal-dropping speed in the coal seams with different Protodyakonov coefficients under different cutting pressures can be summarized, as shown in **Table 2**.

By fitting the above data according to the negative exponent curve, the change curves between the jet pressure and the coal-dropping speed in coal seams with different Protodyakonov coefficients can be attained, as shown in **Figure 6**.

As shown in **Figure 6**, the larger the cutting pressure is, the larger the coal-dropping speed during hydraulic cutting; moreover, with the growth of the cutting pressure, the coal-dropping speed during hydraulic cutting exponentially rises. Therefore, during high pressure cutting, the coal output dramatically increases due to the growth of the cutting pressure, thus leading to the borehole jamming and borehole outburst. The determination of a reasonable cutting pressure decisively influences the hydraulic cutting technology.

PRESSURE SELECTION FOR COORDINATED SLAG DISPOSAL DURING HYDRAULIC CUTTING

Critical Flow Velocity at the Moving Laminar Flow Regime

According to the mechanical analysis on coal particles in *Relationship Between Cutting Pressure and Coal-Dropping Speed*, it can be seen that coal particles are mainly subjected to the uplift force of fluids, effective gravity of particles and the drag force of fluids. The drag force of fluids drives coal particles to move forward while the effective gravity and the uplift force of fluids are forces with contrary directions in the vertical direction.

Therefore, the critical flow velocity V_{\min} at the moving laminar flow regime when coal particles are transformed from the rolling state to the sliding state needs to satisfy the following condition:

$$F_D - \mu F_g = 0 \quad (11)$$

where, F_g , F_d and μ separately refer to the effective gravity, the drag force of fluids and the friction coefficient between coal particles and the pipe wall.

Thus,

$$(u_w - w_s)^2 \propto \frac{4}{3C_D} \times \frac{\rho_s - \rho_w}{\rho_w} \times \frac{d_s}{D} \times \mu g D \quad (12)$$

where, g denotes the gravitational acceleration and P_s and P_w refer to the densities of coal particles and water; D stands for the equivalent diameter of the annular pipes ($D = \sqrt{(R^2 - r^2)}$); R and r represent the diameters of the boreholes and drill pipes, respectively; d_s denotes the average diameter of coal particles; U_s and U_w separately stand for flow velocities of coal particles and water and C_D refers to the drag force coefficient of fluids.

The drag force coefficient of coal particles can be determined according to the following equation:

$$C_D = \frac{4gd_s(S-1)}{3v_t^2} \quad (13)$$

where, v_t denotes the deposition velocity (m/s) of coal particles; $S = \rho_s/\rho_w$ refers to the density ratio of the transported particles to the carrying liquids.

Therefore, **Eq. 12** can be transformed as follows:

$$(u_w - w_s) \propto \sqrt{2gD(S-1)} \cdot \left(\frac{d_s}{D}\right)^{0.5} \quad (14)$$

Owing to $(u_w - u_s) \propto V_{\min}$ and the critical flow velocity of coal particles transformed from the rolling state to the sliding state is related to the volume concentration of particles, particle size and borehole diameter, **Eq. 15** can be attained.

$$\begin{cases} V_{\min} \propto \left(\frac{d_s}{D}\right)^{0.25} \\ V_{\min} \propto C_V^{0.2} \end{cases} \quad (15)$$

Thus, the critical flow velocity at the moving laminar flow regime can be obtained by using the dimensional analysis.

$$V_{\min} = a \sqrt{2gD(S-1)} \cdot \left(\frac{d_s}{D}\right)^{0.75} C_V^{0.2} \quad (16)$$

where, a stands for the comprehensive factor for characterizing the shape factors of coal particles.

Critical Relationship Between the Flow Rate and the slag-Disposal Capacity

To calculate the numerical relationship between the flow rate and the slag-disposal capacity, the dimensionless analysis is employed to solve **Eq. 16**. The annular solid-liquid two-phase flow model for coal particles and water is solved according to **Eq. 16** based on

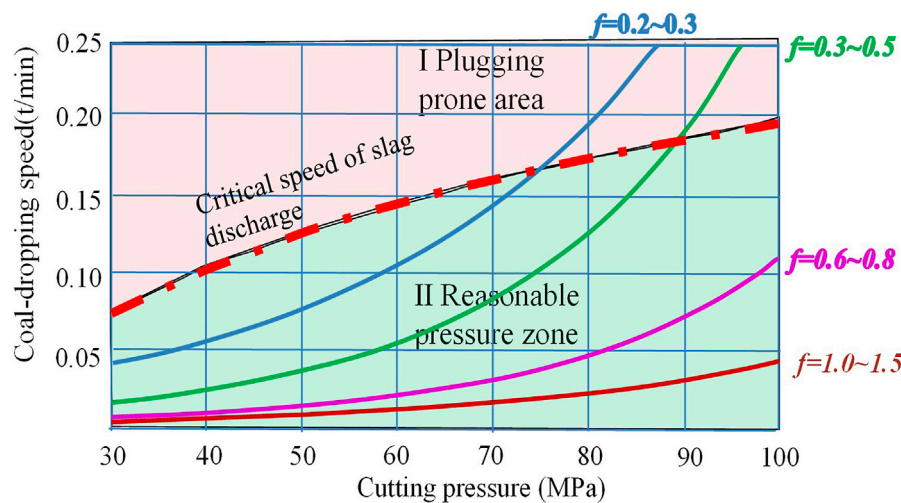


FIGURE 7 | Model for the coordinated slag disposal during the cutting.

various parameters. To be specific, R and r are 0.113 m and 0.073 m and thus $D = 0.086$ m; d_s and S equal 0.001 m and 1.42. By substituting them into Eq. 16, it can be attained that:

$$V_{\min} = 2.97 \times 10^{-2} a C_V^{0.2} \quad (17)$$

By substituting $V_{\min} = 4Q/(\pi D^2)$ and $C_V = v_s(v_s + v_w)^{-1}$ into the above equation, it is obtained that:

$$Q = 1.72 \times 10^{-4} a \cdot \left(\frac{v_s}{v_s + v_w} \right)^{0.2} \quad (18)$$

where, v_p and v_f separately denote the volumes of coal particles and liquid, respectively.

By substituting $v_s = T_0 \rho_s^{-1}$ and $v_w = Q \rho_w^{-1}$ into Eq. 18, it can be attained that:

$$T_0 = \frac{1.42 Q^6 \times 10^{19}}{1.51 a^5 - Q^5 \times 10^{19}} \quad (19)$$

By substituting Eq. 3 into Equation (23), it can be obtained that:

$$T_0 = \frac{1.8 P^3 \times 10^{-5}}{1.51 a^5 - 1.22 \times 10^{-1} P^{5/2}} \quad (20)$$

Through the above calculation, the relationship between the cutting pressure and the critical slag disposal amount is obtained.

Model for the Coordinated slag Disposal During Hydraulic Cutting

By substituting Eq. 20 into Figure 7, the model for the coordinated slag disposal during the cutting can be attained, as shown in Figure 7.

Through analysis according to the results of theoretical calculation and the field data, it is found that by taking the critical curve for the slag disposal as the boundary, zone I is the position where the borehole jamming is likely to occur. When the

selected pressure corresponds to the zone I, the coal output from boreholes is quite large and exceeds the critical slag disposal amount, thus easily leading to the borehole jamming; in the case that the pressure corresponds to the zone II, the coal output is lower than the critical slag disposal amount. On this condition, it is possible to achieve the expected cutting effect and also successfully discharge coal cinders from boreholes. Therefore, when selecting the cutting parameters, it is necessary to select the cutting pressure within the zone II, thus realizing the optimal cutting effect. It can be seen from the figure that the critical pressure inducing the borehole jamming is in the range of 70–75 MPa when Protodyakonov coefficient of coal seams ranges from 0.2 to 0.3 and it is within 80–85 MPa in the case that Protodyakonov coefficient of coal seams is in the range of 0.3–0.5.

FIELD TEST

Selection of Test Schemes

The No. 2 mine in China Coal Xinji Energy Co., Ltd. (Xijin coal mine No. 2) was used as the test mine and the 220112 working face was taken as the test area, as shown in Figure 8. The 1[#] coal seam group in 2201 mining area was divided into the 1[#] upper coal seam and 1[#] coal seam, with the average thicknesses of 3.4 and 3.9 m, respectively. The 1[#] upper coal seam and 1[#] coal seam showed an average spacing of 0.9 m and a dip angle of 5°. Through measurement, the maximum gas pressure, the gas content and Protodyakonov coefficient of 1[#] coal seam were 1.65 MPa, 6.8–8.2 m³/t and 0.48, respectively. As for the borehole design, 25 horizontal test boreholes (G1 ~ G25) were distributed in the machinery roadway of the working face and 20 boreholes (D1 ~ D20) were used for comparison, showing the spacing of 10 m and borehole depth of 120 m; the spacing between the boreholes for hydraulic cutting and those for comparison was set as 20 m. The boreholes G1 ~ G5 were test boreholes for exploring the

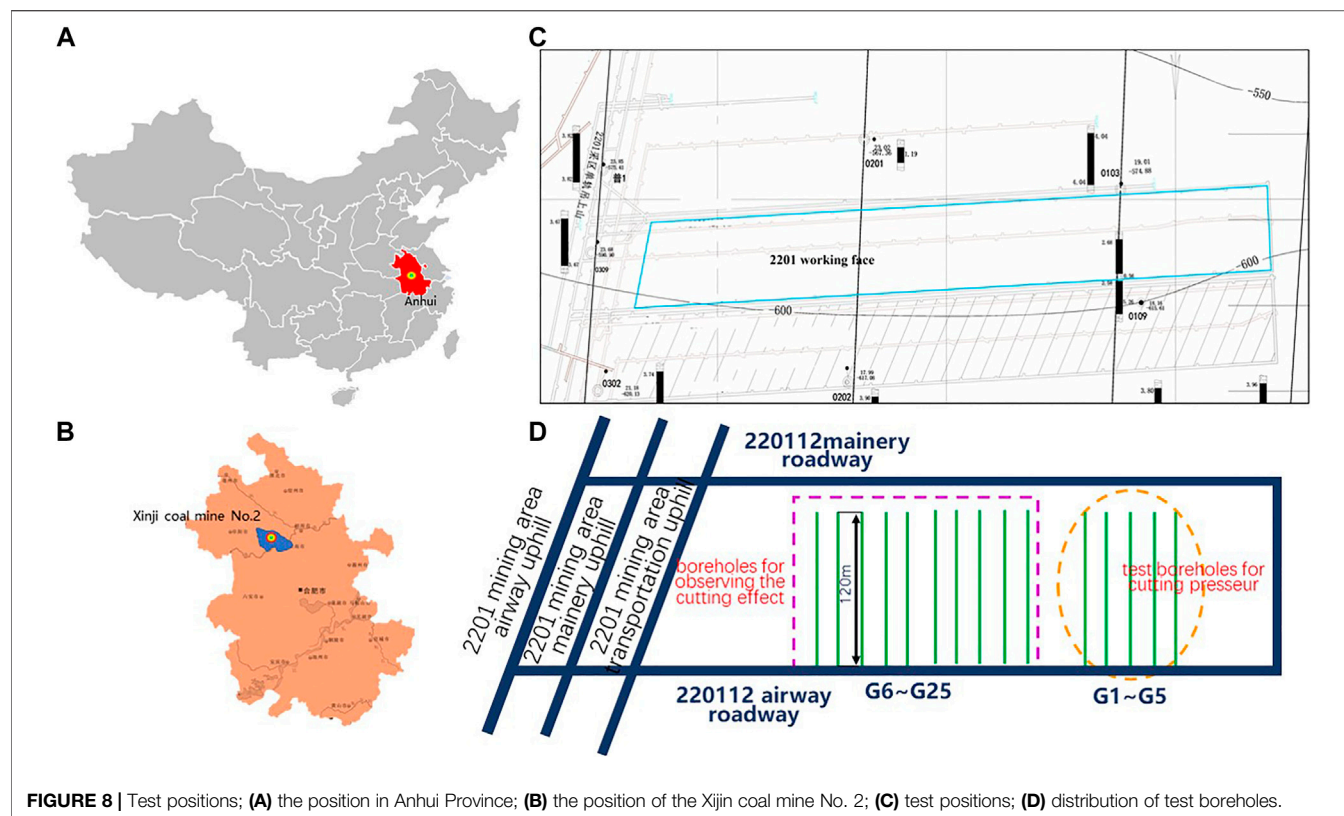


FIGURE 8 | Test positions; **(A)** the position in Anhui Province; **(B)** the position of the Xinji coal mine No. 2; **(C)** test positions; **(D)** distribution of test boreholes.

TABLE 3 | Cutting condition based on the test boreholes for the reasonable cutting pressure.

Serial number of boreholes	Protodyakonov coefficient of coal seams	Pressure/MPa	Flow rate L/min	Time/min	Coal output/t	Water- and slag-return conditions
G1	0.48	50	79	7	0.22	A small number of coal-cinder particles
G2	0.48	60	88	7	0.37	Normal water- and slag-return conditions
G3	0.48	70	97	8	0.74	Normal water- and slag-return conditions
G4	0.48	80	105	7	0.85	Borehole outburst and borehole jamming
G5	0.48	90	112	~	~	Severe borehole outburst and borehole jamming

reasonable cutting pressure. The cutting test was separately carried out under different cutting pressures, during which the cutting time, slag disposal amount and the water- and slag-return conditions were recorded. After determining the reasonable cutting pressure, the ultra-high pressure hydraulic cutting test was conducted to explore the coal output and net gas extraction; afterwards, the comparative analysis was made with those from boreholes for comparison.

Result Analysis of Test Boreholes for the Reasonable Cutting Pressure

The cutting parameters and conditions obtained from the test boreholes G1 ~ G5 for the reasonable

As shown in **Table 3**, as for test boreholes G1 and G2, the coal output is low under the cutting pressure of 50–60 MPa while it significantly rises when the cutting pressure is in the range of

70–80 MPa; after the pressure grows to 90 MPa, the severe borehole jamming and borehole outburst appear in the borehole G5. It indicates that the reasonable cutting pressure should be about 80 MPa for coal seams with the Protodyakonov coefficient of about 0.48, which conforms to the result obtained according to the model for the coordinated slag disposal during hydraulic cutting.

Analysis of the Coal Output From the Boreholes for Hydraulic Cutting

Figure 9 displays the coal output from boreholes for hydraulic cutting. It can be seen from the figure that the average coal output per cutting of 20 boreholes for hydraulic cutting (G6 ~ G25) reaches the minimum of 0.69 t and the maximum of 1.06 t, with the mean value of 0.87 t. The equivalent radius is calculated as 2.15 m. During hydraulic cutting of 20 boreholes, the poor slag



FIGURE 9 | Coal output from boreholes for hydraulic cutting.

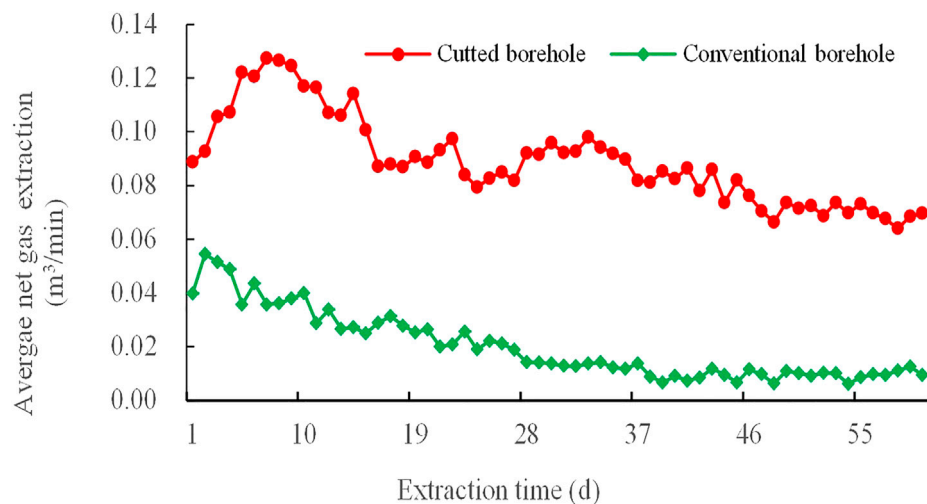


FIGURE 10 | Changes curves of the average net gas extraction from a single borehole for hydraulic cutting and a conventional borehole.

disposal conditions (such as borehole jamming and borehole outburst) do not occur, which also validates the selection rationality of the cutting pressure.

min, respectively. The average net gas extraction from boreholes for hydraulic cutting is 4.5 times larger than that from conventional boreholes.

Comparative Analysis of the Gas Extraction Effect

Figure 10 shows the change curves of the average net gas extraction from a single borehole for hydraulic cutting and a conventional borehole within 60 days of extraction.

It can be seen from the figure that the maximum and minimum of the average net gas extraction from boreholes for hydraulic cutting are 0.127 and 0.064 m³/min, with the mean value of 0.089 m³/min, while those from conventional boreholes are 0.054 and 0.006 m³/min, with the mean value of 0.020 m³/min, respectively.

Observation on the Permeability of Coal Seams

Before performing the ultra-high pressure hydraulic cutting, the original gas permeability coefficient of 1[#] coal seam of the machinery roadway in the 220,112 working face is calculated as 0.03962 m²/MPa²·d based on the method proposed by China University of Mining and Technology. After conducting the ultra-high pressure hydraulic cutting, the gas permeability coefficient of the 1[#] coal seam is measured as 0.9905 m²/MPa²·d, which increases by 25 times than the original one.

TABLE 4 | Comparison of the effective extraction radiuses around boreholes for hydraulic cutting and conventional boreholes.

Extraction time (d)	Effective extraction radius (m) hydraulic boreholes for cutting	Effective extraction radius (m) hydraulic conventional boreholes
30	5.5	2.38
60	7.1	3.36

Comparison of the Effective Extraction Radius

The effective extraction radiuses around the boreholes for hydraulic cutting and conventional boreholes after extraction for 30 and 60 days are shown in **Table 4**. After the cutting, the impact area of the boreholes for hydraulic cutting greatly increases and the effective extraction radius is more than doubled relative to conventional boreholes.

In summary, the field tests were conducted after determining a reasonable cutting pressure. The comparison of the coal output from the boreholes for hydraulic cutting, the gas extraction effect, the permeability of coal seams, and the comparison of the effective extraction radius for hydraulic cutting was analyzed. The field test results show that the reasonable cutting pressure can ensure the safety of cutting operation and improve the extraction effect.

CONCLUSION

In this paper, a model for coordinated slag disposal during hydraulic cutting based on coal-water two-phase flow was established according to the annular solid-liquid two-phase flow theory. Besides, the model for selecting the reasonable cutting pressure was used to guide the field test. The primary conclusions are displayed as follows.

- (1) By analyzing the test data on four mines containing coal seams with different Protodyakonov coefficients obtained through the field cutting test, the relationship curves between the coal-dropping speed and the cutting pressure under different Protodyakonov coefficients were attained; moreover, it suggested that the coal-dropping speed during hydraulic cutting exponentially increases with the growth of the cutting pressure.
- (2) By constructing the annular solid-liquid two-phase flow model with coal-water mixture, the mechanical condition of coal particles at different motion stages was analyzed. The result showed that the concentration and flow velocity of coal-water two-phase flow are main factors influencing the slag disposal from boreholes; the critical flow velocity at the moving laminar flow regime is considered as that for the coordinated slag disposal from boreholes.
- (3) Through mechanical analysis of the moving laminar flow regime of coal-cinder particles, the critical flow velocity at the moving laminar flow regime was obtained. In addition, the model for selecting the reasonable cutting pressure based on the coordinated slag disposal theory was established according to

the curve relationship with the coal-dropping speed, which guided the cutting test on the 220112 working face. When the reasonable cutting pressure during the slag disposal in the coal seam with Protodyakonov coefficient of 0.48 was determined as about 80 MPa, no borehole outburst and borehole jamming were found during the cutting of test boreholes, with the average coal output per cutting of 0.87 t and the equivalent radius of 2.15 m. The average net gas extraction from boreholes for hydraulic cutting was 4.5 times of that from conventional boreholes; additionally, relative to conventional boreholes, the gas permeability coefficient rose by 25 times and the effective extraction radius is more than doubled.

- (4) The test results showed that the model for selecting the reasonable cutting pressure based on the coordinated slag disposal theory clarified the relationships of the cutting pressure, coal-dropping speed and the critical slag disposal amount. It can ensure the safety of the cutting operation while improving the extraction effect during hydraulic cutting, which effectively guides the selection of the cutting pressure in field tests.

DATA AVAILABILITY STATEMENT

The raw data supporting the conclusions of this article will be made available by the authors, without undue reservation.

AUTHOR CONTRIBUTIONS

The authors have made a significant contribution to the manuscript. YZ was responsible for the framework design and writing of the paper, FJ was responsible for the theoretical analysis in the manuscript and QZ was responsible for the revision of the manuscript.

FUNDING

This work is financially supported by the Tiandi Technology Co., Ltd. for the special funding of Science and Technology Innovation and Entrepreneurship Fund (2021-2-TD-ZD008), the Regional Innovation Development Joint Fund Key Project (U21A20110), the State Key Laboratory Open Fund Project (SKLMRDPC20KF01), and the National Natural Science Foundation of China (52074041), which are gratefully acknowledged.

REFERENCES

- Cheng, Y., Fu, J., and Yu, Q. (2009). Development of Coal Mine Gas Drainage Technology in China. *J. Mining Saf. Eng.* 26 (2), 127–139.
- Guo, D., Lv, P., Zhao, J., and Zhang, C. (2020). Research Progress on Permeability Improvement Mechanisms and Technologies of Coalbed Deep-Hole Cumulative Blasting. *Int. J. Coal Sci. Technol.* 7 (2), 329–336. doi:10.1007/s40789-020-00320-5
- Guo, H., Wang, K., Wu, Y., Tang, H., Wu, J., Guan, L., et al. (2021). Evaluation of the Weakening Behavior of Gas on the Coal Strength and its Quantitative Influence on the Coal Deformation. *Int. J. Mining Sci. Technol.* 31 (03), 451–462. doi:10.1016/j.ijmst.2021.03.005
- Han, S. M., Woo, N. S., Ha, J. H., Kim, T., Kim, Y. J., and Kim, S. M. (2020). Flow Characteristics of a Solid-Liquid Non-newtonian Fluid for Directional Drilling. *J. Nanosci Nanotechnol* 20 (1), 384–395. doi:10.1166/jnn.2020.17239
- He, M., Zhang, Z., Zhu, J., and Li, N. (2021). Correlation between the Constant Mi of Hoek-Brown Criterion and Porosity of Intact Rock. *Rock Mech. Rock Eng.* 55, 923–936. doi:10.1007/s00603-021-02718-2
- He, M., Zhang, Z., Zhu, J., Li, N., Li, G., and Chen, Y. (2021). Correlation between the Rockburst Proneness and Friction Characteristics of Rock Materials and a New Method for Rockburst Proneness Prediction: Field Demonstration. *J. Pet. Sci. Eng.* 205, 108997. doi:10.1016/j.petrol.2021.108997
- Hu, Q., Jiang, S., and Su, W. (2000). Countermeasures for Prevention and Control of Coal Mine Gas Disaster in China. *Mining Saf. Environ. Prot.* 2000 (01), 58–61.
- Ilker, P., and Sorgun, M. (2020). Performance of Turbulence Models for Single Phase and Liquid-Solid Slurry Flows in Pressurized Pipe Systems. *Ocean Eng.* 2020, 214. doi:10.1016/j.oceaneng.2020.107711
- Jia, L., Li, K., Shi, X., Zhao, L., and Jianshe, L. (2021). Application of Gas Wettability Alteration to Improve Methane Drainage Performance: A Case Study. *Int. J. Mining Sci. Technol.* 31 (04), 621–629. doi:10.1016/j.ijmst.2021.04.002
- Kramer, O. J. I., Padding, J. T., van Vugt, W. H., de Moel, P. J., Baars, E. T., Boek, E. S., et al. (2020). Improvement of Voidage Prediction in Liquid-Solid Fluidized Beds by Inclusion of the Froude Number in Effective Drag Relations. *Int. J. Multiphase Flow* 127. doi:10.1016/j.ijmultiphaseflow.2020.103261
- Liang, Y., Ran, Q., Zou, Q., Zhang, B., and Hong, Y. (2022). Experimental Study of Mechanical Behaviors and Failure Characteristics of Coal under True Triaxial Cyclic Loading and Unloading and Stress Rotation. *Nat. Resour. Res.* doi:10.1007/s11053-022-10022-1
- Lin, B., Fazhi, Y., Zhu, C. J., Zhou, Y., Quanle, Z., Chang, G., et al. (2015). Cross-borehole Hydraulic Slotting Technique for Preventing and Controlling Coal and Gas Outbursts during Coal Roadway Excavation. *J. Nat. Gas Sci. Eng.* 26, 518–525.
- Liu, J. H., and Zhu, M. Y. (2011). Numeration Simulation of Solid-Liquid Two-phase Flow in Centrifugal Sewerage Pump. *Amm* 44-47, 345–348. doi:10.4028/www.scientific.net/AMM.44-47.345
- Shen, C., Lin, B., Sun, C., Zhang, Q., and Li, Q. (2015). Analysis of the Stress-Permeability Coupling Property in Water Jet Slotting Coal and its Impact on Methane Drainage. *J. Pet. Sci. Eng.* 126, 231–241. doi:10.1016/j.petrol.2014.11.035
- Wang, K., and Zhang, X. (2006). Development Status and prospect of China's Coal Mine Gas Drainage Technology. *China Coal Bed Methane* 2006 (01), 13–16+39.
- Wang, Q., He, M., Li, S., Jiang, Z., Wang, Y., Qian, Q., et al. (2021). Comparative Study of Model Tests on Automatically Formed Roadway and Gob-Side Entry Driving in Deep Coal Mines. *Int. J. Mining Sci. Technol.* 31 (04), 591–601. doi:10.1016/j.ijmst.2021.04.004
- Wang, Y., Sun, Y., Chun, L., He, Z., and Wang, Z. (2016). Dynamic Characteristics and Application of Drilling Cuttings Migration in Soft Coal Seam Drilling Hole Area. *J. Mining Saf. Eng.* 33 (06), 1138–1144.
- Wei, N., Xu, H., Sun, W., Zhao, J., Zhang, L., Fu, Q., et al. (2017). Migration Law of Solid Particles of Natural Gas Hydrate with Different Abundances in Horizontal Well Section. *Nat. Gas Industry* 37 (12), 75–80.
- Yamaguchi, H., Niu, X., Shogo, N., and Florian, D. V. (2011). Solid-liquid Two-phase Flow_measurement Using An_electromagnetically Induced Signal Measurement Method. *J. Fluids Engineering-Transactions Asme* 133 (4), 041302. doi:10.1115/1.4003856
- Yang, X. (1994). Study on Cuttings Migration and Critical Speed in Spiral Drilling. *J. China Univ. Mining Technol.* 1994 (04), 101–108.
- Yang, X., Zhang, Y., and Ren, C. (2012). The Numerical Simulation for Seepage Rule of Coal-Bed Methane with Hydraulic Cutting Seam Mining Based on Matlab. *Adv. Mater. Res.* 2012, 1792. doi:10.4028/www.scientific.net/amr.524-527.485
- Yi, M., Wang, L., Hao, C., Liu, Q., and Wang, Z. (2021). Method for Designing the Optimal Sealing Depth in Methane Drainage Boreholes to Realize Efficient Drainage. *Int. J. Coal Sci. Technol.* 8 (6), 1400–1410. doi:10.1007/s40789-021-00448-y
- Zhang, B., Sun, H., Liang, Y., Wang, K., and Zou, Q. (2019). Characterization and Quantification of Mining-Induced Fractures in Overlying Strata: Implications for Coalbed Methane Drainage. *Nat. Resour. Res.* 29 (4). doi:10.1007/s11053-019-0960-7
- Zhang, T., Zou, Q., Jia, X., Liu, T., Jiang, Z., Tian, S., et al. (2022). Effect of Cyclic Water Injection on the Wettability of Coal with Different SiO₂ Nanofluid Treatment Time. *Fuel* 312. doi:10.1016/j.fuel.2021.122922
- Zhang, X., Li, J., Zhou, Z., and Zhao, W. (2017). Numerical Analysis and Experimental Study on Micro-holes in Solid-Liquid Two-phase Abrasive Flow Machining. *J. Measurements Eng.* 5 (3), 176–181. doi:10.21595/jme.2017.19103
- Zhao, Y., Lin, B., Liu, T., Kong, J., and Zheng, Y. (2020). Gas Flow in Hydraulic Slotting-Disturbed Coal Seam Considering Stress Relief Induced Damage. *J. Nat. Gas Sci. Eng.* 75. doi:10.1016/j.jngse.2020.103160
- Zhou, A., Zhang, M., Wang, K., and Elsworth, D. (2021). Near-source Characteristics of Two-phase Gas-Solid Outbursts in Roadways. *Int. J. Coal Sci. Technol.* 8 (4), 685–696. doi:10.1007/s40789-020-00362-9
- Zou, Q., Han, L., Jiang, Z., and Wu, X. (2021). Gas Flow Laws in Coal Subjected to Hydraulic Slotting and a Prediction Model for its Permeability-Enhancing Effect. *Energy Sourc. A: Recovery, Utilization, Environ. Effects* 2021. doi:10.1080/15567036.2021.1936692
- Zou, Q., Liu, H., Zhang, Y., Li, Q., Fu, J., and Hu, Q. (2020). Rationality Evaluation of Production Deployment of Outburst-Prone Coal Mines: A Case Study of Nantong Coal Mine in Chongqing, China. *Saf. Sci.* 122, 104515. doi:10.1016/j.ssci.2019.104515
- Zou, Q., Zhang, T., Cheng, Z., Jiang, Z., and Tian, S. (2022). A Method for Selection Rationality Evaluation of the First-Mining Seam in Multi-Seam Mining. *Geomech. Geophys. Geo-energ. Geo-resour.* 8 (1), 17. doi:10.1007/s40948-021-00314-w

Conflict of Interest: The authors declare that this study received funding from the Tiandi Technology Co., Ltd. The funder had the following involvement in the study: study design, collection, analysis, interpretation of data.

Publisher's Note: All claims expressed in this article are solely those of the authors and do not necessarily represent those of their affiliated organizations, or those of the publisher, the editors and the reviewers. Any product that may be evaluated in this article, or claim that may be made by its manufacturer, is not guaranteed or endorsed by the publisher.

Copyright © 2022 Zhang, Ji and Zou. This is an open-access article distributed under the terms of the Creative Commons Attribution License (CC BY). The use, distribution or reproduction in other forums is permitted, provided the original author(s) and the copyright owner(s) are credited and that the original publication in this journal is cited, in accordance with accepted academic practice. No use, distribution or reproduction is permitted which does not comply with these terms.



Surrounding Rock Damage Characteristics and Support Optimization of Roadway in Soft Gas-Rich Coal Seam Under the Condition of Penetrating Hydraulic Reaming

Xu Han^{1,2}, Kai Zhang^{1,2*}, Xinran Xue^{1,2} and Bailong Ma^{1,2}

¹State Key Laboratory of Geomechanics and Deep Underground Engineering, China University of Mining and Technology, Xuzhou, China, ²School of Mechanics and Civil Engineering, China University of Mining and Technology, Xuzhou, China

OPEN ACCESS

Edited by:

Wei Liu,
Chongqing University, China

Reviewed by:

Jun Wang,
Shandong University of Science and
Technology, China
Fanzhen Meng,
Qingdao University of Technology,
China

*Correspondence:

Kai Zhang
kzhang@cumt.edu.cn

Specialty section:

This article was submitted to
Geohazards and Georisks,
a section of the journal
Frontiers in Earth Science

Received: 10 November 2021

Accepted: 16 March 2022

Published: 26 April 2022

Citation:

Han X, Zhang K, Xue X and Ma B
(2022) Surrounding Rock Damage
Characteristics and Support
Optimization of Roadway in Soft Gas-
Rich Coal Seam Under the Condition of
Penetrating Hydraulic Reaming.
Front. Earth Sci. 10:812687.
doi: 10.3389/feart.2022.812687

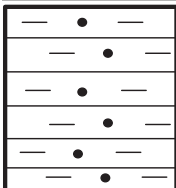
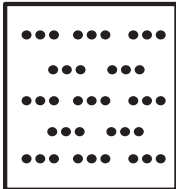

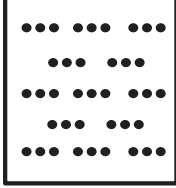
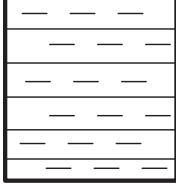
The support of roadways in soft coal seams is a challenge in deep coal mines. For gas-rich coal seams, many methods are developed to drain the gas before mining. The penetrating hydraulic reaming (PHR) is one of the most efficient methods to reduce the gas content and pressure in the coal seams. However, the PHR method will cause many large holes in the coal seam, which brings difficulty to in-seam roadways control. The strength parameters of the coal are essential for roadway stability analysis. However, in soft coal seams, the sampling of the coal is difficult, and the direct evaluation of the coal strength parameters is unfeasible. In the present research, the surrounding rock damage characteristics of the holes induced by PHR are first evaluated by ground-penetrating radar (GPR). Then, the strength parameters of the coal are determined *via* the back-analysis method. After that, the deformation and failure of the roadway are analyzed, and an optimized support scheme is proposed. According to the monitored displacement and measured damage zone of the roadway, the roadway is well controlled by the proposed support scheme.

Keywords: soft-rock mass roadway, support optimization, EDZ, ground support, numerical simulation

INTRODUCTION

In deep coal mines with soft coal seams, the control of roadway stability is a challenge due to the high *in situ* stress and surrounding rock with low strength. (He et al., 2005; Yang et al., 2013; Zong et al., 2014). Although many technologies have been proposed for the roadway support in recent years, the accidents caused by the failure of roadway are still a main threat to the deep coal mines in China (Cai and Kaiser, 2004; Tan et al., 2013; Yang et al., 2013; Felix et al., 2014; Zong et al., 2014). During the excavation of the roadways, the surrounding rock mass will undergo plastic deformation and damage, and an excavation damage zone (EDZ) will arise around the roadway (Melkounian et al., 2009; Sriapai et al., 2013; Yu et al., 2020). The support structure, such as rockbolt or cable, is used to control the extent of EDZ and prevent the deformation of rock mass. Therefore, the estimate of the extent of EDZ in the surrounding rock mass is essential for the support design of roadway. If the mechanical parameters of the rock mass are determined, the EDZ can be analyzed by theoretical analysis or numerical simulation (Coggan et al., 2012; Du et al., 2019; Qin et al., 2019). However, due

TABLE 1 | Condition of coal seam roof and floor.

Column	Name	Rock type	Thickness/m	Rock features
	Main roof	Medium grained sandstone	4.9	Light gray, medium-thick, containing plant fossil
	Immediate roof	Mudstone	10.6	Gray in color, contains coal particles
	Coal	Coal seam	5.3	Massive, developed lower cracks
	Immediate floor	Mudstone	4.5	Gray in color, contains coal particles
	Main floor	Siltstone	2.7	Dark gray, horizontal texture

to the low strength of the coal and distribution of joints, it is difficult to estimate the mechanical parameters of the rock mass either *in situ* or laboratory. Alternatively, many researchers attempt to measure the extent of EDZ directly in the field *via* ground-penetrating radar (GPR) or Goodman jack, et al. However, the *in situ* tests are quite time-consuming and can only evaluate the EDZ, while the roadway has been supported.

For gas-rich coal seams, penetrating hydraulic reaming (PHR) has been one of the most efficient methods to reduce the gas content and pressure in the coal seams (Gao and Xie, 2009; Spearing et al., 2013; Zhang et al., 2015; Jiang et al., 2019). During the excavation of the roadway in the coal seam, the holes induced by PHR may be revealed. The damage zone around the holes can reflect the mechanical properties of the rock mass. Therefore, in the present research, the surrounding rock damage characteristics

of the holes induced by PHR are first determined by GPR. Then, the strength parameters of the rock mass are determined *via* the back-analysis method. Based on the aforementioned analysis, the deformation and failure of the roadway are analyzed, and an optimized support scheme is proposed.

DETECTION OF DAMAGE ZONE AROUND PHR INDUCED HOLES

Geological Conditions

The coal mine of this research is located in Yuzhou City, Shanxi Province, China. The tests were carried out in the # 32051 preparation roadway, which belongs to 32 working faces in the Liangbei coal mine, and its buried depth was -637 m. The roof of

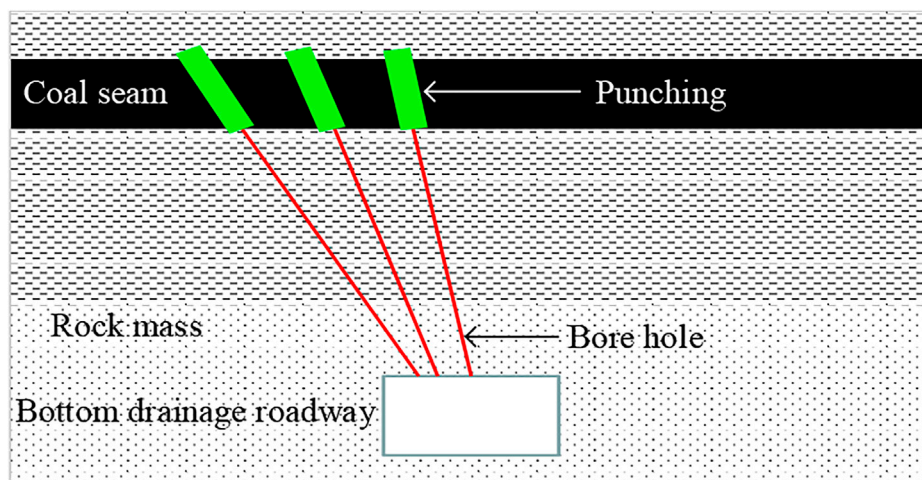


FIGURE 1 | Profile map of PHR.

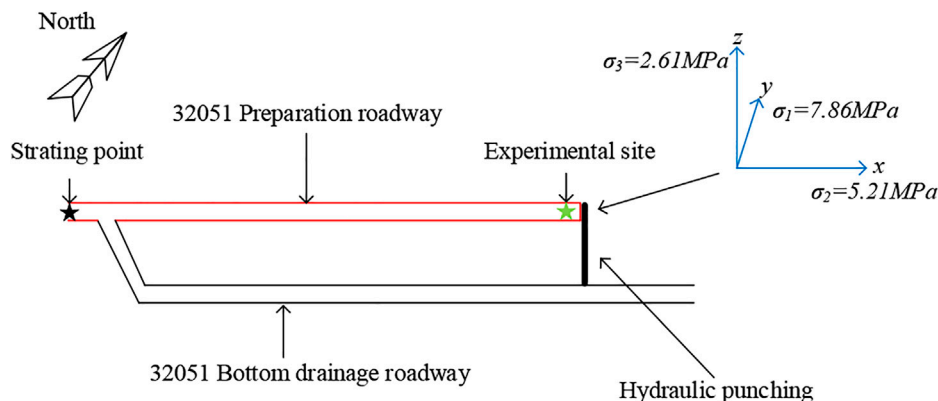


FIGURE 2 | Sketch map of experimental site and ground stress.

the roadway was made of medium-grained sandstone (4.98 m thick) and mudstone (10.64 m thick), while the coal seam floor was mudstone or siltstone (4.51 m thick). The coal seam was 5 m thick on average, with an average compressive strength of 1.63 MPa. They can therefore be considered as soft coal seam (Table 1). The dip angle of the roadway was 0° – 7° . The height of the roadway was 5.3 m, and the width was 5.1 m. In the coal seam, hydraulic reaming with a distance of 6 m was distributed. Before the excavation of the preparation roadway, the reaming hole was drilled in the bottom drainage roadway (Figure 1). In order to determine the damaged zone of the coal seam, three measuring surfaces were chosen before mining.

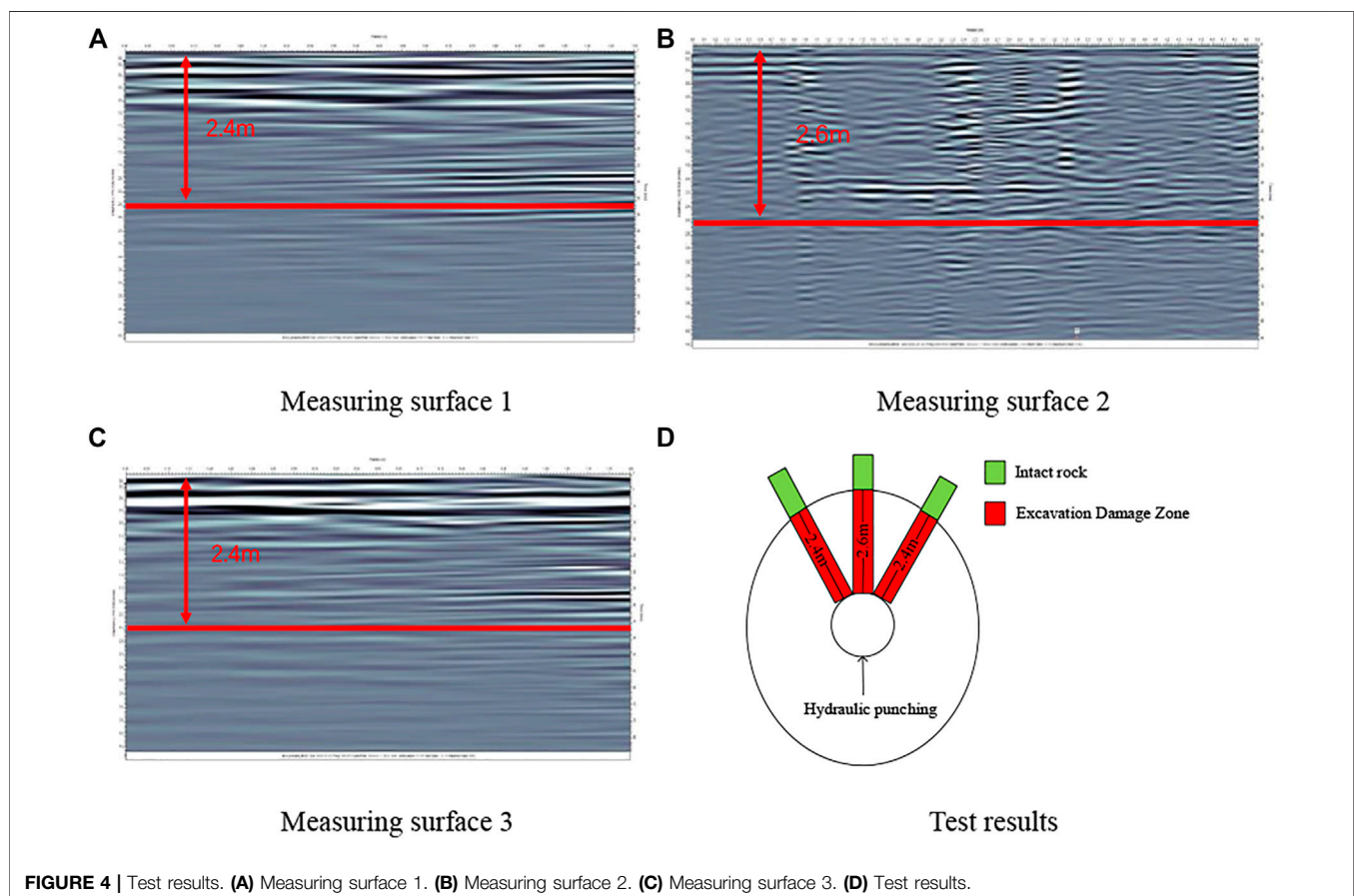
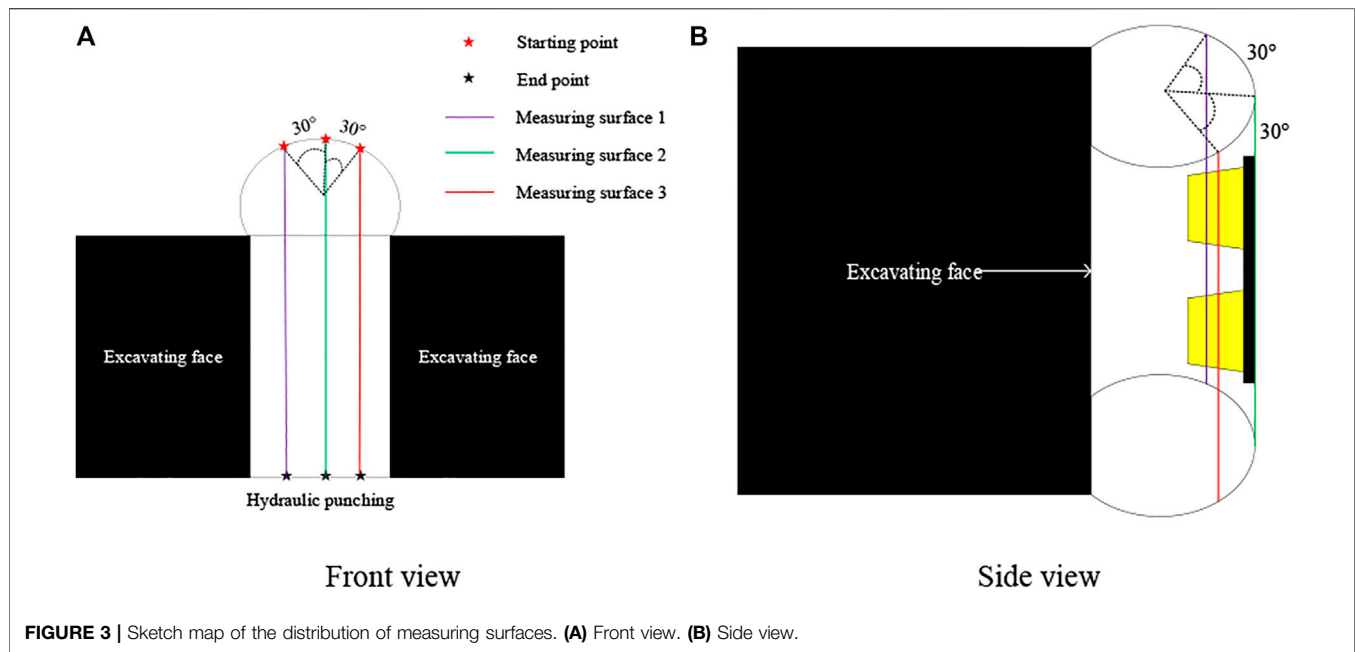
Before the experiment was carried out, the ground stress at the experimental site should be determined. The initial stress was referred to the adjacent Pingdingshan coal mine which has similar geological history and depth. The vertical stress is 2.61 MPa, the maximum and minimum horizontal stresses are 7.86 and 5.21 MPa, respectively. The directions of ground stress are presented (Figure 2).

Experimental Equipment

The Pulse EKKO100 Ground Penetrating Radar (GPR) is used to measure the plastic zone which has an accuracy of 0.01 m. The radar can estimate the EDZ by receiving electromagnetic wave in different mediums. In particular, when electromagnetic waves pass through different mediums, part of them will be reflected. The interfaces among different media can be then analyzed.

Test Scheme and Results

In order to avoid the disturbance caused by the excavation of the roadway, the EDZ was tested immediately once the borehole was finished. Since three points can determine the elliptical extent of the plastic zone, three measuring surfaces were selected at the same borehole for testing, namely, the excavation direction of the roadway and the two directions with an angle of 30° from this axis. During the test, the GPR was slowly moved along the measuring surface from the starting point to the end point (Figure 3).



It can be seen from the image that the electromagnetic wave fluctuates significantly within 2.4 m at measuring surface 1. This shows that this is the junction between the EDZ and the total rock

mass, and the radius of the EDZ of the reaming is then determined. Similarly, the EDZ radius of measuring surfaces 2 and 3 are 2.6 and 2.4 m, respectively. The test results are shown in **Figure 4**.

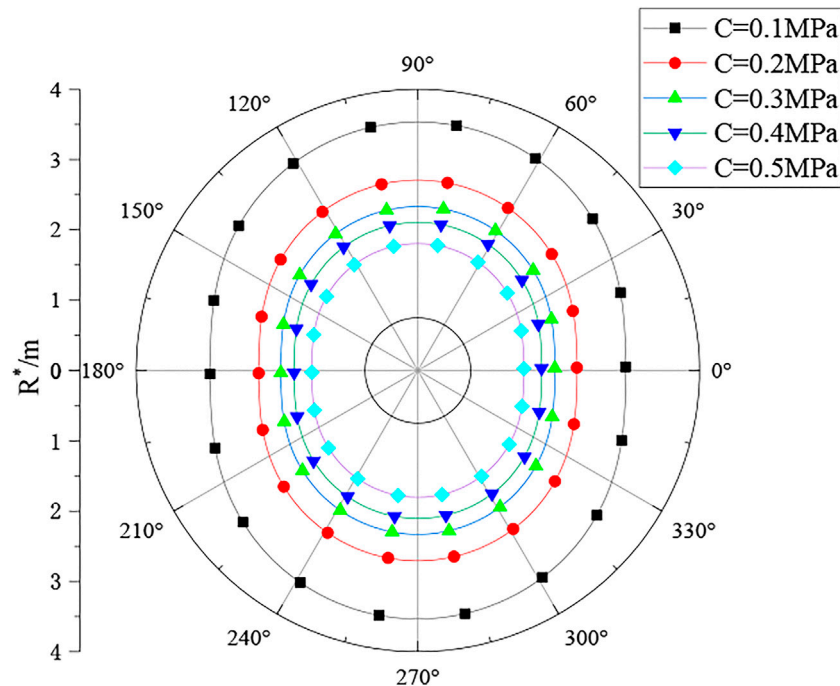


FIGURE 5 | Radius distribution of plastic zone around hydraulic reaming.

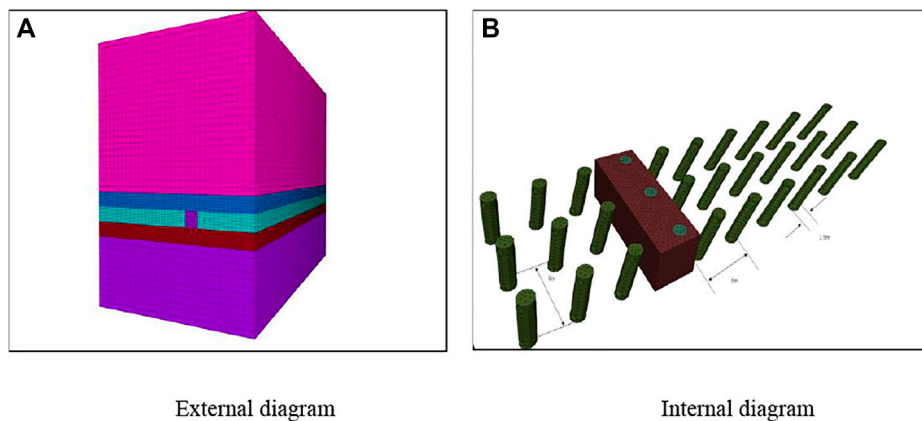


FIGURE 6 | Schematic diagram of the model. **(A)** External diagram. **(B)** Internal diagram.

DETERMINATION OF MECHANICAL PARAMETERS

Since the reaming can be regarded as a long cylinder, the cross section and the constraints parallel to the cross section do not change with the length. Therefore, the analysis of hydraulic reaming can be simplified as a plane strain problem. Due to the unequal horizontal force on the reaming, the side pressure coefficient in the horizontal direction will be considered. Therefore, the function of complex variable is used to reflect the EDZ around the hole. The formulas for calculating the stress

and plastic zone of a borehole in the surrounding rock were established by previous scholars.

$$R^* = \left\{ \sigma_y [(1 + \lambda) + 2(\lambda - 1) \cos 2\theta] + C \cot \eta \right\} \frac{1 - \sin \eta}{(1 - \sin \eta) C \cot \eta} \frac{1 - \sin \eta}{2 \sin \eta} r, \quad (1)$$

There are seven parameters in Eq. 1, where σ_y is the stress along the y-axis, λ is the side pressure coefficient, θ is the angle of the surrounding rock coordinate system, C is the cohesive force, η is the internal friction angle, and r is the radius of the borehole.

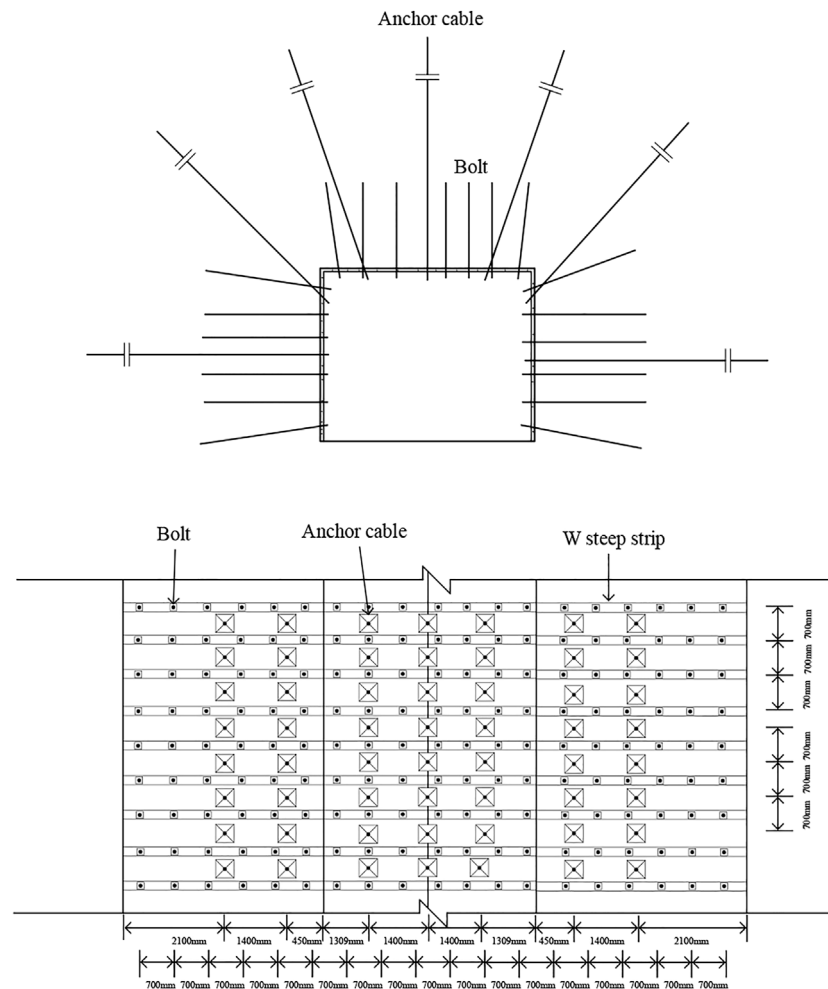


FIGURE 7 | Schematic diagram of cross-sectional support.

In order to calculate the EDZ of the borehole, pass the formula by the analytical solution. It is necessary to explore the size and shape of the EDZ of the borehole under different cohesive forces. According to the geological conditions, the parameter σ_y is 10 MPa, the λ is 1.2, the parameter $r = 0.75$ m, and the internal friction angle $\eta = 27.67^\circ$. Therefore, the parameter C is the only variable in Eq. 1. According to the characteristics of coal seam, the cohesive force C is determined as 0.1, 0.2, 0.3, 0.4, and 0.5 MPa, respectively. Therefore, the EDZ is calculated under different cohesion forces.

The results from Figure 5 showed that the distribution of the EDZ is elliptical, especially the long axis is along the σ_y direction where the ground stress is smaller, and the short axis is along the direction where the ground stress is higher. The distribution of values is regular: $(0^\circ, 180^\circ) > 45^\circ > \text{both sides } (90^\circ, 270^\circ)$. With the increase in cohesive force, the range of EDZ shrinks gradually. Moreover, the degree of change becomes smaller. When the local cohesion C is higher than 0.2 MPa, the changing trend of the radius is obviously reduced with the increase in cohesion and the distribution of the EDZ can be obtained from the results.

Therefore, the long axis of the plastic zone is 5.2 m. The value of the cohesive force C is 0.3 MPa.

SURROUNDING ROCK DAMAGE CHARACTERISTICS OF ROADWAY

In this section, the commercial software FLAC3D was used. The rock mechanics parameters obtained before were used to calculate the EDZ of the roadway.

Model Establishment and Parameter Selection

A numerical simulation model was established based on the geological conditions of Liangbei coal mine, having length, width, and height of 100 m, 70, and 100 m, respectively. The displacement of the model base was 0. Gravity stress was applied on the surface according to the buried depth of the roadway and both the bottom and lateral displacement of the model were fixed.

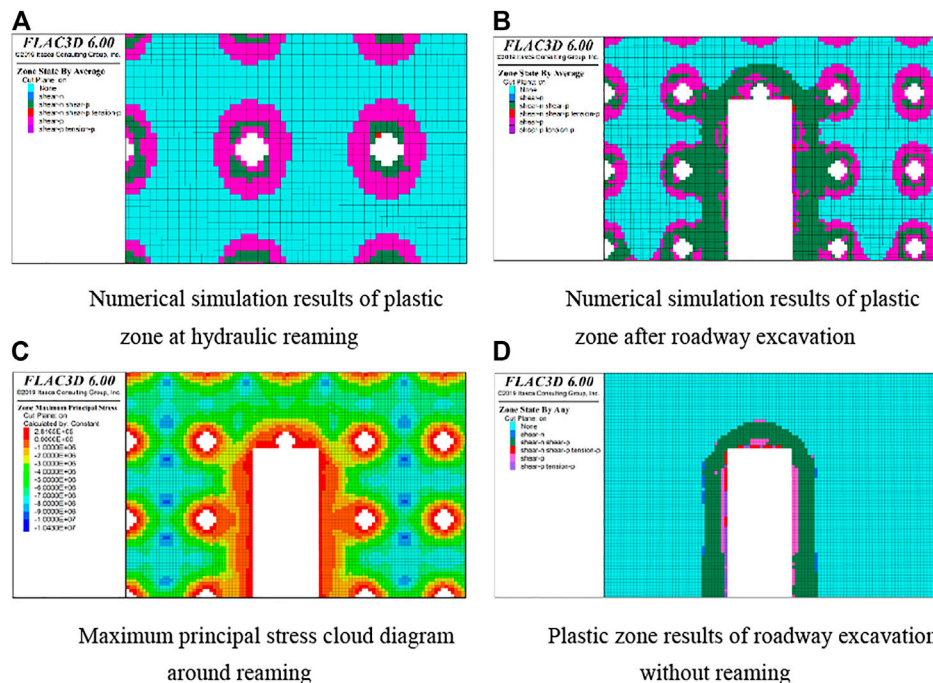


FIGURE 8 | Numerical simulation results. **(A)** Numerical simulation results of plastic zone at hydraulic reaming. **(B)** Numerical simulation results of plastic zone after roadway excavation. **(C)** Maximum principal stress cloud diagram around reaming. **(D)** Plastic zone results of roadway excavation without reaming.

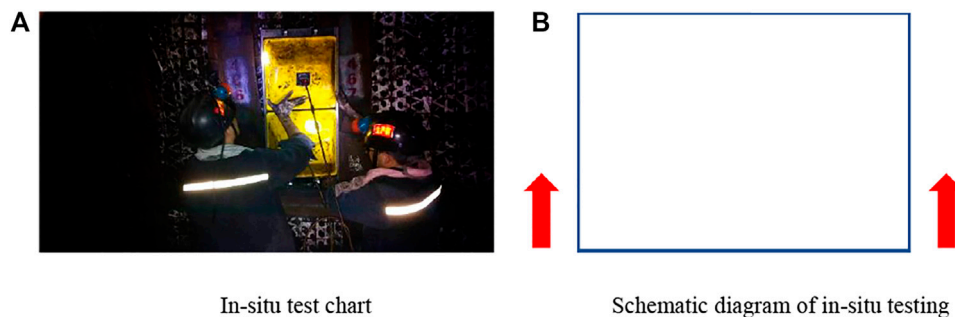


FIGURE 9 | Schematic diagram of *in situ* test. **(A)** *In situ* test chart. **(B)** Schematic diagram of *in situ* testing.

The element mesh model is shown in **Figure 6**. The Mohr–Coulomb failure criterion was used for calculation. According to the conditions on-site, the excavation distance of each step was 3 m. The excavation was carried out step by step. The supporting diagram is shown in **Figure 7**.

Numerical Simulation Results and Analysis

The plastic zone and stress cloud diagrams obtained by numerical simulation are sliced along the horizontal direction and shown in. It can be seen that after the excavation of the hydraulic reaming, the stress in a particular range around the reaming was redistributed. The surrounding plastic zone can match the shape of the plastic zone calculated by **Eq. 1**. The reamed plastic zone under unequal horizontal force presents an

approximately elliptical shape. The long and short axes are perpendicular to the direction of maximum principal stress and minimum principal stress, respectively.

Based on the results, the excavation of the roadway will not increase the radius of the plastic zone at the measuring surfaces. In contrast, the roadway without reaming is excavated, and the cloud graph of the plastic zone is shown in **Figure 8**. It can be seen that the subsequent excavation of the roadway will not affect the range of the plastic zone at the measuring surface.

Simulation Result Verification

In order to verify the results obtained by the numerical simulation, the field test was then carried out. The section at the working face of the roadway is used for measurement. The

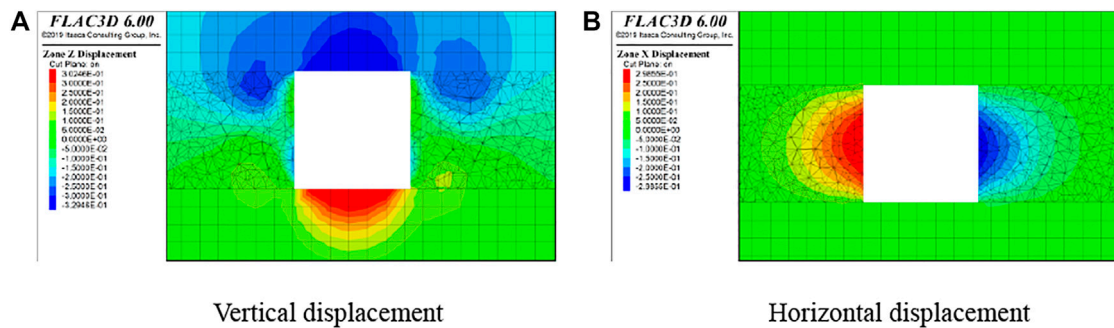


FIGURE 10 | Displacement cloud diagram of initial scheme. **(A)** Vertical displacement. **(B)** Horizontal displacement.

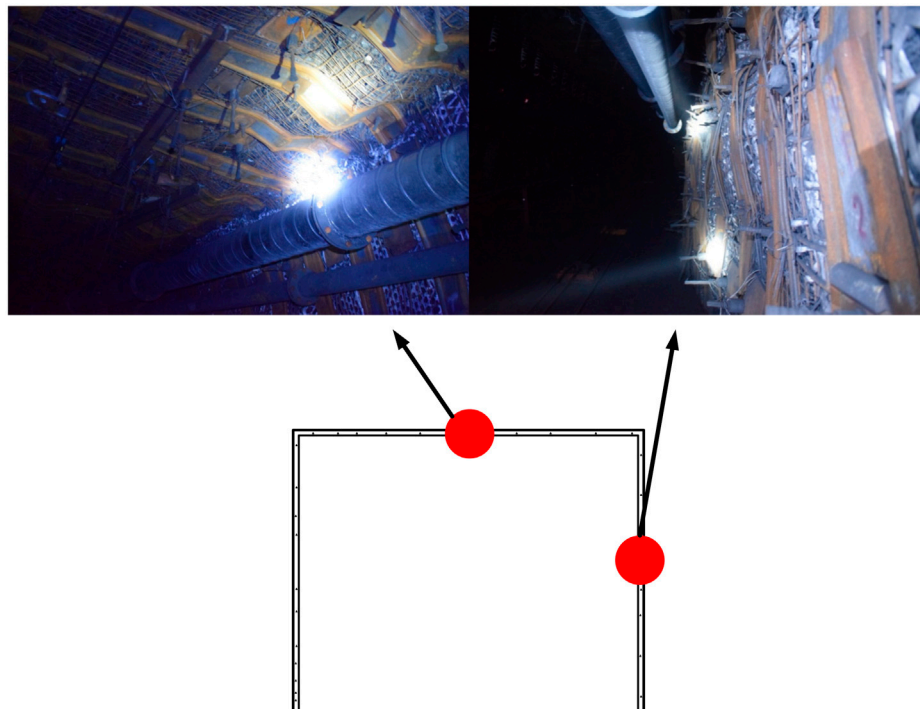


FIGURE 11 | Supporting effect of improve scheme.

GPR was used on both sides of the roadway, and the schematic diagram is shown in **Figure 9**. By analyzing the image obtained using the GPR, the plastic zone radius of both sides of the roadway is 2.8 m, which was similar to the results of the numerical simulation.

RESULTS AND DISCUSSION

Since the parameters obtained before are close to the rock mass on-site, this method can better reflect the distribution of the plastic zone. In this section, the parameters obtained before will be used for the roadway supporting method and parameters

selection. The anchor rod and anchor cable are selected as the primary support tools, and the steel belt joist is the auxiliary support tool.

Mechanism of Anchor Rod and Anchor Cable

- 1) Mechanism of anchor rod: A large number of studies have shown that the primary function of the bolt is to increase the strength, elastic modulus, internal friction angle, and cohesion of the surrounding rock mass after failure. For the tensile and shear areas of the surrounding rock of the



2) Mechanism of anchor cable: The role of the anchor cable is mainly to connect the surrounding rock after the anchor rod is reinforced with the bearing layer of the deep surrounding rock. In this way, the load-bearing capacity of the deep rock mass can be fully improved, and the rock mass in a larger area can be controlled together.

According to the Mining Engineering Design Manual, a mesh reinforcement anchor cable-combined support scheme is carried out in the roadway. The initial support scheme is provided by mesh reinforcement and anchor cable. The roof is supported with a steel mesh, W-type steel belt, thread steel anchor, and anchor cable. A left-handed non-longitudinal rebar normal-strength thread steel anchor is modified to strengthen the support with a diameter of 20 mm and a length of 2600 mm. The anchor cable has a diameter of 21.6 mm and a length of 8000 mm, composed of steel strands. The type of W-type steel belt is BHW-280-4.00 steel belt with a length of 5400 mm. The diameter, length, and width of the steel mesh are 6, 1540, and 840 mm, respectively. The row spacing and column spacing of the thread steel anchor are both 700 mm. The row spacing of the anchor cable is 1400 mm, and the column spacing is 700 mm. The W-type steel belt of two sides adopts the BHW-280-4.00 steel belt with a length of 2500 mm and the BHW-280-4.00 steel belt with a length of 1800 mm. The pre-stressing of anchor cables of two sides is not less than 100 kN,

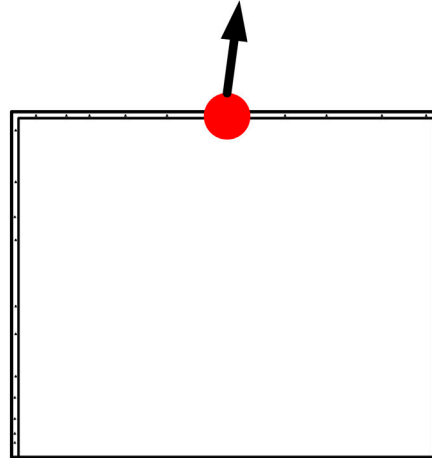


FIGURE 13 | Supporting effect diagram of improved scheme.

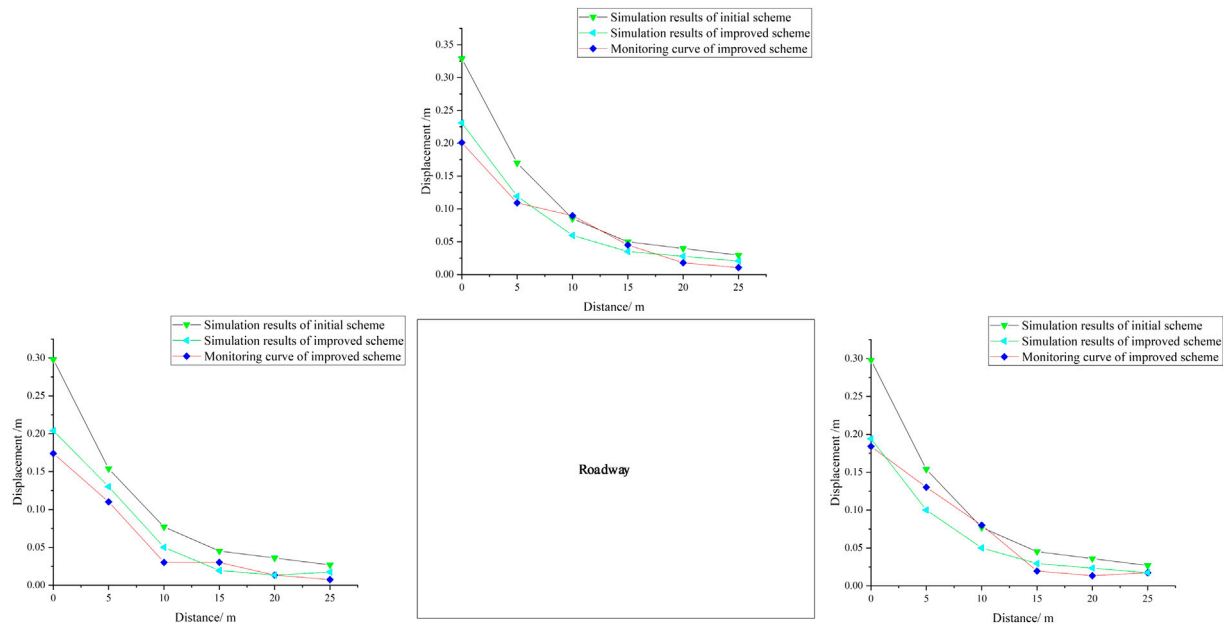


FIGURE 14 | Comparison of two support schemes.

and the pre-stressing of anchor cables of the roof is not less than 300 kN.

Under this support scheme, ground stress balance and excavation are carried out. In order to reduce the influence of boundary conditions on the model, the monitoring section is taken at $y = 5$ m. The displacement cloud diagrams around the roadway obtained by the numerical simulation are shown in **Figure 10**. Moreover, the initial support scheme is implemented, and the results are shown in **Figure 11**.

According to the numerical simulation results and the on-site support schematic diagram, the displacement of the two sides and roof in the first support scheme is large. This is because the anchor cable is located in the middle of the two rows of anchor rods and each tool bears load separately. This means anchor cables and anchor rods are not taken as a whole. The component with larger stiffness can be destructed first, and then other support tools bear loads and damage. This situation will cause the losses of the whole support structure.

The initial scheme only focuses on the support effect of a single element. At the same time, the synergetic effect is ignored. Therefore, in order to improve the outcome of supporting, the bolts strength and density of the anchor are increased blindly. In fact, by appropriately adjusting the acting position of the anchor cable and the connection mode between the anchor cable and the steel anchor, the synergetic support effect can be achieved. It is important to achieve the cooperation between the anchor cable's and anchor rod's design strength. This can improve the safety of the roadway and accelerate the construction schedule. In addition, according to the theory of "Anchor cable pull-out force attenuation during group anchoring" proposed by Professor Shan Renliang of China University of Mining and Technology, the short distance of the anchor cables will cause the stress loss of adjacent anchor cables after tensioning. Therefore, the distance between the anchor cables should be reasonably controlled to fully mobilize the performance of anchor cables and the steel anchors and get the synergetic effect.

Based on the drawbacks of the initial support scheme and the aforementioned theoretical basis, the scheme was optimized. The mesh reinforcement and anchor cable are considered as the main element in the support structure. The steel mesh, W-type steel belt, steel anchor, and anchor cable combined support were used in the roadway. Furthermore, the steel joists are used on both sides of the roadway. The steel joist is made of miner steel, with a total length of 2600 mm and a distance between ends of 600 mm. Moreover, the two rows of steel joists are arranged alternately. In addition, the anchor rods in the top and bottom are inclined upward and downward, respectively, by 15° – 30° . The diagrams of improved support schemes are shown in **Figure 12**.

The effect of the improved scheme is shown in **Figure 13**. The cross-monitoring method is used for displacement

monitoring, and infrared displacement monitoring instruments are placed on the roof and side of the roadway. The displacement of roadway by different support schemes is indicated in **Figure 14**. The top-bottom distance has been reduced by 232 mm, and the two-side distance has been reduced by 208 mm. The improvement is noticeable and the moving amount of the roof and the two sides of the roadway can be limited within 500 mm according to the Mining Engineering Design Manual. The improved scheme can control the excessive deformation of the roadway and maintain the stability of the surrounding rock.

CONCLUSION

- 1) Based on GPR tests, the range of the EDZ at the measuring surfaces of hydraulic reaming was measured, which can be used to calculate the strength parameters through the plastic zone formula based on the complex variable function. The parameters were verified by field experiments and were consistent with the measurement results.
- 2) According to the strength parameters, the displacement in surrounding rock under different support schemes was calculated by means of FALC 3D. The results were verified by field experiments and found to be consistent with the field test results.
- 3) A reasonable joint support scheme and support parameters were designed according to the strength parameters, which can improve bearing performance and ensure the long-term stability of the soft coal seam roadway.

DATA AVAILABILITY STATEMENT

The original contributions presented in the study are included in the article/Supplementary Material, further inquiries can be directed to the corresponding author.

AUTHOR CONTRIBUTIONS

Conception and design of study: XH, KZ and XX. Drafting of the manuscript: XH, KZ and XX. Analysis and/or interpretation of data: XH, KZ and BM.

FUNDING

This work was supported by the National Natural Science Foundation of China (No. 52074260).

REFERENCES

- Cai, M., and Kaiser, P. K. (2004). Assessment of Excavation Damaged Zone Using a Micromechanics Model. *Tunnelling Underground Space Technology* incorporating *Trenchless Technology Res.* 20 (4), 301–310. doi:10.1016/j.tust.2004.12.002
- Coggan, J., Gao, F., Stead, D., and Elmo, D. (2012). Numerical Modelling of the Effects of Weak Immediate Roof Lithology on Coal Mine Roadway Stability. *Int. J. Coal Geology*. 90–91, 100–109. doi:10.1016/j.coal.2011.11.003

- Du, S., Li, D., and Sun, J. (2019). Stability Control and Support Optimization for a Soft-Rock Roadway in Dipping Layered Strata. *Geotech Geol. Eng.* 37 (3), 2189–2205. doi:10.1007/s10706-018-0753-y
- Felix, K., Rüdiger, G., Catherine, A., and Stefan, B. (2014). Seismic Travel-Time and Attenuation Tomography to Characterize the Excavation Damaged Zone and the Surrounding Rock Mass of a Newly Excavated Ramp and Chamber. *INT. J. ROCK MECH. MIN* 70, 524–532. doi:10.1016/j.ijrmms.2014.06.010
- Gao, F.-Q., and Xie, Y.-S. (2009). Resist-decreasing Effects of Rock Bolts on Strength of Rock Mass Around Roadway-Insight from Numerical Modeling. *Mining Sci. Technology (China)* 19 (4), 425–429. doi:10.1016/S1674-5264(09)60079-X
- He, M. C., Xie, H. P., Peng, S. P., and Jiang, Y. D. (2005). Study on Rock Mechanics in Deep Mining Engineering. *Yanshilixue Yu Gongcheng Xuebao/Chinese J. Rock Mech. Eng.* 24 (16), 2803–2813.
- Jiang, L., Kong, P., Shu, J., and Fan, K. (2019). Numerical Analysis of Support Designs Based on a Case Study of a Longwall Entry. *ROCK MECH. ROCK ENG.* 52 (9), 3373–3384. doi:10.1007/s00603-018-1728-2
- Melkounian, N., Priest, S. D., and Hunt, S. P. (2009). Further Development of the Three-Dimensional Hoek-Brown Yield Criterion. *ROCK MECH. ROCK ENG.* 42 (6), 835–847. doi:10.1007/s00603-008-0022-0
- Qin, Z., Fu, H., and Chen, X. (2019). A Study on Altered Granite Meso-Damage Mechanisms Due to Water Invasion-Water Loss Cycles. *ENVIRON. EARTH SCI* 78 (14), 1–10. doi:10.1007/s12665-019-8426-6
- Spearing, A. J. S., Hyett, A. J., Kostecki, T., and Gadde, M. (2013). “New Technology for Measuring the *In Situ* Performance of Rock Bolts,” *Int. J. rock Mech. mining Sci.* 57, 153–166. doi:10.1016/j.ijrmms.2012.07.027
- Sriapai, T., Walsri, C., and Fuenkajorn, K. (2013). “True-triaxial Compressive Strength of Maha Sarakham Salt,” *Int. J. rock Mech. mining Sci.* 61, 256–265. doi:10.1016/j.ijrmms.2013.03.010
- Tan, Y. L., Yu, F. H., and Chen, L. (2013). A New Approach for Predicting Bedding Separation of Roof Strata in Underground Coalmines. *INT. J. ROCK MECH. MIN* 61, 183–188. doi:10.1016/j.ijrmms.2013.02.005
- Yang, X., Pang, J., Liu, D., Liu, Y., Tian, Y., Ma, J., et al. (2013). Deformation Mechanism of Roadways in Deep Soft Rock at Hegang Xing'an Coal Mine. *Int. J. Mining Sci. Technology* 23 (02), 307–312. doi:10.1016/j.ijmst.2013.04.002
- Yu, K., Ren, F., Puscasu, R., Lin, P., and Meng, Q. (2020). Optimization of Combined Support in Soft-Rock Roadway. *Tunnelling Underground Space Technology* 103, 103502. doi:10.1016/j.tust.2020.103502
- Zhang, K., Zhang, G., Hou, R., Wu, Y., and Zhou, H. (2015). Stress Evolution in Roadway Rock Bolts during Mining in a Fully Mechanized Longwall Face, and an Evaluation of Rock Bolt Support Design. *Rock Mech* 48 (1), 333–344. doi:10.1007/s00603-014-0546-4
- Zong, Y., Han, L., Qu, T., and Yang, S. (2014). Mechanical Properties and Failure Characteristics of Fractured sandstone with Grouting and anchorage. *Int. J. Mining Sci. Technology* 24 (02), 165–170. doi:10.1016/j.ijmst.2014.01.004

Conflict of Interest: The authors declare that the research was conducted in the absence of any commercial or financial relationships that could be construed as a potential conflict of interest.

Publisher's Note: All claims expressed in this article are solely those of the authors and do not necessarily represent those of their affiliated organizations, or those of the publisher, the editors, and the reviewers. Any product that may be evaluated in this article, or claim that may be made by its manufacturer, is not guaranteed or endorsed by the publisher.

Copyright © 2022 Han, Zhang, Xue and Ma. This is an open-access article distributed under the terms of the Creative Commons Attribution License (CC BY). The use, distribution or reproduction in other forums is permitted, provided the original author(s) and the copyright owner(s) are credited and that the original publication in this journal is cited, in accordance with accepted academic practice. No use, distribution or reproduction is permitted which does not comply with these terms.



Severe Damage Law on the Ground Surface Induced by High-Strength Mining: A Case Study From the Shendong Coal Field in China

Weitao Yan^{1,2}, Junting Guo¹, Junjie Chen^{2*}, Yi Tan^{2*}, Shaoge Yan² and Yueguan Yan³

¹State Key Laboratory of Groundwater Protection and Utilization by Coal Mining, Beijing, China, ²State Collaborative Innovation Center of Coal Work Safety and Clean-efficiency Utilization, Henan Polytechnic University, Jiaozuo, China, ³College of Geoscience and Surveying Engineering, China University of Mining and Technology (Beijing), Beijing, China

OPEN ACCESS

Edited by:

Wei Liu,
Chongqing University, China

Reviewed by:

R. M. Yuan,
China Earthquake Administration,
China

Qiang Sun,
Xi'an University of Science and
Technology, China

Geng Jiabo,
Jiangxi University of Science and
Technology, China

*Correspondence:

Junjie Chen
chenjj@hpu.edu.cn
Yi Tan
tanyi@hpu.edu.cn

Specialty section:

This article was submitted to
Geohazards and Georisks,
a section of the journal
Frontiers in Earth Science

Received: 02 December 2021

Accepted: 31 March 2022

Published: 29 April 2022

Citation:

Yan W, Guo J, Chen J, Tan Y, Yan S
and Yan Y (2022) Severe Damage Law
on the Ground Surface Induced by
High-Strength Mining: A Case Study
From the Shendong Coal Field
in China.
Front. Earth Sci. 10:827826.
doi: 10.3389/feart.2022.827826

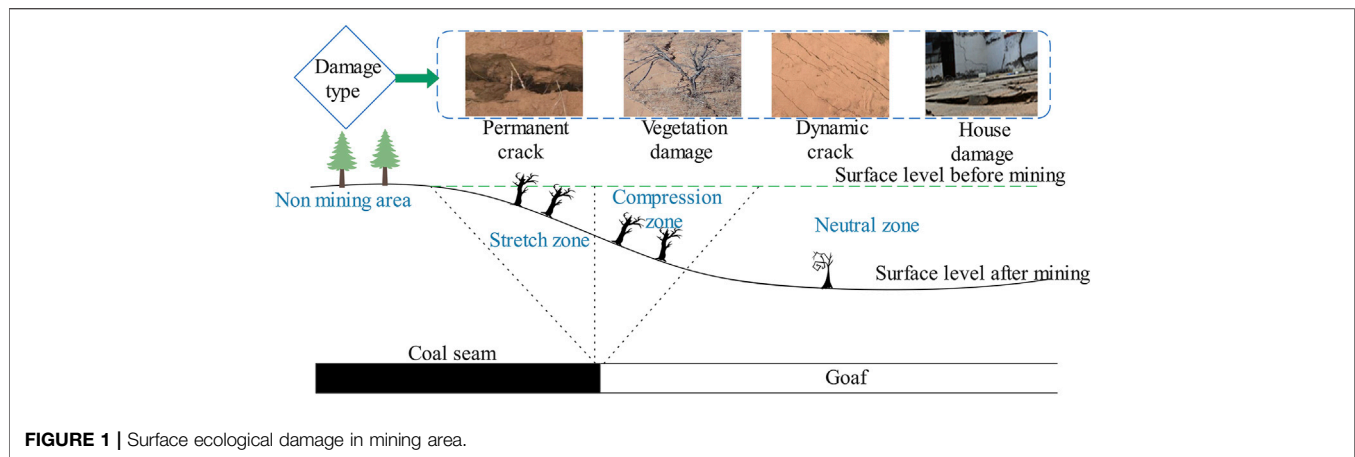
High-strength mining has the characteristics of shallow buried depth, large mining height, and fast mining speed. Under the condition of high-strength mining, the overburden moves violently and the surface damage is serious. It has caused serious ecological security problems in the mining area. In order to solve this problem, it is necessary to adopt the technology of restoration while mining. The key to the effective implementation of this technology is to clarify the real-time distribution law and generation mechanism of surface damage. In this paper, field investigation and the theoretical analysis method are used for related research. The results show that the surface strenuous move duration is long, the strenuous move area is large, and the surface discontinuous deformation is fully developed. With the characteristics of stepped crack lags behind the location of the working face, the stepped crack spacing and periodic weighting interval are equivalent. Through discussion and analysis, it is found that the cause of serious damage is the strata movement mode of high-strength mining in “two zones” mode. Under the “two zones” mode, the roof has easy-to-slip instability, the bedrock is completely broken along the direction of the bedrock breaking angle, and the weak anti-disturbance ability of the loose layer leads to the surface becoming severely damaged. The research results can provide reference for the formulation of follow-up ecological real-time restoration measures in similar mines.

Keywords: severe damage, crack, dynamic distribution, high-strength mining, “two zones” mode

1 INTRODUCTION

China is the largest coal producer and coal consumer in the world. Coal accounted for about 60% of China's primary energy structure in 2019. The mining of a large number of underground coal resources brings about large-scale overburden movement and surface subsidence, which badly disturbs the original ecology and environment, and seriously affects the safe use of buildings, railways, and highways in the subsidence area. A series of economic, ecological, and environmental problems caused by mining have attracted many people's attention (Figure 1).

At present, surface ecological restoration technology is mainly used for the treatment of surface ecological damage in the mining area, but it is usually repaired after mining. There are problems such as poor repair timeliness and low repair rate in this repair mode. In order to solve those problems, the



technology of “restoration while mining” has been put forward in recent years. This technology emphasizes the timeliness and accuracy of repair, and has good application and promotion. The key to the effective implementation of this technology is to grasp the real-time distribution law of surface damage. This is also the content of this paper.

According to the mining subsidence theory (He et al., 1991; Peng, 1992; National Bureau of Coal Industry, 2017), when the ratio of mining depth to mining height is large and mining velocity is fast, the surface subsidence is generally continuous and regular in time and space. For this continuous surface subsidence, many scholars have undertaken a lot of research on its distribution law (Zhang and Chong, 2012; Cui et al., 2014; Thongprapha et al., 2015; Vervoort, 2016; Yan et al., 2018; Bai et al., 2020), generation mechanism (Wang et al., 1999; Ma et al., 2013; Yu et al., 2015; Suchowska Iwaniec et al., 2016; Salmi et al., 2017; Lian et al., 2020), prediction method (Ren et al., 1989; Ramesh and Ram, 1995; Luo and Cheng, 2009; Yan et al., 2019), and the mining-induced social and ecological problem (Bell et al., 2000; Sinha et al., 2007; Tang, 2009; Saha et al., 2011; Sasaoka et al., 2015). An abundance of research results have been obtained and some important results have been extended to the engineering application. But when the ratio of mining depth to mining height is small and the mining velocity is slow, the surface subsidence will often be accompanied by discontinuous movement, and the surface will often produce tensile cracks, stepped cracks, collapse pits, and other disasters (Fan et al., 2011; Ju and Xu, 2013; Fan et al., 2015; Yan et al., 2018; Chen et al., 2019), which will destroy the soil construction, lower the underground aquifer, reduce agricultural production, and endanger the safety of residents in the subsidence area. This highly destructive mining mode is called high-strength mining. The adverse phenomenon induced by high-strength mining can be divided into two kinds, static and dynamic. The static damage distribution law has been fully studied, and related achievements have been obtained and included in textbooks (He et al., 1991; Peng, 1992). But at present, the research results on the dynamic damage distribution law are still few and insufficient.

Under high-strength mining, the ratio of mining depth to mining height is small, the mining velocity is fast, and the

above-mentioned adverse phenomenon is more serious. To deeply study the dynamic law of severe surface damage induced by high-strength mining, this paper selected working face 22,407 in the Shendong coal field, a typical high-strength mining working face, as the sample. By collecting the relevant information of working face 22,407, we studied the dynamic severe damage distribution law and analyzed its subsidence mechanism.

2 ENGINEERING BACKGROUND OF STUDY AREA

The Halagou coal mine is located in Daliuta Town, Shenmu county, Shaanxi Province, at the junction of Mu Us Desert and Loess Plateau, with an annual output of 10 million tons of coal. Working face 22,407, which belongs to the Halagou coal mine is located in the middle of panel 4. The northwest is the central return air roadway of coal seam 22, the northeast is the designed working face 22,408, the southeast is working face 22,610 designed by the Daliuta coal mine, and the southwest is the goaf of working face 22,406. The ground surface of working face 22,407 has little fluctuation and is covered by aeolian sand. Working face 407 mainly mines coal seam 22.

The coal seam within the mining range of working face 22,407 has a simple structure and is a stable coal seam. The coal seam minability index is 1. The geological structure within the minable range of the working face is simple, without the occurrence of large geological events and the existence of large geological structures.

The working face is mainly affected by the water of the Quaternary loose aquifer. The Quaternary loose aquifer is mainly composed of aeolian sand. The aquifer is 10–24 m thick and has a strong water yield. The normal water inflow of the working face is 75 m³/h.

The size of working face 22,407 is 3224 m × 284 m. The bedrock thickness is 73 m, alluvium thickness is 57 m, and the aquifer thickness is 10–24 m. The average thickness, depth, and dip angle are 5.2 m, 130 m and 1°, respectively. According to the geo-mining conditions and borehole histogram of working face 22,407 (Figure 2), the lithology of the overlying strata in this working face is evaluated as medium hard. The comprehensive

Geological time	Numbers of rock layers	Names of rocks	Thickness (m)	Lithology
Quaternary System	20	Aeolian sand	15.66	
	19	Loess	26.34	
	18	Gritstone	13.47	
Zhiluo Formation	17	Sandy mudstone	4.89	
	16	Siltstone	5.35	
	15	Medium sandstone	6.47	
	14	Fine sandstone	4.57	
	13	Siltstone	4.88	
Yan'an Formation	12	Medium sandstone	13.98	
	11	Siltstone	2.02	
	10	Fine sandstone	6.87	
	9	Fine sandstone	3.64	
	8	Medium sandstone	4.42	
	7	Fine sandstone	5.66	
	6	Sandy mudstone	3.29	
	5	Medium sandstone	2.84	
	4	Siltstone	6.68	
	3	2-2 coal seam	5.39	
	2	Siltstone	5.80	
	1	Fine sandstone	4.41	

FIGURE 2 | The borehole log of working face 22407.

mechanized coal mining method is used for mining and the all caving method is used to manage the roof. The average mining velocity of working face 22,407 is 15 m/d.

From the above conditions, we can see that the ratio of mining depth to mining height of working face 22,407 is small and the mining velocity is fast. It is a typical high-strength mining face. Therefore, we chose the data of working face 22,407 to analyze the dynamic damage distribution law and reveal its generation mechanism.

3 MONITORING METHODS AND DATA ACQUISITION

In order to obtain surface movement data, a surface movement observation station was set up on one side of the stoping line of working face 22,407 according to the mine survey regulations. The observation station included one strike surface movement

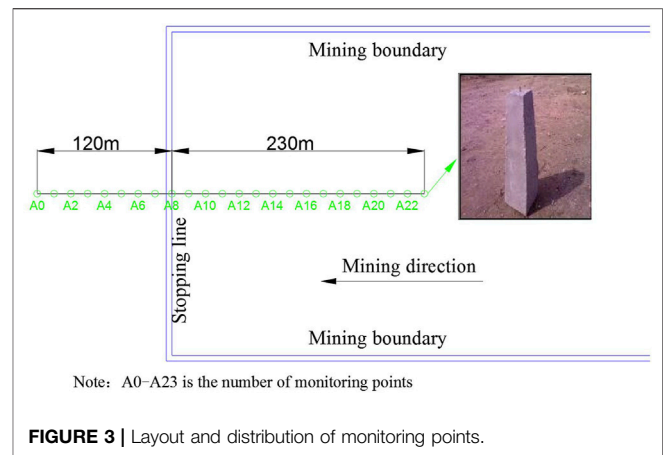


FIGURE 3 | Layout and distribution of monitoring points.

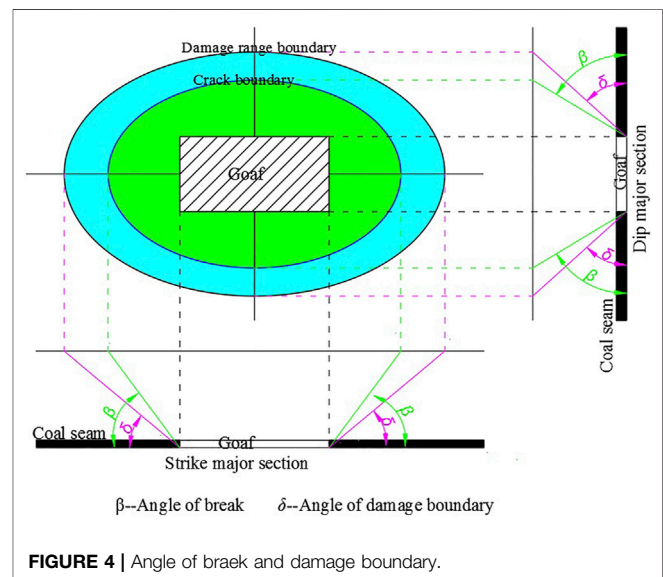


FIGURE 4 | Angle of break and damage boundary.

observation line. The total length of the strike observation line was 350 m, with 24 monitoring points in total, and the density of monitoring points was 15 m. The point layout is shown in Figure 3.

After the monitoring points were arranged, the following monitoring methods were used for data collection (Table 1).

4 RESULTS

4.1 Surface Damage Range

After the exploitation of underground coal resources, the area of surface mining damage was much larger than that of underground mining. According to the knowledge of mining subsidence, the angle of the damage boundary is often used to characterize the range of ground surface movement, and the angle of break is used to characterize the distribution range of surface damage, as shown in Figure 4.

The angle of the damage boundary value can be calculated with Formula (1).

TABLE 1 | Monitoring items and means.




Numbers	Monitoring items	Monitoring means	Corresponding measured photos
1	Subsidence	Leveling	
2	Horizontal displacement	Differential GPS real-time kinematic positioning	
3	Crack	Tape measurement	

TABLE 2 | Duration of each movement period.

	Initial period(d)	Active period(d)	Weakening period(d)
Halagou 22407	9	150	200

$$\beta = \arctan \frac{H}{L_1} \quad (1)$$

Where β is the angle of damage boundary; H is the mining depth; and L_1 is the horizontal distance from the boundary of goaf to the boundary point of 10 mm subsidence. Generally, the value of the boundary angle is approximately $50\text{--}60^\circ$. The angle of the break value can be calculated with **Formula (2)**.

$$\delta = \arctan \frac{H}{L_2} \quad (2)$$

Where δ is the angle of the break and L_2 is the horizontal distance from the boundary of goaf to the surface critical deformation point. The surface critical deformation point is determined from the outermost point with the inclination of 3 mm/m, curvature of 0.2 mm/m^2 , and horizontal movement of 2 mm/m. Generally, the value of boundary angle is approximately 75° .

The inclination, curvature, and horizontal movement value can be calculated with **Formula (3)**.

$$\begin{aligned} i_{12} &= \frac{w_2 - w_1}{l_{12}} \\ K_{123} &= \frac{i_{23} - i_{12}}{\frac{1}{2}(l_{12} + l_{23})} \\ \varepsilon_{12} &= \frac{u_2 - u_1}{l_{12}} \end{aligned} \quad (3)$$

Where w is the subsidence value; i is the inclination value; ε is the horizontal movement value; and u is the horizontal displacement value.

Through field measurement, it is found that the angle of damage boundary of working face 22,407 is 46° , and the angle of break is 70° . Compared with the angular parameters under general conditions, the corresponding angular parameters under high-strength mining conditions are small and the influence range is large.

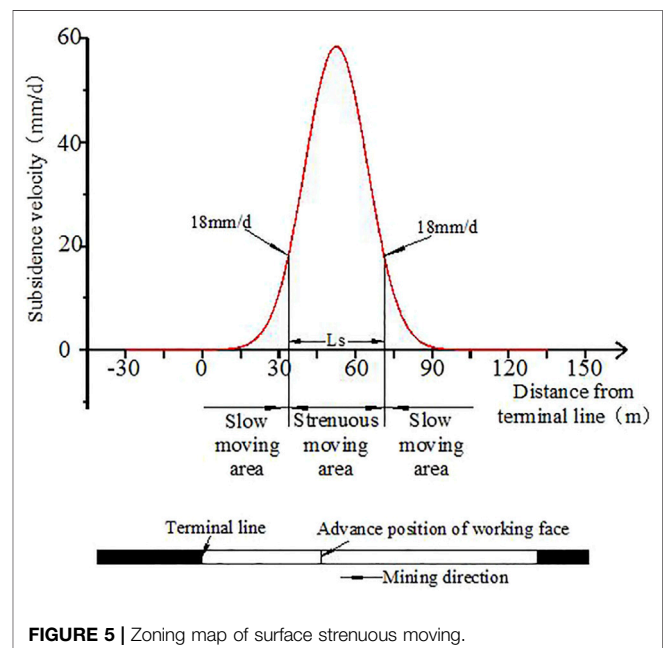
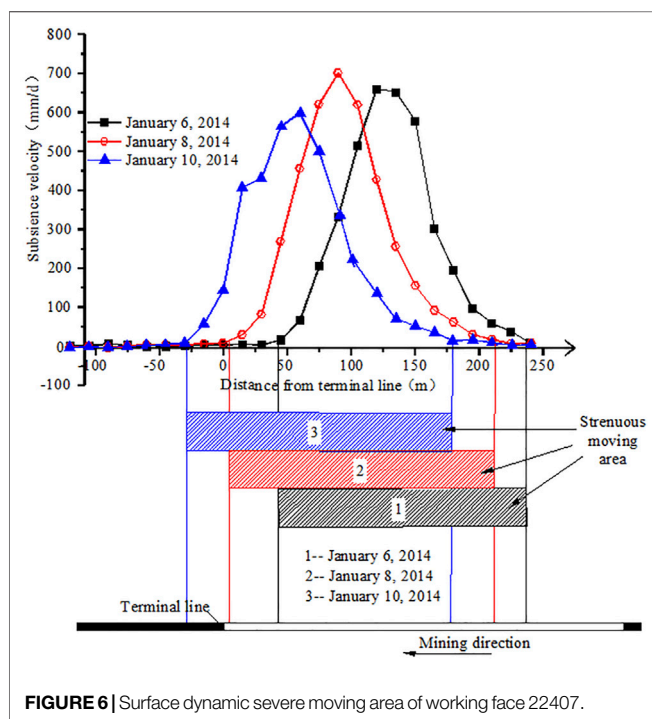
**FIGURE 5** | Zoning map of surface strenuous moving.

TABLE 3 | Width of strenuous moving area.

	Width of strenuous moving area/m	Mining depth/m	Ratio of the strenuous moving area width to mining depth
2014-01-06	197	130	1.52
2014-01-08	205	130	1.58
2014-01-10	203	130	1.56
Average	201.7	130	1.55

TABLE 4 | Location of strenuous moving area.

Date	Distance between the advanced position of the working face and the left boundary of the strenuous moving area/L (m)	Width of strenuous moving area/L _s (m)	L/L _s
2014-01-06	40	191	0.209
2014-01-08	38	198	0.192
2014-01-10	38	202	0.188
Average	38.67	197	0.196

**FIGURE 6** | Surface dynamic severe moving area of working face 22407.

4.2 Surface Damage Degree

The damage degree of the ground surface above the gob can be reflected by the magnitude of surface subsidence velocity. The surface subsidence velocity can be calculated by the following formula.

$$v_n = \frac{w_{i+1} - w_i}{t} \quad (4)$$

Where v_n is the subsidence velocity of point n ; w_{i+1} , w_i is the subsidence value of point n measured at $i + 1$ and i times, mm; and t is the interval between two measurements, d.

The maximum subsidence velocity of working face 22,407 is 700 mm/d, so the surface has undergone strenuous movement and violent deformation during the mining process under the condition of high-strength mining. To analyze the dynamic distribution laws of ground surface severe damage, we evaluated two aspects: the temporal and spatial distribution

characteristics of severe surface damage and the dynamic distribution laws of surface cracks.

4.2.1 Temporal Distribution of Surface Single Point Severe Damage

The surface point in the subsidence trough experiences the process from when it begins to move to the end of movement. The movement process of a surface point can be described by the subsidence velocity. The whole movement duration, according to the subsidence velocity, can be divided into three periods: initial period, active period, and weakening period (He et al., 1991; Peng, 1992; National Bureau of Coal Industry, 2017).

Initial period. From the beginning of the movement of the surface to the time when subsidence velocity reaches 1.67 mm/d or 50 mm/month.

Active period. Time interval when subsidence velocity is greater than 1.67 mm/d.

Weakening period. From the time when the movement of the surface decreases to 1.67 mm/d to the time when subsidence ends.

During these three periods, the surface points in the active period had the largest subsidence velocity and suffered the most damage. The longer the active period lasts, the more severe the damage to the surface points. The movement duration of working face 22,407 is shown in **Table 2**.

As can be seen from **Table 2**, the whole movement duration was 359 days, and the initial period, active period, and weakening period accounted for 2.5, 41.8, and 55.7% of the whole movement duration, respectively. The initial period was very short. The surface point entered the active period soon after it was affected by mining activities. The duration of the active period and weakening period was close to half of the whole movement duration. Compared with the traditional law (He et al., 1991; Peng, 1992; National Bureau of Coal Industry, 2017), it can be seen that under high-strength mining conditions, the active period was longer, and the severe damage to the surface point was more serious.

4.2.2 Spatial Distribution Law of Severe Surface Damage

At a certain time, the subsidence velocity differed for each point on the major section of the subsidence trough. According to the subsidence velocity, its strenuous movement degree can be

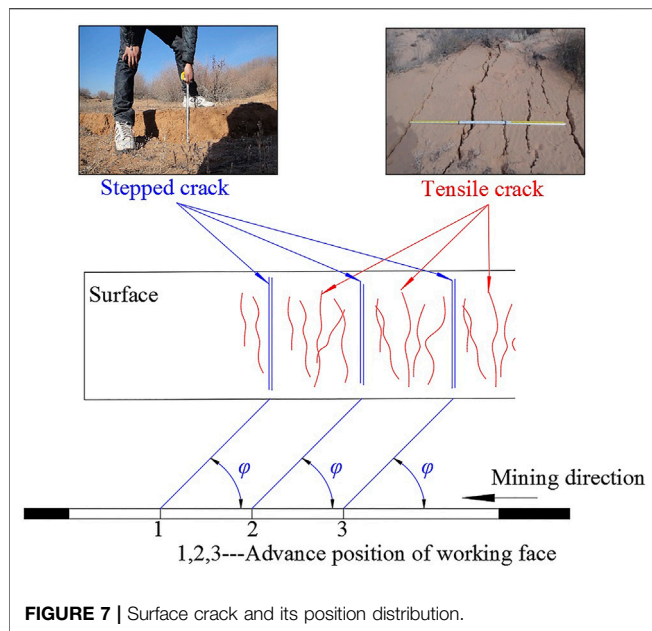


FIGURE 7 | Surface crack and its position distribution.

described by partition. A subsidence velocity of 18 mm/d was given as the critical value to define level IV damage to buildings. This paper also uses it to divide the dynamic subsidence trough into two zones (Figure 5).

Slow moving area: the surface subsidence velocity in this area is not greater than 18 mm/d; Strenuous moving area: the surface subsidence velocity in this area is larger than 18 mm/d.

When the face advances a sufficient distance, the width of strenuous moving area reaches its maximum possible value. The field-measured width of the strenuous moving area is shown in Table 3.

It can be seen from the above table that the strenuous moving area width was approximately 1.55 times the mining depth. That is, under high-strength mining conditions, the scope of the ground surface point moved violently and severe damages were generally large. The development of the strenuous moving area as the face advanced is shown in Figure 6.

The distance between the advanced position of the working face and the left boundary of the strenuous moving area under various advance positions of the working face measured in the Halagou coal mine are shown in Table 4.

From Table 3, the distance between the advanced position of the working face and the left boundary of the strenuous moving area for all three periods were equal to 1/5 of the strenuous moving area width. That is, the advanced position of working face was located at the left 1/5 of the strenuous moving area width.

In summary, under high-strength mining conditions, the time duration of severe damage to the surface points was relatively long, and the area where the surface was severely damaged was relatively wide. The severely damaged area was a dynamic area, which continuously moved forward as the working face advanced.

4.2.3 Surface Dynamic Crack and Its Development Rules

The ratio of mining depth to mining thickness of the high-strength mining working face was small and the dynamic crack was fully developed. The dynamic crack mainly had tensile cracks and stepped cracks as shown in Figure 7. The development of tensile crack had high density and small width. In addition, a stepped crack appeared in cycles.

The development of dynamic crack has the following characteristics:

- 1) A stepped crack lags behind the advanced position of working faces.

The overburden layer failure is developed along the direction of the bedrock fracture angle in the bedrock and along the similar vertical direction in the loose layer. The failure directly reaches to the surface and forms a stepped crack. A stepped crack lags behind the advanced position of the working face. The lag distance is called the lag distance of the stepped crack (Eq. 5), the corresponding angle is called the lag angle of the stepped crack (Eq. 6).

$$L_t = H_j \times \cot \gamma \quad (5)$$

$$\varphi = \arctan\left(\frac{L_t}{H_0}\right) \quad (6)$$

Where L_t is the lag distance of the stepped crack (m), φ is the lag angle of the stepped crack ($^\circ$), H_j is the thickness of bedrock (m), H_0 is the average mining depth (m), and γ is the bedrock fracture angle ($^\circ$).

A bedrock fracture angle of 52–57° at the side of the working face was measured (Yan et al., 2018). An average angle value of 55° was used as the bedrock fracture angle value. According to Eqs 2, 3, the lag distance of the stepped crack is 62.3 m and the lag angle of the stepped crack is 64.6°.

The field-measured lag distance of the stepped crack under various advanced positions of the working face are shown in Table 5. It can be seen from Table 5 that the calculation results are basically consistent with the field measurement results.

- 2) Stepped crack spacing and periodic weighting interval fairly.

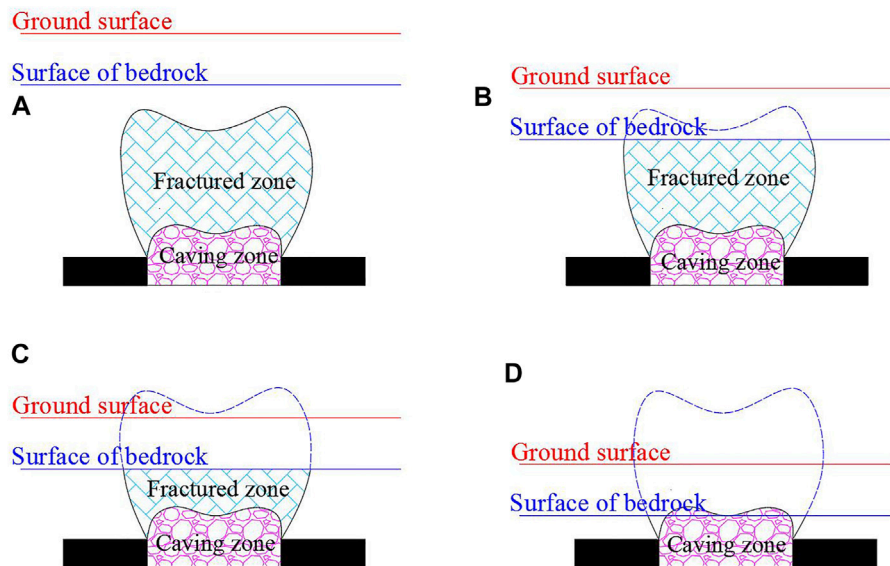
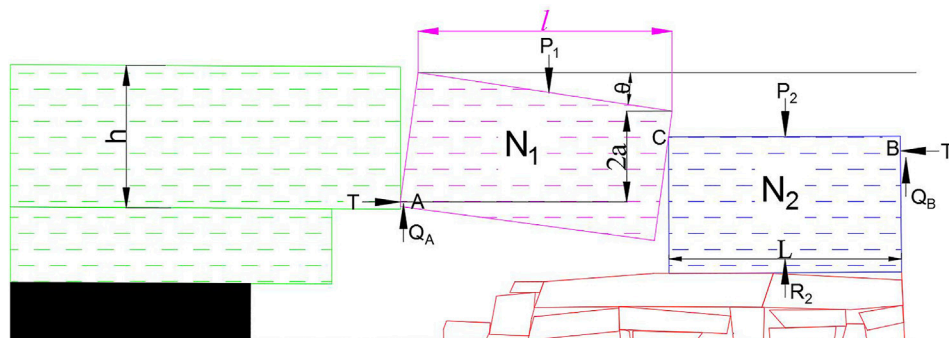
The measured spacing between stepped cracks is 8–11 m along the advance direction of the working face. The periodic weighting interval is 10 m, which is basically the same as the former.

5 DISCUSSION

In the vertical direction, under the condition of general geological mining, after rock strata movement, the overlying strata can be divided into three different mining influence areas: caving zone, fractured zone, and sagging zone. Because the caving zone and fractured zone easily conduct water, they are jointly called the water conducting fractured

TABLE 5 | Relative position of the stepped crack and the working face.

Date	Horizontal distance between the working face and terminal line/m	Horizontal distance between the outside stepped crack and terminal line/m	Horizontal distance between the outside stepped crack and working face/m
6 January 2014	77–94	146	52–69
8 January 2014	40–60	117	57–77
10 January 2014	3–19	78	59–75

**FIGURE 8** | Develop types of overlying strata.**FIGURE 9** | Failure mode and mechanics model of overlying strata.

zone. However, under special geological and mining conditions, the movement law of overlying strata is different, and the three mining influence zones in overburden strata do not exist at the same time. Which can be summarized as four types, as shown in **Figure 8**.

Type one: The “three zones” of overlying rock are fully developed. The caving zone, fractured zone, and sagging zone exist at the same time (**Figure 8A**).

Type two: The fracture zones directly reach the top surface of the bedrock, but do not reach the ground surface (**Figure 8B**).

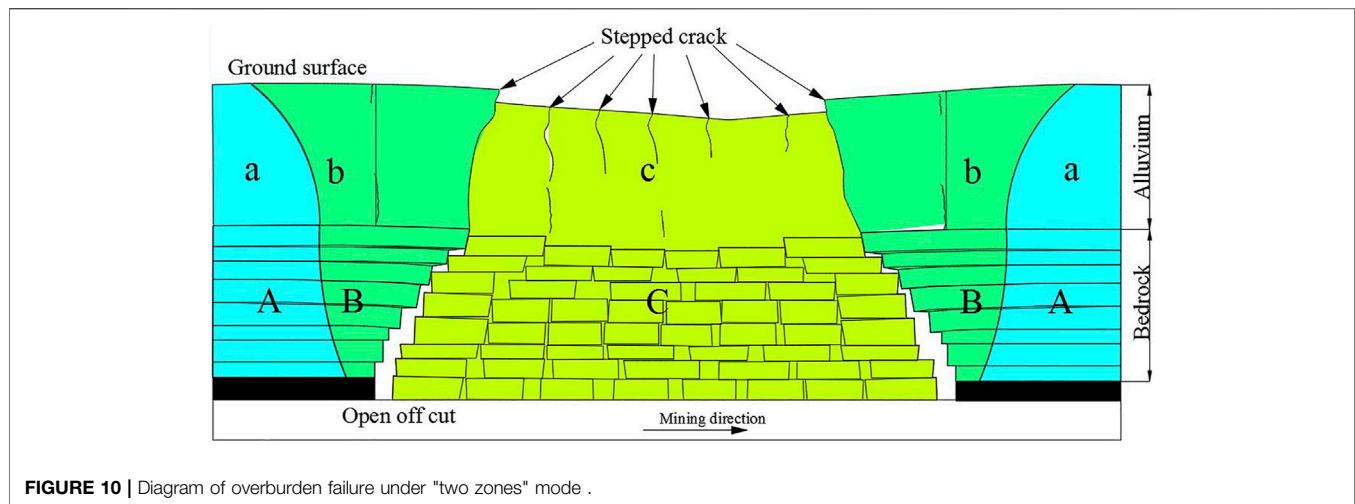


FIGURE 10 | Diagram of overburden failure under "two zones" mode .

Type three: The fracture zone directly reaches the ground surface (**Figure 8C**).

Type four: The caving zone directly reaches the top surface of bedrock (**Figure 8D**).

Under high-strength mining, the calculation formula of the height of caving zone and fracture zone is as follows (Yan et al., 2018).

$$H_c = (6.94M - 17.3) \pm 4.7 \quad (7)$$

$$H_f = (2.62M + 53.77) \pm 8.7 \quad (8)$$

Where H_c is the height of the caving zone; H_f is the height of the fracture zone; and M is the mining thickness.

Through calculation, it was found that the fracture zone height of working face 22,407 was greater than the bedrock thickness. The fractured zone directly reached the surface of bedrock. Therefore, the type of overlying strata movement of the working face conformed to type two. That is to say, the type of overlying strata movement of high-strength mining was the "two zones" mode.

Under the "two zones" mode, the migration of the roof is shown in **Figure 9**.

According to the moment equilibrium, **Formulas 9–12** can be derived.

$$Q_A + Q_B = P_1 \quad (9)$$

$$T = \frac{lP_1}{2(h-a-w)} = \frac{P_1}{i - 2 \sin \theta_{\max} + \sin \theta} \quad (10)$$

$$Q_B = T \sin \theta_2 \quad (11)$$

$$a = 0.5(h - l \sin \theta) \quad (12)$$

Where Q is the shear force; P is the suffered load; T is the horizontal thrust; l is the length of rock block; h is the height of rock block; θ is the rotation angle of rock block; and i is the rock fragmental size, $i = l/h$.

Since θ_2 is very small, Q_B can be ignored, so $Q_A = P_1$. According to a previous study (Qian et al., 2012), the maximum value of θ in this area is $8-12^\circ$, i is greater than 1, and the tangent value of the friction angle is 0.5. When these

values are brought into the above formula, the following relationship can be obtained:

$$i - 2 \sin \theta_{\max} + \sin \theta > 0.584 \quad (13)$$

Therefore, the relationship between the shear force and friction force of the arch foot is calculated as follows.

$$T \tan \varphi = \frac{P_1}{i - 2 \sin \theta_{\max} + \sin \theta} < \frac{0.5P_1}{0.584} < P_1 = Q_A \quad (14)$$

It can be seen that the sliding instability easily occurs in the "two zones" mode. The sliding instability of the roof can easily lead to the stepped subsidence of strata and induce the overburden to break in full thickness. As seen in **Figure 10**, because the loose layer is prone to shear failure, the stepped subsidence of strata easily leads to the formation of stepped cracks on the ground surface.

Besides, the loose layer above working face 22,407 is thick, up to 55 m. And the cohesion between particles in the loose layer such as aeolian sand is small. This will lead to the following two situations.

- 1) The thick loose layer is equivalent to softening of the rock stratum, which increases the influence range and degree of surface mining.
- 2) Due to the weak anti-disturbance ability of the loose layer, the ground surface will be seriously damaged by underground high-strength mining, and it is easy for many small irregular tension cracks to appear on the ground surface between stepped cracks (**Figure 7**).

6 CONCLUSION

Through analysis of field-measured data, the characteristics of severe surface damage induced by high-strength mining were summarized. The main conclusions are as follows:

- 1) Severe surface damage lasts for a long time and has a wide range. The duration of the active period is close to half of the whole movement duration. The width of the strenuous moving area is equal to 1.55 times the mining depth. The advanced position of the working face is located at the left 1/5 of the strenuous moving area width. The strenuous moving area is a dynamic area, which continuously moves forward as the working face advances.
- 2) The dynamic crack types of surface and their periodic distribution laws induced by high-strength mining are summarized. The development of tensile cracks has high density and small width. In addition, stepped cracks appear in cycles, and the step crack spacing and the periodic weighting interval is consistent. The surface dynamic tensile cracks reflect the surface tension process between the two roof breakages.
- 3) The overburden strata failure in the “step beam” model and the strata move in the “two zones” mode. The sliding instability of the roof results in stepped subsidence of rock strata and further stepped cracks on the ground surface. In addition, rock strata are completely broken, resulting in severe surface damage.

DATA AVAILABILITY STATEMENT

The raw data supporting the conclusion of this article will be made available by the authors, without undue reservation.

REFERENCES

- Bai, E. H., Guo, W. B., Tan, Y., Huang, G. S., Guo, M. J., and Ma, Z. B. (2020). Roadway Backfill Mining with Super-high-water Material to Protect Surface Buildings: a Case Study. *Appl. Sci.* 10, 107. doi:10.3390/app10010107
- Bell, F. G., Stacey, T. R., and Genske, D. D. (2000). Mining Subsidence and its Effect on the Environment: Some Differing Examples. *Environ. Geol.* 40, 135–152. doi:10.1007/s002540000140
- Chen, C., Hu, Z. Q., Wang, J., and Jia, J. T. (2019). Dynamic Surface Subsidence Characteristics Due to Super-large Working Face in Fragile-Ecological Mining Areas: A Case Study in Shendong Coalfield, China. *Adv. Civ. Eng.* 2019, 1–16. doi:10.1155/2019/8658753
- Cui, X., Gao, Y., and Yuan, D. (2014). Sudden Surface Collapse Disasters Caused by Shallow Partial Mining in Datong Coalfield, China. *Nat. Hazards* 74, 911–929. doi:10.1007/s11069-014-1221-5
- Fan, G. W., Zhang, D. S., and Ma, L. Q. (2011). Overburden Movement and Fracture Distribution Induced by Longwall Mining of the Shallow Coal Seam in the Shendong Coalfield. *J. China Univ. Min. Tech.* 40, 196–201.
- Fan, L. M., Zhang, X. T., and Xiang, M. X. (2015). Characteristics of Ground Fissure Development in High-Intensity Mining Area of Shallow Seam in Yushenfu Coal Field. *J. China Coal Soc.* 40, 1442–1447. doi:10.13225/j.cnki.jccs.2014.1707
- He, G. Q., Yang, L., and Ling, G. D. (1991). *Mining Subsidence Theory*. Xuzhou, China: China University of Mining and Technology Press.
- Ju, J., and Xu, J. (2013). Structural Characteristics of Key Strata and Strata Behaviour of a Fully Mechanized Longwall Face with 7.0m Height Chocks. *Int. J. Rock Mech. Min. Sci.* 58, 46–54. doi:10.1016/j.ijrmms.2012.09.006
- Lian, X., Zhang, Y., Yuan, H., Wang, C., Guo, J., and Liu, J. (2020). Law of Movement of Discontinuous Deformation of Strata and Ground with a Thick Loess Layer and Thin Bedrock in Long Wall Mining. *Appl. Sci.* 10, 2874. doi:10.3390/app10082874
- Luo, Y., and Cheng, J. W. (2009). An Influence Function Method Based Subsidence Prediction Program for Longwall Mining Operations in Inclined Coal Seams. *Min. Sci. Tech.* 19, 0592–0598. doi:10.1016/s1674-5264(09)60110-1

AUTHOR CONTRIBUTIONS

Conceptualization, WY; methodology, JC; software, WY; validation, YT and JG; formal analysis, WY; investigation, SY; resources, YY; data curation, JG; writing—original draft preparation, WY; writing—review and editing, WY; visualization, JG; supervision, YT; project administration, JC; funding acquisition, JC. All authors have read and agreed to the published version of the manuscript.

FUNDING

This research was funded by the Open Fund of State Key Laboratory of Water Resource Protection and Utilization in Coal Mining (grant numbers WPUKFJ2019-20 and WPUKFJ2019-17), the Henan Scientific and Technological Projection (grant number 212102310012), the National Natural Science Foundation of China (grant numbers U21A20108 and 51974105), the Fundamental Research Funds for the Universities of Henan Province (grant number NSFRF200314), the Youth Backbone Teacher Support Program of Henan Polytechnic University (2019XQG-07), and Doctoral Fund Program of Henan Polytechnic University (B2017-07, B2019-03).

- Ma, L., Zhang, D., Sun, G., Cui, T., and Zhou, T. (2013). Thick Alluvium Full-Mechanized Caving Mining with Large Mining with Large Mining Height Face Roof Control Mechanism and Practice. *J. China Coal Soc.* 38, 199–203. doi:10.13225/j.cnki.jccs.2013.02.017
- National Bureau of Coal Industry (2017). *Pillars and Mining Regulation of Building, Water, Railway and Main Shaft and Tunnel*. Beijing, China: China Coal Industry Publishing House.
- Peng, S. S. (1992). *Surface Subsidence Engineering*. New York, USA: Society of Mining Engineers.
- Qian, M. G., Shi, P. W., and Xu, J. L. (2012). *Mining Pressure and Strata Control*. Xuzhou: China Uni Min Tech Pub, 374.
- Ramesh, P. S., and Ram, N. Y. (1995). Prediction of Subsidence Due to Coal Mining in Raniganj Coalfield, West Bengal, India. *Eng. Geol.* 39, 103–111. doi:10.1016/0013-7952(94)00062-7
- Ren, G., Whittaker, B. N., and Reddish, D. J. (1989). Mining Subsidence and Displacement Prediction Using Influence Function Methods for Steep Seams. *Min. Sci. Technol.* 8, 235–251. doi:10.1016/s0167-9031(89)90393-9
- Saha, S., Pattanayak, S. K., Sils, E. O., and Singha, A. K. (2011). Under-mining Health: Environmental Justice and Mining in India. *Health & Place* 17, 140–148. doi:10.1016/j.healthplace.2010.09.007
- Salmi, E. F., Nazem, M., and Karakus, M. (2017). The Effect of Rock Mass Gradual Deterioration on the Mechanism of Post-mining Subsidence over Shallow Abandoned Coal Mines. *Int. J. Rock Mech. Min. Sci.* 91, 59–71. doi:10.1016/j.ijrmms.2016.11.012
- Sasaoka, T., Takamoto, H., Shimada, H., Oya, J., Hamanaka, A., and Matsui, K. (2015). Surface Subsidence Due to Underground Mining Operation under Weak Geological Condition in Indonesia. *J. Rock Mech. Geotechnical Eng.* 7, 337–344. doi:10.1016/j.jrmge.2015.01.007
- Sinha, S., Bhattacharya, R. N., and Banerjee, R. (2007). Surface Iron Ore Mining in Eastern India and Local Level Sustainability. *Resour. Policy* 32, 57–68. doi:10.1016/j.resourpol.2007.06.001
- Suchowska Iwanec, A. M., Carter, J. P., and Hambleton, J. P. (2016). Geomechanics of Subsidence above Single and Multi-Seam Coal Mining. *J. Rock Mech. Geotechnical Eng.* 8, 304–313. doi:10.1016/j.jrmge.2015.11.007

- Tang, F.-q. (2009). Research on Mechanism of Mountain Landslide Due to Underground Mining. *J. Coal Sci. Eng. China* 15, 351–354. doi:10.1007/s12404-009-0403-3
- Thongprapha, T., Fuenkajorn, K., and Daemen, J. J. K. (2015). Study of Surface Subsidence above an Underground Opening Using a Trap Door Apparatus. *Tunn. Undergr. Space Technol.* 46, 94–103. doi:10.1016/j.tust.2014.11.007
- Vervoort, A. (2016). Surface Movement above an Underground Coal Longwall Mine after Closure. *Nat. Hazards Earth Syst. Sci.* 16, 2107–2121. doi:10.5194/nhess-16-2107-2016
- Wang, J. Z., Kang, J. R., and Chang, Z. Q. (1999). The Mechanism Analysis on the Dissymmetry of the Surface Subsidence Basin. *J. China Coal Soc.* 24, 252–255.
- Yan, W., Chen, J., and Yan, Y. (2019). A New Model for Predicting Surface Mining Subsidence: the Improved Lognormal Function Model. *Geosci. J.* 23, 165–174. doi:10.1007/s12303-018-0008-1
- Yan, W., Dai, H., and Chen, J. (2018). Surface Crack and Sand Inrush Disaster Induced by High-Strength Mining: Example from the Shendong Coal Field, China. *Geosci. J.* 22, 347–357. doi:10.1007/s12303-017-0031-7
- Yu, B., Zhao, J., Kuang, T., and Meng, X. (2015). *In Situ* investigations into Overburden Failures of a Super-thick Coal Seam for Longwall Top Coal Caving. *Int. J. Rock Mech. Min. Sci.* 78, 155–162. doi:10.1016/j.ijrmms.2015.05.009
- Zhang, J., and Chong, L. (2012). The Discussion of the Surface and Building Deformation in the Coal Mining Subsidence Area. *Shanxi Archit.* 38 (09), 83–84. doi:10.13719/j.cnki.cn14-1279/tu.2012.09.012

Conflict of Interest: The authors declare that the research was conducted in the absence of any commercial or financial relationships that could be construed as a potential conflict of interest.

Publisher's Note: All claims expressed in this article are solely those of the authors and do not necessarily represent those of their affiliated organizations, or those of the publisher, the editors and the reviewers. Any product that may be evaluated in this article, or claim that may be made by its manufacturer, is not guaranteed or endorsed by the publisher.

Copyright © 2022 Yan, Guo, Chen, Tan, Yan and Yan. This is an open-access article distributed under the terms of the Creative Commons Attribution License (CC BY). The use, distribution or reproduction in other forums is permitted, provided the original author(s) and the copyright owner(s) are credited and that the original publication in this journal is cited, in accordance with accepted academic practice. No use, distribution or reproduction is permitted which does not comply with these terms.



Research on 3D Development Characteristics of Water-Conducting Fractured Zone Based on Field Measurement

Dong Feng^{1,2*}, Enke Hou^{1,2*}, Shuangming Wang^{1,2}, Xiaoshen Xie^{1,2}, Feng Yuan³, Liangliang Guo⁴, Gang Wang⁴, Yongli Xie⁵ and Zhen Chen⁵

¹College of Geology and Environment, Xi'an University of Science and Technology, Xi'an, China, ²Shaanxi Provincial Key Laboratory of Geological Support for Coal Green Exploitation, Xi'an, China, ³Shaanxi Institute of Geological Survey, Xi'an, China, ⁴Shaanxi 185 Coal Field Geology Co., Ltd, Yulin, China, ⁵Shaanxi Xiaobaodang Mining Co., Ltd, Yulin, China

OPEN ACCESS

Edited by:

Wei Liu,
Chongqing University, China

Reviewed by:

Gang Wang,
Shandong University of Science and
Technology, China
Iman Hajirasouliha,
The University of Sheffield,
United Kingdom

*Correspondence:

Dong Feng
zyfd20180619@163.com
Enke Hou
houek@xust.edu.cn

Specialty section:

This article was submitted to
Geohazards and Georisks,
a section of the journal
Frontiers in Earth Science

Received: 04 November 2021

Accepted: 21 April 2022

Published: 26 May 2022

Citation:

Feng D, Hou E, Wang S, Xie X, Yuan F,
Guo L, Wang G, Xie Y and Chen Z
(2022) Research on 3D Development
Characteristics of Water-Conducting
Fractured Zone Based on
Field Measurement.
Front. Earth Sci. 10:808931.
doi: 10.3389/feart.2022.808931

With the large-scale mining of coal resources in western China, coal resources are gradually shifting from shallow to deep mining. In coal seam mining, the overlying rock water-conducting fractured zone (WCFZ) is the main factor causing mine water damage and water resource damage. Accurately grasping the development height of the water-conducting fissure zone is the key to the prevention of water hazards and the protection of water resources in medium-deep coal seams. In this study, the 3D development form of the WCFZ in the middle and deep coal seam mining is studied by the integrated method of drilling and 3D seismic survey, taking the first mining face of Xiaobodang No.1 mine in Yushen such that the height of the WCFZ measured by drilling is 81.50–177.07 m. The height of WCFZ development in the 3D seismic survey was 79.83–178.03 m, and the morphology of the WCFZ was saddle-shaped. This study provides methodological guidance for predicting the 3D morphology and developmental characteristics of the WCFZ. The results obtained are of great significance for the safe, green, and efficient mining of coal seams in medium and deep buried ecologically fragile environments.

Keywords: field measurement, 3D seismic survey, water-conducting fractured zone, 3D development characteristics, medium-deep coal seam

INTRODUCTION

As the most important disposable energy source in China, according to forecasts, coal will remain the major contributor to more than 50% of China's primary energy, so the coal-based energy mix will not change for a long time (Zhou et al., 2020; Dong et al., 2021).

When the coal seam is mined, the overlying rock layer will inevitably be damaged and the coal seam goaf was divided into three zones: caved zone, fracture zone, and continuous bending zone (Figure 1). The caved zone and fracture zone will be interconnected to form the WCFZ (Zhang et al., 2018). If the development of the WCFZ penetrates the overlying bedrock aquifer or the ground surface, it will cause the groundwater level to drop (Wang G et al., 2017; Gui et al., 2020; Wang S et al., 2017), ground collapse (Yan et al., 2018; Yang et al., 2019; Zhou et al., 2020; Dawei et al., 2019), land desertification (Sun et al., 2017; Li et al., 2018), and other environmental issues and even cause mine water gushing accidents, threatening the safety of mining. Mastering the development characteristics of the WCFZ is the key to ensuring the safe, green, and efficient mining of coal resources, and it is the

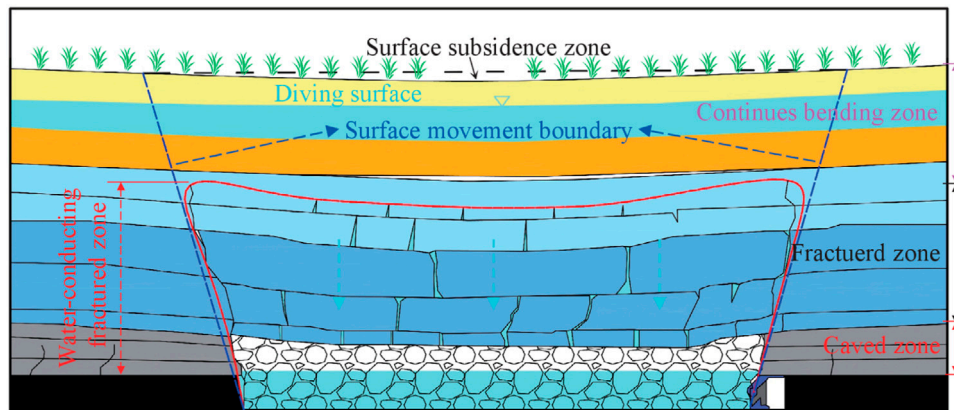


FIGURE 1 | Division zones of the coal-roof strata after mining.

basic condition to reduce the ecological environment damage. In response to the aforementioned hot issues, some scholars have explored the characteristics of the WCFZ using different methods. Development height of the WCFZ was analyzed by field actual measurement of drilling leakage fluid, borehole TV observation, and theoretical calculation (Sui et al., 2015; Zhang et al., 2018). Also, there are scholars who use UDEC (Gao et al., 2014; Du and Gao, 2017), FLAC (Gao et al., 2014; Liu et al., 2019), PFC (Liu et al., 2015), RPPA (Liu et al., 2019; Fan et al., 2020), similar material simulation (Liu et al., 2019; Xie et al., 2021), and other methods to study the development height of the WCFZ.

Most of the currently carried out methods include field measurements, theoretical calculations, numerical simulations, similar material simulations, and empirical formulae calculation. Although the use of geological drilling combined with logging curves to determine H_{WCFZ} development is highly accurate, the detection effect is only seen in one hole, and the cost of drilling is high. With the development of mining equipment and advances in coal mining technology, some empirical formulas and theoretical studies are no longer sufficient to predict H_{WCFZ} development in existing mines related to high-intensity mining. Physical and numerical modeling methods are scaled to actual mining conditions, and these methods are mainly suitable for predicting the height of H_{WCFZ} in mines with relatively simple geological conditions; in complex and variable geological conditions, the simulation results may differ significantly from the field results due to scaling effects. In recent years, 3D seismic exploration technology is mostly used for geological formations, resource endowment, and exploration of stratigraphic undulations (Li et al., 2017; Pei, 2020). With the update of 3D seismic data processing software, the resolution accuracy of 3D seismic data is continuously improved, which achieves clearer imaging and more accurate location of underground exploration targets.

There are relatively few studies related to the developmental characteristics of the WCFZ generated after coal seam retrieval by means of 3D seismic technology. In summary, this study uses 3D seismic exploration to investigate its spatial morphology and a new method guide for predicting the 3D developmental

morphology of the WCFZ. The 3D seismic survey results were also compared with the field actual WCFZ measurements to further verify the reliability of the 3D seismic survey results.

The Jurassic coalfield in northern Shaanxi is the largest coal base in China. The ecological environment is fragile and water resources are scarce. It is urgent to accurately grasp the 3D shape and development characteristics of the WCFZ to provide a theoretical reference for safe, green, and efficient mining of coal resources and down the ecological environment. This study takes the first mining face of Xiaobaodang No.1 as an example to carry out the study on the 3D morphology and development characteristics of the WCFZ.

BACKGROUND

The Yushen mine is located in the abdomen of the Jurassic coalfield in northern Shaanxi, with large reserves, simple geological structure, and excellent coal quality.

The Xiaobaodang No. 1 mine is located in the northeastern part of the Phase III planning area of the Yushen mine (Figure 2). Most of the surface is covered by quaternary wind-deposited semi-fixed sand dunes and fixed sand dunes, with wind erosion and wind-deposited desert hills as the main landforms. The general topographic trend is high in the southwest and low in the northeast, with the highest elevation at 1,346.60 m and the lowest elevation at 1,198 m and the general elevation at 1,250–1,300 m, with a maximum relative height difference of 148.60 m.

According to the geomorphic cause, geomorphic form, and composition material, the geomorphic unit of the Xiaobaodang No. 1 mine can be divided into three types of geomorphic features: sand dunes, windy sandy land, and sand-covered red soil mount landforms, among which sand dunes are divided into fixed sand dunes accounting for 14.3%; semi-fixed sand dunes accounting for 69.6%; flowing sand dunes accounting for 5.1%; windy sandy landforms accounting for 10.9%; and sand-covered red soil mount landforms accounting for 0.1%.

The first coal seam in the Xiaobaodang mine is 2⁻² coal, with an average recoverable thickness of 5.80 m. The lithology of the

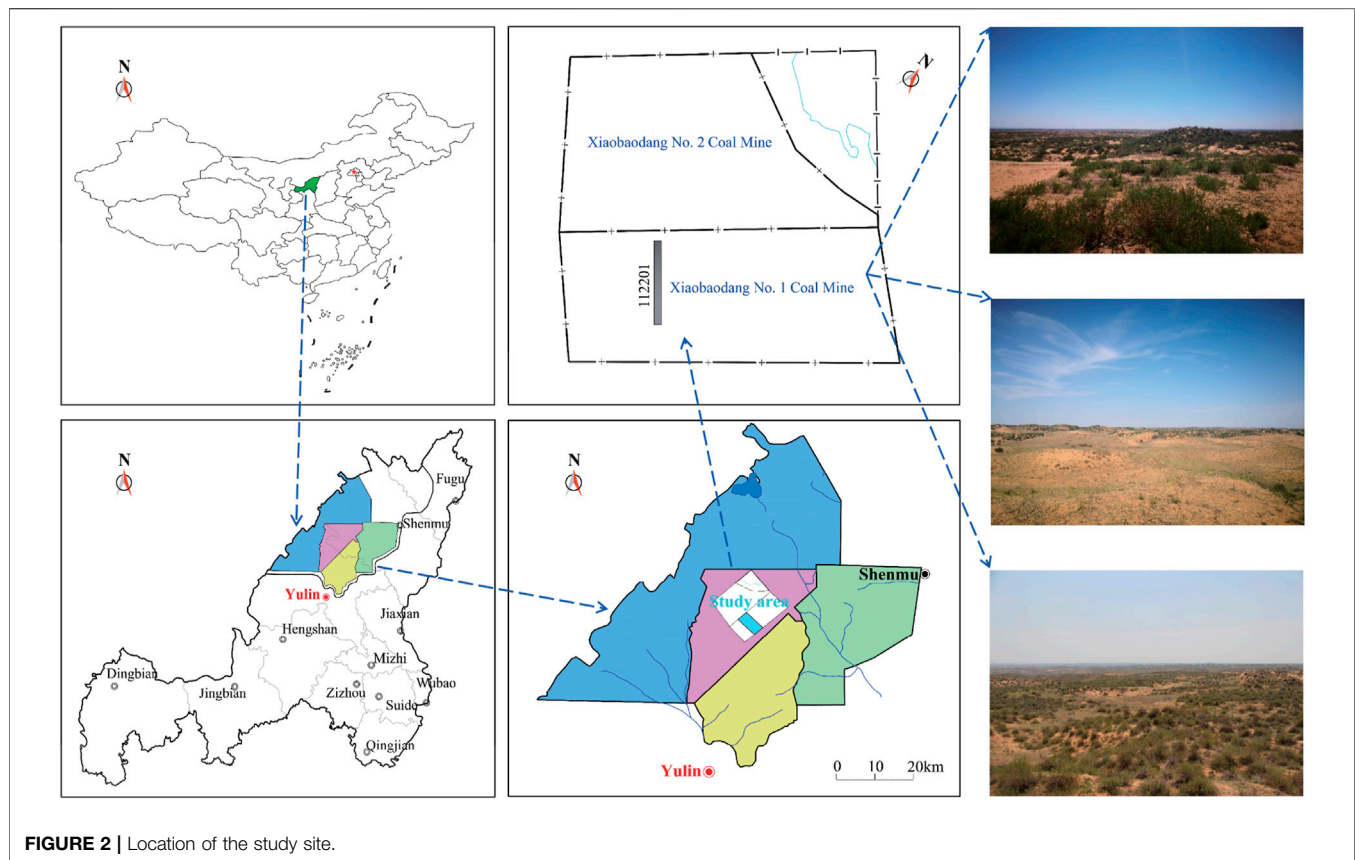


FIGURE 2 | Location of the study site.

coal seam roof is mainly siltstone and fine-grained sandstone, and the burial depth is about 199.69–401.22 m. The first working face is 112,201, with a strike length of 4,660 m and a width of 350 m, and uses a full-height integrated mining process with an average coal seam thickness of 5.8 m. The overlying bedrock of the 2⁻² coal seam is mainly sandstone, with a thickness of about 180–260 m. A comprehensive bar chart of the stratigraphy of the study site is shown in **Figure 3**.

DRILLING MEASURED WCFZ

Drilling Construction Location

The 112,201 working face is the first of the Xiaobaodang coal mine. The previous holes D1 and D2 were drilled on the inclination of the workings, and only the development characteristics of the WCFZ in the dip direction were obtained. In order to further grasp the 3D development characteristics of the WCFZ, combined with the previous construction of boreholes, the drilling location of this arrangement satisfies the vertical arrangement along the advancing direction, the inclination direction of the working face, and the drilling location in **Figure 4**.

The development height of the WCFZ was analyzed and studied using the leakage of flushing fluid and borehole TV during the construction of the drilling. **Figure 4** shows the location of the drilling construction.

Field Measurement Results

Figure 5 shows the extent of flushing fluid leakage and borehole TV detection results during the construction of different boreholes.

From **Figure 5A**, it can be seen that the flushing fluid leakage in borehole D4 varies from 0.0 to 0.46 L/s, with an average value of 0.16 L/s at a depth of 95 m. This indicates a very low leakage of borehole flushing fluid within 95 m, mainly due to development of fractures in the primary formation. When the depth is greater than 95 m, the leakage fluid suddenly rises to 1.95 L/s. The variation of flushing fluid leakage during drilling from 114.25 m to 121.84 m ranged from 0.18 to 0.3443 L/s, with an average value of 0.26 L/s. The amount of flushing fluid leakage during drilling was from 121.84 to 124.46 m, with the range varying from 0.7803 to 1.1475 L/s and the average value increased to 0.9639 L/s. Then, from 124.46 m drilling to 124.80 m, the flushing fluid circulation was suddenly interrupted, and all leakage fluid suddenly was lost. This indicates that the drill bit has entered the top boundary of the WCFZ. From this, it is determined that the top boundary position for the development of the WCFZ is 124.80 m. The borehole TV result shows that 123.3 m is the top boundary of the WCFZ in D4.

From **Figure 5B**, it can be seen that the flushing fluid circulates normally when the depth of the D5 borehole is less than 229.40 m, and the consumption ranges from 0.00 to 0.63 L/s, with an average value of 0.083 L/s. At a depth of 229.40 m, all the drilling flushing fluid was lost, and the leakage amount was

Layer	Columnar	Average thickness/m	Lithology
Q ₄ ^{col}		14.26	sand
Q ₃ ^S		26.66	clayey silt sand
N _{2b}		65.00	red clay
J _{2a}		52.30	mudstone and siltstone
J _{2z}		80.30	mainly mudstone, siltstone, fine-grained feldspar sandstone, and feldspar complex sandstone
		1.16	1 ⁻¹ coal
		25.67	mainly medium-fine-grained and coarse-grained sandstone
J _{2y} ⁵		31.60	mainly siltstone and mudstone
		5.8	2 ⁻² coal

FIGURE 3 | Comprehensive bar chart of the stratigraphy of the study site.

3.33 L/s. The drill bit has entered the top boundary of the WCFZ. From this, it is determined that the top boundary position for the development of the WCFZ is 229.40 m. The borehole TV result shows that 222.3 m is the top boundary of the WCFZ in D5.

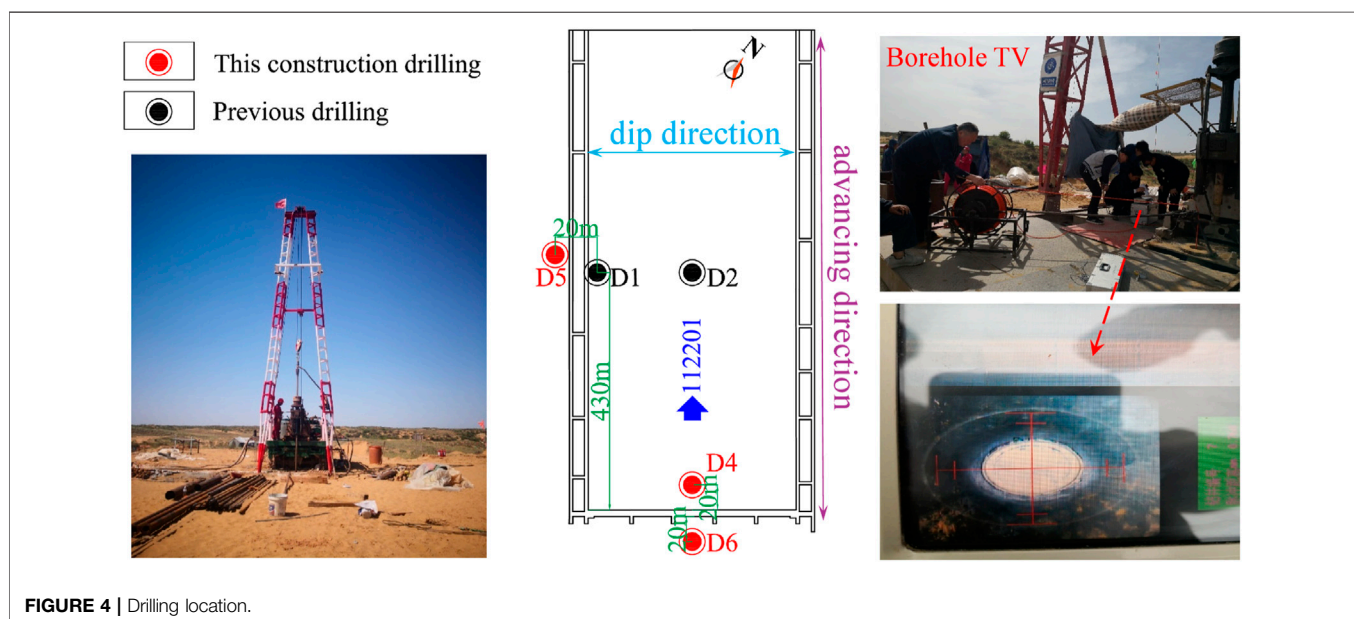
From **Figure 5C**, it can be seen that the flushing fluid circulates normally in drilling D6 during drilling, and the flushing fluid leakage varies from 0.00 to 0.315 L/s, with an average value of 0.06 L/s. This means that the mining-induced WCFZ was not developed in D6. The borehole TV results in D6: the borehole wall was smooth without cracks, and no cracks were produced.

The borehole TV is a continuous real-time observation of the whole hole section and can intuitively locate and quantitatively describe WCFZ development and distribution position of the rock body accurately, with high accuracy, which can realize the visualization and digitalization of mining. When recording the flushing fluid loss in segments during drilling, there is an observation lag error, resulting in some deviation from the recorded result, which can only determine the approximate range of the developed height of the WCFZ. Therefore, the height of the WCFZ measured by borehole TV is the final result in this study, and the WCFZ development height of each drilling is shown in **Table 1**.

High-Density 3D Seismic Exploration of the WCFZ

The 3D development characteristics of the WCFZ and 3D seismic exploration are carried out on the basis of the actual measurement of the WCFZ in the drilling. The development height of the WCFZ obtained by two different methods is compared to verify the accuracy of the interpretation results of 3D seismic exploration.

Based on this, the high-density 3D seismic field data acquisition range is arranged within the scope of the working face drilling construction, which is convenient for comparison and research. The data acquisition area is about 0.31 km². The scope of 3D seismic construction is shown in **Figure 6**.



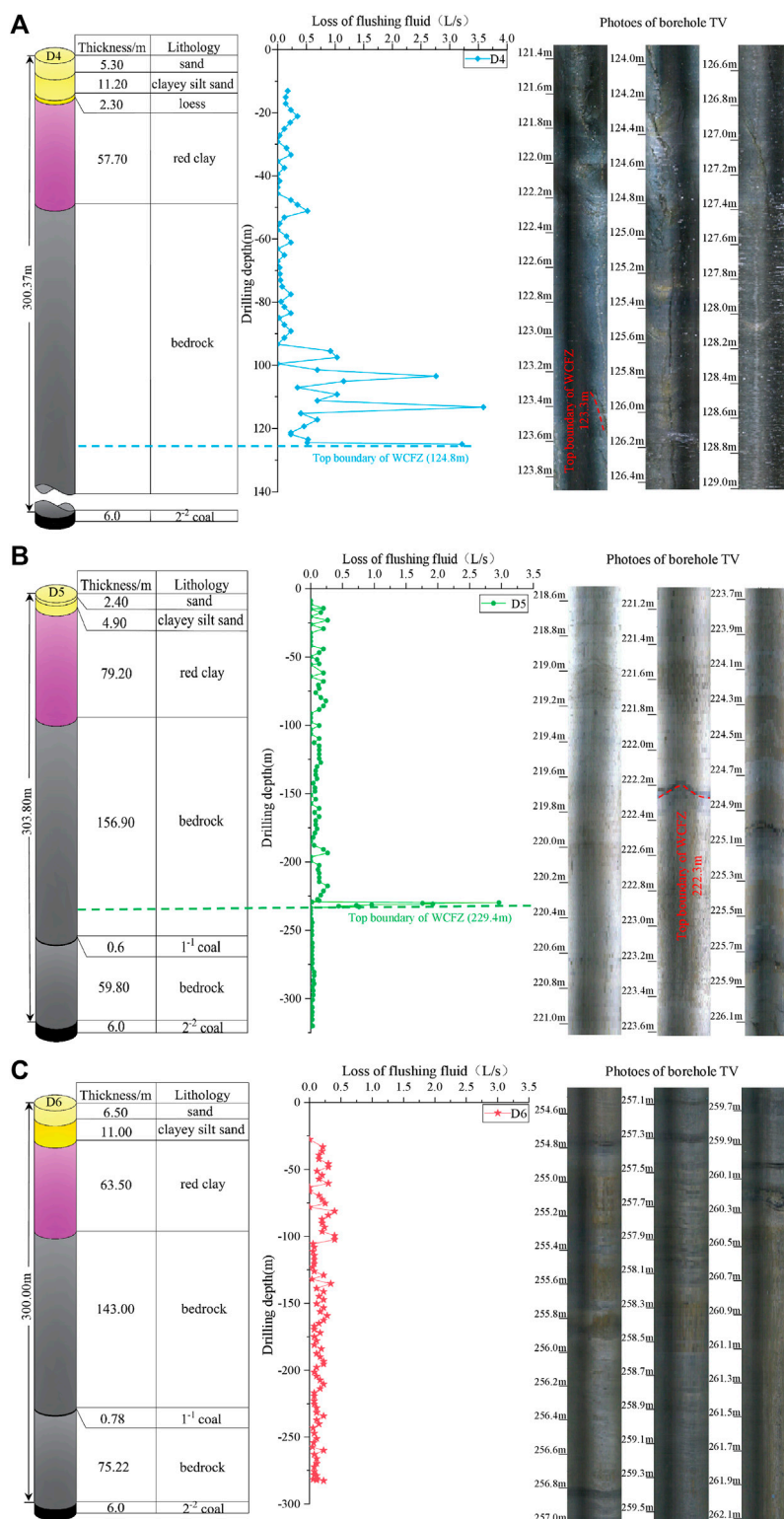
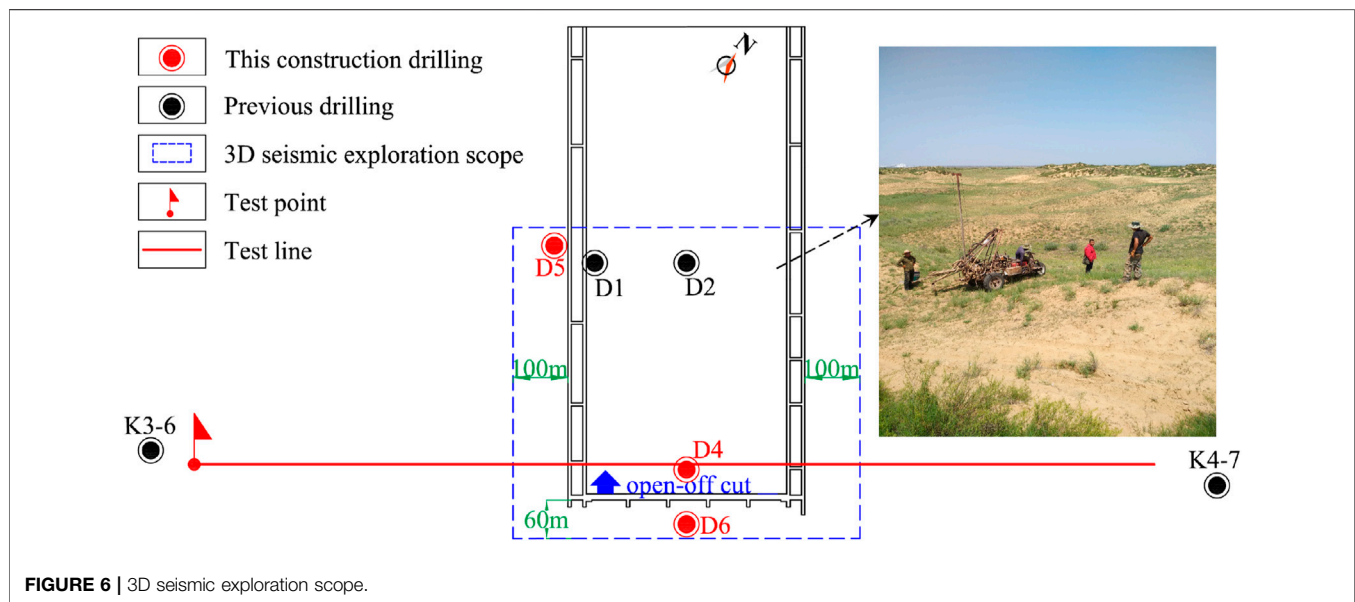


FIGURE 5 | Hole flushing fluid leakage and borehole TV results: (A) D4, (B) D5, and (C) D6.

TABLE 1 | Height of WCFZ development.

Drill	Depth of 2 ⁻² coal seam (D ₂ ⁻²)	The result of fluid leakage and the depth of top boundary of the WCFZ (D _{T1})	The result of borehole TV and the depth of top boundary of the WCFZ (D _{T2})	H _W (D ₂ ⁻² - D _T)			H _W /T _M 2 ⁻²
				Fluid leakage (m)	Borehole TV (m)	Comprehensive result (m)	
D1	309.96	151.18 m	155.95	158.78	154.01	158.78	27.38
D2	294.61	137.53 m	142.60	157.08	152.01	157.08	27.08
D4	300.37	124.80 m	123.30	175.57	177.07	177.07	30.53
D5	303.80	229.40 m	222.30	74.40	81.50	81.50	14.05
D6	300.00			No cracks			

**FIGURE 6** | 3D seismic exploration scope.

Field Data Collection

Whether the observation system is selected correctly or not will directly affect the efficiency of field construction, accuracy of results, and cost of exploration. 3D seismic acquisition is an area acquisition technology, which is characterized by using a reasonable combination of shot grid and geophone grid to obtain a uniformly distributed grid of underground data points and required coverage times. Based on this, the seismic geological conditions of the selected test site locations are representative, no fracture structures are developed in the vicinity of the test site, and the test site is located at or near the borehole or through the borehole, as a result of actual field investigations and analysis of geological data prior to data acquisition. One test point and one test line were selected for testing in the exploration area, and the selected location is shown in **Figure 6**. It is better to ensure that the observed target layer is complete and continuous, facilitating the comparative analysis of test data and the analysis of reflected waves from the target layer.

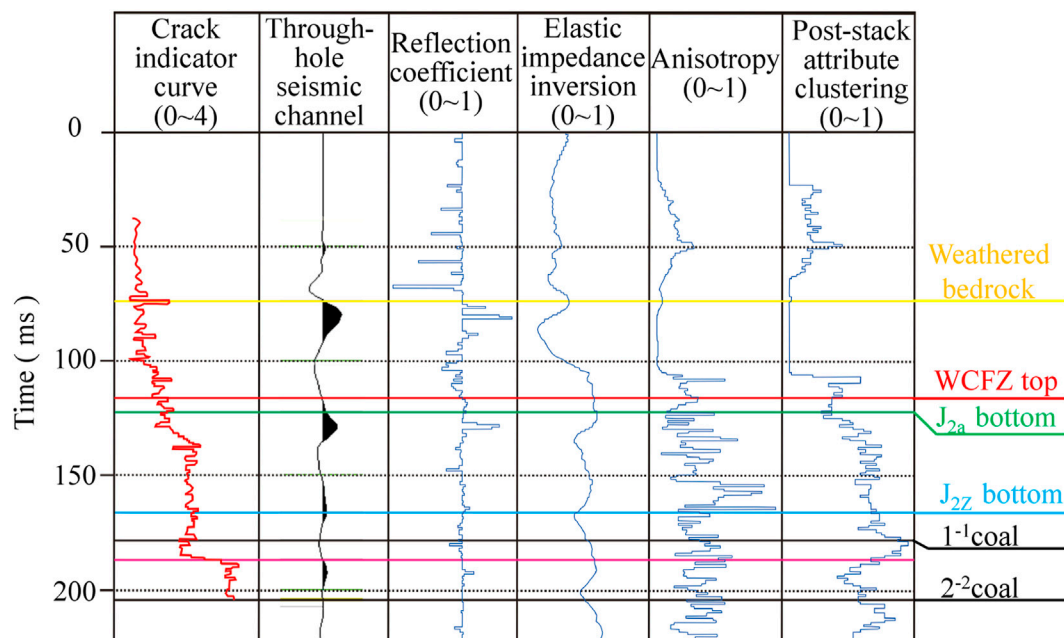
The 3D seismic exploration test finally divided the optimal excitation parameters of the exploration area into two situations: excitation at 3 m below the red soil layer, drug dosage, phreatic well depth of 3 m, and chemical dosage of 2 kg. By comparing 10 Hz, 60 Hz, high-sensitive single-point 7 Hz geophone and digital geophone to the sensitivity of the information in this area, a high-sensitivity geophone with a natural frequency of 7 Hz is finally used for signal reception. An e-428 high-resolution digital seismometer with a sampling interval of 0.5 ms, a recording length of 2.0 s, recording format SEG-D, and full-band reception is used. The parameters of the observation system are shown in **Table 2**.

3D Seismic Exploration and Interpretation Results of the WCFZ

In order to quantitatively interpret the developmental pattern of the WCFZ, seismic data, multi-attribute data, pre-stack elastic inversion, anisotropic interpretation, and fracture indicator

TABLE 2 | Main parameters of the observation system.

Name	Parameter
Types of observation systems	16-line × 4-gun (midpoint firing) × 96-channel orthogonal bundle observation system
Number of receiving lines	Each wire harness 10
Receiving line distance	40 m
Offset distance	10 m
CDP	5 × 5 m
Effective aspect ratio from the offset	1:1

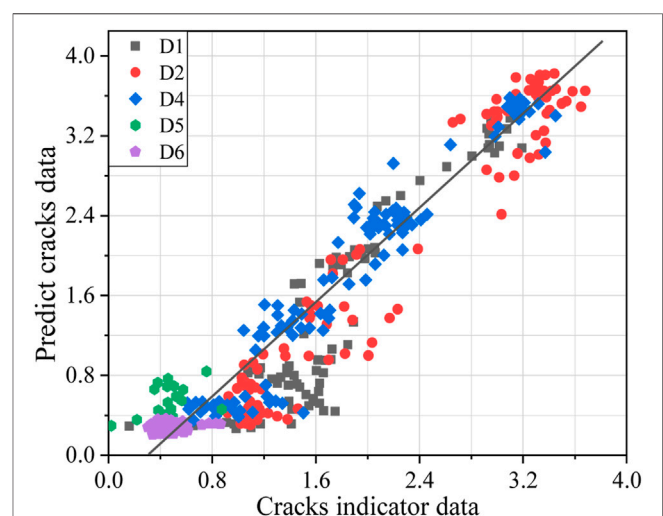
**FIGURE 7** | Training data for fracture inversion.

curves were inverted using probabilistic neural network techniques.

Figure 7 shows the training data of the fracture inversion. Before training the neural network, the fracture indication curves of all boreholes were normalized to eliminate the influence caused by the difference in sampling value.

This 3D seismic survey has achieved good results within the study area, with the similarity coefficient between the inversion results, and the similarity coefficient is 0.97, with high accuracy (**Figure 8**) combined with the fracture indication curve to divide the fracture zone and caved zone. In the fracture indicator data, the value in the range of 0–1 denotes the undeveloped area of the fracture and is divided into the curved subsidence zone and normal zone. Values between 1 and 2.5 are classified as fracture zone; values greater than 2.5 are classified as the caved zone.

The results of the fracture-indicating inversion profiles obtained by seismic geological interpretation are shown in **Figure 9**. As can be seen in **Figure 9**, in terms of depth, the development density in the upper area of the WCFZ to some extent is compared to that of the lower area as the distance

**FIGURE 8** | PNN inversion similarity coefficient (the similarity coefficient is 0.97).

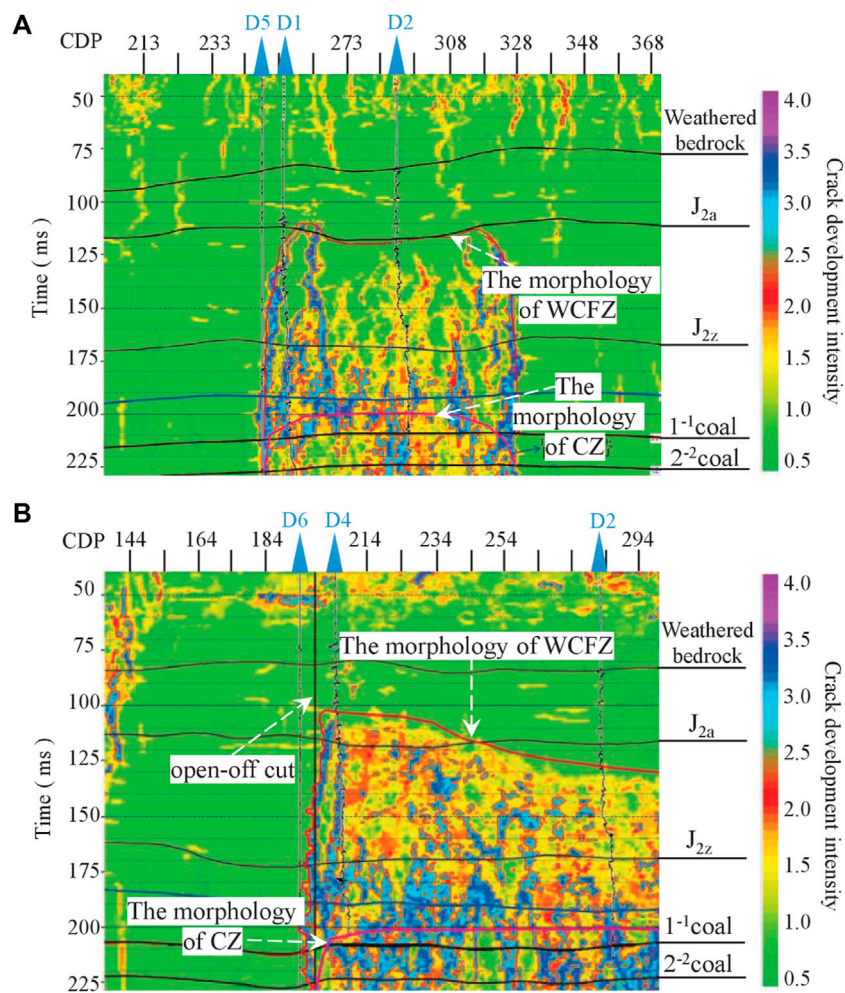


FIGURE 9 | Fracture indicator inversion profile: **(A)** Inversion profile of working face incline and fissure indication and **(B)** inversion profile of working face strike crack indication.

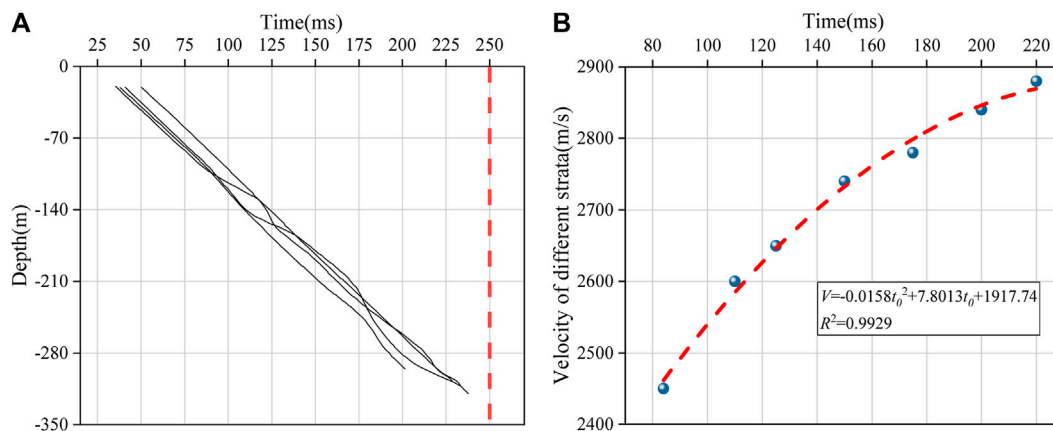
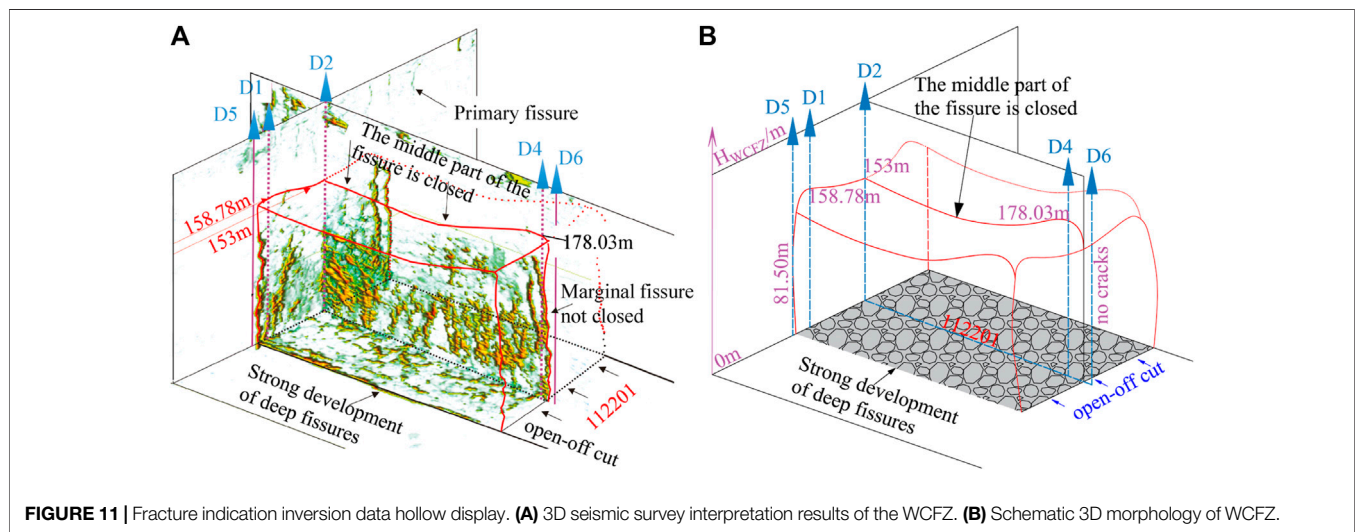


FIGURE 10 | Time-depth conversion of the WCFZ: **(A)** Velocity field establishment and **(B)** time-depth conversion velocity diagram of the WCFZ.

TABLE 3 | WCFZ obtained by different methods.

Drilling	$T_M \text{ s}^{-2}/\text{m}$	H_W/m		Deviation	$H_W/T_M \text{ s}^{-2}$	
		Drilling measurement	3D seismic survey		Drilling measurement	3D seismic survey
D1	6.00	158.78	156.36	2.42	27.38	26.96
D2		157.08	158.82	-1.74	27.08	27.38
D4		177.07	178.03	-0.96	30.53	30.69
D5		81.50	79.83	1.67	14.05	13.76
D6				No cracks		

**FIGURE 11** | Fracture indication inversion data hollow display. **(A)** 3D seismic survey interpretation results of the WCFZ. **(B)** Schematic 3D morphology of WCFZ.

between the H_{WCFZ} and the mined coal seam increases. The characteristic of the development density of the WCFZ in the edge regions on both sides of the working face is higher than that in the inner working face.

The propagation velocity of seismic reflection waves is an important parameter for seismic data processing and interpretation, and it is the basis for time-depth conversion. Its accuracy directly affects the accuracy of interpretation results.

First of all, the velocity field is established according to the time-depth relationship calibrated by synthetic records (Figure 10A). According to the drilling data that have been constructed within the 3D seismic exploration range, the burial depth of the stratum and the t_0 time of the corresponding stratum reflection wave are used to inversely calculate the interfacial velocity of the stratum and perform coefficient correction to obtain the final time-depth conversion velocity.

In this study, a large number of experiments and parameter tests have been carried out to correct the time-depth conversion velocity of D1, D2, D4, D5, and D6 boreholes in the process of 3D seismic exploration and interpretation. The Green Mountain static correction method based on refractive wave theory uses the original single-gun first-arrival refractive wave data to first strip away the low-velocity layer and correct to the near-surface floating surface. The floating data are corrected to the uniform data by selecting uniform data of +1,300 in the whole area and using a substitution speed of 2000 m/s. After correction, the first arrivals were smooth, and the correction effect was obvious.

The final determination of the unified static calibration datum elevation for the whole region is +1300 m, and the alternative velocity is 2000 m/s to calibrate the floating data to the unified data. The mathematical equation for the velocity calibration is determined (Eq. 1).

$$V = \frac{2000 \times (1300 - H)}{t_0}, \quad (1)$$

where V is the calibration velocity of the borehole point.

H is the elevation of the stratum corresponding to the borehole point, and t_0 is the two-way travel time of the reflected wave of the stratum corresponding to the borehole.

As can be seen in Figure 10, all boreholes in the survey area were back-calculated for stratigraphic interface velocities using their burial depth and the corresponding two-way travel time t_0 of the stratigraphic reflected waves, and the resulting time-to-depth converted velocity data were finally fitted using Origin (Figure 10B).

It was found that there was a positive correlation between the calibration velocity V and the two-way travel time t_0 of the corresponding stratigraphic reflected waves for boreholes in the medium-deep buried zone; however, the rate of increase of the calibration velocity V at the borehole sites decreased with time. The fitted time-to-depth conversion rate relationship for the WCFZ in the study area is specified in Eq. 2.

$$V = -0.0158t_0^2 + 7.8013t_0 + 1917.7417. \quad (2)$$

Combining Eq. 1 with Eq. 2 yields Eq. 3.

$$H = 1300 - \frac{(-0.0158t_0^2 + 7.8013t_0 + 1917.7417) \times t_0}{2000}. \quad (3)$$

It can be seen from Figure 9 that after the mining of the 2⁻² coal seam, the top time t_0 of the development height of the WCFZ in different positions is 105–175 ms.

Substituting the obtained t_0 into Eq. 3, the elevation range of the top of the WCFZ in different boreholes is 1,055.08 ~ 1,165.46 m, and the development height relative to the coal bed roof is 79.83 ~ 178.03 m.

DISCUSSION

Table 3 shows the comparison of the development heights of the WCFZ in D1, D2, D4, D5, and D6 obtained by field measurement and 3D seismic exploration.

It can be seen from Table 3 that the development height of the WCFZ obtained by 3D seismic exploration is basically consistent with the field measurement results, and the absolute value of the error is between 0.962 and 2.42 m. Therefore, it is considered that it is feasible to judge the 3D shape and development characteristics of the WCFZ after coal seam mining by 3D seismic exploration. This method can visually and clearly observe the spatial development of the WCFZ.

The specific interpretation result of 3D seismic exploration is that the development form of the water-conducting fractured zone is relatively high near the open-off cut. The height of development along the working face gradually decreases in the direction of pushing and mining and is “half saddle-shaped.” The development pattern of the WCFZ in the direction perpendicular to the working face is characterized by being high on both sides and slightly low in the middle, similar to “saddle-shaped” (Figure 11). The development of the WCFZ in the area on both sides of the working face and at the open-off cut is relatively strong during the mining process, and the area in the middle of the working face is relatively weakened. This result provides an important reference for the corresponding water resource protection in the mining process of other surrounding mines in the future.

CONCLUSION

This study presents a method to interpret the 3D development characteristics of the WCFZ in the mining area by using the 3D seismic exploration method, and the results of borehole exploration and 3D seismic exploration are compared and analyzed to determine the 3D development characteristics of the WCFZ in the study site after coal seam mine. The conclusions are as follows:

REFERENCES

- Dawei, Z., Kan, W., Zhihui, B., Zhenqi, H., Liang, L., Yuankun, X., et al. (2019). Formation and Development Mechanism of Ground Crack Caused by Coal

- 1) By comparing the results of H_{WCFZ} of field measurement and 3D seismic survey, the error range between the results of the 3D seismic survey and field measurement is within ± 7 m, which shows the reliability and reasonableness of the 3D seismic survey, and the research results provide a new method to grasp the 3D morphological characteristics of the WCFZ of coal seam mining.
- 2) In this study, it is found that the development density of the upper area of the WCFZ decreases to a certain extent compared with the lower area as the distance between the H_{WCFZ} and the mined coal seam increases, and the development density of the WCFZ as a whole is characterized by higher development density of the WCFZ in the marginal area on both sides of the working face than in the area inside the working face.
- 3) The results of this study of 3D morphology of H_{WCFZ} after mining of the medium-deep buried coal seam. Specifically, the H_{WCFZ} gradually decreases along the advancing direction in a “semi-saddle shape,” and the H_{WCFZ} along the dip direction is characterized by being high on both sides and slightly low in the middle, similar to “saddle-shaped.” The development pattern of the WCFZ perpendicular to the working face direction is characterized by being high on both sides and slightly low in the middle, similar to a “saddle-shaped.”

DATA AVAILABILITY STATEMENT

The original contributions presented in the study are included in the article/Supplementary Material; further inquiries can be directed to the corresponding authors.

AUTHOR CONTRIBUTIONS

DF, EH, and SW designed the study; DF, XX, FY, and YX completed the analysis of the 3D seismic survey; DF, LG, GW, and ZC obtained the field measurement data and analyzed; DF, EH, and SW improved the manuscript draft; all authors have read and agreed to the published version of the manuscript.

FUNDING

This research was supported by the National Natural Science Foundation of China (No. 42177174), the Scientific Research Fund of the Shaanxi Coal Chemical Industry Group (2018MHKJ-B-J-24), the Central Government Guides, the Special Project of Local Science and Technology Innovation (2020ZY-JC-03), and the Shaanxi Province Joint Fund Project (2021JLM-09).

Mining: Effects of Overlying Key Strata. *Bull. Eng. Geol. Environ.* 78, 1025–1044. doi:10.1007/s10064-017-1108-2

Dong, S., Wang, H., Guo, X., and Zhou, Z. (2021). Characteristics of Water Hazards in China's Coal Mines: A Review. *Mine Water Environ.* 40, 325–333. doi:10.1007/s10230-021-00770-6

- Du, F., and Gao, R. (2017). Development Patterns of Fractured Water-Conducting Zones in Longwall Mining of Thick Coal Seams-A Case Study on Safe Mining under the Zhuozhang River. *Energies* 10, 1856–1916. doi:10.3390/en10111856
- Fan, H., Wang, L., Lu, Y., Li, Z., Li, W., and Wang, K. (2020). Height of Water-Conducting Fractured Zone in a Coal Seam Overlain by Thin Bedrock and Thick Clay Layer: a Case Study from the Sanyuan Coal Mine in North China. *Environ. Earth Sci.* 79, 1–11. doi:10.1007/s12665-020-8873-0
- Gao, F., Stead, D., and Coggan, J. (2014). Evaluation of Coal Longwall Caving Characteristics Using an Innovative UDEC Trigon Approach. *Comput. Geotechnics* 55, 448–460. doi:10.1016/j.compgeo.2013.09.020
- Gui, H., Qiu, H., Chen, Z., Ding, P., Zhao, H., and Li, J. (2020). An Overview of Surface Water Hazards in China Coal Mines and Disaster-Causing Mechanism. *Arab. J. Geosci.* 13, 1–11. doi:10.1007/s12517-019-5046-0
- Li, H., Zhang, B., Bai, H., Wu, J., Meng, Q., Xiao, N., et al. (2018). Surface Water Resource Protection in a Mining Process under Varying Strata Thickness-A Case Study of Buliangou Coal Mine, China. *Sustainability* 10, 4634–4715. doi:10.3390/su10124634
- Li, J., Li, F., Hu, M., Zhang, W., and Pan, D. (2017). Evaluation of Geological Conditions for Coalbed Methane Occurrence Based on 3D Seismic Information: a Case Study in Fowa Region, Xinjing Coal Mine, China. *Acta Geophys.* 65, 345–351. doi:10.1007/s11600-017-0027-8
- Liu, W.-r. (2019). Experimental and Numerical Study of Rock Stratum Movement Characteristics in Longwall Mining. *Shock Vib.* 2019, 1–15. doi:10.1155/2019/5041536
- Liu, X., Tan, Y., Ning, J., Tian, C., and Wang, J. (2015). The Height of Water-Conducting Fractured Zones in Longwall Mining of Shallow Coal Seams. *Geotech. Geol. Eng.* 33, 693–700. doi:10.1007/s10706-015-9851-2
- Liu, Z., Fan, Z., and Zhang, Y. (2019). Fracture Characteristics of Overlying Bedrock and Clay Aquiclude Subjected to Shallow Coal Seam Mining. *Mine Water Environ.* 38, 136–147. doi:10.1007/s10230-018-0549-6
- Pei, X. (2020). Signal Acquisition Method for 3D Seismic Exploration in High Density Coal Mining Area. *Arab. J. Geosci.* 13, 1–11. doi:10.1007/s12517-020-05599-x
- Sui, W., Hang, Y., Ma, L., Wu, Z., Zhou, Y., Long, G., et al. (2015). Interactions of Overburden Failure Zones Due to Multiple-Seam Mining Using Longwall Caving. *Bull. Eng. Geol. Environ.* 74, 1019–1035. doi:10.1007/s10064-014-0674-9
- Sun, Q., Zhang, J., Zhang, Q., and Zhao, X. (2017). Analysis and Prevention of Geo-Environmental Hazards with High-Intensive Coal Mining: A Case Study in China's Western Eco-Environment Frangible Area. *Energies* 10, 786–815. doi:10.3390/en10060786
- Wang, G., Wu, M., Wang, R., Xu, H., and Song, X. (2017). Height of the Mining-Induced Fractured Zone above a Coal Face. *Eng. Geol.* 216, 140–152. doi:10.1016/j.enggeo.2016.11.024
- Wang, S., Li, X., and Wang, S. (2017). Separation and Fracturing in Overlying Strata Disturbed by Longwall Mining in a Mineral Deposit Seam. *Eng. Geol.* 226, 257–266. doi:10.1016/j.enggeo.2017.06.015
- Xie, X., Hou, E., Wang, S., Sun, X., Hou, P., Wang, S., et al. (2021). Formation Mechanism and the Height of the Water-Conducting Fractured Zone Induced by Middle Deep Coal Seam Mining in a Sandy Region: A Case Study from the Xiaobaodang Coal Mine. *Adv. Civ. Eng.* 2021, 1–11. doi:10.1155/2021/6684202
- Yan, W., Dai, H., and Chen, J. (2018). Surface Crack and Sand Inrush Disaster Induced by High-Strength Mining: Example from the Shendong Coal Field, China. *Geosci. J.* 22, 347–357. doi:10.1007/s12303-017-0031-7
- Yang, X., Wen, G., Dai, L., Sun, H., and Li, X. (2019). Ground Subsidence and Surface Cracks Evolution from Shallow-Buried Close-Distance Multi-Seam Mining: A Case Study in Bulianta Coal Mine. *Rock Mech. Rock Eng.* 52, 2835–2852. doi:10.1007/s00603-018-1726-4
- Zhang, Y., Cao, S., Wan, T., and Wang, J. (2018). Field Measurement and Mechanical Analysis of Height of the Water Flowing Fracture Zone in Short-Wall Block Backfill Mining beneath the Aquifer: A Case Study in China. *Geofluids* 2018, 1–12. doi:10.1155/2018/7873682
- Zhou, A., Hu, J., and Wang, K. (2020). Carbon Emission Assessment and Control Measures for Coal Mining in China. *Environ. Earth Sci.* 79, 1–15. doi:10.1007/s12665-020-09189-8

Conflict of Interest: Authors LG and GW were employed by Shaanxi 185 Coal Field Geology Co., Ltd. Authors YX and ZC were employed by Shaanxi Xiaobaodang Mining Co., Ltd. Authors FY was employed by the company Shaanxi Institute of Geological Survey.

The remaining authors declare that the research was conducted in the absence of any commercial or financial relationships that could be construed as a potential conflict of interest.

Publisher's Note: All claims expressed in this article are solely those of the authors and do not necessarily represent those of their affiliated organizations, or those of the publisher, the editors, and the reviewers. Any product that may be evaluated in this article, or claim that may be made by its manufacturer, is not guaranteed or endorsed by the publisher.

Copyright © 2022 Feng, Hou, Wang, Xie, Yuan, Guo, Wang, Xie and Chen. This is an open-access article distributed under the terms of the Creative Commons Attribution License (CC BY). The use, distribution or reproduction in other forums is permitted, provided the original author(s) and the copyright owner(s) are credited and that the original publication in this journal is cited, in accordance with accepted academic practice. No use, distribution or reproduction is permitted which does not comply with these terms.

Frontiers in Earth Science

Investigates the processes operating within the major spheres of our planet

Advances our understanding across the earth sciences, providing a theoretical background for better use of our planet's resources and equipping us to face major environmental challenges.

Discover the latest Research Topics

[See more →](#)

Frontiers

Avenue du Tribunal-Fédéral 34
1005 Lausanne, Switzerland
frontiersin.org

Contact us

+41 (0)21 510 17 00
frontiersin.org/about/contact

